รายงานวิจัยฉบับสมบูรณ์

โครงการ

ผลของสนามแม่เหล็กไฟฟ้าต่อปรากฏการณ์การถ่ายโอนในวัสดุพรุน (วัสดุวิศวกรรมและวัสดุชีวภาพ

Electromagnetic Field Effects on Transport Phenomena in Porous Media (Engineering Materials and Bio-Tissues)

โดย ศาสตราจารย์ ดร. ผดุงศักดิ์ รัตนเดโช

5 กรกฎาคม 2559

สัญญาเลขที่ RTA 5680007

รายงานวิจัยฉบับสมบูรณ์

ผลของสนามแม่เหล็กไฟฟ้าต่อปรากฏการณ์การถ่ายโอนในวัสดุพรุน (วัสดุวิศวกรรมและวัสดุชีวภาพ

Electromagnetic Field Effects on Transport Phenomena in Porous Media (Engineering Materials and Bio-Tissues)

โดย ศาสตราจารย์ ดร. ผดุงศักดิ์ รัตนเดโช
ภาควิชาวิศวกรรมเครื่องกล คณะวิศวกรรมศาสตร์ มหาวิทยาลัยธรรมศาสตร์

สนับสนุนโดยสำนักงานกองทุนสนับสนุนการวิจัย

ความเห็นในรายงานนี้เป็นของผู้วิจัย สกว. ไม่จำเป็นต้องเห็นด้วยเสมอไป

ผลของสนามแม่เหล็กไฟฟ้าต่อปรากฏการณ์การถ่ายโอนในวัสดุพรุน

(วัสดุวิศวกรรมและวัสดุชีวภาพ)

บทคัดย่อ

งานวิจัยโครงการนี้เน้นการวิเคราะห์กระบวนการถ่ายเทความร้อนและมวลภายในวัสดุพรุนที่มีหลายชั้นภายใต้พลังงานสนามแม่เหล็กไฟฟ้าทั้งในเชิงคำนวณและเชิงทดลอง งานวิจัยนี้ได้มีการจำลองร่วมระหว่างการถ่ายเทความร้อน (2มิติ) และคลื่นแม่เหล็กไฟฟ้า (3มิติ) เพื่อจำลองอันตรกิริยาที่เกิดขึ้นระหว่างคลื่นแม่เหล็กไฟฟ้าและวัสดุพรุนที่สภาวะทดสอบแบบต่าง ๆ โดยได้ศึกษาพฤติกรรมของปรากฏการณ์ถ่ายโอนที่เกิดขึ้นภายในวัสดุพรุนบนพื้นฐานโครงสร้างระดับจุลภาค การคำนวณผลเฉลยที่ได้จากสมการควบคุมการถ่ายเทความร้อนและมวลโดยใช้ระเบียบวิธีไฟไนท์วอลลุม คำนวณผลเฉลยที่ได้จากสมการควบคุมการแพร่ของคลื่นแม่เหล็กไฟฟ้าโดยใช้ระเบียบวิธีไฟไนท์เอลิเมนต์ไทม์โดเมน นอกจากนี้ยังได้ออกแบบการทดลองเพื่อทำการวัดค่าการซึมผ่านและค่าการซึมผ่านสัมพัทธ์ในวัสดุพรุน ค่าสมบัติทางฟิสิกส์ สมบัติทางเทอร์โมไดนามิกส์ สมบัติทางความร้อน และสมบัติไดอิเล็กตริกที่นำมาใช้ในการจำลองปรากฏการณ์ที่เกิดขึ้นในแพคเบดของวัสดุพรุนนั้นเป็นค่าได้มาจากการวัดหรือการอ้างอิงจากเอกสารที่เกี่ยวข้องนอกจากนี้งานวิจัยโครงการนี้ยังมีการประยุกต์ศึกษาถึงปัญหาทางด้านชีวกลศาสตร์ที่เกี่ยวข้องกับการถ่ายโอนความร้อนในเนื้อเยื่อมนุษย์ที่มีหลายชั้นภายใต้พลังงานคลื่นแม่เหล็กไฟฟ้า เช่น การศึกษาอิทธิพลของชนิดท่อนำคลื่นที่มีผลต่อการดูดกลืนพลังงานไมโครเวฟ อัตราการดูดกลืนพลังงานจำเพาะ และการกระจายตัวเชิงอุณหภูมิภายในเนื้อเยื่อประเภทต่างๆตับระหว่างการรักษาโรคด้วยพลังงานไมโครเวฟ ในทางทฤษฎีแบบจำลองทางคณิตศาสตร์ที่มีการจำลองร่วมระหว่างการแพร่ของคลื่นแม่เหล็กไฟฟ้าและการถ่ายเทความร้อนนั้นสามารถหาผลเฉลยโดยใช้ระเบียบวิธีไฟไนท์อิลิเมนต์แบบสมมาตรรอบแกนได้ นอกจากนี้ยังได้ทำการจำลองอัตราการดูดกลืนพลังงานจำเพาะและอุณหภูมิที่เพิ่มขึ้นในแบบจำลองร่างกายมนุษย์ที่มีหลายชั้นภายใต้พลังงานคลื่นแม่เหล็กไฟฟ้าอีกด้วย

คำสำคัญ: แม่เหล็กไฟฟ้า การคำนวณเชิงตัวเลข วัสดุพรุน เนื้อเยื่อ การถ่ายเทความร้อน

Electromagnetic Field Effects on Transport Phenomena in Porous Media

(Engineering Materials and Bio-Tissues)

Abstract

In this project, the analysis of heat and mass transfer in a multi-layered porous materials under conventional energy and electromagnetic energy is investigated numerically and experimentally. The coupled heat transfer (2 D) and electromagnetic wave (3 D) model is developed to simulate the interaction between electromagnetic wave and various kinds of porous samples. The relevant transport mechanisms are analyzed by examining the microstructure and possible transport passages in the porous media. The resulting governing equations are numerically solved with the Finite Volume Method (FVM) for heat and mass transfer model and Finite Difference Time Domain (FDTD) for electromagnetic wave model. An experiment is designed to measure both the intrinsic and the relative permeability of porous media. All the physical, thermodynamic, thermal, transport, and dielectric properties used in the simulation are for porous packed beds and are either from our measurements or from the literature. The other works on this project are concerned to biomechanics problems which related to heat transfer in human tissues (multi-layered tissues) during subjected to electromagnetic energy. Namely, in the problem of microwave ablation process (MWA), the influence of antenna type on microwave power absorbed, SAR and temperature distribution in liver tissue during MWA, are investigated systematically. Theorically, mathematical models based on coupled equations of electromagnetic wave propagation and bioheat equation are solved by using an axisymetric finite element method (FEM). Furthermore, the simulations of the specific absorption rate (SAR) and the temperature increase in the human body (multi-layered tissues) exposed to leakage microwave energy are also done.

Keywords: Electromagnetic, Numerical Method, Porous Media, Tissue, Heat Transfer

Content

	Page
Abstract	
Executive Summary	**1**
Outline of Research	**5**
Research Outputs	**8**
Appendix	
Publications (Full text)	
Article for Social	
Award	

1. Executive Summary

1.1 Project Title: Electromagnetic Field Effects on Transport Phenomena in Porous Media (Engineering Materials and Bio-Tissues)

1.2 Principal Investigator: Dr. Phadungsak Ratanadecho (Professor)

Education

- B. Eng. (Mechanical Engineering), King Mongkut Institute of Technology, Thonburi, March 1991.
- M. Eng. (Mechanical Engineering), Chulalongkorn University,Thailand, March 1994.
- Research Student (Computational Heat and Fluid Flow in Porous Media), Mechanical Engineering Department, Nagaoka University of Technology, Japan, 1999 (Japanese Government Scholarship (Monbusho))
- Ph.D (Program of Energy and Environment Science), Mechanical Engineering Department, Nagaoka University of Technology, Japan, 2002 (Japanese Government Scholarship (Monbusho))
- Post Doctoral Fellow in Chemical Engineering and Material Science, University of Minnesota, Twin Cities, USA, 2002-2003

Contact Address:

Center of Excellence in Electromagnetic Energy Utilization in Engineering (CEEE)

Department of Mechanical Engineering, Faculty of Engineering

Thammasat University (Rangsit Campus), Pathumthani 12120

Tel: 0-2564-3001-9; Fax: 0-2564-3010; E-mail: ratphadu@engr.tu.ac.th

1.3 Research area / sub area of this project:

Computational modeling / Heat transfer / Fluid flow/Numerical method/physic of electromagnetic

1.4 Keywords:

Heat and Mass Transport, Porous Media, Energy, Dielectric Heating, Mathematical Model, Numerical Method, Multi-Layered Model

1.5 Budget:

7,500,000 Baht

1.6 Project Duration: 3 years

1.7 Objectives

1) To develop a coupled model of heat transfer, fluid flow and electromagnetic fields emitted by various sources in engineering materials and anatomically based human organs by using both simplified and porous media approach.

2) To investigate the effects of electromagnetic fields on transport phenomena in porous media for case of engineering applications and therapeutic and health implication of electromagnetic wave exposures applications.

3) To study the effects of various parameters, namely, typical radiated electromagnetic fields, configuration of porous structure and external heat sources, on heat transfer and fluid flow or moisture transport in porous media.

4) To compare the numerical results in the propose domain obtained with those of the results obtained from the literature survey or in house experimental result.

5) To provide guidelines that will help the physician and related personnel in design and development of new safety surgical procedure to prevent harmful ocular adverse effects in human organs.

6) To help (expected) the government organizations in Thailand in implementing policies for the management of standard for safety levels with respect to human exposure to electromagnetic wave.

7) To give some collaboration and exchange of knowledge between researchers and public organization.

1.8 Research Methodology

The numerical work based on proposed mathematical model and some experimental work will be carried out in this project. The effects of electromagnetic fields from the various electromagnetic sources on temperature transfer and fluid flow or moisture transport in the porous media for the case of engineering applications and therapeutic applications, and health implications of electromagnetic fields exposures, will be performed in details. Below, we will show only the case of therapeutic applications, and health implications of electromagnetic fields exposures.

The first step in evaluating the effects of a certain exposure to electromagnetic fields in the human eye is the determination of the induced internal electromagnetic field and its spatial distribution. Thereafter, electromagnetic energy absorption which results in temperature increases within the porous media, i.e., human organs and other interactions can be considered. In this study, a human organs model is used to simulate the SAR and temperature distribution over this human organs model. Electromagnetic wave propagation in the human organs is investigated by using Maxwell's equations. An analysis of heat transfer in the human organs exposed to electromagnetic fields is investigated using a developed heat transfer model (conduction, natural convection, and porous media model). In the human organs model, the effects of radiated electromagnetic fields, operating frequencies, wave propagation modes and distance from the sources on distributions of SAR, fluid flow and temperature profile within the human organs is systematically investigated. Moreover, the numerical results are then compared with the experimental results. The finite element as well as finite control volume methods are used to analyze the transient problems. The computational scheme is to assemble numerical scheme model and compute a local heat generation term by performing an electromagnetic calculation using tissue properties. The system of governing equations as well as initial and boundary conditions are then solved. All computational processes are implemented to demonstrate the phenomenon that occurs within the human organs exposed to electromagnetic fields.

The study and research procedures consist of the following steps:

1) Review literature.

2) Study the fundamental of transport phenomena in porous media, i.e.,biological tissue and engineering materials.

3) Develop a mathematical model and numerical scheme that considers electromagnetic wave propagation, heat transfer of biological tissue considered heat conduction, natural convection and porous media theory.

4) Compare the simulated results of tissue temperature against the experimental results or simulated results obtained from the literatures or experiment in order to verify the accuracy of the developed mathematical model.

5) Study the effects of various parameters on distributions of specific absorption rate and temperature profile and velocity field within the porous media, i.e., human organs.

6) Explain and discuss on electromagnetic field effects on transport phenomena in porous media, i.e.,biological tissue and engineering materials.

1.9 Research Schedule

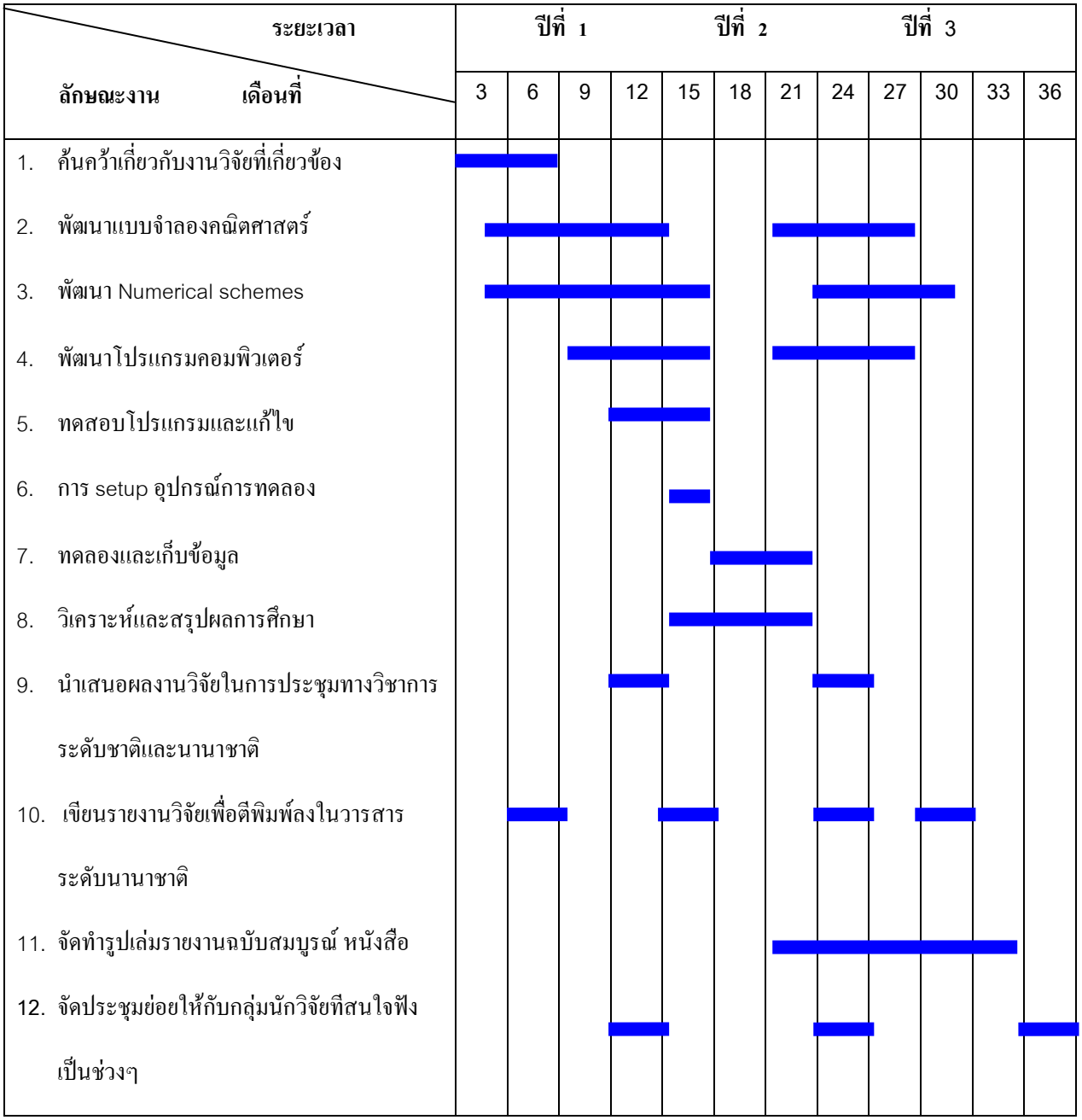

1.10 Expected Benefits

The main outputs of the project are publications in refereed international journals. The obtained knowledge should also be useful as a guideline to understand the phenomena of the interaction between electromagnetic wave and various kinds of dielectric materials at a fundamental level. Furthermore, the major impact of the project is the enhanced competitive advantage of the Thai industry.

2.Outline of Research

The research in “Electromagnetic Field Effects on Transport Phenomena in Porous Media” in this proposal can be separated in two major categories; engineering applications and therapeutic and health implication of electromagnetic wave exposures applications.

We focus first on the case of engineering applications. There are many successful examples of electromagnetic energy application including industrial heating (such as drying of foods, freeze drying, drying of textiles, drying of wood and paper products, thermosetting, preheating rubber and vulcanizations of rubber), enhancing catalytic reactions (isomerization and oxidation), sterilization, and the further electromagnetic energy processing. Generally, electromagnetic energy processing is a novel alternative method of heating or drying, allowing to obtain products of acceptable quality. It permits a shorter drying time and a substantial improvement in the quality of dried materials, in relation to those dried with convective air and microwaves drying methods. Furthermore, other advantages including environmental friendliness at low temperature, which not only over-comes the limitation of low thermal conductivity of the material under continuous cavity due to the absence of drying medium, but also avoids the defect of internal crack and interior burning caused by excessive heating in microwave drying, and acquires a wide range of application on the biomaterial and food industries. Although an application of electromagnetic energy processing has found some application in the heating or dehydration of materials, more research and development is needed before the process is used in large commercial scale. In particular, the effect of convective air and feed magnetron positioned on the drying kinetics should be known quantitatively, so that the drying system can be optimized from the cost and quality standpoints. The main objective of this research was to examine the feasibility of using novel electromagnetic processing driers to dry porous material, i.e., agricultural products and experimentally explore drying characteristics in different drying processing and drying conditions. The experimental results from this study could help to identify some of the potential problems during the practical design stage. This study is of great importance from the practical point of view because it shows the possibility of application of electromagnetic or dielectric heating-drying of porous materials on an industrial scale, especially in a continuous system.

Since microwave devices are commonly used in various aspects of everyday life and there is an increasing public concern about the interaction between the human body and electromagnetic fields. Next, we will focus on the case the therapeutic and health implication of electromagnetic wave exposures applications. In recent years, there is an increasing public concern about the interaction between the human body and electromagnetic fields.

Recently, EM environments have become very complex because of the rapid spread and wide use of a number of electric and electronic devices, including recent widespread use of cellular telephones. These devices have created an increasing number of EM wave interference problems. Also, there is a growing concern in the population about the possible biological effects induced by such radiation. Increasing use of EM energy results in the necessity to identify the limits of safe exposure with respect to thermal hazards. The amount of energy absorbed by a tissue depends on many factors including frequency, dielectric property of the tissue, duration of exposure, intensity of electromagnetic radiation, and water content of the tissue. The power absorption in human tissues induces temperature increase inside the tissues. The severity of the physiological effect produced by small temperature increases can be expected to worsen in sensitive organs.

An EM interaction mechanism in biological tissues is important because the effects of this interaction are the result of the penetration of the EM waves into the living system and their propagation into it. The fact is stressed that only the fields inside a material can influence it, so that only the fields inside tissues and biological bodies can possibly interact with these. The biological effects of electromagnetic waves do not depend solely on the external power density; they depend on the dielectric field inside the tissue or the body. Hence, the internal fields have to be determined for any meaningful and general quantification of biological data obtained experimentally. Domestic studies that attempt to quantify the interactions of RF fields with biological tissues and bodies are reported.

More recently, however, other subjects have received as much attention, in particular EM energy absorption in human subjects, especially in the human head, interaction of electromagnetic waves with the nervous system, influence of the fields of mobile phone on membrane channels, and molecular effects. An increasing amount of evidence, derived from in vitro and in vivo studies, indicates that electromagnetic waves affect living systems directly. The experimental electromagnetic wave ablation cannot be carried out in living human. There are some experimental studies in animal, such as rats, cows and pigs. However, the results may not represent the practical behavior of human tissues. Therefore, the modeling of heat transport in human tissue is needed. At the same time, some doctors around the world use microwaves in cancer treatments such as breast cancer. There is scientific and medical evidence to support this treatment. The heating by microwaves enhances the blood circulation and enhances the locally supply of treatment drugs that are applied to enhance the death rates cancer cells. Some doctors simply as microwaves or they can treatment. They believe and they observe that this reduces the cancer tumors. Almost all of them do not know what the side effect of this electromagnetic radiation.

This research provides an electromagnetic and thermal analysis of the human tissue in several case studies. The research aims to illustrate the advancement of bioheat transport application in Therapeutic applications and Health implication of electromagnetic wave exposures. Electromagnetic wave propagation in tissues is investigated by using Maxwell's equations. An analysis of heat transfer in tissues subjected to electromagnetic waves is investigated by using the bioheat equation. Moreover, the case study of bioheat transfer in several human organs induced by EM wave based on the theory of porous media is also systematically investigated. In the therapeutic applications, the obtained knowledge would then reduce further the need for surgical or invasive procedures, substituting non-invasive and minimally invasive techniques. In health implication of electromagnetic wave exposures, the obtained values provide an indication of limitations that must be considered for the temperature increases due to localized electromagnetic energy absorption

3. Research Outputs

ได้ตีพิมพ์บทความวิจัยลงในวารสารนานาชาติ 22 บทความ แล้วดังนี้

Jindarat, W., Sungsoontorn, S. and Rattanadecho, P., " **Analysis of Energy Consumption in A Combined Microwave-Hot Air Spouted Bed (CMHS) Drying of Biomaterial: Coffee Beans** " Experimental Heat Transfer, Vol. 28 pp. 107-124, 2015 Impact Factor: 0.979

Jindarat., W. , Sungsoontorn., S. and Rattanadecho., P. **"Analysis of Energy Consumption in Drying Process of Biomaterials Using a Combined Unsymmetrical Double-Feed Microwave and Vacuum System (CUMV) (Case Study: Tea Leaves)"**, Drying Technology An International J.,Vol.31, pp.1138-1147, 2013 : Impact factor 2.084

Keangin. P., Vafai. K., and Rattanadecho. P "**Electromagnetic field effects on biological materials** " International Journal of Heat and Mass Transfer, Vol 65, pp.389-399, 2013 : Impact factor 2.52

Siriwitpreecha, A., Rattanadecho, P. and Wessapan, T., " **The influence of wave propagation mode on specific absorption rate and heat transfer in human body exposed to electromagnetic wave**" International Journal of Heat and Mass Transfer, Vol.65 , pp.423-434, 2013 : Impact factor 2.52

Chaiyo. K. and Rattanadecho, P. "**Numerical analysis of heat-mass transport and pressure buildup of unsaturated porous medium in a rectangular waveguide subjected to a combined microwave and vacuum system**" International Journal of Heat and Mass Transfer, Vol.65 , pp.825-844, 2013 : Impact factor 2.52

Keangin, P. and Rattanadecho, P. "**Analysis of heat transport on local thermal non-equilibrium in porous liver during microwave ablation**" International Journal of Heat and Mass Transfer, Vol.67 , pp.46-60, 2013 : Impact factor 2.52

Suttisong S., Montienthong, P. and Rattanadecho.P. **"Comparison of Stefan Model with Single-Phase model of Water Infiltration Process in Unsaturated Porous Media (Theory and Experiment)"** Journal of Hydrology, 497, pp.145-151, 2013 : Impact factor 3.654

Klayborworn., S., Pakdee., W., Rattanadecho., P.and Vongpradubchai, S.**"Effects of material properties on heating processes in two-layered porous media subjected to microwave energy "**, International Journal of Heat and Mass Transfer, : Vol.61, pp.397-408, 2013 : Impact factor **2.598**

Rattanadecho, P., Suttisong, S.and Somtawin, T. "**The Numerical and experimental analysis of heat transport and water infiltration in a granular packed bed due to supplied hot water**" Numerical Heat Transfer; Part A: Applications 65 (10), pp. 1007-1022, 2014.: Impact Factor: 1.975

Natt Makul, Phadungsak Rattanadecho, Dinesh K Agrawal. "**Applications of microwave energy in cement and concrete - A review**". Renewable & Sustainable Energy Reviews, Vol.37, pp.715-733, 2014 : Impact Factor: 6.577

Wessapan, T. and Rattanadecho, P. "**Specific absorption rate and temperature increase in the human eye due to electromagnetic fields exposure at different frequencie**s" International Journal of Heat and Mass Transfer, Vol.64 , pp.426-435, 2013 : Impact factor **2.52**

Wessapan, T. and Rattanadecho, P., **"Aqueous Humor Natural Convection of the Human Eye induced by Electromagnetic Fields: In the Supine Position"**, Journal of Medical and Bioengineering,Vol.3(4), pp.251-258, 2014: Impact factor **1.287**

Intra, P., Yawootti, A. and Rattanadecho, P., "**Numerical and experimental studies of collection efficiency of an ion electrostatic collector for a mini-volume electrical PM detector**", Journal of Electrostatics, pp.477-486, 2014,: Impact factor 1.287

Intra, P., Yawootti, A. and Rattanadecho, P., "**Influence of the corona-wire diameter and length on corona discharge characteristics of a cylindrical tri-axial charger**", Journal of Electrostatics, Vol.74, pp.37-46, 2015: Impact factor 1.287

Wessapan, T., and Rattanadecho, P.**"Heat transfer of human eye during exposure to sauna therapy"** Numerical Heat Transfer; Part A: Applications, Vol68(5), pp.566-582, 2015.: Impact Factor: 1.975

Wessapan, T., Rattanadecho, P. and Wongchadakul, P.**"Effect of body position on natural convection within anterior of the human eye during exposure to electromagnetic fields"** Numerical Heat Transfer; Part A: Applications, Vol.xx, pp.1-15, 2016.: Impact Factor: 1.847

Yawootti, A., Intra, P., Tippayawong, N. and Rattanadecho, P., **"An experimental study of relative humidity and air flow effects on positive and negative corona discharges in a corona-needle charger"**, Journal of Electrostatics, Vol.77, pp.1-7, 2015: Impact factor 1.287

Natt Makul and Phadungsak Rattanadecho "**Microwave-assisted Drying: A review of the state-of-the-art**" Drying Technology An International J., Vol 34, pp.1-38, 2016: Impact factor 2.084

Waraporn Klinbun and Phadungsak Rattanadecho , "**Investigation into Heat Transfer and Fluid Flow Characteristics of Liquid Two-Layer and Emulsion in Microwave Processing**", International Communications in Heat and Mass Transfer, Vol70, January 2016, pp. 115–126 : Impact factor 2.316

Sudaporn Sudprasert, Chatchawin Chinsorranant and Phadungsak Rattanadecho, "**Numerical Study of Vertical Solar Chimneys with Moist Air in a Hot and Humid Climate",** International Journal of Heat and Mass Transfer, Vol102, pp. 645-656, 2016: Impact Factor 2.598

Rattanadecho, P., Makul, N., Pichaicherd, A., Chanamai, P. and Rungroungdouyboon B. **"A novel rapid microwave-thermal process for accelerated curing of concrete: Prototype design, optimal process and experimental investigations**" Construction & Building Materials, 123, pp. 768-784, 2016: Impact Factor 2.421

S. Sungsoontorn, P. Rattanadecho, S. Jumrat and Y.Pianroj , "**Design and Analysis of Doubly Corrugated Filter for a Combined Multi-Feed Microwave-Hot Air and Continuous Belt System (CMCB),** Songklanakarin Journal of Science and Technology, 2016 (Accepted)

ได้ตีพิมพ์บทความวิจัยลงใน Book Chapter 1 **บทความ แล้วดังนี้**

Wessapan, T. and Rattanadecho, P. "**Effects of electromagnetic fields on specific absorption rate and heat transfer in the human eye**", Book Chapter, Ophthalmology Imaging and Applications, 2014 by CRC Press, Taylor &Francis Group.

ได้สิทธิบัตรการประดิษฐ์ 2 รายการ
เครื่องกำเนิดความร้อนด้วยคลื่นไมโครเวฟชนิดป้อนคลื่นหลายตำแหน่งร่วมกับระบบสายพานลำเลียง
อุปกรณ์บ่มสีเส้นจราจรด้วยคลื่นไมโครเวฟ

ได้ตำรา 1 เล่ม แล้วดังนี้
การทำความร้อนด้วยไมโครเวฟ: ทฤษฎีและนวัตกรรม

รางวัลระดับชาติ

รางวัลผลงานวิจัยระดับดีมาก จากสภาวิจัยแห่งชาติ 1 รายการ

Analysis of Specific Absorption Rate and Heat Transfer in Human Eye Subjected to Electromagnetic Field (Theory and Applications)

รางวัลนวัตกรรมนานาชาติ 7 รายการ

- เหรียญเงิน "The Liver Cancer Treatment Using Microwave Coaxial Antenna: Computer Simulation Based on FEM and Experiment" "44nd International Exhibition of Inventions of Geneva" 2016 ณ กรุงเจนีวา สมาพันธรัฐสวิส

- FIRI award for the best invention (special prize from Iran), "Computer Simulation Based on FEM of Laser-induced Thermotherapy in Human Layered Skin-Tissue"
"44nd International Exhibition of Inventions of Geneva" 2016 ณ กรุงเจนีวา สมาพันธรัฐสวิส

- เหรียญทองแดง "Computer Simulation Based on FEM of Laser-induced Thermotherapy in Human Layered Skin-Tissue"
"44nd International Exhibition of Inventions of Geneva" 2016 ณ กรุงเจนีวา สมาพันธรัฐสวิส

- เหรียญทอง " Nanoparticle Material Charge"
"43nd International Exhibition of Inventions of Geneva" 2015 ณ กรุงเจนีวา สมาพันธรัฐสวิส

- เหรียญเงิน "Simulated Software for Predicting Specific Absorption Rate (SAR) and Heat Transfer in Human Head Subjected to Mobile Phone Radiation"
"42nd International Exhibition of Inventions of Geneva" 2014 ณ กรุงเจนีวา สมาพันธรัฐสวิส

รางวัลเหรียญทองแดง " Commercailized Drier Processing Using a Combine Unsymmetrical Double Feed low Power Microwave and Vacuum System (CUMV)" 2014 ณ กรุงเจนีวา สมาพันธรัฐสวิส

- เหรียญเงิน "A Combined Double Feed-Microwave Power and Hot Air-Spouted Bed Drier" 2013
ณ กรุงโซล เกาหลี

PUBLICATIONS

This article was downloaded by: [Thammasat University Libraries]
On: 19 November 2014, At: 18:20
Publisher: Taylor & Francis
Informa Ltd Registered in England and Wales Registered Number: 1072954 Registered office: Mortimer House, 37-41 Mortimer Street, London W1T 3JH, UK

Experimental Heat Transfer: A Journal of Thermal Energy Generation, Transport, Storage, and Conversion
Publication details, including instructions for authors and subscription information:
http://www.tandfonline.com/loi/ueht20

Analysis of Energy Consumption in a Combined Microwave-hot Air Spouted Bed Drying of Biomaterial: Coffee Beans

W. Jindarat[a], S. Sungsoontorn[a] & P. Rattanadecho[a]
[a] Department of Mechanical Engineering, Faculty of Engineering, Center of Excellence in Electromagnetic Energy Utilization in Engineering (CEEE), Thammasat University (Rangsit Campus), Pathumthani, Thailand
Accepted author version posted online: 28 Oct 2013.Published online: 31 Jul 2014.

To cite this article: W. Jindarat, S. Sungsoontorn & P. Rattanadecho (2015) Analysis of Energy Consumption in a Combined Microwave-hot Air Spouted Bed Drying of Biomaterial: Coffee Beans, Experimental Heat Transfer: A Journal of Thermal Energy Generation, Transport, Storage, and Conversion, 28:2, 107-124, DOI: 10.1080/08916152.2013.821544

To link to this article: http://dx.doi.org/10.1080/08916152.2013.821544

PLEASE SCROLL DOWN FOR ARTICLE

Taylor & Francis makes every effort to ensure the accuracy of all the information (the "Content") contained in the publications on our platform. However, Taylor & Francis, our agents, and our licensors make no representations or warranties whatsoever as to the accuracy, completeness, or suitability for any purpose of the Content. Any opinions and views expressed in this publication are the opinions and views of the authors, and are not the views of or endorsed by Taylor & Francis. The accuracy of the Content should not be relied upon and should be independently verified with primary sources of information. Taylor and Francis shall not be liable for any losses, actions, claims, proceedings, demands, costs, expenses, damages, and other liabilities whatsoever or howsoever caused arising directly or indirectly in connection with, in relation to or arising out of the use of the Content.

This article may be used for research, teaching, and private study purposes. Any substantial or systematic reproduction, redistribution, reselling, loan, sub-licensing, systematic supply, or distribution in any form to anyone is expressly forbidden. Terms &

Conditions of access and use can be found at http://www.tandfonline.com/page/terms-and-conditions

Downloaded by [Thammasat University Libraries] at 18:20 19 November 2014

Experimental Heat Transfer, 28:107–124, 2015
Copyright © Taylor & Francis Group, LLC
ISSN: 0891-6152 print/1521-0480 online
DOI: 10.1080/08916152.2013.821544

Downloaded by [Thammasat University Libraries] at 18:20 19 November 2014

ANALYSIS OF ENERGY CONSUMPTION IN A COMBINED MICROWAVE–HOT AIR SPOUTED BED DRYING OF BIOMATERIAL: COFFEE BEANS

W. Jindarat, S. Sungsoontorn, and P. Rattanadecho
Department of Mechanical Engineering, Faculty of Engineering, Center of Excellence in Electromagnetic Energy Utilization in Engineering (CEEE), Thammasat University (Rangsit Campus), Pathumthani, Thailand

In this study, an energy model based on the first law of thermodynamics is developed to evaluated energy efficiency and specific energy consumption. The influences of hot air temperature and initial weight of coffee beans on energy consumption are considered. Furthermore, a comparison between combined microwave–hot air spouted bed drying and hot air spouted bed drying methods on energy consumption is also investigated in detail. The results show that energy efficiency as well as energy consumption depends on hot air temperature, initial weight of coffee bean, and typical drying methods (combined microwave–hot air spouted bed and hot air spouted bed). The optimum drying condition is also achieved in this study.

Keywords specific energy consumption, energy efficiency, microwave energy

INTRODUCTION

Presently, the most important goal of industries, other than producing high-quality products for markets, is to increase productivity and reduce production cost. In general, several production processes of agricultural and industrial products are related with drying either by a natural method or using energy from other sources resulting in a low production rate or high-cost products. Microwave drying is one of the most interesting methods in terms of mechanisms and economics for heating and drying in various kinds of products. A combined microwave–hot air spouted bed (CMHS) drying method is a novel alternative method of drying and produces products of acceptable quality. It permits a shorter drying time and substantial improvement in the quality of dried materials in comparison to those dried with hot air and microwave drying methods. Other advantages include environmental friendliness at low temperatures, which not only overcomes the limitation of low thermal conductivity of the material but avoids the defect of internal cracking and interior burning caused by excessive heating in microwave drying, and its applicability within a wide range

Received 12 November 2012; accepted 27 June 2013.
Address correspondence to Prof. Phadungsak Rattanadecho, Department of Mechanical Engineering, Faculty of Engineering, Thammasat University (Rangsit Campus), Pathumthani 12120, Thailand. E-mail: ratphadu@engr.tu.ac.th
Color versions of one or more of the figures in the article can be found online at www.tandfonline.com/ueht

NOMENCLATURE

C_p	specific heat of the dielectric material (kJ/kg K)
c_m	material specific heat (kJ/kg K)
E	electromagnetic field intensity (V/cm)
D_p	penetration depth (m)
f	microwave frequency (Hz)
h	enthalpy (kJ/kg)
h_{fg}	latent heat of vaporization (kJ/kg$_{water}$)
h_{fw}	enthalpy of water (kJ/kg)
h_m	enthalpy of material (kJ/kg)
$\dot{m}$	mass flow rate (kg/s)
$\dot{m}_a$	mass flow rate of dry air (kg/s)
$\dot{m}_w$	mass flow rate of water from the spouted bed (kg/s)
M_p	particle moisture content dry basis (kg$_{water}$/kg$_{solid}$)
P_1	density of microwave power absorbed by dielectric material (kW/cm^3)
P_2	energy is required to heat up material (kW)
P_{in}	microwave power incident (microwave energy emitted from a microwave oscillator; kW)
$\dot{Q}_{evap}$	heat transfer rate due to water evaporation (kW)
$\dot{Q}_{loss}$	heat transfer rate to environment (kW)
$\dot{Q}_{MW}$	microwave energy (kW)
SEC	specific energy consumption (MJ/kg)
t	time (sec)
T	temperature (°C)
tan δ	loss tangent coefficient
W	weight of the dielectric material (kg)
W_b	weight of material before drying (kg)
W_d	weight of dry material (kg)
X	absolute humidity (kg$_{vapor}$/kg$_{dry\ air}$)

Greek Letters

ΔT	increment temperature (°C)
ε_0	permittivity of air (F/m)
ε_r'	relative dielectric constant
ε_r''	relative dielectric loss factor
η_e	energy efficiency (%)
η_m	microwave efficiency device (%)
υ	velocity of propagation (m/s)
ω	angular velocity of microwave (rad/s)

Subscripts

0	free space
1	inlet
2	outlet
a	air
ab	absorb
d	dry material
da	drying air
db	dry basis
fg	difference in property between saturated liquid and saturated vapor
g	gas
in	input
l	liquid water
m	material
o	standard state value
out	output
r	relative
s	solid
v	vapor
w	water

of herbal and food industries. It is also easily integrated into flexible, automated manufacturing systems. A CMHS drying method has been investigated as a potential method for obtaining high-quality dried foodstuffs, including fruits, vegetables, and herbs. The reasons for interest in the interaction of microwaves with porous materials have been reported in the recent literature [1–21]. Excellent reviews of the drying techniques in dielectric materials using microwave energy were presented in [1–5].

Rattanadecho et al. [6] developed a mathematic model and experimental test rig for microwave drying processing for described moisture migration and temperature gradient in unsaturated porous media. The temperature profiles and drying rate during microwave–fluidized bed drying of macaroni beads with various drying conditions were investigated in [7]. The heat and mass transfer model was developed to simulate the kinetics of microwave and spouted bed drying of hygroscopic porous material (diced apples) in [8]. The total gas–pressure equation was introduced to account for internal vapor generation during microwave drying. The governing equation for heat and mass transfer were simplified using a scaling technique and numerically solved with the finite-difference method.

Downloaded by [Thammasat University Libraries] at 18:20 19 November 2014

Downloaded by [Thammasat University Libraries] at 18:20 19 November 2014

Microwave-assisted spouted bed (MWSB) drying on the quality of dried lettuce cubes was studied in [9], where the dielectric properties of lettuce were measured for the analysis. Response surface methodology was used to optimize the drying process conditions with chlorophyll content as the response value. Based on such properties as rehydration rate, chlorophyll content, color, drying time, and dielectric properties, the MWSB-dried products were compared with that from other drying technologies. Furthermore, the models were proposed for thermodynamic analysis of a drying process based on the energy and exergy concept [10, 11]. An analysis of microwave energy consumption in drying process was performed in [12]. Specific energy consumption (SEC) in microwave drying of garlic cloves has been examined. A comparative study of SEC with two different drying methods, namely microwave–hot air and conventional hot air drying, has also been conducted. Another related study presents microwave energy and hot air drying processes, considering the combined microwave and hot air drying of peeled longan [13]. The influence of moisture content on SEC was examined. In another important study [14], a comparison of SEC in cooking rice was presented among the microwave oven, electric rice cooker, and pressure cooker.

Investigations of energy efficiency of microwave drying of porous media have been performed since the late 1950s. Many authors [15–22] have emphasized the advantages of microwave drying over convective drying.

Although microwave drying of porous media has found some application in the dehydration of biomaterials and engineering products, more research and development was needed before the process was used on a large commercial scale. In particular, the effect of hot air temperature, initial weight of coffee beans, and typical drying methods (CMHS and hot air spouted bed [HASB]) on the drying kinetics should be quantitatively known, so that the drying system can be optimized from the cost and quality standpoints.

The main objective of this research is to examine the feasibility of using CMHS and HASB drying methods to dry coffee beans and to experimentally explore drying characteristics of coffee beans in different drying conditions, considering the hot air temperature and initial weight of coffee bean. The research results are beneficial in presenting a theory basis for further study and for industrial applications of a CMHS drying method of biomaterials in the future.

RELATED THEORIES

Microwave Heat Generation

Microwave heating involves heat dissipation and microwaves propagation, which causes the dipoles to vibrate and rotate. When the microwave energy from a microwave oscillator (P_{in}) is irradiated inside the microwave applicator, the dielectric material has a property of dielectric loss factor that absorbs the energy and the internal heat generation then takes place. The basic equation calculating the density of microwave power absorbed by dielectric material (P_1) is given by [23]

$$P_1 = \omega\varepsilon_0\varepsilon_r'' E^2 = 2\pi \cdot f \cdot \varepsilon_0 \cdot \varepsilon_r'(\tan\delta)E^2, \tag{1}$$

where E is the electromagnetic field intensity, f is the microwave frequency, ω is the angular velocity of microwave, ε_r' is the relative dielectric constant, ε_0 is the dielectric constant of air in free space, and $\tan\delta$ is the loss tangent coefficient.

Downloaded by [Thammasat University Libraries] at 18:20 19 November 2014

From Eq. (1), P_1 is directly proportional to the frequency of the applied electric field, loss tangent coefficient, and root-mean-square value of the electric field; this means that increasing tanδ of specimen, energy absorption, and heat generation are also increased. While tanδ is small, the microwave will penetrate into a specimen without heat generation. However, the temperature increase depends on other factors, such as specific heat, size, and characteristic of the specimen.

As the material is unilaterally heated, it is found that when the dielectric constant and loss tangent coefficient vary, the penetration depth will be changed and the electric field within the dielectric material will be altered. The penetration depth is used to denote the depth at which the power density decreased to 37% of its initial value at the surface [23]:

$$D_p = \frac{1}{\frac{2\pi f}{\upsilon}\sqrt{\frac{\varepsilon_r'\left(\sqrt{1+\left(\frac{\varepsilon_r''}{\varepsilon_r'}\right)^2}-1\right)}{2}}} = \frac{1}{\frac{2\pi f}{\upsilon}\sqrt{\frac{\varepsilon_r'\left(\sqrt{1+(\tan\delta)^2}-1\right)}{2}}} \tag{2}$$

where D_P is penetration depth, ε_r'' is relative dielectric loss factor, and υ is microwave speed. The penetration depth of the microwave power is calculated according to Eq. (2), which shows how it depends on the dielectric properties of the material. It is noted that products with huge dimensions and high loss factors may occasionally be overheated to a considerably thick layer on the outer layer. To prevent such a phenomenon, the power density must be chosen so that enough time is provided for the essential heat exchange between boundary and core. If the thickness of the material is less than the penetration depth, only a fraction of the supplied energy will be absorbed. Furthermore, the dielectric properties of dielectric materials typically show moderate lossiness, depending on the actual composition of the material. With a large amount of moisture content, greater potential for absorbing microwaves is revealed. For typical dielectric materials, a decrease in the moisture content typically decreases ε_r'', accompanied by a slight increment in D_p.

In the analysis, energy P_2 is required to heat up the dielectric material $W(g)$ placed in a microwave applicator. The initial temperature of material T_1 is raised to T_2. The energy P_2 can be estimated by the following calorific equation [24]:

$$P_2 = \frac{4.18 \cdot W \cdot C_p \cdot \Delta T}{t}, \tag{3}$$

where W is the weight of the dielectric material, C_p is the specific heat of the dielectric material, ΔT is the increment of temperature ($T_2 - T_1$), and t is heating time.

Assuming an ideal condition, all of the oscillated microwave energy (P_{in}) is absorbed into the dielectric material; such internal heat generation as shown in Eq. (1) takes place. In this case, the relation between P_{in} and P_2 is shown as [24]

$$P_{in} = P_2. \tag{4}$$

From a practical point of view, however, the transformation energy in the applicator exists due to (1) the rate of microwave energy absorbed by means of the dielectric loss factor of the sample and (2) the energy loss in the microwave devices. Accordingly, by taking this transformation efficiency into account, the microwave oscillation output can be

calculated by the following equations [24]:

$$P_{in} = \frac{P_2}{\eta_m}, \tag{5}$$

$$\eta_m = \frac{P_2}{P_{in}}. \tag{6}$$

Mass and Energy Balance Equation for Drying Process

For analyzing mass transfer in the drying process, the law of conservation of mass for the control volume is applied, as shown in Figure 1. The mass balance equation can be written as [24]

$$\frac{dm_{cv}}{dt} = \dot{m}_{g1} - \dot{m}_{g2}. \tag{7}$$

Equation (7) is the mass rate balance for the control volume, where $\dot{m}_{g1}$ and $\dot{m}_{g2}$ denote the mass flow rate at inlet (1) and exit at (2), respectively. Similarly, a balance of water in air flowing through the drying spouted bed leads to [24]

$$W_d \frac{dM_p}{dt} = \dot{m}_a(X_1 - X_2), \tag{8}$$

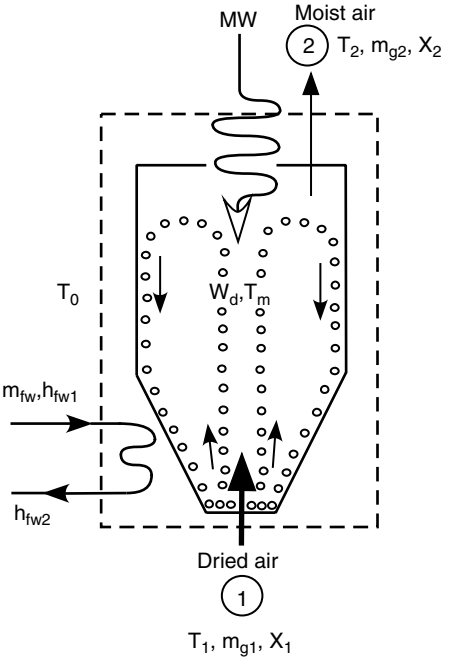

Figure 1. Physical control volume of CMHS drying process for energy analysis.

Downloaded by [Thammasat University Libraries] at 18:20 19 November 2014

where W_d is weight of dry material, and M_p is particle moisture content, dry basis; this can be expressed as [24]

$$M_p = \frac{W_b - W_d}{W_d}, \tag{9}$$

where W_b is the weight of material before drying, $\dot{m}_a$ is the mass flow rate of dry air, and X_1 and X_2 denote absolute humidity of inlet and exit air, respectively. The left-hand side of the mass balance equation (Eq. (10)) is the mass flow rate of water in the air flowing from the spouted bed and can be written as

$$\dot{m}_w = \dot{m}_a(X_2 - X_1). \tag{10}$$

For analyzing energy transfer in the drying process, the first law of thermodynamics (the law of conservation of energy) is applied for the control volume, as shown in Figure 1. The significant heat transfer is due to the internal heat generation due to microwave energy and heat of evaporation between the porous structure and the drying air, and there is also heat rejection to the surroundings. The energy rate balance is simplified by ignoring kinetic and potential energies. Since the mass flow rate of the dry air and the mass of dry material within the control volume remain constant with time, the energy rate balance can be expressed as

$$\frac{W_d(h_{m2} - h_{m1})}{\Delta t} = \dot{Q}_{evap} + \dot{m}_a(h_1 - h_2) + \dot{Q}_{MW} + \dot{Q}_{loss} + \dot{m}_{fw}(h_{fw1} - h_{fw2}), \tag{11}$$

where $\dot{Q}_{evap}$ is the heat transfer rate due to water evaporation, $\dot{Q}_{MW} = P_{in}$ is microwave energy, h_m is the enthalpy of material, t is time, $\dot{m}_a$ is the mass flow rate of dry air, h is the enthalpy of dry air, and $\dot{Q}_{loss}$ the is heat transfer rate to the environment.

The differences in specific enthalpy are as follows, assuming air as an ideal gas:

$$h_{m1} - h_o = c_m(T_{m1} - T_o), \tag{12}$$

$$h_{m2} - h_o = c_m(T_{m2} - T_o). \tag{13}$$

The material enthalpy term of the energy rate balance can be expressed as [24]

$$h_{m2} - h_{m1} = c_m(T_{m2} - T_{m1}), \tag{14}$$

where c_m represents the specific heat of the material. The enthalpy of moist air can be calculated by adding the contribution of each component as it exits the mixture; thus the enthalpy of moist air is [24]

$$h = h_a + Xh_v, \tag{15}$$

$$h_{fw} = 0.1163 + 4.1861T. \tag{16}$$

The heat transfer rate due to phase change is [24]

$$\dot{Q}_{evap} = \dot{m}_w h_{fg}, \tag{17}$$

where h_{fg} is the latent heat of vaporization.

SEC and Energy Efficiency in Drying Process

The drying of biomaterial, a process of simultaneous heat and mass transfer, represents an energy-intensive operation of some industrial significance. The SEC is

Downloaded by [Thammasat University Libraries] at 18:20 19 November 2014

estimated in CMHS drying processes as a relationship between two values considering the total energy supplied to drying processes and the amount of water removed during drying. A CMHS drying process is conducted in the same drying conditions, keeping the microwave power output of 800 W at air velocity of 12 m/s. SEC is as follows:

$$SEC = \frac{\text{Total energy supplied in drying process}}{\text{Amount of moisture removed during drying}}, \frac{kJ}{kg}, \tag{18}$$

$$SEC = \frac{[P_{\text{in}} + \dot{m}_{da}(h_1 - h_0)]\Delta t}{\text{Amount of moisture removed during drying}}, \frac{kJ}{kg}. \tag{19}$$

The energy efficiency (η_e) for the drying process is described by

$$\eta_e = \frac{W_d[h_{fg}(M_{p1} - M_{p2}) + c_m(T_{m2} - T_{m1}) + \dot{m}_{fw}(h_{fw2} - h_{fw1})]}{\dot{m}_{da}(h_1 - h_o)\Delta t + \Delta t \dot{Q}_{MW}}, \tag{20}$$

where c_m is material-specific heat.

EXPERIMENTAL APPARATUS

An experimental stand for the lab-scale biomaterial drier using a CMHS drying method is shown in Figure 2. This drying method is modified from the work of [8]. The system consists of a microwave power source, multimode microwave cavity, hot air convective source, spouted bed, and water-dummy load. The microwave is generated by a one-feed magnetron with a maximum power of 800 W operating at a frequency of

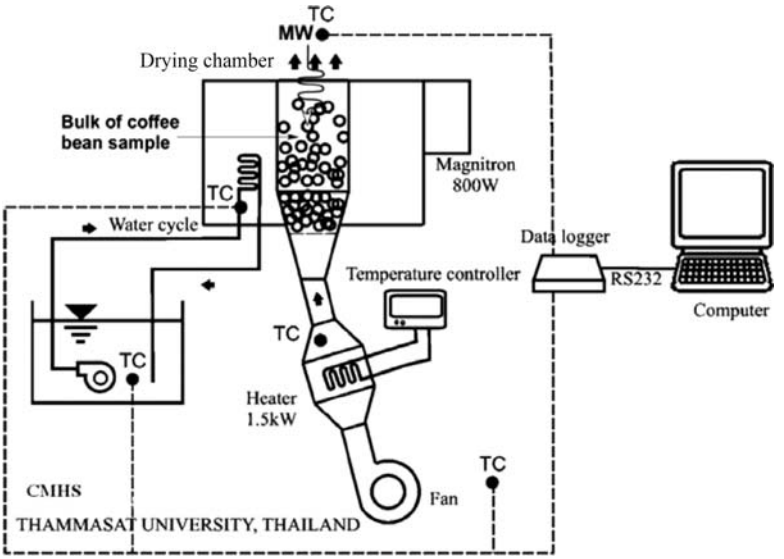

Figure 2. Schematic diagram of CMHS drying system.

Downloaded by [Thammasat University Libraries] at 18:20 19 November 2014

Table 1. SEC under various drying conditions

Test condition	Drying methods	Weight of coffee bean (g)	Hot air temperature (°C)	SEC (MJ/kg)
Case 1	CMHS	200	50	114.046
Case 2	HASB	200	50	149.930
Case 3	CMHS	200	60	111.762
Case 4	HASB	200	60	136.697
Case 5	CMHS	200	70	105.892
Case 6	HASB	200	70	125.207
Case 7	CMHS	280	60	83.238
Case 8	HASB	280	60	104.302

Downloaded by [Thammasat University Libraries] at 18:20 19 November 2014

2,450 MHz. The multimode microwave cavity had dimensions of $30 \times 30 \times 19$ cm. The spouted bed installed in multimode microwave cavity is constructed with glass that cannot absorb waves. The bottom of the spouted bed is made from polypropylene meshes to hold the particulate samples and to provide a pass for the convective hot air. The spouted bed is supported by a metal sheet and a metal screen with holes small enough to cut off microwave leaking. The circulating water load system is installed to protect the magnetron from overheating, especially in the final stage of the drying process. In this study, the microwave power output from the generator is calibrated following the method recommended in [8] (International Microwave Power Institute). Inlet and outlet temperatures of the water load are measured by high-precision thermometers. At the bottom of multimode microwave cavity as well as the spouted bed, a blower is used to provide an air velocity of up to 12 m/s in the spouted bed. The ambient air is pre-heated by a 1.5-kW electric heater before entering the spouted bed. Experimentally, the samples to be dried can be circulated in the spouted bed with a designed terminal velocity to enhance the interaction between the microwave and dielectric load. In this study, the system can be operated in either a CMHS drying or pure HASB drying mode in each experiment under different drying conditions as listed in Table 1.

The moisture content (dry basis) and dry matter content are measured according to Association of Official Analytical Chemists (AOAC) [26] standards using a laboratory scale system to an accuracy of 0.01 g. Optical fiber (LUXTRON Fluroptic Thermometer, model 790, (Luxtron Corp., Santa Clara, USA) accurate to ± 0.5°C) is employed for measuring the average temperature of the bulk load in the spouted bed. Optical fibers are used instead of conventional thermocouples because the latter absorb microwave energy and produce erroneous temperature indications. During the experimental (CMHS) drying processes, the uncertainty of data might come from the variations in humidity and room temperature. The uncertainty in drying kinetics is assumed to result from errors in the measured weight of the sample. The calculated drying kinetic uncertainties in all tests are less than 3%. The uncertainly in temperature is assumed to result from errors in measured input power, ambient temperature, and ambient humidity. The calculated uncertainty associated with temperature was less than 2.85%. Three test runs are repeatedly carried out to obtain accurate data. In CMHS, the leakage of microwaves is controlled below the U.S. Department of Health and Human Services standard of 5 mW/cm^2. The dielectric properties for coffee bean samples are measured at 25°C using a portable dielectric measurement (network analyzer) over a frequency band of 1.5 to 2.6 GHz to estimate microwave power absorbed in the dielectric load, as shown in Figure 3.

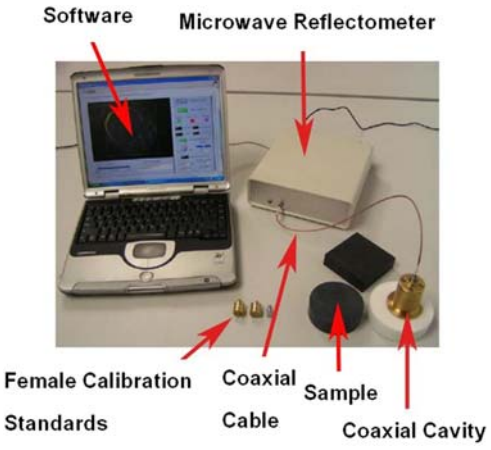

Figure 3. Portable dielectric measurement (network analyzer).

RESULTS AND DISCUSSION

According to testing condition cases shown in Table 1, Figures 4–6 show the temperature and moisture variations with respect to elapsed times with an initial weight coffee bean of 200 g, where the temperature is measured at the center of bulk load within the spouted bed. It should be noted that the energy efficiency seems to be very low in all testing conditions. This is because all testing conditions are done on a very small load (initial weight of coffee bean is 200 g/batch), which is much lower than the optimum

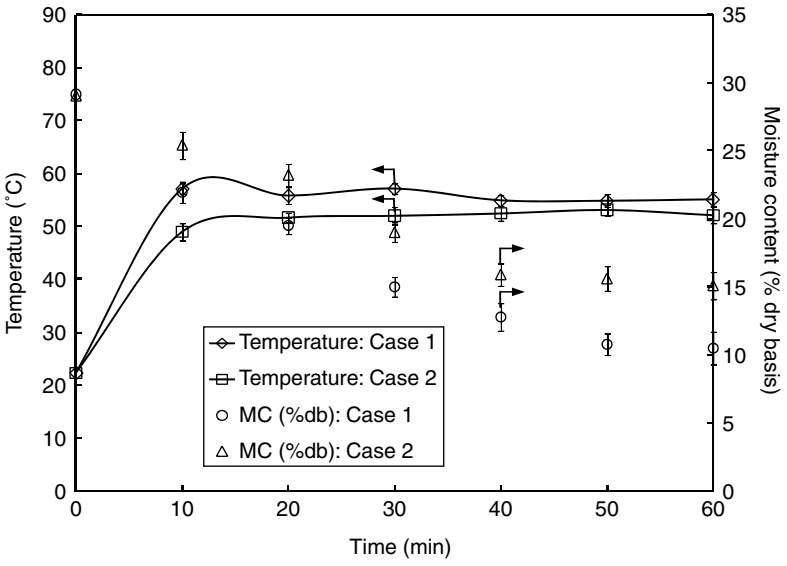

Figure 4. Temperature and moisture variations versus elapsed times with different drying methods ($W = 200$ g, $T_1 = 50$°C).

Downloaded by [Thammasat University Libraries] at 18:20 19 November 2014

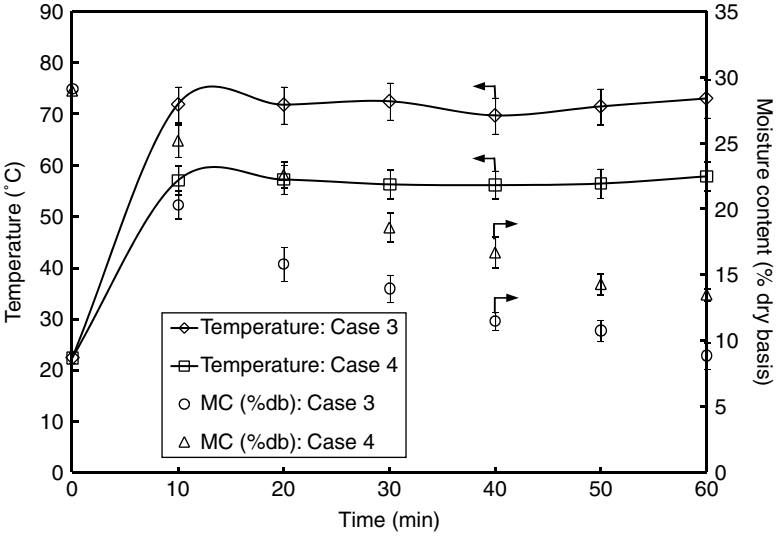

Figure 5. Temperature and moisture variations versus elapsed times with different drying methods ($W = 200$ g, $T_1 = 60$°C).

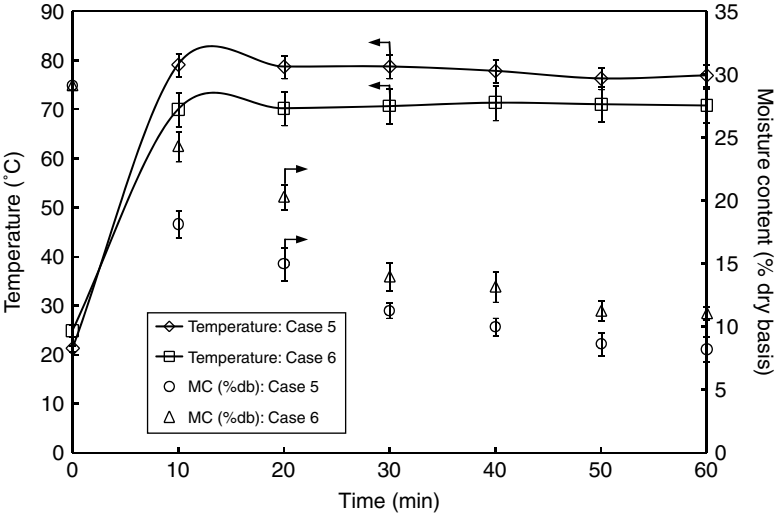

Figure 6. Temperature and moisture variations versus elapsed times with different drying methods ($W = 200$ g, $T_1 = 70$°C).

designed load. Actually, the energy efficiency will be increased with an increasing load when it approaches optimum design load. This is because the increasing bulk of coffee beans corresponds to the highest rate of water evaporation using CMHS drying. In future work, the effects of initial weight on analyzing energy consumption demand as well as energy efficiency will be investigated. It is found that in the CMHS at microwave power of 800 W with hot air temperatures of 50°C, 60°C, and 70°C, respectively, the moisture

Downloaded by [Thammasat University Libraries] at 18:20 19 November 2014

Downloaded by [Thammasat University Libraries] at 18:20 19 November 2014

content inside the spouted bed continuously decreases faster than that in all cases of the hot air temperature in the spouted bed drying (HASB) at 50°C, 60°C, and 70°C, respectively. This is because in the CMHS case, the bulk of this sample absorbed the largest amount of microwave energy. This phenomenon corresponds to the level of absorbed energy in the samples, as described in Eq. (1). It is observed the temperature profile within the spouted bed for both cases (CMHS and HASB) rises quickly in the early stages of the drying process (about 0–12 min); however, its rise slows down after this stage. It is evident from the figures that near the end stages of drying, the moisture content inside the spouted bed for both cases is continuously reduced. Additionally, in the CMHS case, when the process nearly reaches the end stage of drying, the moisture content inside the sample is reduced, and hence the absorption of microwave energy decreases [6]. Thus, during this stage, microwave power should adjust into lower level (or shut off) to reduce power consumption in the drying system. Furthermore, in the CMHS case, the temperature profile within the spouted bed (Figures 4–6) corresponds to the moisture content profile, where the temperature continuously rises faster than that in the HASB case, and the temperature remains higher throughout all drying methods.

Figures 7–10 show the energy efficiency with respect to elapsed times. It seems that high energy efficiency occurs near the starting period about 0–10 min due to the high quantity of moisture content within bulk of coffee bean in the spouted bed; thus, the microwave power absorbed is effectively converted to internal heat generation in the spouted bed. Throughout the drying process, after the vapor within the spouted bed is progressing from the top of the spouted bed, the moisture content within the spouted bed quickly decreases, and the corresponding low quantity of absorbed waves which leads to decrease energy efficiency. The energy efficiency profile for both cases rises quickly in the early stages of the drying process (about 10 min); however, it continuously falls after this stage (about 10–60 min). It is evident from the figures that near the end stages of drying, as the moisture content inside the sample is reduced, the microwave power absorbed

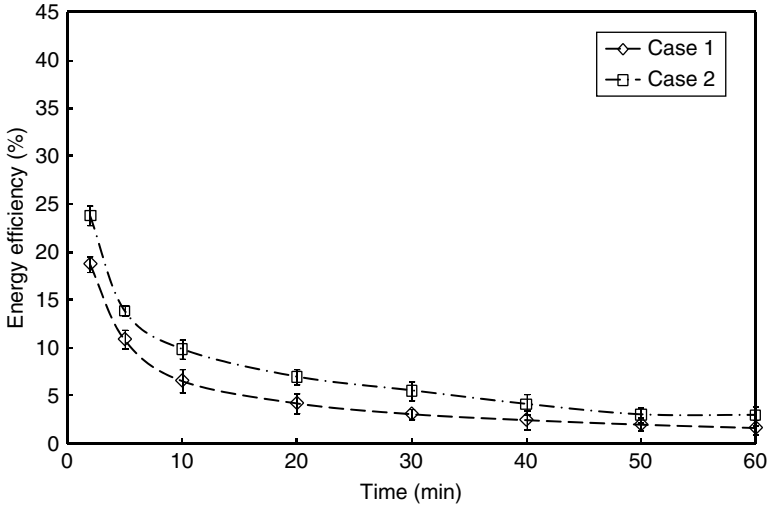

Figure 7. Energy efficiency versus elapsed times with different drying methods ($W = 200$ g, $T_1 = 50$°C).

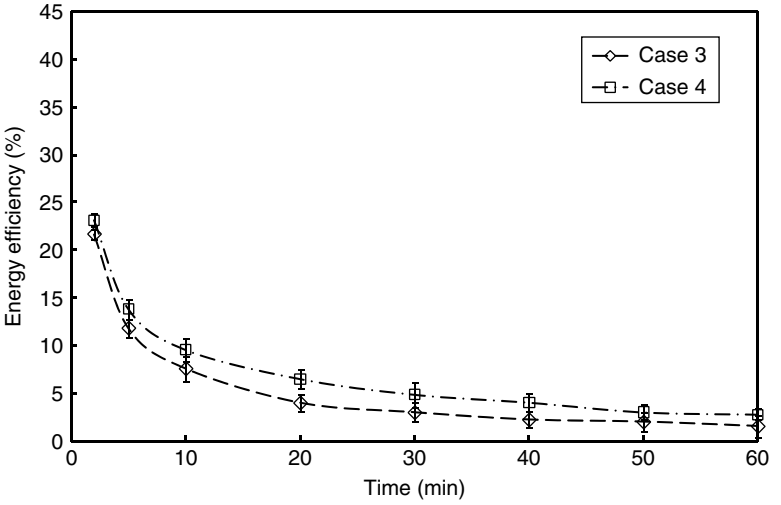

Figure 8. Energy efficiency versus elapsed times with different drying methods ($W = 200\,\text{g}$, $T_1 = 60°\text{C}$).

decreases. Although the process continuously feeds microwaves into the cavity with fixed microwave power supplied (800 W), it is noted that in this stage, most unused waves are directly absorbed by the water load (as shown in Figure 2). Further, since the microwave power supplied is fixed, the portion of useful microwave power for evaporating moisture inside the spouted bed is significantly reduced (Eq. (20)) due to the dried sample acting as a low lossy material, which explains why the energy efficiency profiles are decreased in this stage of the drying process. It can be observed from Figures 7–10 that the highest energy efficiency is presented in the HASB case throughout the drying method. This is because more waste energy is achieved in the CMHS case since the supplied energy sources are

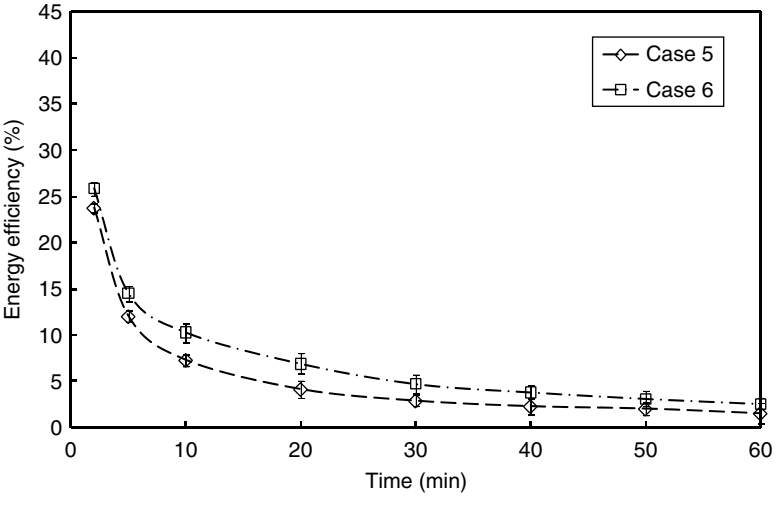

Figure 9. Energy efficiency versus elapsed times with different drying methods ($W = 200\,\text{g}$, $T_1 = 70°\text{C}$).

Downloaded by [Thammasat University Libraries] at 18:20 19 November 2014

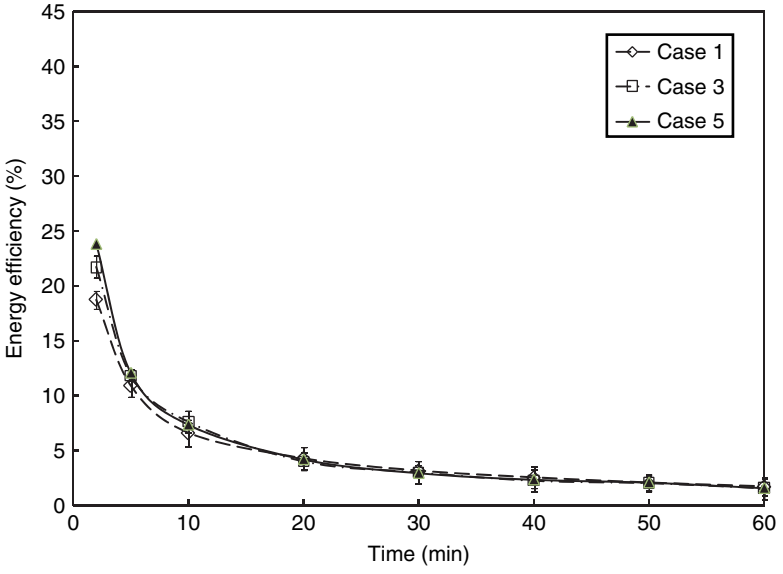

Figure 10. Energy efficiency at various hot air temperature with CMHS ($W = 200$ g).

incoming from the both modes, namely the microwave energy mode and hot air convective mode, during the drying process with a low initial weight of coffee bean. The next presentation will address the influences of the initial weight of coffee bean sample on the overall drying kinetics as well as the energy consumption rate.

Figure 11 shows the temperature and moisture variations with respect to elapsed time with an initial coffee bean weight of 280 g. A drying curve, exhibits the change in the

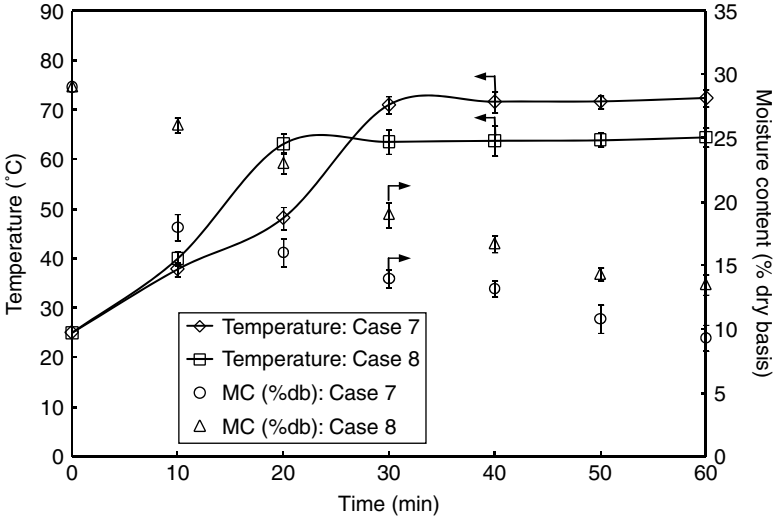

Figure 11. Temperature and moisture variations versus elapsed times with different drying methods ($W = 280$ g, $T_1 = 60$°C).

Downloaded by [Thammasat University Libraries] at 18:20 19 November 2014

Downloaded by [Thammasat University Libraries] at 18:20 19 November 2014

temperature and moisture content of the sample with time under different drying conditions. In the HASB case, drying rates are more in the beginning of the drying process where the air stream easily evaporates moisture from the bulk of coffee beans. The moisture content exponentially decreased with the drying time, where substantial drying takes place in the constant drying period. The drying time required to reduce the moisture from initial moisture content of about 29% (db) to a desired moisture in the final product, approximately 14% (db), was about 1 h with drying temperature of 62°C. The CMHS drying behavior of coffee beans followed the similar trend to that of the HASB case in that drying occurred mainly in the constant rate period.

It is found that drying rates are higher for the CMHS case. The accelerated drying rates may be attributed to internal heat generation and so-called liquid movement within the material when it is exposed to microwave energy. Generally, microwave power absorption by the sample depends on its moisture content. The moisture content of the coffee beans is relatively high during the early stage of drying, which resulted in higher microwave power absorbed and led to an increased sample temperature. This results in a higher drying rate due to higher moisture diffusion. As the drying progressed, *i.e.*, falling rate period, microwave power absorbed is decreased due to the dried sample acting as the low lossy material during the end stage of drying [8], as explained in previous figures. Consequently, the energy efficiency is decreased in this stage of drying; this will be discussed again in Figure 12.

In Figure 12, the energy efficiency profiles for the sample in cases 7 and 8 are higher in the early stages of drying (about 0–5 min) and continuously drop after this period; this is in contrast to the previous drying case, where energy efficiency for the HASB case is always higher than the CMHS case with a low initial weight (200 g; Figures 7–10). In this case (280 g), the energy efficiency in the CMHS case is higher than HASB case, especially at the early stage of drying (constant drying period). This is because the majority of moisture content within the bulk of coffee beans has been removed in this stage. After 20 min, the energy efficiency in the HASB case becomes a little bit higher than the CMHS

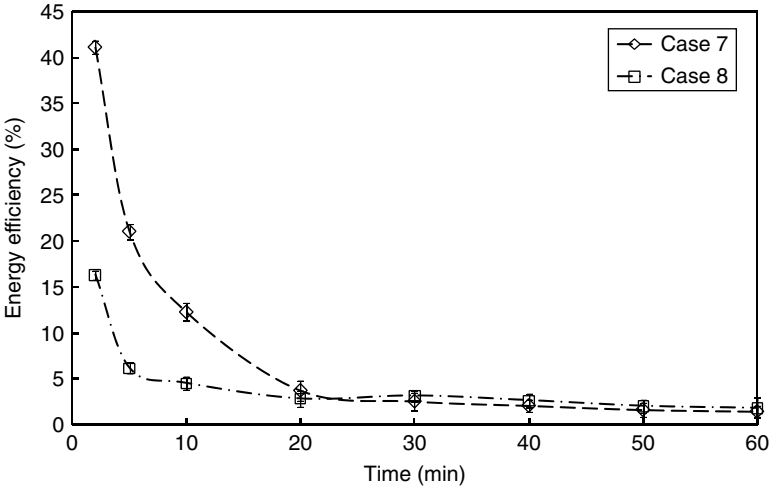

Figure 12. Energy efficiency versus elapsed times with different drying methods ($W = 280$ g, $T_1 = 60$°C).

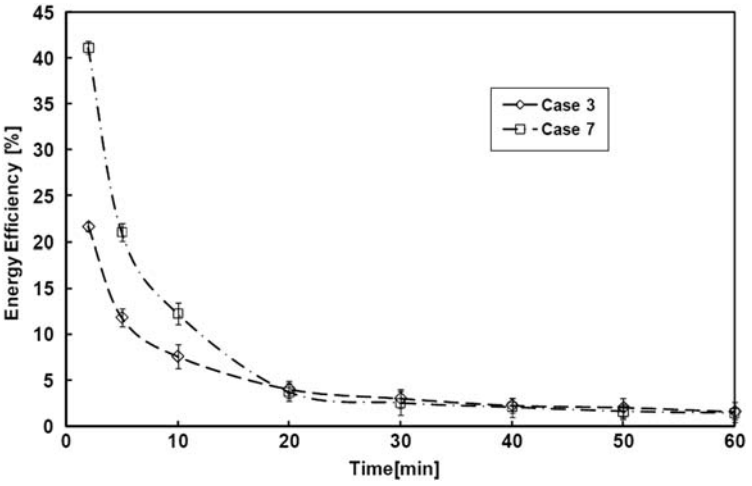

Figure 13. Energy efficiency at various elapsed times with different initial coffee beans weight when dried with CMHS ($T_1 = 60°C$).

case. In Fig. 13, the energy efficiency profiles for both cases (case 3 and case 7) with varying initial coffee bean weight are performed. The clear difference for both cases has been shown before drying time of 20 min, similarly trend as mentioned in Fig. 12.

The experimental data are analyzed to obtain the SEC under different drying conditions as listed in Table 1. Figure 14, redrawn from Table 1, shows the variations of SEC as a function of different drying conditions during the CMHS and HASB coffee bean drying methods. The lowest value in all drying conditions regarding energy consumption is noted in case 7 (83.238 MJ/kg), whereas the highest value is noted in case 2 (149.930 MJ/kg). The lowest SEC is occurred in case 7 (83.238 MJ/kg), followed by case 8 (104.302 MJ/kg), case 5 (105.892 MJ/kg), case 3 (111.762 MJ/kg), case 1 (114.046 MJ/kg), case 6

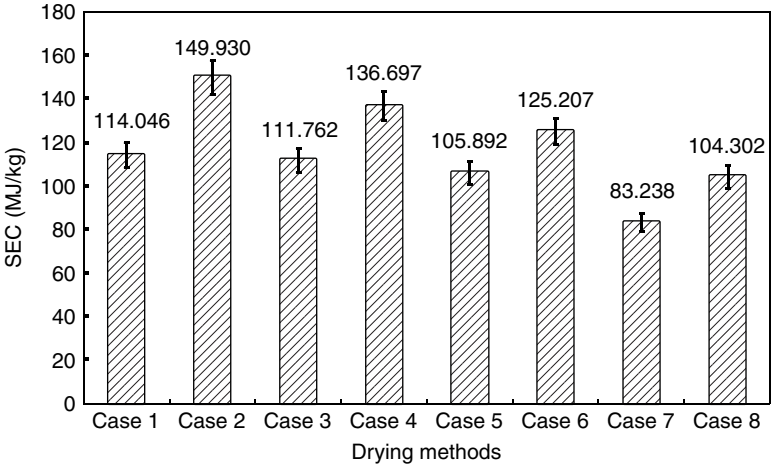

Figure 14. Variation in SEC for a different drying conditions (drying time = 60 min).

Downloaded by [Thammasat University Libraries] at 18:20 19 November 2014

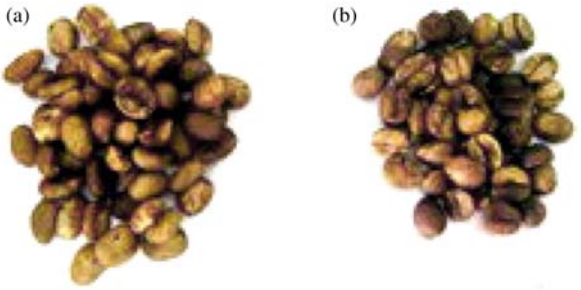

Figure 15. Color parameters of coffee beans before and after drying with CMHS (weight of coffee bean 280 g and hot air temperature of 60°C): (a) coffee beans before drying and (b) coffee beans after drying.

(125.207 MJ/kg), case 4 (136.697 MJ/kg), and case 2 (149.930 MJ/kg). To summarizes, the SEC for during the CMHS drying method is always lower than the HASB drying method considered at the same hot air temperature and coffee bean initial weight. This is because the CMHS drying method supplied microwave energy through the cavity, which leads to more volumetric heating inside the bulk of the coffee beans, resulting in a higher rate of water evaporation compared to the HASB drying method.

Figure 15 shows that the best color values are achieved during the CMHS drying method. Figures 15a and 15b show the rough color shades of the coffee beans before and after drying with the CMHS, respectively. It is observed that drying with CMHS gives better product quality in physical appearance. It should be mentioned again that the drying condition at high initial coffee bean weight increase the drying rate and decrease the average temperature of the bulk load.

It is mentioned again that the energy consumption by using the CMHS can obviously save more than purely conventional drying with optimum drying conditions, i.e., initial weight of load and inlet hot air temperature. Furthermore, this study attempted drying biomaterials to find essential factors for the assessment of energy consumption and biomaterials, and coffee beans have been used as the dried sample. This study confirms that the estimation of energy consumption in different drying conditions should be done to obtain the optimum drying point before expanding to a commercial-sized drying process.

CONCLUSIONS

The application of microwave energy for drying coffee beans is investigated. A CMHS drying method has been developed and operated at different hot air temperature and initial coffee bean weight. Experimentally the coffee beans are of uniform size and are used in the drying experiments, which are carried out in several drying conditions: at hot air temperatures of 50°C, 60°C, and 70°C; with air velocity of 12 m/s; and a microwave power level of 800 W. CMHS drying is performed until the moisture content of the coffee bean reduced from the initial moisture content of 29% (db) to a level of approximately 10% (db). The energy efficiency and SEC related to drying kinetics involving all drying conditions are also estimated in drying process. The quality attributes of the fresh and dehydrated coffee bean are evaluated for color shades. The process parameters for CMHS

Downloaded by [Thammasat University Libraries] at 18:20 19 November 2014

drying are optimized for the coffee bean using initial weight variable tests (200 and 280 g). The results reveal that the CMHS drying method with the drying conditions of hot air temperature of 60°C, air velocity of 12 m/s, and initial coffee bean weight of 280 g gave a good quality dehydrated coffee bean and involved low SEC in the drying method. Further, the quality of coffee beans dehydrated by the CMHS drying method is found to be superior to the HASB drying method.

FUNDING

This work was supported by the Thailand Research Fund and National Research University Project of Thailand, Office of the Higher Education Commission.

Downloaded by [Thammasat University Libraries] at 18:20 19 November 2014

REFERENCES

1. R. F. Schiffmann, Microwave and Dielectric Drying, in A. S. Mujumdar (ed.), *Handbook of Industrial Drying*, 2nd ed., Marcel Dekker, New York, 1995.
2. A. C. Metaxas and R. J. Meridith, *Industrial Microwave Heating*, Peter Peregrinus, Ltd., London, pp. 5–103, 1983.
3. A. K. Datta and R. C. Anantheswaran, *Handbook of Microwave Technology for Food Applications*, Marcel Dekker, Inc., New York, pp. 69–114, 2001.
4. I. H. Boyaci, G. Sumnu, and O. Sakiyan, Estimation of Dielectric properties of Cakes Based on Porosity, Moisture Content and Formulations Using Statistical Methods and Artificial Neural Networks, *Food Bioproc. Technol.*, vol. 2, pp. 353–360, 2009.
5. R. Vadivambal and D. S. Jayas, Non-Uniform Temperature Distribution During Microwave Heating of Food Materials—A Review, *Food Bioproc. Technol.*, vol. 3, pp. 161–171, 2009.
6. P. Rattanadecho, K. Aoki, and M. Akahori, Experimental and Numerical Study of Microwave Drying in Unsaturated Porous Material, *Int. Commun. Heat Mass Transf.*, vol. 28, pp. 605–616, 2001.
7. E. I. Goksu, G. Sumnu, and A. Esin, Effect of Microwave on Fluidized Bed Drying of Macaroni Beads, *J. Food Eng.*, vol. 66, pp. 463–468, 2005.
8. H. Feng and J. Tang, Microwave Finish Drying of Diced Apple Slices in a Spouted Bed, *J. Food Sci.*, vol. 47, pp. 1499–1512, 1998.
9. Y. F. Feng, M. Zhang, H. Jiang, and J. C. Sun, Microwave-Assisted Spouted Bed Drying of Lettuce Cubes, *Dry. Technol.*, vol. 30, pp. 1482–1490, 2012.
10. I. Dincer and A. Z. Sahin, A New Model for Thermodynamic Analysis of a Drying Process, *Int. J. Heat Mass Transf.*, vol. 47, pp. 645–652, 2004.
11. R. Prommas, P. Rattanadecho, and D. Cholaseuk, Energy and Exergy Analyses in Drying Process of Porous Media Using Hot Air, *Int. Commun. Heat Mass Transf.*, vol. 37, pp. 372–378, 2010.
12. G. P. Sharma and S. Prasad, Specific Energy Consumption in Microwave Drying of Garlic Cloves, *J. Food Eng.*, vol. 31, pp. 1921–1926, 2005.
13. J. Varith, P. Dijkanarukkul, A. Achariyaviriya, and S. Achariyaviriya, Combined Microwave-Hot Air Drying of Peeled Longon, *J. Food Eng.*, vol. 81, pp. 459–468, 2007.
14. S. Lakshmi, A. Chakkaravarthi, R. Subramanian, and V. Singh, Energy Consumption in Microwave Cooking of Rice and Its Comparison with Other Domestic Appliances, *J. Food Eng.*, vol. 78, pp. 715–722, 2005.
15. I. Alibas, Energy Consumption and Color Characteristics of Nettle Leaves During Microwave, Vacuum and Convective Drying, *Biosyst. Eng.*, vol. 96, pp. 495–502, 2007.
16. G. Poli, R. Sola, and P. Veronesi, Microwave-Assisted Combustion Synthesis of NiAl Intermetallics in a Single Mode Applicator: Modeling And Optimization, *Mater. Sci. Eng.*, vol. 441, pp. 149–156, 2006.

17. J. Cheng, J. Zhou, Y. Li, J. Liu, and K. Cen, Improvement of Coal Water Slurry Property Through Coal Physicochemical Modifications by Microwave Irradiation and Thermal Heat, *Energy Fuels*, vol. 22, pp. 2422–2428, 2008.
18. W. Lipiński, E. Guillot, G. Olalde, and A. Steinfeld, Transmittance Enhancement of Packed-Bed Particulate Media, *Exp. Heat Transf.*, vol. 21, pp. 73–82, 2008.
19. E. Holtz, L. Ahrné, T. H. Karlsson, M. Rittenauer, and A. Rasmuson, The Role of Processing Parameters on Energy Efficiency During Microwave Convective Drying of Porous Materials, *Dry. Technol.*, vol. 27, pp. 173–185, 2009.
20. Y. Soysal, S. Öztekin, and Ö. Eren, Microwave Drying of Parsley: Modeling, Kinetics, and Energy Aspects, *Biosys. Eng.*, vol. 93, pp. 403–413, 2006.
21. M. Leiker and M. A. Adamska, Energy Efficiency and Drying Rates During Vacuum Microwave Drying of Wood, *Holz Roh Werkstoff*, vol. 62, pp. 203–208, 2004.
22. A. Gazis, D. Panousakis, J. Patterson, W. H. Chen, R. Chen, and J. Turner, Using in-Cylinder Gas Internal Energy Balance to Calibrate Cylinder Pressure Data and Estimate Residual Gas Amount in Gasoline Homogeneous Charge Compression Ignition Combustion, *Exp. Heat Transf.*, vol. 21, pp. 257–280, 2008.
23. S. Vongpradubchai and P. Rattanadecho, The Microwave Processing of Wood Using a Continuous Microwave Belt Drier, *Chem. Eng. Process*, vol. 33, pp. 472–481, 2009.
24. W. Jindarat, P. Rattanadecho, S. Vongpradubchai, and Y. Pianroj, Analysis of Energy Consumption in Drying Process of Non-Hygroscopic Porous Packed Bed Using a Combined Multi-Feed Microwave–Convective Air and Continuous Belt System, *Dry. Technol.*, vol. 29, pp. 926–938, 2011.
25. AOAC, *Official Methods of Analysis of AOAC International* (16th ed.), Arlington, VA, p. 42-1–42-2, 1995.

Downloaded by [Thammasat University Libraries] at 18:20 19 November 2014

This article was downloaded by: [Thammasat University Libraries]
On: 06 January 2014, At: 02:20
Publisher: Taylor & Francis
Informa Ltd Registered in England and Wales Registered Number: 1072954 Registered office: Mortimer House, 37-41 Mortimer Street, London W1T 3JH, UK

Drying Technology: An International Journal
Publication details, including instructions for authors and subscription information:
http://www.tandfonline.com/loi/ldrt20

Analysis of Energy Consumption in Drying Process of Biomaterials Using a Combined Unsymmetrical Double-Feed Microwave and Vacuum System (CUMV)—Case Study: Tea Leaves

W. Jindarat [a], S. Sungsoontorn [a] & P. Rattanadecho [a]
[a] Research Center of Microwave Utilization in Engineering (R.C.M.E.), Department of Mechanical Engineering, Faculty of Engineering, Thammasat University, Pathumthani, Thailand
Published online: 27 Jun 2013.

To cite this article: W. Jindarat, S. Sungsoontorn & P. Rattanadecho (2013) Analysis of Energy Consumption in Drying Process of Biomaterials Using a Combined Unsymmetrical Double-Feed Microwave and Vacuum System (CUMV)—Case Study: Tea Leaves, Drying Technology: An International Journal, 31:10, 1138-1147, DOI: 10.1080/07373937.2013.778863

To link to this article: http://dx.doi.org/10.1080/07373937.2013.778863

PLEASE SCROLL DOWN FOR ARTICLE

Taylor & Francis makes every effort to ensure the accuracy of all the information (the "Content") contained in the publications on our platform. However, Taylor & Francis, our agents, and our licensors make no representations or warranties whatsoever as to the accuracy, completeness, or suitability for any purpose of the Content. Any opinions and views expressed in this publication are the opinions and views of the authors, and are not the views of or endorsed by Taylor & Francis. The accuracy of the Content should not be relied upon and should be independently verified with primary sources of information. Taylor and Francis shall not be liable for any losses, actions, claims, proceedings, demands, costs, expenses, damages, and other liabilities whatsoever or howsoever caused arising directly or indirectly in connection with, in relation to or arising out of the use of the Content.

This article may be used for research, teaching, and private study purposes. Any substantial or systematic reproduction, redistribution, reselling, loan, sub-licensing, systematic supply, or distribution in any form to anyone is expressly forbidden. Terms & Conditions of access and use can be found at http://www.tandfonline.com/page/terms-and-conditions

Drying Technology, 31: 1138–1147, 2013
Copyright © 2013 Taylor & Francis Group, LLC
ISSN: 0737-3937 print/1532-2300 online
DOI: 10.1080/07373937.2013.778863

Taylor & Francis
Taylor & Francis Group

Analysis of Energy Consumption in Drying Process of Biomaterials Using a Combined Unsymmetrical Double-Feed Microwave and Vacuum System (CUMV)—Case Study: Tea Leaves

W. Jindarat, S. Sungsoontorn, and P. Rattanadecho
Research Center of Microwave Utilization in Engineering (R.C.M.E.), Department of Mechanical Engineering, Faculty of Engineering, Thammasat University, Pathumthani, Thailand

Downloaded by [Thammasat University Libraries] at 02:20 06 January 2014

An energy analysis of drying of biomaterials (tea leaves) was conducted on a combined unsymmetrical double-feed microwave and vacuum system (CUMV) to optimize the operating conditions and quality of the products. Tea leaves were dried from an initial moisture content of 172 to 7% (db). An energy consumption model based on the first law of thermodynamics was developed to evaluate energy efficiency. The influences of microwave power, vacuum pressure, and microwave operation modes on energy consumption were investigated in detail. The results showed that energy consumption as well as energy efficiency were strongly dependent on vacuum pressure and microwave power. Energy consumption and color parameters of the tea leaves were compared at different drying conditions. In particular, the experiments were carried out at different microwave powers (800 and 1,600 W) at a frequency of 2,450 MHz and different vacuum pressures (535 and 385 torr) to investigate the effects of these factors on the microwave–vacuum drying.

Keywords Energy efficiency; Microwave energy; Specific energy consumption; Vacuum pressure

INTRODUCTION

The most important thing in industry, in addition to producing high-quality products, is to increase productivity and reduce production cost. In general, several production processes for agricultural and industrial products are related to drying either by a natural method or using energy from other sources, resulting in a low production rate or high-cost products. Microwave drying is one of the most interesting methods for heating and drying materials.[1–6]

Microwave–vacuum (MV) drying is a novel alternative method of drying, producing products of acceptable quality. It permits a shorter drying time and a substantial improvement in the quality of dried materials compared to those dried with hot air and microwave drying methods. Other advantages include environmental friendliness at low temperature, which not only overcomes the limitation of low thermal conductivity of the material under vacuum due to the absence of drying medium but avoids defects such as internal cracking and interior burning caused by excessive heating in microwave drying. MV drying has been investigated as a potential method for obtaining high-quality dried foodstuffs, including fruits, vegetables, and grains.[7–14] Drouzas et al.[15] applied the MV technique to investigate the process of model fruit gel drying. They studied drying kinetics under different levels of pressure and microwave power. Sunjka et al.[16] dried cranberries using MV and microwave–hot air drying techniques and obtained a better quality product with MV drying. Alibas[17] studied the microwave, vacuum, and air drying characteristics of collard leaves. This author determined changes in the color values of the product after drying as well as the changes in the ascorbic acid (vitamin C) content of the product after drying and obtained the optimum drying method for the drying of collard. Wang et al.[18] studied corona discharge for stem lettuce cubes. Circular conduits of different diameters were used and compared with flat slab models at a high microwave frequency (2,450 MHz). Excellent reviews of the drying techniques in dielectric materials using microwave energy have been presented by Mujumdar,[19] Metaxas and Meridith,[20] Schubert and Regier,[21] Mejia-Meza et al.,[22] Setiady et al.,[23] Yaghmaee and Durance,[24] Jeni et al.,[25] Jindarat et al.,[26] Dincer and Sahin,[27] Sharma and Prasad,[28] Lakshmi et al.,[29] Alibas,[30] Holtz et al.,[31] Soysol et al.,[32] Leiker and Adamska,[33] Choicharoen et al.,[34] and Balbay and Şahin.[35]

Although combined MV drying has found some application in the dehydration of fruit juices, more research and development is necessary before the process can be used on a commercial scale. In particular, the effect of microwave power, vacuum pressure, and microwave operation modes on the drying kinetics should be known

Correspondence: P. Rattanadecho, Research Center of Microwave Utilization in Engineering (R.C.M.E.), Department of Mechanical Engineering, Faculty of Engineering, Thammasat University (Rangsit Campus), 99 Moo 18, Pathumthani 12120, Thailand; E-mail: ratphadu@engr.tu.ac.th

quantitatively, so that the drying system can be optimized from both cost and quality standpoints.

The main objective of this research is to examine the feasibility of using a combined unsymmetrical double-feed microwave and vacuum system (CUMV) to dry tea leaves and experimentally explore drying characteristics of tea leaves under different drying conditions, including microwave power, vacuum pressure, and microwave operation modes. The energy efficiency of development of the first law of thermodynamics is happen in heating process. At the same time, the research findings will provide a theoretical basis for further study and industrial application of combined microwave and vacuum technology in biomaterials drying.

RELATED THEORIES

Microwave Heat Generation

Microwave heating involves heat dissipation and microwave propagation, which causes the dipoles to vibrate and rotate. When the microwave energy is emitted from a microwave oscillator (P_{in}) and irradiated inside the microwave applicator, the dielectric material, which has a dielectric loss factor, absorbs the energy and is heated up. Then internal heat generation takes place. The basic equation for calculation of the density of microwave power absorbed by dielectric material (P_1) is given by[26]

$$P_1 = \omega \varepsilon_0 \varepsilon_r'' E^2 = 2\pi \cdot f \cdot \varepsilon_0 \cdot \varepsilon_r'(\tan\delta)E^2, \qquad (1)$$

where E is the electromagnetic field intensity; f is the microwave frequency; ω is the angular velocity of microwave; ε'_r is the relative dielectric constant; ε_0 is the dielectric constant of air in free space; and $\tan\delta$ is the dielectric loss tangent coefficient.

From Eq. (1), P_1 is directly proportional to the frequency of the applied electric field and dielectric loss tangent coefficient and root mean square value of the electric field. This means that as the $\tan\delta$ of specimen increases, energy absorption and heat generation are also increased. While $\tan\delta$ is small, microwaves will penetrate into the specimen without heat generation. However, the temperature increase depends on other factors, such as specific heat, size, and characteristics of the specimen.

When the material is heated unilaterally, it is found that as the dielectric constant and loss tangent coefficient vary, the penetration depth will be changed and the electric field within the dielectric material will be altered. The penetration depth is used to denote the depth at which the power density decreased to 37% of its initial value at the surface.[26]

$$D_p = \frac{1}{\frac{2\pi f}{\upsilon}\sqrt{\frac{\varepsilon'_r\left(\sqrt{1+\left(\frac{\varepsilon''_r}{\varepsilon'_r}\right)^2}-1\right)}{2}}} = \frac{1}{\frac{2\pi f}{\upsilon}\sqrt{\frac{\varepsilon'_r\left(\sqrt{1+(\tan\delta)^2}-1\right)}{2}}}, \qquad (2)$$

where D_P is penetration depth; ε''_r is relative dielectric loss factor; and υ is the microwave speed. The penetration depth of the microwave power is calculated according to Eq. (2), which shows how it depends on the dielectric properties of the material. It is noted that products with large dimensions and high loss factors may occasionally be overheated to a considerably thick layer on the outer layer. To prevent such phenomena, the power density must be chosen so that enough time is provided for the essential heat exchange between the boundary and the core. If the thickness of the material is less than the penetration depth, only a fraction of the supplied energy will be absorbed. Furthermore, the dielectric properties of biomaterial specimens typically show moderate lossiness depending on the actual composition of the material. A high moisture content reveals a greater potential for absorbing microwaves. For typical specimens in a porous packed bed, a decrease in the moisture content typically decreases ε''_r, accompanied by a slight increment in D_p.

In the analysis, energy, P_2, is required to heat up the dielectric material, W (g), placed in a microwave applicator. The initial temperature of the material, T_1, is raised to T_2. The energy P_2 can be estimated by the following calorific equation:[26]

$$P_2 = \frac{4.18 \cdot W \cdot C_p \cdot \Delta T}{t}, \qquad (3)$$

where W is the weight of the dielectric material; C_p is the specific heat of the dielectric material; ΔT is the increment of temperature ($T_2 - T_1$); and t is the heating time.

Assuming an ideal condition, all of the oscillated microwave energy (P_{in}) is absorbed into the dielectric material; internal heat generation as shown in Eq. (1) takes place. In this case, the relation between P_{in} and P_2 is shown below:[26]

$$P_{\text{in}} = P_2 \qquad (4)$$

From a practical point of view, however, the transformation energy in the applicator exists due to (1) the rate of microwave energy absorbed by means of the dielectric loss factor of the sample and (2) the energy loss in the microwave devices. Accordingly, by taking this transformation efficiency into account, the microwave oscillation output can be calculated by the following equations[26]:

$$P_{\text{in}} = \frac{P_2}{\eta_m} \qquad (5)$$

$$\eta_m = \frac{P_2}{P_{\text{in}}} \qquad (6)$$

Downloaded by [Thammasat University Libraries] at 02:20 06 January 2014

Downloaded by [Thammasat University Libraries] at 02:20 06 January 2014

Mass and Energy Balance Equations of the Drying Process

To analyze mass transfer in the drying process we applied the law of conservation of mass for the control volume as shown in Fig. 1. The mass balance equation can be written as:[26]

$$\frac{dm_{cv}}{dt} = m_{g1} - m_{g2} \tag{7}$$

Here, Eq. (7) is the mass rate balance for the control volume where m_{g1} and m_{g2} denote the mass flow rate at the inlet (1) and exit (2), respectively. Similarly, a balance of water in air flowing through the drying spouted bed leads to[26]

$$W_d \frac{dM_p}{dt} = m_a(X_1 - X_2), \tag{8}$$

where W_d is the weight of the dry material and M_p is the particle moisture content (db); this can be expressed as[26]

$$M_p = \frac{W_b - W_d}{W_d}, \tag{9}$$

where W_b is the weight of the material before drying; m_a is the mass flow rate of dry air; X_1 and X_2 denote the absolute humidity of inlet and exit air, respectively. The left-hand side of the mass balance equation (Eq. (10)) is the mass flow rate of water in the air flowing from the CUMV and can be written as[26]

$$m_w = m_a(X_2 - X_1). \tag{10}$$

To analyze energy transfer in the drying process, we applied the first law of thermodynamics (the law of conservation of energy) for the control volume as shown in Fig. 1. The significant heat transfer was due to the heat of

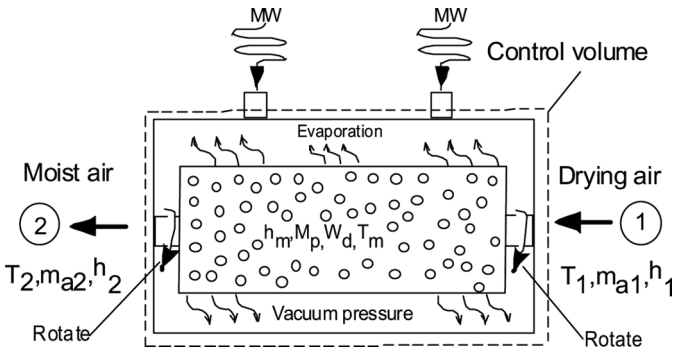

FIG. 1. Schematic of the control volume represented in the drying process using a combined unsymmetrical double-feed microwave and vacuum system (CUMV).

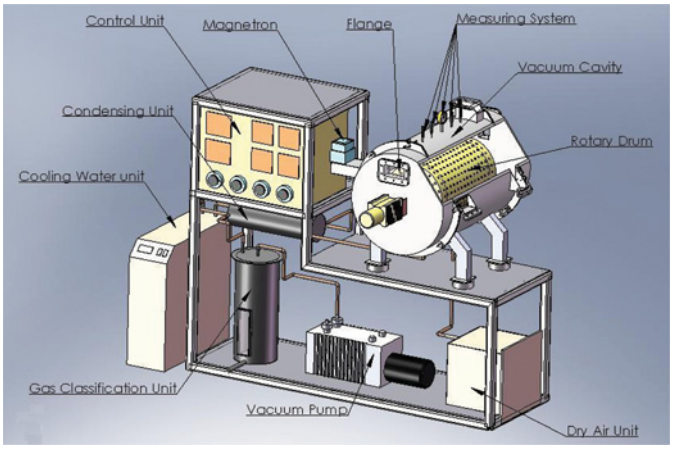

FIG. 2. Details of a combined unsymmetrical double-feed microwave and vacuum system (CUMV) (color figure available online).

evaporation between the solid and the drying air, and there was also heat rejection to the surroundings. The energy rate balance was simplified by ignoring kinetic and potential energies. Because the mass flow rate of the dry air and the mass of dry material within the control volume remain constant with time, the energy rate balance can be expressed as

$$\frac{W_d(h_{m2} - h_{m1})}{\Delta t} = Q_{\text{evap}} + m_a(h_1 - h_2) + Q_{MW} + Q_{\text{loss}}, \tag{11}$$

where Q_{evap} is heat transfer rate due to water evaporation; $Q_{MW} = P_{\text{in}}$ is the microwave energy; h_m is the enthalpy of the material; t is time; m_a is the mass flow rate of dry air; h is the enthalpy of dry air; and Q_{loss} is the heat transfer rate to the environment.

The differences in specific enthalpy are as follows, assuming air as an ideal gas:[26]

$$h_{m1} - h_o = c_m(T_{m1} - T_o) \tag{12}$$

$$h_{m2} - h_o = c_m(T_{m2} - T_o) \tag{13}$$

The material enthalpy term of the energy rate balance can be expressed as[26]

$$h_{m2} - h_{m1} = c_m(T_{m2} - T_{m1}), \tag{14}$$

where c_m represents the specific heat of the material. The enthalpy of moist air can be calculated by adding the contribution of each component as it exist in the mixture; thus, the enthalpy of moist air is[26]

$$h = h_a + Xh_v. \quad (15)$$

The heat transfer rate due to a phase change is[26]

$$Q_{\text{evap}} = m_w h_{fg}, \quad (16)$$

where h_{fg} is the latent heat of vaporization.

Specific Energy Consumption and Energy Efficiency of the Drying Process

The drying of biomaterial, a process of simultaneous heat and mass transfer, represents an energy-intensive operation of some industrial significance. The specific energy consumption is estimated, in CUMV drying processes, as a relationship between two values considering the total energy supplied to dry processes and amount of water removed during drying. A CUMV drying process is conducted in the same drying conditions, keeping the microwave power output at 800 and 1,600 W at an air velocity of 12 m/s. The specific energy consumption is as follows:

$$SEC = \frac{\text{Total energy supplied in drying process}}{\text{Amount of water removed during drying}}, \frac{\text{kJ}}{\text{kg}} \quad (17)$$

$$SEC = \frac{[P_{\text{in}} + m_{da}(h_1 - h_0)]\Delta t}{\text{Amount of water removed during drying}}, \frac{\text{kJ}}{\text{kg}} \quad (18)$$

The energy efficiency (η_e) for the drying process is represented by[26]

$$\eta_e = \frac{W_d[h_{fg}(M_{p1} - M_{p2}) + c_m(T_{m2} - T_{m1})]}{m_{da}(h_1 - h_o)\Delta t + \Delta t Q_{MW}}, \quad (19)$$

where c_m is the specific heat of the material.

MATERIAL AND METHODS

Materials

The experimental materials were tea leaves from a farm located in the northern part of Thailand that were stored at 10°C until the experiments. Three hours before drying, the bulk of tea leaves were left in the ambient air. The initial moisture content of the material was 172% (db). Three kilograms of tea leaves were applied with the CUMV.

Experimental Apparatus

An experimental stand for the commercialized tea leaves dryer using CUMV is shown in Fig. 3. The microwave power was generated by means of unsymmetrical double-feed magnetrons according to the design concept as shown in section 2 (two compressed air-cooled magnetrons of 800 W each for a maximum of 1.6 kW) operating at a frequency of 2,450 MHz. The microwave power setting could be adjusted individually in 800 W. The microwave was conveyed through a series of rectangular (11.0 × 5.5 cm) waveguides to a metallic vacuum cavity of 0.13 m^3 ($\pi \times 0.24^2 \times 0.72$ m) in which the materials to be dried can be rotated by a rotary drum in the cavity. The rotary drum has a maximum capacity of 30 kg (full load). The rotary drum installed in the multimode cavity was made of polypropylene with dimensions of approximately 30 cm radius and 50 cm length. The rotation speed of the rotary drum was controlled at about 10 rpm in order to enhance the interaction between microwave and the dielectric load. The maximum vacuum degree was about 50 torr.

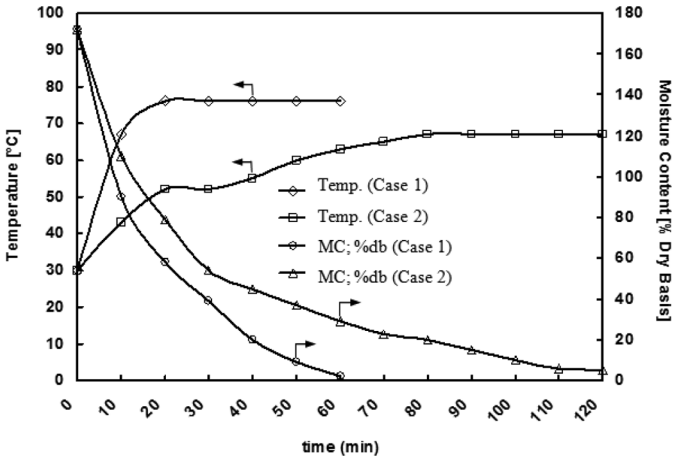

FIG. 3. Temperature and moisture variations versus elapsed times with respect to different drying conditions (microwave power 800 W, vacuum pressure 385 torr).

The CUMV drying experiments were carried out for two levels of microwave power (800 W: one magnetron turned on; 1,600 W: two magnetrons turned on) and two levels of vacuum pressure (385 and 535 torr). In this study, the system could be operated in either continuous or pulse mode. In the intermittent mode or pulsed microwave operation mode, the magnetron was alternately turned on and off for predetermined times. The pulsed microwave operation mode of 60 s on–60 s off was used in each experiment.

The moisture content (db) and dry matter content were measured according to the AOAC International standards,[36] using a laboratory scale with an accuracy of 0.01 g. Optical fiber (LUXTRON Fluoroptic Thermometer, model 790, Luxtron Corporation, Santa Clara, CA, USA; accuracy ±0.5°C) was employed to measure the average temperature of the bulk load in the cavity (the cavity temperature). Optical fibers were used instead of conventional thermocouples because the latter absorb microwave energy and produce erroneous temperature indications. An infrared camera was used to control the temperature in the cavity. An infrared camera (FLIR T200 Infrared Camera, Trek Equipment Corporation, USA) with a PC

Downloaded by [Thammasat University Libraries] at 02:20 06 January 2014

Downloaded by [Thammasat University Libraries] at 02:20 06 January 2014

interface was used to monitor the temperature inside the cavity and to facilitate feedback control of the process.

An infrared camera was used to measure the surface temperature of the samples (accurate to $\pm 0.5^{\circ}C$). In the CUMV process, the leakage of microwaves was prevented by the countermeasure in double with a combination of mechanical blocking filter and microwave absorber zone filter to be provided at the both covers' ends. The microwave leakage was controlled below the U.S. Department of Health and Human Services (DHHS)[37] standard of 5 mW/cm^2.

RESULTS AND DISCUSSION

Drying Kinetics

This section discusses the moisture content and average temperatures of a bulk load (cavity temperature) of tea leaves with respect to elapsed times and various drying conditions. Figures 3–6 show the tea leaf moisture content and average temperature of the bulk load (tea leaves) as influenced by applied microwave power, vacuum pressure, and microwave operation modes. Magnetron power as well as microwave operating mode had strong effects on the internal heat generation and drying rate of the dried samples.

Figures 3 and 4 show the cavity temperatures and tea leaf moisture content with respect to elapsed times at a microwave power of 800 W in case of continuous and pulsed operation modes. It is clear from the figure that the temperature profiles began to reach a steady-state plateau at approximately 20 and 50 min in continuous and pulsed microwave operation modes, respectively. For the continuous microwave operation mode, the cavity temperatures reached 75 and 77°C at vacuum pressures of 385 and 535 torr, respectively.

In the case of pulse microwave operation mode, the cavity temperatures reached 64 and 65°C at the vacuum pressures of 385 and 535 torr, respectively. Furthermore, for a microwave power of 1,600 W, the moisture content profiles of the bulk of tea leaves decreased faster than for a microwave power of 800 W, as shown in Figs. 3 and 4. The higher microwave power level as well as continuous microwave operation mode can increase the temperature and drying rate by providing more energy for water vaporization, thus accelerating moisture removal at higher temperature while the stronger vacuum pressure allows water to evaporate at lower temperature.

Figures 5 and 6 show the cavity temperature and tea leaf moisture content with respect to elapsed time at a microwave power of 1,600 W in case of continuous and pulsed operation modes. It is clear from the figures that the temperature profiles began to reach a steady state plateau at approximately 25 min; after this stage, the temperature remained constant. For the continuous microwave operation mode, the cavity temperatures reached 83 and 85°C at vacuum pressures of 385 and 535 torr, respectively. For the pulsed microwave operation mode, the cavity temperatures reached 64 and 66°C at vacuum pressures of 385 and 535 torr, respectively. The moisture content profiles for the bulk of tea leaves are also presented in both continuous and pulsed operation modes. It is clear from these curves that the moisture content profiles with respect to elapsed times were dependent on microwave operation mode and vacuum pressure. Furthermore, the total drying times were reduced substantially with changing the microwave operation modes compared to the variation in vacuum pressure level. In particular, in the case of continuous microwave operation mode where the supplied microwave energy continuously gives the more microwave energy absorbed rates, which leads to higher temperature and the moisture

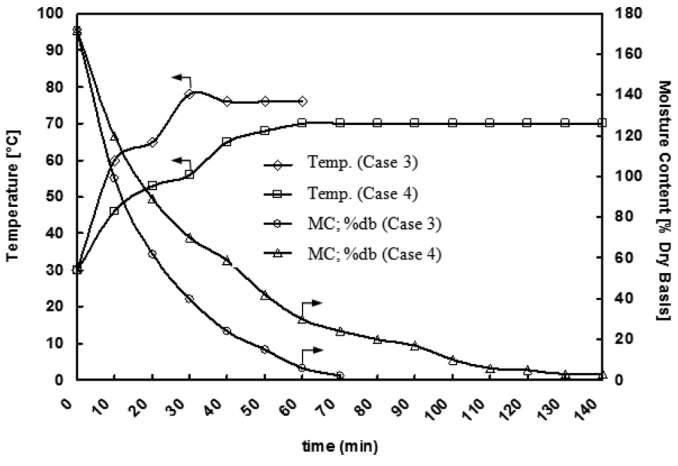

FIG. 4. Temperature and moisture variations versus elapsed times with respect to different drying conditions (microwave power 800 W, vacuum pressure 535 torr).

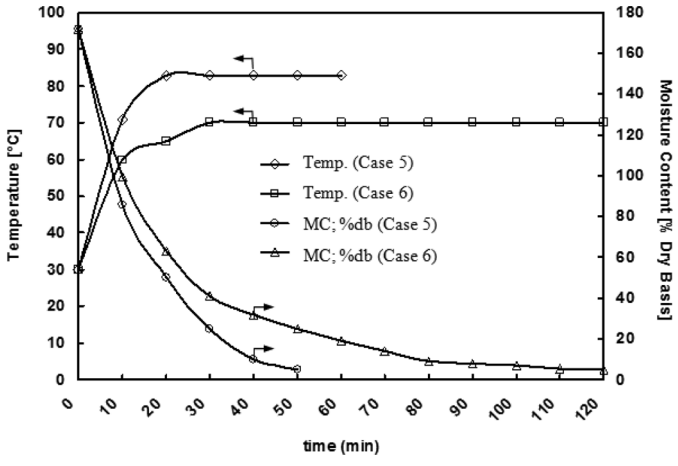

FIG. 5. Temperature and moisture variations versus elapsed times with respect to different drying conditions (microwave power 1,600 W, vacuum pressure 385 torr).

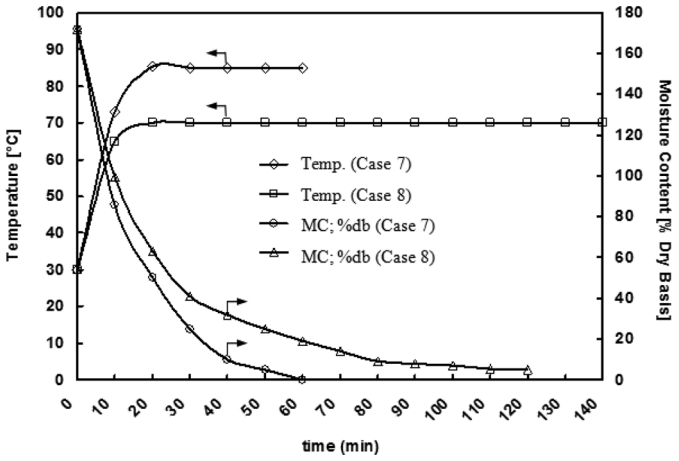

FIG. 6. Temperature and moisture variations versus elapsed times with respect to different drying conditions (microwave power 1,600 W, vacuum pressure 535 torr).

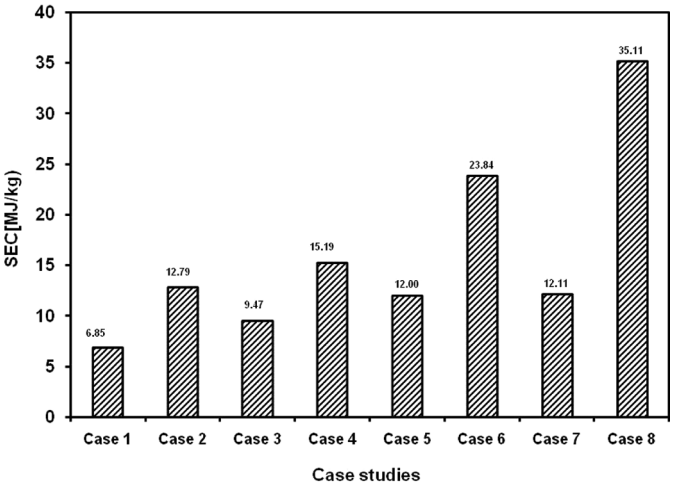

FIG. 7. Variations in specific energy consumption as a function of different drying conditions.

transfer rates within the dried samples. For continuous microwave operation mode at a microwave power of 1,600 W, the drying time for tea leaves was 50 min at a vacuum pressure of 385 torr, and the drying time was 60 min at a vacuum pressure of 535 torr. Nevertheless, the bulk of tea leaves considered as low-lossy dielectric materials, which corresponds to the lower microwave energy absorbed compared to other high-lossy dielectric materials (strawberries, beef, etc.) during CUMV.

Analysis of Specific Energy Consumption

Experimental data were analyzed to obtain the specific energy consumption under different drying conditions as listed in Table 1. Figure 7 shows the variations in specific energy consumption as a function of different drying conditions during CUMV drying of tea leaves. The lowest value in all drying conditions regarding energy consumption was noted in case 1 (6.85 MJ/kg), whereas the highest value noted was in case 8 (35.11 MJ/kg). The order of

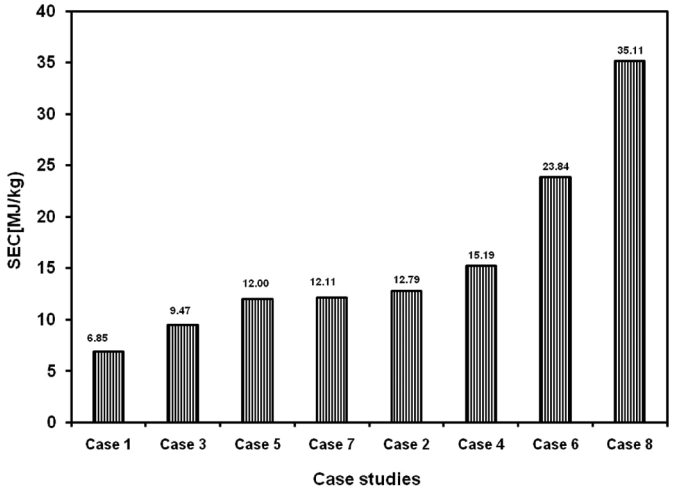

FIG. 8. Ordering of specific energy consumption for different drying conditions.

TABLE 1
Specific energy consumption under various drying conditions

Test condition	Microwave power (W)	Vacuum pressure (torr)	Microwave operation modes	Specific energy consumption (MJ/kg)
Case 1	800	385	Continuous	6.85
Case 2	800	385	Pulsed	12.79
Case 3	800	535	Continuous	9.47
Case 4	800	535	Pulsed	15.19
Case 5	1,600	385	Continuous	12.00
Case 6	1,600	385	Pulsed	23.84
Case 7	1,600	535	Continuous	12.11
Case 8	1,600	535	Pulsed	35.11

Downloaded by [Thammasat University Libraries] at 02:20 06 January 2014

Downloaded by [Thammasat University Libraries] at 02:20 06 January 2014

specific energy consumption for different drying conditions is shown in Fig. 8. The lowest specific energy consumption occurred in case 1 (6.85 MJ/kg), followed by case 3 (9.47 MJ/kg), case 5 (12.00 MJ/kg), case 7 (12.11 MJ/kg), case 2 (12.19 MJ/kg), case 4 (15.19 MJ/kg), case 6 (23.84 MJ/kg), and case 8 (35.11 MJ/kg). To summarize, the specific energy consumption for continuous microwave operation mode was always lower than that for pulsed microwave operation mode at the same microwave power and vacuum pressure. This is because the continuous microwave operation mode continuously supplied microwave energy through the cavity, which led to more microwave energy being absorbed in the bulk of tea leaves, resulting in a higher rate of water evaporation compared to pulsed microwave operation mode.

Energy Efficiency

The influence of microwave power, vacuum pressure, and microwave operation modes on energy efficiency (%) was investigated. The energy efficiency versus elapsed times with respect to different drying conditions of CUMV drying is illustrated in Figs. 9 and 10.

In Figs. 9 and 10, the energy efficiency profiles for all cases of CUMV drying increased quickly in the early stages of drying (about 0–10 min). However, the efficiency decreased rapidly after this stage (about 10–40 min). It is evident from the figures that the moisture content inside the bulk of tea leaves was substantially reduced in the early stages of drying. It is noted that bulk tea leaves have a low moisture content and act as a low dielectric material. During drying, this causes a decrease in the microwave energy absorbed. Consequently, the energy efficiency profiles decrease in this stage of drying. There is a difference between the energy efficiency of a microwave power of 800 W and a microwave power of 1,600 W using CUMV. Observations showed that the energy efficiency of a microwave power of 800 W (Fig. 9) was greater than that at a microwave power of 1,600 W in CUMV drying, as shown in Fig. 10. For the entering continuous microwave operation mode, the efficiency increased with a decrease in vacuum pressure (385 torr), as expected. This was because the stronger vacuum condition led to a higher rate of water evaporation inside the bulk tea leaves. This result of a higher rate of water evaporation corresponds to a higher energy efficiency, as shown in Fig. 9. Nevertheless, the trends of efficiency profiles in both figures displayed an unusual shape. This was due to the interaction between microwave and the dielectric sample (bulk of tea leaves) inside the rotary drum installed in the multimode cavity, which resulted in no control of the internal heat generation in the sample load.

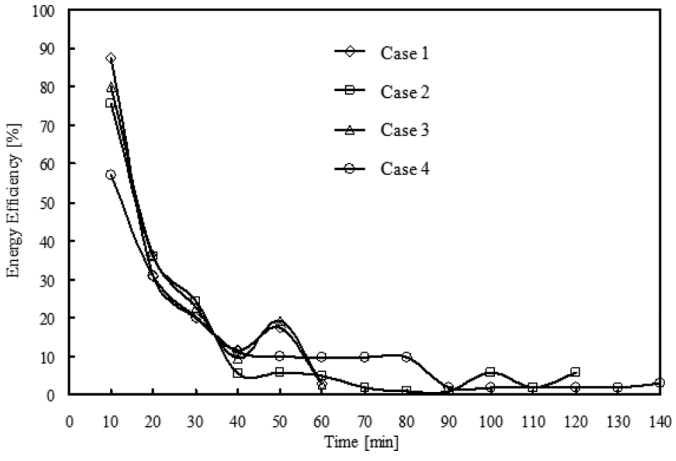

FIG. 9. Energy efficiency versus elapsed times with respect to different drying conditions (microwave power 800 W).

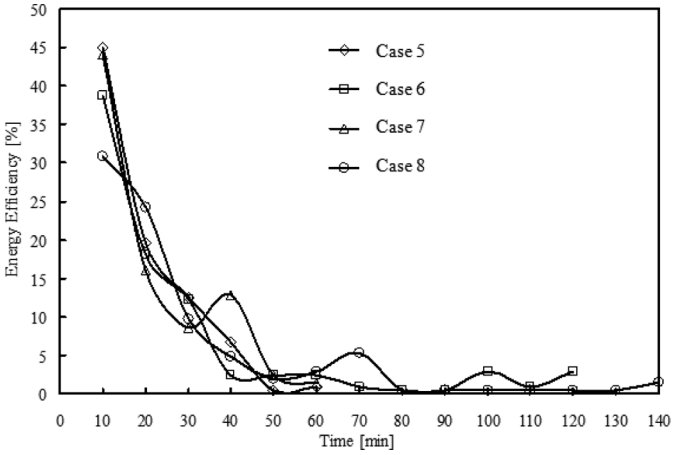

FIG. 10. Energy efficiency versus elapsed times with respect to different drying conditions (microwave power 1,600 W).

It should be noted that the energy efficiency was very low for all testing conditions. This was because all tests were performed on very small loads (initial weight of tea leaves was 3 kg/batch). Actually, the energy efficiency increased with increasing load when it approached the optimum design load (about 30 kg for a full load in the rotary drum). This was due to the increasing bulk of tea leaves corresponding to the highest rate of water evaporation using CUMV drying. In future work, the effects of initial weight on energy consumption as well as energy efficiency will be investigated.

Figure 11 shows that the best color values were achieved during continuous microwave drying. Figures 11a and 11b show the rough color shades of tea leaves dried with pulsed and continuous microwave operation modes, respectively. It can be observed that magnetron control affected the physical appearance of the tea leaves. It is clear from these figures that the pulsed microwave operation mode resulted in a better physical appearance than continuous microwave operation mode. As mentioned in previous work,[26] microwave energy consumption can save potentially more than

FIG. 11. Color parameter of the tea leaves dried in microwave operation mode (vacuum pressure of 385 torr, microwave power of 800 W): (a) pulsed microwave operation mode and (b) continuous microwave operation mode (color figure available online).

the purely conventional drying. Nevertheless, in this primary study aimed on drying of tea leaves, which has a lack of essential factors for assessment the energy consumption and biomaterials; that is, tea leaves has used in specific purpose in food or herb industries is produced in general purpose; therefore, estimate on energy consumption in biomaterials is suitable to perform.

CONCLUSIONS

The influence of drying conditions on the CUMV drying of tea leaves was evaluated based on the drying parameters, such as microwave power, vacuum pressure, and microwave operation modes with drying time. The results showed that energy consumption was dependent on our purpose parameters. Based on the experimental investigation and energy consumption analysis in CUMV drying, the following conclusions were drawn.

1. CUMV drying is more rapid in the continuous microwave operation mode than in the pulsed microwave operation mode.
2. The specific energy consumption values were relatively low in continuous microwave operation mode compared to those obtained for pulsed microwave operation mode. This was because the continuous microwave operation mode continuously supplied microwave energy through the cavity, which led to more microwave energy being absorbed in the bulk tea leaves, resulting in a higher rate of water evaporation compared to pulsed microwave operation mode. In contrast to the energy consumption results, the tea leaves dried with pulsed microwave operation mode had a better physical appearance than those obtained from continuous microwave operation mode.
3. The effects of microwave power, vacuum pressure, and microwave operation modes during CUMV drying on energy consumption as well as energy efficiency under different drying conditions were clarified.

NOMENCLATURE

C_p	Specific heat of the dielectric material (kJ/kg.K)
c_m	Material specific heat (kJ/kg·K)
D_p	Penetration depth (m)
E	Electromagnetic field intensity (V/cm)
f	Microwave frequency (Hz)
h	Enthalpy (kJ/kg)
h_{fg}	Latent heat of vaporization (kJ/kg_{water})
h_m	Enthalpy of material (kJ/kg)
M_p	Particle moisture content, db (kg_{water}/kg_{solid})
m	Mass flow rate (kg/s)
m_a	Mass flow rate of dry air (kg/s)
m_{cv}	Mass rate balance for the control volume (kg/s)
m_w	Mass flow rate of water from the CUMV (kg/s)
P_{in}	Microwave power incident (kW)
P_1	Density of microwave power absorbed by dielectric material (kW/cm^3)
P_2	Energy required to heat up the dielectric material (kW)
Q_{evap}	Heat transfer rate due to water evaporation (kW)
Q_{loss}	Heat transfer rate to the environment (kW)
Q_{MW}	Microwave energy (kW)
SEC	Specific energy consumption (MJ/kg)
T	Temperature (°C)
ΔT	Increment temperature (°C)
t	Time (s)
$\tan\delta$	Loss tangent coefficient
W	Weight of the dielectric material (kg)
W_b	Weight of material before drying (kg)
W_d	Weight of dry material (kg)
X	Absolute humidity (kg_{vapor}/kg_{dryair})

Greek Letters

ε'_r	Relative dielectric constant
ε''_r	Relative dielectric loss factor
ε_0	Permittivity of air (F/m)
η_e	Energy efficiency (%)
η_m	Microwave efficiency device (%)
υ	Velocity of propagation (m/s)
ω	Angular velocity of microwave (rad/s)

Subscripts

o	Surroundings; reference environment
a	Air
ab	Absorb
d	Dry material
da	Drying air
fg	Difference in property between saturated liquid and saturated vapor

Downloaded by [Thammasat University Libraries] at 02:20 06 January 2014

g	Gas
in	Input
l	Liquid water
m	Material
out	Output
r	Relative
s	Solid
v	Vapor
w	Water
0	Free space
1	Inlet
2	Outlet

Downloaded by [Thammasat University Libraries] at 02:20 06 January 2014

ACKNOWLEDGMENTS

The authors gratefully acknowledge the Thailand Research Fund and the National Research University Project of Thailand Office of Higher Education Commission for supporting this research project.

REFERENCES

1. Ayappa, K.G.; Davis, H.T.; Davis, E.A.; Gordon, J. Analysis of microwave heating of materials with temperature dependent properties. *AIChE Journal* **1991**, *37*(3), 313–322.
2. Perre, P.; Turner, W. Microwave drying of softwood in an oversized waveguide. *AIChE Journal* **1997**, *43*(10), 2579–2595.
3. Rattanadecho, P.; Suwannapum, N.; Watanasungsuit, A.; Atong, D. Drying of dielectric materials using microwave–continuous belt furnace. *ASME Journal of Manufacturing Sciences and Engineering* **2007**, *129*(1), 157–163.
4. Rattanadecho, P.; Suwannapum, N.; Chatveera, B.; Atong, D.; Makul, N. Development of compressive strength of cement paste under accelerated curing by using a continuous microwave belt drier. *Material Science and Engineering* **2008**, *472*, 299–307.
5. Vongpradubchai, V.; Rattanadecho, P. The microwave processing of wood using a continuous microwave belt drier. *Chemical Engineering and Processing* **2009**, *33*, 472–481.
6. Suwannapum, N.; Rattanadecho, P. Analysis of heat–mass transport and pressure buildup induced inside unsaturated porous media subjected to microwave energy using a single (TE10) mode cavity. *Drying Technology* **2011**, *29*(9), 1010–1024.
7. Cui, Z.W.; Xu, S.Y.; Sun, D.W. Dehydration of garlic slices by combined microwave–vacuum and air drying. *Drying Technology* **2003**, *21*(7), 1173–1185.
8. Cui, Z.W.; Xu, S.Y.; Sun, D.W. Effect of microwave–vacuum drying on the carotenoids retention of carrot slices and chlorophyll retention of Chinese chive leaves. *Drying Technology* **2004**, *22*(3), 561–574.
9. Drouzas, A.E.; Schubert, H. Microwave application in vacuum drying of fruits. *Journal of Food Engineering* **1996**, *28*, 203–209.
10. Kaensup, W.; Chutima, S.; Wongwises, S. Experimental study on drying of chilli in a combined microwave–vacuum–rotary drum dryer. *Drying Technology* **2002**, *20*(10), 2067–2079.
11. Lin, T.M.; Durance, T.D.; Scaman, C.H. Physical and sensory properties of vacuum microwave dehydrated shrimp. *Journal of Aquatic Food Product Technology* **1999**, *8*(4), 41–53.
12. Wadsworth, J.I.; Velupillai, L.; Verma, L.R. Microwave–vacuum drying of parboiled rice. *Transactions of the ASAE* **1990**, *33*(1), 199–210.
13. Yongsawatdigul, J.; Gunasekaran, S. Pulsed microwave–vacuum drying of cranberries, part I: Energy use and efficiency. *Journal of Food Processing and Preservation* **1996**, *20*(2), 121–143.
14. Yongsawatdigul, J.; Gunasekaran, S. Pulsed microwave–vacuum drying of cranberries, part II: Quality evaluation. *Journal of Food Processing and Preservation* **1996**, *20*(3), 145–156.
15. Drouzas, A.E.; Tsami, E.; Saravacos, G.D. Microwave/vacuum drying of model fruit gels. *Journal of Food Engineering* **1999**, *39*, 117–122.
16. Sunjka, P.S.; Rennie, T.J.; Beaudry, C.; Raghavan, G.S.V. Microwave–convective and microwave–vacuum drying of cranberries: A comparative study. *Drying Technology* **2004**, *22*(5), 1217–1231.
17. Alibas, I. Microwave, vacuum, and air drying characteristics of collard leaves. *Drying Technology* **2009**, *27*(11), 1266–1273.
18. Wang, Y.; Zhang, M.; Mujumdar, A.S.; Mothibe, K.J. Experimental investigation and mechanism analysis on microwave freeze drying of stem lettuce cubes in a circular conduit. *Drying Technology* **2012**, *30*(11–12), 1377–1386.
19. Mujumdar, A.S. *Handbook of Industrial Drying*, 2nd Ed.; Marcel Dekker: New York, 1995.
20. Metaxas, A.C.; Meridith, R.J. *Industrial Microwave Heating*; Peter Peregrinus, Ltd.: London, 1983.
21. Schubert, H.; Regier, M. *The Microwave Processing of Foods*; Woodhead Publishing Limited: Cambridge, UK, 2005.
22. Mejia-Meza, E.I.; Yanez, J.A.; Davies, N.M.; Rasco, B.; Younce, F.; Remsberg, C.M.; Clary, C. Improving nutritional value of dried blueberries (*Vaccinium corymbosum* L.) combining microwave–vacuum, hot-air drying and freeze drying technologies. *International Journal of Food Engineering* **2008**, *4*(5), Art. 5.
23. Setiady, D.; Clary, C.; Younce, F.; Rasco, B.A. Optimizing drying conditions for microwave–vacuum (MIVAC®) drying of russet potatoes (*Solanum tuberosum*). *Drying Technology* **2007**, *25*(9), 1479–1485.
24. Yaghmaee, P.; Durance, T. Efficacy of vacuum microwave drying in microbial decontamination of dried vegetables. *Drying Technology* **2007**, *25*(6), 1099–1104.
25. Jeni, K.; Yapa, M.; Rattanadecho, P. Design and analysis of the commercialized drier processing using a combined unsymmetrical double-feed microwave and vacuum system (case study: Tea leaves). *Chemical Engineering and Processing* **2010**, *49*, 389–395.
26. Jindarat, W.; Rattanadecho, P.; Vongpradubchai, S.; Pianroj, Y. Analysis of energy consumption in drying process of non-hygroscopic porous packed bed using a combined multi-feed microwave–convective air and continuous belt system. *Drying Technology* **2011**, *29*, 926–938.
27. Dincer, I.; Sahin, A.Z. A new model for thermodynamic analysis of a drying process. *International Journal of Heat and Mass Transfer* **2004**, *47*, 645–652.
28. Sharma, G.P.; Prasad, S. Specific energy consumption in microwave drying of garlic cloves. *Journal of Food Engineering* **2005**, *31*, 1921–1926.
29. Lakshmi, S.; Chakkaravarthi, A.; Subramanian, R.; Singh, V. Energy consumption in microwave cooking of rice and its comparison with other domestic appliances. *Journal of Food Engineering* **2005**, *78*, 715–722.
30. Alibas, I. Energy consumption and colour characteristics of nettle leaves during microwave, vacuum and convective drying. *Biosystems Engineering* **2007**, *96*(4), 495–502.
31. Holtz, E.; Ahrné, L.; Karlsson, T.H.; Rittenauer, M.; Rasmuson, A. The role of processing parameters on energy efficiency during microwave convective drying of porous materials. *Drying Technology* **2009**, *27*, 173–185.
32. Soysal, Y.; Öztekin, S.; Eren, Ö. Microwave drying of parsley: Modelling, kinetics, and energy aspects. *Biosystems Engineering* **2006**, *93*(4), 403–413.

33. Leiker, M.; Adamska, M.A. Energy efficiency and drying rates during vacuum microwave drying of wood. *Holz als Roh- und Werkstoff* **2004**, *62*, 203–208.
34. Choicharoen, K.; Devahastin, S.; Soponronnarit, S. Comparative evaluation of performance and energy consumption of hot air and superheated steam impinging stream dryers for high-moisture particulate materials. *Applied Thermal Engineering* **2011**, *31*(16), 3444–3452.
35. Balbay, A.; Şahin, Ö. Microwave drying kinetics of a thin-layer liquorice root. *Drying Technology* **2012**, *30*(8), 859–864.
36. AOAC International. *Official Methods of Analysis of AOAC International*, 16th Ed.; Association of Official Analytical Chemists: Washington, DC; 1995.
37. U.S Department of Health and Human Services (DHHS). National Institute for Occupational Safety and Health (NIOSH) Publication 1979, 80–107.

Downloaded by [Thammasat University Libraries] at 02:20 06 January 2014

International Journal of Heat and Mass Transfer 65 (2013) 389–399

Contents lists available at SciVerse ScienceDirect

International Journal of Heat and Mass Transfer

journal homepage: www.elsevier.com/locate/ijhmt

Electromagnetic field effects on biological materials

Pornthip Keangin [a,b], Kambiz Vafai [b,*], Phadungsak Rattanadecho [a]

[a] Department of Mechanical Engineering, Faculty of Engineering, Thammasat University (Rangsit Campus), 99 moo 18, Klong Luang, Pathum Thani 12120, Thailand
[b] Department of Mechanical Engineering, Faculty of Engineering, University of California, A363 Bourns Hall, Riverside, CA 2507-0425, USA

ARTICLE INFO

Article history:
Received 24 May 2013
Received in revised form 17 June 2013
Accepted 17 June 2013
Available online 9 July 2013

Keywords:
Biological materials
Electromagnetic field
Finite element
Local thermal non-equilibrium
Porous medium
Temperature profiles

ABSTRACT

In this study, the effect of an imposed electromagnetic field on biological media is analyzed. The local thermal non-equilibrium (LTNE) is taken into account by solving the two-energy equation model for tissue and blood phases. A comprehensive examination of heat transport through biological media is carried out including thermal conduction in tissue and vascular system, blood-tissue convective heat exchange, metabolic heat generation and imposed heat flux. The primary biological media, i.e., bone, liver, cornea, fat, skin and brain are considered in our analysis. The effects of variations of dimensionless electromagnetic wave power and dimensionless electromagnetic wave frequency on the dimensionless tissue and blood temperature profiles are systematically investigated. Results are obtained for a range of dimensionless electromagnetic wave power from 1 to 500 and dimensionless electromagnetic wave frequency from 0.2 to 2. The coupled equations of electromagnetic wave propagation and heat transfer under LTNE assumption are solved using the finite element method (FEM). This investigation provides the essential aspects for a fundamental understanding of heat transport within biological materials while experiencing an applied electromagnetic field such as applications related to the cancer thermal ablation and can be used as a guideline for these types of treatments.

© 2013 Elsevier Ltd. All rights reserved.

1. Introduction

The modeling of heat transport within biological materials is quite important and has been used extensively in medical thermal therapeutic applications for predicting the temperature during these processes. In recent years, utilization of an imposed electromagnetic field in various applications has increased since the electromagnetic wave can penetrate the surface and is converted into thermal energy very rapidly within the material. Various electromagnetic wave applications have been used in many industrial and household applications. For example, for drying, pasteurization, sterilization, heating processes, etc. [1]. Recently, electromagnetic wave has been introduced as a rapid method of delivering high temperatures to destroy the cancer cells during thermal ablation [2,3]. The imposed electromagnetic field interacts with the material and results in a variety of thermal effects. Various effects such as an increase in temperature as result of electromagnetic radiation on materials are gaining widespread attention, particularly in biological materials [4,5]. However, the resulting thermo-physiologic response of the biological materials subject to an electromagnetic field is not well understood due to the complexity of the configurations in biological materials. The severity of the physiological effect produced by small temperature increases can be expected to worsen in sensitive organs. An increase of approximately 1–5 °C in human body temperature can cause numerous malformations, temporary infertility in males, brain lesions, and blood chemistry changes [6]. In order to gain insight into the phenomena occurring within the biological materials subject to an imposed electromagnetic field, detailed knowledge of the electromagnetic radiation absorption is necessary. A detailed investigation is necessary to demonstrate the effects of electromagnetic radiation absorption in biological materials. Furthermore, numerical simulation under various conditions can be utilized to demonstrate and indentify the fundamental parameters as well as provide guidance for different applications.

Studies of heat transport through biological materials, involves thermal conduction in tissue and vascular system, blood-tissue convection and perfusion (through capillary tubes within the tissues) as well as metabolic heat generation [6–10]. Wessapan et al. [6] have carried out a numerical analysis of specific absorption rate (SAR) and heat transfer in human body due to an electromagnetic field leakage. Keangin et al. [10] carried out the numerical simulation of liver cancer treatment using the microwave antenna.

A biological tissue can be represented by a microvascular bed with blood flow through many vessels, through which blood flows and can be regarded as a porous structure [7]. Utilizing porous media theory in modeling heat transfer results in fewer

* Corresponding author.
E-mail addresses: vafai@engr.ucr.edu (K. Vafai), ratphadu@engr.tu.ac.th (P. Rattanadecho).

0017-9310/$ - see front matter © 2013 Elsevier Ltd. All rights reserved.
http://dx.doi.org/10.1016/j.ijheatmasstransfer.2013.06.039

Nomenclatures

a_{tb}	specific surface area between the blood and the tissue (m^2/m^3)
Bi	Biot number, $Bi = \frac{h_{tb}a_{tb}H^2}{K_{t,eff}}$
c_p	specific heat capacity (J/kg °C)
E	electric field (V/m)
f	electromagnetic wave frequency (Hz)
h_{tb}	interfacial heat transfer coefficient between the lumen and the tissue (W/m^2 °C)
H	height of the biological material (m)
k_0	free space wave number (m^{-1})
K	thermal conductivity (W/m °C)
L	length of the biological material (m)
P	electromagnetic wave power (W)
q_s	heat flux at the surface (W/m^2)
Q	heat source (W/m^3)
T	temperature (°C)
u	lumen velocity (m/s)
x	longitudinal coordinate (m)
y	transverse coordinate (m)

Greek Symbols

ε	porosity (the ratio of the volume fraction of the vascular space to the space occupied by the extra-vascular space) (–)
η	dimensionless transverse coordinate, $\eta = \frac{y}{D}$
Φ	dimensionless heat generation within the biological material, $\Phi = \frac{(1-\varepsilon)HQ_{met}}{q_s}$
κ	ratio of the effective blood thermal conductivity to that of the tissue, $\kappa = \frac{K_{b,eff}}{K_{t,eff}}$
ρ	density (kg/m^3)
θ	dimensionless temperature, $\theta = \frac{K_{t,eff}\langle\langle T\rangle - T_s\rangle}{q_s H}$
μ	magnetic permeability (H/m)
γ	permittivity (F/m)
σ	electric conductivity (S/m)
ω	angular frequency (rad/s)

Subscripts

b	blood phase
c	cut off
eff	effective property
ext	external
met	metabolic
r	relative
s	surface
t	tissue phase
tb	tissue to blood
0	free space, initial condition

Abbreviations

FEM	finite element method
LTNE	local thermal non-equilibrium

assumptions as compared to different established bioheat transfer models [7–9]. Depiction of heat transport through a porous medium has been of interest for many decades. Two different models are used for analyzing heat transfer in a porous medium; local thermal equilibrium (LTE) and local thermal non-equilibrium (LTNE) [11–15]. The LTE model is based on the assumption that the tissue phase temperature is equal to blood phase temperature everywhere in the porous medium and referred to as the one equation model [7,11–13]. This assumption is not suitable for a number of physical situations [7]. In recent years, the LTNE model has received more attention to demonstrate the heat transport in biological media [7–9,16,17]. Utilizing the porous media theory, LTNE between the tissue and the blood phase is addressed and the tissue-blood convective heat exchange is taken into account. Volume averaging over each of the tissue and blood phases results in energy equations for each individual phase. Studies of heat transport under LTNE in biological media has been established in the literature [8,9]. Mahjoob and Vafai [8] analyzed characterization of heat transport through biological media incorporating hyperthermia treatment, utilizing the LTNE model. They had obtained detailed exact solutions for the tissue and blood temperature profiles. Mahjoob and Vafai [9] analyzed characterization of bioheat transport

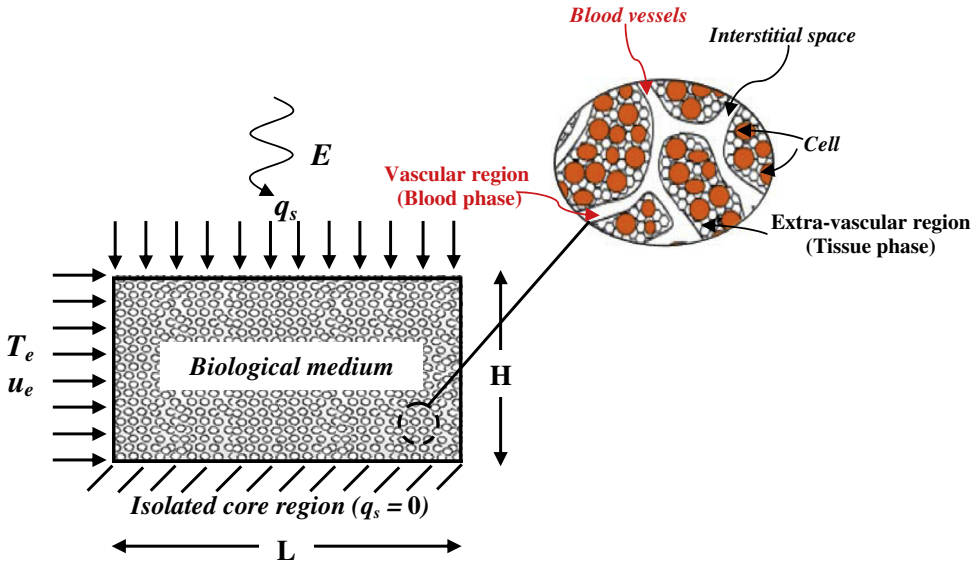

Fig. 1. Schematic diagram of a biological medium subject to an electromagnetic field.

Table 1
Thermal and dielectric properties of biological media used in the computations [6,24–30].

Biological materials	Density ρ (kg/m^3)	Thermal conductivity K (W/m °C)	Specific heat capacity C_p (J/kg °C)	Porosity ε	Relative permittivity γ_r	Electric conductivity σ (S/m)
Liver	1030 [6]	0.497 [6]	3600[6]	0.6 [24]	43.0 [6]	1.69 [6]
Brain	1038 [30]	0.535 [30]	3650 [30]	0.2 [26]	45.805 [30]	0.765 [30]
Cornea	1050 [29]	0.58 [29]	4178 [29]	0.6 [29]	52.0 [29]	1.85 [29]
Skin	1125 [6]	0.35 [6]	3437 [6]	0.2 [27]	44.86 [6]	0.92 [6]
Bone	1038 [6]	0.436 [6]	1300 [6]	0.75 [28]	44.80 [6]	2.10 [6]
Fat	916 [6]	0.22 [6]	2300 [6]	0.17 [25]	5.97 [6]	0.09 [6]
Blood	1058 [6]	0.45 [6]	3960 [6]	1.0 [27]	58.30 [6]	2.54 [6]

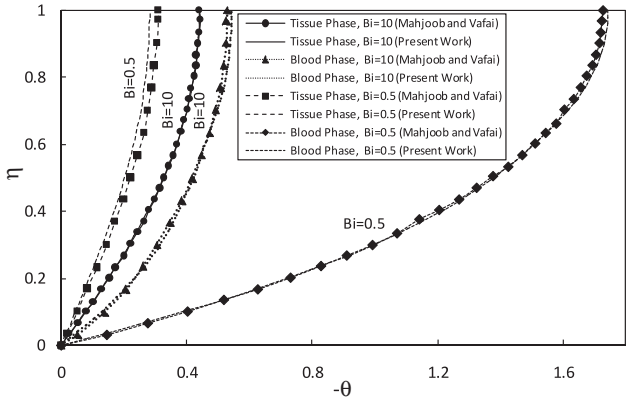

Fig. 2. Comparison of the tissue and blood temperature profiles obtained from the present numerical results and the analytical results by Mahjoob and Vafai [8] for $\varepsilon = 0.1$, $\Phi = 0$ and $\kappa = 0.111$ at Bi = 10 and Bi = 0.5.

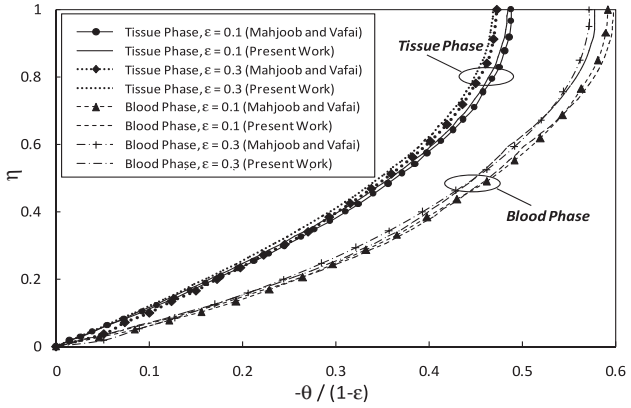

Fig. 3. Comparison of the tissue and blood temperature profiles obtained from the present numerical results and the analytical results by Mahjoob and Vafai [8] for $\Phi(1-\varepsilon) = 0.022$ and $\kappa = 0.111$ at Bi = 10 with $\varepsilon = 0.1$ and $\varepsilon = 0.3$.

through a dual layer biological media. The effect of the vascular volume fraction and metabolic heat generation on the temperature within the biological media was discussed in their work and detailed exact solutions were obtained. Belmiloudi [18] analyzed the temperature distribution in biofluid heat transfer during thermal therapy based on LTNE model. Afrin et al. [19] presented a model of thermal lagging in living biological tissue based on LTNE heat transfer model between tissue, arterial and venous bloods. It was found that the phase lag times for heat flux and temperature gradient are identical for the case when the tissue and blood have the same properties.

While there have been studies on heat transport based on LTNE assumption, very few works have studied electromagnetic wave propagation coupled with heat transfer based on LTNE model. Furthermore, only few prior studies have concentrated on the effect of electromagnetic field such as electromagnetic wave power and electromagnetic wave frequency particularly as applied to biological materials due to the complexity of the problem. To gain insight into the process occurring within the biological tissues subject to an imposed electromagnetic field, it is essential to study temperature distribution within a biological tissue during cancer thermal ablation. As such it is necessary to obtain a detailed knowledge of the electromagnetic radiation absorption coupled with heat transport. Biological tissues have different properties and response times for disturbances, especially when subject to an electromagnetic field. In order to understand the thermal response of the biological tissues subject to an electromagnetic field, knowledge of the thermal response in various biological tissues is required.

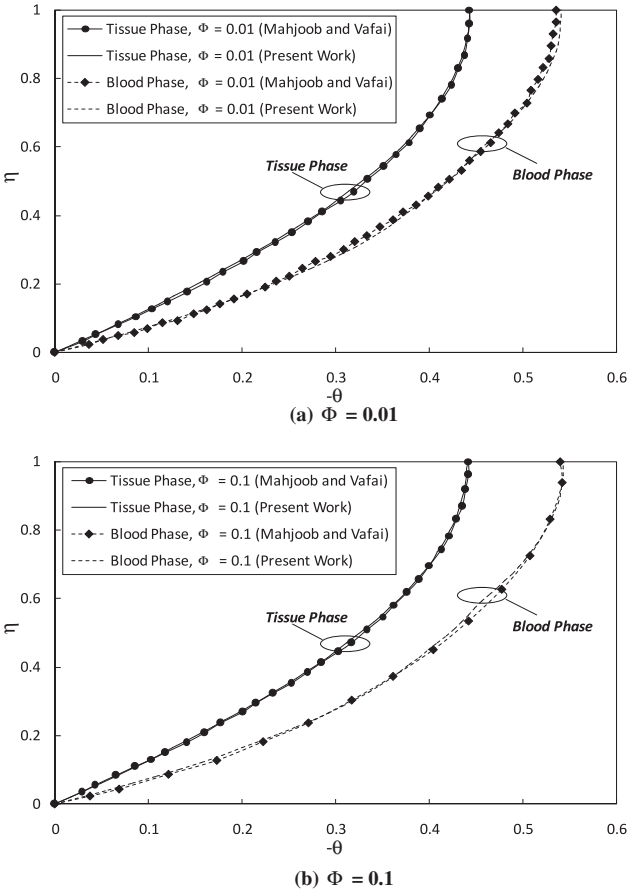

Fig. 4. Comparison of the tissue and blood temperature profiles obtained from the present numerical results and the analytical results by Mahjoob and Vafai [8] for $\varepsilon = 0.1$ and $\kappa = 0.111$ at Bi = 10 where (a) $\Phi = 0.01$ and (b) $\Phi = 0.1$.

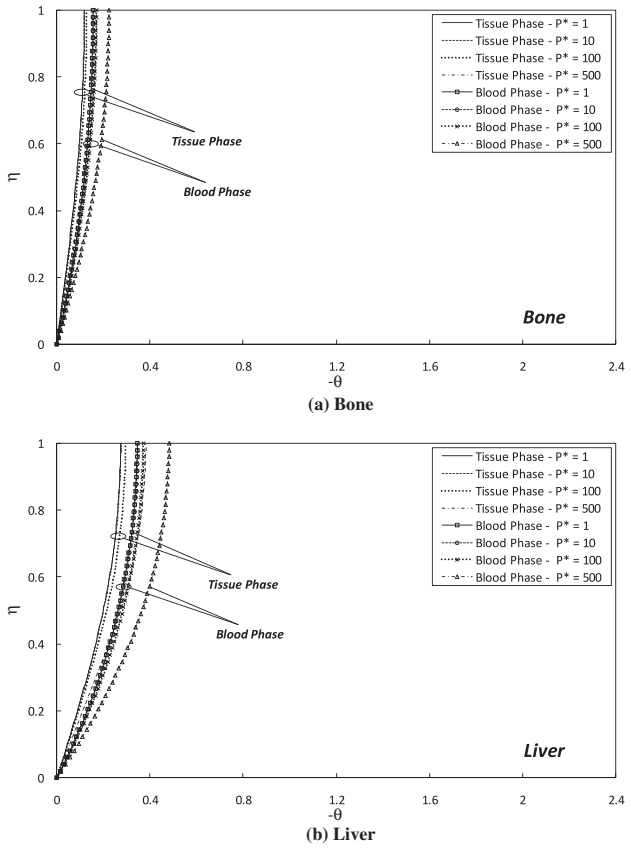

Fig. 5. Effects of the electromagnetic wave power on the tissue and blood temperature profiles in different biological media for $\Phi = 0.1$ and $f^* = 0.6$ at Bi = 10 for (a) Bone and (b) Liver.

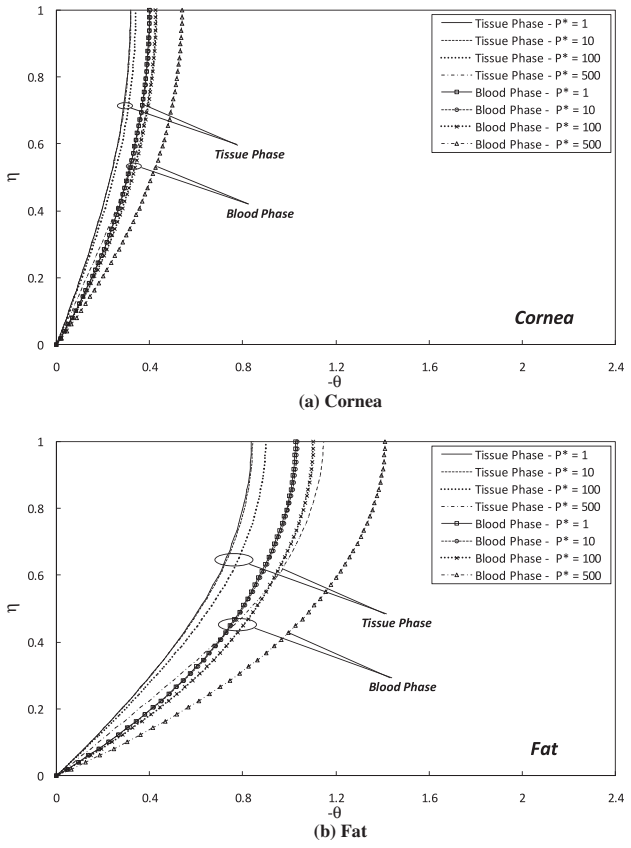

Fig. 6. Effects of the electromagnetic wave power on the tissue and blood temperature profiles in different biological media for $\Phi = 0.1$ and $f^* = 0.6$ at Bi = 10 for (a) Cornea and (b) Fat.

Modeling of heat transport coupled with electromagnetic wave propagation in biological media is required to investigate the cited applications. The aim of this study is to analyze and demonstrate the effect of electromagnetic field, namely the electromagnetic wave power (P^*) and electromagnetic wave frequency (f^*) on the tissue and blood temperature profiles in biological media. The heat flux intensity effects on biological media are investigated and characterized to establish the thermal signature in biomedical applications such as thermal ablation. This study focuses attention on primary biological materials in the human body such as bone, liver, cornea, fat, skin and brain. The dimensionless tissue and blood temperature profiles in various biological materials, obtained by numerical solution of heat transfer coupled with electromagnetic wave propagation under LTNE assumption, are presented. The effects of variations of electromagnetic wave power (P^*) from 1 to 500 and electromagnetic wave frequency (f^*) from 0.2 to 2 on tissue and blood temperature profiles are systematically investigated. (P^*) is chosen in the range of 1–500 for simulations in this study as it corresponds to the input electromagnetic power for destroying cancer cells through a thermal ablation process. In addition, (f^*) is chosen in the range of 0.2–2 for simulations as this frequency range corresponds to the electromagnetic band which is used most frequently in applications related to studies on the effects of electromagnetic field on biological materials. The presented results provide the essential aspects for a fundamental understanding of the effects of an imposed electromagnetic field on biological materials under LTNE. Furthermore, the electromagnetic field effect on heat transport patterns in biological tissues is systematically investigated. The results from this study can be used as a guideline for biomedical applications such as cancer thermal ablation for various biological tissues [30].

2. Problem description

Biological media generally consist of three components i.e. blood vessels, cells and interstitial space [8,20]. Further, biological media can be categorized as vascular region (blood vessels) and extra-vascular region (cells and the interstitial space). The whole anatomical structure can be represented as a blood saturated tissue represented by a porous medium [8], through which the blood infiltrates. The vascular region is regarded as a blood phase and extra-vascular region is regarded as a tissue (solid matrix) phase, as illustrated in Fig. 1.

A two-dimensional model is considered in this work since the biological media is considered homogenous, isotropic and saturated with blood. This model can minimize the computational time while maintaining good resolution and efficiency. In order to investigate the electromagnetic field effects on different biological media, a rectangular slab where H and L denote the height and length of each biological media is considered. The biological medium is subjected to a uniform electromagnetic flux from the top. The electromagnetic external heat source and heat flux represent the imposed energy which is utilized to destroy cancer cells for combined heating during a thermal ablation process. Heat flux represents the heating of a surface while the external heat source represents the electromagnetic energy source such as microwave energy. Electromagnetic irradiation can penetrate the material surface and is converted into thermal energy within the material. This results in a very rapid temperature increase throughout the material that may lead to decomposition of cancer cells. This is a combined heating which can develop into an efficient heating for destroying the cancer cells during the thermal ablation process. The biological media is considered homogenous, isotropic and saturated with

blood. Blood flow is assumed to be hydraulically and thermally fully developed [8]. Natural convection is assumed to be negligible. There is no phase change or chemical reaction within the biological media. The tissue and blood local heat exchange, while the biological medium is subjected to an electromagnetic field, is addressed and the tissue and blood temperature profiles are established in this study.

3. Analysis

Analysis of electromagnetic wave propagation and heat transfer in biological media induced by an electromagnetic field is presented here. The system of governing equations as well as initial and boundary conditions are solved numerically using the finite element method (FEM).

3.1. Electromagnetic wave propagation analysis

The electromagnetic wave propagation in the biological media is modeled on a two-dimensional basis and is calculated using Maxwell's equations, which describe the interdependence of the electromagnetic field. The general form of Maxwell's equations for transverse electric wave (TE) mode is derived assuming a harmonic propagation and is simplified to demonstrate the electromagnetic field in a biological medium [6]:

$$\nabla \times \left(\frac{1}{\mu_r}\nabla \times \vec{E}_z\right) - \left(\gamma_r - \frac{j\sigma}{\omega\gamma_0}\right)k_0^2\vec{E}_z = 0 \tag{1}$$

where $\vec{E}_z$ is the electric field intensity in the z-direction (V/m), μ_r the relative permeability, γ_r the relative permittivity, $\gamma_0 = 8.8542 \times 10^{-12}$ F/m the permittivity of free space, σ the electric conductivity (S/m), $\omega = 2\pi f$ the angular frequency (rad/s) and k_0 is the free space wave number (m^{-1}) and $j = \sqrt{-1}$.

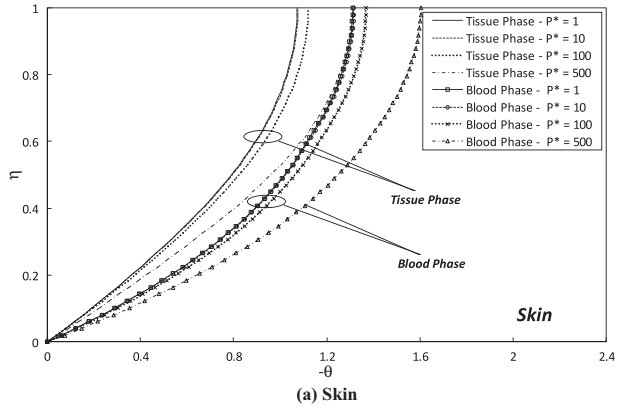

(a) Skin

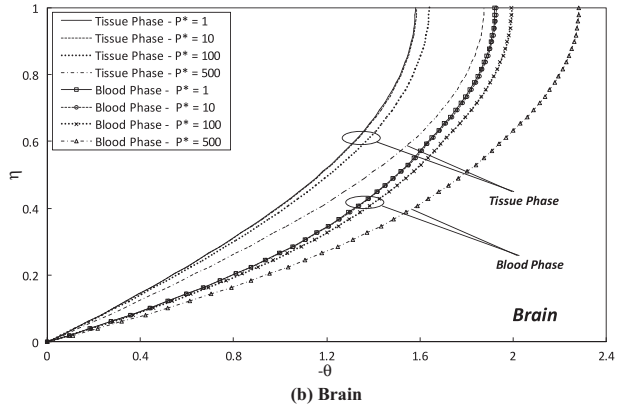

(b) Brain

Fig. 7. Effects of the electromagnetic wave power on the tissue and blood temperature profiles in different biological media for $\Phi = 0.1$ and $f^* = 0.6$ at Bi = 10 for (a) Skin and (b) Brain.

3.1.1. Boundary conditions for the electromagnetic wave propagation analysis

When an electromagnetic field propagates in a biological medium, it is absorbed by the medium and converted into internal heat generation, which causes its temperature to rise. Therefore, boundary conditions for analyzing electromagnetic wave propagation, as shown in Fig. 1, are considered as follows.

The biological medium is subjected to a uniform wave flux from the top. Therefore, at the top boundary of the considered domain, an electromagnetic simulator employs TE wave propagation port with a specified electromagnetic field power:

$$S = \int \left(\vec{E} - \vec{E}_1\right)\cdot\vec{E}_1 \Big/ \int \vec{E}_1 \cdot \vec{E}_1 \tag{2}$$

The outer sides of the biological media are considered as an electric conductor boundary condition. Therefore, electric field intensity in the z-direction vanishes at these sides.

$$\vec{E}_z = 0 \tag{3}$$

3.2. Heat transfer analysis

The anatomical structure is modeled as a biological medium consisting of tissue and blood phases. The steady state volume-averaged governing equations describing the heat transfer phenomenon for tissue and blood phases incorporating metabolic heat generation and an imposed electromagnetic field under LTNE conditions can be represented as [8]:

Tissue phase:

$$K_{t,eff}\nabla_y^2\langle T_t\rangle^t - h_{tb}a_{tb}\left\langle\langle T_t\rangle^t - \langle T_b\rangle^b\right\rangle + (1-\varepsilon)Q_{met} + (1-\varepsilon)Q_{t,ext} = 0 \tag{4}$$

Blood phase:

$$K_{b,eff}\nabla_y^2\langle T_b\rangle^b + h_{tb}a_{tb}\left\langle\langle T_t\rangle^t - \langle T_b\rangle^b\right\rangle + \varepsilon Q_{b,ext} = \varepsilon\rho c_p\langle u\rangle^b\frac{\partial\langle T_b\rangle^b}{\partial x} \tag{5}$$

where,

$$K_{b,eff} = \varepsilon K_b \tag{6}$$

$$K_{t,eff} = (1-\varepsilon)K_t \tag{7}$$

where subscripts *eff*, *t* and *b* represent the effective value, tissue and blood phase, respectively, T the temperature (°C), ρ the density (kg/m^3), c_p the specific heat capacity (J/kg °C), K the thermal conductivity (W/m °C), ε the porosity which is the ratio of the volume fraction of the vascular space, u the blood phase average velocity (m/s), h_{tb} the blood to tissue interfacial heat transfer coefficient (W/m^2 °C) and a_{tb} is the specific surface area between the blood and the tissue (m^2/m^3).

In Eq. (4), the first, second, third and fourth on the left-hand side of equation denote heat conduction, interstitial convection heat transfer, metabolic heat generation and external heat source (heat generation by the electromagnetic field) term, respectively. The bulk blood flow term appears on the right-hand side of the blood phase energy equation (Eq. (5)). It can be seen in Eqs. (4) and (5) that the tissue and blood phases are coupled via the interstitial convective heat transfer term. The interstitial term accounts for the convective heat transfer between the blood and the peripheral tissues. Furthermore, Eqs. (4) and (5) are coupled to the electromagnetic wave propagation equation (Eq. (1)) through Eq. (8).

The computational scheme starts with computing an external heat source term by running an electromagnetic wave propagation calculation and subsequently solving the tissue and blood temperatures in Eqs. (4) and (5) in biological materials. The proposed model is reasonable and adequate for effectively analyzing the essential aspects for a fundamental understanding of heat transport within biological materials subject to an electromagnetic field.

It should be noted that Q_{met} is the metabolic heat generation (W/m^3) while the external heat source is represented by Q_{ext}. The Q_{ext} is equal to the resistive heat generated by electromagnetic field and can be defined as [21]:

$$Q_{ext} = \frac{\sigma|\vec{E}_z|^2}{2} \tag{8}$$

Our external heat source is evaluated in Eq. (8), which is calculated through the electromagnetic wave propagation analysis.

3.2.1. Boundary conditions for the heat transfer analysis

As seen in Fig. 1, the biological medium is subjected to an electromagnetic flux from the top. The imposed heat flux can be represented under the LTNE conditions, based on the work of Mahjoob and Vafai [8], Lee and Vafai [11] and Marafie and Vafai [13] as follows:

$$q_s = -K_{b,eff}\left.\frac{\partial\langle T_b\rangle^b}{\partial y}\right|_{y=H} - K_{t,eff}\left.\frac{\partial\langle T_t\rangle^t}{\partial y}\right|_{y=H} \tag{9}$$

The temperature at the interface of the biological media's surface is likely to be uniform regardless of whether it contacts the tissue solid matrix or the blood. As such the temperature of the tissue and the blood at the biological media's surface will be the same [8,11,13,22,23]:

$$\left.\langle T_b\rangle^b\right|_{y=H} \approx \left.\langle T_t\rangle^t\right|_{y=H} \approx T_s \tag{10}$$

The core region of the biological medium ($y = 0$) is away from the heat transfer interaction used and is considered to act as an insulated boundary as shown in Fig. 1:

$$q_s = 0 \tag{11}$$

The initial temperature of the biological medium is assumed to be uniform and at the normal body temperature:

$$T(t_0) = 37\ ^\circ\mathrm{C} \tag{12}$$

3.3. Non dimensionalization

The numerical results are presented in a dimensionless form. The non-dimensional temperature profiles are plotted against a dimensionless vertical scale, η. These dimensionless variables are defined as:

$$\eta = \frac{y}{D}, \quad \kappa = \frac{K_{b,eff}}{K_{t,eff}}, \quad Bi = \frac{h_{tb}a_{tb}H^2}{K_{t,eff}},$$
$$\theta = \frac{K_{t,eff}\langle\langle T\rangle - T_s\rangle}{q_s H}, \quad \Phi = \frac{(1-\varepsilon)HQ_{met}}{q_s} \tag{13}$$

The dimensionless electromagnetic wave power and dimensionless electromagnetic wave frequency are defined as:

$$P^* = \frac{P}{q_s H^2}, \quad f^* = \frac{f}{f_c} \tag{14}$$

where f_c is the cut off frequency (lowest propagation frequency) of the microwave in TE mode.

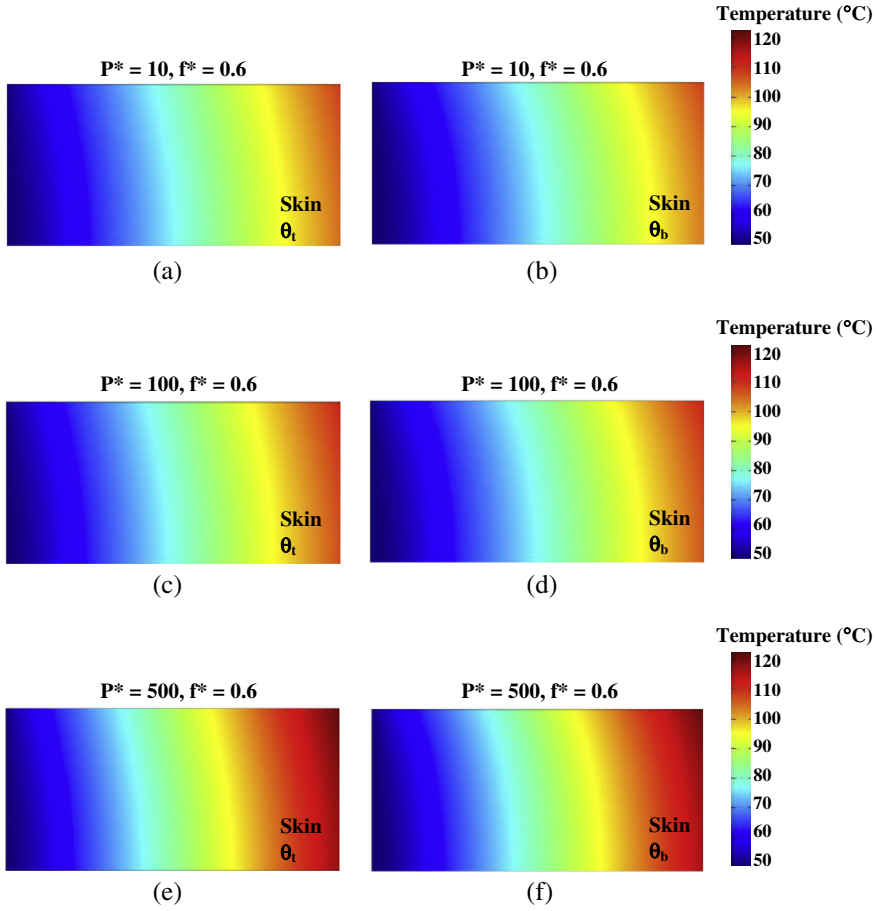

Fig. 8. Effect of the electromagnetic wave power variation on the tissue and blood temperature contours of skin for $\Phi = 0.1$ and $f^* = 0.6$ at Bi = 10.

4. Numerical simulations

The heat transport in a biological medium is expressed through Eqs. (4)–(7). These equations are coupled to Maxwell's equations through Eq. (8). Eqs. (1)–(12) are solved numerically using a FEM via COMSOL^{TM} Multiphysics to demonstrate the phenomenon that occurs in the biological media exposed to an electromagnetic field. The two-dimensional model is discretized using triangular elements, and the Lagrange quadratic is used to approximate temperature profile variations across each element. The biological media comprises six types of tissue including bone, liver, cornea, fat, skin and brain. These biological media have different thermal and dielectric properties and porosities. We assume that the thermal and dielectric properties and porosity of each biological medium are constant. The thermal and dielectric properties and porosities of biological media used in the computations are listed in Table 1 [6,24–30]. Each biological medium is assumed to be homogeneous and electrically as well as thermally isotropic.

5. Results and discussion

5.1. Validation

In order to verify the accuracy of the present model, the numerical results for the case without an electromagnetic field are validated against the analytical results with the same conditions obtained by Mahjoob and Vafai [8]. In the works of Mahjoob and Vafai [8] analytical solutions for heat transport through biological media incorporating hyperthermia treatment and subject to an imposed heat flux are established. The comparison of dimensionless tissue and blood temperature profiles with the analytical results obtained by Mahjoob and Vafai [8] at Bi = 10 and Bi = 0.5 are displayed in Fig. 2. The following parameters are used to generate the results: $\varepsilon = 0.1$, $\Phi = 0$ and $\kappa = 0.111$. It can be seen that the dimensionless tissue and blood temperature profiles are in excellent agreement with the analytical results obtained by Mahjoob and Vafai [8]. Fig. 2 also indicates that a decrease in the internal heat exchange (Bi = 0.5) results in a larger tissue and blood temperature difference while displaying the importance of utilizing the LTNE model.

Fig. 3 illustrates the comparison of dimensionless tissue and blood temperature profiles with the analytical results obtained by Mahjoob and Vafai [8] at different porosities. The tissue and blood temperature profiles for $\Phi(1-\varepsilon) = 0.022$ at Bi = 10 where $\varepsilon = 0.1$ and 0.3 are shown in Fig. 3. A very good agreement is observed for all of the cited comparisons. This figure also shows that a decrease in the porosity results in a larger deviation between the tissue temperature and that of the blood.

Based on the cited values in Mahjoob and Vafai [8], a representative metabolic heat generation is utilized for some of the comparisons. The comparison of dimensionless tissue and blood temperature profiles with the analytical results obtained by Mahjoob and Vafai [8] with variations in the metabolic heat generation for $\varepsilon = 0.1$ at Bi = 10 are displayed in Fig. 4. Fig. 4(a) and 4(b) show the tissue and blood temperature profiles for $\Phi = 0.01$ and 0.1, respectively. Comparing the results for both metabolic heat generation values indicates a very good agreement as seen in Fig. 4. As

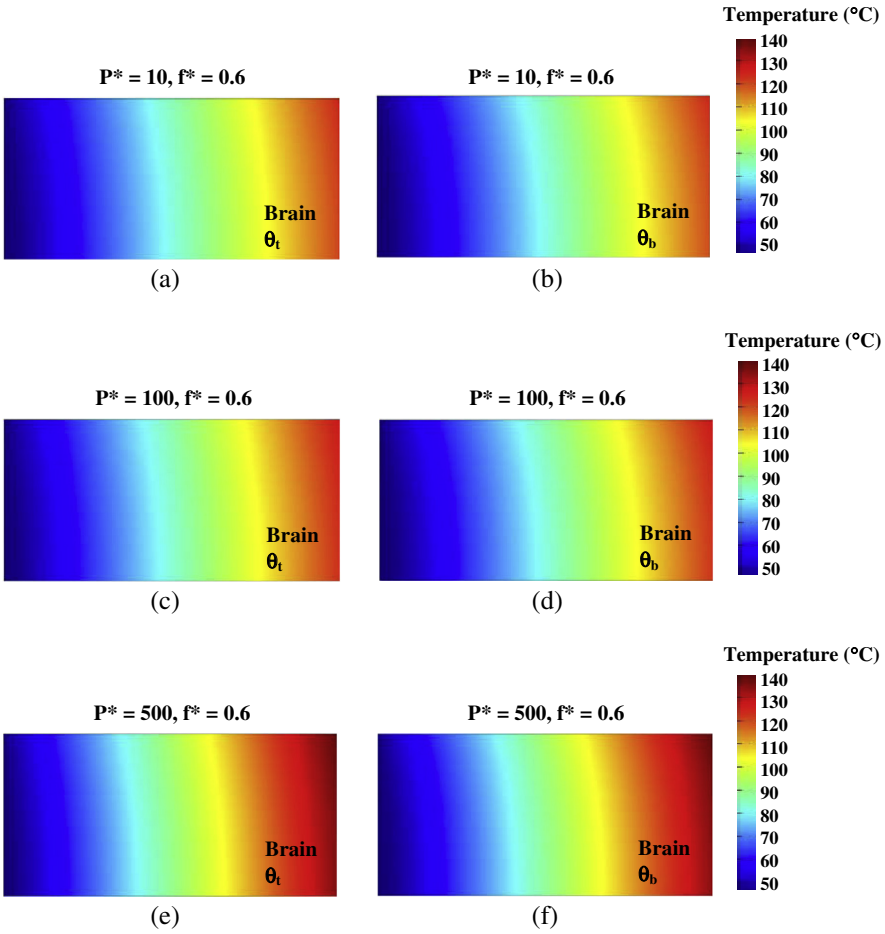

Fig. 9. Effect of the electromagnetic wave power variation on the tissue and blood temperature contours of brain for $\Phi = 0.1$ and $f^* = 0.6$ at Bi = 10.

can be seen an increase in the metabolic heat generation enhances the temperature difference between the two phases. Overall, our results in the present study are in excellent agreement with the analytical results by Mahjoob and Vafai [8]. This highly favorable comparison lends confidence in the accuracy of the present numerical model.

5.2. Dimensionless electromagnetic wave power effects

The effects of electromagnetic wave power on the tissue and blood temperature profiles for different types of biological materials are established. In applications for cancer thermal ablation a detailed description of electromagnetic wave power effects is required to address the effectiveness of thermal ablation technique during the process. The effects of dimensionless electromagnetic wave power on the dimensionless tissue and blood temperature profiles for a variety of different biological media exposed to an electromagnetic field are presented in Figs. 5–7. The physical data utilized in these figures are: $\Phi = 0.1$ and $f^* = 0.6$ at Bi = 10. The electromagnetic wave power varies from 1 to 500. The dimensionless tissue and blood temperature profiles for bone, liver, cornea, fat, skin and brain are depicted in Figs. 5 (a) and (b), 6(a) and (b) and 7(a) and (b), respectively. It is established that the temperature profile patterns are quite similar for all biological media and the temperature profile of the tissue phase is similar to that of the blood phase. It can be seen in these figures that the electromagnetic wave power significantly influences the rate of temperature increase. As expected, the temperature of the tissue and blood increase with an increase in the electromagnetic wave power for all the considered biological media. This is because an increase in the electromagnetic wave power results in a higher heat generation rate in a biological medium. It can be observed that the dimensionless blood temperature values are higher than the tissue tempera-

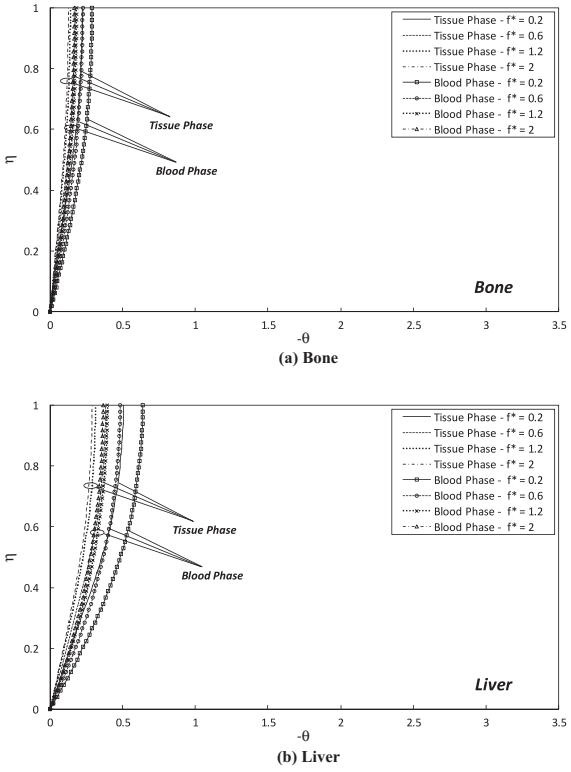

Fig. 10. Effects of the electromagnetic wave frequency on the tissue and blood temperature profiles for $\Phi = 0.1$ and $P^* = 500$ at Bi = 10 for biological media for (a) Bone and (b) Liver.

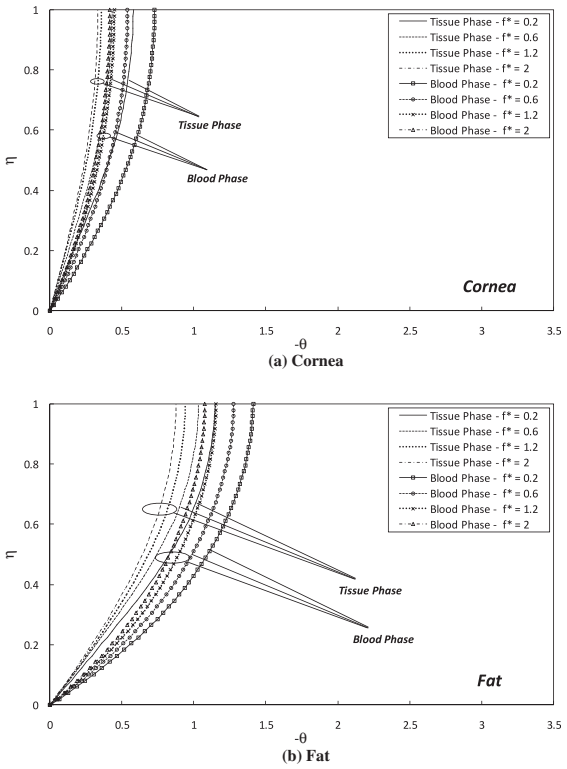

Fig. 11. Effects of the electromagnetic wave frequency on the tissue and blood temperature profiles for $\Phi = 0.1$ and $P^* = 500$ at Bi = 10 for biological media for (a) Cornea and (b) Fat.

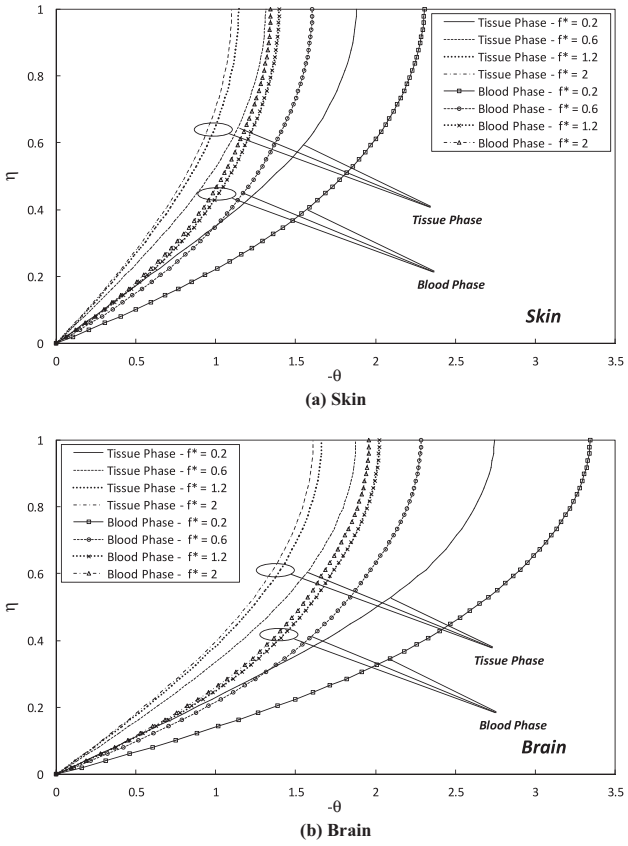

Fig. 12. Effects of the electromagnetic wave frequency on the tissue and blood temperature profiles for $\Phi = 0.1$ and $P^* = 500$ at Bi = 10 for biological media for (a) Skin and (b) Brain.

ture for all of the considered biological media at the same electromagnetic wave power due to the different electromagnetic power absorption of tissue and blood temperatures when subjected to an electromagnetic field. Furthermore, the results in these figures also show that an increase in the electromagnetic wave power results in a larger deviation between the tissue temperature and that of the blood. This shows that the error in utilizing an LTE model for heat transfer investigations increases as the electromagnetic wave power increases when an electromagnetic field is imposed.

Comparing the tissue and blood temperature values in each of the biological materials, it can be seen that the brain has the highest tissue and blood temperature values compared to the other considered biological media followed by skin, fat, cornea, liver and bone, respectively. An increase in the effective thermal conductivity results in an increase in the electromagnetic wave penetration causing an increase in the temperature. Also, the maximum temperature difference between the two phases exists in the brain followed by skin, fat, cornea, liver and bone, respectively due to the highest internal heat exchange. However, as can be seen other factors also affect the tissue and blood temperatures such as thermal and dielectric properties and porosity. For example, in case of fat, although it has a low tissue effective thermal conductivity, it also has the lowest porosity and blood effective thermal conductivity resulting in a high temperature.

Figs. 8 and 9 illustrate the effect of variations in the electromagnetic wave power. The dimensionless electromagnetic wave power of 10, 100 and 500 at $f^* = 0.6$ is considered. Fig. 6 demonstrates the effects of variations in the electromagnetic wave power on the dimensionless temperature contours in the two-dimensional plane of skin. The dimensionless tissue temperature contours are shown in Fig. 8(a), (c) and (e) while Fig. 8(b), (d) and (f) display the dimensionless blood temperature contours. The results clearly show that the tissue and blood temperature values increase with an increase in the electromagnetic wave power. Moreover, an increase in the electromagnetic wave power provides a larger temperature difference between tissue and blood phases as also seen in Fig. 7(a). As can be seen in Fig. 8, the hot spots occur downstream (right-hand side) of the skin slab. The effects of variations in the electromagnetic wave power on the dimensionless temperature contours in the x-y plane of brain are shown in Fig. 9. The dimensionless tissue temperature contours are illustrated in Fig. 9(a), (c) and (e) while Fig. 9(b), (d) and (f) demonstrate the dimensionless blood temperature contours. As can be clearly seen in Fig. 9, once again in an increase in the electromagnetic wave power results in an increase in the tissue and blood temperature values in the brain. Furthermore, an increase in the electromagnetic wave power creates a larger temperature difference between the two phases. These results are consistent with those shown in Fig. 7(b). Similar to the results for the skin the hot spots occur downstream (right-hand side) of the brain slab. It should be noted that for the same impose power, higher temperatures occur within the brain as compared to the skin slab.

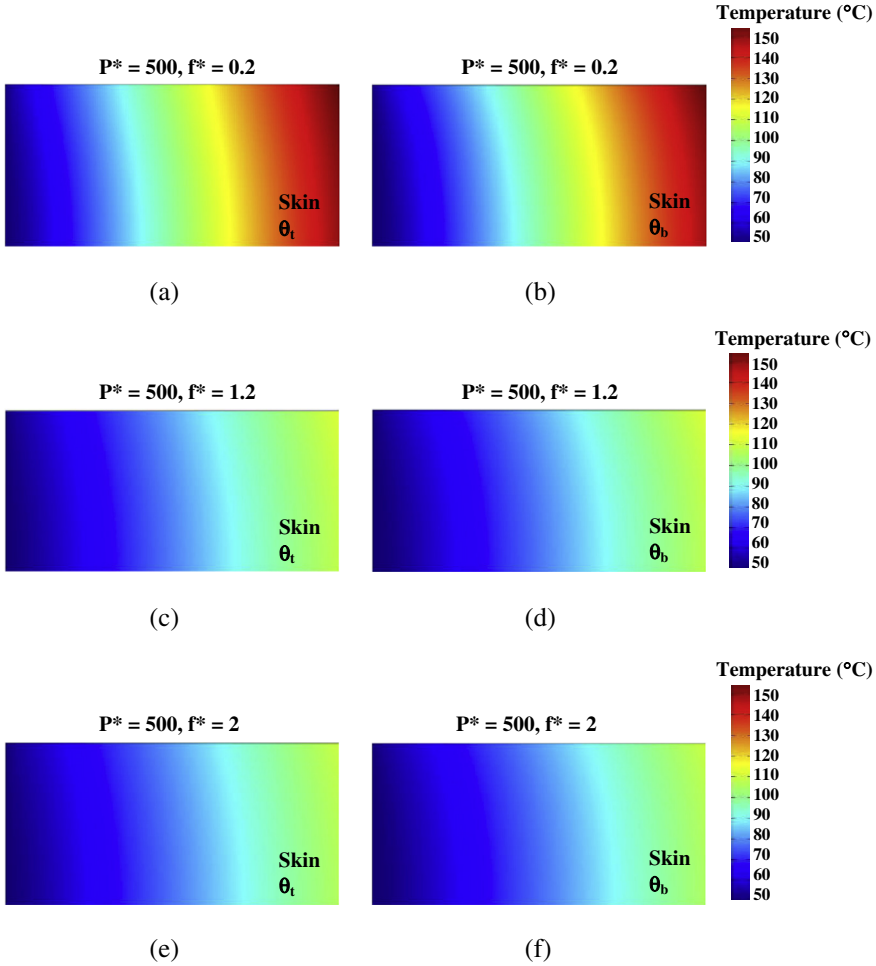

Fig. 13. Tissue and blood temperature contours for skin for $\Phi = 0.1$, $P^* = 500$, Bi = 10 at various electromagnetic wave frequencies.

5.3. Dimensionless electromagnetic wave frequency effects

Figs. 10–12 shows the effect of variations in the dimensionless electromagnetic wave frequency on the dimensionless tissue and blood temperature profiles for different biological media exposed to an electromagnetic field. The results are shown for: $\Phi = 0.1$ and $P^* = 500$ at Bi = 10. The dimensionless electromagnetic wave frequency is varied from 0.2 to 2. The dimensionless tissue and blood temperature profiles for bone, liver, cornea, fat, skin and brain are depicted in Figs. 10(a) and (b), 11(c) and (d) and 12(e) and (f), respectively. The results in these figures show that the temperature profile trend and characteristics are quite similar for all the considered biological media. Note that the highest temperature values do not correspond to the highest electromagnetic wave frequencies. As it can be seen a higher electromagnetic wave frequency produces a lower dimensionless tissue and blood temperature values in all materials. This is because at higher frequencies electromagnetic wave has a shorter wavelength and a smaller penetration depth as compared to lower frequencies. Thus most of electromagnetic energy is absorbed at the entrance region of the biological media. Also it can be seen that the dimensionless blood temperature values are higher than the tissue temperature values for all of the considered biological media subjected to the same electromagnetic wave frequency. Likewise, a decrease in the electromagnetic wave frequency results in a larger deviation between the tissue temperature and that of the blood. This shows that the error in utilizing a LTE model for heat transfer investigations increases as the wave frequency decreases when an electromagnetic field is imposed. Therefore, the LTNE model needs to be utilized for investigating transport through biological media.

Figs. 13 and 14 demonstrate the effect of variations in the electromagnetic wave frequency. The dimensionless temperature contour plots (Figs. 13 and 14) qualitatively confirm the dimensionless temperature profiles in Fig. 12. The dimensionless electromagnetic wave frequency varies at 0.2, 1.2 and 2 at $P^* = 500$. The influence of dimensionless electromagnetic wave frequency on the temperature contours for the skin at different frequencies are displayed in Fig. 13. The dimensionless tissue temperature contours are shown in Fig. 13(a), (c) and (e) while Fig. 13(b), (d) and (f) depict the dimensionless blood temperature contours. The results show that the tissue and blood temperature values decrease with an increase in the electromagnetic wave frequency. Additionally, a decrease in the electromagnetic wave frequency creates a larger temperature difference between tissue and blood phases which further confirms the results shown in Fig. 12(a). Once again as can be seen in Fig. 13, the hot spots occur on the downstream (right-hand) side of the skin. Fig. 14 shows the effects of variations in the electromagnetic wave frequency on the dimensionless temperature contours of the brain. The dimensionless tissue temperature contours are demonstrated in Fig. 14(a), (c) and (e) whereas Fig. 14(b), (d) and (f) display the dimensionless blood temperature contours. The pattern of temperature contours of the brain are somewhat similar to that of the skin shown in Fig. 13. Again it

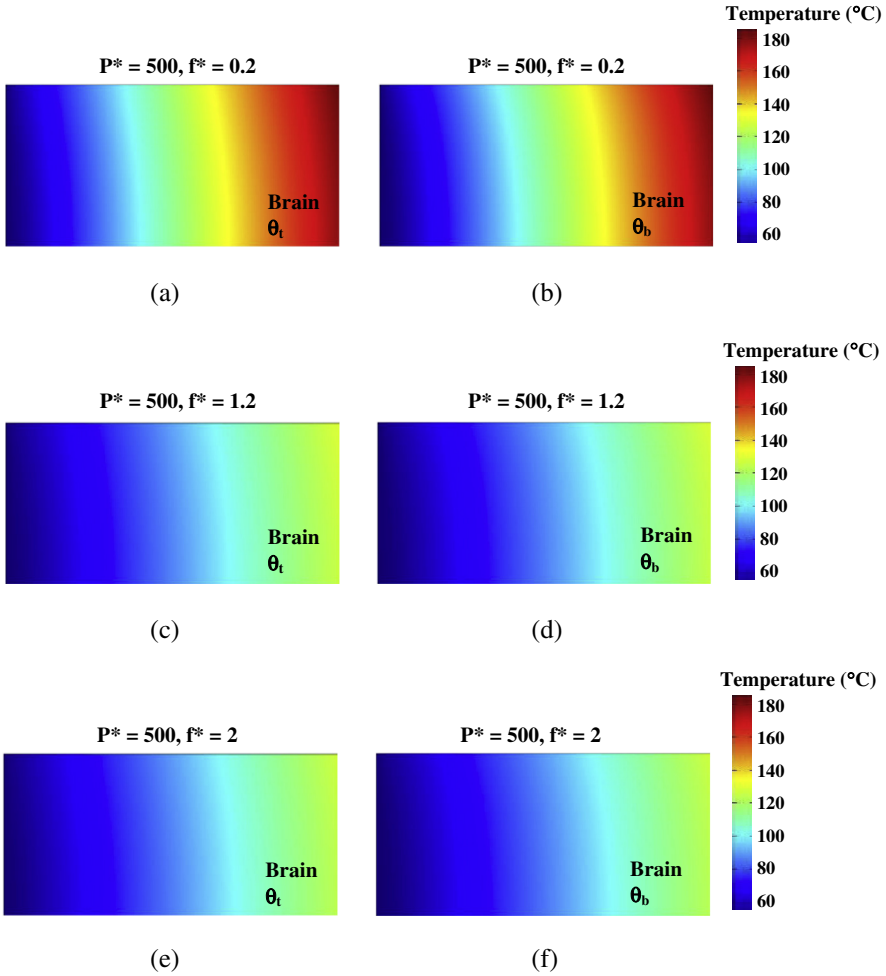

Fig. 14. Tissue and blood temperature contours for brain for $\Phi = 0.1$, $P^* = 500$, Bi = 10 at various electromagnetic wave frequencies.

can be observed that a decrease in the electromagnetic wave frequency results in an increase in the tissue and blood temperature values in the brain. In addition, a decrease in the electromagnetic wave frequency results in a larger temperature difference between the two phases. The results in this figure further confirm the results shown in Fig. 12(b). Similar to the situation for the skin, the hot spots occur downstream (right-hand) of the brain slab. It should be noted that the temperature values for the brain are higher than those for the skin at all electromagnetic wave frequencies.

6. Conclusions

In this work, the effects of an imposed electromagnetic field on different biological media is analyzed. The LTNE model is employed to express the heat transport phenomena in a biological medium. The effect of electromagnetic wave power and frequency on heat transport through a biological medium are analyzed. The simulation results are in excellent agreement with the analytical results obtained by Mahjoob and Vafai [8]. The results provide the fundamental attributes of the transport phenomena in biological media subject to an imposed electromagnetic field. The results demonstrate the importance of utilizing the LTNE model especially at lower internal heat exchange values (Bi = 0.5), lower porosities and higher metabolic heat generation rates for biological media. The magnitude of electromagnetic wave power and frequency has a substantial impact on the temperature of a biological medium. An increase in the electromagnetic wave power produces a higher tissue and blood temperature and enhances a larger temperature difference between tissue and blood phases. On the other hand, a decrease in the electromagnetic wave frequency produces a higher tissue and blood temperature and results in a larger deviation between the tissue temperature and that of the blood. Our results show that an imposed electromagnetic field has a substantial effect in altering the LTE between tissue and blood phases in biological materials.

Acknowledgments

The authors gratefully acknowledge the financial support for this work provided by the Thailand Research Fund (TRF) and Thammasat University and the Higher Education Research Promotion and National Research University Project of Thailand, Office of the Higher Education Commission.

References

[1] S. Chatterjee, T. Basak, S.K. Das, Microwave driven convection in a rotating cylindrical cavity: a numerical study, J. Food Eng. 79 (2007) 1269–1279.
[2] G. Carrafiello, D. Laganà, M. Mangini, F. Fontana, G. Dionigi, L. Boni, F. Rovera, S. Cuffari, C. Fugazzola, Microwave tumors ablation: principles, clinical applications and review of preliminary experiences, Int. J. Surgery 6 (2008) S65–S69.
[3] C. Jones, S.A. Badger, G. Ellis, The role of microwave ablation in the management of hepatic colorectal metastases, The Surgeon 9 (2011) 33–37.
[4] G.J. Beers, Biological effects of weak electromagnetic fields from 0 Hz to 200 MHz: a survey of the literature with special emphasis on possible magnetic resonance effects, Mag. Res. Imaging 7 (1989) 309–331.
[5] I.A. Cotgreave, Biological stress responses to radio frequency electromagnetic radiation: are mobile phones really so (heat) shocking?, Arch Biochem. Biophys. 435 (2005) 227–240.
[6] T. Wessapan, S. Srisawatdhisukul, P. Rattanadecho, Numerical analysis of specific absorption rate and heat transfer in the human body exposed to leakage microwave power at 915 MHz and 2450 MHz, ASME J. Heat Transfer 133 (2011) 051101-1–051101-13.
[7] A.-R.A. Khaled, K. Vafai, The role of porous media in modeling flow and heat transfer in biological tissues, Int. J. Heat Mass Transfer 46 (2003) 4989–5003.
[8] S. Mahjoob, K. Vafai, Analytical characterization of heat transport through biological media incorporating hyperthermia treatment, Int. J. Heat Mass Transfer 52 (2009) 1608–1618.
[9] S. Mahjoob, K. Vafai, Analysis of bioheat transport through a dual layer biological media, ASME J. Heat Transfer 132 (2010) 031101-1–031101-14.
[10] P. Keangin, P. Rattanadecho, T. Wessapan, An analysis of heat transfer in liver tissue during microwave ablation using single and double slot antenna, Int. Commun. Heat Mass Transfer 38 (2011) 757–766.
[11] D.Y. Lee, K. Vafai, Analytical characterization and conceptual assessment of solid and fluid temperature differentials in porous media, Int. J. Heat Mass Transfer 42 (1999) 423–435.
[12] B. Alazmi, K. Vafai, Analysis of variants within the porous media transport models, ASME J. Heat Transfer 122 (2000) 303–326.
[13] A. Marafie, K. Vafai, Analysis of non-Darcian effects on temperature differentials in porous media, Int. J. Heat Mass Transfer 44 (2001) 4401–4411.
[14] A. Amiri, K. Vafai, Analysis of dispersion effects and non-thermal equilibrium non-Darcian, variable porosity incompressible flow through porous medium, Int. J. Heat Mass Transfer 37 (1994) 939–954.
[15] A. Amiri, K. Vafai, Transient analysis of incompressible flow through a packed bed, Int. J. Heat Mass Transfer 41 (1998) 4259–4279.
[16] S. Mahjoob, K. Vafai, Analytical characterization and production of an isothermal surface for biological and electronic applications, ASME J. Heat Transfer 131 (2009) 052604-1–052604-12.
[17] S. Mahjoob, K. Vafai, Analysis of heat transfer in consecutive variable cross-sectional domains-applications in biological media and thermal management, ASME J. Heat Transfer 133 (2011) 011006-1–011006-9.
[18] A. Belmiloudi, Parameter identification problems and analysis of the impact of porous media in biofluid heat transfer in biological tissues during thermal therapy, Nonlinear Anal. Real World Appl. 11 (2010) 1345–1363.
[19] N. Afrin, Y. Zhang, J.K. Chen, Thermal lagging in living biological tissue based on nonequilibrium heat transfer between tissue, arterial and venous bloods, Int. J. Heat Mass Transfer 54 (2011) 2419–2426.
[20] A. Nakayama, F. Kuwahara, A general bioheat transfer model based on the theory of porous media, Int. J. Heat Mass Transfer 51 (2008) 3190–3199.
[21] W. Klinbun, K. Vafai, P. Rattanadecho, Electromagnetic field effects on transport through porous media, Int. J. Heat Mass Transfer 55 (2012) 325–335.
[22] K. Yang, K. Vafai, Analysis of temperature gradient bifurcation in porous media-an exact solution, Int. J. Heat Mass Transfer 53 (2010) 4316–4325.
[23] K. Yang, K. Vafai, Analysis of heat flux bifurcation inside porous media incorporating inertial and dispersion effects-an exact solution, Int. J. Heat Mass Transfer 54 (2011) 5286–5297.
[24] P. Rattanadecho, P. Keangin, Numerical study of heat transfer and blood flow in two-layered porous liver tissue during microwave ablation process using single and double slot antenna, Int. J. Heat Mass Transfer 58 (2013) 457–470.
[25] M. Rüegg, B. Blanc, The fat globule size distribution in human milk, BBA – Lipids Lipid Metab. 666 (1981) 7–14.
[26] M.A. Bauman, G.T. Gillies, R. Raghavan, M.L. Brady, C. Pedain, Physical characterization of neurocatheter performance in a brain phantom gelatin with nanoscale porosity: steady-state and oscillatory flows, Nanotechnology 15 (2004) 92–97.
[27] Y. He, H. Liu, R. Himeno, J. Sunaga, N. Kakusho, H. Yokota, Finite element analysis of blood flow and heat transfer in an image-based human finger, Comput. Biol. Med. 38 (2008) 555–562.
[28] R.P. Gilbert, Y. Liu, J.-P. Groby, E. Ogam, A. Wirgin, Y. Xu, Computing porosity of cancellous bone using ultrasonic waves. II: The muscle, cortical, cancellous bone system, Math. Comput. Model. 50 (2009) 421–429.
[29] T. Wessapan, P. Rattanadecho, Specific absorption rate and temperature increase in human eye subjected to electromagnetic fields at 900 MHz, ASME J. Heat Transfer 134 (2012) 91101-1–91101-11.
[30] T. Wessapan, S. Srisawatdhisukul, P. Rattanadecho, Specific absorption rate and temperature distributions in human head subjected to mobile phone radiation at different frequencies, Int. J. Heat Mass Transfer 55 (2012) 347–359.

International Journal of Heat and Mass Transfer 65 (2013) 423–434

Contents lists available at SciVerse ScienceDirect

International Journal of Heat and Mass Transfer

journal homepage: www.elsevier.com/locate/ijhmt

The influence of wave propagation mode on specific absorption rate and heat transfer in human body exposed to electromagnetic wave

Apichart Siriwitpreecha, Phadungsak Rattanadecho *, Teerapot Wessapan

Center of Excellence in Electromagnetic Energy Utilization in Engineering (CEEE), Department of Mechanical Engineering, Faculty of Engineering, Thammasat University (Rangsit Campus), Pathumthani 12120, Thailand

ARTICLE INFO

Article history:
Received 4 January 2013
Accepted 8 June 2013

Keywords:
Propagation mode
SAR
Heat transfer
Human body

ABSTRACT

In recent years, the utilization of electromagnetic wave in various applications is increasing rapidly because of its advantages. There is concern about the human health due to electromagnetic wave because it can damage human tissue by damaging molecular structure which is interacted with this electromagnetic wave. In this study, the 2-D computational analysis is used to study the distribution of the specific absorption rate (SAR) and temperature on organs in human body exposed to electromagnetic wave which are propagated from source in Transverse Electric mode (TE mode) and Transverse Magnetic mode (TM mode). The mathematical models consist of a coupled electromagnetic wave equation and bioheat equation. In numerical simulation, these coupled mathematical models are solved by using a finite element method (FEM) with thermal and dielectric properties to describe SAR and temperature distributions in the human body. The effects of wave propagation mode, operating frequency, radiated power of electromagnetic wave and exposure time are systematically investigated. This study focuses attention on organs in the human trunk. It is found that the maximum SAR on organs exposed to electromagnetic wave which are propagated in TM mode is higher than that of TE mode for all organs and frequencies of electromagnetic wave. The electromagnetic wave at the frequency of 300 MHz propagated in TM mode is the most significant exposure condition to produce the maximum SAR and temperature increase in fat. Moreover, the maximum SAR and temperature increase are proportional to the power of heating source. The lower frequency of electromagnetic wave has an ability to penetrate through the human body deeper than that of the high frequency.

© 2013 Elsevier Ltd. All rights reserved.

1. Introduction

Electromagnetic wave is a one heat source that is an attractive alternative over conventional heating methods because electromagnetic wave in range of microwave that penetrates the surface is converted into thermal energy within the material. The utilizations of electromagnetic wave have been used in many industrial and household applications such as heating process or drying process. In recent years, these utilizations are increasing rapidly because of the several advantages of electromagnetic wave heating source such as high speed start up, selective energy absorption, instantaneous electric control, no pollution, high energy efficiency and high product quality [1,2]. Rapid development of electromagnetic energy applications causes an increase in public concern about health risks from electromagnetic energy emitted from various sources [5–8]. The power absorption of electromagnetic wave induces temperature increase on organs in the human body. The specific absorption rate (SAR) criteria have been used to obtain the dosimetric data and to gain further understanding of the biological tissues absorption characteristic of the human body [9]. The temperature increase of organs is one of the main tasks in the evaluation of the human risk related to the exposure to the human body to electromagnetic wave [10].

The computational analysis is used to study the distributions of SAR and temperature in human body because these distributions cannot be measured directly to the alive human body due to ethical consideration. In present day, the experimental data on the correlation of SAR levels to the temperature increase on organs in the human body are still sparse. Most previous studies of a human body exposed to an electromagnetic wave did not consider heat transfer cause an incomplete analysis to result. The earlier studies of heat transfer in human tissues used the general bioheat equation to investigate that [13]. Thereafter, coupled model of Maxwell's equation and bioheat equation were used to model human tissues exposed to electromagnetic wave to explain the electromagnetic wave propagation and heat transfer in tissues in the human body. There are some research have been studied temperature distribution over the surface and various biotissues exposed to electromagnetic wave [14-19]. Nishizawa et al. simulated SAR

* Corresponding author. Tel.: +66 2564 3001 9; fax: +66 2564 3010.
E-mail address: ratphadu@engr.tu.ac.th (P. Rattanadecho).

0017-9310/$ - see front matter © 2013 Elsevier Ltd. All rights reserved.
http://dx.doi.org/10.1016/j.ijheatmasstransfer.2013.06.015

Nomenclature

c_p	specific heat capacity (J/kg K)
E	electric field intensity (V/m)
H	magnetic field intensity (A/m)
f	frequency of microwave (Hz)
k	thermal conductivity (W/m K)
n	refractive index
Q	heat (W/m^3)
s	poynting vector (W/m^2)
t	time (s)
T	temperature (°C)
v	velocity of propagation (m/s)
tan δ	dielectric loss coefficient

Greek letters

ε	permittivity (F/m)
ε_r	dielectric constant of tissue
μ	permeability (H/m)
ρ	density (kg/m^3)
σ	electric conductivity (S/m)
ω	perfusion rate (1/s)

Subscripts

b	blood
ext	external
met	metabolism

distributions of skin, fat and muscle tissues in human body with three-layer physical model [9]. Keangin et al. studied heat transfer in liver tissue for liver cancer treatment using microwave coaxial antenna [3,4]. However, most studies of temperature increase induced by electromagnetic wave have not been considered in a realistic domain of the human body with complicated organs of several types of tissues. Our research group has tried to numerically investigate the temperature increase in human tissue subjected to electromagnetic fields in many problems, such as Wessapan et al. studied SAR and temperature distributions in the human head and the human eye due to mobile phone radiation at several frequencies [6,7]. Moreover, they used the human body model which has 10 organs in the human trunk to simulate the SAR and heat transfer in these organs exposed to electromagnetic wave at frequencies of 915 MHz and 2450 MHz which are characterized propagation in TE mode [5], and studied the effects of dielectric shield on SAR and temperature increase in the human body at the frequencies of 300 MHz, 915 MHz, 1300 MHz and 2450 MHz [8]. However, these works were not considered these effects on organs when the electromagnetic wave propagated from source in different propagation mode.

The work described in this paper is substantially extended from our previous work [6] by further puts the focus on the effects of wave propagation mode, operating frequency, radiated power of electromagnetic wave and exposure time. In this paper, a 2-D human cross section model [11] is used to simulate the distribution of SAR and temperature in these organs exposed to electromagnetic wave. There are four frequencies of electromagnetic wave in range of microwave at 300 MHz, 915 MHz, 1300 MHz and 2450 MHz are chosen to simulate these distributions because the energy of these frequencies can be converted to thermal energy. Each frequency has radiated power of 10 W, 50 W and 100 W. Furthermore, the comparison of biological effects on organs due to particular mode of electromagnetic wave propagation, TE mode and TM mode, are considered. The Maxwell's equation and the bioheat equation are used to investigate electromagnetic wave propagation and heat transfer on organs exposed to electromagnetic wave, respectively. The obtained values provide an indication of limitations that must be considered for temperature increases due to localized electromagnetic wave energy absorption.

2. Numerical simulation

Most of industrial electromagnetic wave heating systems generate high power electromagnetic wave to use in various applications such as industrial microwave system as shown in Fig. 1. The leakage electromagnetic wave from the heating source can cause significant thermal damage on sensitive organs within the human body. Therefore, to approach reality, it is necessary to investigate the temperature distribution on organs in the human trunk due to the leakage electromagnetic wave. It is assumed that the propagation of electromagnetic wave is uniform plane wave. For ethical consideration, it is difficult to measure these distributions directly to the alive human body. The computational analysis is selected to investigate the distributions of SAR and temperature in human body. The system of governing equations as well as initial and boundary conditions are solved numerically using the finite element method (FEM) via COMSOL™ Multiphysics to demonstrate the phenomenon occurs within the human body exposed to electromagnetic wave.

2.1. Human model

Fig. 2 shows the 2-D human body model which is used in this study is obtained by image processing technique from the work of *Shiba* and *Higaki* [11]. The side view cross section through the middle plane of the human trunk model has a dimension of 400 mm in width and 525 mm in height which composes of nine internal organs in human trunk which are skin, fat, muscle, bone, large intestine, small intestine, bladder, stomach and liver. These organs have different dielectric and thermal properties. The thermal properties of tissues are given in Table 1 and the dielectric properties of tissues at the frequencies of 300 MHz, 915 MHz, 1300 MHz and 2450 MHz are given in Table 2. The thermal properties of these tissues are constant because there are only a slight change of temperature is noticed along the exposure time.

2.2. Equation of electromagnetic wave propagation analysis

The mathematical models are developed to predict SAR and temperature distributions within the human body exposed to electromagnetic wave. It is assumed that electromagnetic wave leaks from industrial electromagnetic wave heating system. This electromagnetic wave propagates in x-direction and penetrates into the human body from front to back of human body as shown in Fig. 1. To simplify the computational analysis, some of the following assumptions are used in this paper,

1. It is assumed that the electromagnetic wave is plane wave.
2. The human body in which electromagnetic wave interact with human proceeds in free space.
3. The free space is truncated by scattering boundary condition.
4. The dielectric properties of tissues are uniform and constant.

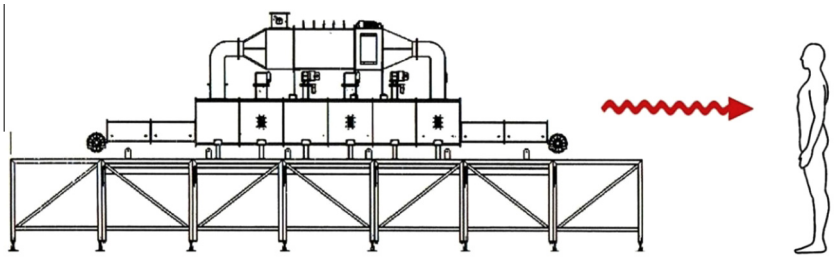

Fig. 1. The leakage electromagnetic wave from the industrial microwave.

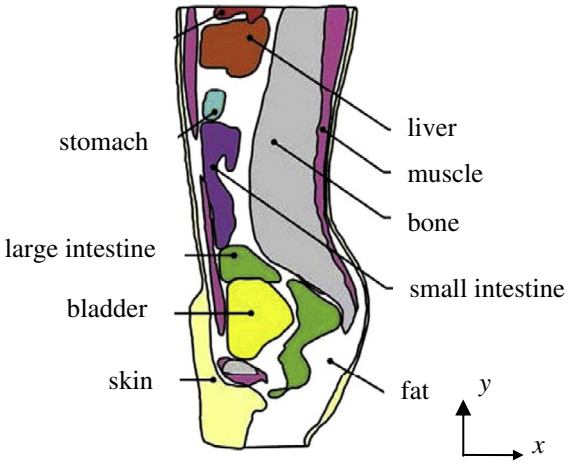

Fig. 2. Cross sectional model of human body.

Table 1
Thermal properties of tissues [8].

Organs	ρ (kg/m^3)	K (W/m K)	c (J/kg K)	ω_b (1/s)
Skin	1125	0.35	3437	2.00×10^{-2}
Fat	916	0.22	2300	4.58×10^{-4}
Muscle	1047	0.60	3500	8.69×10^{-3}
Bone	1038	0.44	1300	4.36×10^{-4}
Large intestine	1043	0.60	3500	1.39×10^{-2}
Small intestine	1043	0.60	3500	1.74×10^{-2}
Bladder	1030	0.56	3900	0.000
Stomach	1050	0.53	3500	7.00×10^{-3}
Liver	1030	0.50	3600	1.72×10^{-2}

2.2.1. Governing equations

In this study, the two propagation characteristic of electromagnetic wave which leaks from electromagnetic wave heating system to the human body is assumed in two circumstances: (i) TE mode and (ii) TM mode. The induced biological effects on organs in human body due to the two propagation modes of electromagnetic wave are compared. The propagation of electromagnetic wave in human body is calculated by Maxwell's equation [12], which mathematically describes the interdependence between electric and magnetic fields. The general forms of Maxwell's equation are simplified to the following expressions:

- Transverse Electric mode (TE mode) [5,8]

$$\nabla \times \left(\frac{1}{\mu_r}\nabla \times E_z\right) - \left(\varepsilon_r - \frac{j\sigma}{\omega\varepsilon_o}\right)k_o^2 E_z = 0. \tag{1}$$

- Transverse Magnetic mode (TM mode)

$$\nabla \times \left(\left(\frac{1}{\varepsilon_r - \frac{j\sigma}{\omega\varepsilon_o}}\right)(\nabla \times H_z)\right) - \mu_r k_o^2 H_z = 0 \tag{2}$$

where $\varepsilon_o = 8.8542 \times 10^{-12}$ F/m is the permittivity of free space and $j = \sqrt{-1}$ is imaginary number.

2.2.2. Boundary conditions

The electromagnetic wave is emitted from the high power electromagnetic wave heating system and leaks to the environment. It propagates in x-direction to strike in front of the human body and moves through the back. It is assumed that the electromagnetic wave which strikes the human body is characterized by uniform plane wave with the power the same as source. Fig. 3 shows an electromagnetic wave propagation port in the left boundary of considered domain with a specified power,

$$S = \frac{\int^{(E-E_1)} \cdot E_1}{\int_1^E \cdot E_1}. \tag{3}$$

For the boundary conditions along the interfaces between different medium such as air and organs or organs and organs, they are considered continuity boundary conditions,

$$n \times (H_1 - H_2) = 0. \tag{4}$$

For the outer sides of the tissue boundaries are truncated as scattering boundary conditions,

Table 2
Dielectric properties of tissues [8].

Organs	300 MHz		915 MHz		1300 MHz		2450 MHz	
	σ (S/m)	ε_r	σ (S/m)	ε_r	σ (S/m)	ε_r	σ (S/m)	ε_r
Skin	0.35	48.41	0.92	44.86	1.25	43.56	2.16	41.79
Fat	0.06	6.55	0.09	5.97	0.10	5.80	0.13	5.51
Muscle	1.08	55.45	1.33	50.44	1.42	48.96	1.60	46.40
Bone	2.10	44.80	2.10	44.80	2.10	44.80	2.10	44.80
Large intestine	2.04	53.90	2.04	53.90	2.04	53.90	2.04	53.90
Small intestine	3.17	54.40	3.17	54.40	3.17	54.40	3.17	54.40
Bladder	0.69	18.00	0.69	18.00	0.69	18.00	0.69	18.00
Stomach	2.21	62.20	2.21	62.20	2.21	62.20	2.21	62.20
Liver	1.69	43.00	1.69	43.00	1.69	43.00	1.69	43.00

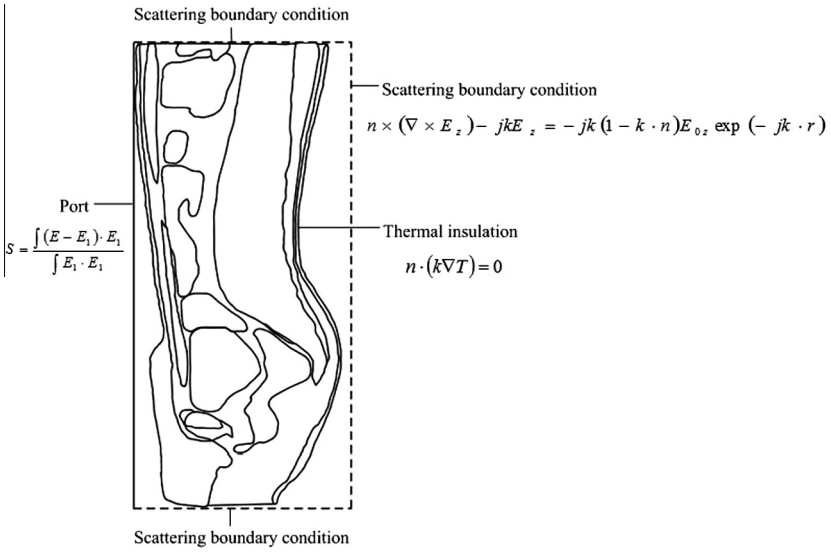

Fig. 3. Boundary conditions for electromagnetic wave propagation and heat transfer.

$$n \times (\nabla \times E_z) - jkE_z = -jk(1 - k \cdot n)E_{oz}e^{-jk \cdot r} \tag{5}$$

2.3. Equation of heat transfer in human body

To solve the thermal problem, the temperature distribution in the human body has been evaluated by the bioheat equation according to Maxwell's equations. The temperature distribution corresponds to the SAR. This is because the SAR within the human body distributes, owing to energy absorption. Thereafter, the absorbed energy is converted to thermal energy, which increases the organs temperature. Heat transfer analysis of the human body is modeled in two dimensions. To simplify the problem, the following assumptions are made:

1. Human organ is bio-material with uniform and constant thermal properties.
2. There is no phase change of substance within the organ.
3. There is no energy exchange throughout the human model.
4. There is no chemical reaction within the organ.

2.3.1. Governing equations

The energy of electromagnetic wave is absorbed by tissue organs, when it penetrates into the human body. The temperature of tissues in human body will be increased, according to the absorbed energy is converted to thermal energy. These temperature distributions inside the human model are obtained by Pennes' bioheat equation as Eq. (3). The transient bioheat equation effectively explains the phenomenon of heat transfer within the human body, it can be written as [13]:

$$\rho C\frac{\partial T}{\partial t} = \nabla \cdot (k\nabla T) + \rho_b C_b \omega_b (T_b - T) + Q_{met} + Q_{ext}. \tag{6}$$

where ρ is the organ density (kg/m^3), C is the heat capacity of organ (J/kg K), k is thermal conductivity of orgas (W/m K), T is the organ temperature (°C), T_b is the temperature of blood (°C), ρ_b is the density of blood (kg/m^3), C_b is the specific heat capacity of blood (J/kg K), ω_b is the blood perfusion rate (1/s), Q_{met} is the metabolism heat source (W/m^3) and Q_{ext} is the external heat source term (electromagnetic wave heat-source density) (W/m^3).

In this analysis, the metabolism heat source is negligible, heat conduction and blood flow in each organ is approximated by the term $\nabla \cdot (k\nabla T)$ and $\rho_b C_b \omega_b (T_b - T)$, respectively. For the external heat source, Q_{ext}, this analysis is electromagnetic wave heat source density (W/m^3). It is equal to the resistive heat which is generated by the electromagnetic wave power absorbed, which is defined as

$$Q_{ext} = \frac{1}{2}\sigma_{\text{organ}}|E|^2 \tag{7}$$

where $\sigma_{\text{organ}} = 2\pi f \varepsilon_r' \varepsilon_o$.

2.3.2. Boundary conditions

Heat transfer is considered only in the human body domain, which is not including the surrounding space. The boundary of human body which contacts the air is considered to be a thermal insulation boundary condition, defined as,

$$N \cdot (k\nabla T) = 0. \tag{8}$$

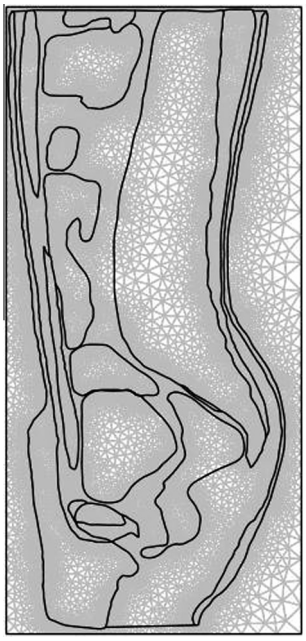

Fig. 4. An initial two-dimensional finite element mesh of human cross section model.

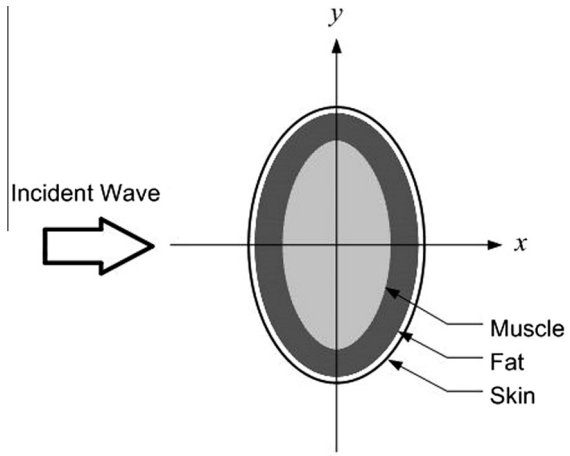

Fig. 5. Geometry of the validation model obtained from the paper [5].

It is assumed that no contact resistance occurs between the internal organs in human body. Therefore, the boundary conditions of the internal organs are assumed to be a continuous.

$$n \cdot (k_u \nabla T_u - k_d \nabla T_d) = 0. \tag{9}$$

2.3.3. Interaction of electromagnetic wave and human organs

Human organs are generally lossy mediums for electromagnetic wave with finite electric conductivity. When electromagnetic wave propagates into these organs, the energy of electromagnetic wave propagation is absorbed by the tissue. SAR of electromagnetic wave energy in organ is defined as a power dissipation rate normalized by organs density [8], which is given by the following equation:

$$\mathrm{SAR} = \frac{\sigma}{\rho}|E|^2. \tag{10}$$

2.3.4. Initial condition for heat transfer

In this analysis, the temperature distribution inside the human body is assumed to be uniform. The thermoregulation mechanisms and the metabolic heat generation of each organ have been neglected to illustrate the clear temperature distribution. Therefore, the initial temperature of the human body is defined as

$$T(t_o) = 37\ ^\circ\mathrm{C} \tag{11}$$

Table 3
Comparison of the results obtained in the present work with those of Nishizawa and Hashimoto.

Power (W)	Present work	Published work [9]	% difference
SAR_{max} in skin	0.212	0.220	3.63
SAR_{max} in fat	0.198	0.206	3.88
SAR_{max} in muscle	0.116	0.120	3.33

2.3.5. Penetration depth

The penetration depth (D_p) is defined as the distance within material at which the electromagnetic wave density has decreased to 37% of its initial value at the surface [8]:

$$D_p = \frac{1}{\frac{2\pi f}{v}\sqrt{\frac{\varepsilon_r'\left(\sqrt{1+(\tan)^2}-1\right)}{2}}} \tag{12}$$

where ε_r' is the relative dielectric constant, tan δ is the loss tangent which provides an indication of how well the material can be penetrated by an electrical field and how it dissipates electrical energy as heat, and υ is the speed of electromagnetic wave (m/s).

The penetration depth of the electromagnetic wave which penetrates within the material is calculated using Eq. (12), which shows how it depends on the dielectric properties of the dielectric material and frequency of electromagnetic wave. It is shown that the penetration depth is greatly dependent on the frequency of electromagnetic wave, it will be increased if the frequency of electromagnetic wave is decrease.

2.4. Simulation procedure

The finite element method is used to analyze the transient problems. The computational scheme is to assemble a finite element model and compute a local heat generation term by performing an electromagnetic calculation using organ properties. In order

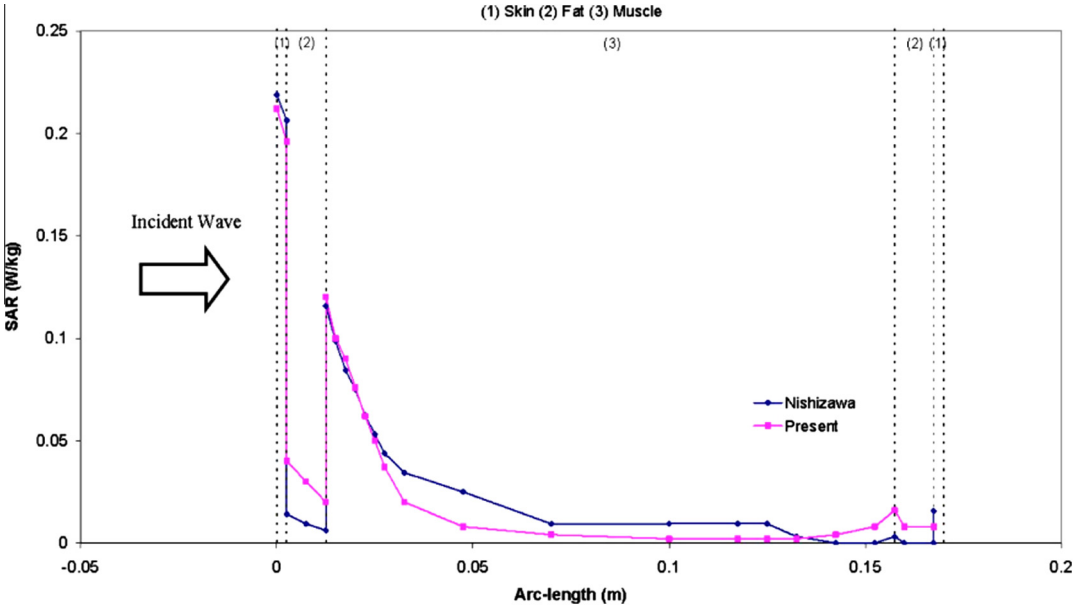

Fig. 6. Comparison of the calculated SAR distribution to the SAR distribution from the paper [5].

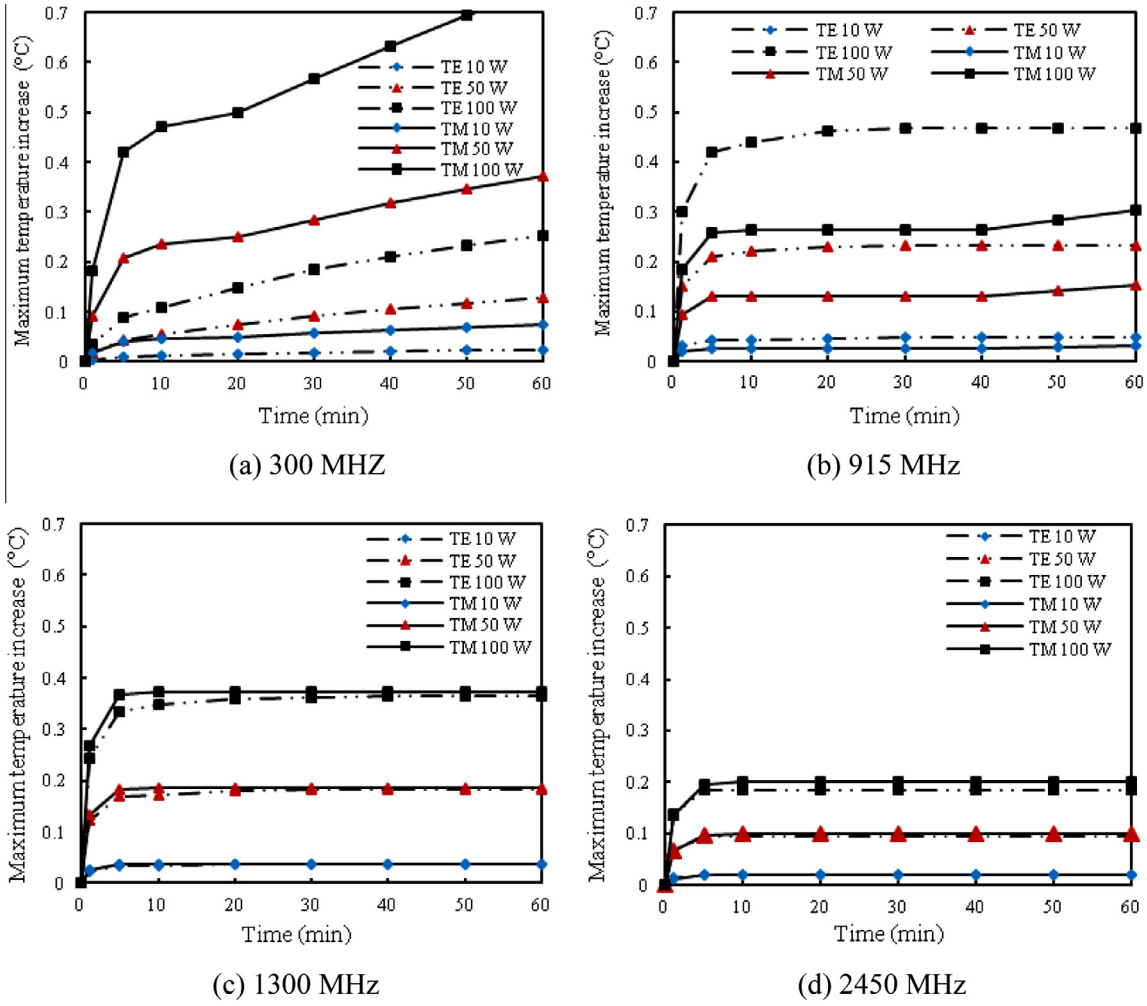

Fig. 7. The maximum temperature increase on organs in human body due to electromagnetic wave at frequencies of 300 MHz, 915 MHz, 1300 MHz and 2450 MHz in various exposure time.

to obtain a good approximation, a fine mesh is specified in the sensitive areas. This study provides a variable mesh method for solving the problem as shown in Fig. 4. The model of bioheat equation and Maxwell's equation are solved. All computational processes are implemented using COMSOL™ Multiphysics, to demonstrate the phenomena that occur within the human body exposed to electromagnetic fields. The electromagnetic power absorption at each point is computed and used to solve the time-dependent temperature distribution. All steps are repeated, until the required exposure time is reached. The 2-D model is discretized using triangular elements and the Lagrange quadratic is used to approximate temperature and SAR variation across each element. Convergence tests are carried out to identify a suitable number of elements required. The convergence test leads to a grid with approximately 90,000 elements. It is reasonable to assume that, with this element number, the accuracy of the simulation results is independent of the number of elements and therefore save computation memory and time.

3. Results and discussions

The coupled mathematic models of heat transfer and electromagnetic wave propagation is used to simulate SAR and temperature distributions on organs in human body exposed to electromagnetic wave which have four frequencies of 300 MHz, 915 MHz, 1300 MHz and 2450 MHz. The influence of wave propagation mode, operating frequency, and radiated power of the electromagnetic wave source are systematically investigated.

3.1. Verification of the model

It must be noted in advance that it is not possible to make a direct comparison of the model in this study and the experimental results. In order to verify the accuracy of the present numerical model, the simple case of the simulated results is then validated against the numerical results with the same geometric model obtained by *Nishizawa* and *Hashimoto* [9]. The horizontal cross section of three-layer human tissues as shown in Fig. 5 is used in the validation case. In the validation case, the leakage power density exposed to the electromagnetic frequency of 1300 MHz is 1 mW/cm^2. The results of the selected test case are illustrated in Fig. 6 for SAR distribution in the human body. Table 3 clearly shows good agreement in the maximum value of the SAR of tissues between the present solution and that of *Nishizawa* and *Hashimoto*. This favorable comparison lends confidence in the accuracy of the present numerical model. It is important to note that there may be some errors occurring in the simulations that are generated by the input dielectric properties and the numerical scheme.

It is shown that the maximum SAR of organs calculated in the present study and Nishisawa's models are in good agreement, the

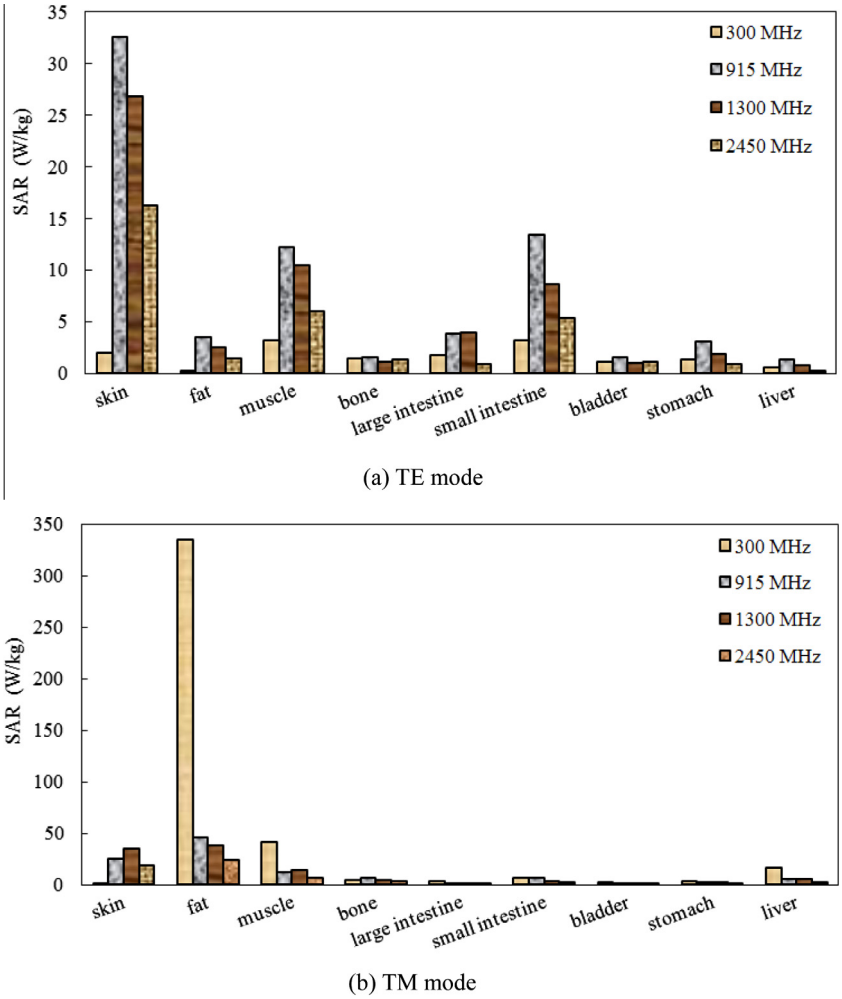

Fig. 8. SAR distribution on organs in human body exposed to electromagnetic wave which are propagated in (a) TE mode and (b) TM mode at power 100 W and exposure time 20 min in various frequencies.

maximum difference is about 3.88%. This comparison lends confidence in the accuracy of these models to simulate SAR and temperature distributions in human body in this study.

3.2. Influence of exposure time of electromagnetic wave

Fig. 7 shows the maximum temperature increases in human body exposed to electromagnetic wave propagation in TE and TM mode plane wave at the frequency of 300 MHz, 915 MHz, 1300 MHz and 2450 MHz in various exposure times. It is found that the maximum temperature increases in the human body at these frequencies are approach to steady state after five minutes of exposure time, except for the frequency of 300 MHz from both of propagation mode, the temperature is rising continuously. This is because the high penetration depth of the 300 MHz frequency causes localizing thermal runaway in deep organs which is shown in Eq. (12). The SAR distributions at low frequency are higher than that of high frequency, but at 300 MHz has low SAR value because its penetration depth is too high compared to that of other frequencies. The electromagnetic wave can penetrate into the human body and the absorbed energy is distributed in each organ of the human body as shown in Fig. 8.

The maximum temperature increases at the high frequency of 1300 MHz and 2450 MHz for both TE and TM mode propagation have a very similar distribution trend at each radiated power as shown in Fig. 7(c) and (d). This is because in this frequency range they have low penetration depth of the electromagnetic wave into the human body. While at the low frequency of 300 MHz, the maximum temperature increases in case of TM mode, is higher than that of TE mode. This is because the resonance of standing wave is becoming a dominant phenomenon in the fat (which will be discussed later). The energy of this resonance ability to be absorbed in the fat, thereafter, it is converted to thermal energy and its transfer to other organs. This phenomenon causes significant high temperature increase within organs.

At the frequency of 915 MHz, it is illustrated the different behavior of the maximum temperature increases to the frequency of 300 MHz. It is found that the temperature increases of TE mode are higher than that of TM mode. This is because the maximum SAR obtained from TE mode occurred in the skin, is very different from fat as shown in Fig. 8(a). Therefore, a significant amount of thermal energy transfers from skin to fat. It is found that the maximum temperature occurs in the fat because it has low thermal conductivity and low blood perfusion rate. While the maximum SAR obtained from TM mode occurs in the fat, but not much different from the contiguous organs. This is because thermal energy spread out from fat to these organs. Thus, the maximum temperatures of organ in human body exposed to electromagnetic wave at 915 MHz of TM mode are lower than that of TE mode.

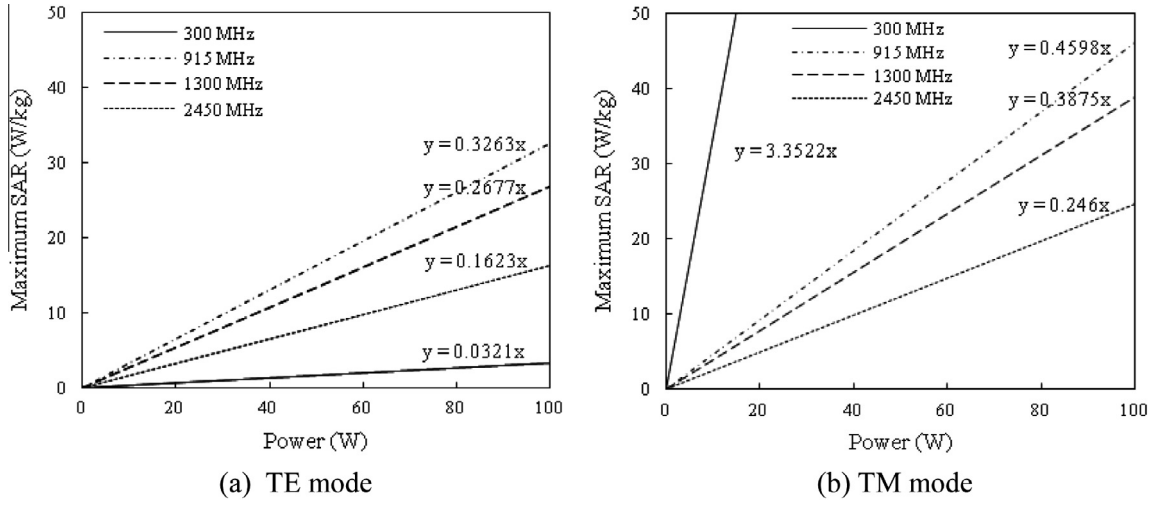

Fig. 9. The maximum SAR on organs of each electromagnetic wave power of heating source which are propagated in (a) TE mode and (b) TM mode.

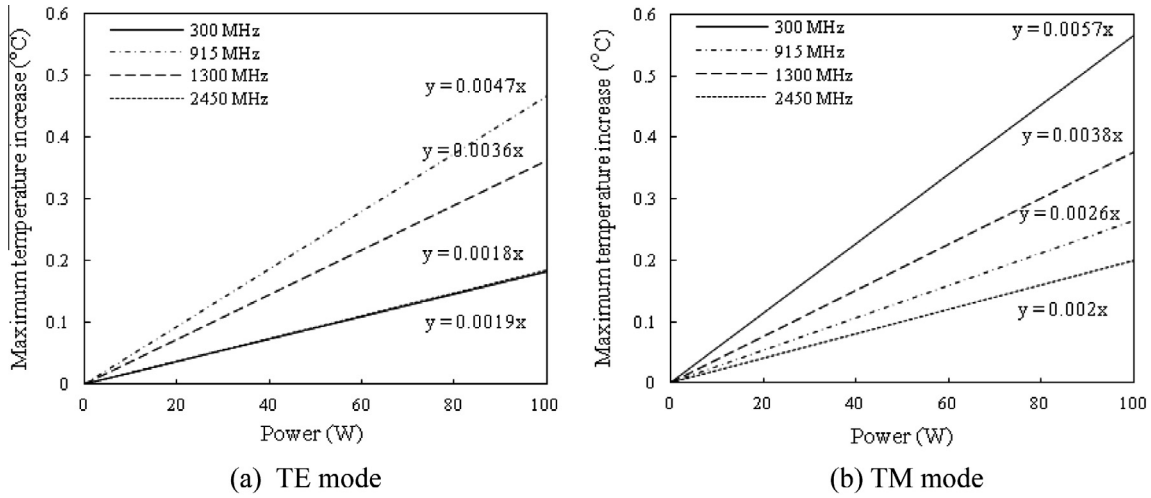

Fig. 10. The maximum temperature increase on organs of each power of heating source which are propagated in (a) TE mode and (b) TM mode.

3.3. Influence of the power of electromagnetic wave

The relation between the maximum SAR and electromagnetic wave radiated power which is propagated in TE and TM mode is shown in Fig. 9. The exposure times at 20 min are selected to study because the maximum temperature increases in human body due to electromagnetic wave are steady for both of frequencies and propagation mode, except at 300 MHz which are shown in Fig. 7.

Fig. 9 shows the maximum SAR depends on the radiated power, it will be increased if the radiated power is higher. The increasing is inversely to the frequency of electromagnetic wave, because the penetration depth in human body of the lower frequency is high, except at frequency 300 MHz in TE mode, it is the most slowly increasing of the maximum SAR because it is very high of penetration depth. This is because the energy of electric field distributes many organs in human body. The maximum SAR at frequency 300 MHz in TM mode is the most rapidly increasing in various powers of source, because the resonance of the electric field standing wave in the fat is very strong due to the large different thermal and dielectric properties with each others as shown in Tables 1 and 2. From electromagnetic theory, the reflection to the first medium and the transmission to the next medium of electromagnetic wave can be occurred at the surface when it propagates in discontinuous medium. The standing wave of electric or magnetic field will be occurred at the first medium due to the combination of incident and reflected field if they have opposite phase, normally when it propagates from low density to strike high density medium. The dominant standing wave of electromagnetic field which is propagated in TE mode is magnetic field, while propagated in TM mode is electric field. These fields will be increased in the medium which has many standing waves due to the resonance of these standing waves inside. Thus, the total electric and magnetic field of each organ are from the penetration field and the resonance. Therefore, SAR value of organ is obtained from electric field, its dielectric property and density as shown in Eq. (10). Moreover, the maximum SAR from TM mode is higher than that of TE mode at each frequency because the dominant standing wave of TM mode is electric field which causes to SAR value.

For consideration of the maximum temperature increases, it is found that most of them are corresponding to the maximum SAR as shown in Fig. 10. For TE mode, the maximum temperatures at the extremely high and low frequencies are slowly increases, while at 915 MHz is the most rapidly increase in this propagation mode. For TM mode, the maximum temperature increase at 300 MHz is

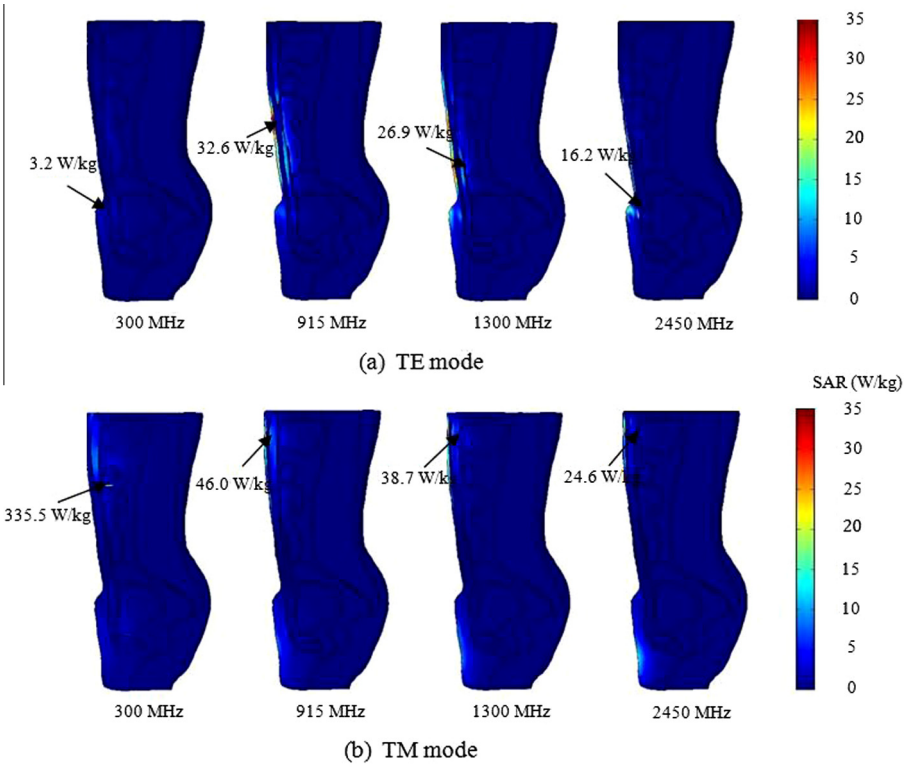

Fig. 11. SAR distribution of human body exposed to electromagnetic wave at frequencies of 300 MHz, 915 MHz, 1300 MHz and 2450 MHz which are propagated in (a) TE mode and (b) TM mode at power 100 W and exposure time 20 min.

the most rapidly while 2450 MHz is the most slowly temperature increase, corresponding to the maximum SAR.

3.4. SAR distribution in human body

Fig. 11 shows the SAR distribution evaluated on the vertical section of the human body in which the maximum SAR value occurs. For consideration of the SAR distribution on organs in human body exposed to electromagnetic wave at frequencies of 300 MHz, 915 MHz, 1300 MHz and 2450 MHz, the cases of 100 W and exposure time at 20 min are investigated. It is evident that the dielectric properties, as shown in Table 2, can become significant to SAR distributions in human organ when electromagnetic energy is exposed in these organs. The electric field is attenuated within the human body, owing to the energy absorbed in organs. The SAR in particular organ is given by Eq. (10), it is found that the high values of SAR occur in the periphery region of the body, skin and fat. The SAR distributions at low frequency are higher than that of high frequency of electromagnetic wave in the same organs, because the penetration depth of low frequency is high. But at frequency 300 MHz in TE mode has low SAR because it is very high penetration depth of this frequency when compares with other frequencies, the electromagnetic wave can moves through many organs in human body and distributes the energy on each organ, as shown in Fig. 11(a).

For TM mode, it is found that the SAR values on each organ which is exposed to electromagnetic wave in TM mode are higher than that of TE mode for all organs and frequencies. This is because the standing wave on each organ can be occurred by the summation of the transmitted electromagnetic field from previous organ and reflected electromagnetic field from the boundary of the next organ. It contributes to the resonance of standing wave in each organ, the energy of the resonance of standing wave will be absorbed by organs. The dominant standing wave on organs from wave propagation in TE mode is magnetic field, while from wave propagation in TM mode is electric field. Thus, the absorbed energy from electric field on each organ which exposed to electromagnetic wave in TM mode is higher than that of TE mode. Fig. 11(b) shows the SAR value at frequency 300 MHz in TM mode is too high on fat when compares with other frequencies and organs, because the dielectric constant of fat is too different from the contiguous organs while the others are similar to each contiguous organ as shown in Table 2, the reflected coefficient of electric field is very high, it causes strong standing wave on fat. The resonance of standing wave on fat at frequency 300 MHz in TM mode is significant because it has high penetration depth and strong standing wave, it has very high SAR when compare to other organs, frequencies of electromagnetic wave and propagation mode.

3.5. Temperature distribution in the human body

Fig. 12 shows the temperature distribution in the human body at the same cases of the SAR consideration. It is found that the temperature increases are corresponding to the SAR distributions because the absorbed energy on each organ is converted to thermal energy. Although the SAR on the inner organs are quite different from the periphery organs of the body as shown in Fig. 8, but the temperature increases are not quite different. Not only SAR is important value to cause the temperature increase in the human body, but the thermal and dielectric properties which are shown in Tables 1 and 2 are also important. The bioheat equation in Eq. (6) shows that thermal energy can be transfer to the contiguous organs due to conduction and blood perfusion terms. The heat source of each tissue is SAR, while heat sink is heat transfer to other organs by factors of thermal conductivity and blood perfusion rate.

For TE mode, the maximum temperature increases are inversely to frequency, except at 300 MHz because it has low SAR in this case. The maximum temperature of high frequencies of 915 MHz

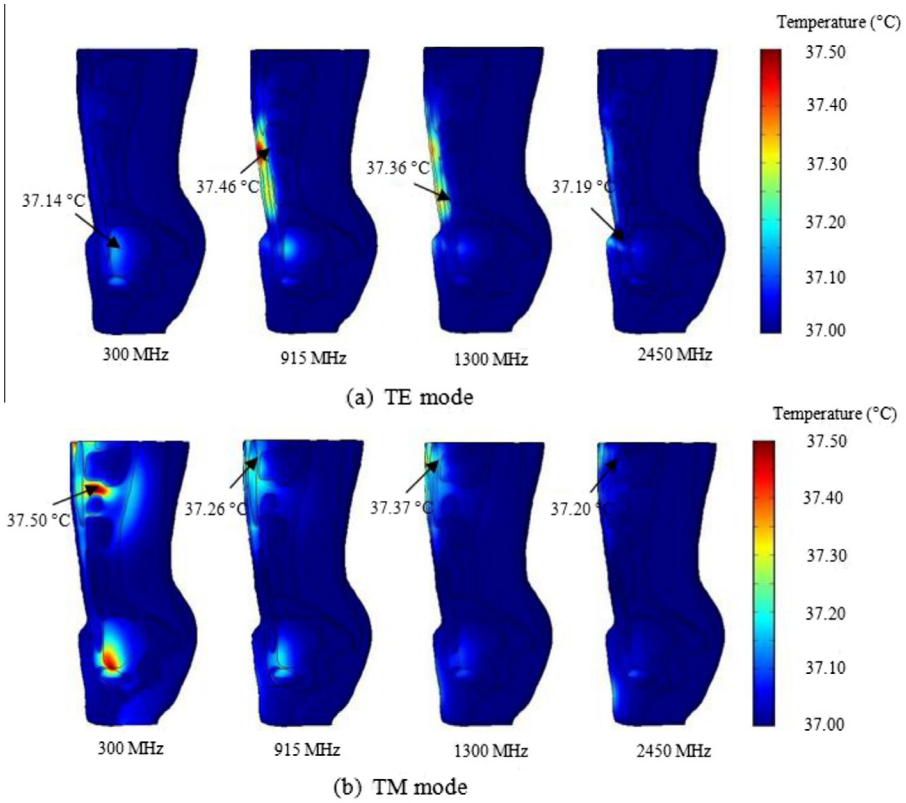

Fig. 12. Temperature distribution of human body exposed to electromagnetic wave at frequencies of 300 MHz, 915 MHz, 1300 MHz and 2450 MHz which are propagated in (a) TE mode and (b) TM mode at power 100 W and exposure time 20 min.

and 1300 MHz are occurred on fat at 37.46 °C and 37.36 °C, respectively. For the frequency of 2450 MHz is occurred on skin at 37.19 °C as shown in Fig. 13(a). This is because fat has low thermal conductivity and blood perfusion rate as shown in Table 1, causes low heat sink on fat. While the maximum temperature at frequency 300 MHz is occurred on bladder, 37.14 °C. This is because this frequency has high penetration depth, it can penetrate into bladder. This organ is very large and do not have blood perfusion rate.

For TM mode, the most of maximum temperature is obtained from 300 MHz at 37.50 °C on fat because it has very high SAR on fat. Fig. 13(b) shows that the temperature increases on organs of 300 MHz are not quite different, although the SAR value on fat is very high when compare with other organs. This is because of heat transfer from fat to the contiguous organs. The maximum temperatures which are obtained from 915 MHz, 1300 MHz and 2450 MHz are occurred on skin at 37.26 °C, 37.37 °C and 37.20 °C, respectively. It is found that the temperature increases which are obtained from both of TE mode and TM mode at high frequency are not different. The maximum temperature increase from all frequencies and propagations mode in this work is 0.50 °C, this temperature is much lower than the thermal damage temperature within the range of 1–5 °C.

3.6. The maximum SAR and temperature on organs in the human body

From the previous section, the steady state temperature after exposure for 20 min at the radiated power of 100 W, are selected to study the organs which have the maximum SAR and temperature. Tables 4 and 5 show the organs which have the maximum SAR and temperature from TE mode and TM mode, respectively. It is found that the maximum SAR from TE mode at frequencies of 915 MHz, 1300 MHz and 2450 MHz occur in the skin. These values are 32.6 W/kg, 26.9 W/kg and 16.2 W/kg, respectively. Thereafter, thermal energy transfers from skin to fat, the maximum temperatures occur on fat, because at low conductivity and blood perfusion rate on fat. These values are 37.46 °C, 37.36 °C and 37.19 °C, respectively. At 300 MHz, which has high penetration depth, the maximum SAR occurs on muscle, 3.2 W/kg, and the maximum temperature occurs on the next organ, bladder, 37.14 °C.

For TM mode, it is found that the maximum SARs occur on fat at all frequencies, because of the resonance of the electric field standing wave is very strong. These values are 335.5 W/kg, 46.0 W/kg, 38.7 W/kg and 24.6 W/kg, respectively. The maximum temperatures occur in the skin because thermal energy from fat spread out to the contiguous organs, except at 300 MHz is still on fat because of very high SAR when compared to the others. These values are 37.50 °C, 37.26 °C, 37.37 °C and 37.20 °C, respectively.

Comparing to the ICNIRP limit [20], SAR value for occupational exposure is 10 W/kg. It is found that most of the resulting of SAR values are exceeded the ICNIRP limit for all cases of frequencies and propagation modes when the electromagnetic radiated power is 100 W, especially at 300 MHz in TM mode.

4. Conclusions

This study presents the numerical simulation of SAR and temperature distributions on organs in human body exposed to electromagnetic wave at the frequencies of 300 MHz, 915 MHz, 1300 MHz and 2450 MHz. The influence of electromagnetic wave propagation mode at each frequency in various exposure time and power of electromagnetic wave are investigated. The results show that the maximum temperature are approch to steady after

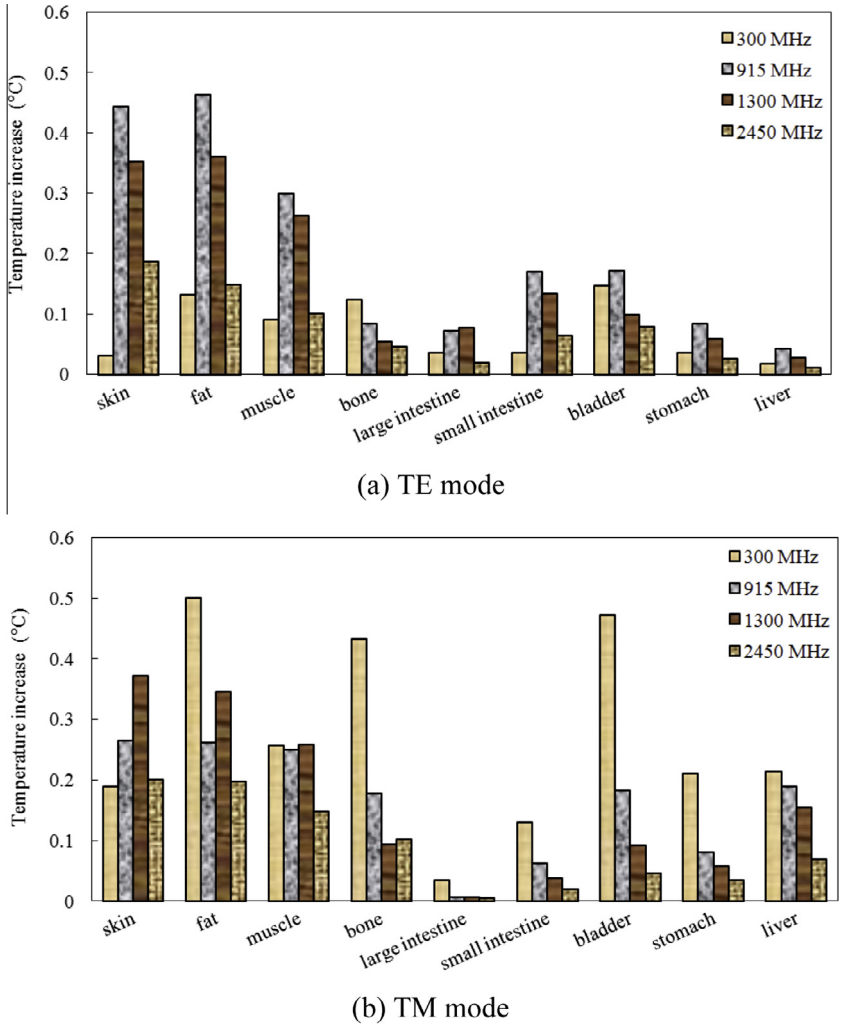

Fig. 13. Temperature distribution on tissues in human body exposed to electromagnetic wave at frequencies of 300 MHz, 915 MHz, 1300 MHz and 2450 MHz which are propagated in (a) TE mode and (b) TM mode at power 100 W and exposure time 20 min.

Table 4
The organ in human body which has the maximum SAR and temperature in TE mode.

Power (W)	300 MHz		915 MHz		1300 MHz		2450 MHz	
	SAR	*T*	SAR	*T*	SAR	*T*	SAR	*T*
10	Muscle	Bladder	Skin	Fat	Skin	Fat	Skin	Fat
50	Muscle	Bladder	Skin	Fat	Skin	Fat	Skin	Fat
100	Muscle	Bladder	Skin	Fat	Skin	Fat	Skin	Fat

Table 5
The organ in human body which has the maximum SAR and temperature in TM mode.

Power (W)	300 MHz		915 MHz		1300 MHz		2450 MHz	
	SAR	*T*	SAR	*T*	SAR	*T*	SAR	*T*
10	Fat	Fat	Fat	Skin	Fat	Skin	Fat	Skin
50	Fat	Fat	Fat	Skin	Fat	Skin	Fat	Skin
100	Fat	Fat	Fat	Skin	Fat	Skin	Fat	Skin

5 min of exposure time, it depends on the power of electromagnetic wave.

For the distribution of SAR consideration, the maximum SARs within the human body which are exposed to electromagnetic wave propagation in TM mode are higher than that of TE mode at each frequency for all cases of radiated power. The maximum SARs occur at skin when electromagnetic wave propagated in TE mode for all frequencies, except at the frequency 300 MHz. It occurs at muscle because it has high penetration depth. In TM mode, they occur at fat for all frequencies because of the resonance of electric field standing wave on fat. These maximum SAR values are proportional to the power of electromagnetic wave but the power of electromagnetic wave is not affected to the organs which have the maximum SAR, it is the same organ for all frequencies and propagation modes even though the power of electromagnetic wave is increasing.

For the distribution of temperature consideration, the maximum temperatures in the human body occur at the contiguous organs of the organs which have the maximum SAR, because of heat transfer of these organs. They occur at bladder from the frequency 300 MHz and fat from the frequencies of 915 MHz, 1300 MHz and 2450 MHz for all powers of electromagnetic wave in TE mode. These organs has the lareg size, the effect of heat is increasing of temperature more than transfer to other organs. While they occur at skin from the frequencies of 915 MHz, 1300 MHz and 2450 MHz for all powers of electromagnetic wave in TM mode. This is because fat is a tiny region at the position of the maximum SAR. Except at the frequency 300 MHz in TM mode, the maximum temperature still occurs at fat. This is because it has very high SAR and the large size of fat.

Moreover, it is found that the temperature distribution is not related only electric field, but the dielectric property, thermal property, blood perfusion and penetration depth of organs at each frequency of electromagnetic wave are significant too. However, mode of electromagnetic wave propagation is important to cause the SAR and temperature distributions. The electromagnetic wave at frequency 300 MHz which is propagated in TE mode is little affected to SAR and temperature distributions in human body, while 300 MHz in TM mode is significant to cause the SAR and temperature distributions.

For the future work, these models will be developed for 3-D simulation for better understanding of the realistic situation of the interaction between the electromagnetic wave and the organs in human body. Moreover, these effects will be calculated from other electromagnetic sources such as electromagnetic wave which is propagated from high power transmission lines.

Acknowledgement

The authors gratefully acknowledge the financial support provided by Thailand Research Fund.

References

[1] P. Rattanadecho, N. Suwannapum, W. Cha-um, Interactions between electromagnetic and thermal fields in microwave heating of hardened Type I-cement paste using a rectangular waveguide (influence of frequency and sample size), ASME J. Heat Transfer 131 (2009) 082101.
[2] N. Suwannapum, P. Rattanadecho, Analysis of heat-mass transport and pressure buildup induced inside unsaturated porous media subjected to microwave energy using a single (TE10) mode cavity, Drying Technol. Int. J. 29 (09) (2011) 1010–1024.
[3] P. Keangin, T. Wessapan, P. Rattanadecho, Analysis of heat transfer in deformed liver cancer modeling treated using a microwave coaxial antenna, Appl. Therm. Eng. 31 (16) (2011) 3243–3254.
[4] P. Keangin, T. Wessapan, P. Rattanadecho, An analysis of heat transfer in liver tissue during microwave ablation using single and double slot antenna, Int. Commun. Heat Mass Transfer 38 (2011) 757–766.
[5] T. Wessapan, S. Srisawatdhisukul, P. Rattanadecho, Numerical analysis of specific absorption rate and heat transfer in the human body exposed to leakage electromagnetic field at 915 MHz and 2450 MHz, J. Heat Transfer 133 (5) (2011). 051101.1-13.
[6] T. Wessapan, P. Rattanadecho, Specific absorption rate and temperature increase in human eye subjected to electromagnetic fields at 900 MHz, ASME J. Heat Transfer (2011).
[7] T. Wessapan, S. Srisawatdhisukul, P. Rattanadecho, Specific absorption rate and temperature distributions in human head subjected to mobile phone radiation at different frequencies, Int. J. Heat Mass Transfer 55 (1–3) (2012) 347–359.
[8] T. Wessapan, S. Srisawatdhisukul, P. Rattanadecho, The effects of dielectric Shield on specific absorption rate and heat transfer in the human body exposed to leakage microwave energy, Int. Commun. Heat Mass Transfer 38 (2011) 255–262.
[9] S. Nishizawa, O. Hashimoto, Effectiveness analysis of lossy dielectric shields for a three-layered human model, IEEE Trans. Microwave Theory Tech. 47 (3) (1999) 277–283.
[10] T. Samaras, A. Christ, A. Klingenbock, N. Kuster, Worst case temperature rise in a one-dimensional tissue model exposed to radiofrequency radiation, IEEE Trans. Biomed. Eng. 54 (3) (2007) 492–496.
[11] Shiba, K., Higaki, N., Analysis of SAR and current density in human tissue surrounding an energy transmitting coil for a wireless capsule endoscope. In: 20th International Zurich Symposium on Electromagnetic Compatibility, Zurich, 2009, pp. 321–324.
[12] R.J. Spiegel, A review of numerical models for predicting the energy deposition and resultant thermal response of humans exposed to electromagnetic fields, IEEE Trans. Microwave Theory Tech. 32 (8) (1984) 730–746.
[13] H.H. Pennes, Analysis of tissue and arterial blood temperatures in the resting human forearm, J. Appl. Physiol. 85 (1) (1998) 5–34.
[14] D. Yang, M.C. Converse, D.M. Mahvi, J.W. Webster, Measurement and analysis of tissue temperature during microwave liver ablation, IEEE Trans. Biomed. Eng. 54 (1) (2007) 150–155.
[15] S. Ozen, S. Helhel, O. Cerezci, Heat analysis of biological tissue exposed to microwave by using thermal wave model of bio-heat transfer (TWMBT), Burns 34 (1) (2008) 45–49.
[16] H. Kanai, H. Marushima, N. Kimura, T. Iwaki, M. Saito, H. Maehashi, et al., Extracorporeal bioartificial liver using the radial-flow bioreactor in the treatment of fatal experimental hepatic encephalopathy, Artif. Organs 31 (2) (2007) 148–151.
[17] J. Wang, O. Fujiwara, FDTD computation of temperature rise in the human head for portable telephones, IEEE Trans. Microwave Theory Tech. 47 (8) (1999) 1528–1534.
[18] D. Yang, M.C. Converse, D.M. Mahvi, J.G. Webster, Expanding the bioheat equation to include tissue internal water evaporation during heating, IEEE Trans. Biomed. Eng. 54 (8) (2007) 1382–1388.
[19] V.L. Dragun, S.M. Danilova-Tret'yak, S.A. Gubarev, Simulation of heating of biological tissues in the process of ultrahigh-frequency therapy, J. Eng. Phys. Thermophys. 78 (1) (2005) 109–114.
[20] G. Ziegelberger, ICNIRP statement on the guidelines for limiting exposure to time-varying electric, magnetic, and electromagnetic (fields up to 300 GHz), Health Phys. 97 (3) (2009) 257–258.

Provided for non-commercial research and education use.
Not for reproduction, distribution or commercial use.

This article appeared in a journal published by Elsevier. The attached copy is furnished to the author for internal non-commercial research and education use, including for instruction at the authors institution and sharing with colleagues.

Other uses, including reproduction and distribution, or selling or licensing copies, or posting to personal, institutional or third party websites are prohibited.

In most cases authors are permitted to post their version of the article (e.g. in Word or Tex form) to their personal website or institutional repository. Authors requiring further information regarding Elsevier's archiving and manuscript policies are encouraged to visit:

http://www.elsevier.com/authorsrights

Author's personal copy

International Journal of Heat and Mass Transfer 65 (2013) 826–844

Contents lists available at SciVerse ScienceDirect

International Journal of Heat and Mass Transfer

journal homepage: www.elsevier.com/locate/ijhmt

Numerical analysis of heat-mass transport and pressure buildup of unsaturated porous medium in a rectangular waveguide subjected to a combined microwave and vacuum system

Khomgris Chaiyo, Phadungsak Rattanadecho *

Research Center of Microwave Utilization in Engineering (R.C.M.E.), Department of Mechanical Engineering, Faculty of Engineering, Thammasat University (Rangsit Campus), Pathumthani 12120, Thailand

ARTICLE INFO

Article history:
Received 13 December 2012
Received in revised form 23 June 2013
Accepted 27 June 2013
Available online 25 July 2013

Keywords:
Microwave
Vacuum
Porous media

ABSTRACT

This paper presents two-dimensional numerical analysis of heat-mass transport and pressure buildup inside an unsaturated porous packed bed which is filled in a rectangular waveguide and subjected to a combined microwave and vacuum system. A microwave system supplies a monochromatic wave in a fundamental TE_{10} mode. The unsaturated porous media is composed of glass beads, water and air. The finite difference time domain method is used to determine the electromagnetic field distribution in the rectangular waveguide by solving the transient Maxwell's equations. The finite difference method together with Newton–Rephson technique is employed to predict the heat, multiphase flow and pressure buildup. The influences of vacuum pressure and operating microwave frequency on temperature, microwave power absorbed, saturation and pressure buildup distribution, and movement of fluid inside the unsaturated porous media are investigated during microwave vacuum drying process.

© 2013 Elsevier Ltd. All rights reserved.

1. Introduction

Microwave technology has been applied to many drying processes for several decades. In microwave drying, that heat is generated by directly transforming the electromagnetic energy into kinetic energy, thus heat is generated deep within the material to be dried. Some of the successful examples of microwave drying are in a ceramics process for drying and sintering, drying of paper, freeze drying and vulcanization of rubber. Furthermore, excellent reviews of microwave drying are presented by Mujumdar [1], Metaxas and Meridith [2] and Datta and Anantheswaran [3]. In vacuum drying processes can offer reduced drying times and higher end-product quality in comparison with a conventional drying [4–5]. Indeed, operating at low pressure reduces the boiling point of water, and provides low temperature to treat product throughout drying process. Vacuum drying is well known in the metallurgical industries for processing of high purity alloys. It is apparent that microwaves can provide a substantial increase rate of heating in a vacuum environment compared with other methods. However it may be limited not only by the usual restraint of mass transfer but also by the onset breakdown electric filed. Fundamental to the operation of a vacuum drying system is the operating pressure to control the temperature of the product below a prescribed limit.

Fig. 1 shows the boiling point temperature of water versus pressure range of 1–133 kPa (about 0.1–1000 torr). For vacuum drying, the pressure range of 1.33–26.6 kPa (about 10–200 torr) is more successful application to dry heat sensitive materials such as pharmaceutical products and other chemicals. The critical breakdown electric field should be also carefully selected to avoid breakdown electric field responses causing the effect of breakdown in gas such air or water vapor [2].

Microwave vacuum drying provides higher product qualities and an improved drying rate compared to conventional drying processing by experimentally investigated of many researchers. Some of the successful researches of experimental microwave vacuum drying are as followings. Drouzas and Schubert [6] investigated experimentally microwave vacuum dying of banana slices that dehydrated products of excellent quality as examined by taste, color, aroma, smell and rehydration tests compared to conventional drying. Drouzas et al. [7] used a laboratory microwave vacuum drier to investigate drying kinetics experiments with model fruit gel, simulating orange juice concentrate that drying rate constant of the thin-layer drying model is increased with increasing microwave power output and decreasing absolute pressure in vacuum drying. Péré and Rodie [8] presented experimental results obtained by microwave vacuum drying of a packing of initially water saturated glass beads and a packing of initially unsaturated pharmaceutical granules. Sunjka et al. [9] investigated two drying methods of cranberries such microwave-vacuum and

* Corresponding author. Tel.: +66 2564 30019x3153; fax: +66 2564 3010.
E-mail address: ratphadu@engr.tu.ac.th (P. Rattanadecho).

0017-9310/$ - see front matter © 2013 Elsevier Ltd. All rights reserved.
http://dx.doi.org/10.1016/j.ijheatmasstransfer.2013.06.066

Author's personal copy

Nomenclatures

C	velocity of light (m/s)
C_p	specific heat capacity (J/kg K)
D	binary mass diffusion (m^2/s)
D_m	effective molecular mass diffusion (m^2/s)
E	electromagnetic field intensity (V/m)
f	frequency of the microwave (Hz)
g	gravitational constant (m/s^2)
H_v	specific heat of evaporation (J/kg)
h_c	Heat transfer coefficient (W/m^2 K)
h_m	mass transfer coefficient (m/s)
J	Leverett functions
K	permeability (m^2)
M	molecular weight (kg/mol)
$\dot{n}$	phase change term (kg/m^3 s)
P	microwave power (W)
p	pressure (Pa)
p_{vs}	partial pressure of the saturation vapor (Pa)
Q	microwave power absorbed term (W/m^3)
R	universal gas constant (J/mol K)
S	water saturation
S_e	effective water saturation
S_{ir}	irreducible water saturation
T	temperature (°C)
t	time (s)
u, w	velocity (m/s)

Greek letters

α	attenuation constant
tan δ	loss tangent coefficient
δ_s	skin depth
ε	complex permittivity (F/m)
ε'	permittivity or dielectric constant
ε''	dielectric loss factor
ϕ	porosity
λ_{eff}	effective thermal conductivity (W/m K)
μ	magnetic permeability (H/m) or Dynamic viscosity (Pa s)
ρ	density (kg/m^3)
σ	gas–liquid interfacial tension

Subscripts

0	free space
a	air
c	capillary
g	gas
l	liquid
p	particle
r	relative
v	water vapor
x, z	Cartesian coordinate

microwave-convective that microwave vacuum drying exhibited to enhance characteristics in almost all observed parameters (color, textural characteristics, organoleptic properties) and was more energy-efficient when compared to microwave-convective drying. Hu et al. [10] compared the characteristics of hot air and microwave vacuum combination drying using edamame as the raw material, it was found that combined hot air and microwave vacuum is enable to increase drying rate and enhance product quality.

In a theoretical analysis of heat and mass transfer in porous materials has been studied for several decades and it can be classified into three difference fundamentals as following details.

(1) The single variable model: one diffusion equation of moisture content is used for simple configuration.
(2) The two variables model: two dependent variables as temperature and moisture content are employed, and effect of pressure buildup can be neglected.
(3) The three variables model: three dependent variables as temperature, moisture content, and pressure buildup are used; this model provides better transport phenomena details than other models.

The single variable and two variables model are mostly applied to investigate for a conventional drying because they are not complicated to manipulate numerical scheme. However, a few studies used the three variables model are Datta and Anantheswaran [3], Perré and Turner [11], Rattanadecho [12], and Ni et al. [13].

A few of researchers have numerically studied heat and mass transport phenomena of porous material under microwave drying processing, and most previous works have not mentioned pressure buildup within porous material [14–19]. Some of previous researches [20–21] revealed pressure buildup by using the three variables model for microwave drying of an unsaturated porous media. However, the studies in case of numerically microwave vacuum drying of unsaturated porous material in a rectangular waveguide of a microwave system supplies a monochromatic wave in a fundamental mode (TE_{10} mode) with operating frequency of 2.45 GHz have not been investigated before. Therefore, this research studies the influence of vacuum pressure and operating microwave frequency to affect internal phenomena of unsaturated porous medium when apply microwave energy.

The objective of this study is carried out to predict temperature, microwave power absorbed and pressure buildup distribution, moisture profile, and movement of fluid inside the unsaturated porous media at vacuum and atmospheric pressures. Furthermore, the influence of material properties is investigated.

2. Experimental apparatus

Fig. 2 shows the experimental apparatus is used. The microwave system is a monochromatic wave of TE_{10} mode at operating frequency of 2.45 GHz. Microwave energy is generated by magnetron, and it is transmitted along z-direction of the rectangular waveguide with inside dimensions of 110 mm × 54.61 mm toward water load that is situated at the end of the waveguide. In addition,

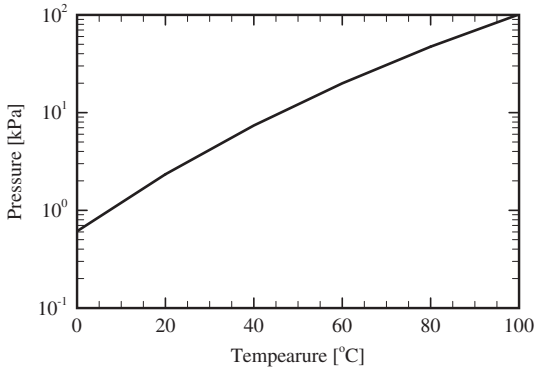

Fig. 1. Saturation vapor pressure of water as a function of temperature.

Author's personal copy

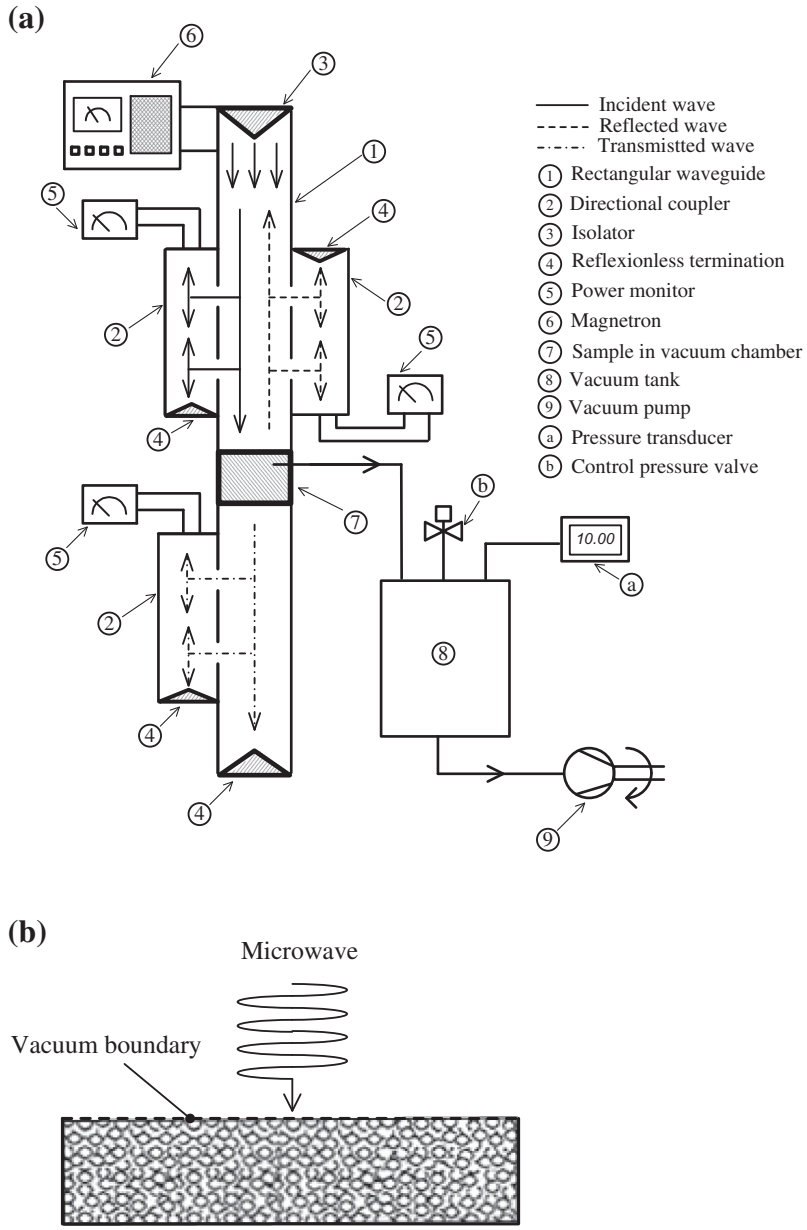

Fig. 2. Schematic of experimental apparatus: (a) a combined microwave and vacuum system, and (b) single-layered porous packed bed (sample) in rectangular waveguide.

an isolator is used to trap any microwave reflected from the sample to prevent it from damaging the magnetron. The powers of incident, reflected and transmitted waves were measured by a wattmeter using a directional coupler.

As shown in Fig. 2(c), the sample is a single-layered porous packed bed, which is composed of glass beads and water. A sample container is made from quartz. The sample of packed bed is inserted in the rectangular waveguide. The distributions of temperature within the sample are measured using fiber-optical temperature. The water saturations in the packed bed were defined as the fraction of the volume occupied by water to volume of the pores, and can be described in the following:

$$s = \frac{\rho_p(1-\phi)(m_w - m_d)}{\rho_l \phi m_d} \quad (1)$$

where s is water saturation, m_w and m_d are wet and dry mass of the sample, respectively, ϕ is porosity, ρ_l and ρ_p are densities of water and particle, respectively.

3. Analysis of mathematical modeling

Generally, studies on the microwave drying involve solutions of the equations governing electromagnetic propagation, i.e., Maxwell's equations, either by themselves or coupled with the heat transport equation. The surface of a sample is exposed to the monochromatic wave of TE_{10} mode with operating frequency of 2.45 GHz (shown as Fig. 2(a)).

3.1. Analysis of electromagnetic model

Fig. 3 shows the physical model used for analyzing microwave drying of capillary porous materials in a rectangular waveguide. The proposed model is based on the following assumptions:

(1) Since the microwave field in the TE_{10} mode has no variation of field in the direction between the broad faces, a two-dimensional model over the x–z plane is applicable to analysis of electromagnetic field inside a rectangular waveguide [22,23]

Author's personal copy

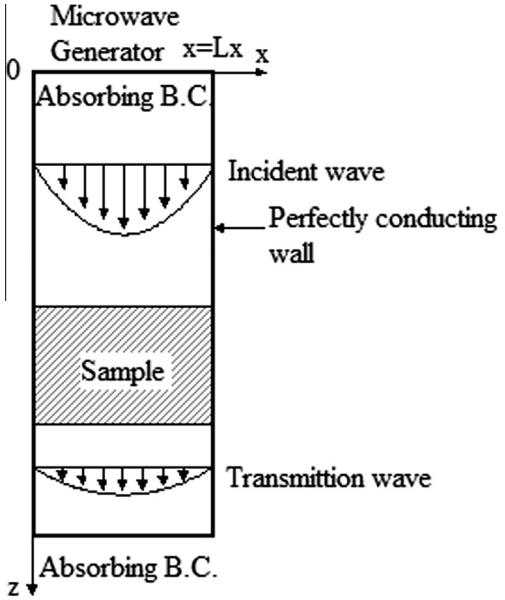

Fig. 3. Physical model for the microwave and dielectric material interactions inside a rectangular waveguide.

(2) The absorption of microwave energy by the cavity (including air) in the rectangular waveguide is negligible
(3) The walls of a rectangular waveguide are perfect conductors
(4) The effect of the sample container (made of quartz) on the electromagnetic field can be neglected because it did not absorb microwave energy

3.1.1. Basic equations of electromagnetic

The electromagnetic field is solved according to the theory of Maxwell's equations. In this study, the microwave of a fundamental TE_{10} mode is considered; therefore the Maxwell's equations in terms of the electric field intensity E and magnetic intensity H are given by:

$$\frac{\partial E_y}{\partial z} = \mu \frac{\partial H_x}{\partial t} \tag{2}$$

$$\frac{\partial E_y}{\partial x} = -\mu \frac{\partial H_z}{\partial t} \tag{3}$$

$$-\left(\frac{\partial H_z}{\partial_x} - \frac{\partial H_x}{\partial z}\right) = \sigma E_y + \varepsilon \frac{\partial E_y}{\partial t} \tag{4}$$

where the permittivity ε, magnetic permeability μ and electric conductivity σ as:

$$\varepsilon = \varepsilon_0 = \varepsilon_r, \quad \mu = \mu_0 \mu_r, \quad \sigma = 2\pi f \varepsilon \tan\delta \tag{5}$$

Additionally if magnetic effects are negligible, which is proven to be a valid assumption for most dielectric materials used in microwave heating applications, the magnetic permeability μ is well approximated by its value μ_0 in the free space. Let tan δ is the loss tangent

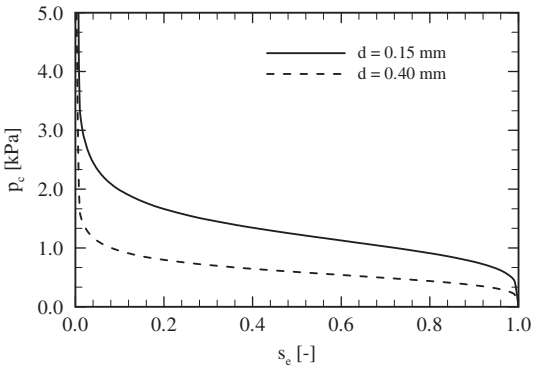

Fig. 5. Typical relationship between p_c and S_e.

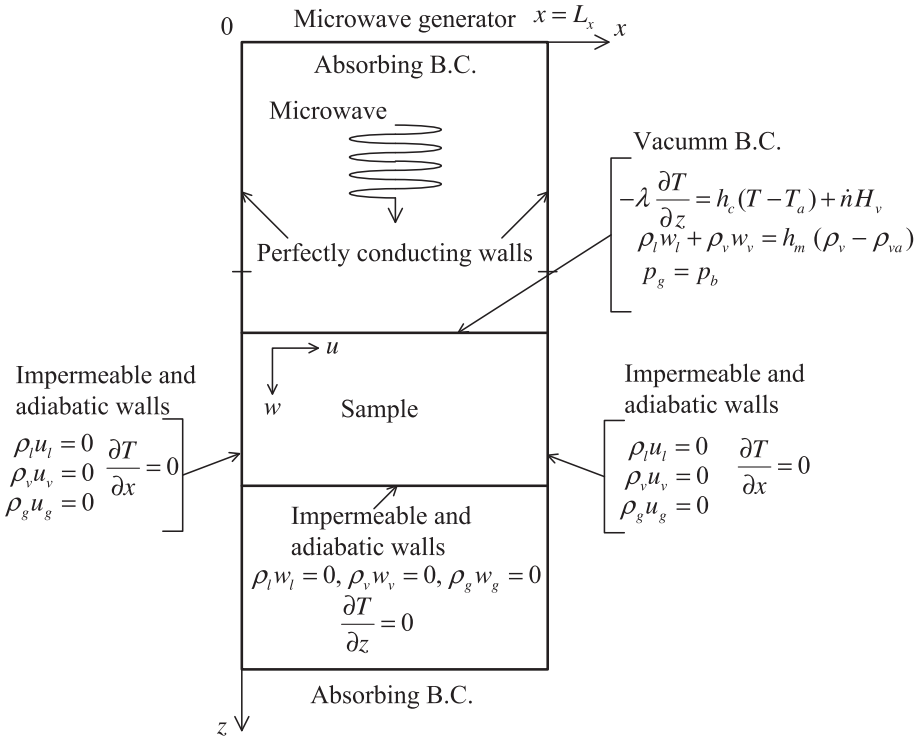

Fig. 4. Physical single layer model.

Author's personal copy

Table 1
Thermophysical and electromagnetic properties (at microwave frequency of 2.45 GHz) used in the computations.

Properties	Air	Water	Glass bead
ρ(kg/m^3)	1.205	1000.0	2500.0
C_p(J/kg K)	1.007	4.186	0.80
λ(W/m K)	0.0262	0.609	0.14
ε'_r(F/m)	1.0	$88.15 - 0.414T + 3.13\times10^{-3}T^2 - 4.60\times10^{-6}T^3$	5.1
$\tan\delta$ (–)	0.0	$0.323 - 9.499\times10^{-3}T + 1.27\times10^{-4}T^2 - 6.13\times10^{-2}T^3$	0.01

coefficient. In this work, the dielectric properties are assumed to vary with temperature only.

In this study, the effects on the overall drying kinetics are examined by selecting the dielectric properties as a function of moisture content and temperature. In order to determine the functional dependence of the combination of moisture content and temperature, the theory surrounding mixing formulas is used [24] in which the volume fractions (v) of water saturation, water vapor and glass particle were considered, as follows:

$$\varepsilon(s,T) = \varepsilon'(s,T) - j\varepsilon''(s,T) \tag{6}$$

where

$$[\varepsilon'(s,T)]^m = \sum_{i=1}^{3} v_i[\varepsilon'_{ri}(T)]^m = \phi.s[\varepsilon'_{rl}(T)]^m + = \phi(1-s)[\varepsilon'_{ra}]^m + (1-\phi)[\varepsilon'_{rp}]^m \tag{7}$$

$$[\varepsilon''(s,T)]^m = \sum_{i=1}^{3} v_i[\varepsilon''_i(T)]^m = \phi.s[\varepsilon''_{rl}(T)]^m + = \phi(1-s)[\varepsilon''_{ra}]^m + (1-\phi)[\varepsilon''_{rp}]^m \tag{8}$$

In above equations, the parameter m is likely to vary over the range 0–1, as suggested by Wang and Schmugge [24]. A value of $m = 0.33$ has been used throughout in this study. The loss tangent coefficient can be expressed as follow:

$$\tan\delta = \frac{\varepsilon''_r(s,t)}{\varepsilon'_r(s,t)} \tag{9}$$

When the material is heated unilaterally, it is found that as the dielectric constant and loss tangent coefficient vary, the penetration depth and the electric field within the dielectric material varies. The penetration depth is used to denote the depth at which the power

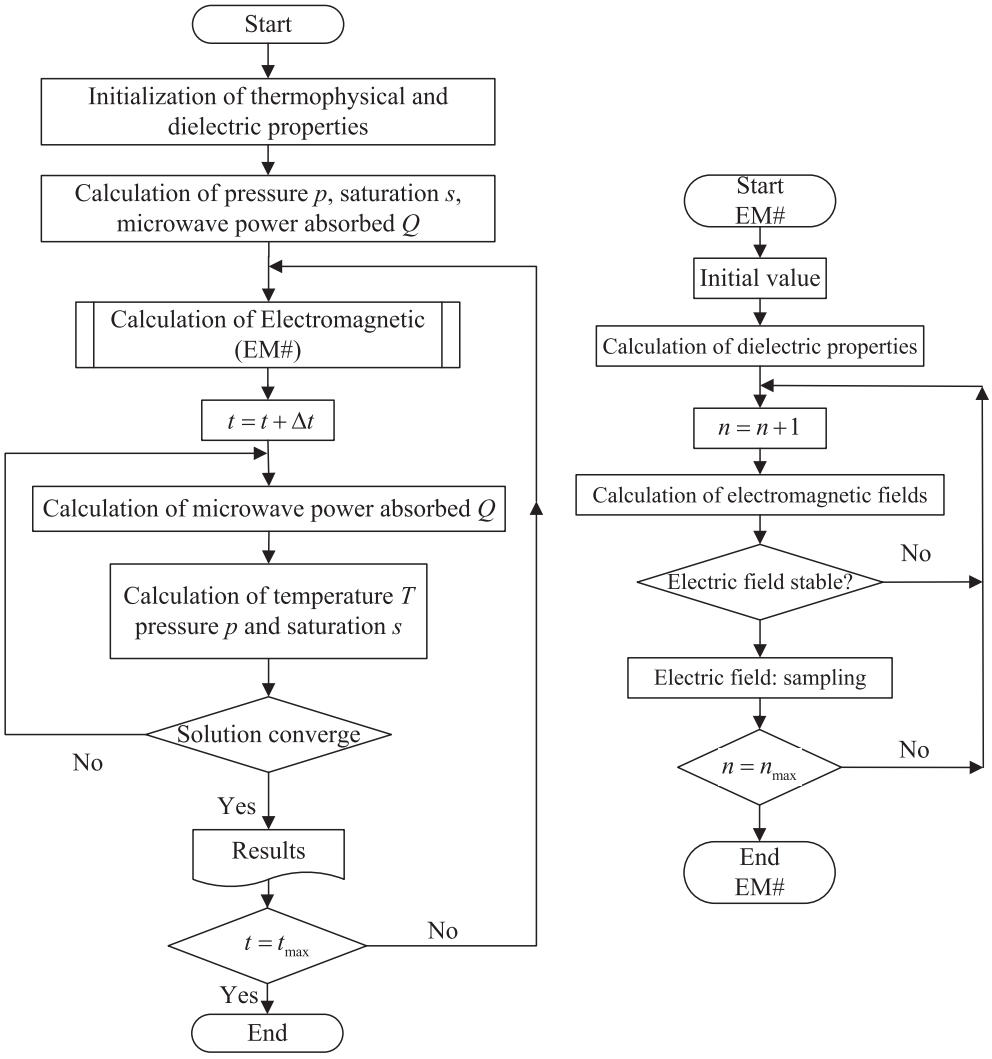

Fig. 6. Computational scheme.

Author's personal copy

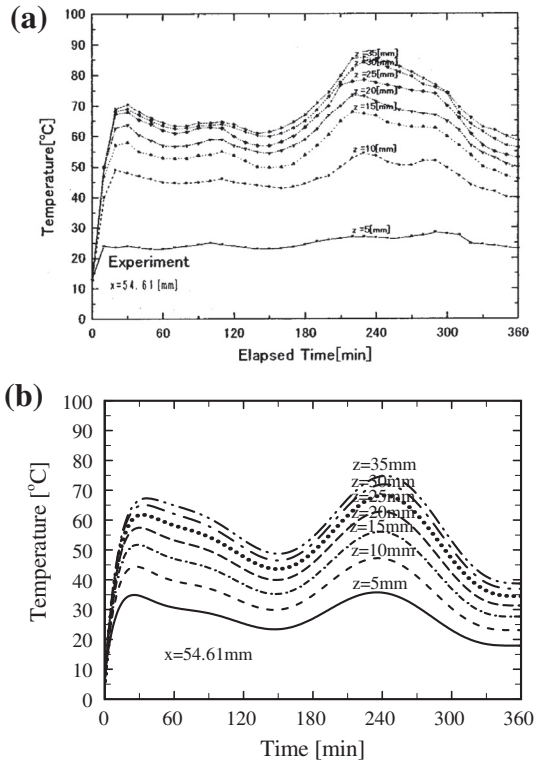

Fig. 7. Temperature profile in times at various depths ($P = 50$ W, $d = 0.15$ mm, $S_0 = 0.6$): (a) experiment result obtained by Ratanadecho et al. [26]; and (b) numerical result of the present study.

density has decreased to 37% of its initial value at the surface [25,26]

$$D_p = \frac{1}{\frac{2\pi f}{\upsilon}\sqrt{\frac{\varepsilon'_r\left(\sqrt{1+tan^2\delta}-1\right)}{2}}} \tag{10}$$

3.1.2. Boundary conditions

Corresponding to the physical model shown in Fig. 4, boundary conditions are given in the following list.

(a) Perfectly conducting boundaries; boundary conditions on the inner wall surface of a rectangular waveguide are given by using Faraday's law and Gauss' theorem:

$$E_t = 0, \quad H_n = 0 \tag{11}$$

where subscripts t and n denote the components of tangential and normal direction, respectively.

(b) Continuity boundary condition; boundary conditions along the interface between different materials, for example between air and dielectric material surface, are given by using Ampere's law and Gauss' theorem:

$$E_t = E'_t, \quad H_t = H'_t, \quad D_n = D'_n, \quad B_n = B'_n \tag{12}$$

where D is the electric flux density and B is the magnetic induction. The superscript $'$ denotes one of the different materials.

(c) Absorbing boundary condition; at both ends of the rectangular waveguide, the first order absorbing conditions proposed by Mur [27] are applied:

$$\frac{\partial E_y}{\partial t} = \pm\upsilon\frac{\partial E_y}{\partial z} \tag{13}$$

Here, the symbol ± represents forward or backward waves and υ is phase velocity of the microwave.

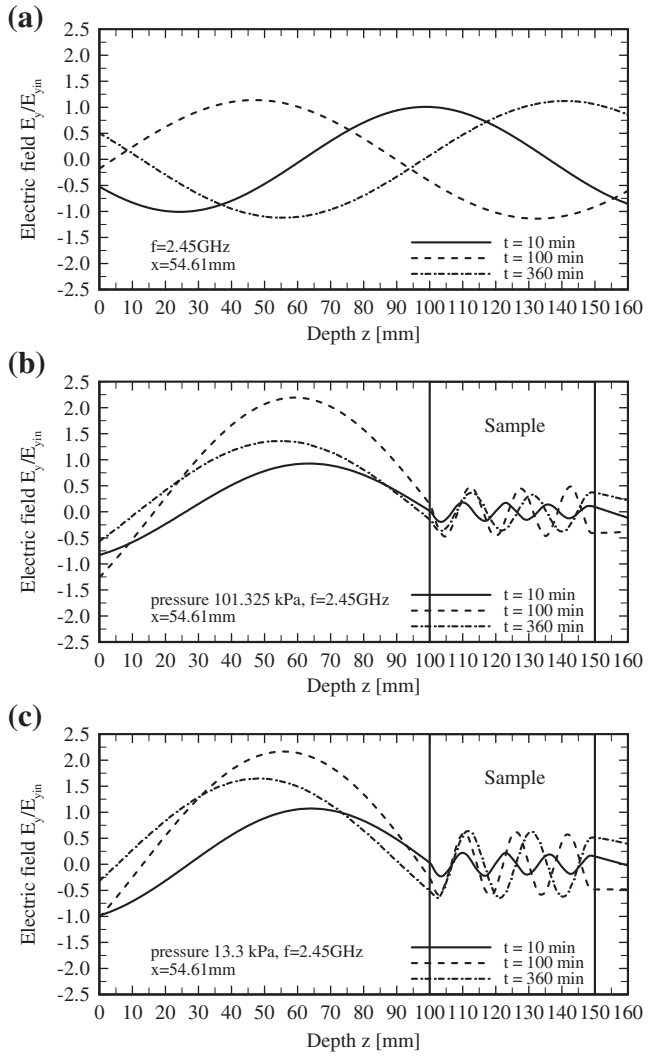

Fig. 8. Electric field distribution in case of microwave frequency of 2.45 GHz: (a) the rectangular waveguide is empty, (b) the sample is inserted in the waveguide rectangular at pressure of 101.325 kPa, (c) the sample is inserted in the rectangular waveguide at pressure of 13.3 kPa.

(d) Oscillation of the electric and magnetic field intensities by magnetron; incident wave due to magnetron is given by the following equations:

$$E_y = E_{yin}\sin\left(\frac{\pi x}{L_x}\right)\sin(2\pi ft) \tag{14a}$$

$$H_x = \frac{E_{yin}}{Z_H}\sin\left(\frac{\pi x}{L_x}\right)\sin(2\pi ft) \tag{14b}$$

where Z_H is the wave impedance defined as

$$Z_H = \frac{\lambda_g Z_I}{\lambda_0} = \frac{\lambda_g}{\lambda_0}\sqrt{\frac{\mu_0}{\varepsilon_0}} \tag{15}$$

3.2. Analysis of heat and mass transfer

A schematic diagram of model is illustrated in Fig. 4. By conservations of mass and energy in the capillary porous sample, the governing equation of mass and energy for all phases can be derived by using the volume average technique [28]. The main transport mechanisms that enable moisture movement during microwave

Author's personal copy

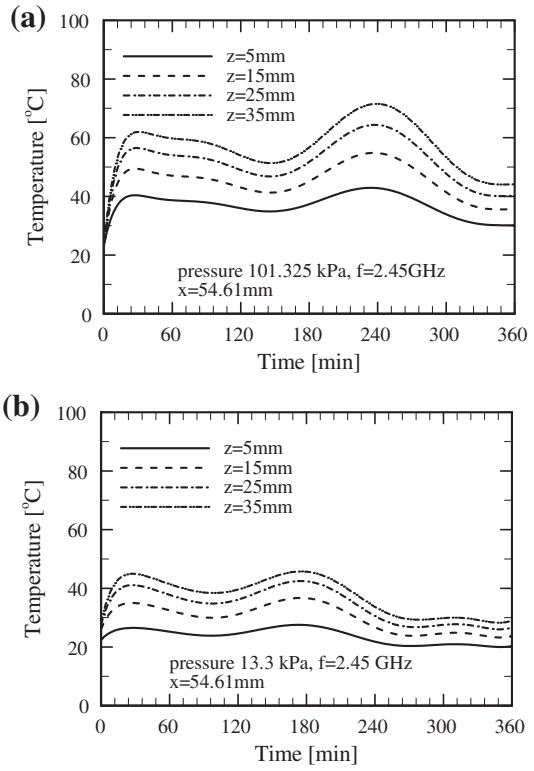

Fig. 9. Temperature profile in times with different z-depths at x-width of 54.61 mm: (a) atmospheric pressure, (b) vacuum pressure of 13.3 kPa.

drying of sample are: liquid flow driven by capillary pressure gradient and gravity while the vapor is driven by the gradient of the partial pressure of the evaporating species. The surface of the sample is exposed to external vacuum condition. Microwaves in the form of plane wave also incident on this surface. Other surfaces are insulated, and the heat and mass fluxes are set equal to zero. In this study, several simplifying assumptions are made in order to obtain a closed set of governing macroscopic equations:

(1) The capillary porous material is rigid, no chemical reactions take place in the sample.
(2) Local thermodynamic equilibrium is assumed.
(3) Simultaneous heat and mass transport occurs at a constant pressure, where the dominant mechanisms are capillary transport, vapor diffusion and gravity: such is generally the case in drying of capillary porous medium at specified vacuum pressure or atmospheric pressure when the temperature is lower than the boiling point.
(4) The gas binary mixture of air and water vapor behaves like an ideal gas.
(5) Darcy's law holds for the liquid and gas phases.
(6) Gravity is included for the liquid and gas phases.
(7) Permeability of liquid and gas can be expressed in term of relative permeability.
(8) The solid matrix is further assumed to be rigid and nondeformable.
(9) In a macroscopic sense, the porous packed bed is assumed to be homogeneous and isotropic, and water not bound to the solid matrix. Therefore, the volume average model for a homogeneous and isotropic material can be used in the theoretical modeling and analysis.
(10) Corresponding to electromagnetic field, temperature and moisture profiles also can be assumed to be two-dimensional in the x–z plane.

The governing equations based on a volume average approach led to the following conservation equations describing the drying process of capillary porous materials:

3.2.1. Mass conservation

The microscopic mass conservation equations for liquid, water vapor, and air phase, are written, respectively, as

$$\text{Liquid phase}: \quad \frac{\partial}{\partial t}(\rho_l \phi s) + \frac{\partial}{\partial x}(\rho_l u_l) + \frac{\partial}{\partial z}(\rho_l w_l) = -\dot{n} \tag{16}$$

$$\text{Vapor phase}: \quad \frac{\partial}{\partial t}[\rho_v \phi(1-s)] + \frac{\partial}{\partial x}(\rho_v u_v) + \frac{\partial}{\partial_z}(\rho_v w_v) = \dot{n} \tag{17}$$

$$\text{Air phase}: \quad \frac{\partial}{\partial t}[\rho_a \phi(1-s)] + \frac{\partial}{\partial x}(\rho_a u_a) + \frac{\partial}{\partial z}(\rho_a w_a) = 0 \tag{18}$$

where $\dot{n}$ is the condensation rate or evaporation rate during phase change and ϕ is the porosity of porous medium. The water vapor and air mass flux is the sum of the convective term with the gas superficial velocity and diffusive term. Additionally, the gas phase is assumed to be an ideal mixture of air and vapor phase.

3.2.2. Energy conservation

Ignoring kinetic energy and pressure terms which are usually unimportant, this can be obtained from the total energy conservation for a combined solid, water vapor and air phase and by invoking the assumption that local thermodynamic equilibrium prevails among the all phases, the temperature of the sample exposed to irradiation is obtained by solving the conventional heat transport equation with the microwave power absorbed included as a local electromagnetic heat generation term.

The governing energy equation describing the temperature rise in the sample is the time dependent equation:

$$\rho C_p \frac{\partial T}{\partial t} + \nabla[\{\rho C_{pl}\vec{u}_l + (\rho_a C_{pa} + \rho_v C_{pv})\vec{u}_g\}T] + H_v \dot{n} = -\nabla q + Q \tag{19}$$

where H_v is the latent heat of vaporization of water and Q is the microwave power absorbed term, which is a function of the electric field and defined as:

$$Q = 2\pi f \varepsilon_0 \varepsilon_r' (\tan\delta) E_y^2 \tag{20}$$

where ε_r' denotes relative dielectric constant, ε_0 denotes the permittivity of free space and tan δ denotes the loss tangent coefficient.

3.2.3. Phenomenological relation

In order to complete the system of equations, the expressions for the superficial average velocity of the liquid and gas phases the generalized Darcy's law in the following vector form is used:

$$\vec{u}_l = -\frac{KK_{rl}}{\mu_l}[\nabla p_g - \nabla p_c - \rho_l \vec{g}] \tag{21}$$

$$\vec{u}_g = -\frac{KK_{rg}}{\mu_g}[\nabla p_g - \rho_g \vec{g}] \tag{22}$$

The velocity of vapor water and air phase the generalized Fick's law for a two component gas mixture can be expressed in vector form as:

$$\rho_v \vec{u}_v = \rho_v \vec{u}_g - \rho_g D_m \nabla\left(\frac{\rho_v}{\rho_g}\right) \tag{23}$$

$$\rho_a \vec{u}_a = \rho_a \vec{u}_g - \rho_g D_m \nabla\left(\frac{\rho_v}{\rho_g}\right) \tag{24}$$

Author's personal copy

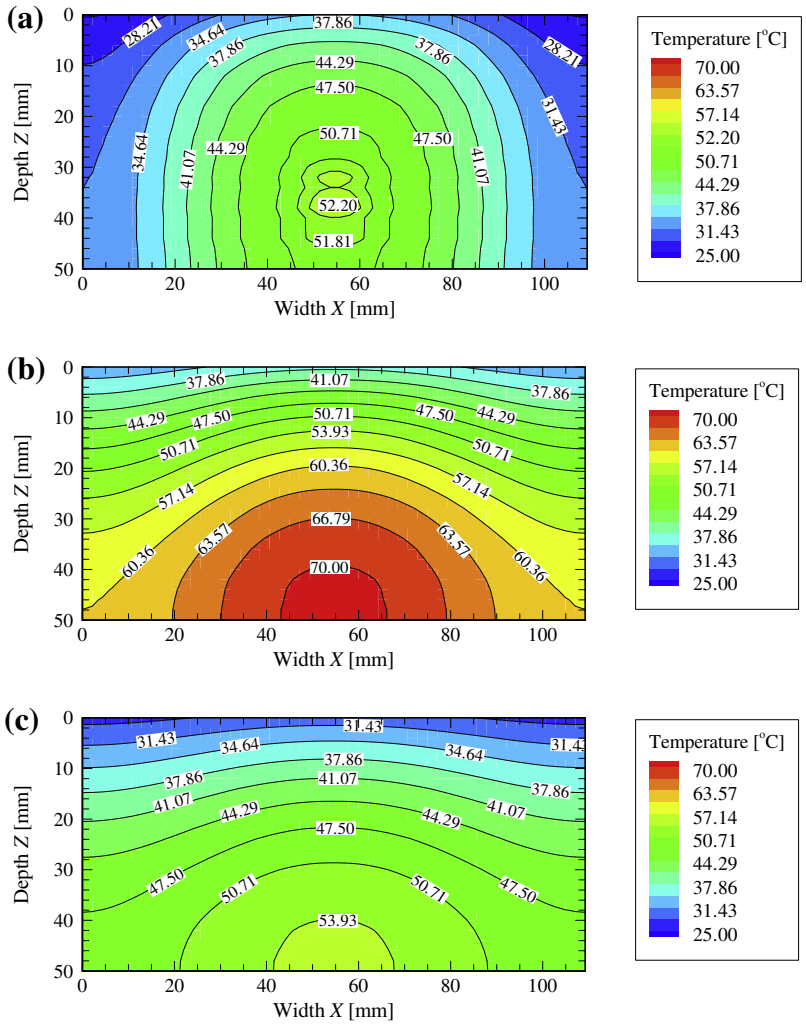

Fig. 10. Temperature distribution inside the sample at atmospheric pressure and microwave frequency of 2.45 GHz: (a) t = 10 min, (b) t = 100 min, and (c) t = 360 min.

where the capillary pressure p_c is related to the gas and liquid phases can be written by

$$p_c = p_g - p_l \tag{25}$$

and D_m is the effective molecular mass diffusion [29] as:

$$D_m = \frac{2\phi}{3-\phi}(1-s)D \tag{26}$$

where D is the binary mass diffusion in plain media, and can be defined as:

$$D = D_0\left(\frac{p_0}{p}\right)\left(\frac{T}{T_0}\right)^{2.2} \tag{27}$$

Fourier's law is used to define the heat flux through the porous material

$$q = -\lambda_{eff}\nabla T \tag{28}$$

3.2.4. Equilibrium relation

The system of conservation equations obtained for multiphase transport mode requires constitutive equation for relative permeability K_r, capillary pressure p_c, capillary pressure functions or Leverett functions $J(s_e)$, and the effective thermal conductivity λ_{eff}. A typical set of constitutive relationships for liquid and gas system is given by Kaviany and Mittal [30]

$$K_{rl} = s_e^3, K_{rg} = (1-s_e)^3 \tag{29}$$

where s_e is the effective water saturation considered the irreducible water saturation s_{ir} and defined by

$$s_e = \frac{s - s_{ir}}{1 - s_{ir}} \tag{30}$$

The capillary pressure p_c is further assumed to be a function of water saturation or Leverett functions $J(s_e)$ and surface tension $\xi(T)$. The Leverett functions $J(s_e)$ is dependent on the internal structure of the porous materials and defined by Aoki et al. [31]:

$$J(s_e) = 0.325(1/s_e - 1)^{0.217} \tag{31}$$

The relationship between the capillary pressure and the water saturation is defined by using Leverett functions $J(s_e)$:

$$p_c = p_g - p_l = \frac{\xi}{\sqrt{K/\phi}}J(s_e) \tag{32}$$

where K the permeability of capillary porous materials is found from the Carman–Kozeny equation [32]:

$$K = \frac{d^2}{180}\frac{\phi^3}{(1-\phi)^2} \tag{33}$$

Fig. 5 shows the typical moisture characteristic curve for different particle sizes obtained from present experiments. It is seen that,

Author's personal copy

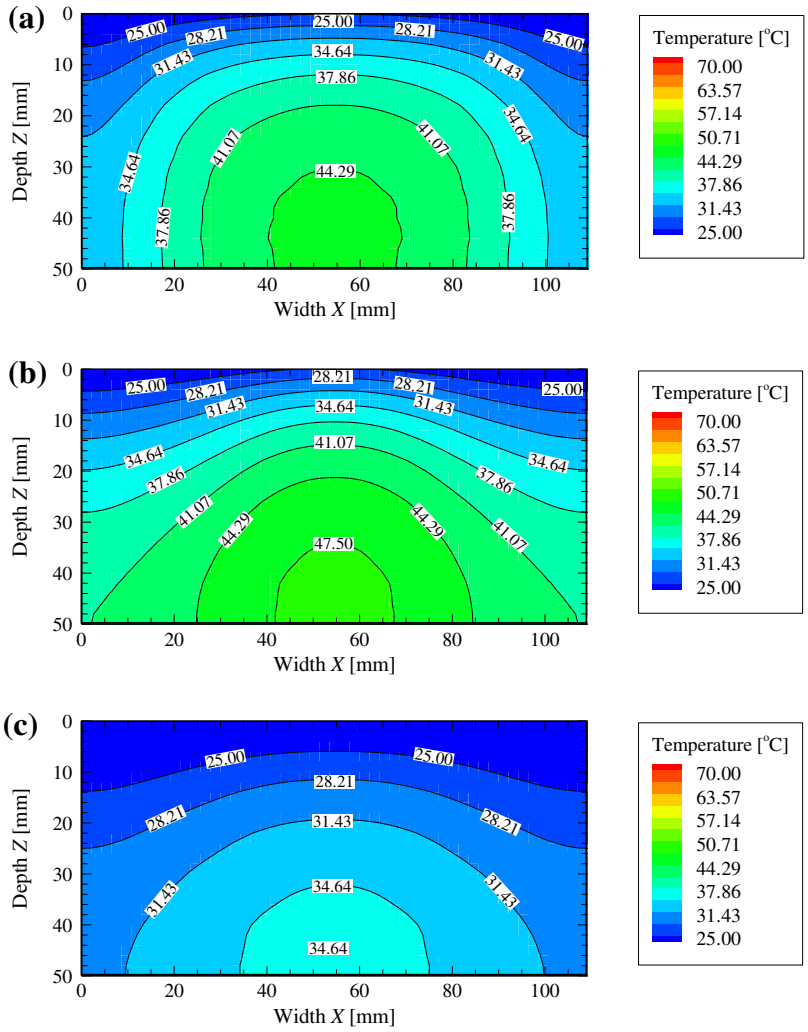

Fig. 11. Temperature distribution inside the sample at vacuum pressure of 13.3 kPa and microwave frequency of 2.45 GHz: (a) t = 10 min, (b) t = 100 min, and (c) t = 360 min.

in the case of the same water saturation, a smaller particle size corresponds to a higher capillary pressure.

Based on the experimental results of Aoki et al. [31] using a glass beads unsaturated with water, the effective thermal conductivity is further assumed to be a function of water saturation and defined by

$$\lambda_{eff} = \frac{0.8}{1 + 3.78e^{-5.95s}} \tag{34}$$

3.2.5. State equation

The gas phase is assumed to be an ideal mixture of perfect gases, so that the species density can be determined by the state equations, with the classical definitions for total density of the gas, ρ_g, and the mass average velocity of the gas:

$$\rho_a = \frac{p_a M_a}{R_0 T} \tag{35}$$

$$\rho_v = \frac{p_v M_v}{R_0 T} \tag{36}$$

$$\rho_g = \rho_a + \rho_v \tag{37}$$

$$p_a = \rho_a R_a T \tag{38}$$

$$P_v = \rho_v R_v T \tag{39}$$

$$p_g = p_a + p_v \tag{40}$$

$$\rho_g u_g = \rho_a u_a + \rho_v u_v \tag{41}$$

The partial pressure of the vapor is given by Kelvin's equation considered the capillary force defined by:

$$p_v = p_{vs} exp\left(\frac{p_c}{\rho_l R_v T}\right) \tag{42}$$

where p_{vs} is the partial pressure of the saturation vapor as a function of temperature [14,33] that shown in Fig. 1 and defined by

$$p_{vs} = C_0 + C_1 T + C_2 T^2 + C_3 T^3 + C_4 T^4 + C_5 T^5 \tag{43}$$

where

$$C_0 = 610.8, \quad C_1 = 43.87, \quad C_2 = 1.47, \quad C_3 = 0.025,$$
$$C_4 = 2.88 \times 10^{-4}, \quad C_5 = 2.71 \times 10^{-6}$$

3.2.6. Moisture transport equation

The phenomenon of moisture transport in the sample is described by the mass conservation equations for the liquid phase (Eq. (15)), and the vapor portion of the gas phase (Eq. (16)). Since the total water content is interested, these equations in two-dimensional scalar forms can be added together to yield an equation for the total moisture content as follows:

Author's personal copy

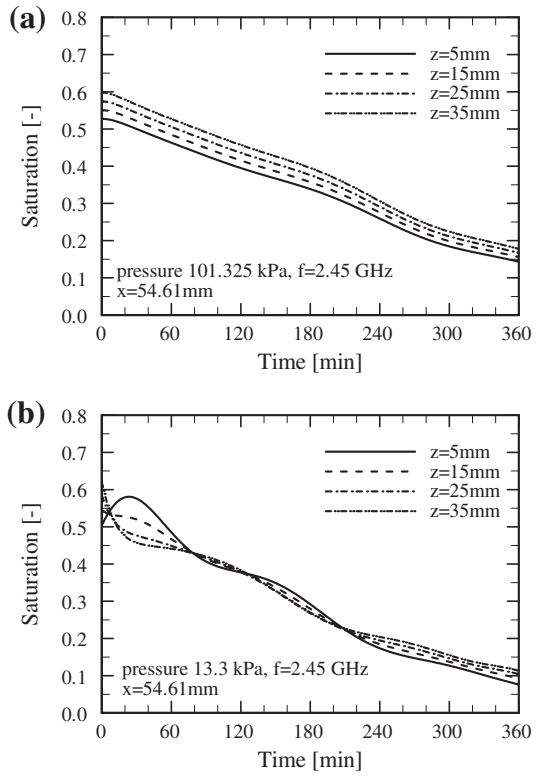

Fig. 12. Saturation profile in times with different z-depths at x-width of 54.61 mm: (a) atmospheric pressure, (b) vacuum pressure of 13.3 kPa.

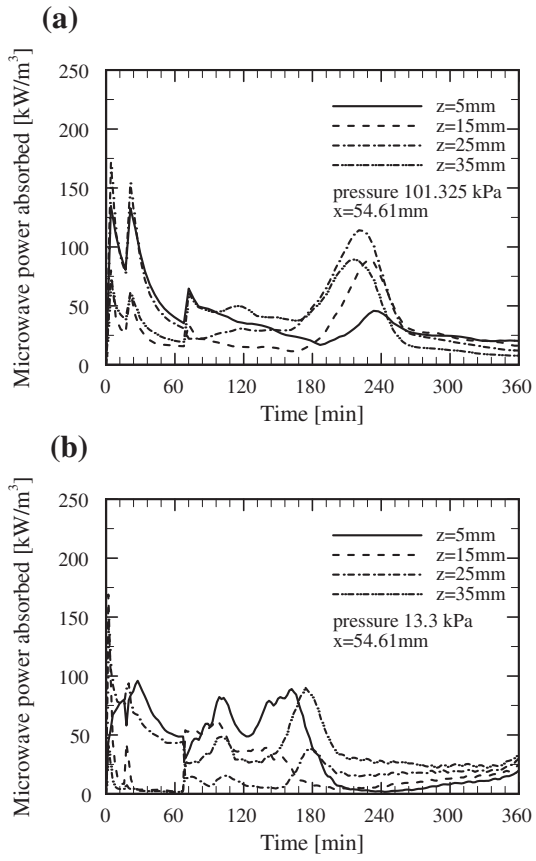

Fig. 13. Microwave power absorbed profile in times with different z-depths at x-width of 54.61 mm: (a) atmospheric pressure, (b) vacuum pressure of 13.3 kPa.

$$\phi\frac{\partial}{\partial t}[\rho_l s+\rho_v(1-s)]+\frac{\partial}{\partial x}(\rho_l u_l+\rho_v u_v)+\frac{\partial}{\partial z}(\rho_l w_l+\rho_v w_v)=0 \tag{44}$$

Using Darcy's generalized equation (Eqs.(20) and (21)) and Fick's law (Eqs.(22) and (23)), the moisture transport equation is written as:

$$\begin{aligned}&\phi\frac{\partial}{\partial t}[\rho_l s+\rho_v(1-s)]\\&+\frac{\partial}{\partial x}\left[\rho_l\frac{KK_{rl}}{\mu_l}\left(\frac{\partial p_c}{\partial x}-\frac{\partial p_g}{\partial x}+\rho_l g_x\right)+\rho_v\frac{KK_{rg}}{\mu_g}\left(-\frac{\partial p_g}{\partial x}+\rho_g g_x\right)-D_m\frac{\partial \rho_v}{\partial x}\right]\\&+\frac{\partial}{\partial z}=\left[\rho_l\frac{KK_{rl}}{\mu_l}\left(\frac{\partial p_c}{\partial_z}-\frac{\partial p_g}{\partial_z}+\rho_l g_z\right)+\rho_v\frac{KK_{rg}}{\mu_g}\left(-\frac{\partial p_g}{\partial z}+\rho_g g_z\right)-D_m\frac{\partial \rho_v}{\partial z}\right]=0\end{aligned} \tag{45}$$

In addition, it is assumed that gravitational effect in x-direction is negligible. Thus, Eq. (38) becomes:

$$\begin{aligned}&\phi\frac{\partial}{\partial t}\{\rho_l s+\rho_v(1-s)\}\\&+\frac{\partial}{\partial x}\left[\rho_l\frac{KK_{rl}}{\mu_l}\left(\frac{\partial p_c}{\partial x}-\frac{\partial p_g}{\partial x}\right)+\rho_v\frac{KK_{rg}}{\mu_g}\left(-\frac{\partial p_g}{\partial x}\right)-D_m\frac{\partial \rho_v}{\partial x}\right]\\&+\frac{\partial}{\partial z}\left[\rho_l\frac{KK_{rl}}{\mu_l}\left(\frac{\partial p_c}{\partial z}-\frac{\partial p_g}{\partial x}+\rho_l g_z\right)+\rho_v\frac{KK_{rg}}{\mu_g}\left(-\frac{\partial p_g}{\partial x}+\rho_g g_z\right)-D_m\frac{\partial \rho_v}{\partial z}\right]=0\end{aligned} \tag{46}$$

3.2.7. Total pressure equation

Considering the Darcy's law and Fick's law, and assuming that the gaseous phase is an ideal mixture of perfect gases, Eq. (17) becomes:

$$\begin{aligned}&\phi\frac{\partial}{\partial t}[\rho_a(1-s)]+\frac{\partial}{\partial x}\left[\rho_a\frac{KK_{rg}}{\mu_g}\left(-\frac{\partial p_g}{\partial x}\right)-D_m\frac{\partial}{\partial x}(\rho_a)\right]\\&+\frac{\partial}{\partial z}\left[\rho_a\frac{KK_{rg}}{\mu_g}\left(-\frac{\partial p_g}{\partial z}+\rho_g g_z\right)-D_m\frac{\partial}{\partial z}(\rho_a)\right]=0\end{aligned} \tag{47}$$

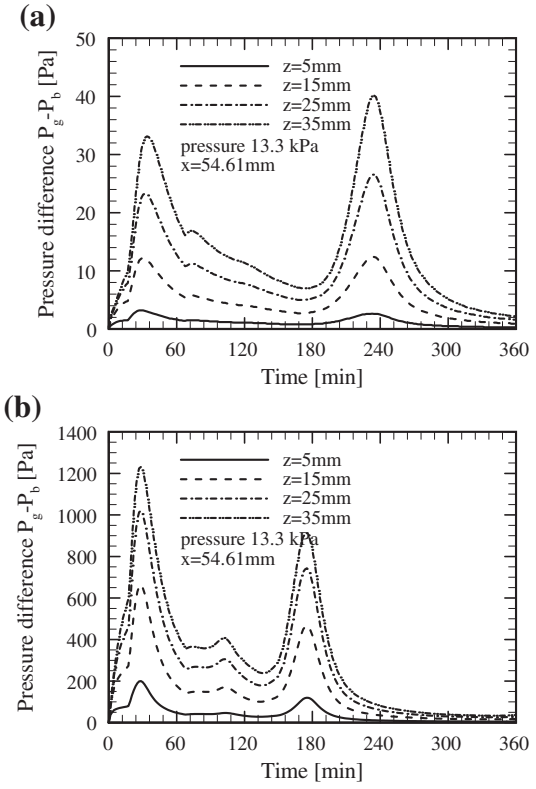

Fig. 14. Pressure difference profile in times with different z-depths at x-width of 54.61 mm: (a) atmospheric pressure, (b) vacuum pressure of 13.3 kPa.

Author's personal copy

3.2.8. Heat transport equation

For a nonisothermal flow, we must add temperature as a dependent variable. The conservation of energy equation for the two-dimensional model allows prediction of the temperature. Thus, Eq. (18) leads to:

$$\rho C_p \frac{\partial T}{\partial t} + \frac{\partial}{\partial x}\left[\{\rho_l C_{pl} u_l + (\rho_a C_{pa} + \rho_v C_{pv}) u_g\} T\right] + \frac{\partial}{\partial z}\left[\{\rho_l C_{pl} w_l + (\rho_a C_{pa} + \rho_v C_{pv}) w_g\} T\right] + H_v \dot{n} = \frac{\partial}{\partial x}\left[\lambda_{eff} \frac{\partial T}{\partial x}\right] + \frac{\partial}{\partial z}\left[\lambda_{eff} \frac{\partial T}{\partial z}\right] + Q \quad (48)$$

where ρC_p is the effective heat capacitance of water–gas matrix mixtures:

$$\rho C_p = \rho_l C_{pl} \phi s + (\rho_a C_{pa} + \rho_v C_{pv}) \phi (1 - s) + \rho_p C_{pp} (1 - \phi) \quad (49)$$

Also, the phase change term is given by

$$\dot{n} \frac{\partial}{\partial t}\{\rho_v \phi (1 - s)\} + \frac{\partial}{\partial x}\left[-D_m \frac{\partial \rho_v}{\partial x}\right] + \frac{\partial}{\partial z}\left[\rho_v \frac{KK_{rg}}{\mu_g} \rho_g g_z - D_m \frac{\partial \rho_v}{\partial z}\right] \quad (50)$$

3.2.9. Boundary and initial conditions

In Fig. 4 two types of boundary conditions for solution of the governing equations are formulated at the open and impermeable boundaries. At open boundary (as vacuum boundary), the liquid and vapor flux reaching the boundary from the interior is fully evaporated and convected away as vapor to the ambient. Regardless of the volumetric evaporation rate inside, any remaining liquid flux arriving at the surface is evaporated at the open boundary. The exchanger of energy at the open boundary which can be described in the following form:

$$-\lambda_{eff} \frac{\partial T}{\partial z} = h_c (T - T_\infty) + \dot{n} H_v \quad (51)$$

where h_c is the local heat transfer coefficient, and T_∞ is the reference temperature in the gas phase surrounding the vacuum boundary.

Mass transfer at the open boundary is modeled by means of a locally constant mass transfer coefficient, which is related to the local vapor flux density, and is described as:

$$\rho_l w_l + \rho_v w_v = h_m (\rho_v - \rho_\infty) \quad (52)$$

where ρ_v is the density of vapor at the open boundary and ρ_∞ is reference vapor density in the gas phase surrounding the open bound-

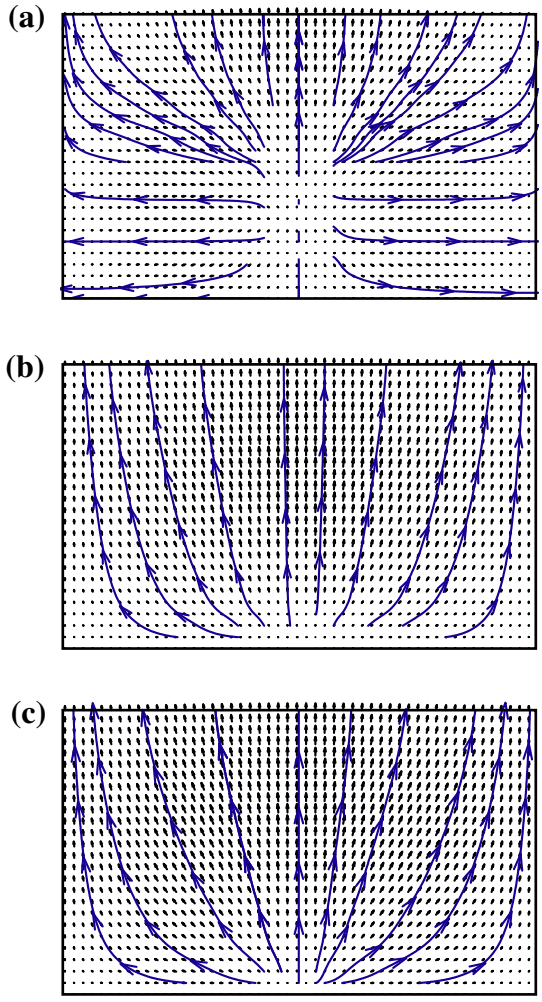

Fig. 15. Vector and streamline of vapor flux inside the sample at atmospheric pressure (scale × 9,000,000): (a) t = 10 min, (b) t = 100 min, and (c) t = 360 min.

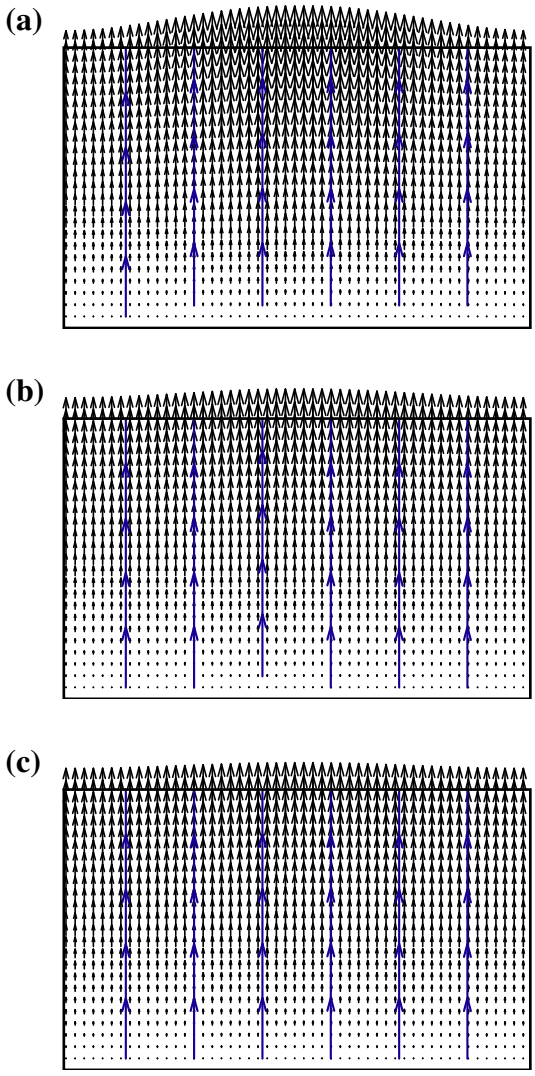

Fig. 16. Vector and streamline of liquid flux inside the sample at atmospheric pressure (scale × 2500): (a) t = 10 min, (b) t = 100 min, and (c) t = 360 min.

Author's personal copy

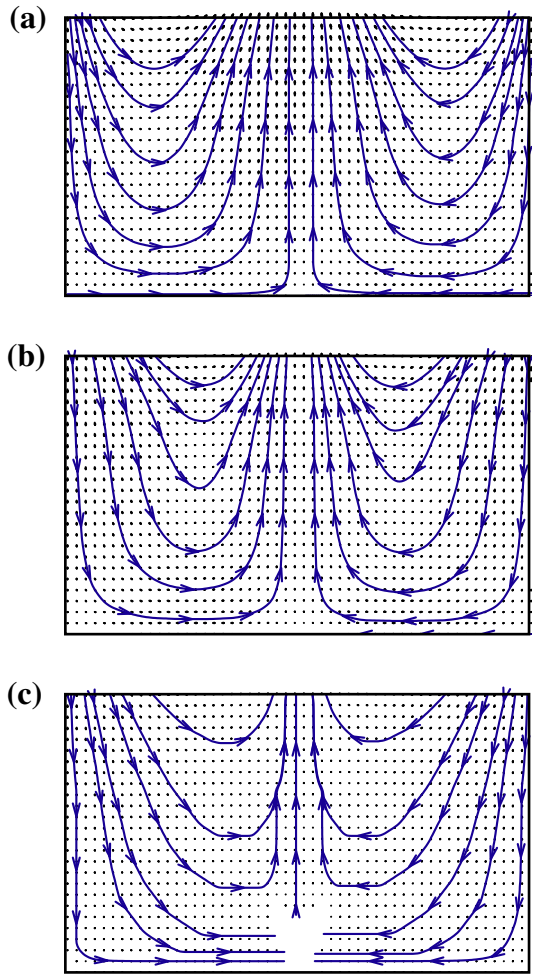

Fig. 17. Vector and streamline of air flux inside the sample at atmospheric pressure (scale × 30,000,000): (a) t = 10 min, (b) t = 100 min, and (c) t = 360 min.

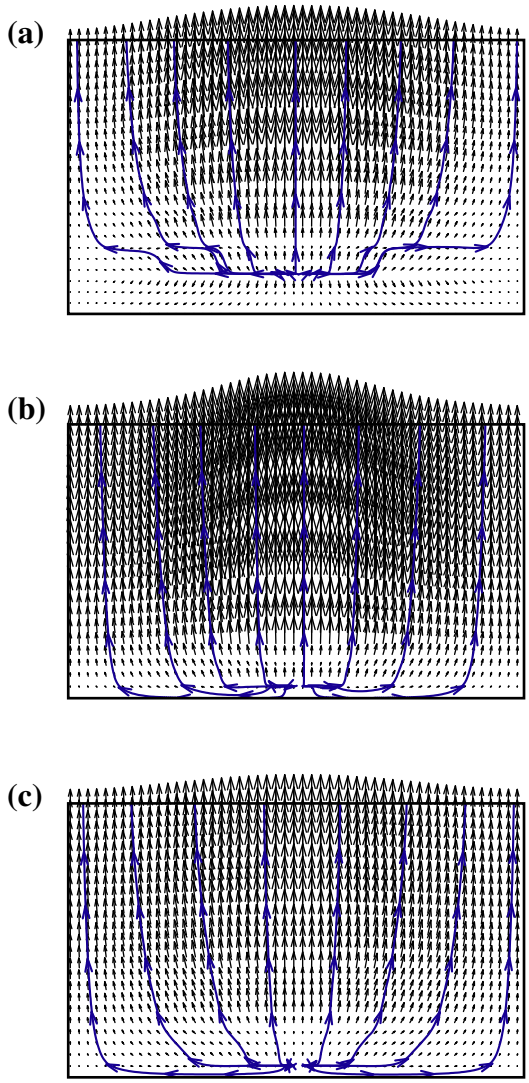

Fig. 18. Vector and streamline of vapor flux inside the sample at vacuum pressure of 13.3 kPa (scale × 9,000,000): (a) t = 10 min, (b) t = 100 min, and (c) t = 360 min.

ary, and assuming in this case the analogy between heat and mass transfer [32], the local mass transfer coefficient, h_m can be expressed as:

$$h_m = \frac{h_c}{\rho_g C_{pg} Le^{2/3}} \tag{53}$$

where

$$Le = \frac{\alpha_g}{D} \tag{54}$$

The total pressure at open boundary (the external drying surface) is fixed at boundary pressure, p_b as:

$$p_g = p_b \tag{55}$$

where p_b is equal to or less than 101.325 kPa in case of atmospheric pressure and vacuum pressure, respectively. Considering boundary conditions at the impermeable boundary that no heat and mass exchange taken place are given by:

$$\frac{\partial T}{\partial x} = \frac{\partial T}{\partial z} = 0, \quad \rho u = \rho w = 0 \tag{56}$$

The initial conditions are given by uniform initial temperature and moisture content.

4. Numerical solution procedure

4.1. Model discretization

The description of heat, mass transfer and total pressure equations (Eqs. (39)–(41)) requires specification of temperature (T), total pressure (p_g) and the moisture content (s) within the sample. These equations are coupled to the Maxwell equations (Eqs. (2)–(4) by Eq. (19)). The later equation represents the local microwave power absorbed in the sample.

In order to predict the electromagnetic field (Eqs. (2)–(4)), a finite difference time domain (FDTD) method is applied. The system of nonlinear partial differential equations (Eqs. (39)–(41)) are solved by a finite difference method. The Newton Raphson method is employed at each iteration to quicken the convergence. Initially, the temperature and moisture profiles were set to be equal at all nodes at values corresponding to the measured capillary porous medium conditions. Considering the microwave drying in TE_{10} mode, it is the lowest mode of the supported microwave field for waves transmitted in the present rectangular waveguide without power dissipation. The type of wave mode is prescribed by the frequency and waveguide dimension.

Author's personal copy

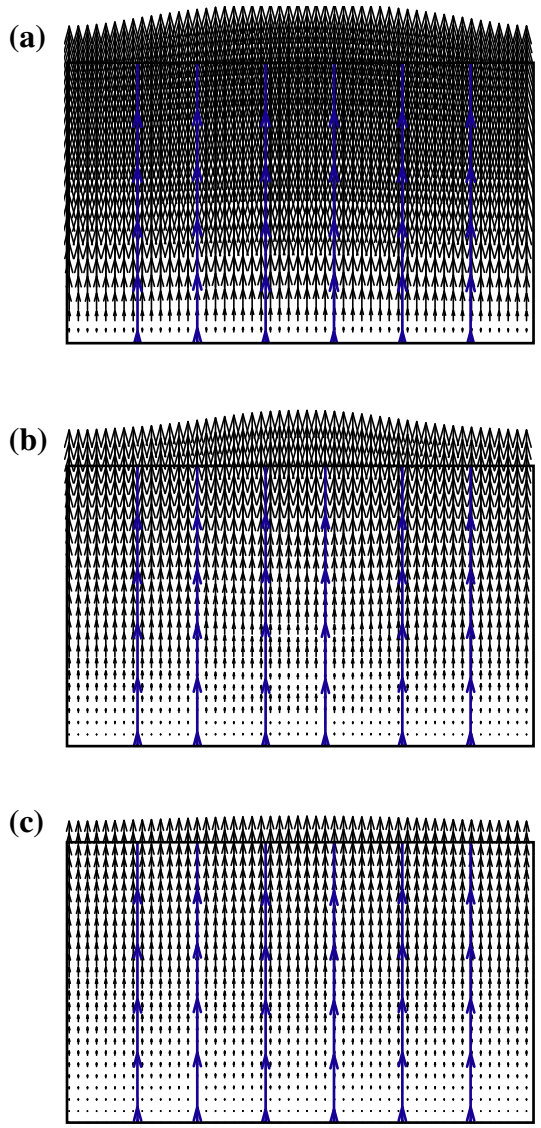

Fig. 19. Vector and streamline of liquid flux inside the sample at vacuum pressure of 13.3 kPa (scale × 2500): (a) t = 10 min, (b) t = 100 min, and (c) t = 360 min.

4.2. The stability and accuracy of calculation

Spatial and temporal resolution is selected to ensure of stability and accuracy. Eqs. (2)–(4) are solved on a grid system, and temporally they are solved alternatively for both the electric and magnetic fields. To insure stability of the time-stepping algorithm, Δt was chosen to satisfy the courant stability condition:

$$\Delta t \leq \frac{\sqrt{(\Delta x)^2 + (\Delta z)^2}}{\upsilon} \tag{57}$$

and the spatial resolution of each cell defined as

$$\Delta x, \Delta z \leq \frac{\lambda_g}{10\sqrt{\varepsilon_r}} = \frac{\lambda_{mg}}{10} \tag{58}$$

The relative errors in the iteration procedure of 10^{-8} are chosen. One aspect of model verification is to compare drying data from experiments run under different conditions with mathematical simulations using parameter values obtained from Table 1. The details of computational scheme and strategy are illustrated in Fig. 6.

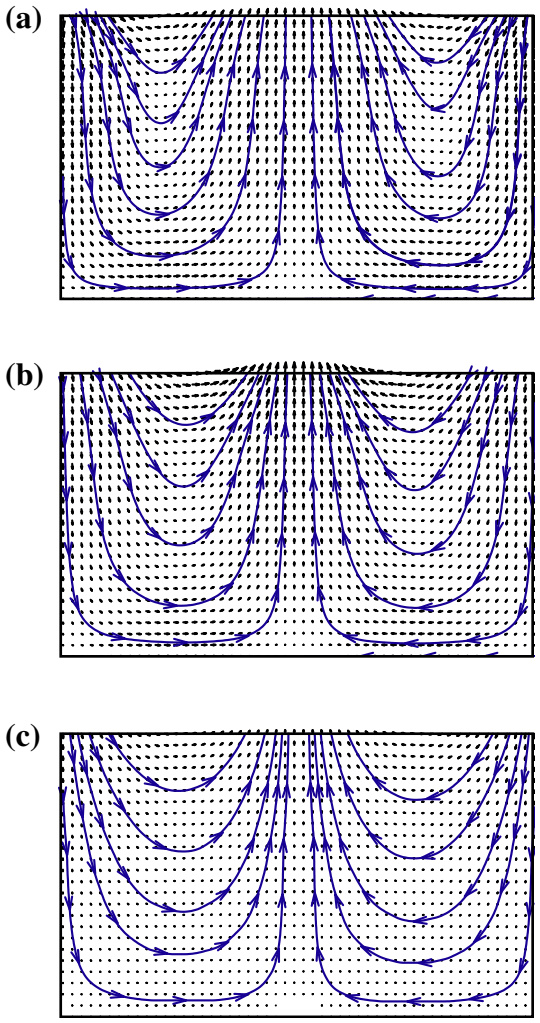

Fig. 20. Vector and streamline of air flux inside the sample at vacuum pressure of 13.3 kPa (30,000,000): (a) t = 10 min, (b) t = 100 min, and (c) t = 360 min.

5. Results and discussion

The numerical results for heat, multiphase flow and pressure buildup in an unsaturated porous packed bed (composed of glass beads, water, and air) filled in a rectangular waveguide and subjected to a combined microwave and vacuum system are investigated. A microwave system supplies a monochromatic wave in a fundamental mode (TE_{10} mode) with operating frequency of 2.45 GHz and input microwave power of 50 W.

5.1. Numerical validation

Fig. 7(a) and (b) shows the present simulation results compared with experimental data from Ratanadecho et al. [26] of temperature profiles within the sample, corresponding to the initial temperature of 10.4 °C, initial saturation s_{in} of 0.6, particle size d_p of 0.15 mm and input microwave power of 50 W. It is observed that the trends of results are in good agreement. The source of the discrepancy is the non-uniform heating effect along the axis, which accounts for the fact that the incident microwave at the surface of the sample is non-uniform. Numerically, the discrepancy may be attributed to uncertainties in the thermal and dielectric property database. On the other hand during the experiment of microwave drying process, the impact on the uncertainty of our data

Author's personal copy

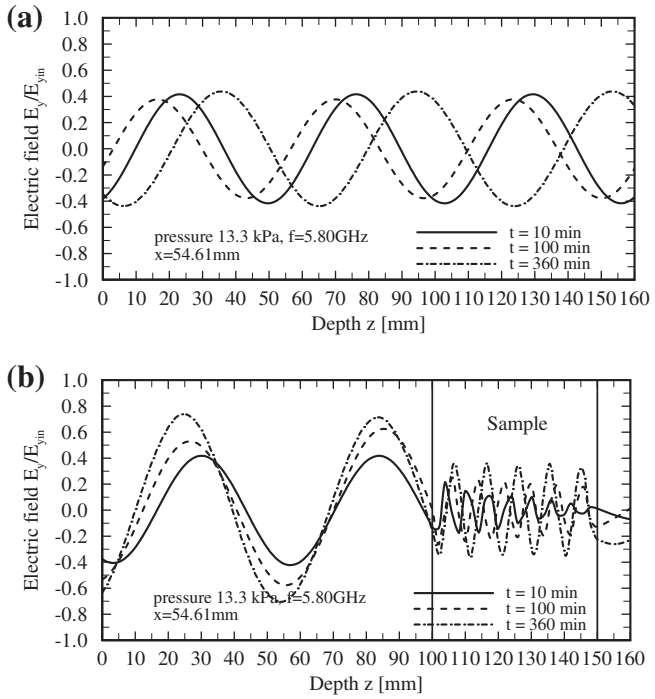

Fig. 21. Electric field distribution in case of vacuum pressure of 13.3 kPa and microwave frequency of 5.8 GHz: (a) the rectangular waveguide is empty, (b) the sample is inserted in the rectangular waveguide.

Table 2
Penetration depth of unsaturated packed bed at various times.

Time (min)	Penetration depth D_p (mm)	
	f = 2.45 GHz	f = 5.80 GHz
0	200.12	52.18
10	265.73	57.02
100	377.09	94.86
360	946.67	258.62

may cause by variations in humidity, room temperature and another effects.

5.2. The effect of vacuum pressure level

The numerical results for heat, multiphase flow and pressure buildup in an unsaturated porous packed bed subjected to microwave energy are investigated at vacuum pressure of 13.3 kPa (100 torr) compared with atmospheric pressure condition. However, two drying processes using the operating microwave frequency of 2.45 GHz, the input microwave power of 50 W, initial temperature of 25 °C, initial saturation of 0.6, and particle size of 0.15 mm are selected. In the selected vacuum pressure of 13.3 kPa is in typical range of pressure (1.33–26.66 kPa) in vacuum processing and is similar to Changrue [34] in which microwave vacuum processing is applied to investigate drying of carrots cubes. The input microwave power of 50 W is also lower than the critical breakdown electric field [2]. Therefore, the effect of gas breakdown is not appeared in this drying condition.

Fig. 8(a) illustrates the electric field distribution along the center axis (x = 54.61 mm) of the empty rectangular waveguide at different drying times (t = 10, 100 and 360 min) in case of atmospheric pressure which is similar to vacuum pressure of 13.3 kPa. In this figure, the vertical axis represents the intensity of the electric fields E_y, which is normalized to the amplitude of

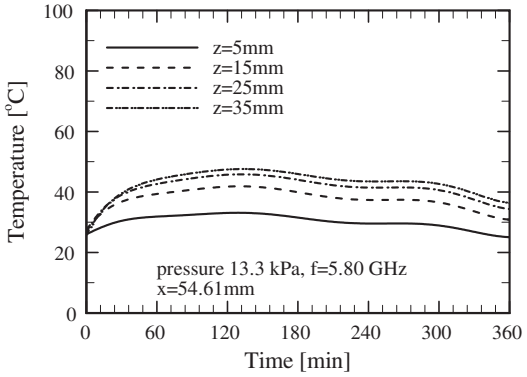

Fig. 22. Temperature profile in times with different z-depths at x-width of 54.61 mm in case of vacuum pressure of 13.3 kPa and microwave frequency of 5.80 GHz.

the input electric fields E_{yin}, it is seen that the stationary wave inside the empty waveguide with completely power is absorbed by water load at the end of the waveguide.

Fig. 8(b) and (c) shows the electric filed distribution along the center axis (x = 54.61 mm) of the rectangular waveguide when inserted the sample at different drying times (t = 10, 100 and 360 min) in case of atmospheric pressure and vacuum pressure of 13.3 kPa, respectively. Since the sample is composed of glass beads, water and air that is implied to be a lossy material (moist porous material). For the case of atmospheric pressure, it is observed from Fig. 8(b) that the resonance of standing wave configuration inside the sample is weak as compared to left-hand side of the sample. Focusing attention of the electric filed distribution inside the cavity (left-hand side), a stronger standing wave with large amplitude is formed by interference between the incident waves and reflected waves from the surface of sample due to the different dielectric properties of materials (air and sample) at the interface. It is evident from the results that the electric filed distribution within the sample attenuates owing to the microwave power absorbed, and thereafter the microwave power absorbed is converted to the thermal energy. The some part of microwaves is transmitted through the sample and then absorbed by water load at the end of the waveguide. At drying time t = 10 min, the sample having moist porous material, the electric field attenuates due to microwave power absorbed to the sample and then the microwave power absorbed is converted to thermal energy, causing increase temperature within the sample. Furthermore the electric field within the sample is almost extinguished lead to short wavelength and small amplitude of electric field. As drying proceed t = 100 and 360 min, a majority of the moist content has been removed, the effect of reflected waves from the surface of sample is reduced which increases the large part of microwaves inside the sample. Consequently, the reflected and transmitted wave at each interface will contribute to the resonance of standing wave configuration with the larger amplitude and wavelength inside the sample where the moisture content is small in comparison with early stage of drying time (t = 10 min).

For the case of vacuum pressure of 13.3 kPa (as seen in Fig. 8(c)), the electric fields with small amplitude are formed within the sample, while the stronger standing wave outside the sample (left-hand side) with a lager amplitude is formed by interference between the incident waves and reflected waves from the surface of sample. In addition, the electric field within the sample attenuates owing to microwave power absorbed, and thereafter the microwave power absorbed is converted to thermal energy (similar to atmospheric pressure condition). However, it is interesting to observe that the electric field intensity in case of vacuum

Author's personal copy

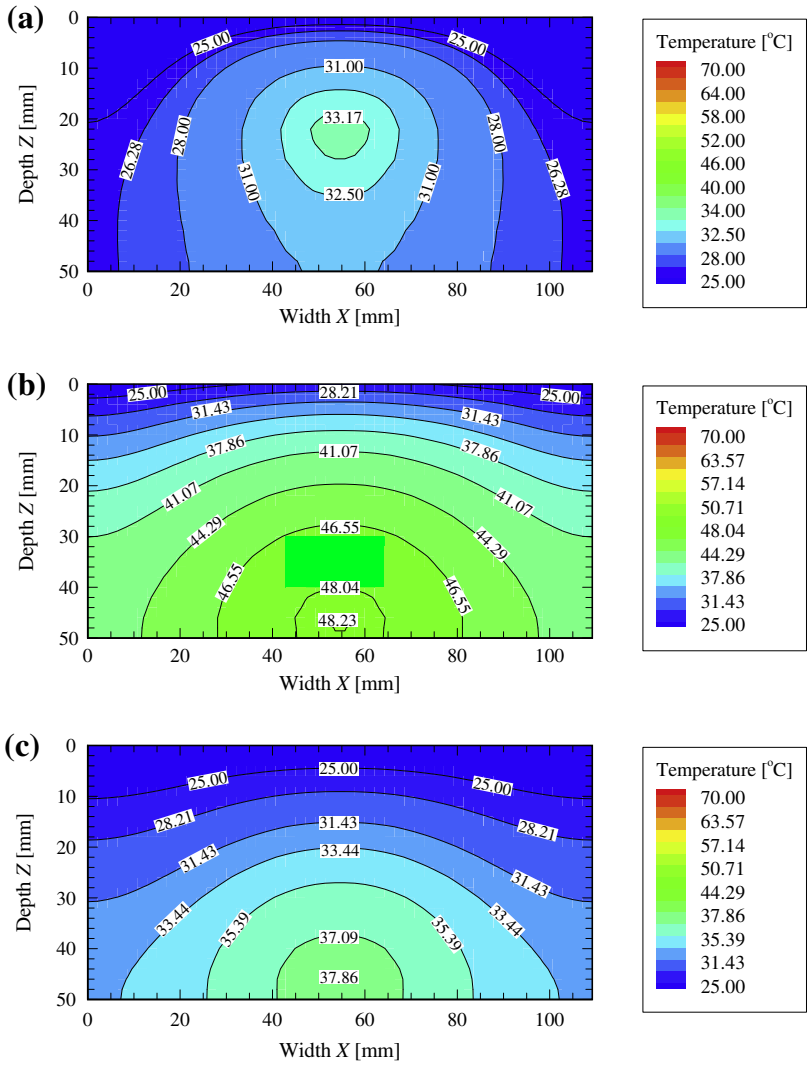

Fig. 23. Temperature distribution inside the sample at vacuum pressure of 13.3 kPa and microwave frequency of 5.80 GHz: (a) t = 10 min, (b) t = 100 min, and (c) t = 360 min.

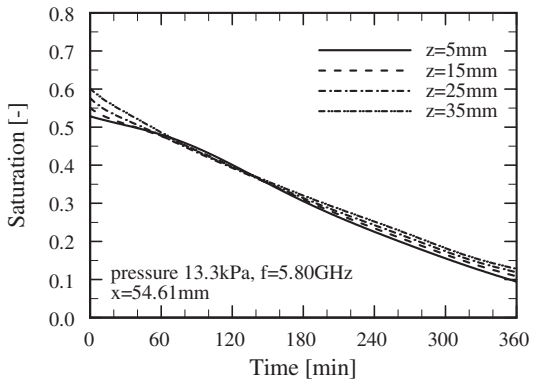

Fig. 24. Saturation profile in times with different z-depths at x-width of 54.61 mm in case of vacuum pressure of 13.3 kPa and microwave frequency of 5.80 GHz.

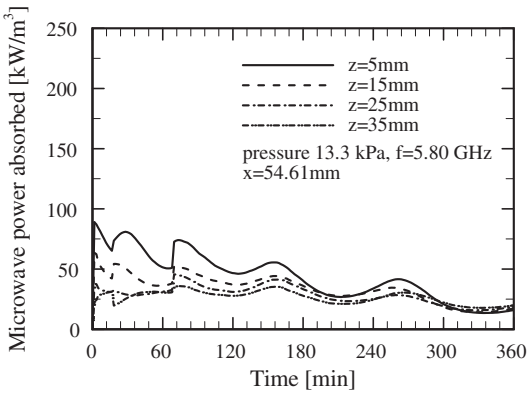

Fig. 25. Microwave power absorbed profile in times with different z-depths at x-width of 54.61 mm in case of vacuum pressure of 13.3 kPa and microwave frequency of 5.80 GHz.

pressure of 13.3 kPa is greater than in case of atmospheric pressure when drying proceed (such as t = 100 and 360 min). This is because moisture content is removed with higher rate as compared to atmospheric pressure.

Fig. 9 shows temperature profile at various times in case of vacuum pressure of 13.3 kPa and atmospheric pressure. In contrast to that in a conventional drying, a microwave drying provides higher temperature inside the drying sample while the surface temperature stays colder due to effect of surrounding air. At same time the evaporation takes place at the surface of sample at lower temperature due to evaporative cooling. It is seen that the temperature

Author's personal copy

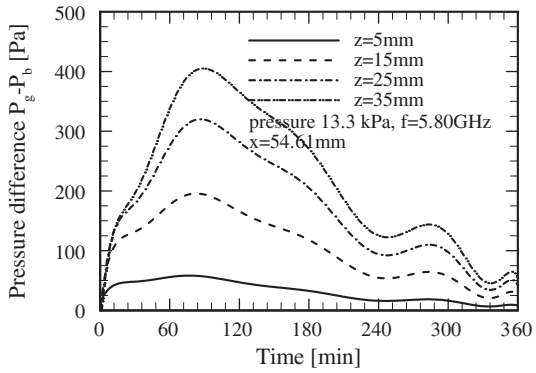

Fig. 26. Pressure difference profile in times with different z-depths at x-width of 54.61 mm in case of vacuum pressure of 13.3 kPa and microwave frequency of 5.80 GHz.

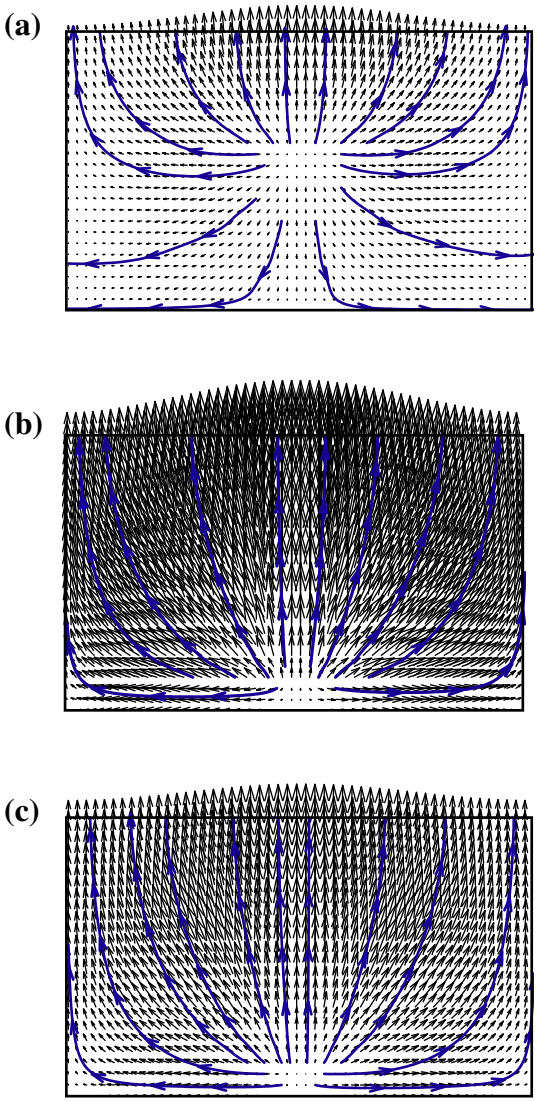

Fig. 27. Vector and streamline of vapor flux inside the sample at vacuum pressure of 13.3 kPa and microwave frequency of 5.80 GHz (scale × 9,000,000): (a) t = 10 min, (b) t = 100 min, and (c) t = 360 min.

profile within the sample rise up steadily in the early stages of drying. Due to the large initial moisture content, the skin depth heating effect causes a majority of microwave to be decay, resulting in a

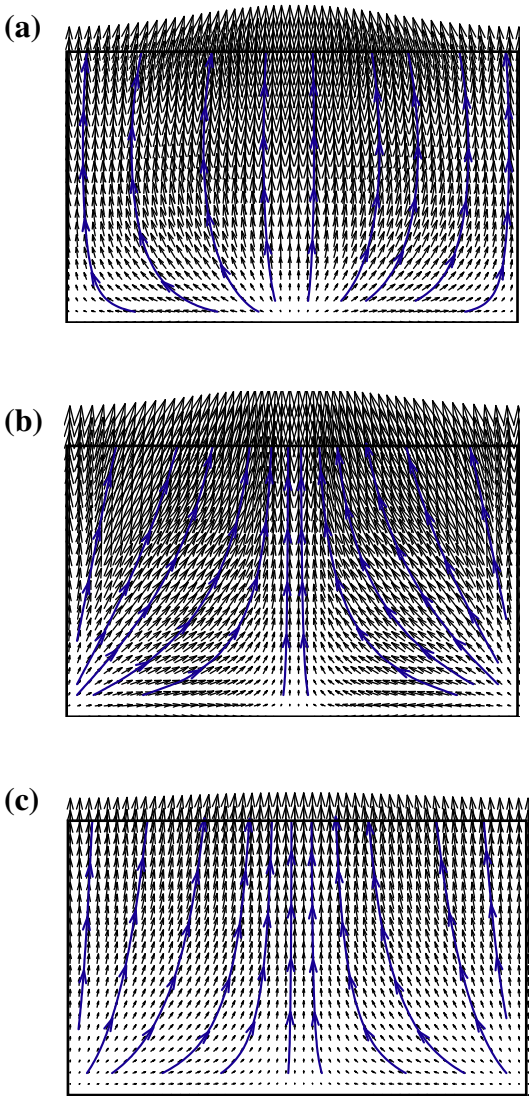

Fig. 28. Vector and streamline of liquid flux inside the sample at vacuum pressure of 13.3 kPa and microwave frequency of 5.80 GHz (scale × 2,500): (a) t = 10 min, (b) t = 100 min, and (c) t = 360 min.

lower rate of microwave power absorbed in the interior. As the drying process proceeds, moisture content is removed from the sample; the microwave can penetrate further into the sample as material dries. During this state of drying, temperature profile slows down considerably because moisture inside the sample is significant reduced, reducing dielectric loss factor as well as microwave power absorbed also. Nevertheless, temperature profiles at vacuum pressure are lower than atmospheric pressure as shown in Figs. 9–11 because the boiling point of water is fallen down under vacuum condition. It is found that at vacuum pressure of 13.3 kPa, water evaporation takes place within the sample and the temperature of sample is always lower than the boiling point of water which is equal to 56.02 °C. Consequently the sample processing temperature can be significant lower than atmospheric condition.

Fig. 12 presents the moisture profile in term of saturation profile at vacuum and atmospheric pressure. In the early state of drying, the internal movement of moisture is due to liquid flow by capillary action and vapor flow by molecular diffusion. As the drying process proceeds, the capillary action plays an important role in the moisture migration mechanism and maintains a good supply of liquid to the surface, and would cause the average moisture

Author's personal copy

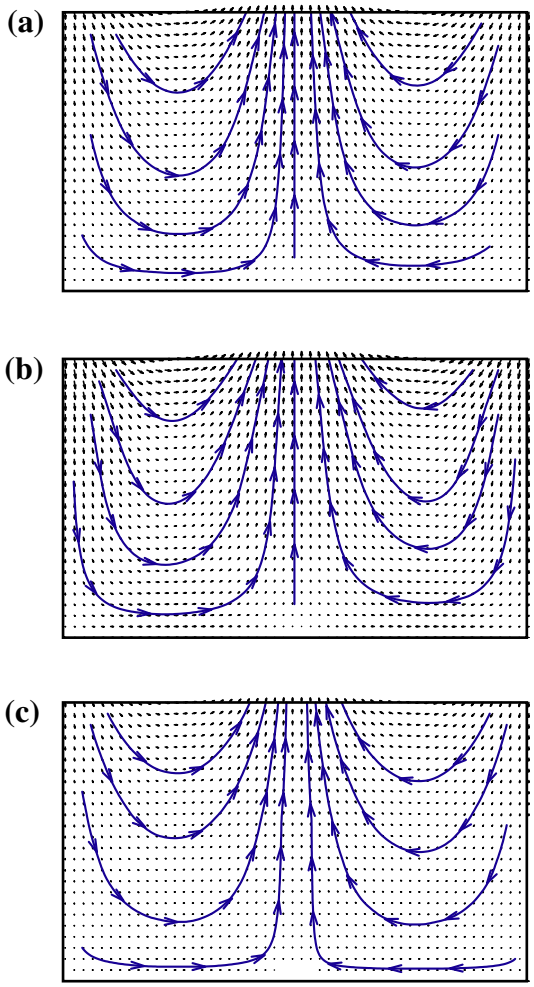

Fig. 29. Vector and streamline of air flux inside the sample at vacuum pressure of 13.3 kPa and microwave frequency of 5.80 GHz (scale × 30,000,000): (a) t = 10 min, (b) t = 100 min, and (c) t = 360 min.

content inside the sample to decrease. However, at long stages of drying about 180 min, the vapor diffusion effect plays important role in the moisture migration mechanism because of the sustained evaporation that is generated within the sample. The observed moisture profiles in case of vacuum pressure is lower than atmospheric pressure with following reasons. First, at vacuum processing provides the lower boiling point to increase rate of the water evaporation, and so causes moisture to transport upward. Second, vapor flow is greatly improved by increased total pressure gradients, and the effective molecular mass diffusion and binary mass diffusion (as displayed in Eqs. (25) and (26)). Finally, vacuum pressure enhances the mass transfer because of an increased pressure gradient between inside and outside of the sample to be dried.

Fig. 13 shows the microwave power absorbed profile in case of at vacuum pressure of 13.3 kPa and atmospheric pressure, it can be seen that the maximum of microwave power absorbed is occurred for early stage of drying time and is decreased with increasing the elapsed time. As the drying process proceeds, it would eventually cause the average moisture content to decrease and lead to a microwave power absorbed is decreased. The microwave power absorbed is directly affected by dielectric properties as a function of temperature and moisture content. The dielectric loss coefficient is significantly decreased with increasing temperature (further details shown in [35]). Therefore, the microwave power absorbed in case of vacuum pressure is lower than atmospheric pressure because of vacuum pressure corresponding to lower moisture content and higher pressure gradient between inside and outside the sample.

Fig. 14 shows pressure difference profile within the sample at vacuum and atmospheric pressure drying condition. The pressure difference is defined as total gas pressure p_g is subtracted by boundary pressure p_b. It is found that p_b is equal to 13.3 kPa and 101.325 kPa in case of vacuum and atmospheric pressure, respectively. As the drying process proceeds, total pressure is rapidly buildup within the sample and is increasingly contributed by the amount of accumulated vapor owing to the high diffusive vapor flux. It is seen that high temperature and pressure gradient are generated within the sample during particularly the constant rate period. As a result, the capillary action plays an important role in the moisture migration mechanism, and maintains a good supply of liquid to the surface. However, in vacuum pressure drying provides the greater pressure gradient than atmospheric pressure drying, because water evaporation within the sample is accelerated by the higher microwave power absorbed together with the lower boiling point of water.

In order to get more insight into the fluid transport, it is important to investigate the fluid movements within the sample in depth. The vapor, liquid and air flux profiles in case of atmospheric and vacuum pressure at various drying times as 1 of 10, 100 and 360 min are shown in Figs. 15–20, respectively. It can be seen that the vapor flux flows within the sample toward the surface which water evaporation is taken place inside the sample and on the surface. As drying process proceeds, the vapor flux flows throughout the sample migrates in the direction of decreasing saturation. For the liquid flux, it can be observed that almost all of the liquid has migrated toward the upper surface of the sample due to capillary pressure and gas pressure buildup, which are simultaneously changed due to the effect of saturation and temperature distribution in each time period. The air flux moves toward the heated surface with a lower than the vapor flux because the air diffusion is decreased by the convective air flux whereas the vapor diffusion is enhanced by the convective vapor flux. As the rate of liquid supply to the surface becomes lower than the water evaporation rate lead to the void volume is increased; therefore, allowing air flows away from heated surface toward the other surface. The results of all flux profiles in case of vacuum pressure is greater than atmospheric pressure because water evaporation within the sample is accelerated by lower boiling point of water together with higher microwave power absorbed, and higher pressure gradient.

5.3. The effect of microwave frequency

The investigated microwave frequencies are 2.45 and 5.8 GHz in discussion the effect of microwave frequency, which are chosen to show microwave heating phenomena because there are in set of frequencies reserved for industrial, scientific, and medical (ISM band) use. The dielectric properties of water at microwave frequency of 5.8 GHz is refer to Meissner and Wentz [36]. The penetration depth for operating microwave frequencies of 2.45 GHz and 5.8 GHz are 200.11 mm and 52.05 mm, respectively, at initial saturation of S_{in} = 0.6.

Fig. 8(c) shows the electric field distribution inside a rectangular waveguide when the sample is inserted within the waveguide during microwave heating with operating microwave frequency of 2.45 GHz and vacuum pressure of 13.3 kPa. Since the typical depth of sample (50.0 mm) is less than the penetration depth of microwave (200.11 mm), so a large part of microwave is able to penetrate through the sample. The reflected waves occur on each interface, from air (cavity) to upper surface and from lower surface of sample to air (cavity). The reflection and transmission components at each interface contribute to the resonance of standing wave configuration inside the sample and give rise to a microwave

Author's personal copy

power absorbed peak further from the surface exposed to incident microwaves as seen in Fig. 13(b). Thereafter the microwave power absorbed is converted to the thermal energy and temperature is increased.

Fig. 8(c) presents the electric field distribution inside a rectangular waveguide when the sample is inserted inside the waveguide during microwave heating with the frequency of 2.45 GHz. The penetration of this microwave is higher than the typical depth of sample as seen in Table 2, thus a large part of microwaves are able to penetrate through the sample. The reflected wave occurs on each interface, from air (cavity) to upper surface and from lower surface of sample to air (cavity). The reflection and transmission components at each interface contribute to the resonance of standing wave configuration inside the sample and give rise to a microwave absorption peak further from the surface exposed to incident microwaves. Thereafter the microwave power absorbed is converted to the thermal energy, which increases the sample temperature.

Fig. 21(b) illustrates the electric field distributions inside a rectangular waveguide when the sample is inserted in the waveguide during microwave heating with the microwave frequency of 5.8 GHz. In contrast to the electric field configuration in case of 2.45 GHz, this is a result of a transmitted wave at the incident face and a reflected wave from the lower surface of the sample. This is due to the fact that microwave operating at a high frequency has a short wavelength which corresponds to a smaller penetration depth of microwave as compared with in case of 2.45 GHz (as seen in Table 2) and slightly higher than the depth of sample. Consequently, most microwaves are absorbed by the sample.

Fig. 22 shows the temperature profiles with different z-depths at x-width of 54.61 mm in case of vacuum pressure of 13.3 kPa and microwave frequency of 5.80 GHz. Fig. 23 shows temperature distribution inside the sample at various drying time as 10, 100 and 360 min. Since the higher microwave frequency, 5.8 GHz, has a short wavelength which corresponds to a smaller penetration of microwave. Consequently, most microwaves are absorbed by the sample. Therefore the microwave power absorbed is the greatest at the surface exposed to incident microwave as shown in Fig. 25, and decays exponentially along the propagating direction with a small wavelength. As a result, maximum temperatures are occurred at depth-z of 22.0, 46.0 and 46.0 mm for exposure time of 10, 100 and 360 min, respectively, as shown in Fig. 23. In contrast that to in case of 2.45 GHz illustrated in Fig. 11, maximum temperatures are at the depth-z of 44.0, 48.0 and 48.0 mm for drying time of 10, 100 and 360 min, respectively.

Fig. 24 presents saturation profiles at vacuum pressure of 13.3 kPa and operating microwave frequency of 5.8 GHz. The observed moisture profiles in case of 5.8 GHz are higher than 2.45 GHz because of lower microwave power absorbed.

Fig. 25 shows microwave power absorbed profile within the sample in case of operating microwave frequency of 5.8 GHz. The microwave power absorbed is lower than in case of 2.45 GHz because of a smaller penetration of microwave.

Fig. 26 shows pressure difference profile within the sample in case of operating microwave frequency of 5.8 GHz. Total pressure is lower than in case of 2.45 GHz because it is lower microwave power absorbed profiles taken place inside the sample.

Figs. 27–29 illustrate fluid movement patterns inside the sample in case of microwave frequency of 5.8 GHz at various times as 10, 100 and 360 min. For fluid transport phenomena in terms of liquid, vapor and air flux are explained in previous subsection.

This study shows the capability of the numerical analysis to handle heat-mass transport and pressure buildup in two-dimensional porous medium subjected to a combined microwave and vacuum system. With further quantitative validation of the present method, this method can be used as a tool for investigating in detail this particular microwave drying under vacuum pressure of phase change in an unsaturated porous media at a fundamental level.

6. Conclusions

The numerical analysis presented describes many important interactions within the sample (as an unsaturated porous media) during microwave vacuum drying. A generalized 2D mathematical model for analysis of heat and mass transfer, and pressure buildup in the sample subjected to microwave energy can be used successfully to descript transport phenomena under vacuum pressure condition. The vacuum pressure significant influences to temperature, microwave power absorbed, saturation and pressure buildup distribution, and movement of fluid inside the sample.

Acknowledgments

The authors gratefully acknowledge the Thailand Research Fund (TRF) for supporting this research project.

References

[1] A.S. Mujumdar, Handbook of Industrial Drying, second ed., Marcel Dekker, New York, 1995.
[2] A.C. Metaxas, R.J. Meridith, Industrial Microwave Heating, Peter Peregrinus Ltd., London, 1983.
[3] A.K. Datta, R.C. Anantheswaran, Handbook of Microwave Technology for Food Applications, Marcel Dekker, New York, 2001.
[4] P. Perré, S. Mosnier, I.W. Turner, Vacuum drying of wood with radiative heating. I. Experimental procedure, AIChE J. 50 (2004) 97–107.
[5] W. Jomaa, O. Baixeras, Discontinuous vacuum drying of oak wood: modelling and experimental investigations, Drying Technol. 15 (9) (1997) 2129–2144.
[6] A.E. Drouzas, H. Schubert, Microwave application in vacuum drying of fruits, J. Food Eng. 28 (1996) 203–209.
[7] A.E. Drouzas, E. Tsami, G.D. Saravacos, Microwave/vacuum drying of model fruit gels, J. Food Eng. 39 (1999) 117–122.
[8] C. Péré, E. Rodier, Microwave vacuum drying of porous media: experimental study and qualitative considerations of internal transfers, Chem. Eng. Process. 41 (2002) 427–436.
[9] P.S. Sunjka, T.J. Rennie, C. Beaudry, G.S.V. Raghavan, Microwave-convective and microwave-vacuum drying of cranberries: a comparative study, Drying Technol. 22 (5) (2004) 1217–1231.
[10] Q. Hu, M. Zhang, A.S. Mujumdar, G. Xiao, J. Sun, Drying of edamames by hot air and vacuum microwave combination, J. Food Eng. 77 (2006) 977–982.
[11] P. Perré, I.W. Turner, A 3-D version of TransPore: a comprehensive heat and mass transfer computational model for simulating the drying of porous media, Int. J. Heat Mass Transfer 42 (1999) 4501–4521.
[12] P. Rattanadecho, W. Pakdee, J. Stakulcharoen, Analysis of multiphase flow and heat transfer: pressure buildup in an unsaturated porous slab exposed to hot gas, Drying Technol. 26 (2008) 39–53.
[13] H. Ni, A.K. Datta, K.E. Torrance, Moisture transport in intensive microwave heating of biomaterials: a multiphase porous media model, Int. J. Heat Mass Transfer 42 (1999) 1501–1512.
[14] P. Ratanadecho, K. Aoki, M. Akahori, A numerical and experimental investigation of the modeling of microwave drying using a rectangular wave guide, Drying Technol. 19 (9) (2001) 2209–2234.
[15] L.A. Campañone, N.E. Zaritzky, Mathematical analysis of microwave heating process, J. Food Eng. 69 (3) (2005) 359–368.
[16] W. Cha-um, P. Rattanadecho, W. Pakdee, Experimental analysis of microwave heating of dielectric materials using a rectangular waveguide (MODE: TE10) (case study: water layer and saturated porous medium), Exp. Therm. Fluid Sci. 33 (3) (2009) 472–481.
[17] P. Rattanadecho, N. Suwannapum, W. Cha-um, Interactions between electromagnetic and thermal fields in microwave heating of hardened type I-cement paste using a rectangular waveguide (influence of frequency and sample size), ASME J. Heat Transfer 131 (2009) 082101–082112.
[18] L. Hansson, L. Antti, Modeling microwave heating and moisture redistribution in wood, Drying Technol. 26 (2010) 552–559.
[19] D. Jia, M.T. Afzal, Modeling the heat and mass transfer in microwave drying of white oak, Drying Technol. 26 (2008) 1103–1111.
[20] S. Sungsoontorn, P. Rattanadecho, W. Pakdee, One-dimensional model of heat and mass transports and pressure buildup in unsaturated porous materials subjected to microwave energy, Drying Technol. 29 (2011) 189–204.
[21] N. Suwannapum, P. Rattanadecho, Analysis of heat–mass transport and pressure buildup induced inside unsaturated porous media subjected to microwave energy using a single (TE10) mode cavity, Drying Technol. 29 (2011) 1010–1024.

Author's personal copy

[22] P. Ratanadecho, K. Aoki, M. Akahori, A numerical and experimental investigation of the modeling of microwave heating for liquid layers using a rectangular waveguide (effects of natural convection and dielectric properties), Appl. Math. Model. 26 (3) (2002) 449–472.
[23] S. Tada, R. Echigo, Y. Kuno, H. Yoshida, Numerical Analysis of Electromagnetic Wave in Partially Loaded Microwave Applicator, Int. J. Heat Mass Transfer 41 (1998) 709–718.
[24] J. Wang, T. Schmugge, An empirical model for the complex dielectric permittivity of soil as a function of water content, IEEE Trans. Geosci. Remote Sens. GE-18 (4) (1980) 288–295.
[25] T. Basak, K. Aparna, A. Meenakshi, A.R. Balakrishnan, Effect of ceramic supports on microwave processing of porous food samples, Int. J. Heat Mass Transfer 49 (2006) 4325–4339.
[26] P. Ratanadecho, K. Aoki, M. Akahori, Influence of irradiation time, particle sizes, and initial moisture content during microwave drying of multi-layered capillary porous materials, ASME J. Heat Transfer 124 (2002) 151–161.
[27] G. Mur, Absorbing boundary conditions for the finite-difference approximation of the time-domain electromagnetic-field equations, IEEE Trans. Electromagn. Compat. EMC-23 (4) (1981) 377–382.
[28] S. Whitaker, A theory of drying in porous media, Adv. Heat Transfer 13 (1977) 119–203.
[29] M. Kaviany, Principle of Heat Transfer in Porous Media, Springer, New York, 1991.
[30] M. Kaviany, M. Mittal, Funicular state in drying of porous slab, Int. J. Heat Mass Transfer 30 (7) (1987) 1407–1418.
[31] K. Aoki, M. Hattori, M. Kitamura, N. Shiraishi, Characteristics of heat transport in porous media with water infiltration, ASME/JSME Therm. Eng. Proc. 4 (1991) 303–308.
[32] J.A. Rogers, M. Kaviany, Funicular and evaporative-front regimes in convective drying of granular beds, Int. J. Heat Mass Transfer 35 (1992) 469–479.
[33] J. Watanuki, Fundamental study of microwave heating with rectangular wave guide, M.S. Thesis, Nagaoka University of Technology, Japan, 1998, p. 85.
[34] V. Changrue, Hybrid (osmotic, microwave-vacuum) drying of strawberries and carrots, Ph.D. Thesis, Macdonald Campus of McGill University, Canada, 2006.
[35] P. Ratanadecho, K. Aoki, M. Akahori, Experimental and numerical study of microwave drying in unsaturated porous material, Int. Commun. Heat Mass Transfer 28 (2001) 605–616.
[36] T. Meissner, F.J. Wentz, The complex dielectric constant of pure and sea water from microwave satellite observations, IEEE Trans. Geosci. Remote Sens. 42 (9) (2004) 1836–1849.

International Journal of Heat and Mass Transfer 67 (2013) 46–60

Contents lists available at ScienceDirect

International Journal of Heat and Mass Transfer

journal homepage: www.elsevier.com/locate/ijhmt

Analysis of heat transport on local thermal non-equilibrium in porous liver during microwave ablation

Pornthip Keangin [a], Phadungsak Rattanadecho [b,*]

[a] Department of Mechanical Engineering, Faculty of Engineering, Mahidol University, 25/25 Phutthamomthon 4 Rd., Salaya, Nakhon Pathom 73170, Thailand
[b] Department of Mechanical Engineering, Faculty of Engineering, Thammasat University (Rangsit Campus), 99 moo 18, Khlong Luang, Pathum Thani 12120, Thailand

ARTICLE INFO

Article history:
Received 24 January 2013
Received in revised form 12 July 2013
Accepted 19 July 2013
Available online 28 August 2013

Keywords:
Finite element
Local thermal non-equilibrium
Microwave ablation
Porous liver
Temperature distribution

ABSTRACT

Microwave ablation (MWA) is a process that uses the heat from microwave energy to kill cancer cells without damaging the surrounding tissue. The effectiveness of this technique is related to the temperature achieved during the process, as well as the input microwave power and heating time of treatment. The modeling of heat transport within biological tissues are key issues and have been used extensively in medical thermal therapeutic applications, for instance MWA treatment for predicting the temperature distribution during process. In this work, the interstitial MWA in porous liver by single slot microwave coaxial antenna (MCA) is carried out. A mathematical model of MWA of the porous media approach is proposed, which uses transient energy equation coupled with electromagnetic wave propagation equation to describe the temperature distribution within porous liver under local thermal non-equilibrium (LTNE) assumption. The LTNE assumption is taken into account by solving the two energy equations for tissue and blood phases. The thermal model considers the tissue with its blood vessel distribution as a porous medium and employs both the interfacial convective heat transfer and blood perfusion rate terms in the transient energy equations for both tissue and blood phases. The coupled nonlinear set of these equations is solved using the axisymmetric finite element method (FEM). The influences of blood velocities, porosities, input microwave powers and positions within the porous liver (distance from a MCA) on the tissue and blood temperature distributions have been investigated. Furthermore, the tissue and blood temperatures of LTNE model are compared with the tissue temperature of Pennes model and Klinger model. Through an accuracy comparison, the temperature results of the one-energy equation under local thermal equilibrium (LTE) model and Pennes model are compared with the experimental results from previous work in order to show the validity of the numerical results. The results show that the LTE assumption is found to be suitable for predicting the temperature distribution when the blood velocities to be 0.4 cm/s and 2 cm/s in all porosities, whilst, in case of blood velocities to be 3 cm/s and 3.4 cm/s the LTNE assumption for heat transfer analysis needs to be utilized. In addition, the LTE model is suitable for predicting a distribution of temperature when the high porosity for this model. This investigation provides the essential aspects for a fundamental understanding of heat transport within biological tissues while experiencing an applied electromagnetic field such as applications in the thermal ablation.

© 2013 Elsevier Ltd. All rights reserved.

1. Introduction

Microwave ablation (MWA) techniques have become a extensive choice for the treatment of cancer, including liver, where the majority of the patients are not candidates for surgical resection due to restrictions, such as multifocal disease, tumor size, and position of tumor to key vessels. MWA can improve outcomes with few side effects [1] and also particularly useful when the tumor is located in an area that cannot be removed for functional purposes. The main advantages of MWA technology, when compared with existing thermal ablation technologies, include consistently higher intratumoral temperatures, larger tumor ablation volumes and faster ablation times [2]. In MWA treatments, the un-wanted tissue will be overheated to a therapeutic value, typically 50 °C to damage or kill the cancer cells and affect metastases [3]. The effectiveness of MWA process is related to the temperature achieved during the process. In order to kill cancer cells without damage to normal tissues, the ability to predict the temperature of the tumor and surrounding tissue is important in MWA. However, before real experimental cancer therapy, there should be basis numerical simulation. Therefore, the modeling of MWA in tissue is needed. The numerical simulation has important roles on the MWA

* Corresponding author. Tel.: +66 02 5643001 to 9x3153; fax: +66 02 5643023.
E-mail address: ratphadu@engr.tu.ac.th (P. Rattanadecho).

0017-9310/$ - see front matter © 2013 Elsevier Ltd. All rights reserved.
http://dx.doi.org/10.1016/j.ijheatmasstransfer.2013.07.064

Nomenclature

a	volumetric transfer area between the blood and the tissue (m^2/m^3)
C_p	specific heat capacity (J/(kg °C))
E	electric field (V/m)
f	microwave frequency (Hz)
H	magnetic field (A/m)
h	heat transfer coefficient (W/m^2 °C)
k	propagation constant (m^{-1})
K	thermal conductivity (W/(m °C))
P	input microwave power (W)
Q	heat source (W/m^3)
r	dielectric radius (m)
t	time (s)
T	temperature (°C)
u	blood velocity (cm/s)
Z	wave impedance in the dielectric of the coaxial cable (Ω)

Greek letters

μ	magnetic permeability (H/m)
ε	permittivity (F/m)
σ	electric conductivity (S/m)
λ	wave length (m)
ϖ	angular frequency (rad/s)
ω	blood perfusion rate (1/s)
ρ	density (kg/m^3)
ϕ	porosity (–)

Subscripts

b	blood
eff	effective
ext	external
inner	inner
met	metabolic
outer	outer
r	relative
r,*z*, and φ	components of cylindrical coordinates
s	solid
t	tissue
tb	tissue to blood
0	free space, initial condition

performance prediction in order to demonstrate the relationship between the microwave power deposited in the tissue and the resulting tissue status post treatment is highly complex, particularly in organs with high blood perfusion such as the liver. Furthermore, numerical simulation under various conditions can be studied for effective use in identifying the fundamental parameters as well as provide guidance for more realistic consideration in experiments.

In the past, the studies of MWA dealt with homogeneous material and focused on heat conduction (using Pennes's bioheat equation) within a medium. These models usually need many assumptions which may limit their applications in reality. Pennes's bioheat equation, introduced by Pennes [4] based on the heat diffusion equation, involves thermal conduction in tissue and vascular system, blood perfusion (through capillary tubes within the tissues) and also metabolic heat generation. The Pennes's bioheat models has been extensively used in many works for analysis of heat transfer in biological tissues, particularly in thermal ablation models [5–7]. Due to simplifications and shortcomings of this model, the Pennes's bioheat equation assumes the temperature of the blood within the capillaries equal to the body's core temperature. This means that all of the heat loss/gain occurs in the capillary bed and there are no losses or gains in the thermal energy of the blood in the higher order systemic components (large and intermediate sized vessels or veins) [8]. Therefore, other studies have investigated new models that substitute, modify the Pennes model model or coupled Pennes model with other models. For example, Klinger [9] developed a mathematical procedure which us to gain an exact analytical solution of the bioheat equation with convection terms. Yang et al. [10] proposed a new method to study high temperature tissue ablation using a modified bioheat equation to include tissue internal water evaporation during heating. The simulation result of modified bioheat equation is found in agreement well to the experimental result. After that Keangin et al. [11] carried out on the numerical simulation of liver cancer treated using the complete mathematical model considered the coupled model of bioheat model with electromagnetic wave propagation and mechanical deformation model in liver tissue during MWA process in the couple way.

In realistic, the biological tissue including cell and microvascular bed with the blood flow direction contains many vessels, assuming that the tissue is like a sponge, through which blood flows and can be regarded as a porous structure [12,13]. Thus, the study of heat transport in biological tissue should used porous media theory. The advantages of utilizing porous media theory in modeling of heat transfer is a fewer assumptions as compared to different established bioheat transfer models. Description of heat transport through porous media has been of interest for many decades. Two different models are used for analyzing heat transfer in a porous medium; local thermal equilibrium (LTE) and local thermal non-equilibrium (LTNE). Most of the prior works are based on invoking the LTE model based on the assumption that the tissue phase temperature is equal to fluid phase temperature everywhere in the porous medium. This assumption occurs when heat exchange between the tissue and the blood is efficient, it is a valid assumption in a capillary bed having many micro vessels (of small diameter) and a large area of heat transfer [14]. Explanation of the established LTE models can be found in the literature [15–18]. Alazmi and Vafai [15] investigated the effect of Darcy number, inertia parameter, Reynolds number, porosity, particle diameter, and the fluid-to-solid conductivity ratio on the velocity and temperature distributions within the porous media transport models. Later, Kou et al. [17] presented the effects of directional blood flow and heating schemes on the distributions of temperature and thermal dose during thermal therapy. A modified bioheat transfer equation based on the porous medium concept on LTE assumption by using a Green's function method was proposed to obtain the temperature distribution and thermal dose. The results showed that the domain of the thermal lesion might extend to the downstream normal tissue when the porosity and the averaged blood velocity are large. Recently, analyzed of heat transfer and blood flow on LTE assumption in two-layered porous liver tissue during MWA using single and double slot antenna was presented by Rattanadecho and Keangin [18]. The results show that the maximum specific absorption rate (SAR), temperature and blood velocity appears in the porous liver when using a single slot MCA is higher than when using a double slot antenna.

However, the LTE assumption is not valid for a number of physical situations such as when the fluid flows at a high speed through the porous medium [19]. Moreover, this assumption is not considered the temperature difference between the tissue and blood phases within the porous media. Which the temperature difference significantly influence on the heat transfer, especially during thermal ablation treatment. The criterion of LTE assumption during thermal ablation treatment may be different from that in the normal situation where metabolic heat source or external heat source occurs. In such cases, the LTNE assumption for heat transfer analysis needs to be utilized. This assumption based on heat transfer is convectively transferred between the two phases, making the two equations coupled. In recent years, the LTNE model in a porous medium has received more attention as demonstrated, such as Fan and Wang [20] developed a general bioheat transport model at macroscale for biological tissues based on porous media model. The model shows that both blood and tissue macroscale temperatures satisfy the derived the dual-phase-lag (DPL) energy equations. In the same year, Afrin et al. [21] presented a model of thermal lagging in living biological tissue based on LTNE heat transfer model between tissue, arterial and venous bloods. It was found that the phase lag times for heat flux and temperature gradient are the identical for the case that the tissue and blood have the same properties. Moreover, the LTNE model was used extensively in biomaterials during hyperthermia therapy [1,14,22–24]. Mahjoob and Vafai [22] analyzed characterization of heat transport through biological media incorporating hyperthermia treatment, utilizing the LTNE model of porous media theory, exact solutions for the tissue and blood temperature profiles were established. An equivalent heat transfer coefficient between tissue and blood in a porous model for simulating a biological tissue in a hyperthermia therapy based on the LTNE model was investigated by Yuan [23]. The results indicate that the equivalent heat transfer coefficient was not a strong function of the perfusion rate, blood velocity and heating conditions, but was inversely related to the blood vessel diameter. Next, Belmiloudi [24] analyzed the temperature distribution in biofluid heat transfer of porous non homogeneous tissues during thermal therapy based on LTNE model.

However, a few studies concentrated the heat transport of porous medium subjected to electromagnetic fields as in thermal ablation under LTNE model. Therefore, to approach reality, modeling of heat transport in porous tissue during thermal ablation is must be cooperating with the modeling of electromagnetic in order to completely these analysis. In addition, there are various effects related to the tissue and blood temperature, such as blood velocities, porosities and input microwave powers in a porous medium that still not well understood and several pertinent issues remain unresolved. The complete mathematical model is useful for the development of biomedical technologies especially.

In this study, investigates the transient distribution of tissue and blood temperatures within porous liver during MWA process using a single slot microwave coaxial antenna (MCA) based on LTNE model. Two equations of tissue and blood phases are used in the current study, to determine the implication of this new model for practical implementation. Mathematical model of MWA process of the porous media approach is proposed, which uses transient energy equation coupled with electromagnetic wave propagation equation. The coupled nonlinear set of governing equations as well as initial and boundary conditions are solved using the axisymmetric finite element method (FEM) via COMSOL^{TM} Multiphysics. The effect of blood velocities, porosities, input microwave powers and positions within the porous liver (distance from a MCA) in affecting the tissue and blood temperature distributions are analyzed. In order to verify the accuracy of the presented mathematical model of MWA, the resulting data of temperature from LTE model and Pennes model are validated against the experimental results, obtained by Yang et al. [10]. Furthermore, the tissue and blood temperatures of LTNE model are compared with the tissue temperature of Pennes model and Klinger model. The analysis from this study serves as essential fundament for the development of mathematic models of heat transfer for temperature prediction during MWA therapies that can be modified to present a more accurate temperature distribution within other biological tissues and can be used as a guideline for the practical treatment.

2. Problem Description

MWA is a process that uses the heat from microwave energy to kill cancer cells. The energy from the microwave frequency waves emitted by the microwave antenna creates heat in the local cancerous tissue cancer without the damaging surrounding tissue. This study uses a single slot MCA, to transfer microwave power into the porous liver for the treatment of liver cancer. The single slot MCA has a diameter of 1.79 mm, the thin antenna is required in the interstitial treatments because it is a minimally invasive and capable of delivering a large amount of electromagnetic power. A ring-shaped slot, 1 mm wide is cut off the outer conductor 5.5 mm in length from the short circuited tip because the effective heating around the tip of the antenna is very important to the interstitial heating and because the electric field becomes stronger near the slot [25]. The single slot MCA is composed of an inner conductor, a dielectric and an outer conductor. The single slot MCA is enclosed in a catheter (made of polytetrafluorethylene; PTFE), for hygienic and guidance purposes. Fig. 1 shows the model geometry of a single slot MCA. The single slot MCA operates at the frequency of 2.45 GHz, a widely used frequency in MWA, and the various input microwave powers. The goal of MWA is to elevate the temperature of un-wanted tissue (tumor) to 50 °C where cancer cells are destroyed [3]. Dimensions of a single slot MCA are given in Table 1. While the dielectric properties of a single slot MCA are given in Table 2.

In realistic, the structure of a tumor has been found to be different from that of normal tissue [26]. The structure of the tumors is very complicated. Therefore, the structures of tumor and normal tissue have been assumed to be the same in order to simplify the physical model to that of a uniform porous medium. In this study, the porous liver is considered as a cylindrical geometry. It has a 30 mm radius and 80 mm in height and a single slot MCA is inserted into the porous liver with 70.5 mm depth [11]. The vertical axis is oriented along the longitudinal axis of the single slot MCA, and the horizontal axis is oriented along the radial direction. The coaxial slot antenna exhibits rotational symmetry around the

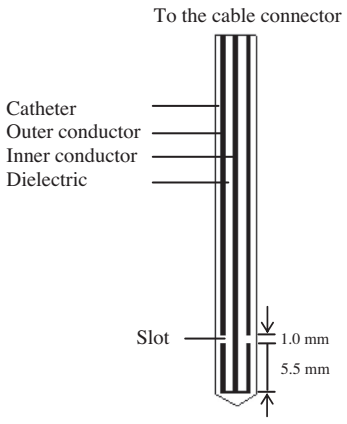

Fig. 1. Model geometry of a single slot MCA.

Table 1
Dimensions of a single slot MCA.

Materials	Dimensions (mm)
Inner conductor	0.135 (radial)
Dielectric	0.335 (radial)
Outer conductor	0.460 (radial)
Catheter	0.895 (radial)
Slot	1.000 (wide)

Table 2
The dielectric properties of a single slot MCA.

Properties	Relative permittivity ε_r	Electric conductivity σ (S/m)	Relative permeability μ_r
Dielectric	2.03	0	1
Catheter	2.1	0	1
Slot	1	0	1

longitudinal axis, therefore an axially symmetric model is considered in this study, which minimized the computation time while maintaining good resolution and represents the full three-dimensional result. Fig. 2 shows the axially symmetrical model geometry for analysis in this study. Three positions of the slot center are considered at p1 (2.5 mm, 16 mm), p2 (4.5 mm, 16 mm) and p3 (8.5 mm, 16 mm) to determine the tissue and blood temperatures.

In an anatomical view, biological tissues usually consist of three compartments, namely, blood vessels, cells and interstitial space [13,22]. The interstitial space can be further divided into the extracellular matrix and the interstitial fluid. However, for sake of simplicity, the biological tissues are divided into two distinctive regions, namely, the vascular region (blood vessels) and the extra-vascular region (cells and the interstitial space) and treat the whole anatomical structure as a blood saturated tissue represented by a porous medium [22], through which the blood infiltrates. The vascular region is regarded as a blood phase and extra-vascular region is regarded as a tissue (solid matrix) phase, as illustrated in Fig. 2. In this work, the tissue and blood local heat exchange, while the porous liver subjected to electromagnetic fields as in MWA process, is addressed and the tissue and blood temperature distributions are established analytically. Fundamental formulations of the governing equations based on LTNE model between the tissue (solid matrix) phase and blood phases within porous media have been presented in the literature [14,22,27].

The dielectric properties and thermal properties of the tissue and blood phases are assumed to be isotropic and constant are listed in Table 3 according to the study by Wessapan et al. [28] where the microwave frequency of 2.45 GHz is considered. Moreover, the heat transfer coefficient and blood velocity are assumed to be constant throughout the calculated domain.

Yuan [14] investigated the temperature and thermal dose response of biological tissue during hyperthermia therapy by using a range of porosities from 0.005 to 0.05. The range of porosities are corresponds to the capillaries, arterioles, terminal arteries, terminal branches, and tertiary branches. While, the range of porosities from 0.05 to 0.3 were selected for analyzed the heat transport through biological media incorporating hyperthermia therapy in work of Mahjoob and Vafai [22]. Therefore, a range of porosities from 0.025 to 0.1 are selected for investigating the tissue and blood temperature distributions within porous liver during MWA in this study. The relationship between blood velocity, porosity and volumetric transfer area between the blood and the tissue are given in Table 4 [14,29]. The blood velocity and volumetric transfer area are constant and are relevant to the different generations of the vasculature which taken from the literature [1,29].

3. The formulation of the mathematical model

In this section, an analysis of electromagnetic wave propagation and heat transfer within the porous liver during MWA process will be illustrated. The system of governing equations as well as initial and boundary conditions are solved numerically using the FEM via COMSOL^{TM} Multiphysics. The relevant boundary conditions are described in Fig. 3.

3.1. Equations for electromagnetic wave propagation analysis

This study investigates the transient temperature distribution within porous liver during MWA process. The microwave energy applied to the tumor causes water molecules to vibrate and rotate, resulting in heat to a temperature high enough to cause cell death. The electromagnetic wave propagation equation is solved for

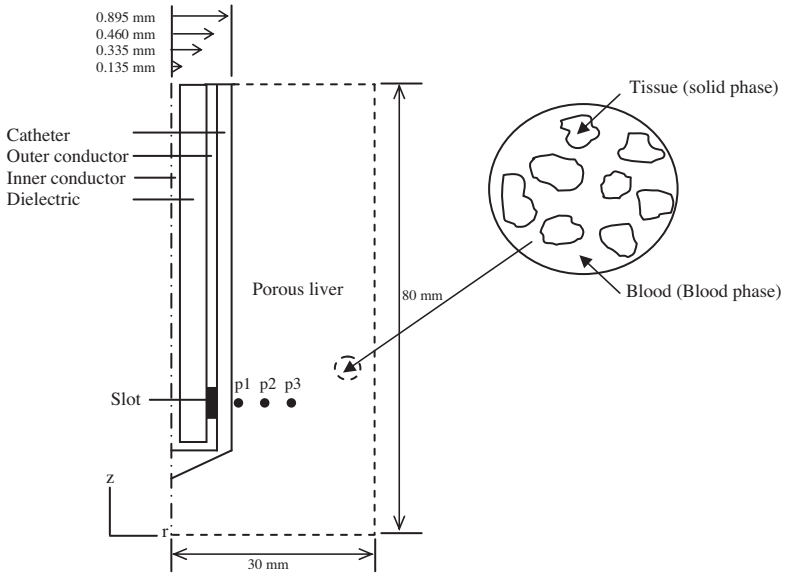

Fig. 2. Axially symmetrical model geometry. Three positions of the slot center are considered at p1 (2.5 mm, 16 mm), p2 (4.5 mm, 16 mm) and p3 (8.5 mm, 16 mm) to determine the tissue and blood temperatures.

Table 3
The thermal properties and dielectric properties of tissue and blood phases from Wessapan et al. [28].

Properties	Thermal conductivity K (W/m °C)	Density ρ (kg/m^3)	Specific heat capacity C_p (J/kg °C)	Relative permittivity ε_r	Electric conductivity σ (S/m)
Tissue phase (t)	0.497	1030	3600	43.00	1.69
Blood phase (b)	0.45	1058	3960	58.30	2.54

Table 4
The relationship between blood velocity, porosity and volumetric transfer area between the blood and the tissue [14,29].

Porosity (–)	Volumetric transfer area between the blood and the tissue (m^2/ m^3)			
	u = 0.4 cm/s	u = 2 cm/s	u = 3 cm/s	u = 3.4 cm/s
ϕ = 0.025	667	400	200	143
ϕ = 0.05	1333	800	400	286
ϕ = 0.1	6667	4000	2000	1429

microwave energy which is applied to porous liver during process. From the Fig. 2, this study is based on the following assumptions:

1. Electromagnetic wave propagation is modeled in 2D axially symmetrical cylindrical coordinates (r-z).
2. An electromagnetic wave, propagating in a MCA, is characterized by transverse electromagnetic fields (TEM) [30,31].
3. In the porous liver, an electromagnetic wave is characterized by transverse magnetic fields (TM) [30,31].
4. The model assumes that the wall of a MCA is a perfect electric conductor (PEC).
5. The outer surface of the porous liver is truncated by a scattering boundary condition.
6. The model assumes that dielectric properties of the porous liver are uniform and constant.

The axisymetric finite element (FE) model used in this study is adapted from a single slot MCA general model [10,32]. In this model, the electric and magnetic fields associated with the time-varying TEM wave are expressed in 2D axially symmetrical cylindrical coordinates:

$$\text{Electric field}(\vec{E}) \quad \vec{E} = e_r \frac{C}{r} e^{j(\varpi t - kz)} \tag{1}$$

$$\text{Magnetic field}(\vec{H}) \quad = e_\phi \frac{C}{rZ} e^{j(\varpi t - kz)} \tag{2}$$

where $C = \sqrt{\frac{ZP}{\pi . \ln(r_{outer}/r_{inner})}}$ is the arbitrary constant, Z is the wave impedance(Ω), P is the input microwave power (W), r_{inner} is the dielectric inner radius (m), r_{outer} is the dielectric outer radius (m), $\varpi = 2\pi f$ is the angular frequency (rad/s), f is the frequency (Hz), k is the propagation constant (m^{-1}) which relates to the wave length (λ) in the medium (m); $k = \frac{2\pi}{\lambda}$.

In the porous liver, the electric field also has a finite axial component, whereas the magnetic field is purely in the azimuth direction. The electric field is in the radial direction only inside the coaxial cable and in both radial and the axial direction inside the tissue. This allows for a single slot MCA to be modeled using an axisymmetric TM wave formulation. The wave equation then becomes scalar in H_ϕ:

$$\nabla \times \left(\left(\varepsilon_r - \frac{j\sigma}{\omega \varepsilon_0} \right)^{-1} \nabla \times \vec{H}_\phi \right) - \mu_r k_0^2 \vec{H}_\phi = 0 \tag{3}$$

where $\varepsilon_0 = 8.8542 \times 10^{-12}$ F/m is the permittivity of free space, ε_r is the relative permittivity, σ is the electric conductivity (S/m), μ_r is the relative permeability and k_0 is the free space wave number (m^{-1}).

3.1.1. Boundary condition for electromagnetic wave propagation analysis

Microwave energy is emitted from the MCA slot, which connected to the microwave generator, and propagates through the MCA into the porous liver from the MCA slot. Therefore, boundary condition for analyzing electromagnetic wave propagation, as shown in Fig. 3, is considered as follows:

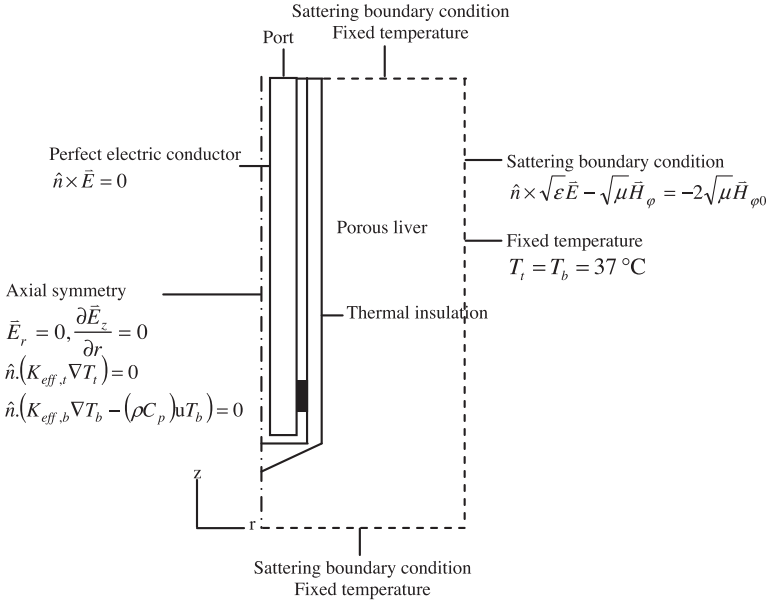

Fig. 3. Boundary condition for analysis of electromagnetic wave propagation and heat transfer.

At the inlet of the MCA, TM wave propagation with various input microwave powers is considered. An axial symmetry boundary is applied at $r = 0$:

$$\vec{E}_r = 0 \tag{4}$$

$$\frac{\partial \vec{E}_z}{\partial r} = 0 \tag{5}$$

The first order scattering boundary conditions for $\vec{H}_\phi$ were used along the outer sides of the porous liver boundaries to prevent reflection artifacts [11]:

$$\hat{n} \times \sqrt{\varepsilon}\,\vec{E} - \sqrt{\mu}\vec{H}_\phi = -2\sqrt{\mu}\vec{H}_{\phi 0} \tag{6}$$

where $\vec{H}_{\phi 0} = C/Zr$ is the excitation magnetic field.

For simplicity and to eliminate numerical error, the inner and outer conductors of the MCA are modeled as the PEC boundary conditions:

$$\hat{n} \times \vec{E} = 0 \tag{7}$$

3.2. Equations for heat transfer analysis

In analysis of heat transfer, the tissue and blood temperatures within the porous liver during MWA process are obtained by solving the two energy equations under LTNE assumption where the microwave power absorbed is included. The temperature distribution corresponds to the microwave power absorbed. This is because when microwave propagates in the porous liver, microwave energy is absorbed by the porous liver and converted into internal heat generation which causes the porous liver temperature to rise. To simplify the problem, the following assumptions are made:

1. Corresponding to electromagnetic wave propagation analysis, blood flow and heat transfer analysis in the liver is assumed in 2D axially symmetrical cylindrical coordinates (r–z).
2. The porous liver is considered homogenous, thermally isotropic and is saturated with a fluid (blood).
3. The blood flow is an incompressible and Newtonian [13,20].
4. There is no phase change occurs within the porous liver, no energy exchange through the outer surface of the porous liver, and no chemical reactions occur within the porous liver.
5. The porosities and thermal properties of the porous liver are assumed to be constant.

The transient temperature distribution within the porous liver is obtained by solving the energy equations of tissue and blood phases where the microwave power absorbed and an internal heat sources (namely metabolic heat source) are included. However, the metabolic heat source includes only in tissue phase energy equation [13,22,27]. The governing equations describing the heat transfer phenomenon for tissue and blood phases incorporating with LTNE conditions can be represented as [27]:

Tissue phase:

$$(1-\phi)(\rho C_p)_t \frac{\partial T_t}{\partial t} = \nabla \cdot (K_{t,eff} \nabla T_t) - h_{tb} a_{tb}(T_t - T_b) - \omega_b C_b \times (T_t - T_b) + (1-\phi) Q_{met} + (1-\phi) Q_{ext,t} \tag{8}$$

Blood phase:

$$\phi(\rho C_p)_b \left(\frac{\partial T_b}{\partial t} + \mathrm{u} \cdot \nabla T_b \right) = \nabla \cdot (K_{b,eff} \nabla T_b) + h_{tb} a_{tb}(T_t - T_b) + \omega_b C_b (T_t - T_b) + \phi Q_{ext,b} \tag{9}$$

where

$$K_{t,eff} = (1-\phi) K_t \tag{10}$$

$$K_{b,eff} = \phi K_b \tag{11}$$

where subscripts *eff*, *t* and *b* represent the effective value, tissue and blood phase, respectively, T is the temperature averaged (°C), ρ is the density (kg/m^3), C_p is the specific heat capacity (J/kg °C), K is the thermal conductivity (W/m °C), ϕ is the porosity which is the ratio of the blood volume to the total volume (–) [13], u is the blood phase average velocity (cm/s), ω is the blood perfusion rate (1/s), h_{tb} is the blood to tissue interfacial heat transfer coefficient (W/m^2 °C) and a_{tb} is thevolumetric transfer area between the blood and the tissue (m^2/m^3). The h_{tb} depends on the nature of the porous matrix and the saturating fluid and the value of this coefficient has been the subject of intense experimental interest. Large values of h_{tb} correspond to a rapid transfer of heat between the phases (LTE assumption) and small values of h_{tb} gives rise to relatively strong LTNE effects [33]. In this study, the blood to tissue interfacial heat transfer coefficient is selected to be 170 W/m^2 °C for all cases [14].

From the Eq. (8), the first, second, third, fourth and fifth terms on the right-hand side of equation denote heat conduction term, interstitial convection heat transfer term, blood perfusion term, metabolic heat source and external heat source (heat generation by the electric field), respectively. On the other hand, the first and second terms on the left-hand side of Eq. (9) denotes the transient term and convection term due to blood flow, respectively. While, bulk blood flow term appears on the left side of the blood phase energy equation (Eq. (9)), as part of the total temporal derivative.

As seen from two energy equations for tissue and blood phases are coupled by the interstitial convective heat transfer term and blood perfusion term. The interstitial convective heat transfer term and blood perfusion term are different processes and should not be confused [13]. The blood perfusion term is the process of nutritive delivery of arterial blood to a capillary bed in the biological tissue [27]. The temperature of the blood is decreased from T_b to T_t in the perfusion process and the energy change in this process. The blood perfusion term is added in both tissue and blood phases, accounting for the heat transfer associated with the transcapillary fluid exchange via arterial-venous anastomoses that was included in Nakayama and Kuwahara [13] and Zhang [27]. In this study, the blood perfusion rate is selected to be 0.0036 1/s for all cases [34]. On the other hand, the interstitial convective heat transfer term is the process of the temperature changes as result of convective heat transfer between the blood and the peripheral tissues. The effects of vascular geometry and size can also be accounted for by blood to tissue interfacial heat transfer coefficient (h_{tb}) and the volumetric transfer area between the blood and the tissue (a_{tb}).

The metabolic heat source (Q_{met}) is 33,800 W/m^3 [35,36], while the external heat source (Q_{ext}) is equal to the resistive heat generated by electric field and can be defined as [37]:

$$Q_{ext} = \frac{\sigma |\vec{E}|^2}{2} \tag{12}$$

When LTE assumption is maintained, the temperature of the tissue is equal to that of the blood temperature ($T_t = T_b = T$). Therefore, the above Eqs. (8) and (9) can be combined into a one equation as follows:

$$((1-\phi)(\rho C_p)_t + \phi(\rho C_p)_b) \frac{\partial T}{\partial t} + \phi(\rho C_p)_b (\mathrm{u} \cdot \nabla T) = \nabla \cdot ((1-\phi) K_t + \phi K_b) \nabla T + (1-\phi) Q_{met} + Q_{ext} \tag{13}$$

The Pennes's bioheat equation which the metabolic heat source and the external heat source are applied to the tissue can be written as [28,31]:

$$(\rho C_p)_t \frac{\partial T_t}{\partial t} = \nabla \cdot (K_t \nabla T_t) + (\rho C_p)_b \omega_b (T_b - T_t) + Q_{met} + Q_{ext} \quad (14)$$

where T_b is the blood temperature and is assumed to be uniform throughout the tissue, normally taken as body temperature 37 °C [18]. Eq. (14) is one of the earliest heat transfer equations that describes the temperature distribution in biological tissue. The blood perfusion effect is assumed to be homogeneous and isotropic, i.e., the effect of directional blood flow cannot be described by the Pennes's bioheat equation.

The Klinger model with the assumption of quasi-steady state [1]:

$$(\rho C_p)_t \frac{\partial T_t}{\partial t} + \phi (\rho C_p)_b (\mathrm{u}.\nabla T) = \nabla \cdot (K_t \nabla T_t) + Q_{met} + Q_{ext} \quad (15)$$

The main difference between Eq. (14) and Eq. (15) is found in their convection term due to blood flow, this term in Eq. (15) accounts for the directional effect of blood flow on the tissue temperature distribution, whilst, that of Eq. (14) acts as a blood perfusion term.

3.2.1. Boundary condition for heat transfer analysis

The heat transfer analysis under LTNE assumption is considered only in the porous liver, which does not include the MCA. As shown in Fig. 3, the boundaries of porous liver corresponds to the assumption are considered as follows:

An axial symmetry boundary is applied at $r = 0$ for the heat transfer analysis:

$$\hat{n} \cdot (K_{eff,t} \nabla T_t) = 0 \quad (16)$$

$$\hat{n} \cdot (K_{eff,b} \nabla T_b - (\rho C_p)_b \mathrm{u} T_b) = 0 \quad (17)$$

At the outer surface between the MCA and the porous liver is considered as adiabatic boundary condition. While, the tissue and the blood temperatures at surroundings of the porous liver will be the same at fixed temperature at 37 °C

$$T_t = T_b = 37\,^{\circ}C \quad (18)$$

The initial temperature of the porous liver is assumed to be uniform:

$$T(t_0) = 37\,^{\circ}C \quad (19)$$

4. Numerical simulations

In this study, the FEM is used to analyze the transient problems. The computational scheme is to assemble axisymmetric FEM model with suitable time and spatial step size. The coupled model of electromagnetic wave propagation and heat transfer analysis are solved by the FEM, to demonstrate the phenomenon that occurs within the porous liver during MWA. Analysis of heat transfer can be modeled by solving a conjugate problem containing a tissue and blood phases. Both initial tissue and blood temperatures are set to be body temperature 37 °C at the beginning of the ablation. The computational scheme starts with computing an external heat source term by running an electromagnetic wave propagation calculation and subsequently solves the time dependent temperature in the porous liver. All the steps are repeated until the required heating time is reached.

The description of heat transfer pattern, Eqs. (8)–(11), (13)–(19) requires specification of tissue temperature (T_t) and blood temperature (T_b). These equations are coupled to the electromagnetic wave propagation equations Eqs. (1)–(7) and energy equation by Eq. (12). The time-steps used to solve the system of equations describing electromagnetic wave propagation and heat transport are $\Delta t = 2 \times 10^{-12}$ s and $\Delta t = 0.01$ s, respectively.

The axisymmetric FEM model is discretized using triangular elements with the Lagrange quadratic shape functions. In order to obtain a good approximation, a fine mesh has been generated in the vicinity of the tip of the antenna, where the temperature is more concentrated. The set of partial differential equations along with their related boundary conditions are coupled and are solved numerically by the FEM via COMSOL™ multiphysics. FEM models can provide users with quick, accurate solutions to multiple systems of differential equations and as such, are well suited to heat transfer problems like ablation [30]. The system of governing equations as well as initial and boundary conditions are solved with the Unsymmetric Multifrontal Method (UMFPACK) solver to approximate tissue and blood temperatures variation across each element. The predicted tissue temperature of the Pennes model and the Klinger model, with the same model parameters and the same initial and boundary conditions as the LTNE model, are also simulated in three blood velocity cases to provide a direct comparison. The convergence test is carried out to identify the suitable numbers of element required. The convergence curve resulting from the convergence test is shown in Fig. 4. This figure shows the relationship between temperature and number of elements from simulations at a critically sensitive point, of the slot center (insertion depth of 64 mm). This convergence test leads to a grid with approximately 20,471 elements. It is reasonable to confirm that, at this number of element, the accuracy of the simulation results is independent from the number of elements through the calculation process. Cases with higher numbers of elements are not tested due to a lack of computational memory and performance.

5. Results and discussion

In this analysis, the influences of blood velocities ($u = 0.4$, 2, 3 and 3.4 cm/s), porosities ($\phi = 0.025$, 0.05 and 0.1), input microwave power ($P = 5$, 10, 15, 20 W) and positions within the porous liver (distance from MCA) (p1 (2.5 mm, 16 mm), p2 (4.5 mm, 16 mm) and p3 (8.5 mm, 16 mm)) on distributions of tissue and blood temperatures within the porous liver are systematically investigated. A parametric study has been carried out to assess the effect of each of these factors separately and analyze their contributions in determining the tissue and blood temperature distributions.

5.1. Validation of the model

It must be noted in advance that it is very difficult to make direct comparison of the model in this study and the experimental results because it is not possible to directly measure the temperature increase in the liver tissue, especially in the case where electromagnetic field is effected during MWA ablation is taken into account. In order to verify the accuracy of the presented mathematical model, the simulation results of tissue temperature of the porous liver based on LTE model and tissue temperature of bioheat model are then validated against the experimental results with the same geometric model and the same testing condition obtained by Yang et al. [10]. The geometry of the validation case as shown in Fig. 5. In the validation case, the input microwave power of 75 W with frequency of 2.45 GHz and the initial liver tissue temperature of 8 °C are used. The single slot MCA with a radius of 1.25 mm is inserted into liver tissues 20 mm in depth. The axially symmetrical model is used to analyze the MWA process with the heating time of 50 s. The validation results of the selected test case are illustrated in Fig. 6 for temperature distribution in the liver tissue, with respect to the heating time of 50 s with the positions of 4.5 mm and 9.5 mm away from the MCA. From the figures, it can be observed that the simulated results of the tissue temperature of the porous liver based on LTE model corresponds well to the

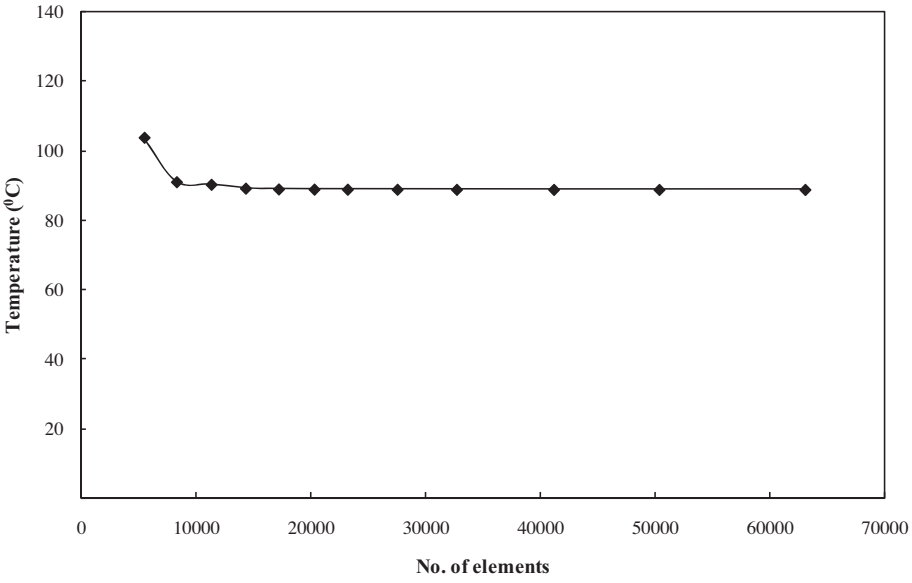

Fig. 4. Grid convergence curve of the model.

experimental results with similar trends in temperature distribution over the same approximate time range at both positions, especially at the end stage. This is due to the fact that the porous media model is based on convective heat mode coupled with conduction heat mode. While the bioheat model is manly governed by conduction heat mode. Considering the fact that the convective heat is influence increases at the end stage, it is obvious that the porous media model yields better results. Table 5 shows the comparisons of the root mean square error (RMSE) of the liver tissue temperature between the tissue temperature from LTE model and tissue temperature from bioheat model in present study with experimental data obtained from Yang et al. [10]. From the table, it is observed that the bioheat model gives greater error than the simulated temperature obtained from porous media model. However, at the position of 9.5 mm away from the MCA, the temperature distribution match the experimental results better than the temperature distribution at the position of 4.5 mm. Therefore, the selected developed model based on porous media approach is reasonable and can be used effectively for this problem. This is important to obtain the approaching realistic tissues modeling during MWA.

Although the simulation result of temperature based on LTE model agree well with the experimental data obtained from Yang et al. [10], the LTE model is not considered the temperature difference between the tissue and blood phases within the biological tissue that significant in to heat transfer, especially during thermal ablation treatment. Therefore, the analysis of heat transport in biological tissue during thermal ablation should consider the LTNE model. These simulated results will contribute to a greater clarity concerning attributes more closely to actual behavior of thermal ablation.

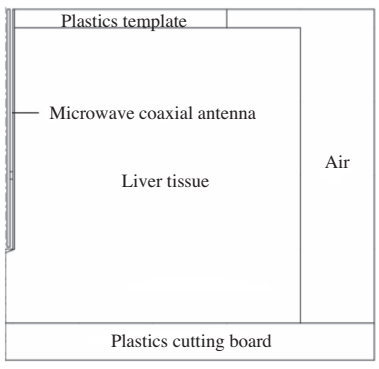

Fig. 5. Geometry of the validation model obtained from the Yang et al. [10].

5.2. Comparison of tissue and blood temperature of LTNE model and tissue temperature of Pennes model and Klinger model

The prediction of tissue and blood temperature distributions within the porous liver is crucial for an effective MWA therapy. The tissue and blood temperature distributions obtained from the numerical simulation correlations effectively address this need.

Fig. 7 depicts the simulation results of temperature distribution the center of the slot exit (z = 16 mm) versus models at three positions based on P = 10 W, f = 2.45 GHz, ϕ = 0.05, u = 2 cm/s and t = 300 s. Fig. 7(a) and (b) shows the tissue and blood temperature distributions of the LTNE model, respectively. While, Fig. 7(c) and (d) shows the tissue temperature distribution of the Pennes model and Klinger model, respectively. It can seen that the tissue and blood temperature distributions of the LTNE model and the tissue temperature distribution of the Pennes model have similar trends with a slight difference in magnitude. The distribution of temperature in three cases are increases with an increases in heating time. Therefore, the predicted tissue temperature distribution pattern of the Pennes model (Fig 7(c)) is shown to be almost identical to that of the that tissue and blood temperature distributions of the LTNE model, whilst, the parallel simulated temperature distribution pattern of the Klinger model (Fig. 7(d)) is, in contrast, very different. This demonstrates that the Pennes model is much closer in equivalence to the tissue and blood temperature distributions of LTNE model in case of blood velocity to be 2 cm/s. Consider the different of tissue and blood temperature distributions from LTNE model, it is found that the pattern of temperature distribution are very similar trends. It can be concluded that the LTE model is suitable for a predicted the distribution of temperature when the blood velocity to be 2 cm/s for this condition.

Fig. 8 illustrates the simulation results of temperature distribution the center of the slot exit (z = 16 mm) versus models at three positions based on P = 10 W, f = 2.45 GHz, ϕ = 0.05, u = 3.4 cm/s and t = 300 s. Fig. 8(a) and (b) shows the tissue and blood temperature distributions of the LTNE model, respectively. While, Fig. 8(c) and (d) shows the tissue temperature distribution of the Pennes model

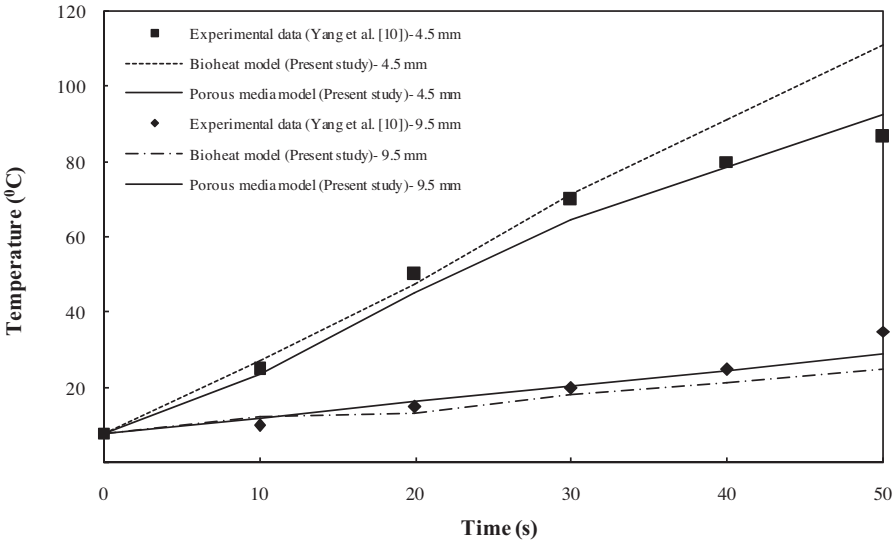

Fig. 6. The validation results of tissue temperature of the porous liver based on LTE model and tissue temperature of bioheat model, against the experimental results obtained by Yang et al. [10].

Table 5
Comparisons of RMSE of the liver tissue temperature between the present study and Yang et al. [10].

Position (mm)	Comparisons of RMSE with experimental data obtained from Yang et al. [10] (°C)	
	Bioheat model (present study)	Porous media model (present study)
4.5 mm	11.10	3.87
9.5 mm	4.52	2.73

and Klinger model, respectively. It can observed that the tissue temperature distribution (Fig. 8(a)) and the blood temperature distribution (Fig. 8(b)) are significantly different, especially at position of p1. Due to this position is close to the MCA that hot spot zone occurs. This demonstrates that the LTE model is not suitable for a predicted the distribution of temperature, suggesting the importance of utilizing the LTNE model when the blood velocity to be 3.4 cm/s for this condition. Referring to Table 4, at blood velocity to be 3.4 cm/s is lower the volumetric transfer area between the blood and the tissue as a result of lower heat exchange between two phases in all porosities, therefore, it can conclude that a low heat exchange lead to a large difference between the tissue and blood temperatures. A similar conclusion has been achieved by Peng et al. [1] and Mahjoob and Vafai [22] when studying the heat transport through biological media. Although the tissue temperature distribution of the Pennes model Fig. 8(c) has similar trends with a tissues temperature distribution of the LTNE model (Fig. 8(a)), a difference in magnitude. While, the simulated temperature of Klinger model (Fig. 8(d)) is also in contrast from the other models corresponds to the results in Fig. 7.

5.3. Comparison of tissue and blood temperature profiles of LTNE model and tissue temperature profile of LTE model

The comparison of tissue and blood temperature profiles of LTNE model and tissue temperature profile of LTE model within the porous liver for heating times of 60 s, 180 s, and 300 s based on $P = 10$ W, $f = 2.45$ GHz, $\phi = 0.05$ and $u = 3.4$ cm/s, are shown in Fig. 9. In all cases, the temperature profile forms a nearly ellipsoidal shape around the slot and the highest value occurs in the vicinity of the slot MCA and decreases with the distance from the MCA. Moreover, the temperature profile in three cases are increases with an increases in heating time. It is interesting to observe that the temperature of tissue and blood from LTNE models and the temperature of tissue from LTE models that far from the MCA are found to be close to the initial temperatures 37 °C. By comparison between tissue and blood temperature profile from LTNE models, it is clear that the difference of temperature profile pattern with a slight difference in magnitude at all heating times. The comparison between the maximum temperatures in three cases, it can be seen that the maximum tissue temperature of LTNE model has a higher maximum temperatures value within the porous liver than that of the maximum blood temperature of LTNE model and maximum tissue temperature of LTE model, respectively at all duration times. The maximum temperature differences for the temperature of tissue and blood from LTNE models are 0.514% and the maximum temperature differences for the temperature of tissue from LTNE and LTE models are 4.167%, respectively at the end of process. Although the patterns of temperature profile of tissue from LTNE is similar to the temperature profile of tissue from LTE models, the maximum temperature values are quite different. Therefore, the LTNE assumption for heat transfer analysis needs to be utilized for this condition.

5.4. Effect of porosity

During thermal ablation treatments, the porosities is likely to change as a part of the natural body temperature regulation system [22]. The natural cooling system in the body, the blood regulates the body temperature during thermal ablation by arterial blood with the cold body core temperature, while modifying the porosity of the biological structure. The natural body thermal regulation system increases or decreases the porosity of the biological structure when exposed to a higher or lower temperature, respectively. A change in the porosity also translates in a change in the and blood and effective thermal conductivities as shown in Eqs. (10) and (11). Therefore, the investigation of the effect of porosities on the temperature distribution may have large practical significance. In this section discusses the effect of porosities on the tissue and blood temperature distributions.

Fig. 10 shows the tissue and blood temperature distributions of the LTNE model versus time for different blood velocities at the position p1 ($r = 2.5$ mm, $z = 16$ mm) based on $P = 10$ W, $f = 2.45$ GHz, $\phi = 0.1$ and $t = 300$ s. In this figure, the difference be-

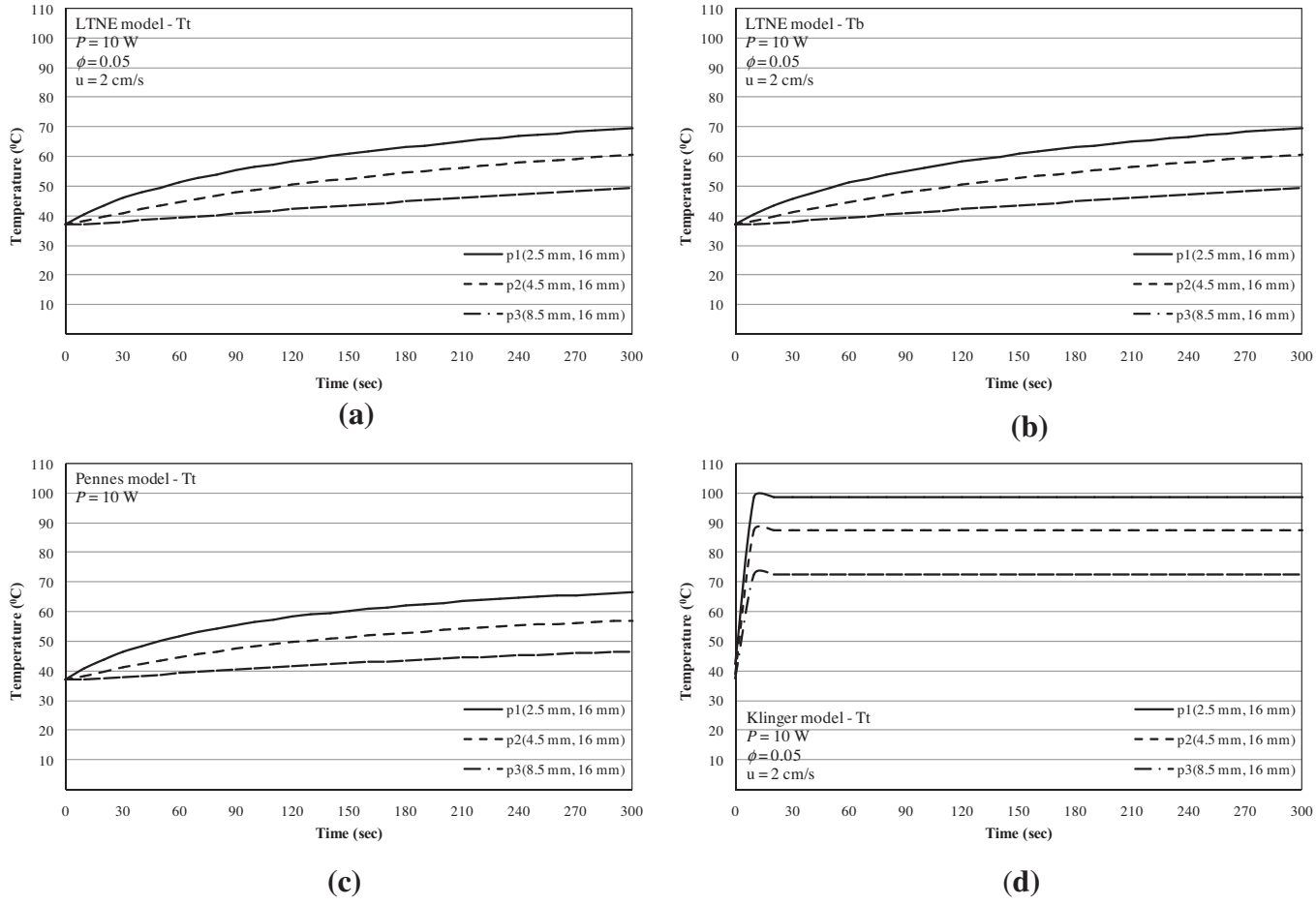

Fig. 7. The temperature distribution at the center of the slot exit (z = 16 mm) versus models (a) and (b) tissue and blood temperature distributions of the LTNE model; (c) tissue temperature distribution of the Pennes model and (d) tissue temperature distribution of the Klinger model, respectively at three positions; (P = 10 W, f = 2.45 GHz, ϕ = 0.05, u = 2 cm/s and t = 300 s).

tween tissue and blood temperature distributions hardly varies for the same blood velocities when the porosity to be 0.1. The distribution of tissue and blood temperatures of all blood velocities are increases with an increases in heating time. Therefore, it can be concluded that the LTE assumption is suitable for a predicted the distribution of temperature when the porosity to be 0.1 for this condition. Consider the effect of blood velocity on the tissue and blood temperature distributions, it is found that the lower blood velocity provides a higher tissue and blood temperature distributions within the porous liver. This is because the lower blood velocity have a higher internal heat exchange, as given in Table 4 results in a higher tissue and blood temperatures.

The effect of lower porosity (ϕ = 0.05) on tissue and blood temperature distributions of the LTNE model versus time for different blood velocities are illustrates in Fig. 11. From the Fig. 11, it is can seen that the tissue and blood temperature distributions in Fig. 11 are similar trends to the tissue and blood temperature distributions in Fig. 10. The distribution of temperature of two phases increases with an increases in heating time. The tissue and blood temperature distributions have similar trends in case blood velocity to be 0.4 cm/s and 2 cm/s. On the other hand, the tissue temperature distribution is different from blood temperature distribution in case blood velocity to be 3 cm/s and 3.4 cm/s. Which the tissue temperature distribution is different from blood temperature distribution in case blood velocity to be 3.4 cm/s more than that in case blood velocity to be 3 cm/s when the porosity to be 0.05 is used. This implies that the LTE assumption is suitable for in case blood velocity to be 0.4 cm/s and 2 cm/s at the porosity to be 0.05. In Eq. (9), the second term on the left of the equation represents the convection heat transferred out by the blood flow, and it depends on the porosity, blood properties, blood velocity, and temperature gradient. When the blood velocity in the tissue is low, the porous medium easily approaches the LTE assumption of equal temperatures of the tissue and blood because of an increase in the internal heat exchange between the tissue and blood. Besides, the comparison of tissue and blood temperatures within porous liver, it is can observed the blood temperature must be lower than the tissue temperature due to the different microwave power absorbed of tissue and blood during the MWA process. That the microwave power absorbed of blood is less than that of tissue during thermal therapy [38].

Fig. 12 depicts the tissue and blood temperature distributions of the LTNE model versus time for different blood velocities with ϕ = 0.025. In Fig. 12, it is clear that the LTE assumption is suitable for blood velocity to be 0.4 cm/s and 2 cm/s when the porosity to be 0.025 due to the tissue temperature match with the blood temperature. While, the difference between the temperature of two phases can see clearly in case blood velocity to be 3 cm/s and 3.4 cm/s. Moreover, the difference between the temperature of two phases with blood velocity to be 3 cm/s and 3.4 cm/s when the porosity to be 0.025 in Fig. 12 is higher than the difference between the temperature of two phases in same two blood velocities when the porosity to be 0.05 in Fig. 11.

Referring to the simulation result in Figs. 10–12, the tissue temperature match the result of blood temperature with blood velocity

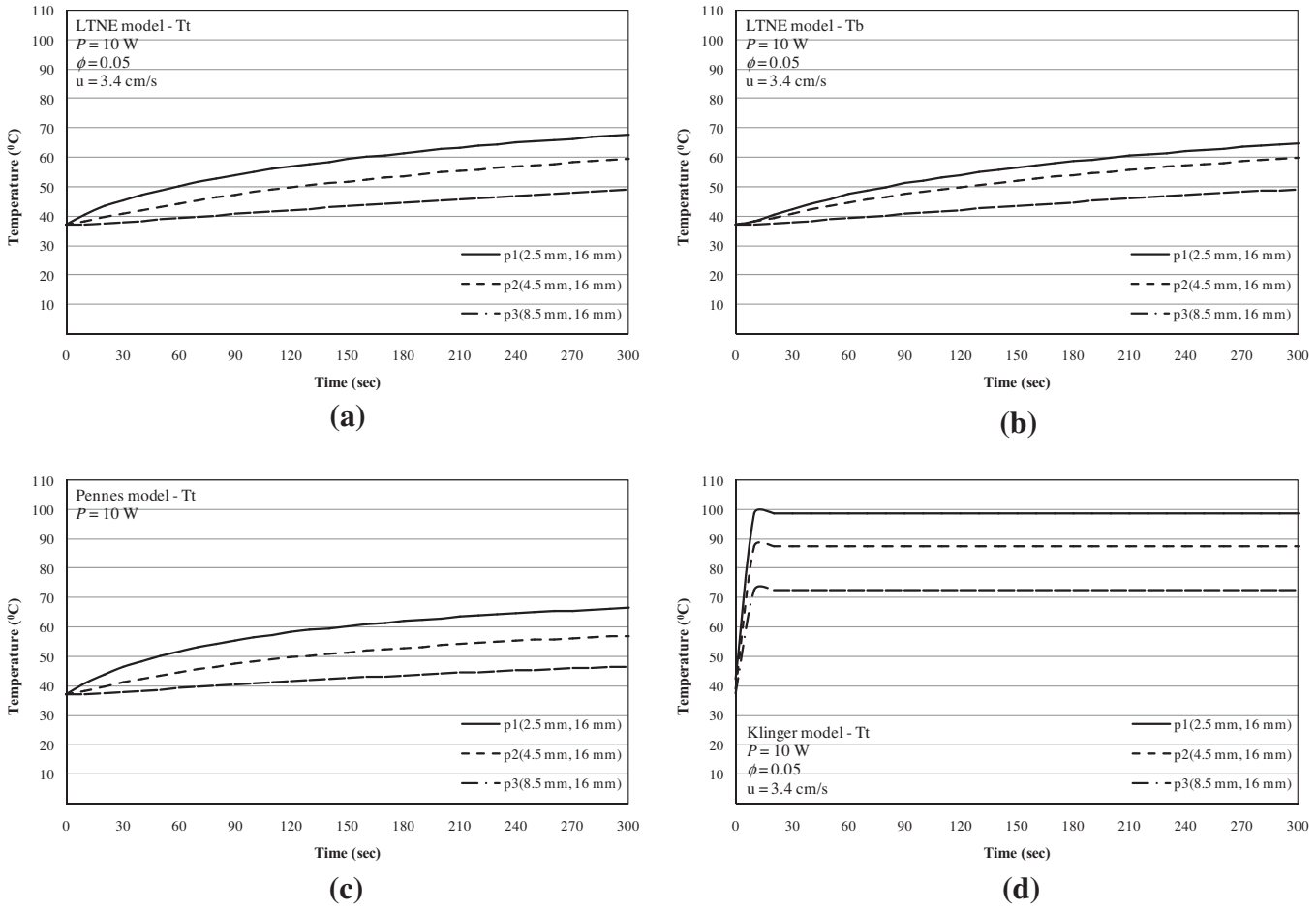

Fig. 8. The temperature distribution at the center of the slot exit (z = 16 mm) versus models (a) and (b) tissue and blood temperature distributions of the LTNE model; (c) tissue temperature distribution of the Pennes model and (d) tissue temperature distribution of the Klinger model, respectively at three positions; (P = 10 W, f = 2.45 GHz, ϕ = 0.05, u = 3.4 cm/s and t = 300 s).

to be 0.4 cm/s and 2 cm/s in every conditions. This show that the LTE assumption is valid for all porosities used in this study when blood velocity to be 0.4 cm/s and 2 cm/s. On the other hand, when blood velocity to be 3 cm/s and 3.4 cm/s the LTNE assumption for heat transfer analysis needs to be utilized. Because the difference of temperature in two phase varies significantly.

Furthermore, referring to the literature [1,14,29], the vasculature with a large blood velocity (blood velocities are 3 cm/s and 3.4 cm/s) will has a larger vessel diameters than that the small blood velocity (blood velocities are 0.4 cm/s and 2 cm/s). Therefore, from the result in the Figs. 10–12, can provides an alternative way to estimate the analysis of heat transport of the whole vasculature during thermal ablation. For the analysis of heat transport in biological media including multiple vessel types, the temperature of a large vessel diameters should be calculated directly from the LTNE assumption, while the heat transport of small vessel diameters or the microvasculature may be neglected because they are completely thermally equilibrated with the surrounding tissue.

Because of the difference in tissue and blood temperatures is the most obvious with blood velocity is 3.4 cm/s, Fig. 13 explains the comparison of the tissue and blood temperature distributions of the LTNE model versus time for different porosities at the position p1 (r = 2.5 mm, z = 16 mm) at blood velocity is 3.4 cm/s. When the porosities is large (ϕ = 0.1), there is little difference between the tissue and blood temperatures, in which case the model prediction could be approximated by that of LTE model. Because higher porosity implies having more blood to carry the heat away from the tissue, consequently the tissues temperature to be close to the blood temperature. The temperature uniformity can be achieved within a biological structure with a larger porosity resulting in a more effective thermal treatment [22]. On the other hand, the larger difference between the tissue and blood temperatures when an decrease in the porosities (ϕ = 0.05 and 0.025) completely breaks down the LTE assumption between the tissue temperature and the blood temperature are better approximated by the assumption of LTNE. Due to a higher porosity leads to a lower microwave power absorbed, hence the time-varying tissue and blood temperature distributions of higher porosity are lower than those of lower porosity the heating duration time and blood velocity maintain the same input.

5.5. Effect of input microwave power

In this section, discusses the effect of input microwave power on tissue and blood temperatures of LTNE model. The input microwave powers of 5 W, 15 W and 20 W are selected for study and demonstration. These input microwave powers are selected during MWA in order to estimate the appropriate power setting of MWA applied treatment for liver cancer. While, the effect of input microwave power is 10 W on tissue and blood temperatures of LTNE model can be seen in the section of 5.4. In addition, the porosity of 0.025 and blood velocity of 3.4 cm/s are selected in this section due to in this condition it is clear that the difference of tissue and blood temperatures. With regard to the tissue and blood temperatures at the three positions are shown in Fig. 2. Fig. 14 shows the tissue and blood temperature distributions of the LTNE

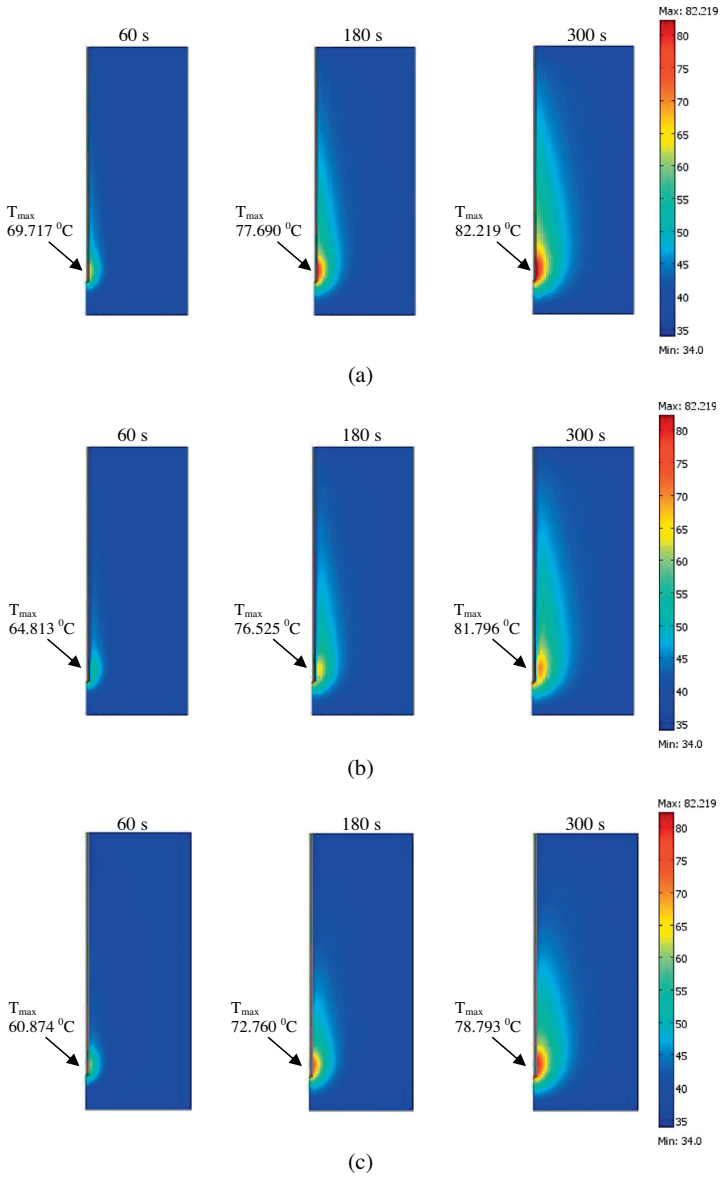

Fig. 9. The temperature profiles in the porous liver at various times where (a) the tissue temperature profiles of LTNE model (b) the blood temperature profiles of LTNE model and (c) the tissue temperature profiles of LTE model based on the same condition in the figure.

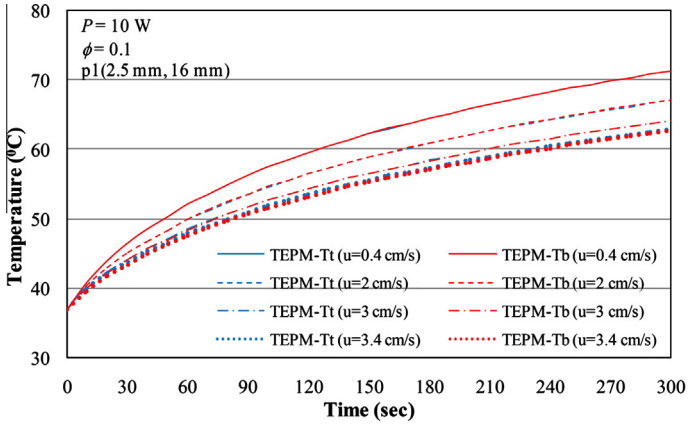

Fig. 10. The tissue and blood temperature distributions of the LTNE model versus time for different blood velocities at the position p1 (r = 2.5 mm, z = 16 mm); (P = 10 W, f = 2.45 GHz, ϕ = 0.1 and t = 300 s).

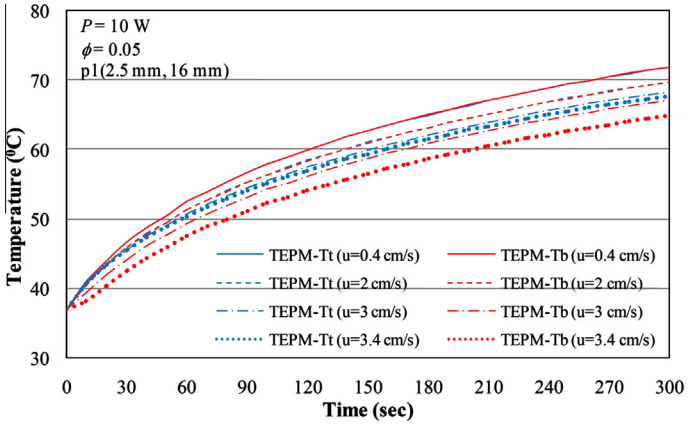

Fig. 11. The tissue and blood temperature distributions of the LTNE model versus time for different blood velocities at the position p1 (r = 2.5 mm, z = 16 mm); (P = 10 W, f = 2.45 GHz, ϕ = 0.05 and t = 300 s).

model within porous liver base on P = 5 W, f = 2.45 GHz, ϕ = 0.025, u = 3.4 cm/s and t = 300 s. From this figure, it is seen that the distribution of tissue and blood temperatures for three positions are increases with an increases in heating time. It is clear that the difference of tissue and blood temperature distributions results at the position of p1 due to position is close to the MCA that hot spot zone occurs. However, the pattern of tissue and blood temperature distributions are similar trends at the position of p2 and p3. Similarly, the temperature at the position of p1has a higher than that of the temperature at the position of p2 and p3, respectively.

In Fig. 15 illustrates the simulated results of tissue and blood temperature distributions of the LTNE model within porous liver at the versus positions when input microwave power is 15 W. The condition is used in this figure based on a same condition as Fig. 14. It is found that the simulation results of Fig. 15 are similar trends to the simulation results in Fig. 14, the distribution of tissue and blood temperatures for three positions are increases with an increases in heating time. Furthermore, the temperature at the position of p1has a higher than that of the temperature at the position of p2 and p3, respectively that are the similar results in Fig. 14. It is clear that the difference of tissue and blood temperatures at the position of p1, a slight difference at the position of p2, whilst, a hardly difference at the position of p3. Greater input microwave power leading to higher difference of temperature for each positions.

The tissue and blood temperature distributions within porous liver at the versus positions when input microwave power is 20 W based on a same condition as Fig. 14 and Fig. 15 is shown in Fig. 16. From the figure, it is seen that the tissue and blood temperature distributions for three positions are increases with an increases in heating time. The temperature at the position of p1has a higher than that of the temperature at the position of p2 and p3, respectively that are the similar results in Fig. 14 and 15. It this figure, the difference of temperature of two phases can be clearly seen at the position of p1 and p2.

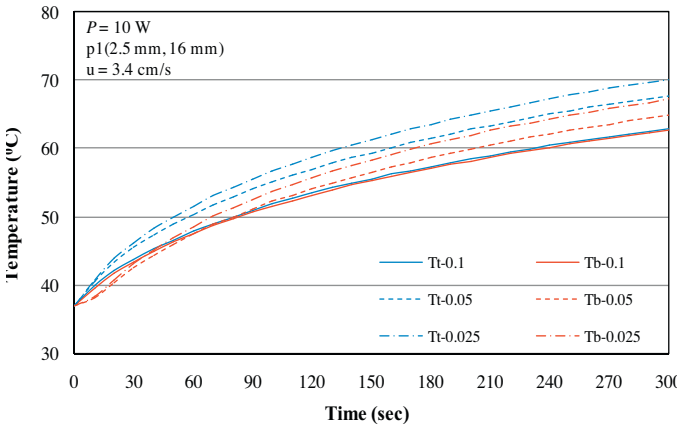

Fig. 13. The tissue and blood temperature distributions of the LTNE model versus time for different porosities at the position p1 (r = 2.5 mm, z = 16 mm); (P = 10 W, f = 2.45 GHz, u = 3.4 cm/s and t = 300 s).

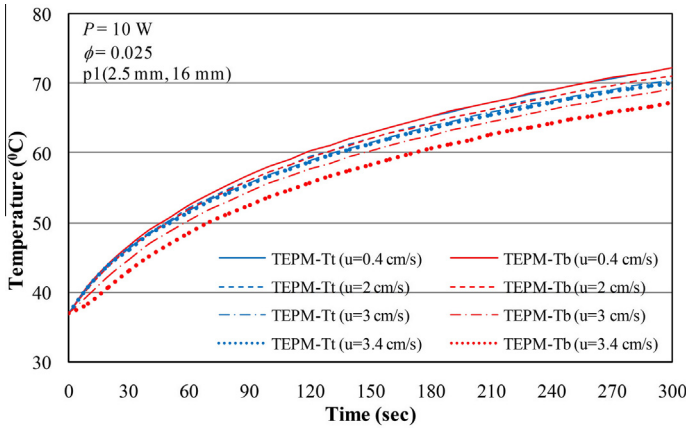

Fig. 12. The tissue and blood temperature distributions of the LTNE model versus time for different blood velocities at the position p1 (r = 2.5 mm, z = 16 mm); (P = 10 W, f = 2.45 GHz, ϕ = 0.025 and t = 300 s).

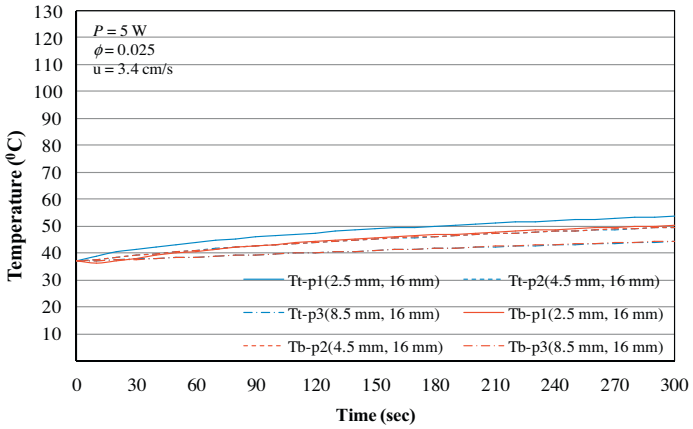

Fig. 14. The tissue and blood temperature distributions of the LTNE model at the versus positions; (P = 5 W, f = 2.45 GHz, ϕ = 0.025, u = 3.4 cm/s and t = 300 s).

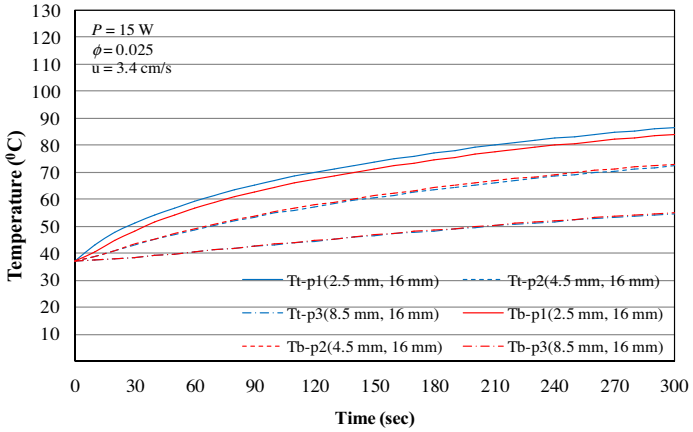

Fig. 15. The tissue and blood temperature distributions of the LTNE model at the versus positions; (P = 15 W, f = 2.45 GHz, ϕ = 0.025, u = 3.4 cm/s and t = 300 s).

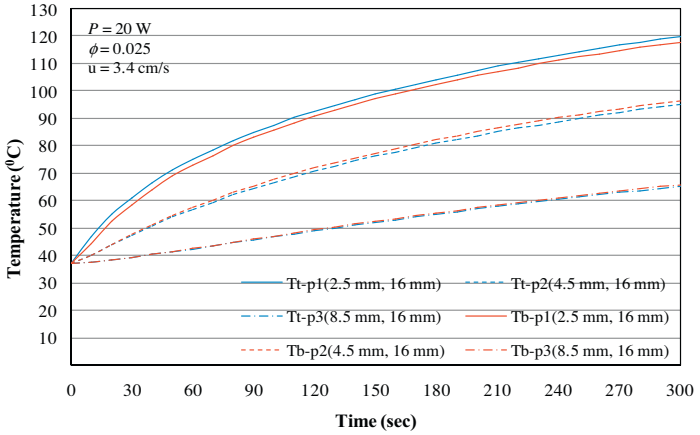

Fig. 16. The tissue and blood temperature distributions of the LTNE model at the versus positions; (P = 20 W, f = 2.45 GHz, ϕ = 0.025, u = 3.4 cm/s and t = 300 s).

Referring to the simulation result in Fig. 14–16, the tissue and blood temperatures in Fig. 16 is higher than that the tissue and blood temperatures in Fig. 14 and Fig. 15 for the same condition and same position. Because of the greater input microwave power leading to higher strength of electric field provides greater heat generation within the porous liver, thereby increasing the tissue and blood temperatures during the MWA process. Furthermore, the greater input microwave power leading to greater difference temperature between the different position. Consider the criterion for use the LTE assumption of the effect of input microwave power, it is difficult to estimate. Because the factors affecting the tissue and blood temperatures include the position. However, it concludes that the input microwave power significantly influence on the tissue and blood temperature distributions within porous liver during MWA process. Nevertheless, in a treatment is often used the heating time for a short time with a higher input microwave power is the trend in thermal therapy [14]. Because of treatment for a longer heating time at low input microwave power will induce a feeling of discomfort and pain for the patient.

Consequently, the above results indicate that the tissue and blood temperatures variation within the porous liver depend on the heating duration, the porosity, the blood velocity, input micro-

wave power and positions within the porous liver during thermal therapy. Although this study analyzes the heat transport within porous media that used only four blood velocities which may not be able to conclude the whole behavior of biological tissue when subjected to electromagnetic fields during thermal ablation. The obtained results can be used as a guideline for the practical treatment.

6. Conclusions

In this study, investigates the transient distribution of tissue and blood temperatures within porous liver during MWA process based on LTNE model undergoing MWA process by MCA. The thermal model considers the tissue with its blood vessel distribution as a porous medium and employs both the convection term due to heat exchange in two phases and blood perfusion term in the transient energy equations for both tissue and blood phases. The tissue and blood temperatures of LTNE model are compared with the tissue temperature of Pennes model and Klinger model. According to the results, the tissue temperature distribution of the Pennes model and the tissue and blood temperature distributions of the LTNE model for blood velocities to be 2 cm/s and 3.4 cm/s when porosity to be 0.05 have similar trends with a difference in magnitude. On the other hand, the temperature distribution pattern of the Klinger model is, very different with the tissue and blood temperatures of LTNE model for all blood velocities. Moreover, the LTE assumption is found to be suitable for predicting the temperature during MWA process when the blood velocities to be 0.4 cm/s and 2 cm/s in all porosities. Conversely, in case blood velocities to be 3 cm/s and 3.4 cm/s the LTNE assumption for heat transfer analysis needs to be utilized. Consistent with the influence of porosity on the different of tissue and blood temperatures, the results show that the lower porosity leading to higher different of tissue and blood temperatures. Therefore, the LTE model is suitable for predicting a distribution of temperature when the high porosity. However, when consider the criterion for use the LTE assumption of the effect of input microwave power, it is difficult to estimate. Because the factors affecting the tissue and blood temperatures include the position. Nevertheless, it concludes that the input microwave power significantly influence on the tissue and blood temperature distributions within porous liver during MWA process.

In next step of this research, will to develop a three-dimensional modeling for approaching realistic liver tissue will be performed. A study will also develop a more realistic model for simulations and study the temperature dependency of and thermal properties of liver tissue.

Acknowledgement

The authors gratefully acknowledge the financial support for this work provided by the Thailand Research Fund (TRF).

References

[1] T. Peng, D.P. O'Neill, S.J. Payne, A two-equation coupled system for determination of liver tissue temperature during thermal ablation, Int. J. Heat Mass Transf. 54 (9–10) (2011) 2100–2109.
[2] C.J. Simon, D.E. Dupuy, W.W. Mayo-Smith, Microwave ablation: principles and applications, Radiographics 25 (Special Issue) (2005) S69–S83.
[3] J.P. McGahan, J.M. Brock, H. Tesluk, W.Z. Gu, P. Schneider, P.D. Browing, Hepatic ablation with use of radio-frequency electrocautery in the animal model, J. Vasc. Intervent. Radiol.: JVIR 3 (2) (1992) 291–297.
[4] H.H. Pennes, Analysis of tissue and arterial blood temperatures in the resting human forearm, J. Appl. Physiol. 85 (1) (1998) 5–34.
[5] J. Okajima, S. Maruyama, H. Takeda, A. Komiya, Dimensionless solutions and general characteristics of bioheat transfer during thermal therapy, J. Therm. Biol 34 (8) (2009) 377–384.
[6] P. Phasukkit, S. Tungjitkusolmun, M. Sangworasil, Finite-element analysis and in vitro experiments of placement configurations using triple antennas in microwave hepatic ablation, IEEE Trans. Biomed. Eng. 56 (11) (2009) 2564–2572.
[7] M. Liangruksa, R. Ganguly, I.K. Puri, Parametric investigation of heating due to magnetic fluid hyperthermia in a tumor with blood perfusion, J. Magn. Magn. Mater. 323 (6) (2011) 708–716.
[8] S. Becker, Analytic one dimensional transient conduction into a living perfuse/non-perfuse two layer composite system, Heat Mass Transf. 48 (2) (2012) 317–327.
[9] H. Klinger, Heat transfer in perfused biological tissue I: general theory, Bull. Math. Biol. 36 (4) (1974) 403–415.
[10] D. Yang, M. Converse, D. Mahvi, Expanding the bioheat equation to include tissue internal water evaporation during heating, IEEE Trans. Biomed. Eng. 54 (8) (2007) 1382–1388.
[11] P. Keangin, T. Wessapan, P. Rattanadecho, Analysis of heat transfer in deformed liver cancer modeling treated using a microwave coaxial antenna, Appl. Therm. Eng. 31 (16) (2011) 3243–3254.
[12] W. Roetzel, Y. Xuan, Transient response of the human limb to an external stimulust, Int. J. Heat Mass Transf. 41 (1) (1998) 229–239.
[13] A. Nakayama, F. Kuwahara, A general bioheat transfer model based on the theory of porous media, Int. J. Heat Mass Transf. 51 (2008) 3190–3199.
[14] P. Yuan, Numerical analysis of temperature and thermal dose response of biological tissues to thermal non-equilibrium during hyperthermia therapy, Med. Eng. Phys. 30 (2) (2008) 135–143.
[15] B. Alazmi, K. Vafai, Analysis of variants within the porous media transport models, ASME J. Heat Transfer 122 (2000) 303–326.
[16] A.-R.A. Khaled, K. Vafai, The role of porous media in modeling flow and heat transfer in biological tissues, Int. J. Heat Mass Transf. 46 (2003) 4989–5003.
[17] H.S. Kou, T.C. Shih, W.L. Lin, Effect of the directional blood flow on thermal dose distribution during thermal therapy: an application of a Green's function based on the porous model, Phys. Med. Biol. 48 (11) (2003) 1577–1589.
[18] P. Rattanadecho, P. Keangin, Numerical study of heat transfer and blood flow in two-layered porous liver tissue during microwave ablation process using single and double slot antenna, Int. J. Heat Mass Transf. 58 (1–2) (2013) 457–470.
[19] W. Klinbun, K. Vafai, P. Rattanadecho, Electromagnetic field effects on transport through porous media, Int. J. Heat Mass Transf. 55 (1–3) (2012) 325–335.
[20] J. Fan, L. Wang, A general bioheat model at macroscale, Int. J. Heat Mass Transf. 54 (1–3) (2011) 722–726.
[21] N. Afrin, Y. Zhang, J.K. Chen, Thermal lagging in living biological tissue based on nonequilibrium heat transfer between tissue, arterial and venous bloods, Int. J. Heat Mass Transf. 54 (11–12) (2011) 2419–2426.
[22] S. Mahjoob, K. Vafai, Analytical characterization of heat transport through biological media incorporating hyperthermia treatment, Int. J. Heat Mass Transf. 52 (5–6) (2009) 1608–1618.
[23] P. Yuan, Numerical analysis of an equivalent heat transfer coefficient in a porous model for simulating a biological tissue in a hyperthermia therapy, Int. J. Heat Mass Transf. 52 (7–8) (2009) 1734–1740.
[24] A. Belmiloudi, Parameter identification problems and analysis of the impact of porous media in biofluid heat transfer in biological tissues during thermal therapy, Nonlinear Anal.: Real World Appl. 11 (3) (2010) 1345–1363.
[25] K. Saito, Y. Hayashi, H. Yoshimura, K. Ito, Heating characteristics of array applicator composed of two coaxial-slot antennas for microwave coagulation therapy, IEEE Trans. Microw. Theory Tech. 48 (2000) 1800–1806 (1 PART 1).
[26] C.W. Song, Role of blood flow in hyperthermia, in: M. Urano, E. Douple (Eds.), Hyperthermia and Oncology Interstitial Hyperthermia: Physics, Biology and Clinical Aspects, Utrecht, VSP, 1992, pp. 275–315.
[27] Y. Zhang, Generalized dual-phase lag bioheat equations based on nonequilibrium heat transfer in living biological tissues, Int. J. Heat Mass Transf. 52 (21–22) (2009) 4829–4834.
[28] T. Wessapan, S. Srisawatdhisukul, P. Rattanadecho, The effects of dielectric shield on specific absorption rate and heat transfer in the human body exposed to leakage microwave energy, Int. Commun. Heat Mass Transfer 38 (2) (2011) 255–262.
[29] J. Crezee, J.J.W. Lagendijk, Temperature uniformity during hyperthermia: the impact of large vessels, Phys. Med. Biol. 37 (6) (1992) 1321–1337.
[30] J.M. Bertram, D. Yang, M.C. Converse, Antenna design for microwave hepatic ablation using an axisymmetric electromagnetic model, Biomed. Eng. Online 5 (2006).
[31] P. Keangin, P. Rattanadecho, T. Wessapan, An analysis of heat transfer in liver tissue during microwave ablation using single and double slot antenna, Int. Commun. Heat Mass Transfer 38 (6) (2011) 757–766.
[32] J.M. Bertram, M.C. Converse, A.P. O'Rourke, J.G. Webster, S.C. Hagness, J.A. Will, D.M. Mahvi, A floating sleeve antenna yields localized hepatic microwave ablation, IEEE Trans. Biomed. Eng. 53 (3) (2006) 533–537.
[33] M.S. Malashetty, M. Swamy, R. Heera, Double diffusive convection in a porous layer using a thermal non-equilibrium model, Int. J. Therm. Sci. 47 (9) (2008) 1131–1147.
[34] A. Vera, L. Leija, Microcoaxial Double slot antenna for interstitial hyperthermia: design, modeling and validation, in: International Conference on Advances in Electronics and Micro-electronics ENICS'08, 2008, pp. 138–143.
[35] Y. Rabin, A. Shitzer, Numerical solution of the multidimensional freezing problem during cryosurgery, J. Biomech. Eng. 120 (1) (1998) 32–37.
[36] J. Lienhard, A Heat Transfer Textbook, Lexington, Phlogiston, MA, 2005.
[37] C. Thiebaut, D. Lemonnier, Three-dimensional modelling and optimisation of thermal fields induced in a human body during hyperthermia, Int. J. Therm. Sci. 41 (6) (2002) 500–508.
[38] F.A. Duck, A.C. Baker, H.C. Starrit, Ultrasound in Medicine, Institute of Physics Publishing, London, 1998. 57-88.

Provided for non-commercial research and education use.
Not for reproduction, distribution or commercial use.

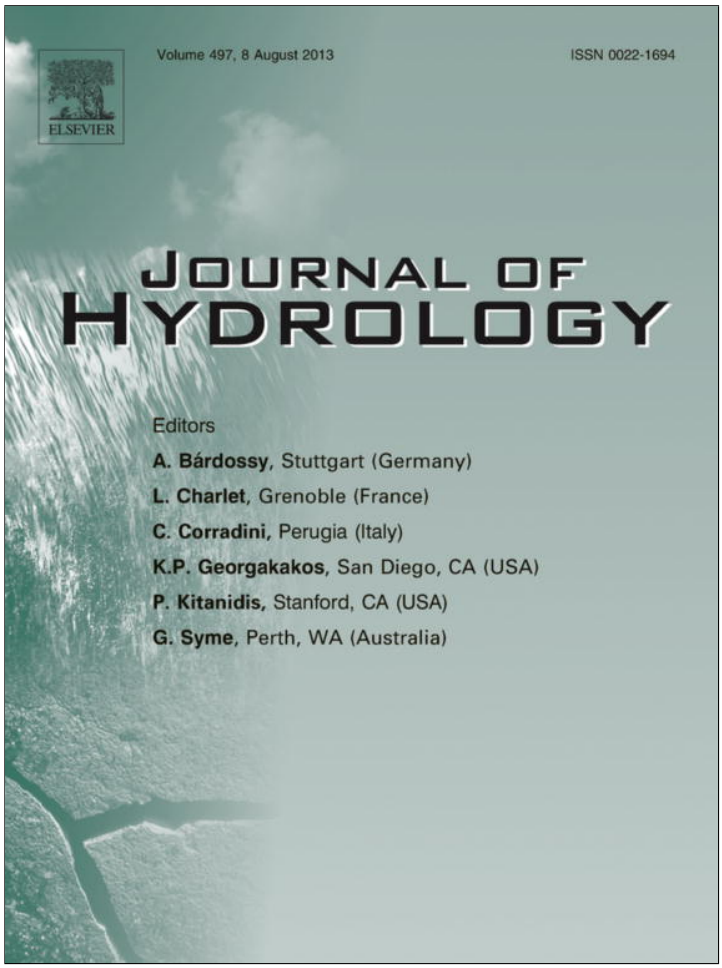

This article appeared in a journal published by Elsevier. The attached copy is furnished to the author for internal non-commercial research and education use, including for instruction at the authors institution and sharing with colleagues.

Other uses, including reproduction and distribution, or selling or licensing copies, or posting to personal, institutional or third party websites are prohibited.

In most cases authors are permitted to post their version of the article (e.g. in Word or Tex form) to their personal website or institutional repository. Authors requiring further information regarding Elsevier's archiving and manuscript policies are encouraged to visit:

http://www.elsevier.com/authorsrights

Author's personal copy

Journal of Hydrology 497 (2013) 145–151

Contents lists available at SciVerse ScienceDirect

Journal of Hydrology

journal homepage: www.elsevier.com/locate/jhydrol

Comparison of Stefan model with Single-phase model of water infiltration process in unsaturated porous media (theory and experiment)

Seksan Suttisong, Phadungsak Rattanadecho *, Prempreeya Montienthong

Center of Excellence in Electromagnetic Energy Utilization in Engineering (CEEE), Department of Mechanical Engineering, Faculty of Engineering, Thammasat University (Rangsit Campus), Pathumthani 12120, Thailand

ARTICLE INFO

Article history:
Received 16 December 2011
Received in revised form 23 May 2013
Accepted 30 May 2013
Available online 11 June 2013
This manuscript was handled by Corrado Corradini, Editor-in-Chief

Keywords:
Water infiltration
Moving boundary
Single-phase flow
Porous media

SUMMARY

Stefan models have been used for many problems such as freezing and melting processes. However, there are few research reports on using Stefan model for the problem of unsaturated flow in a granular packed bed, but the Stefan model has never been used before for considering the effects of particle sizes and supplied water flux to water saturation and moving infiltration fronts. The purpose of this work is to present novel mathematical models and numerical schemes for solving one-dimensional infiltration flow problems. A systematic development and comparison of two proposed models (Single-phase model and Stefan model) is performed. The influences of particle sizes and supplied water flux on water infiltration, i.e., the infiltration layer are studied in detail. It is found that the results of the comparison between these two models are in good agreement. Furthermore, the Stefan model shows better agreement with the experimental results than the Single-phase model. This study shows that the Stefan model can be used effectively for many physical phenomena involving flow infiltration coupled with a moving boundary, compared with other conventional models, i.e., the Single-phase model.

© 2013 Elsevier B.V. All rights reserved.

1. Introduction

Water infiltration is an important process in many fields, such as hydrology, soil science, agriculture, civil engineering, and chemical engineering. The infiltration characteristics of water are of prime interest for a variety of concerns, including water conservation, flooding, runoff, erosion, recovery of isothermal energy, temperature control of soil, and food preservation processes. The infiltration of water is affected by several intrinsic and extrinsic factors. The intrinsic factors that affect water infiltration are the hydraulic conductivity function, water retention characteristics, porosity, capillary pressure gradient, and texture of media.

The models of water infiltration in unsaturated porous media have been studied by many researchers. Abriola and Pinder (1985) proposed an infiltration model of porous media contamination by organic compounds. They considered the effects of the matrix and fluid compressibility, phase composition and the mechanism of driving forces, i.e., capillarity, diffusion and dispersion on flow phenomena in porous media. Stauffer and Dracos (1986) presented an experimental and numerical study of water and solute infiltration in layered porous media, which was restricted to two-dimensional flow in a vertical plane. They highlighted the relation between capillary pressure and the degree of saturation. Haverkamp et al. (1977) compared the numerical simulation models for one-dimensional infiltration. They reported that the implicit or explicit evaluation of the hydraulic conductivity and water capacity functions appear to have the widest range of applicability for predicting water movement in soil with both saturated and unsaturated regions. Other reviews concerning the problem of mass transport in porous media have been performed by Aoki et al. (1991), Ma et al. (2010), Henry and Smith (2006), Binning and Celia (1999), Parlange (1972), Gvirtzman et al. (2008), Ratanadecho et al. (2001, 2002), and Suttisong and Rattanadecho (2011).

Most previously proposed models of water infiltration in porous media have used conventional numerical methods to solve the nonlinear equations. Few studies (Broadrige et al., 2009; Borsi et al., 2004) that have been proposed modeling water infiltration in porous media based on the moving boundary model, or the "Stefan model", owing to the complexity of handling both the flow phenomena and the variation over time of the moving infiltration front. Stefan models have been used for many problems concerning the moving boundary condition, such as the freezing or thawing of soil, ice formation, crystal growth, aerodynamic ablation, casting of metal, food processing and numerous others. Generally, the solution of the moving boundary problem with phase transition has been of special interest because of the inherent difficulties associated both with the nonlinearity of the interface conditions and

* Corresponding author. Tel.: +66 0 2564 3001 9; fax: +66 0 2564 3010.
E-mail address: ratphadu@engr.tu.ac.th (P. Rattanadecho).

0022-1694/$ - see front matter © 2013 Elsevier B.V. All rights reserved.
http://dx.doi.org/10.1016/j.jhydrol.2013.05.048

Author's personal copy

Nomenclature

s	water saturation (–)
s_e	effective water saturation (–)
s_{ir}	irreducible water saturation (–)
ρ_p	density of particle (kg/m^3)
ρ_l	density of water (kg/m^3)
ε	porosity (–)
$F_{l,in}$	supplied water flux (kg/m^2 s)
g	gravity (m^2/s)
K	saturated hydraulic conductivity (m^2)
K_{rl}	relative permeability
v_l	fluid velocity (m/s)
p_c	capillary pressure (Pa)
p_l	fluid pressure (Pa)
p_g	gas pressure (Pa)
μ_l	dynamic viscosity of liquid (Pa s)
υ_l	kinematic viscosity (m^2/s)
σ	surface tension (N/m)
η	coordinate tranformation

Subscripts

s	solid
l	liquid
p	particle

with the unknown locations of the arbitrary moving boundaries. The advantage of the Stefan model is that it is able to handle the moving boundary front in the various kinds of engineering problems, mentioned above. Crank and Gupta (1975) provide a good introduction to the Stefan problems and elaborate a collection of numerical methods. Lyczkowski and Chao (1984) present a comparison of the Stefan model with a two-phase model of a coal drying process in Cartesian and axisymmetric cylindrical coordinates. Javierre et al. (2006) report on the exciting numerical techniques for solving one-dimensional Stefan problems in phase transformation problems. To date, the related problems of Stefan models have been investigated by many researchers: Charn-Jung and Kaviany (1992), Chellaiah and Viskanta (1988), Crowley (1978), Shamsundar and Sparrow (1976), Cheung et al. (1984), Weaver and Viskanta (1986), Afshar and Shobeyri (2010), Saeedpanah et al. (2011), Rattanadecho (2004a,b, 2006), and Rattanadecho and Wongwises (2007). They have introduced various numerical techniques in attempting to overcome the difficulties in handling these moving boundary problems.

Although Stefan models have been used for many problems, relatively few researches report on the problem of unsaturated flow in a granular packed bed based on a Stefan model. In particular, the effects of particle sizes and supplied water flux on water infiltration in porous media and on the infiltration front have never been studied before. The purpose of this work is to: (1) solve numerically the two models (Single-phase model and Stefan model) for describing the one-dimensional infiltration of water in porous media; (2) compare the predicted results obtained for the two models; and (3) compare the predicted results obtained from these two models with the experimental results. The results presented here provide a basis for the fundamental understanding of infiltration flow in porous media.

2. Theory and numerical schemes

The mathematical models derived from mass conservation and Darcy's laws based on Buckley–Leverett function are performed. The main transport mechanisms that enable water infiltration of supplied water into a porous media, i.e., a granular packed bed are water flow driven by the capillary pressure gradient and gravity. Subsequently, a comparison is undertaken of the water infiltration process in unsaturated porous media, between the Single-phase model and the Stefan model.

2.1. Single-phase model

By conservation of mass in the unsaturated porous media, the governing equation of infiltration flow can be derived by using the volume averaged technique (Rattanadecho, 2004a,b).

The main assumptions involved in the formulations of the transport model are:

1. The unsaturated granular packed bed is rigid.
2. No chemical reactions occur in the granular packed bed.
3. Darcy's law holds for the liquid phase.
4. Gravity is included for the flow analysis.
5. Permeability of liquid can be expressed in terms of relative permeability.

Fig. 1 shows a schematic diagram of the Single-phase model or Buckley–Leverett problem. This is an unsaturated flow of water, supplied uniformly at the top surface of a granular packed bed, which is initially composed of glass particles and voids with uniform porosity throughout.

In this study, it is noted that the supplied water flux during unsaturated flow is considered to be lower than the supplied water flux owing to gravity (Aoki et al., 1991), namely:

$$F_l \leqslant g \cdot K \tag{1}$$

where F_l is the supplied water flux, g is the gravity and K is the saturated hydraulic conductivity (permeability). This expression means that the supplied water always infiltrates into the granular packed beds throughout the infiltration process.

2.1.1. Mass conservation

Regarding the infiltration flow in a granular packed bed, the microscopic mass conservation equation for liquid flow in such a packed bed is expressed as:

$$\varepsilon \frac{\partial}{\partial t}[\rho_l s] + \frac{\partial}{\partial z}[\rho_l v_l] = 0 \tag{2}$$

where ε is the porosity, s is the water saturation, ρ_l is the density of water, v_l is the fluid velocity. The generalized Darcy's law, which is the expression for the superficial average velocity of the liquid phase, is defined as (Rattanadecho, 2002):

$$v_l = -\frac{KK_{rl}}{\mu_l}\left[\frac{\partial p_g}{\partial z} - \frac{\partial p_c}{\partial z} - \rho_l g\right] \tag{3}$$

where K_{rl} is the relative permeability, p_g is the gas pressure and μ_l is the liquid viscosity. In Eq. (3), the capillary pressure, p_c is related to the liquid and gas phases which can be written as:

$$p_c = p_g - p_l \tag{4}$$

where p_l is the liquid pressure and p_g is the gas pressure. Using Darcy's generalized equation (Eq. (3)), the mass conservation equation for the Single-phase model (Eq. (2)) can then be rewritten in its final form as:

Author's personal copy

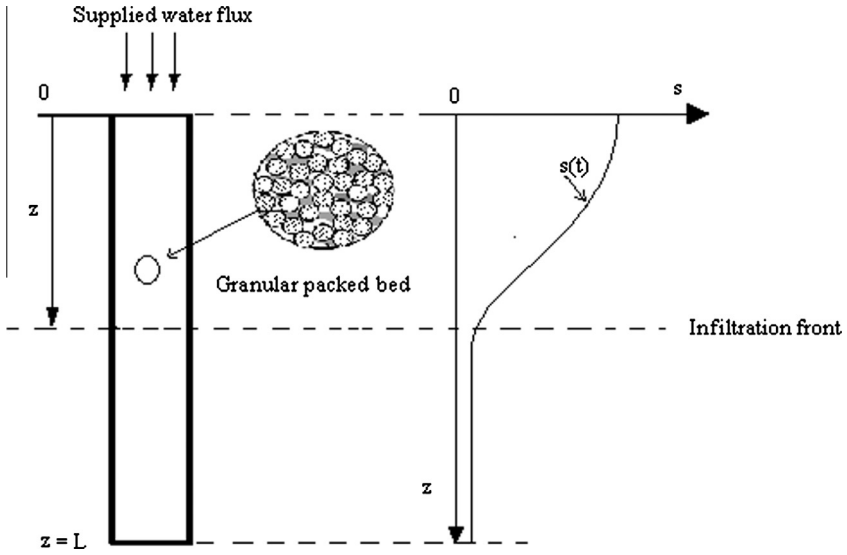

Fig. 1. Schematic representation of the water infiltration in porous media described by the Single-phase model.

$$\varepsilon\frac{\partial}{\partial t}[\rho_l s]-\frac{\partial}{\partial z}\left[\frac{KK_{rl}}{\upsilon_l}\left(\frac{\partial p_g}{\partial z}-\frac{\partial p_c}{\partial z}-\rho_l g\right)\right]=0 \tag{5}$$

where υ_l is the kinematic viscosity. Assuming the effect of gas pressure is negligible, Eq. (5) is reduced to:

$$\varepsilon\frac{\partial}{\partial t}[\rho_l s]+\frac{\partial}{\partial z}\left[\frac{KK_{rl}}{\upsilon_l}\left(\frac{\partial p_c}{\partial z}+\rho_l g\right)\right]=0 \tag{6}$$

2.1.2. Equilibrium relations

The system of conservation equations obtained for the Single-phase transport model requires a constitutive equation for the relative permeability, K_{rl}, capillary pressure, p_c, and capillary pressure functions (Buckley–Leverett functions), J. A typical set of constitutive relation for liquid system is given by:

$$K_{rl}=s_e^3 \tag{7}$$

where s_e is the effective water saturation, considered as the irreducible water saturation, s_{ir}, which can be defined by:

$$s_e=\frac{s-s_{ir}}{1-s_{ir}} \tag{8}$$

The relation between relative permeability in each phase following Eq. (8) is shown in Fig. 2.

Furthermore, the capillary pressure, p_c, is further assumed to be represented adequately by Buckley–Leverett's well known $J(s_e)$ functions. The relation between the capillary pressure and the water saturation is defined by using the Buckley–Leverett functions, $J(s_e)$ Rattanadecho et al., 2002:

$$p_c=p_g-p_l=\frac{\sigma}{\sqrt{K/\varepsilon}}J(s_e) \tag{9}$$

where σ is the surface tension and $J(s_e)$ is correlated to capillary pressure data obtained by Buckley–Leverett and can be expressed as follows (Aoki et al., 1991):

$$J(s_e)=0.325(1/s_e-1)^{0.217} \tag{10}$$

2.1.3. Initial condition and boundary conditions

Assuming that the initial effective water saturation and initial temperature are constant and uniform throughout the granular packed bed:

$$t<0,\quad z\geqslant 0: s_e=s_0,\quad T=T_0 \tag{11}$$

Based on experimental conditions, the initial effective water saturation s_e is given as $s_0=0.001$ and the initial temperature T_0 is given as $T_0=25\ ^\circ C$. The boundary conditions at the top and bottom of granular packed bed are:

$$\begin{aligned} &t>0,\quad z=0: F_{l,in}=const,\\ &z=L: F_{l,out}=\rho_l\upsilon_l \end{aligned} \tag{12}$$

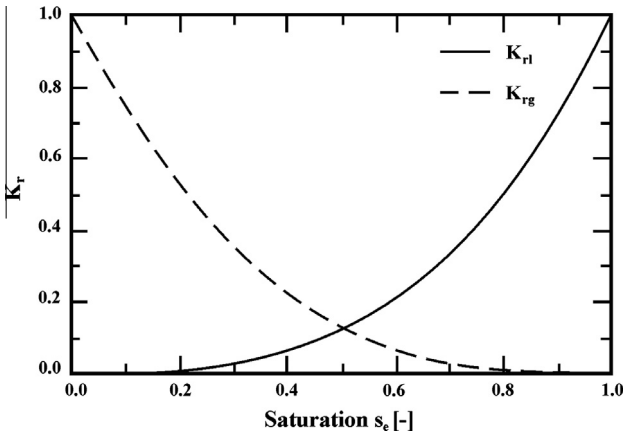

Fig. 2. The relationship between, K_r and s_e.

2.2. Stefan model

Fig. 3 shows a schematic diagram representing the water infiltration in a granular packed bed, as described by the Stefan model. This is one of the more powerful models that can solve the problems involved with the moving boundary, i.e., the infiltration front in this study, because it can simultaneously capture directly the infiltration front together with the infiltration layer during the water infiltration process in porous media.

The study of the water infiltration process in a granular packed bed based on the Stefan model is difficult because the interface between the wet and dry zones, or the infiltration front, is moving from the top of the granular packed bed to the bottom. For solving this moving boundary problem, the original governing equations are transformed into the coordinate transformation equations, which are based on a boundary fixing method. Refer to the original equations (Eqs. (6), (11), and (12)), as shown again below:

Author's personal copy

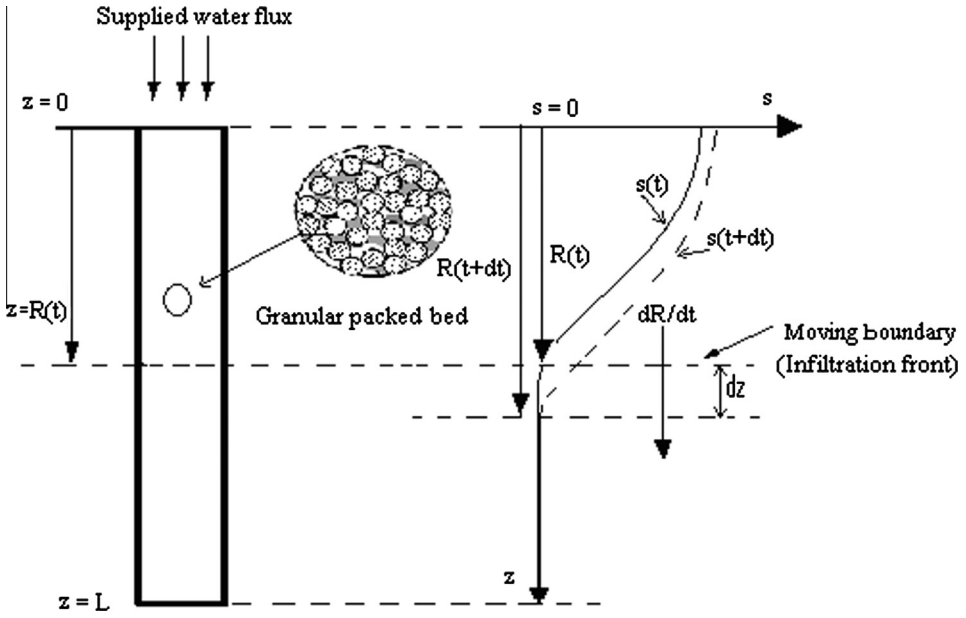

Fig. 3. Schematic representation of the water infiltration in porous media described by the Stefan model.

$$\varepsilon\frac{\partial}{\partial t}[\rho_l s]+\frac{\partial}{\partial z}\left[\frac{KK_{rl}}{\upsilon_l}\left(\frac{\partial p_c}{\partial z}+\rho_l g\right)\right]=0 \tag{6}$$

$$t<0,\quad z\geqslant 0: s_e=s_0,\quad T=T_0 \tag{11}$$

$$\begin{aligned} &t>0,\quad z=0: F_{l,in}=const,\\ &z=L: F_{l,out}=\rho_l \upsilon_l \end{aligned} \tag{12}$$

Considering the moving boundary front or water infiltration front, when the mass balance in performed at this interface, the equation representing the infiltration front (Stefan equation) is described by:

$$\varepsilon s\frac{\partial R}{\partial t}=\frac{KK_{rl}}{\mu_l}\left(\frac{\partial P_c}{\partial z}+\rho_l g\right) \tag{13}$$

With the concept of coordinate transformation technique, the following normalized form is applied (Rattanadecho 2004a):

$$\eta=z/R(t),\quad 0\leqslant z\leqslant R(t) \tag{14}$$

as shown in Fig. 3, where $R(t)$ is the distance between the top surface ($z=0$), and the moving boundary front ($z=R(t)$). For a time step, the infiltration front moves in the z direction. At the moving boundary front ($z=R(t)$), the initial effective water saturation s_e is given as $s_0=0.001$. By using the coordinate transformation technique, the physical space (z, t) is then transformed to the mapping space [$\eta(z, t)$, t]. The differential operators with the coordinate transformation are mathematically related to the following equations (Rattanadecho 2004a):

$$\frac{\partial}{\partial z}=\frac{\partial}{\partial \eta}\frac{\partial \eta}{\partial z}=\frac{1}{R}\frac{\partial}{\partial \eta} \tag{15}$$

$$\frac{\partial}{\partial t}=\frac{\partial}{\partial \eta}\frac{\partial \eta}{\partial t}+\frac{\partial}{\partial t}=\frac{\partial}{\partial t}-\frac{\eta\dot{R}}{R}\frac{\partial}{\partial \eta} \tag{16}$$

where $\dot{R}$ is the time derivative of the water infiltration front. Finally, Eq. (6) in coordinate transformation form is rewritten as (Rattanadecho 2004a):

$$\varepsilon\left(\frac{\partial}{\partial t}-\frac{\eta\dot{R}}{R}\frac{\partial}{\partial \eta}\right)[\rho_l s]+\frac{1}{R}\frac{\partial}{\partial \eta}\left[\frac{KK_{rl}}{\upsilon_l}\left(\frac{1}{R}\frac{\partial p_c}{\partial \eta}+\rho_l g\right)\right]=0 \tag{17}$$

Eq. (13) in coordinate transformation form is also rewritten as:

$$\varepsilon s\left(\frac{\partial R}{\partial t}-\frac{\eta\dot{R}}{R}\frac{\partial R}{\partial \eta}\right)=\frac{KK_{rl}}{\mu_l}\left(\frac{1}{R}\frac{\partial P_c}{\partial \eta}+\rho_l g\right) \tag{18}$$

2.3. Numerical schemes

Corresponding to the method of finite differences, based on the notion of control volume, the generalized systems of nonlinear equations with a coordinate transformation form are integrated over a typical computational domain. These equations within this system can be cast into a numerical discretization of the generalized conservation equation. To solve the nonlinear equations, the Newton–Raphson iteration procedure is used for each element. After integration over each control volume within the computational mesh, a system of nonlinear equation results whereby each equation can be cast into a numerical discretization of the generalized conservation equation.

The Single-phase model (Eq. (6)) for the internal nodes can be cast into a numerical discretization as:

$$\begin{aligned} &\frac{\varepsilon}{\Delta t}(1-s_{ir})\left(\rho_l\left(s_{ei}^{n+1}-s_{ei}^{n}\right)\right)+\frac{1}{\Delta z}\left(\rho_l\left(\frac{KK_{rl}}{\mu_l}\Big|_{i+\frac{1}{2}}\left(\frac{P_{ci+1}^{n+1}-P_{ci}^{n+1}}{\Delta z}+\rho_l g\right)\right.\right.\\ &\left.\left.-\frac{KK_{rl}}{\mu_l}\Big|_{i-\frac{1}{2}}\left(\frac{P_{ci}^{n+1}-P_{ci-1}^{n+1}}{\Delta z}+\rho_l g\right)\right)\right)=0 \end{aligned} \tag{19}$$

The Stefan model (Eq. (17)) can be cast into a numerical discretization as:

$$\begin{aligned} &\frac{\varepsilon}{\Delta t}(1-s_{ir})\left(\rho_l\left(s_{ei}^{n+1}-s_{ei}^{n}\right)\right)-\frac{n\dot{R}}{R}(1-s_{ir})\left(\rho_l\left(s_{ei}^{n+1}-s_{ei}^{n}\right)\right)\\ &+\frac{1}{R\Delta\eta}\left(\rho_l\left(\frac{KK_{rl}}{\mu_l}\Big|_{i+\frac{1}{2}}\left(\frac{P_{ci+1}^{n+1}-P_{ci}^{n+1}}{R\Delta\eta}+\rho_l g_z\right)\right.\right.\\ &\left.\left.-\frac{KK_{rl}}{\mu_l}\Big|_{i-\frac{1}{2}}\left(\frac{P_{ci}^{n+1}-P_{ci-1}^{n+1}}{R\Delta\eta}+\rho_l g_z\right)\right)\right)=0 \end{aligned} \tag{20}$$

where n is the current iteration index and $n+1$ is the new iteration index. The discretized form of the moving boundary interface in Eq. (18) can be written as:

Author's personal copy

$$\varepsilon s\frac{3R^{n+1}-4R^{n}+R^{n-1}}{2\Delta t}=\frac{KK_{rl,i+1}+KK_{rl,i}}{2\mu_l}\left(\frac{P_{c,i+1}-P_{c,i}}{R\Delta\eta}+\rho_l g\right) \quad (21)$$

Finally, to obtain values for all stage variables at the matching time, the system of nonlinear equations (Eqs. (19–21)) must be resolved by the Newton–Raphson method.

3. Experimental apparatus

Fig. 4 shows the experimental apparatus for the one-dimensional water infiltration in a granular packed bed (Aoki et al., 1991). The test column is designed to achieve the one-dimensional flow of infiltrating water. It has an inner diameter of 60 mm, is 400 mm long and is made of rigid acrylic plastic tubing. The dry porous-ceramic disk at the bottom of the granular packed bed support the granular particles in the column while allowing air to escape in advance of the infiltration front. A thick plug of insulation is also placed again the ceramic disk at the bottom of the column. Spherical soda lime glass beads with average sizes (d) of 0.15 and 0.4 mm, are used as a sample of the granular packed bed. The water is supplied (supplied water flux, f) from a water tank to the top surface of the granular packed bed through a distributor with controlled rates of 0.05 and 0.1 kg/m^2 s. The test column is covered with insulation.

The position of the infiltration depth in the packed bed is captured by digital camera relative to a time-based reference, as shown in Fig. 4. At the end of the test run, the granular packed bed is cut into five sections, each with volume of 183 cm^3, in order to measure the water saturation. The water saturation in the non-hygroscopic porous packed bed was defined as the fraction of the volume occupied by water to the volume of the pores. This water saturation was obtained by weighing the dry and wet mass of the sample. Before the experiment, each section was weighed individually to record its dry mass. The porous packed bed was weighed again at 5 min after the test run. The water saturation formula can be described in the following form (Rattanadecho, 2004a and Aoki et al., 1991):

$$s=\frac{\rho_p\cdot(1-\varepsilon)\cdot(m_w-m_d)}{\rho_l\cdot\varepsilon\cdot m_d} \quad (22)$$

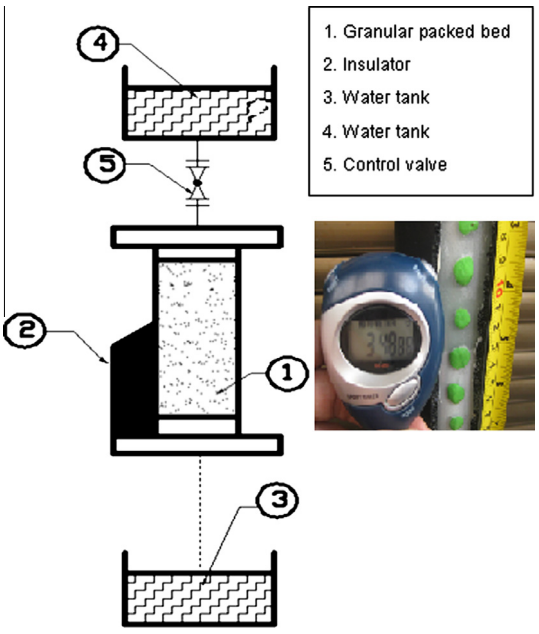

Fig. 4. Experimental apparatus for measuring unsaturated flow in one dimension porous layered.

where s is water saturation, ρ_p is the density of the particles, ρ_l is the density of water, ε is porosity, and m_w and m_d are the wet and dry mass of the sample, respectively.

4. Results and discussion

In this study, the numerical results of a Single-phase model and a Stefan model are described for the one-dimensional infiltration of water in porous media. The numerical results between the Stefan model and Single-phase model are carried out in this study. Subsequently, these numerical results are compared with the experimental results. The effects of particle size (d) and supplied water flux (f) on water infiltration, i.e., the infiltration layer and the infiltration front are studied in detail.

Fig. 5 shows the comparison of the progress of the infiltration layer through the granular packed bed (d = 0.15 mm) between the two models at various elapsed times, as a parameter of supplied water flux (f = 0.05 kg/m^2 s and 0.1 kg/m^2 s). It is evident that the infiltration layer or water distribution can be regarded as a parameter of the supplied water flux. Greater supplied water flux results in a faster infiltration rate and forms a wider infiltration layer with time. The main transport mechanisms that enable fluid movement in porous media are liquid flow driven by capillary pressure gradient and gravity, as mentioned in Eq. (3). The predicted infiltration layers in both models are in good agreement, especially in the case of the lower supplied water flux. This is because the movement of the infiltration front is not as fast for the case of lower supplied water flux where no difference of computing performance of these two models has been found. Nevertheless, for the case of the higher supplied water flux, the differences of predicted results obtained from both models are clearly shown. In contrast with the case of the lower supplied water flux, the movement of the infiltration front for the case of the higher supplied water flux is faster owing to the hydrodynamic characteristics. In this case, the difference between the computing performances of these two models is clearly evidenced. The com-

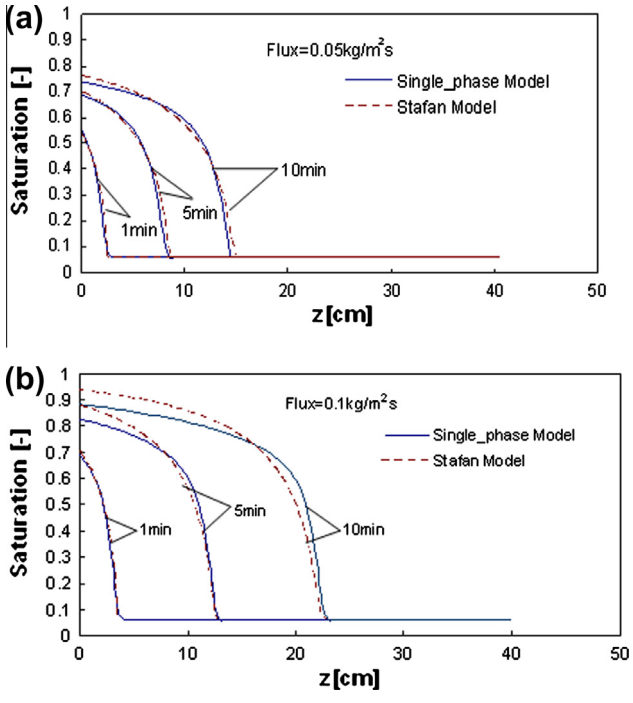

Fig. 5. Comparison of infiltration layer along granular packed bed (d = 0.15 mm) between two models at various elapsed times as a parameter of supplied water flux: (a) f = 0.05 kg/m^2 s and (b) 0.1 kg/m^2 s.

Author's personal copy

puting performance from the both models will be discussed again in the following paragraphs.

Figs. 6 and 7 show the influences of the supplied water flux and particle sizes on the infiltration layer for the two models. The larger particle size and greater supplied water flux results in a faster infiltration rate and forms a wider infiltration layer in the granular packed bed. The effect of the fast response depends on hydrodynamic characteristics, i.e., capillary pressure gradient, permeability and gravity.

Fig. 8 shows the comparison of the infiltration front ($d = 0.15$ mm and $d = 0.4$ mm) between the two models as a parameter of the supplied water flux ($f = 0.05$ kg/m^2 s and 0.1 kg/m^2 s). Numerically, it is observed that for all testing cases, the predicted results obtained from both models are in good agreement, especially in the case of the lower supplied water flux, mentioned with regard to Fig. 5. This means that the proposed calculation technique based on the Stefan model is appropriate for modeling flow infiltration, especially in the case of sensitively moving boundary front.

Fig. 9 shows the comparison of the infiltration layer through the granular packed bed with different particle sizes between the numerical results and the experimental result ($t = 5$ min and $f = 0.1$ kg/m^2 s). It is evident that the predicted results from both models are in agreement with the experimental results. Furthermore, the numerical results based on the Stefan model seem to be nearer the experimental results than do those of the Single-phase model in the case of sensitively moving boundary fronts. This is because the Stefan model can solve accurately the problems involved with the moving boundary, because it can simultaneously capture directly the moving front together with the infiltration layer during the water infiltration process in a granular packed bed. However, the conventional method, i.e., the Single-phase model, aims to predict the saturation profile or infiltration layer, but it cannot capture directly the moving front and infiltration layer at the same time.

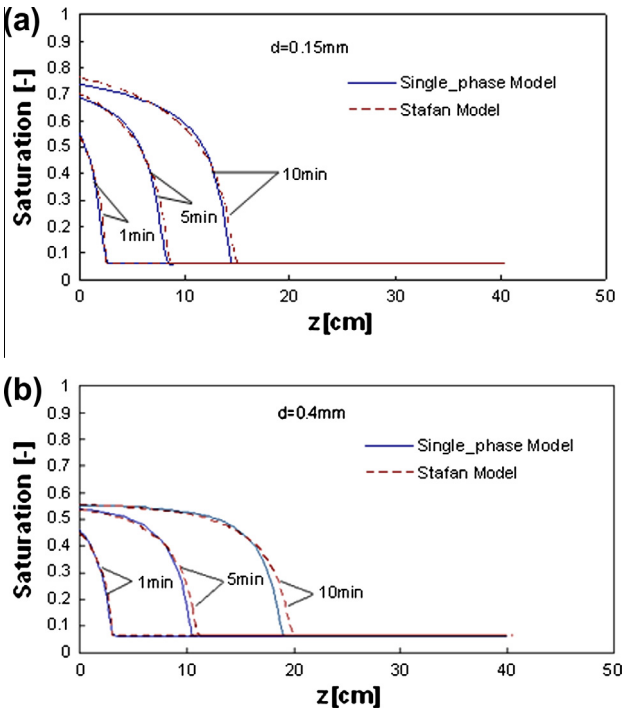

Fig. 6. Comparison of infiltration layer along granular packed bed ($f = 0.05$ kg/m^2 s) between two models at various elapsed times as a parameter of particle sizes: (a) $d = 0.15$ mm and (b) 0.4 mm.

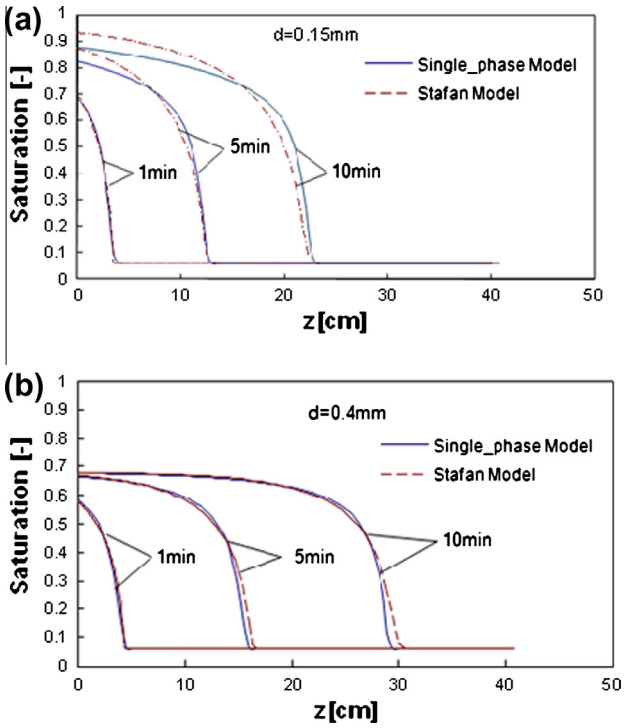

Fig. 7. Comparison of infiltration layer along granular packed bed ($f = 0.1$ kg/m^2 s) between two models at various elapsed times as a parameter of particle sizes: (a) $d = 0.15$ mm and (b) 0.4 mm.

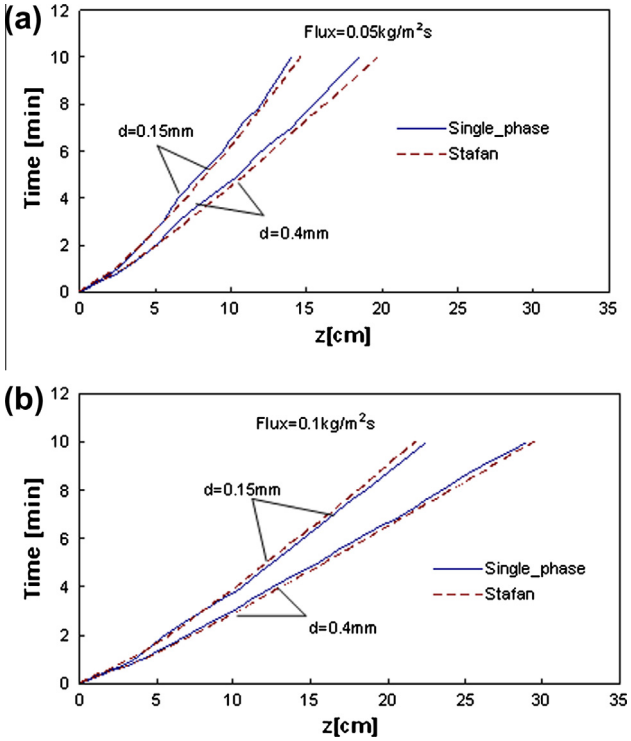

Fig. 8. Comparison of infiltration front ($d = 0.15$ mm and $d = 0.4$ mm) between two models as a parameter of supplied water flux: (a) $f = 0.05$ kg/m^2 s and (b) 0.1 kg/m^2 s.

Again, these results confirm that the troublesome numerical errors in the conventional method (Eqs. (2–12) and (19): Single-phase model) are reduced effectively if the solution procedure is linked with the discontinuities condition and if a special formula

Author's personal copy

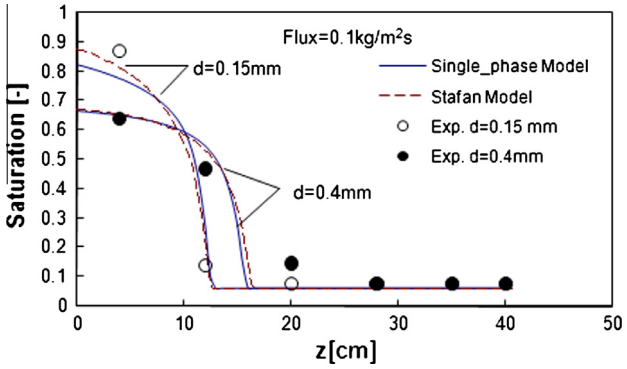

Fig. 9. Comparison of infiltration layer along granular packed bed with different particle size between numerical results and experimental result (t = 5 min, f = 0.1 kg/m^2 s).

is used to incorporate the jump conditions directly into the numerical model (Eqs. (14–18), (20) and (21): Stefan model). This is the main idea behind this work in considering the moving boundary as a prior parameter, because the water infiltration process is the moving boundary problem that involve infiltration front. Even though, the Stefan model seems more accurate than that Single-phase model, the relative computation times are slightly higher than for performing the calculation using the Single-phase model because of the greater memory usage. This issue needs to be improved in further research.

5. Conclusions

Water infiltration in a granular packed bed with unsaturated flow is investigated numerically using the Single-phase and the Stefan models. The results show that for all test cases the predicted results obtained from both models are in good agreement. Furthermore, the predicted results obtained from these two models are also in good agreement with the experimental results. The proposed calculation technique, based on the Stefan model is appropriate for modeling the flow infiltration process, especially in the cases of a sensitively moving boundary front. Furthermore, the larger particle size and a greater supplied water flux in the granular packed bed correspond to a faster infiltration flow, compared with smaller particle size and a lower supplied water flux. Gravity and capillary pressure are shown clearly to have an influence on the infiltration flow.

Acknowledgement

This work was supported by Thailand Research Fund (TRF).

References

Abriola, M., Pinder, F., 1985. A multiphase approach to the modeling of porous media contamination by organic compounds 1. Equation development. Water Resources Research 21, 11–18.
Afshar, M.H., Shobeyri, G.R., 2010. Efficient simulation of free surface flows with discrete least-squares meshless method using a priori error estimator. International Journal of Computation Fluid Dynamics 24 (9), 349–367.
Aoki, K., Hattori, M., Kitamura, M., Shiraishi, N., (1991). Characteristics of heat transport in porous media with water infiltration. ASME/JSME Thermal Engineering Proceeding 4, 303–308.
Binning, Philip, Celia, Michael A., 1999. Practical implementation of the fractional flow approach to multi-phase flow simulation. International Journal of Advances in Water Resources 22, 461–478.
Borsi, I., Farina, A., Fasano, A., 2004. On the infiltration of rain water through the soil with runoff of the excess water. Nonlinear Analysis: Real World Applications 5, 763–800.
Broadrige, P., Triadis, D., Hill, J.M., 2009. Infiltration from supply at constant water content: an integrable model. Journal of Engineering Mathematics 64, 193–206.
Charn-Jung, K., Kaviany, M., 1992. Numerical method for phase-change problems with convection and diffusion. International Journal of Heat and Mass Transfer 35, 457–467.
Chellaiah, S., Viskanta, R., 1988. Freezing of saturated and superheated liquid in porous media. International Journal of Heat and Mass Transfer 31, 321–330.
Cheung, F.B., Chawla, T.C., Pedersen, D.R., 1984. The effect of heat generation and wall interaction on freezing and melting in finite slab. International Journal of Heat and Mass Transfer 27, 29–37.
Crank, J., Gupta, R.S., 1975. Isotherm migration method in two dimensions. International Journal of Heat and Mass Transfer 18, 1101.
Crowley, A.B., 1978. Numerical solution of Stefan problems. International Journal of Heat and Mass Transfer 21, 215.
Gvirtzman, Haim., Shalev, Eyal., Dahan, Ofer., Hatzor, Yossef.H., 2008. Large-scale infiltration experiments into unsaturated stratified loess sediment: monitoring and modeling. International Journal of Hydrology 349, 214–229.
Haverkamp, R., Vauclin, M., Touma, J., Wierenga, P.J., Vanchaud, G., 1977. A comparison of numerical simulation models for one-dimension infiltration. Soil Sci. Soc. Am. J. 41, 285–294.
Henry, E.J., Smith, J.E., 2006. Numerical demonstration of surfactant concentration-dependent capillarity and viscosity effects on infiltration from a constant flux line source. International Journal of Hydrology 329, 63–74.
Javierre, E., Vuik, C., Vermolen, F., 2006. A comparison of numerical models for one-dimensional Stefan problems. Journal of Computational and Applied Mathematics 2006 (192), 445–459.
Lyczkowski, R.W., Chao, Y.T., 1984. Comparison of Stefan model with two-phase model of coal drying. International Journal of Heat and Mass Transfer 27, 1157–1169.
Ma, Ying., Feng, Shaoyuan., Dongyuan, Su., Gao, Guangyao, Huo, Zailin, 2010. Modeling water infiltration in a large layered soil column with a modified Green-Ampt model and HYDRUS-1D. Int. J. Computer and Electronics in Agriculture 71S, S40–S47.
Parlange, J.Y., 1972. Theory of water movement in soils: one-dimensional infiltration. Soil Science 111, 170–174.
Ratanadecho, P., Aoki, K., Akahori, M., 2001. Experimental and numerical study of microwave drying in unsaturated porous material. International Communications in Heat and Mass Transfer 28, 605–616.
Ratanadecho, P., Aoki, K., Akahori, M., 2002. Influence of irradiation time, particle sizes and initial moisture content during microwave drying of multi-layered capillary porous materials. ASME Journal of Heat Transfer 124, 151–161.
Rattanadecho, P., 2004a. Experimental and numerical study of solidification process in unsaturated granular packed bed. Journal of Thermophysics and Heat Transfer 18, 87–93.
Rattanadecho, P., 2004b. Theoretical and experimental investigation of microwave thawing of frozen layer using a microwave oven (effects of layered configurations and layer thickness). International Journal of Heat and Mass Transfer 47, 937–945.
Rattanadecho, P., 2006. Simulation of melting of ice in a porous media under multiple constant temperature heat sources using a combined transfinite interpolation and PDE methods. Chemical Engineering Science 61, 4571–4581.
Rattanadecho, P., Wongwises, S., 2007. Moving boundary-moving mesh analysis of freezing process in water-saturated porous media using a combined transfinite interpolation and PDE mapping methods. ASME Journal of Heat Transfer 31, 318–333.
Saeedpanah, I., Jabbari, E., Shayanfar, M.A., 2011. Numerical simulation of ground water flow via a new approach to local radial point interpolation meshless method. International Journal of Computation Fluid Dynamics 24 (1), 17–30.
Shamsundar, N., Sparrow, E.M., 1976. Effect of density change on multi-dimensional conduction phase change. ASME Journal of Heat Transfer 105, 550.
Stauffer, F., Dracos, T., 1986. Experimental and numerical study of water and solute infiltration in layered porous media. Journal of Hydrology 84, 9–34.
Suttisong, S., Ratanadecho, P., 2011. The experimental investigation of heat transport and water infiltration in granular packed bed due to supplied hot water from tom top: influence of supplied water flux, particle sizes and supplied water temperature. Experimental and Thermal Fluid Science. http://dx.doi.org/10.1016/j.expthermflusci.2011.07.003.
Weaver, J.A., Viskanta, R., 1986. Freezing of liquid-saturated porous media. ASME Journal of Heat Transfer 108, 654–659.

Provided for non-commercial research and education use.
Not for reproduction, distribution or commercial use.

This article appeared in a journal published by Elsevier. The attached copy is furnished to the author for internal non-commercial research and education use, including for instruction at the authors institution and sharing with colleagues.

Other uses, including reproduction and distribution, or selling or licensing copies, or posting to personal, institutional or third party websites are prohibited.

In most cases authors are permitted to post their version of the article (e.g. in Word or Tex form) to their personal website or institutional repository. Authors requiring further information regarding Elsevier's archiving and manuscript policies are encouraged to visit:

http://www.elsevier.com/authorsrights

Author's personal copy

International Journal of Heat and Mass Transfer 64 (2013) 426–435

Contents lists available at SciVerse ScienceDirect

International Journal of Heat and Mass Transfer

journal homepage: www.elsevier.com/locate/ijhmt

Specific absorption rate and temperature increase in the human eye due to electromagnetic fields exposure at different frequencies

Teerapot Wessapan [a], Phadungsak Rattanadecho [b,*]

[a] School of Aviation, Eastern Asia University, Pathumthani 12110, Thailand
[b] Center of Excellence in Electromagnetic Energy Utilization in Engineering (CEEE), Department of Mechanical Engineering, Faculty of Engineering, Thammasat University (Rangsit Campus), Pathumthani 12120, Thailand

ARTICLE INFO

Article history:
Received 25 December 2012
Received in revised form 24 April 2013
Accepted 25 April 2013

Keywords:
Electromagnetic fields
Temperature distribution
Specific absorption rate
Human eye
Heat transfer

ABSTRACT

This study presents a numerical analysis of the specific absorption rate (SAR) and the heat transfer in a heterogeneous human eye model exposed to electromagnetic (EM) fields of 900 and 1800 MHz. In this study, the effect of operating frequency on the SAR and temperature distributions in the eye was systematically investigated. The SAR value and the temperature distribution in various tissues in the eye during exposure to EM fields were obtained by numerical simulation of EM wave propagation and a heat transfer model was then developed based on the natural convection and porous media theories. The study highlights two transport phenomena: heat and mass transfer in the eye during exposure to EM fields at different frequencies. This study indicated that when the eye exposed to EM fields at the frequencies of 900 and 1800 MHz, the highest SAR values at two chosen frequencies was in the cornea, and the highest temperature at the frequency of 900 MHz was in the anterior chamber while the highest for the frequency of 1800 MHz was in the vitreous. The temperature distribution in the eye induced by EM fields was not directly related to the SAR distribution due to the effect of the interaction among the dielectric properties, thermal properties, blood perfusion, and penetration depth of the EM power. Moreover, this study also showed that the exposure time had an influence on the temperature increase in the eye.

© 2013 Elsevier Ltd. All rights reserved.

1. Introduction

The electromagnetic (EM) waves of different power levels and frequencies penetrate deep into the human body causing health risks. In recent years, there has been increasing public concern with the interaction between the human body and the EM fields. Since the human eye is one of the most sensitive organs to the EM radiation. The high intensity EM fields can lead to a number of ocular effects. However, the resulting thermo-physiologic response of the eye to EM fields is still not well understood. In order to gain insight into the phenomena of heat and mass transfer in the eye concerned with the temperature distribution induced by EM fields, a detailed knowledge of the absorbed power distribution as well as the temperature distribution are necessary. Therefore, this study investigates the ocular effects occurred during exposure to EM fields. Although the safety standards in term of the maximum SAR values are regulated, but they are not stated in term of the maximum temperature increase in the eye caused by EM energy absorption which is an actual influence of the dominant factors inducing the adverse physiological effects. The severity of these effects produced by increasing a small temperature can cause eyesight to worsen. There have been medical case reports of the formation of cataracts in humans following accidental exposure to microwave radiation [1]. Actually, a small temperature increase of 3–5 °C in the eye leads to induce cataracts formation [2]. Additionally, it is reported that the temperature above 41 °C is necessary for production of posterior lens opacities [3]. Numerical analysis of the heat and mass transfer in the eye exposed to EM fields has provided useful information on absorption of EM energy for the eye under a variety of exposure conditions.

In the past, there have been reports on the effects of EM fields on the eye [4,5]. Nevertheless, the analysis generally was conducted based on the maximum SAR values permitted by public safety standards [6,7]. The experimental data on the correlation between the SAR levels and the temperature increase in the human tissue was still sparse. Most previous studies of human exposed to EM fields hardly considered the heat transfer causing an incomplete analysis to the results. Therefore, modeling of heat transport in human tissue is needed to cooperate with the modeling of EM in order to completely explain their interaction characteristics for approaching such phenomena.

The topic of temperature increase in human tissue when exposed to EM fields, particularly those radiated to the eye, has been of inter-

* Corresponding author. Tel.: +66 2564 3001 9; fax: +66 2564 3010.
E-mail addresses: teerapot@yahoo.com (T. Wessapan), ratphadu@engr.tu.ac.th (P. Rattanadecho).

0017-9310/$ - see front matter © 2013 Elsevier Ltd. All rights reserved.
http://dx.doi.org/10.1016/j.ijheatmasstransfer.2013.04.060

Author's personal copy

Nomenclatures

C	specific heat capacity (J/(kg K))
E	electric field intensity (V/m)
e	tear evaporation heat loss (W/m^2)
f	frequency of incident wave (Hz)
H	magnetic field (A/m)
h	convection coefficient (W/m^2 K)
j	current density (A/m^2)
k	thermal conductivity (W/(m K))
n	normal vector
p	pressure (N/m^2)
Q	heat source (W/m^3)
T	temperature (K)
u	velocity (m/s)
t	time

Greek letters

B	volume expansion coefficient (1/K)
μ	magnetic permeability (H/m)
ε	permittivity (F/m)
σ	electric conductivity (S/m)
ω	angular frequency (rad/s)
ρ	density (kg/m^3)
ω_b	blood perfusion rate (1/s)
Γ	external surface area

Subscripts

am	ambient
b	blood
ext	external
i	subdomain
met	metabolic
r	relative
ref	reference
0	free space, initial condition

est for many years. Recently, the modeling of heat transport in human tissue has been investigated by many researchers [8–21]. The thermal modeling of human tissue is important as a tool to investigate the effect of external heat sources and to predict the abnormalities in the tissue. In the past, most studies of heat transfer analysis in the eye used heat conduction equation [8–14]. Some studies carried out on the natural convection in the eye based on heat conduction model [15,16]. Ooi and Ng [16,17] studied the effect of aqueous humor (AH) hydrodynamics on the heat transfer in the eye based on heat conduction model. Meanwhile, the bioheat equation, introduced by Pennes [18,19] based on the heat diffusion equation for a blood perfused tissue, is used for modeling of the heat transfer in the eye as well [20,21]. Ooi and Ng also developed a three-dimensional model of the eye [22], extending their two-dimensional model [21]. Recently, porous media models have been utilized to investigate the transport phenomena in biological media instead of a simplified bioheat model [23–25]. Shafahi and Vafai [26] proposed the porous media along with a natural convection model to analyze the eye thermal characteristics during exposure to thermal disturbances. The other research groups have been tried to conduct the advanced model using a coupled model of heat and EM dissipation in the eye [10–14]. Ooi et al. have been tried to conduct the advanced model using the coupled model of heat and laser irradiation in the eye [27]. Results from a similar model of Ooi et al. [27] for various applications were also presented in continuation [28–31].

Our research group has tried to numerically investigate the temperature increase in the human tissue subjected to EM fields in many problems [32–38]. Wessapan et al. [32,33] utilized a 2D finite element method to obtain the SAR and temperature increase in the human body exposed to leakage EM waves. Wessapan et al. [34,35] developed a three-dimensional human head model in order to investigate the SAR and temperature distributions in human head during exposure to the mobile phone radiation. Keangin et al. [36,37] carried out on the numerical simulation of the liver cancer treated using the complete mathematical model considered the coupled model of EM wave propagation, heat transfer and mechanical deformation in the biological tissue in the couple's way. Wessapan et al. [38] investigated the SAR and temperature distributions in the eye during exposed to EM waves at 900 MHz using the porous media theory.

Most previous studies of the interaction between the EM fields and the eye mainly focused on SAR. They have not been considered heat transfer causing an incomplete analysis of results. Therefore, the modeling of the heat transport is needed to completely explain the actual process of interaction between the EM fields and the eye. Although the porous media and natural convection models of the eye have been used in the previous biomedical studies [15,16,26], most studies of the human eye exposed to the EM fields, especially at different frequencies, have not been considering the porous media and natural convection approaches is sparse or non-existent.

There are few studies on the temperature and EM field interaction in a realistic physical model of the human organs especially the eye due to the complexity of the problem, even though it is directly related to the thermal injury of tissues. Therefore, in order to provide information on the levels of exposure and health effects from the different frequencies of EM field exposure adequately, it is essential to simulate both of the EM fields and the heat transfer based on the porous media theory in an anatomical model particularly the eye.

This study presents the simulation of the SAR and temperature distributions in an anatomical human eye exposed to EM fields based on the porous media theory. The work described in this paper is substantially extended from our previous work [38] by further enhancing the focus on the effect of operating frequency. In this study, a two-dimensional human eye model was used to simulate the SAR and temperature distributions in the eye model. The EM wave propagation in the eye was investigated by using Maxwell's equations. An analysis of the heat transfer in the eye exposed to TM-mode of EM fields at different frequencies was investigated using a developed heat transfer model (included the conduction and natural convection heat transfer modes) which was firstly proposed by Shafahi and Vafai [26]. In the heterogeneous eye model, the effect of operating frequency on the SAR and temperature distributions in the eye is systematically investigated. The SAR and temperature distributions are studied in various parts of the eye during exposure to EM fields of 900 and 1800 MHz. They are obtained by numerical simulation of the EM wave propagation and heat transfer equations, are presented. In this study, the frequencies of 900 and 1800 MHz were chosen for our simulations and the frequencies used globally in a wide range of applications including Global System for Mobile Communications (GSM) services. In this work, the model excluded the presence of eyelid as well as the metabolic heat generation in order to ease the modeling procedures. The obtained

Author's personal copy

values represent the accurate phenomena to determine the temperature increase in the eye and indicate the limitations that must be considered as the temperature increase due to EM energy absorption from EM field exposure at different frequencies.

2. Formulation of the problem

Fig. 1 shows the radiation of the EM fields from an EM radiation device to the eye. These EM fields fall on the eye that causes heating in the deeper tissue, which leads to tissue damage and cataract formation. Due to ethical consideration, exposing the human to EM fields for experimental purposes is limited. It is more convenient to develop a realistic human eye model through the numerical simulation. A highlight of this work is the illustration of the transport phenomena, including the heat and mass transfer in the eye during exposure to EM fields at different frequencies. The analyses of the SAR and the heat transfer in the eye exposed to EM fields will be illustrated in Section 3. The system of governing equations as well as the initial and boundary conditions are solved numerically using the finite element method (FEM) via COMSOL™ Multiphysics.

3. Methods and model

The first step in evaluating the effects of a certain exposure to EM fields in the eye is to determine the induced internal EM fields and its spatial distribution. Thereafter, EM energy absorption which results in temperature increase in the eye and other interactions will be able to be considered.

3.1. Physical model

In this study, the two-dimensional model of the eye, which follows the physical model in the previous research [26], is developed. Fig. 2 shows the two-dimensional eye model used in this study. This model comprises seven types of tissue including cornea, anterior chamber, posterior chamber, iris, sclera, lens and vitreous. These tissues have the different dielectric and thermal properties. In the sclera layer, there are two more layers known as the choroid and retina which are relatively thin compared to the sclera. To simplify the problem, these layers are assumed to be homogeneous. The iris and sclera, which have the same properties, are modeled together as one homogenous region [16]. The dielectric and thermal properties of tissue are given in Tables 1 and 2, respectively. Each tissue is assumed to be homogeneous and electrically as well as thermally isotropic.

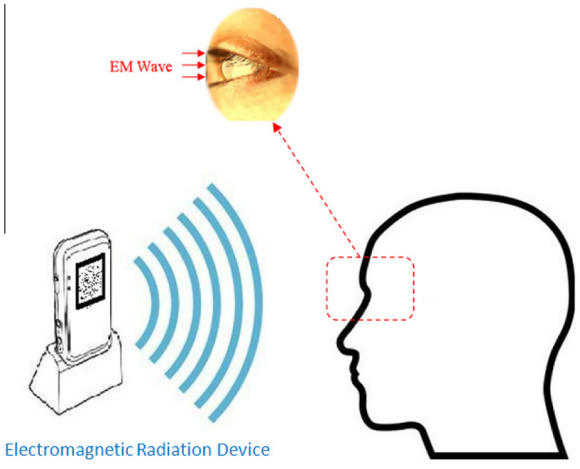

Fig. 1. EM fields from an EM radiation device.

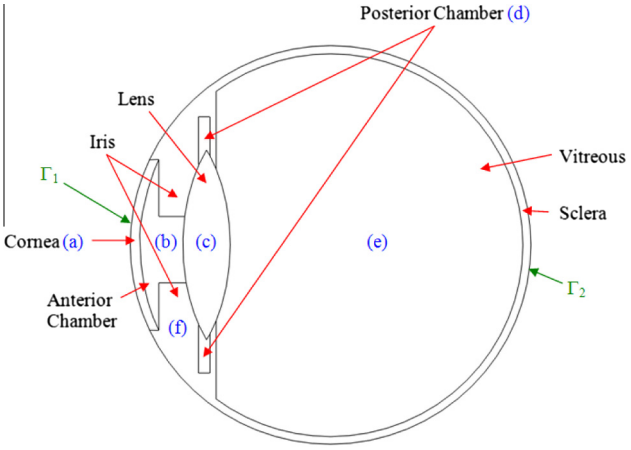

Fig. 2. Human eye vertical cross section.

Table 1
Dielectric properties of tissues at 900 MHz and 1800 MHz [39,40,23].

Tissue	Frequency: 900 MHz		Frequency: 1800 MHz	
	ε_r	σ (S/m)	ε_r	σ (S/m)
Cornea (a)	52.0	1.85	55.0	2.32
Anterior chamber (b)	73.0	1.97	75.0	2.40
Lens (c)	51.3	0.89	41.1	1.29
Posterior chamber (d)	73.0	1.97	75.0	2.40
Vitreous (e)	74.3	1.97	73.7	2.33
Sclera (f)	52.1	1.22	52.7	1.68
Iris (f)	52.1	1.22	52.7	1.68

3.2. Equations for EM wave propagation analysis

The mathematical models are developed to predict the electric fields and the SAR with respect to the temperature gradient in the eye. To simplify the problem, the following assumptions are made:

1. The EM wave propagation is modeled in two dimensions.
2. The eye in which the EM waves interact with the eye proceeds in the open region.
3. The free space is truncated by scattering boundary condition.
4. The model assumes that dielectric properties of each tissue are constant.
5. In the eye, the EM waves are characterized by transverse magnetic fields (TM-mode).

The EM wave propagation in the eye is calculated using Maxwell's equations which mathematically describe the interdependence of the EM waves. The general form of Maxwell's equations is simplified to demonstrate the EM fields penetrated in the eye as the following equation:

$$\nabla \times \left(\left(\varepsilon_r - \frac{j\sigma}{\omega \varepsilon_0}^{-1} \right) \nabla \times H_z \right) - \mu_r k_0^2 H_z = 0 \quad (1)$$

where H is the magnetic field (A/m), μ_r is the relative magnetic permeability, ε_r is the relative dielectric constant, $\varepsilon_0 = 8.8542 \times 10^{-12}$ F/m is the permittivity of free space, k_0 is the free space wave number (m^{-1}).

3.2.1. Boundary condition for wave propagation analysis

EM energy is emitted by an EM radiation device and falls on the eye with a particular power density. Therefore, boundary condition for solving EM wave propagation, as shown in Fig. 3, is described as follows:

Author's personal copy

Table 2
Thermal properties of the eye [16].

Tissue	ρ (kg/m^3)	k (W/m C)	C_p (J/kg C)	μ (N s/m^2)	β (1/K)
Cornea (a)	1050	0.58	4178	–	–
Anterior chamber (b)	996	0.58	3997	0.00074	0.000337
Lens (c)	1000	0.4	3000	–	–
Posterior chamber (d)	996	0.58	3997	–	–
Vitreous (e)	1100	0.603	4178	–	–
Sclera (f)	1050	1.0042	3180	–	–
Iris (f)	1050	1.0042	3180	–	–

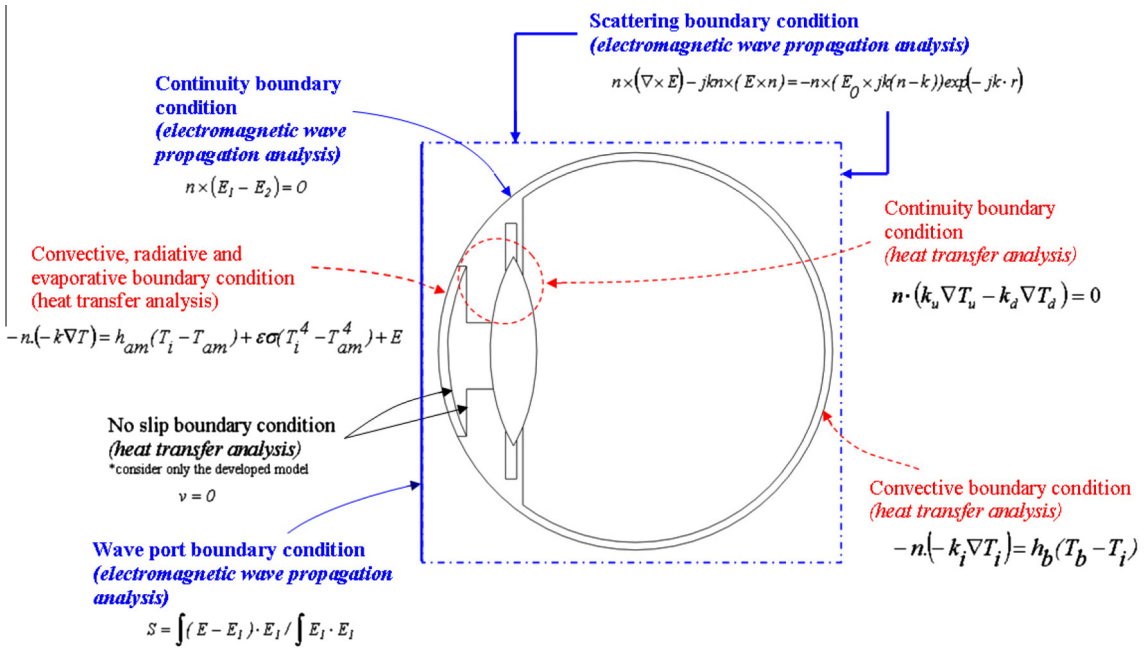

Fig. 3. Boundary condition for analysis of EM wave propagation and heat transfer.

It is assumed that the uniform wave flux falls on the left side of the eye. Therefore, at the left boundary of the considered domain, an EM simulator employs TM wave propagation port with specified power density,

$$S = \int (E - E_1) \cdot E_1 \Big/ \int E_1 \cdot E_1 \tag{2}$$

Boundary conditions along the interfaces between different mediums, for example, between air and tissue or tissue and tissue, are considered as continuity boundary condition,

$$n \times (E_1 - E_2) = 0 \tag{3}$$

The outer sides of the calculated domain, i.e., free space, are considered as scattering boundary condition [25],

$$n \times (\nabla \times E_z) - jkE_z = -jk(1 - k \cdot n)E_{0z}\exp(-jk \cdot r) \tag{4}$$

where k is the wave number (m^{-1}), σ is the electrical conductivity (S/m), n is the normal vector, $j = \sqrt{-1}$, and E_0 is the incident plane wave (V/m).

3.3. Interaction of EM fields and human tissues

Interaction of EM fields with biological tissue can be defined in the term of the SAR. When the EM waves propagate through the tissue, the energy of EM waves is absorbed by the tissue. The SAR is defined as power dissipation rate normalized by material density [25]. The SAR is given by,

$$\mathrm{SAR} = \frac{\sigma}{\rho}|E|^2 \tag{5}$$

where E is the electric field intensity (V/m), σ is the electric conductivity (S/m), and ρ is the tissue density (kg/m^3).

3.4. Equations for heat transfer and flow analysis

To solve the thermal problem, the coupled effects of the EM wave propagation and the unsteady bioheat transfer are investigated. The temperature distribution is corresponded to the SAR. This is because the SAR in the eye distributes owing to energy absorption. Thereafter, the absorbed energy is converted to thermal energy, which increases the tissue temperature.Heat transfer analysis of the eye is modeled in two dimensions. To simplify the problem, the following assumptions are made:

1. The Human tissue is a bio-material with constant thermal properties.
2. There is no phase change of substance in the tissue.
3. There is a local thermal equilibrium between the blood and the tissue.
4. There is no chemical reaction in the tissue.

This study utilized the pertinent thermal model based on the porous media theory [26] to investigate the heat transfer behavior of the eye when exposed to the EM fields.

Author's personal copy

In this study, the motion of fluid is considered only inside the anterior chamber [16]. There is a blood flow in the iris/sclera part, which plays a role to adjust the eye temperature with the rest of the body [26]. For the rest parts, the metabolic heat generation is neglected based on the fact that these comprise mainly water [16]. The equation governing the flow of heat in cornea, posterior chamber, lens and vitreous are resembled the classical heat conduction equation given in Eq. (6)

$$\rho_i C_i \frac{\partial T_i}{\partial t} = \nabla \cdot (k_i \nabla T_i) + Q_{ext}; \quad i = a, c, d, e \tag{6}$$

This model accounts for the existence of AH in the anterior chamber. The heat transfer process consists of both the conduction and natural convections, which can be written as follows:

Continuity equation:

$$\nabla \cdot u_i = 0; \quad i = b \tag{7}$$

Momentum equation:

$$\rho_i \frac{\partial u_i}{\partial t} + \rho_i u_i \nabla \cdot u_i = -\nabla p_i + \nabla \cdot [\mu(\nabla u_i + \nabla u_i^T)] + \rho_i g \beta_i (T_i - T_{ref}); \quad i = b \tag{8}$$

where i denotes each subdomain in the eye model as shown in Fig. 2, ρ is the tissue density (kg/m^3), β is the volume expansion coefficient (1/K), u is the velocity (m/s), p is the pressure (N/m^2), μ is the dynamic viscosity of AH (N s/m^2), t is the time, T is the tissue temperature (K), and T_{ref} is the reference temperature considered here is 37 °C. The effects of buoyancy due to the temperature gradient are modeled using the Boussinesq approximation which states that the density of a given fluid changes slightly with temperature but negligibly with pressure [16].

Energy equation:

$$\rho_i C_i \frac{\partial T_i}{\partial t} - \nabla \cdot (k_i \nabla T_i) = -\rho C_i u_i \cdot \nabla T_i + Q_{ext}; \quad i = b \tag{9}$$

The sclera/iris is modeled as a porous medium with the blood perfusion, which assumes that local thermal equilibrium exits between the blood and the tissue. The blood perfusion rate used is 0.004 1/s. A modified Pennes' bioheat equation [26,23] is used to calculate the temperature distribution in the sclera/iris

$$(1-\varepsilon)\rho_i C_i \frac{\partial T_i}{\partial t} = \nabla \cdot ((1-\varepsilon) k_i \nabla T_i) + \rho_b C_b \omega_b (T_b - T_i) + Q_{ext}; \quad i = f \tag{10}$$

where C is the heat capacity of tissue (J/kg K), k is the thermal conductivity of tissue (W/m K), T_b is the temperature of blood (K), ρ_b is the density of blood (kg/m^3), C_b is the specific heat capacity of blood (J/kg K), ω_b is the blood perfusion rate (1/s), and Q_{ext} is the external heat source term (EM heat-source density) (W/m^3).

In the analysis, the porosity (ε) used is assumed to be 0.6. The heat conduction between the tissue and the blood flow is approximated by the blood perfusion term, $\rho_b C_b \omega_b (T_b - T)$.

The external heat source term is equal to the resistive heat generated by the EM fields (EM power absorbed), which defined as [32]

$$Q_{ext} = \frac{1}{2}\sigma_{tissue}|\bar{E}|^2 = \frac{\rho}{2} \cdot \mathrm{SAR} \tag{11}$$

where σ_{tissue} is the electric conductivity of tissue (S/m).

3.4.1. Boundary condition for heat transfer analysis

The heat transfer analysis excluding the surrounding space is considered only in the eye. The cornea surface as shown in Fig. 3, is considered as the convective, radiative, and evaporative boundary conditions.

$$-n(-k\nabla T) = h_{am}(T_i - T_{am}) + \varepsilon\sigma(T_i^4 - T_{am}^4) + e \ \text{ on } \Gamma_1 \quad i = \alpha \tag{12}$$

where Γ_i is the external surface area corresponding to section i, e is the tear evaporation heat loss (W/m^2), T_{am} is the ambient temperature (K), h_{am} is the convection coefficient (W/m^2 K).

The temperature of blood generally assumed to be the same as the body core temperature causes heat to be transferred into the eye [16]. The surface of the sclera is assumed to be a convective boundary condition

$$-n \cdot (-k_i \nabla T_i) = h_b (T_b - T_i) \text{ on } \Gamma_2 \quad i = f \tag{13}$$

where h_b is the convection coefficient of blood (65 W/m^2 K). Γ_1 and Γ_2 are the corneal surface and sclera surface of the eye, respectively.

3.5. Calculation procedure

In this study, the finite element method is used to analyze the transient problems. The computational scheme is to assemble finite element model and compute a local heat generation term by performing an EM calculation using tissue properties. In order to obtain a good approximation, a fine mesh is specified in the sensitive areas. This study provides a variable mesh method for solving the problem as shown in Fig. 4. The system of governing equations as well as the initial and boundary conditions are then solved. All computational processes are implemented using COMSOL^{TM} Multi-

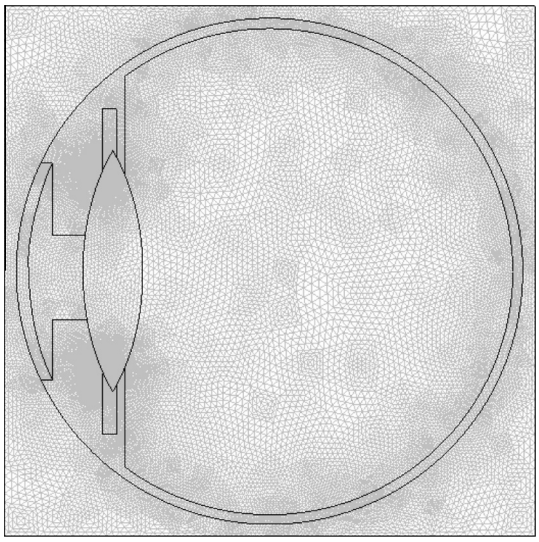

Fig. 4. A two-dimensional finite element mesh of human eye model.

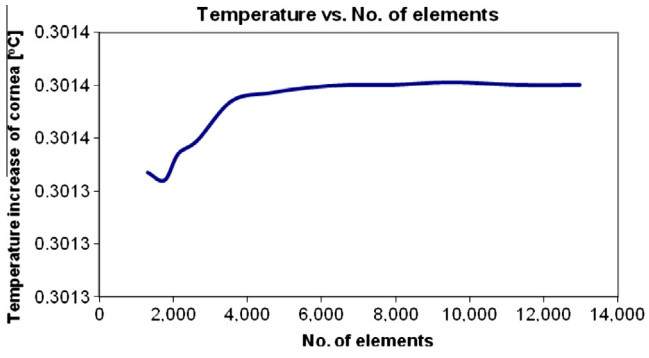

Fig. 5. Grid convergence curve of the 2D model.

Author's personal copy

physics, to demonstrate the phenomenon that occurs in the eye exposed to the EM fields.

The 2D model is discretized using triangular elements and the Lagrange quadratic is then used to approximate the temperature and SAR variations across each element. The convergence test is carried out to identify the suitable number of elements required. The convergence curve resulting from the convergence test is shown in Fig. 5. This convergence test leads to the grid with approximately 10,000 elements. It is reasonable to assume that, at this element number, the accuracy of the simulation results is independent from the number of elements.

4. Results and discussion

In this study, the coupled model of the EM and thermal fields are solved numerically. For the simulation, the dielectric and thermal properties are directly taken from Tables 1 and 2, respectively. The exposed radiated power used in this study refers to the International Commission of Non-Ionizing Radiation Protection (ICNIRP) standard for safety level at the maximum SAR value of 2 W/kg (general public exposure) and 10 W/kg (occupational exposure) [6]. Since most GSM networks use frequencies in the 900 and 1800 MHz spectrum, therefore, in this analysis, the effects of these operating frequencies on distributions of SAR and temperature in the eye are systematically investigated.

4.1. Verification of the model

In order to verify the accuracy of the present numerical models, the case without EM fields of the simulated results from this study are validated against the numerical results with the same geometric model obtained by Shafahi and Vafai [26]. Moreover, the numerical results are then compared to the experimental results of the rabbit obtained from Lagendijk [8]. The validation case assumes that the rabbit body temperature is 38.8 °C, the tear evaporation heat loss is 40 W/m^2, the ambient temperature is 25 °C, and the convection coefficient of ambient air is 20 W/m^2 K. The results of the selected test case are depicted in Fig. 6 for temperature distribution in the eye. Fig. 6 clearly shows a good agreement of the temperature distribution in the eye between the present solution and that of Shafahi and Vafai [26] and Lagendijk [8]. In the figure, the simulated results provides a good agreement with the simulated results obtained from Shafahi and Vafai [26]. This favorable comparison lends confidence in the accuracy of the present numerical model.

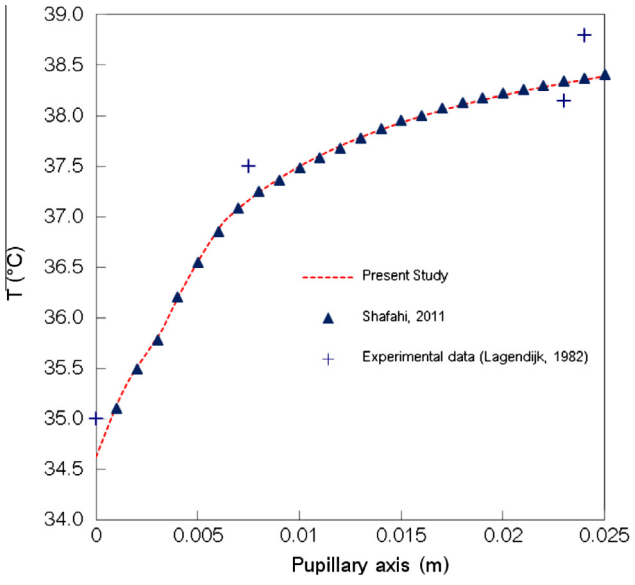

Fig. 6. Comparison of the calculated temperature distribution to the temperature distribution obtained by Shafahi and Vafai, and the Lagendijk's experimental data; h_{am} = 20 W/m^2 K and T_{am} = 25 °C.

4.2. Electric field distribution

In order to study the effect of operating frequency, the eye is exposed to the power density of 100 mW/cm^2 at the frequencies of 900 and 1800 MHz. To illustrate the penetrated electric field distribution inside the eye, the predicted results obtained from our proposed models are required. Fig. 7 shows the simulation of an electric field pattern inside the eye exposed to the EM fields in TM mode operating at the frequencies of 900 and 1800 MHz propagating along the vertical cross section human eye model. Due to the different dielectric characteristics of the various tissue layers at different operating frequencies, a different fraction of the supplied EM energy will become absorbed in each layer in the eye. Consequently, the reflection and transmission components at each layer contribute to the resonance of standing wave in the eye. It can be seen that the higher values of electric fields at the both frequencies occur in the outer part area of the eye, especially in cornea, and lens. By comparison, the maximum electric field intensity in outer parts of the eye at the frequency of 900 MHz displays a higher value than that of 1800 MHz. The maximum electric field intensities are 391.8 and 231.2 V/m at the frequencies of 900 and 1800 MHz, respectively. The maximum value for the frequency of 900 MHz is in the cornea while for the frequency of 1800 MHz is in the lens. Mathematically, this result corresponds to Eq. (1) and the dielectric properties (ε_r) in Table 1 show that the frequency of 900 MHz has lower dielectric properties of cornea, while the frequency of 1800 MHz has lower dielectric properties of lens. It is found that these alterations of electric field distribution between the two chosen frequencies vary in extent with the magnitude of the dielectric property and with the standing-wave pattern. For both frequencies, the electric fields deep inside the eye are extinguished where the electric fields attenuate due to the absorbed EM energy and are then converted to heat. Moreover, the electric field distribution also showed a strong dependence on the dielectric properties of the tissue.

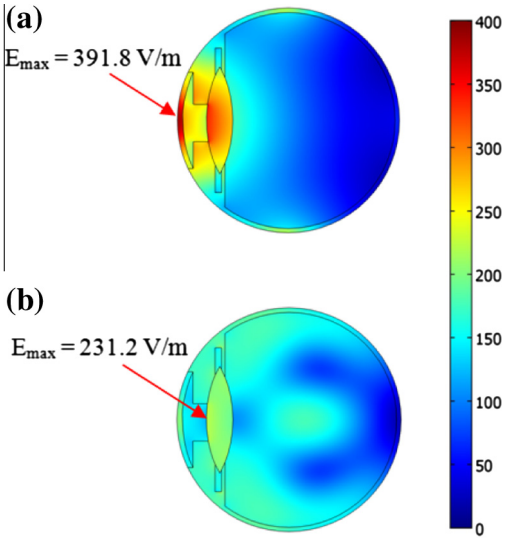

Fig. 7. Electric field distribution (V/m) in human eye exposed to the EM power density of 100 mW/cm^2 at the frequencies of (a) 900 MHz and (b) 1800 MHz.

Author's personal copy

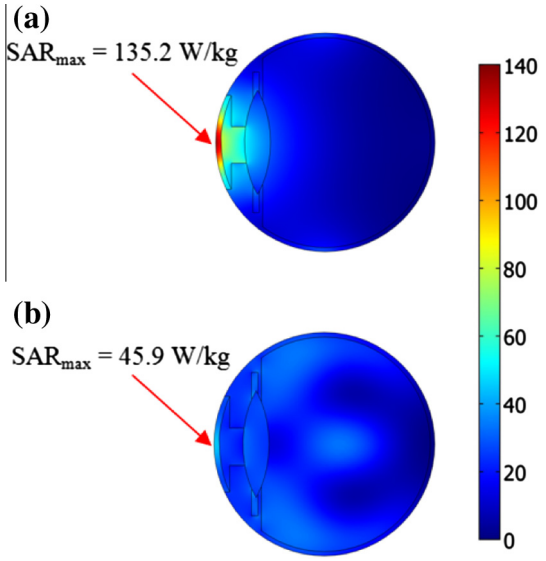

Fig. 8. SAR distribution (W/kg) in human eye exposed to the EM power density of 100 mW/cm^2 at the frequencies of (a) 900 MHz and (b) 1800 MHz.

4.3. SAR distribution

Fig. 8 shows the SAR distribution evaluated on the vertical cross section of the eye exposed to the EM frequencies of 900 and 1800 MHz. It is evident from the figure that the results of the SAR values in the eye (Fig. 8) are increased corresponding to the electric field intensities (Fig. 7). Besides the electric field intensity, the magnitude of the dielectric and thermal properties in each tissue will directly affect SAR values in the eye. For both frequencies, the highest SAR values are obtained in the region of the corneal surface. In this region, the frequencies of 900 and 1800 MHz display SAR values of 135.2 and 45.9 W/kg, respectively. This is because the cornea has a much higher value of its electrical conductivity (σ) than those of lens and iris. The second main reason is the position of the cornea located close to the exposed surface, at which the electric field intensity is strongest. It is found that the SAR distribution pattern in the eye, which corresponds to Eq. (5), is strongly depended on the effect of the dielectric properties (σ, shown in Table 1) and thermal properties (ρ, shown in Table 2). Moreover, the SAR pattern at the frequency of 1800 MHz shows a greater value of the EM power absorption in the deep part of the eye, with less surface heating, compared to those of 900 MHz. Comparing to the ICNIRP standard for safety level at the maximum SAR value of 2 W/kg (general public exposure) and 10 W/kg (occupational exposure) [6], the resulting SAR values from this study are higher than the ICNIRP exposure limits for occupational exposure in all cases.

4.4. Temperature distribution

Since this study has focused on the volumetric heating effect into the multilayer tissues of the eye induced by EM fields, the effect of an ambient temperature variation have been neglected in order to gain insight into the interaction between the EM fields and the tissue as well as the correlation between the SAR and the heat transfer mechanism. For this reason, the ambient temperature has been set to the human body temperature of 37 °C, and the tear evaporation has been neglected. Moreover, the effect of thermoregulation mechanisms has also been neglected due to the small temperature increase occurred during exposure process. The convective coefficient due to the blood flow inside the sclera is set to 65 W/m^2 K [16]. In order to study the heat transfer in the eye, the coupled effects of EM wave propagation and unsteady heat transfer as well as the initial and boundary conditions are then investigated. Due to these coupled effects, the electric field distribution in Fig. 7 and the SAR distribution in Fig. 8 are then converted into heat by absorption of the tissue. Fig. 9 shows the temperature distribution in the vertical cross section human eye at various time exposed to the EM frequencies of 900 (Fig. 9(a)) and 1800 MHz (Fig. 9(b)). For the eye exposed to the EM fields for a period of time, the temperature in the eye (Fig. 9) is increased corresponding to the SAR (Fig. 8). This is because the electric fields in the eye attenuate owing to the energy absorbed and thereafter the absorbed energy is converted to thermal energy, which increases the eye temperature.

It is found that when the eye is subjected to the EM fields at different frequencies, the distribution patterns of temperature at a particular time are quite different. The hot spot zone is strongly displayed at the 10 min for two frequencies. Even the highest level of SAR values in both frequencies appears in the cornea (Fig. 8), the highest temperature for the frequency of 900 MHz is in the anterior chamber and for the frequency of 1800 MHz (Fig. 9) is the vitreous. This behavior is due to the fact that for the different frequency radiation at same radiated power, the temperature distribution pattern is not the same. In this case study, the difference in temperature distribution pattern between two chosen frequencies is caused by the dielectric properties of the tissue as well as

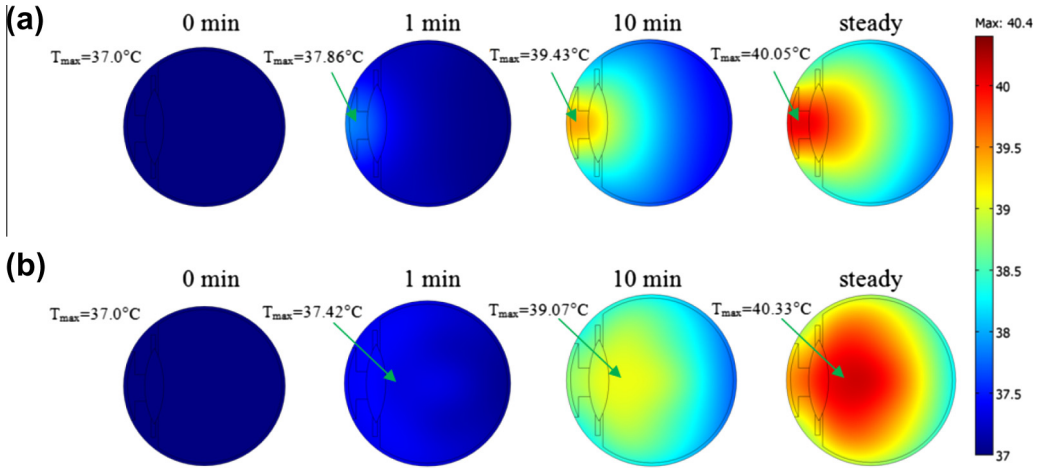

Fig. 9. The temperature distribution in human eye at various time exposed to the EM power density of 100 mW/cm^2 at the frequencies of (a) 900 MHz and (b) 1800 MHz.

Author's personal copy

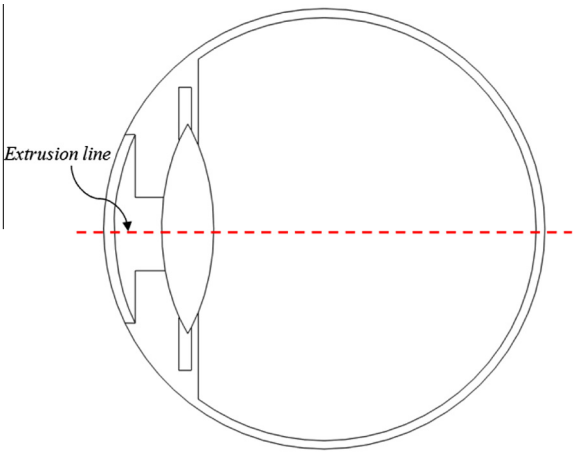

Fig. 10. The extrusion line in the eye where the temperature distribution is considered.

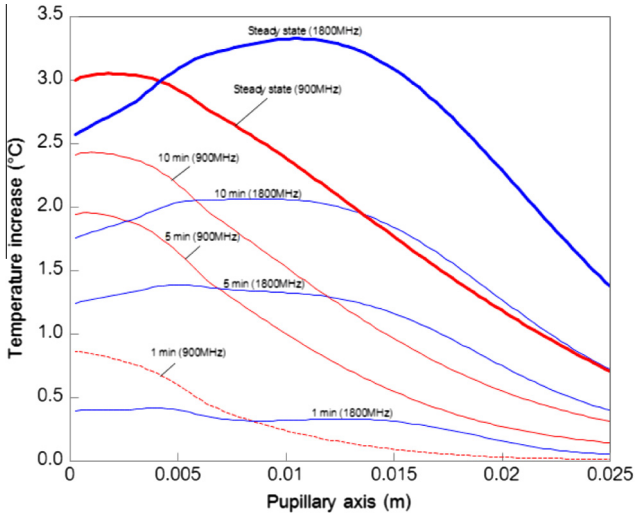

Fig. 11. Temperature increase versus papillary axis of human eye exposed to the EM frequencies of 900 and 1800 MHz at various times.

the electric field distribution pattern in the eye, which become the dominant mechanisms for the heat transfer.

For the 900 MHz frequency, even though the maximum values of the electric fields (Fig. 7(a)) and the SAR (Fig. 8(a)), are the cornea, the highest temperature is the anterior chamber (Fig. 9(a)). This is owing to the extensive penetration of the EM power of the internal regions and the higher dielectric properties (ε_r) of the anterior chamber. This higher dielectric property of the anterior chamber represents the stronger absorption ability of EM fields than those of cornea and lens. Moreover, the outer corneal surface has a lower temperature than that of the anterior chamber, even if it has higher SAR value (Fig. 8(a)). This is because, in this area, the generated heat is dissipated to the ambient via convection and radiation.

While for the 1800 MHz frequency, beside the cornea and lens, the high value of the electric fields is the middle of the vitreous and peripheral vitreous. This is owing to the constructive interference between the forward and reflected waves of the higher frequency of 1800 MHz results in standing wave patterns forming in the EM fields (Fig. 7(b)) in the vitreous area. This high electric field intensity increases the amount of energy absorption in the vitreous area (Fig. 8(b)) and consequently causes the temperature to rise (Fig. 9(b)). In this case, the maximum temperature increase in the peripheral vitreous area has a lower level than that of the middle of the vitreous even if the peripheral vitreous area also has high electric field intensity and the SAR value also. This is due to the presence of blood perfusion in the sclera tissue, which covers an internal surface area of the eye. This blood perfusion provides buffer characteristic to the eye temperature and plays important roles on the cooling processes in the peripheral vitreous area.

From the Fig. 9, it is found that the exposure time significantly influence the temperature increase in the eye. A longer exposure time resulted in a higher heat accumulation inside the eye, thereby increasing its temperature. By using the operating frequency of 900 MHz, the maximum temperatures increase are 0.86, 2.43, and 3.05 °C for the exposure times of 1 min, 10 min, and at steady-state conditions of 60 min, respectively. By using the operating frequency of 1800 MHz, the maximum temperatures increase are 0.42, 2.07, and 3.33 °C for the exposure times of 1 min, 10 min, and at steady-state conditions of 60 min, respectively.

Consider the temperature increase distribution at the extrusion line (Fig. 10). Fig. 11 shows the temperature increase versus papillary axis (along the extrusion line) of the eye exposed to the EM frequencies of 900 and 1800 MHz at various times. From the figure it is found that for every exposure time, the highest temperature for the frequency of 900 MHz is in the anterior chamber (in the front part of the eye) and for the frequency of 1800 MHz is in the vitreous (in the middle part of the eye), as the reasons given previously. In the early stage of exposure (10 min), the temperature increase of the 900 MHz frequency is found to be higher than that of 1800 MHz frequency, especially in the front part of the eye. This is due to the high intensity of the electric fields and the SAR values in this area of the 900 MHz frequency, resulting in a high absorption of the EM energy.

In a steady state, the highest temperature for the frequency of 900 MHz is the anterior chamber, and for the frequency of 1800 MHz is still in the vitreous area. Surprisingly, in a steady state, the maximum temperature increase of the 1800 MHz frequency is higher than that of 900 MHz frequency. This is because not only does the anterior chamber have stronger absorption ability than that of other tissues but also the natural convection and radiation effects at the cornea surface play an important role in heat dissipation from the anterior chamber to the ambient. On the contrary, these heat dissipation effects in the vitreous area have worn off in perception rather than an enhancement. In the first period of exposure with the low flow speed of liquid in the anterior chamber (Fig. 12), the heat transfer in the anterior chamber occurs mainly by conduction across the fluid layer. While in a later time with higher flow speed induced by a higher temperature gradient, different flow regimes are encountered especially in the case of 900 MHz, with a progressively releasing heat into an environment and the connected tissue.

Fig. 12 shows the circulatory patterns in the anterior chamber in the eye exposed to the EM frequencies of 900 and 1800 MHz at various times. These patterns vary corresponding to the temperature gradient in the eye. Therefore, in the case of a lower temperature gradient, the circulatory patterns have a lower speed, where a circulatory pattern with a higher temperature gradient flows faster. For the 900 MHz frequency, it is found that the natural convection and formation of two circulatory patterns with opposite direction in the anterior chamber, shown in Fig. 12(a), play important roles on the cooling processes in the eye, especially in the inner corneal surface. It is observed that a large temperature gradient is significantly produced by the EM fields after 10 min. The circulation pattern implies that the generated heat in the anterior chamber is transferred in two directions; one is to the corneal surface, and the other to the lens surface. While for the 1800 MHz frequency, a counterclockwise circulation thus appears in the anterior chamber, shown in Fig. 12(b). This seemed to imply that the

Author's personal copy

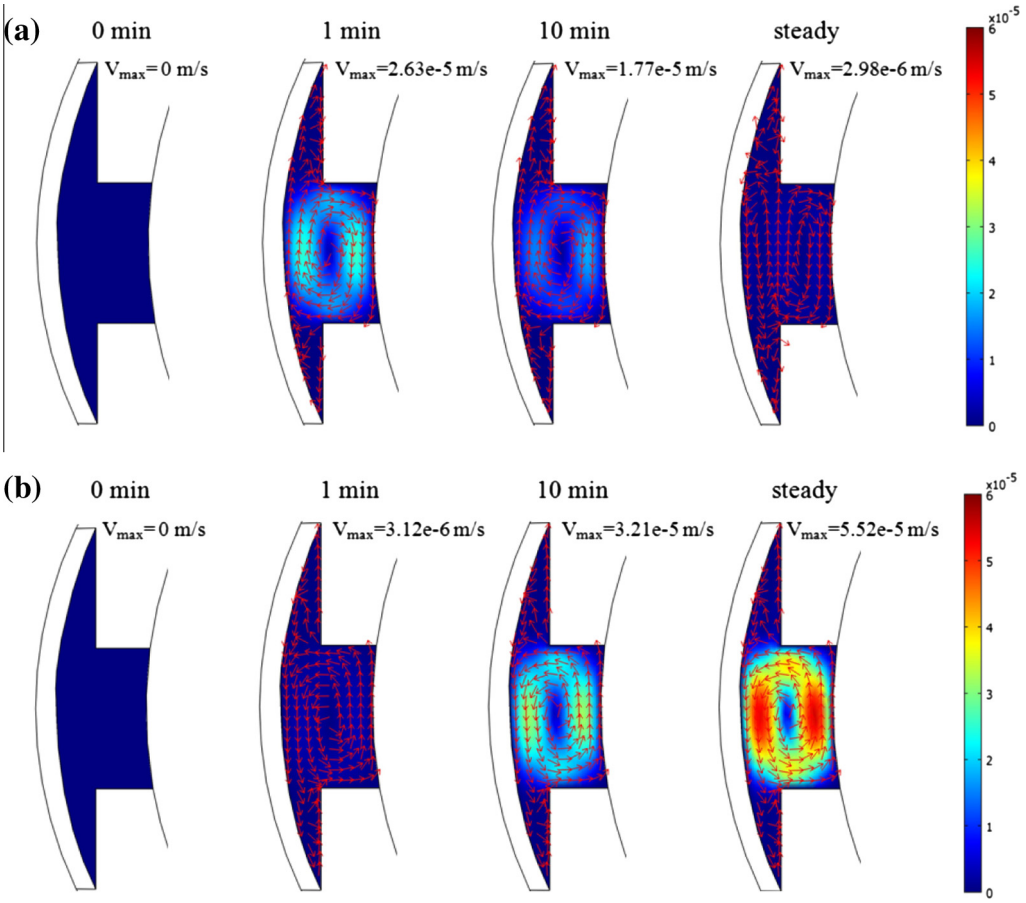

Fig. 12. The velocity distribution inside the anterior chamber at various time exposed to the EM power density of 100 mW/cm^2 at the frequencies of (a) 900 MHz and (b) 1800 MHz.

direction of heat transfer is travels outward from the lens surface. The circulation pattern in the 1800 MHz frequency is quite different from that of that of the 900 MHz frequency because of the different heating pattern in the eye between the two frequencies.

In this study, the maximum temperature increase in the eye exposed to the EM fields with the power density of 100 mW/cm^2 at the frequencies of 900 and 1800 MHz are 3.05 and 3.33 °C, respectively. The obtained temperature increases may leads to the formation of cataract or posterior capsular opacification [2].

5. Conclusions

The numerical simulations of the SAR and temperature distributions in this study show several important features of the energy absorption in the eye during exposed to the TM-mode of EM fields at 900 and 1800 MHz. In this study, the electric field distributions show a strong dependence on the dielectric properties of the tissue. The results of the SAR values are increased corresponding to the electric field intensities. Besides the electric field intensity, the magnitude of the dielectric and thermal properties in each tissue will directly affect the SAR values in the eye. It is found that the temperature distributions in the eye induced by the EM fields are not directly related to the SAR distribution due to the effect of the interaction among the dielectric properties, thermal properties, blood perfusion, and penetration depth of the EM power.

Therefore, health effect assessment of the EM field exposure requires the utilization of the most accurate numerical simulation of the thermal model along with the SAR model. In the future works, the effect of the ambient temperature variation will be included in the analysis to represent the actual heat transfer process which occurs in the realistic situation and will focus on the frequency-dependent dielectric properties of the tissue. A study will also be developed to a more realistic 3D model for simulations and to study the temperature dependency of dielectric property. This will allow a better understanding of the realistic situation of the interaction between the EM fields and the eye.

Acknowledgments

This work has been financially supported by the Thailand Research Fund (TRF), the Commission on Higher Education (CHE) and Eastern Asia University. We thank Dr. Nisakorn Somsuk for grammatical correction of the manuscript.

References

[1] A.F. Emery, P. Kramar, A.W. Guy, J.C. Lin, Microwave induced temperature rises in rabbit eyes in cataract research, ASME J. Heat Transfer 97 (1975) 123–128.
[2] C. Buccella, V.D. Santis, M. Feliaiani, Prediction of temperature increase in human eyes due to RF sources, IEEE Trans. Electromagn. Compat. 49 (4) (2007) 825–833.
[3] J.C. Lin, Cataracts and cell-phone radiation, IEEE Antennas Propag. Mag. 45 (1) (2003) 171–174.
[4] O. Fujiwara, A. Kato, Computation of SAR inside eyeball for 1.5-GHz microwave exposure using finite-difference time domain technique, IEICE Trans. E77-B (1994) 732–737.
[5] O.P. Gandhi, G. Lazzi, C.M. Furse, Electromagnetic absorption in the human head and neck for mobile telephones at 835 and 1900 MHz, IEEE Trans. Microwave Theor. Tech. 44 (10) (1996) 1884–1897.
[6] International Commission on Non-Ionizing Radiation Protection (ICNIRP), Guidelines for limiting exposure to time-varying electric, magnetic and electromagnetic fields (up to 300 GHz), Health Phys. 74, 1998, pp. 494–522.

Author's personal copy

[7] IEEE, IEEE standard for safety levels with respect to human exposure to radio frequency electromagnetic fields, 3 kHz to 300 GHz, IEEE standard C95.1, 1999.
[8] J.J.W. Lagendijk, A mathematical model to calculate temperature distribution in human and rabbit eye during hyperthermic treatment, Phys. Med. Biol. 27 (1982) 1301–1311.
[9] J. Scott, A finite element model of heat transport in the human eye, Phys. Med. Biol. 33 (1988) 227–241.
[10] J. Scott, The computation of temperature rises in the human eye induced by infrared radiation, Phys. Med. Biol. 33 (1988) 243–257.
[11] E.H. Amara, Numerical investigations on thermal effects of Laser–Ocular media interaction, Int. J. Heat Mass Transfer 38 (1995) 2479–2488.
[12] A. Hirata, S. Matsuyama, T. Shiozawa, Temperature rises in the human eye exposed to EM waves in the frequency range 0.6–6 GHz, IEEE Trans. Electromagn. Compat. 42 (4) (2000) 386–393.
[13] K.J. Chua, J.C. Ho, S.K. Chou, M.R. Islam, On the study of the temperature distribution within a human eye subjected to a laser source, Int. Commun. Heat Mass Transfer 32 (2005) 1057–1065.
[14] W. Limtrakarn, S. Reepolmaha, P. Dechaumphai, Transient temperature distribution on the corneal endothelium during ophthalmic phacoemulsification: a numerical simulation using the nodeless variable element, Asian Biomed. 4 (6) (2010) 885–892.
[15] S. Kumar, S. Acharya, R. Beuerman, A. Palkama, Numerical solution of ocular fluid dynamics in a rabbit eye: parametric effects, Ann. Biomed. Eng. 34 (2006) 530–544.
[16] E. Ooi, E.Y.K. Ng, Simulation of aqueous humor hydrodynamics in human eye heat transfer, Comput. Biol. Med. 38 (2008) 252–262.
[17] E.H. Ooi, E.Y.K. Ng, Effects of natural convection inside the anterior chamber, Int. J. Numer. Methods Biomed. Eng. 27 (2011) 408–423.
[18] H.H. Pennes, Analysis of tissue and arterial blood temperatures in the resting human forearm, J. Appl. Physiol. 1 (1948) 93–122.
[19] H.H. Pennes, Analysis of tissue and arterial blood temperatures in the resting human forearm, J. Appl. Physiol. 85 (1) (1998) 5–34.
[20] V.M.M. Flyckt, B.W. Raaymakers, J.J.W. Lagendijk, Modeling the impact of blood flow on the temperature distribution in the human eye and the orbit: fixed heat transfer coefficients versus the pennes bioheat model versus discrete blood vessels, Phys. Med. Biol. 51 (2006) 5007–5021.
[21] E.Y.K. Ng, E.H. Ooi, FEM simulation of the eye structure with bioheat analysis, Comput. Methods Programs Biomed. 82 (2006) 268–276.
[22] E.H. Ooi, E.Y.K. Ng, Ocular temperature distribution: a mathematical perspective, J. Mech. Med. Biol. 9 (2009) 199–227.
[23] A. Nakayama, F. Kuwahara, A general bioheat transfer model based on the theory of porous media, Int. J. Heat Mass Transfer 51 (2008) 3190–3199.
[24] S. Mahjoob, K. Vafai, Analytical characterization of heat transfer through biological media incorporating hyperthermia treatment, Int. J. Heat Mass Transfer 52 (2009) 1608–1618.
[25] K. Khanafer, K. Vafai, Synthesis of mathematical models representing bioheat transport, Adv. Numer. Heat Transfer 3 (2009) 1–28.
[26] M. Shafahi, K. Vafai, Human eye response to thermal disturbances, ASME J. Heat Transfer 133 (2011) 011009.
[27] E.H. Ooi, W.T. Ang, E.Y.K. Ng, A boundary element model of the human eye undergoing laser thermokeratoplasty, Comput. Biol. Med. 28 (2008) 727–738.
[28] E.H. Ooi, W.T. Ang, E.Y.K. Ng, A boundary element model for investigating the effects of eye tumor on the temperature distribution inside the human eye, Comput. Biol. Med. 28 (2009) 727–738.
[29] J.H. Tan, E.Y.K. Ng, U.R. Acharya, C. Chee, Study of normal ocular thermogram using textural parameters, Infrared Phys. Technol. 53 (2010) 120–126.
[30] J.H. Tan, E.Y.K. Ng, U.R. Acharya, Evaluation of tear evaporation from ocular surface by functional infrared thermography, Med. Phys. 37 (2010) 6022–6034.
[31] J.H. Tan, E.Y.K. Ng, U.R. Acharya, Evaluation of topographical variation in ocular surface temperature by functional infrared thermography, Infrared Phys. Technol. 54 (2011) 469–477.
[32] T. Wessapan, S. Srisawatdhisukul, P. Rattanadecho, Numerical analysis of specific absorption rate and heat transfer in the human body exposed to leakage electromagnetic field at 915 MHz and 2450 MHz, ASME J. Heat Transfer 133 (2011) 051101.
[33] T. Wessapan, S. Srisawatdhisukul, P. Rattanadecho, The effects of dielectric shield on specific absorption rate and heat transfer in the human body exposed to leakage microwave energy, Int. Commun. Heat Mass Transfer 38 (2011) 255–262.
[34] T. Wessapan, P. Rattanadecho, Numerical analysis of specific absorption rate and heat transfer in human head subjected to mobile phone radiation, ASME J. Heat Transfer 134 (2012) 121101.
[35] T. Wessapan, S. Srisawatdhisukul, P. Rattanadecho, Specific absorption rate and temperature distributions in human head subjected to mobile phone radiation at different frequencies, Int. J. Heat Mass Transfer 55 (2012) 347–359.
[36] P. Keangin, T. Wessapan, P. Rattanadecho, Analysis of heat transfer in deformed liver cancer modeling treated using a microwave coaxial antenna, Appl. Therm. Eng. 31 (16) (2011) 3243–3254.
[37] P. Keangin, T. Wessapan, P. Rattanadecho, An analysis of heat transfer in liver tissue during microwave ablation using single and double slot antenna, Int. Commun. Heat Mass Transfer 38 (2011) 757–766.
[38] T. Wessapan, P. Rattanadecho, Specific absorption rate and temperature increase in human eye subjected to electromagnetic fields at 900 MHz, ASME J. Heat Transfer 134 (2012) 091101.
[39] P. Bernardi, M. Cavagnaro, S. Pisa, E. Piuzzi, Specific absorption rate and temperature increases in the head of a cellular-phone user, IEEE Trans. Microwave Theor. Tech. 48 (7) (2000) 1118–1126.
[40] S. Park, J. Jeong, Y. Lim, Temperature rise in the human head and brain for portable handsets at 900 and 1800 MHz, in: Proceedings of the Fourth International Conference on Microwave and Millimeter Wave Technology, vol. 1, 2004, pp. 966–969.

This article was downloaded by: [Thammasat University Libraries]
On: 28 April 2014, At: 00:11
Publisher: Taylor & Francis
Informa Ltd Registered in England and Wales Registered Number: 1072954 Registered office: Mortimer House, 37-41 Mortimer Street, London W1T 3JH, UK

Numerical Heat Transfer, Part A: Applications: An International Journal of Computation and Methodology
Publication details, including instructions for authors and subscription information:
http://www.tandfonline.com/loi/unht20

The Numerical and Experimental Analysis of Heat Transport and Water Infiltration in a Granular Packed Bed Due to Supplied Hot Water

Phadungsak Rattanadecho [a], Seksan Suttisong [a] & Thitipan Somtawin [a]

[a] Center of Excellence in Electromagnetic Energy Utilization in Engineering (CEEE), Department of Mechanical Engineering, Faculty of Engineering, Thammasat University (Rangsit Campus), Pathumthani, Thailand

Published online: 14 Mar 2014.

To cite this article: Phadungsak Rattanadecho, Seksan Suttisong & Thitipan Somtawin (2014) The Numerical and Experimental Analysis of Heat Transport and Water Infiltration in a Granular Packed Bed Due to Supplied Hot Water, Numerical Heat Transfer, Part A: Applications: An International Journal of Computation and Methodology, 65:10, 1007-1022, DOI: 10.1080/10407782.2013.850969

To link to this article: http://dx.doi.org/10.1080/10407782.2013.850969

PLEASE SCROLL DOWN FOR ARTICLE

Taylor & Francis makes every effort to ensure the accuracy of all the information (the "Content") contained in the publications on our platform. However, Taylor & Francis, our agents, and our licensors make no representations or warranties whatsoever as to the accuracy, completeness, or suitability for any purpose of the Content. Any opinions and views expressed in this publication are the opinions and views of the authors, and are not the views of or endorsed by Taylor & Francis. The accuracy of the Content should not be relied upon and should be independently verified with primary sources of information. Taylor and Francis shall not be liable for any losses, actions, claims, proceedings, demands, costs, expenses, damages, and other liabilities whatsoever or howsoever caused arising directly or indirectly in connection with, in relation to or arising out of the use of the Content.

This article may be used for research, teaching, and private study purposes. Any substantial or systematic reproduction, redistribution, reselling, loan, sub-licensing,

systematic supply, or distribution in any form to anyone is expressly forbidden. Terms & Conditions of access and use can be found at http://www.tandfonline.com/page/terms-and-conditions

Downloaded by [Thammasat University Libraries] at 00:11 28 April 2014

Numerical Heat Transfer, Part A, 65: 1007–1022, 2014
Copyright © Taylor & Francis Group, LLC
ISSN: 1040-7782 print/1521-0634 online
DOI: 10.1080/10407782.2013.850969

Taylor & Francis
Taylor & Francis Group

THE NUMERICAL AND EXPERIMENTAL ANALYSIS OF HEAT TRANSPORT AND WATER INFILTRATION IN A GRANULAR PACKED BED DUE TO SUPPLIED HOT WATER

Phadungsak Rattanadecho, Seksan Suttisong, and Thitipan Somtawin

Center of Excellence in Electromagnetic Energy Utilization in Engineering (CEEE), Department of Mechanical Engineering, Faculty of Engineering, Thammasat University (Rangsit Campus), Pathumthani, Thailand

The characteristics of heat transport and water infiltration in a granular packed bed due to supplied hot water are investigated experimentally and numerically. The distributions of water saturation and temperature are focused on one-dimensional models assuming the local thermal equilibrium between water and particles at any specific space in a vertical granular packed bed column. This study describes the dynamics of heat transport and water infiltration in various testing condition. The calculated water saturation, temperature distribution, and infiltration depth are compared with the experimental results. Experimentally and numerically, the influence of particle sizes and supplied water flux on heat transport during unsaturated flow are clarified in detail. The results showed that the granular packed bed with a larger particle size results in a faster infiltration rate and forms a wider infiltration depth. However, an extension of the heated layer is not as much as that of the infiltration layer because the temperature of water infiltration gradually drops due to upstream heat transport. It is found that a greater supplied water flux corresponds to a higher water saturation and temperature along a granular packed bed for each time increment. The numerical results closely match the experimental results.

Downloaded by [Thammasat University Libraries] at 00:11 28 April 2014

1. INTRODUCTION

In the past few decades, the problem of heat transport in porous media or a granular packed bed with water infiltration due to capillary action is concerned with a variety of soil science, hydrology, agriculture, civil engineering, and chemical engineering applications, such as in temperature control of soil, recovery of geothermal energy, thermal energy storage, and various reactors in chemical industry. The infiltration of water is affected by several intrinsic and extrinsic factors. The intrinsic

Received 13 December 2012; accepted 17 September 2013.

Address correspondence to Phadungsak Rattanadecho, Center of Excellence in Electromagnetic Energy Utilization in Engineering (CEEE), Department of Mechanical Engineering, Faculty of Engineering, Thammasat University (Rangsit Campus), Pathumthani 12120, Thailand. E-mail: ratphadu@engr.tu.ac.th

Color versions of one or more of the figures in the article can be found online at www.tandfonline.com/unht.

NOMENCLATURE

c_p	specific heat, (J/kg.K)	u	velocity, (m/s)
d	particle diameter, (m)	ε	porosity, (m^3/m^3)
D_m	effective molecular mass diffusion [m^2/s]	ρ	density, (kg/m^3)
f	supplied water flow rate, $(kg/m^2)\cdot s$	λ	effective thermal conductivity, (W/ mK)
g	gravitational acceleration, (m/s^2)	μ	dynamics viscosity of liquid, (Pa s)
K	permeability, (m^2)	σ	surface tension, (N/m)
K_r	relative permeability		
p	pressure, (pa)	**Subscripts**	
q	heat flux, (W/m^3)	0	inlet, atmospheric
s	water saturation	1	first position
t	time, (s)	2	second position
T	temperature, (°C)	l	liquid phase

Downloaded by [Thammasat University Libraries] at 00:11 28 April 2014

factors affecting the infiltration of water are the hydraulic conductivity function, water retention characteristics, and porosity of media. The extrinsic factors mainly refer to climatic conditions, such as water flow pattern, ambient temperature, water flow rate, and surface tension.

Until the present, the related problem of water infiltration in porous media has been investigated both experimentally and numerically by many researchers [1–7]. Pinder and Abriola [8] employed a finite difference approximation of the governing equations to describe non-aqueous phase liquid flow in the saturated zone. Celia and Binning [9] employed a finite element discrestization with fully implicit time stepping and Picard iteration to solve the air water flow equation. In order to consider flow phenomena, measurements were performed to visualize the flow pattern [10–14]. The computation analyses of heat and fluid flows have been studied by many researchers [18–20]. Although water infiltration processes have been studied actively for several decades, relatively few studies report the problem of heat transfer coupled with unsaturated flow in a granular packed bed systematically; especially, considering the effects of particle sizes and supplied water flux on transport phenomena with capturing infiltration depth have not been investigated before. In analysis of water infiltration, the governing equation is written in terms of the pressures in liquid phases through Darcy's equation in the mass balance equation. In analysis heat transport, the governing equation is written in terms of conduction and convection modes in the energy equation. This work is extended from the work of S. Suttisong and P. Rattanadecho [17] based on the work of our group (Aoki et al. [10]) and carried out in experimental and numerical work for analysis of heat transport and water infiltration in a granular pecked bed in several testing conditions. The purpose of this work is to study the influences of the particle size and supplied water flux on heat transport, water infiltration, and infiltration depth during unsaturated flow condition. The results presented here provide of a basis for a fundamental understanding of heat transport and unsaturated flow in porous media.

2. COMPUTATIONAL MODEL

By conservation of mass in the unsaturated porous media, the governing equation of infiltration flow can be derived by using the volume averaged technique [15, 16].

The main assumptions involved in the formulations of the transport model are as follows.

1. The unsaturated granular pack bed is rigid.
2. No chemical reactions occur in the granular packed bed.
3. Darcy's law holds for the liquid phase.
4. Gravity is included for the flow analysis.
5. Permeability of liquid can be expressed in terms of relative permeability.

Figure 1 shows the schematic diagram of a single-phase model or Buckley-Leverett problem. This is an unsaturated flow in a granular pack bed due to supplied water. The water is uniformly supplied at the top surface of the granular packed bed, which is initially composed of a glass particle and void with uniform porosity throughout.

In this study, it is noted that the supplied water flux during unsaturated flow is considered to be lower than the supplied water flux due to gravity (Aoki et al. [15]); namely,

$$f \leq g.k \tag{1}$$

Where f denotes supplied water flux, g denotes gravity, and k denotes saturated hydraulic conductivity (permeability). This expression means that the supplied water always infiltrates into granular packed beds throughout the infiltration process.

2.1. Mass Conservation

Regarding to infiltration flow in granular packed bed, the microscopic mass conservation equation for liquid flow in this packed bed is expressed as follows

$$\varepsilon \frac{\partial}{\partial t}[\rho_l s] + \frac{\partial}{\partial z}[\rho_l u_l] = 0 \tag{2}$$

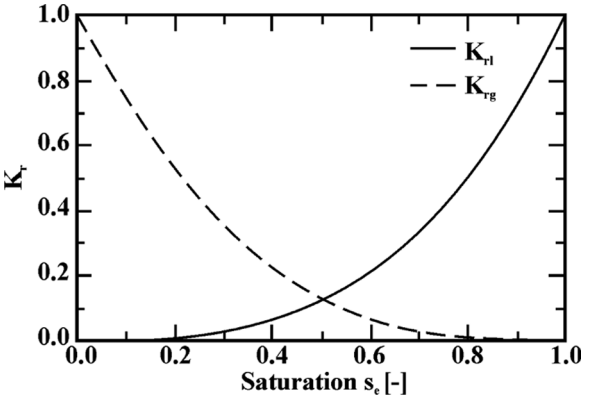

Figure 1. Relationship between K_r and s_e [16].

Downloaded by [Thammasat University Libraries] at 00:11 28 April 2014

Where the generalized Darcy's law which is the expression for the superficial average velocity of the liquid phase, defined [15, 16] as follows.

$$u_l = -\frac{KK_{rl}}{\mu_l}\left[\frac{\partial p_g}{\partial z} - \frac{\partial p_c}{\partial z} - \rho_l g\right] \tag{3}$$

In Eq. (3), the capillary pressure, p_c, is related to the liquid and gas phases which can be written as follows.

$$p_c = p_g - p_l \tag{4}$$

Using Darcy's generalized equation (Eq. (3)), the mass conservation equation for a single-phase model (Eq. (2)) is then rewritten in its final form as follows.

$$\varepsilon\frac{\partial}{\partial t}[\rho_l s] - \frac{\partial}{\partial z}\left[\rho_l\frac{KK_{rl}}{\mu_l}\left(\frac{\partial p_g}{\partial z} - \frac{\partial p_c}{\partial z} - \rho_l g\right)\right] = 0 \tag{5}$$

Assuming the effect of gases pressure is negligible, the Eq. (5) is then reduced to:

$$\varepsilon\frac{\partial}{\partial t}[\rho_l s] + \frac{\partial}{\partial z}\left[\rho_l\frac{KK_{rl}}{\mu_l}\left(\frac{\partial p_c}{\partial z} + \rho_l g\right)\right] = 0 \tag{6}$$

2.2. Equilibrium Relations

The system of conservation equations obtained for Single-phase transport model require constitutive equation for relative permeabilities K_r, capillary pressure p_c, and capillary pressure functions (Brukley-Leverett functions) J. A typical set of constitutive relationships for liquid system is given by the following

$$K_{rl} = s_e^3 \tag{7}$$

Where s_e is the effective water saturation considered the irreducible water saturation, s_{ir}, and can be defined by the following.

$$s_e = \frac{s - s_{ir}}{1 - s_{ir}} \tag{8}$$

The relationship between relative permeability in liquid phase following Eq. (7) is shown in Figure 1.

The capillary pressure p_c is further assumed to be adequately represented by Brukley-Leverett's well know $J(s_e)$ functions. The relationship between the capillary pressure and the water saturation is defined by using Brukley-Leverett functions $J(s_e)$.

$$p_c = p_g - p_l = \frac{\sigma}{\sqrt{K/\varepsilon}}J(s_e) \tag{9}$$

Downloaded by [Thammasat University Libraries] at 00:11 28 April 2014

Where $J(s_e)$ is correlated capillary pressure data obtained by Brukley-Leverett and can be expressed as follows [15, 16].

$$J(s_e) = 0.325(1/s_e - 1)^{0.217} \tag{10}$$

2.3. Initial Condition and Boundary Conditions for Mass Transfer Analysis

Assuming that the initial effective water saturation and initial temperature are constant and uniformed throughout the granular packed bed,

$$t = 0,\ z \geq 0 : s_e = s_0,\ \ T = T_0 \tag{11}$$

Based on experimental conditions, the initial effective water saturation s_0 is given as $s_0 = 0.001$ and the initial temperature T_0 is given as $T_0 = 25$ [°C]. The boundary conditions at the top and the bottom sides of granular packed bed are as follows.

$$\begin{aligned} &t > 0,\ z = 0 :\ F_{l,in} = const \\ &z = L :\ F_{l,out} = \rho_l\ u_l \end{aligned} \tag{12}$$

2.4. Energy Conservation

Ignoring kinetic energy and pressure terms which are usually unimportant, this can be obtained from the total energy conservation of combined solid and liquid phases and by invoking the assumption that the local thermodynamic equilibrium prevails among all volume. The temperature of the sample during unsaturated flow due to supplied hot water is obtained by solving the conventional heat transport equation.

$$\frac{\partial}{\partial t}\left[\left(\rho c_p\right)_T\right] + \frac{\partial}{\partial z}\left[\left(\rho_l c_p u_l\right)T\right] = \frac{\partial}{\partial z}\left[\lambda \frac{\partial T}{\partial z}\right] \tag{13}$$

Where $(\rho c_p)_T$ is the effective heat capacitance of porous layered, and λ is the effective thermal conductivity depending on water saturation. Under thermal equilibrium conditions and using the volume average technique, the effective heat capacitance is given by the following.

$$\left(\rho c_p\right)_T = \rho_l c_{pl} \varepsilon s + \rho_p\ c_{pp}(1 - \varepsilon) \tag{14}$$

Based on the experimental results [15, 16] using glass beads saturated with water, the effective thermal conductivity is represented as a function of the water saturation.

$$\lambda = \frac{0.8}{1 + 3.78e^{-5.95s}} \tag{15}$$

2.5. Initial Condition and Boundary Conditions for Energy Analysis

Assuming that the initial effective water saturation and initial temperature are constant,

$$t = 0,\ z \geq 0 :\ s_e = s_0,\ \ T = T_0 \tag{16}$$

Downloaded by [Thammasat University Libraries] at 00:11 28 April 2014

From experimental conditions, initial effective water saturation s_0 is given as $s_0 = 0.001$ and the initial temperature T_0 is given as $T_0 = 25$ [°C]. The boundary conditions at the top and the bottom sides of porous layered are as follows.

$$t > 0,\ z = 0:\ F_{l,in} = const, \quad q_{l,in} = \rho_l c_{pl} u_l T_{in} \tag{17}$$

2.6. Numerical Schemes

Corresponding to the method of finite differences based on the notion of control volumes, the generalized system of nonlinear equations are integrated over typical rectangular control volumes. After integrating over each control volume within computational mesh, a system of nonlinear equations result whereby each equation within this system can be cast into a numerical discretization of the generalized conservation equation. The equations of heat transport and unsaturated flow are nonlinear because p_c and K_{rl} depend on s. To solve the nonlinear equations the Newton-Raphson iteration procedure are used for each grid. The single-phase model (Eq. (6)) for the internal nodes can be cast into a numerical discretization as follows.

$$\begin{aligned} &\frac{\varepsilon}{\Delta t}(1 - s_{ir})\left(\rho_l(s_{ei}^{n+1} - s_{ei}^{n})\right) \\ &+ \quad \frac{1}{\Delta z}\left(\rho_l\left(\frac{KK_{rl}}{\mu_l}\bigg|_{i+\frac{1}{2}}\left(\frac{P_{ci+1}^{n+1} - P_{ci}^{n+1}}{\Delta z} + \rho_l g_z\right)\right.\right. \\ &\quad \left.\left. - \frac{KK_{rl}}{\mu_l}\bigg|_{i\frac{1}{2}}\left(\frac{P_{ci}^{n+1} - P_{ci-1}^{n+1}}{\Delta z} + \rho_l g_z\right)\right)\right) = 0 \end{aligned} \tag{18}$$

The discretized form of the heat transport equation (Eq. (13)) is given by the following

$$\begin{aligned} &\frac{\left(\rho C_p\right)_{Ti}^{n+1} T_i^{n+1} - \left(\rho C_p\right)_{Ti}^{n} T_i^{n}}{\Delta t} + \frac{\rho_l C_{pl}}{\Delta z}\left(u_{li}^{n+1} T_i^{n+1} - u_{li-1}^{n+1} T_{i-1}^{n+1}\right) \\ &- \frac{1}{\Delta z}\left(\lambda_{i+\frac{1}{2}}^{n+1}\left(\frac{T_{i+1}^{n+1} - T_i^{n+1}}{\Delta z}\right) - \lambda_{i-\frac{1}{2}}^{n+1}\left(\frac{T_i^{n+1} - T_{i-1}^{n+1}}{\Delta z}\right)\right) = 0 \end{aligned} \tag{19}$$

The grid convergence index (GCI) has been used to estimate the uncertainties of grid-spacing for the fine grid solution, which is expressed as follows [21, 22].

$$GCI_{fine}^{21} = \frac{1.25\left|e_a^{21}\right|}{r_{21}^{p} - 1} \tag{20}$$

$$p = \frac{\ln(e_{32}/e_{21})}{\ln(r)} \tag{21}$$

$$e_a^{21} = \left|\frac{\phi_1 - \phi_2}{\phi_1}\right| \tag{22}$$

Where GCI is grid uncertainty, e_a^{21} is approximate relative error, r is refinement ratio, p is apparent order, $e_{32} = \phi_3 - \phi_2$, $e_{21} = \phi_2 - \phi_1$, ϕ_1, ϕ_2, and ϕ_3 is solutions

Downloaded by [Thammasat University Libraries] at 00:11 28 April 2014

for the fine, medium, and coarse grids, respectively. The convergence test carried out using GCI with grid numbers of 80, 40, and 20. These grid numbers represent the coarse, medium, and fine grids with spacing 0.02, 0.01, and 0.005 meters, respectively. The solutions for the fine, medium, and coarse grids are 29.2771, 28.7308, and 27.3773, respectively. From the calculation in Eqs. (20–22), the apparent order is 1.31, the approximate relative error is 1.87%, and the numerical uncertainty in the fine-grid solution is 1.58%. It is reasonable to assume that, at this number of grid, the accuracy of the simulation results is independent from the number of grid for all simulation. This takes 1–5 min on work stations with a dual-core processor (1.73 GHz) and 1 GB of RAM.

Downloaded by [Thammasat University Libraries] at 00:11 28 April 2014

3. EXPERIMENTAL APPARATUS

Figure 2 shows the experimental apparatus for one-dimensional heat transport and water infiltration in granular packed bed. The test column is designed to achieve one-dimensional infiltration flow and heat transport. The test column constructed with inner diameter of 60 mm and 400 mm long column is made of rigid acrylic plastic tubing. The dry porous-ceramic disk at the bottom of the granular packed bed supported the granular particles in the column while allowing a way for air to escape in advance of infiltration depth. Each test column is radially insulated to minimize heat loss through the column walls. A thick plug of insulation is also placed again the ceramic disk of the bottom of column to minimize axial heat loss.

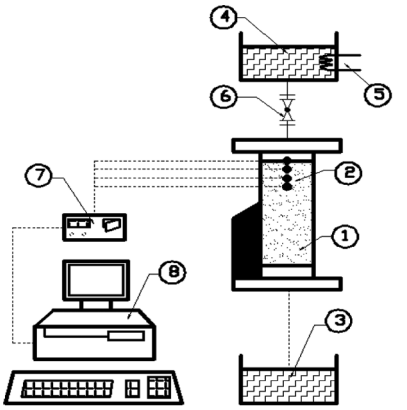

1. Granular packed bed 2.Thermocouples

3. Water tank 4.Hot water tank

5. Heater 6.Control valve

7. Recorder 8.Computer

Figure 2. Experimental apparatus for measuring heat transport and water infiltration in a granular packed bed.

The radial insulation made the columns effectively one-dimensional with respect to heat transfer. Spherical soda lime glass beads with average sizes (d) of 0.15 and 0.4 mm. are used as a sample of granular packed bed. The final assembly thus provided for packing glass beads in the test column with the thermocouples on the axis of the column. The hot water is supplied (supplied water flux, f) from a tank is heated at a certain temperature (T_s) to the top of granular packed bed through a distributor. The hot water supply is controlled by a control valve, where the water flux is calculated from the measured volume used over a period of time. The temperature distributions within test columns are measured with Cu-C thermocouples with diameter of 0.1 mm. These thermocouples are inserted to approximately the center line with 20 mm interval along the vertical axis of test column. The distributions of temperature are recorded by a data logger connected to a computer.

Figure 3 shows the experimental apparatus for measuring water saturation. The position of infiltration depth in the packed bed is captured by digital camera relative to a time-base reference, as shown in Figure 4. At the end of test run, the granular packed bed is cut out into five sections in small volume of 183 cm^3 in order to measure the water saturation. The water saturation in the non-hygroscopic porous packed bed was defined as the fraction of the volume occupied by water to volume of the pores. This water saturation was obtained by weighing dry and wet mass of the sample. Before the experiment, each section was weighed individually to record its dry mass. The porous packed bed was weighed again at 5 and 10 min after the test run. The water saturation formula can be described in the following form [16]:

$$s = \frac{\rho_p \cdot (1 - \varepsilon) \cdot (m_w - m_d)}{\rho_w \cdot \varepsilon \cdot m_d} \tag{23}$$

(a)

(b)

Figure 3. Experimental apparatus for measuring water saturation in a granular packed bed: (a) Weighing scales and (b) the five sections of granular packed bed.

Downloaded by [Thammasat University Libraries] at 00:11 28 April 2014

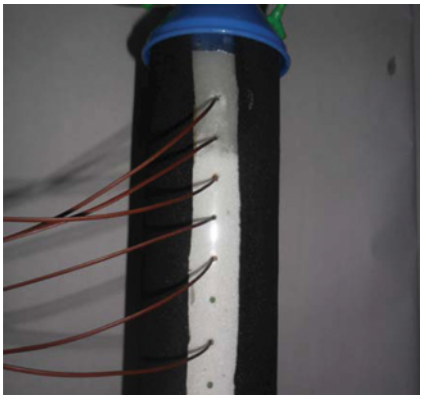

Figure 4. Experimental apparatus for measuring infiltration depth of water.

Where s is water saturation, ρ_p is density of particle, ρ_w is density of water, ε is porosity, and m_w and m_d are wet and dry mass of the sample, respectively.

Initially, the water saturation and the temperature are uniformed within packed bed are 0.06 and 25°C, respectively. The experiments are carried out for the conditions of constant supplied water flux and constant temperature of hot water.

During the experiments, the uncertainty of the data might be due the variations in humidity, room temperature, and human errors. The calculated uncertainties in all tests are less than 2.85%. Additionally, a possible error in the predicted results might be due to the uncertainties in the calculated effective thermal conductivity and the permeability of the porous media.

4. RESULTS AND DISCUSSION

This study described the dynamics of heat transport and water infiltration in various testing condition. The calculated water saturation, temperature distribution, and infiltration depth are compared with the experimental results. Experimentally and numerically, the influences of particle sizes and supplied water flux on heat transport during unsaturated flow are clarified in details. The particle sizes used in this work are 0.15 mm and 0.40 mm in diameter, supplied water fluxes are 0.05 kg/m^{2}s and 0.1 kg/m^{2}s and supplied water temperature is controlled at 55°C and the initial temperature T_0 is given as $T_0 = 25$°C.

The experimental and numerical analysis of heat transport and water infiltration in granular pecked bed in several testing condition are shown in Figures 5–7. Figure 5 shows water saturation at various elapsed times, which corresponds to the diameter of 0.15 mm and supplied water flux of 0.1 kg/m^{2}s. It is found that the experimental results fairly match with numerical results. At elapsed time, the water saturations form wider infiltration layer where the capillary action and gravitational force play an important role on water infiltration process. Figure 6 shows the numerical results for the temperature distributions are in agreement with the experimental results. The temperature distribution at 10 min forms wider and deeper than the temperature distribution at 5 min. The heat conduction and convection from hot water infiltration play an important role on heat transport

Downloaded by [Thammasat University Libraries] at 00:11 28 April 2014

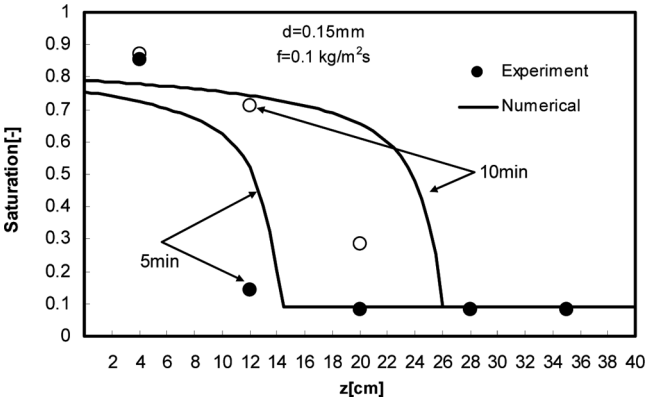

Figure 5. Numerical results of water saturation with the supplied water fluxes 0.1 kg/m^{2}s at 5 and 10 min compared with the experimental results. ($d = 0.15$ mm, and supplied water temperature $T_s = 55$°C.)

phenomena. However, an extension of the heat layer (Figure 6) is not as much as that the infiltration layer (Figure 5). For the infiltration depth, the experimental results is closely match with numerical results, as shown in Figure 7, with supplied water flux of 0.1 kg/m^{2}s and particle size of 0.15 mm.

Figure 8 shows the distributions of water saturation and temperature at various elapsed times as a parameter of supplied water flux, which corresponds to the diameter of 0.15 mm. It is found that a greater supplied water flux in the packed bed corresponds to higher water saturation and forms a wider infiltration layer. The numerical results are in agreement with experimental results. Here, the main transport mechanism that enables water infiltration in granular packed bed is by capillary pressure gradient and gravity. Liquid phase migration is related to capillary pressure gradient as well as temperature (which correspond to that of surface tension, as referred to in Eq. (9). The temperature in the granular packed bed rises

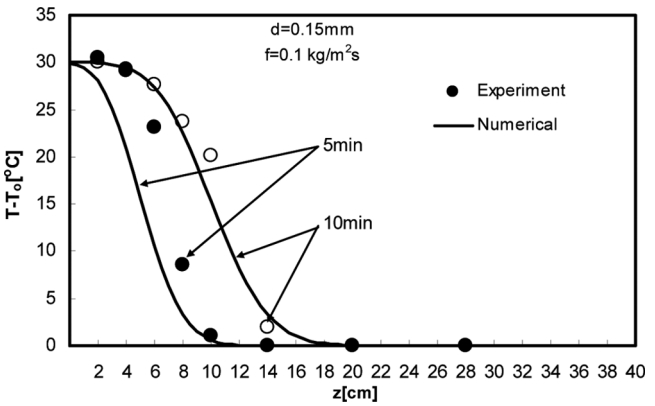

Figure 6. Numerical results of temperature distribution along a granular packed bed with the supplied water fluxes 0.1 kg/m^{2}s at 5 and 10 min compared with the experimental results. ($d = 0.15$ mm, and supplied water temperature $T_s = 55$°C.)

Downloaded by [Thammasat University Libraries] at 00:11 28 April 2014

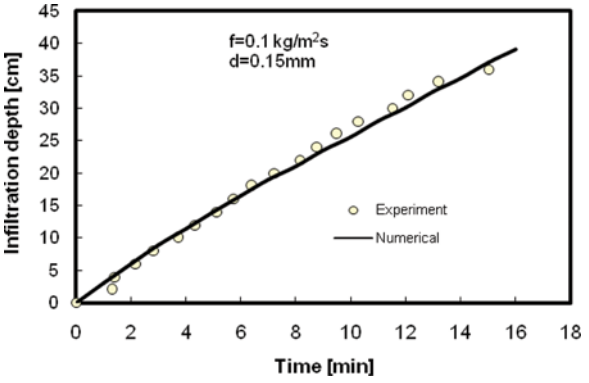

Figure 7. Numerical results of infiltration depth along a granular packed bed with the supplied water fluxes 0.1 kg/m^{2}s, with respect to elapsed times compared with the experimental results ($d = 0.15$ mm, and supplied water temperature $T_s = 55$°C.).

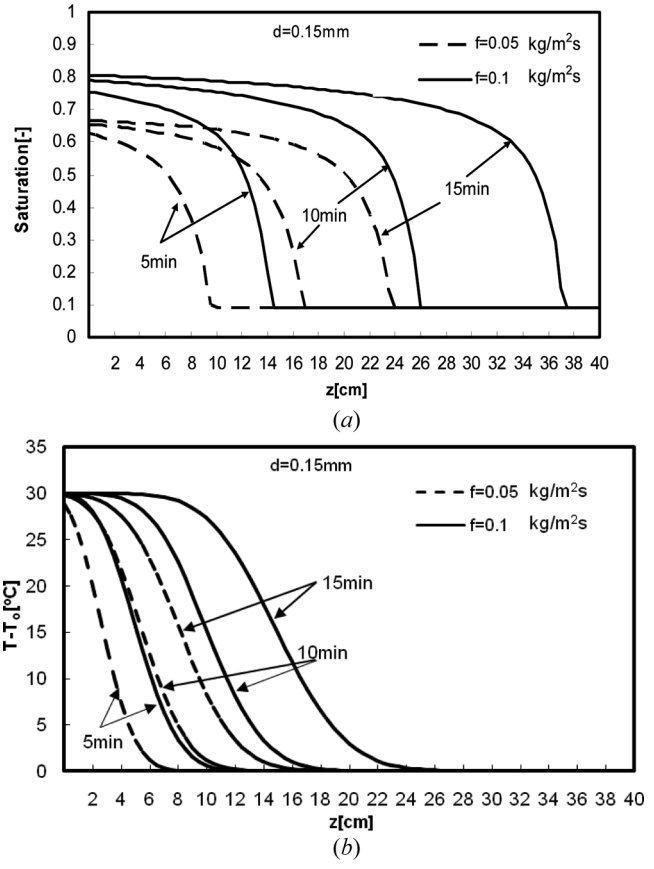

Figure 8. Numerical results of (*a*) temperature profiles and (*b*) water saturation along a granular packed bed with the supplied water fluxes 0.05 kg/m^{2}s and 0.1 kg/m^{2}s with respect to elapsed times. ($d = 0.15$ mm, and supplied water temperature $T_s = 55$°C.)

Downloaded by [Thammasat University Libraries] at 00:11 28 April 2014

due to water infiltration, but the heated layer does not extend as much as the infiltration layer similarly explained in previous figures. Figure 9 shows the distributions of water saturation and temperature at various elapsed times as a parameter of particle size, which corresponds to the supplied water flux of 0.05 kg/m^{2}s. In Figure 9*a*, it is found that using the larger particle size results in lower water saturation but it penetrates much deeper than that of the smaller particle size at each time instant. This is because the larger particle size and hence pore size of these particles reduces the capillary pressure to resist a gravity driven during water infiltration process. In Figure 9*b*, it is found that the temperature distributions of both particle sizes taken at the early stage show nearly the same tendency, that is the temperature decreases to low values within short distance. While in the later stages, the significantly different temperature between the two particles sizes occurs over an infiltration layer. This is because the permeability of the porous medium, as well as the capillary pressure, becomes the strongly dominant factor to the water infiltration and heat transfer in the granular packed bed for the approached steady

Downloaded by [Thammasat University Libraries] at 00:11 28 April 2014

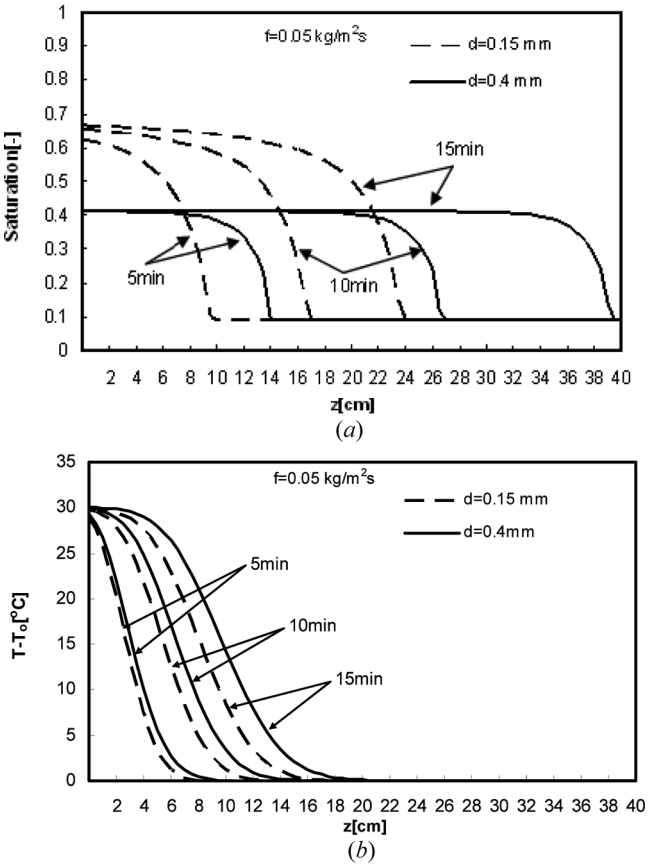

Figure 9. Numerical results of (*a*) temperature profiles and (*b*) water saturation along a granular packed bed with the particle sizes 0.15 and 0.4 mm with respect to elapsed times. (Supplied water flux $f = 0.05$ kg/m^{2}s, and supplied water temperature $T_s = 55$°C.)

state infiltration process. The result shows that a larger particle size leads to faster infiltration rate and forms a wider infiltration layer corresponds to the experimental results.

Figure 10 shows the infiltration depth in a granular packed bed at various elapsed times. The infiltration depth of higher supplied water flux displays a deeper than the infiltration depth of lower supplied water flux, as shown in Figure 10*a*. This figure shows the influence of particle sizes on the distributions of saturation and temperature with respect to elapsed times under the same particle sizes of 0.15 mm with different supplied water flux (0.05 kg/m^2s and 0.1 kg/m^2s). The effect of particle size on infiltration depth is also clearly shown in Figure 10*b*. This figure shows the infiltration depth with respect to elapsed times of the packed bed as a parameter of particle sizes (0.15 mm and 0.4 mm) at supplied water flux of 0.05 kg/m^2s. It is found that the infiltration depth of the larger particle size displays

Downloaded by [Thammasat University Libraries] at 00:11 28 April 2014

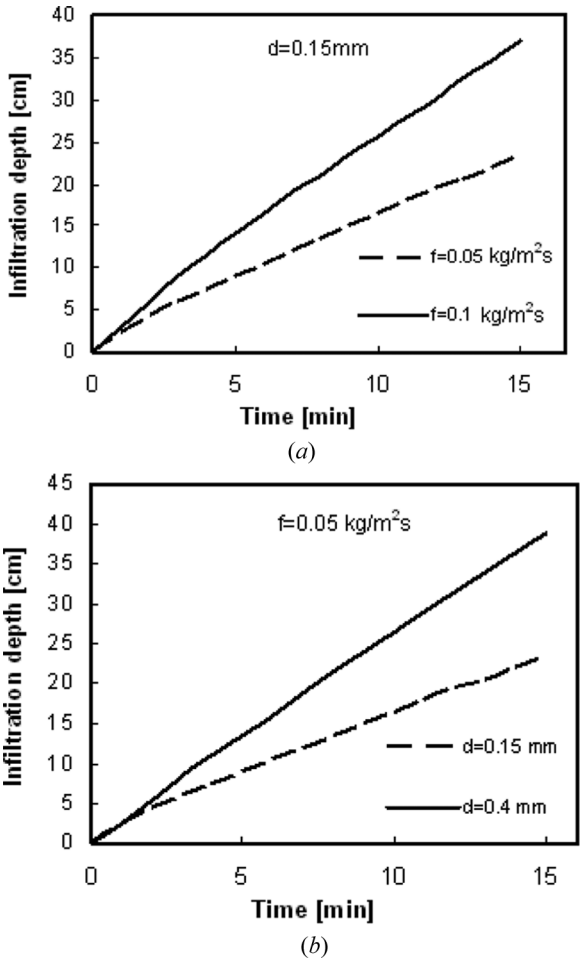

Figure 10. Numerical results of (*a*) infiltration depth as a parameter of supplied water flux and (*b*) particle size along a granular packed bed with respect to elapsed times.

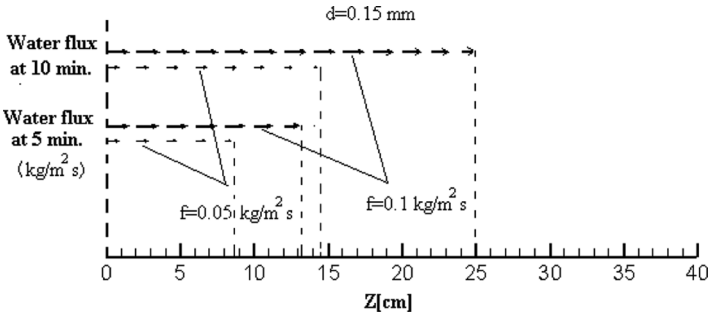

Figure 11. Vectors of water fluxes as a parameter of supplied water flux along a granular packed bed at 5 and 10 min. ($d = 0.15$ mm, $f = 0.05$, and 0.1 kg/m^{2}s.)

a deeper than the infiltration depth of smaller particle size, due to the effect of the hydrodynamic characteristics (Capillary pressure and gravity). Next, the water fluxes flow (vector profiles) will be presented in figures 11 and 12, where it is obtained from numerical results. Figure 11 shows the vectors of water fluxes as a parameter of supplied water flux at 5 and 10 min. As shown in Figure 11, it is found that at 5 min, the infiltration depth of the water flux vectors are 14 cm and 9 cm for the supplied water fluxes of 0.1 kg/m^{2}s and 0.05 kg/m^{2}s, respectively. While at 10 min, the infiltration depth of the water flux vectors are 25 cm and 10 cm for the supplied water fluxes of 0.1 kg/m^{2}s and 0.05 kg/m^{2}s, respectively. This is attributed to the presence of a higher volumetric body force of higher supplied water flux (0.1 kg/m^{2}s) that accelerated a faster water flux than that of 0.05 kg/m^{2}s. Figure 12 shows the vectors of water fluxes as a parameter of particle size at 5 and 10 min, with the water flux at the surface of 0.1 kg/m^{2}s. As shown in Figure 12, it is found that at 5 min, the infiltration depth of the water flux vectors are about 15 cm and 13 cm for the particle size of 0.4 mm and 0.15 mm, respectively. While at 10 min, the infiltration depths of the water flux vectors are about 35 cm and 25 cm for the particle size of 0.4 mm and 0.15 mm, respectively. From the results, the magnitudes of water flux vectors near the surface of the packed bed are found to be higher than that of the infiltration front region. This is because the water saturation is higher near the surface of the

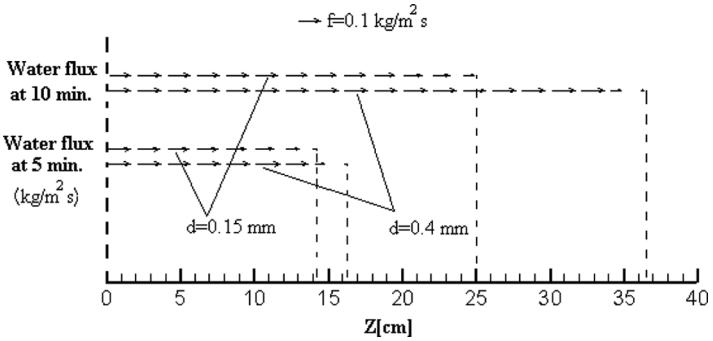

Figure 12. Vectors of water fluxes as a parameter of particle size along a granular packed bed at 5 and 10 min. ($f = 0.05$ kg/m^{2}s, $d = 0.15$, and 0.4 mm.)

Downloaded by [Thammasat University Libraries] at 00:11 28 April 2014

packed bed, and at the infiltration front region where the water saturation is low resulting in the different magnitude of the relative permeability, as shown in Figure 1.

5. CONCLUSION

The heat transport and water infiltration in granular packed bed with unsaturated flow is investigated numerically and experimentally. The following are the conclusions of this work.

1. The heat transport hardly occurs in the layer close to the infiltration front because the temperature of water infiltrating gradually drops due to heat transport upstream. Furthermore, the effect of particle size on the discrepancy of heated layers is smaller compared to that of the water infiltration layers.
2. It is found that the gravity and capillary pressure (with varying particle sizes) have clearly exhibited influence on the water infiltration process in all testing conditions. The numerical results of the distribution temperature, water infiltration, and infiltration depth are in agreement with the experimental results. The numerical results closely match with the experimental results obtained from S. Suttisong and P. Rattanadecho [17].
3. The water flux vectors near the surface of the packed bed are found to be higher than that of the infiltration front region. This is because the water saturation is higher near the surface of the packed bed, and at the infiltration front region where the water saturation is low.
4. The interplay between gravity force and water saturation impacts on water flux vectors, which are essential for numerical study of water infiltration process.

The idea behind this work can be used as guidance for special design of water flow in porous material processes in the future.

Downloaded by [Thammasat University Libraries] at 00:11 28 April 2014

FUNDING

This work was supported by the Nation Research University Project of Thailand Office of Higher Education Commission and Thailand Research Fund.

REFERENCES

1. F. Stauffer and T. Dracos, Experimental and Numerical Study of Water and Solute Infiltration in Layered Porous Media, *J. of Hydrology*, vol. 84, pp. 9–34, 1986.
2. R. Haverkamp, M. Vauclin, J. Touma, P. J. Wierenga, and G. Vanchaud, A Comparison of Numerical Simulation Models for One-Dimensional Infiltration, *Soil Sci. Soc. Am. J.*, vol. 41, pp. 285–294, 1977.
3. J. Y. Parlange, Theory of Water Movement in Soils: One-Dimensional Infiltration, *Soil Science*, vol. 111, pp. 170–174, 1972.
4. B. A. Scherfler and Z. Xiaoyong, A Fully Coupled Model for a Water Flow and Air Flow in Deformable Porous Media, *Water Resources Research*, vol. 29, pp. 155–167, 1993.
5. H. Gvirtzman, E. Shalev, O. Dahan, and Y. H. Hatzor, Large-Scale Infiltration Experiments into Unsaturated Stratified Loess Sediment: Monitoring and Modeling, *Int. J. of Hydrology*, vol. 349, pp. 214–229, 2008.

6. J. T. Kulongoski and J. A. Izbicki, Simulation of Fluid Heat Transport to Estimate Desert Stream Infiltration, *Ground Water*, vol. 46, pp. 462–474, 2008.
7. Z. Xiuqing, M. W. Van Liew, and G. N. Flerchinger, Experimental Study of Infiltration into a Bean Stubble Field During Seasonal Freeze-Thaw Period, *Soil Science*, vol. 166, pp. 3–10, 2001.
8. M. Abriola and F. Pinder, A Multiphase Approach to the Modeling of Porous Media Contamination by Organic Compounds, 1. Equation development, *Water Resources Research*, vol. 21, pp. 11–18, 1985.
9. P. Binning and M. A. Celia, Practical Implementation of the Fractional Flow Approach to Multi-Phase Flow Simulation, *Int. J. Adva. in Water Resources*, vol. 22, pp. 461–478, 1999.
10. P. Ratanadecho, K. Aoki, and M. Akahori, Experimental and Numerical Study of Microwave Drying in Unsaturated Porous Material, *Int. Comm. in Heat and Mass Transfer*, vol. 28, pp. 605–616, 2001.
11. Y. Ma, S. Feng, D. Su, G. Gao, and Z. Huo, Modeling Water Infiltration in a Large Layered Soil Column with a Modified Green-Ampt Model, and HYDRUS-1D, *Int. J. Computer and Electronics in Agriculture*, vol. 71S, pp. S40–S47, 2010.
12. E. J. Henry and J. E. Smith, Numerical Demonstration of Surfactant Concentration-Dependent Capillarity and Viscosity Effects on Infiltration from a Constant Flux Line Source, *Int. J. of Hydrology*, vol. 329, pp. 63–74, 2006.
13. J. H. Eric and E. S. Jame, Numerical Demonstration of Surfactant Consentration-Dependent Capillarity and Viscosity Effects on Infiltration from a Constant Flux Line Source, *Int. J. of Hydrology*, vol. 329, pp. 63–74, 2006.
14. W. Quan-Jiu, R. Horton, and F. Jun, An Analytical Solution for One-Dimensional Water Infiltration and Redistribution in Unsaturated Soil, *Int. J. Pedosphere*, vol. 19, pp. 104–110, 2009.
15. K. Aoki, M. Hattori, M. Kitamura, and N. Shiraishi, Characteristics of Heat Transport in Porous Media with Water Infiltration, *ASME/JSME Thermal Eng. Proceeding*, vol. 4, pp. 303–308, 1991.
16. P. Ratanadecho, K. Aoki, and M. Akahori, Influence of Irradiation Time, Particle Sizes and Initial Moisture Content during Microwave Drying of Multi-Layered Capillary Porous Materials, *ASME J. Heat Transfer*, vol. 124, pp. 151–161, 2002.
17. S. Suttisong and P. Rattanadecho, The Experimental Investigation of Heat Transport, and Water Infiltration in Granular Packed Bed Due to Supplied Hot Water from the Top: Influence of Supplied Water Flux, Particle Sizes and Supplied Water Temperature, *Exp. Them. Fluid Sci.*, vol. 35, pp. 1530–1534, 2011.
18. I. Fayssal and F. Moukalled, A New Numerical Approach for Predicting the Two-Phase Flow of Refrigerants during Evaporation and Condensation, *Numer. Heat Transfer B*, vol. 62, pp. 341–369, 2012.
19. G. Yu, B. Yu, S. Sun, and W. Q. Tao, Comparative Study on Triangular and Quadrilateral Meshes by a Finite-Volume Method with a Central Difference Scheme, *Numer. Heat Transfer B*, vol. 62, pp. 243–263, 2012.
20. N. Georgios, Lygidakis, and K. Ioannis Nikolos, Using the Finite-Volume Method and Hybrid Unstructured Meshes to Compute Radiative Heat Transfer in 3-D Geometries, *Numer. Heat Transfer B*, vol. 62, pp. 289–314, 2012.
21. I. B. Celik, U. Ghia, P. J. Roache, C. J. Freias, H. W. Coleman, and P. E. Raad, Procedure for Estimation and Reporting of Uncertainty Due to Dicrestization in CFD Application, *J. Fluids Eng.—Trans. ASME*, vol. 130, pp. 078001, 2008.
22. T. Xing and F. Stern, Factors of Safety for Richardson Extrapolation, *J. Fluids Eng.—Trans. ASME*, vol. 132, pp. 061403–1, 2010.

Downloaded by [Thammasat University Libraries] at 00:11 28 April 2014

Renewable and Sustainable Energy Reviews 37 (2014) 715–733

Contents lists available at ScienceDirect

Renewable and Sustainable Energy Reviews

journal homepage: www.elsevier.com/locate/rser

Applications of microwave energy in cement and concrete – A review

Natt Makul [a,*], Phadungsak Rattanadecho [b], Dinesh K. Agrawal [c]

[a] Department of Building Technology, Faculty of Industrial Technology, Phranakhon Rajabhat University, Changwattana Road, Bangkhen, Bangkok 10220, Thailand
[b] Center of Excellence in Electromagnetic Energy Utilization in Engineering (CEEE), Thammasat University (Rangsit Campus), Khlong Luang, Prathum Thani 12121, Thailand
[c] Materials Research Institute, Pennsylvania State University, University Park, PA 16802, USA

ARTICLE INFO

Article history:
Received 31 December 2013
Received in revised form
30 April 2014
Accepted 17 May 2014

Keywords:
Microwave processing
Characterization
Electrical properties
Cement
Concrete

ABSTRACT

Microwave heating is a highly efficient technique for various thermal processes. Advantages of microwave heating compared to conventional processing methods include energy-saving rapid heating rates and short processing times, deep penetration of the microwave energy (which allows heat to be generated efficiently without directly contacting the work-piece), instantaneous and precise electronic control, clean heating processes, and no generation of secondary waste. Microwave energy processes for heating, drying, and curing have been developed for numerous laboratory-scale investigations and, in some cases, have been commercialized. Microwave energy use should theoretically be advantageous in the processing of cement and concrete materials (*e.g.*, hydraulic Portland cement, aggregate, and water). These materials exhibit excellent dielectric properties and, therefore, should be able to absorb microwave energy very efficiently and instantaneously convert it into heat.

This paper provides a comprehensive review of the use of microwave energy to process cement and concrete materials, as well as a critical evaluation of currently utilized microwave heating mechanisms and high-performance microwave systems. The current status of microwave applications and future research and development trends are also discussed, including such thermal processing methods as the high-temperature sintering of cement materials, the accelerated curing of precast concrete products, as well as the drilling and cleaning of decontaminated concrete surfaces by the built-up internal pressure. The results of this review indicate that microwave heating is directly associated with dielectric loss by the cement and concrete. Microwave processing can be used to improve clinkering and to reduce the clinkering temperature by about 100 °C. Considerations when constructing mathematical models of microwave heating for cement and concrete should include the influences of heat and mass transfer during microwave curing on the temperature difference in the concrete, the degree of uniformity of the internal structure, and the ultimate performance of the product. Future studies of microwave energy in cement and concrete applications might include investigations of adaptive (time-dependent) dielectric properties, coupling chemical reactions in the presence of microwave energy, the design and construction of suitable microwave systems, and the prediction of related phenomena (*e.g.*, thermal runaway, as a highly regulated safety issue).

© 2014 Elsevier Ltd. All rights reserved.

Contents

1. Introduction . . . 716
2. Dielectric properties . . . 717
 2.1. Dielectric theories . . . 718
 2.2. Measurement techniques and calculation . . . 718
  2.2.1. Measurement techniques . . . 718
  2.2.2. Measurement of cement and concrete . . . 721
  2.2.3. Measurement of blended cement and concrete . . . 722
  2.2.4. Modeling work . . . 722

* Corresponding author. Tel./fax: +66 2 522 6637.
E-mail address: shinomomo7@gmail.com (N. Makul).

http://dx.doi.org/10.1016/j.rser.2014.05.054
1364-0321/© 2014 Elsevier Ltd. All rights reserved.

3. Microwave systems . . . 723
4. Applications of microwave to cement . . . 724
4.1. Cement synthesis . . . 724
4.2. Improving cementitious properties . . . 725
5. Applications of microwave to concrete . . . 725
5.1. Acceleration of curing . . . 725
5.2. Decontamination and decommissioning of concrete . . . 726
5.3. Nondestructive monitoring . . . 727
5.4. Drilling/melting of concrete . . . 727
6. Theoretical investigations of microwave processing . . . 727
6.1. Electromagnetic theories . . . 727
6.2. Numerical techniques and simulation . . . 729
7. Health and safety of microwave processing . . . 729
8. Conclusions . . . 730
8.1. Major review findings . . . 730
8.2. Future trends of research and development . . . 731
Acknowledgments . . . 731
References . . . 732

1. Introduction

Cement and concrete products are well accepted as man-made construction materials. Owing to their numerous advantages (*e.g.*, easy handling of compression forces, brittle nature that enables a rigid structure to be obtained, transportability, and durability/ability to withstand severe environments), these materials are used widely in civilian buildings and universally in infrastructures. A report on global cement use published by Morgan Stanley research [1] (Table 1) found that worldwide cement consumption decreased in the 2006–2013 period due to the economic downturn. The years 2012 and 2014 showed the slowest growth for every country in the world, except China and India, since the crisis years of 2007–2009. However, cement consumption is expected to increase gradually from 2014 forwards.

The increased production of cement and concrete leads to the increased consumption of energy. Conventionally, the cement production procedure includes a clinkering process, consisting of precalcination and pyro-processing steps, as shown in Fig. 1 [2,3]. This process requires energy consumption, especially in the cyclone preheater, precalciner (cyclone preheater plus calciner), and rotary kiln steps (burning consumes 60–70% of the fuel input). The average specific thermal energy consumption in a conventional cement clinker manufacturing process is about 31.5 GJ per ton of clinker [3].

High-level energy consumption, which refers to both a high level of consumption and a long time for the burning process, is affected by the heat transfer mechanism and the thermal conductivity of the cement-making materials (*i.e.*, calcium oxide, CaO; silicon dioxide, SiO_2; alumina oxide, Al_2O_3; and ferric oxide, Fe_2O_3). When cement is made with conventional burning using fuel (*e.g.*, oil and gas), the cement components are heated by an external heat source, and heat is transferred via conduction from the outside inward. Thermal properties, such as the specific heat, latent heat, and so on, regulate the kinetics of the heating process. However, cement-making materials have intrinsically low thermal conductivities and low heat transfer rates. Thus, they must be heated for long times until the inner portion of cement melts and sinters at a high temperature, to become a cement clinker nodule (at $\sim$1450 °C). To overcome this problem, microwave heating may be applied in the burning process of cement.

Unlike conventional heating, microwave heating principally occurs when the electric field of the microwave interacts with a material. Energy from the field is transferred to the molecular bonds of the materials. This energy transfer causes the bonds to vibrate and leads to heat dissipation within the material. Microwave heating is particularly efficient for heating dielectric materials (*e.g.*, microwave heating was at least twice as effective as conventional methods for heating dielectric materials [4,5]). Therefore, microwave heating should be useful in the cement and concrete industry, as cement-making materials exhibit excellent dielectric properties and should be able to absorb microwave energy very efficiently.

Furthermore, internal (volumetric) heating by microwave energy offers many benefits for the cement and concrete industries, including [6,7]:

- Rapid heating rates and short processing times, which save energy and time.
- Deep penetration of the microwave energy (in cement and concrete materials, a microwave system operating at 2.45 GHz can typically penetrate several centimeters), which allows heat to be generated efficiently without directly contacting the cement constituents.
- Instantaneous and precise electronic control, which is convenient for designing and constructing heating systems.
- Unique and fine microstructural development, which permits better properties of produced cement.
- Clean heating processes that do not generate secondary waste.

Based on International Telecommunication Union (ITU) regulations, the electromagnetic frequency band for non-telecommunication (*e.g.* industrial, scientific, and medical) purposes ranges from 6.765 MHz to 246 GHz. Microwaves are electromagnetic waves with frequencies ranging from 300 MHz to 300 GHz (wavelengths from 0.001 to 1.0 m). Microwave systems operate at average frequencies of 896 ± 10 MHz (in the UK), 915 ± 13 MHz (in North and South America), and 2450 ± 5 MHz (worldwide, except where 2375 ± 50 MHz is used), as assigned by the International Microwave Power Institute (IMPI). When used for Industrial, Scientific, and Medical (ISM) purposes, microwave systems are most often operated in the range from 433.92 MHz to 40.00 GHz [4].

Many investigations and practices have recently reported using microwave heating for concrete applications, such as for accelerated curing [8,9], decommissioning and decontaminated surfaces [10,11], and drilling/melting [12,13]. Moreover, microwave systems have been applied as high-performance nondestructive monitoring and surveying methods for cement and concrete structures [14,15].

This paper offers a comprehensive and systematic review of the use of microwave energy in cement and concrete materials. This review systematically summarizes important results from previous experimental and numerical studies, covering such areas as the

Nomenclature

$\vec{B}$	magnetic flux density (Wb/m^2)
$\vec{D}$	electric flux density (C/m)
D_p	penetration depth (m)
$\vec{E}$	electric field intensity (V/m)
$\vec{H}$	magnetic field intensity (A/m)
L	material length
$\vec{P}$	energy flux density (W/m^2)
Q	local electromagnetic heat-generation (J)
T	temperature (°C)
S_{11}	reflected scattering coeffient from Port 1
S_{22}	reflected scattering coeffient from Port 2
S_{21}	transmitted scattering coeffient from Port 1
S_{22}	transmitted scattering coeffient from Port 2
V	volume (m^3)
a	thermal diffusivity (m^2/s)
c_p	heat capacity at constant pressure (J/(kg · K))
f	frequency (Hz)
q	electric charge density (C/m^3)
t	time (s)
e	Euler's number (=2.7182818…)

Greek letters

Γ	reflection coefficient
σ	effective conductivity (S/m)
ε_0	permittivity of free space (=8.8514 × 10^{-12}) (F/m)
ε_∞	permittivity at the high frequency limit
ε_s	static, low-frequency permittivity
ε^*	complex (electric) permittivity, $\varepsilon' - j\varepsilon''$
ε_r	relative permittivity
ε_r'	relative dielectric constant
ε_r''	relative dielectric loss factor
μ^*	complex magnetic permeability, $\mu' - j\mu''$
μ_o	permeability of free space (=4π × 10^{-7})(m kg/s^2 A^2) or (h/m)
μ_r	relative permeability
υ	microwave speed in the dielectric material (m/s)
ω	angular frequency, field's frequency (s^{-1})
tan δ	loss tangent coefficient ($\varepsilon''/\varepsilon'$)
σ	electric conductivity (1/Ohm)
τ	characteristic relaxation time (s)
ρ	density (kg/m^3)
λ_g	wavelength in sample.
$\lambda_{\text{free space}}$	wavelength of free space
λ_{cutoff}	wavelength of cutoff frequency

dielectric properties of cement and concrete, the mechanisms of microwave processing, the applications of microwave systems for cementitious materials, the health and safety of microwave processing, and future Research and Development (R&D) trends. Laboratory-based R&D and a practice-based scale innovation approach are discussed.

On the basis of findings in this review, some topics are recommended for further study and development, including the analysis of adaptive (time-dependent) dielectric properties, the coupling of heating mechanisms with the chemical reactions in cement and concrete, the design and construction of suitable microwave systems for use with cement and concrete, and the prediction of related phenomena (*e.g.*, thermal runaway, as a highly regulated safety issue). Findings from this review can be used to guide future R&D for developing microwave energy applications in the cement and concrete field, in order to decrease energy consumption compared to other energy sources in heating/burning and to reduce the high temperatures needed for producing cement and curing concrete. These findings can also aid in the development of innovative and nondestructive microwave-based methods for monitoring the properties of cement and concrete products, for surveying deteriorated concrete structures, and for selecting suitable methods for concrete repair.

2. Dielectric properties

Microwave heating involves the interactions between electromagnetic energy and the properties of dielectric material, especially

Table 1
Cement consumption growth by region (year over year) (%) [1].

Region	*Year*									
	2006	*2007*	*2008*	*2009*	*2010*	*2011*	*2012*	*2013E[*]*	*2014E*	*2015E*
Western Europe	5.0	0.0	−9.8	−19.5	−6.3	−0.5	−14.2	−6.8	−1.1	1.7
Eastern Europe	15.7	7.6	0.2	−12.6	3.0	8.6	−4.4	2.9	1.5	3.5
Former Soviet Union	13.8	16.8	0.2	23.4	9.5	13.9	9.2	4.3	3.8	4.1
North America	−0.3	−7.9	−15.8	−26.3	0.9	2.5	8.8	3.8	6.4	6.2
Latin America	11.8	8.5	6.4	−2.0	5.9	7.0	3.9	2.1	3.7	3.5
Middle East and North Africa (MENA)	7.6	11.8	10.2	7.8	6.6	1.6	4.1	1.4	3.9	5.1
Sub-Saharan Africa	11.8	15.7	1.9	5.3	3.3	11.4	9.6	7.0	6.8	7.1
China	14.9	13.1	3.3	18.3	14.4	10.8	6.6	7.1	3.5	2.1
India	12.2	8.9	5.0	10.6	7.2	6.2	6.7	3.6	5.2	6.8
North Asia	2.5	−0.8	−4.3	−8.9	2.5	2.0	1.8	3.3	0.0	0.6
South Asia	4.3	5.7	7.5	6.0	8.3	6.3	7.1	2.4	3.7	5.1
Australia/Pacific	−0.5	6.5	3.8	−8.5	1.0	4.9	−2.1	−0.8	3.0	−4.1
World (excl-China)	7.3	5.5	0.4	−4.7	4.0	5.1	3.1	2.1	3.5	4.6
Emerging Markets (excl-China)	9.8	9.3	5.1	0.7	6.2	6.1	4.9	2.8	3.9	4.9

Remark: Source from industry and national sources, Global Cement Report, Morgan Stanley Research estimates ($E^{[*]}$).

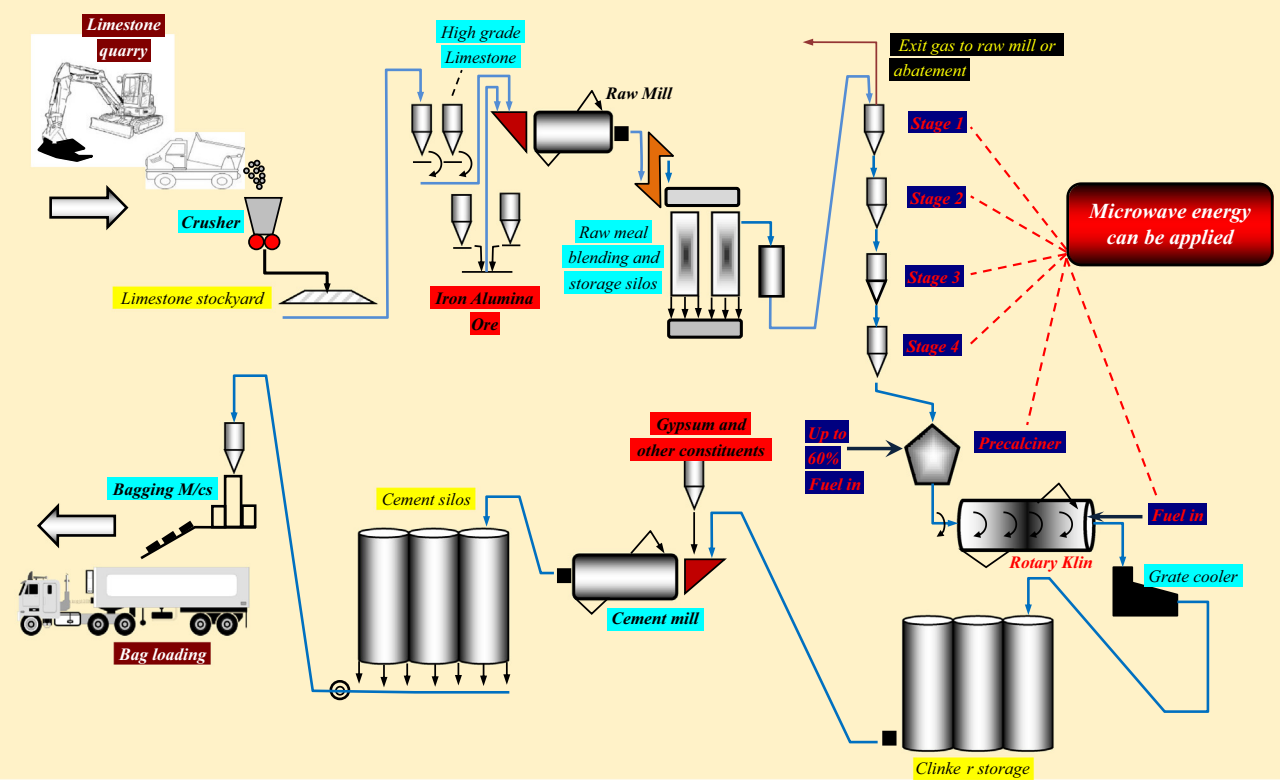

Fig. 1. Overview of a conventional cement manufacturing process [2,3].

dielectric propery. This property plays an important role to describe the behavior of concrete materials when subjected to microwave energy. This section describes theories of dielectric, measurement techniques of cement and concrete, and blended cement and concrete. Modeling work of calculation of cement is also explained.

2.1. Dielectric theories

Cement and concrete are dielectric materials. Their intrinsic properties affect the way they interact with the electric and magnetic fields of the microwaves. Dielectric property can be characterized by two independent electromagnetic properties: the complex (electric) permittivity ε* and the complex (magnetic) permeability μ*. However, most common concrete materials are non-magnetic and yield permeability μ* that is very close to the permeability of free space ($=4\pi\times10^{-7}$)(m kg/s^2 A^2) [16]. Thus, the complex (electric) permittivity ε*, which comprises real and imaginary parts that can be defined as the relationship expressed in Eq. (1):

$$\varepsilon_r^* = \varepsilon_r' - \vec{j}\varepsilon_r'' \tag{1}$$

where ε_r' and ε_r'' are the real part and imaginary parts respectively, of the complex permittivity, and $\vec{j}=\sqrt{-1}$.

The real part of the relative complex permittivity, referred to as the dielectric constant, ε_r', measures how much energy transferred from an external electric field is stored in a material. The imaginary one, ε_r'', measures how lossy a material is to an external electric field and is referred to as the relative loss factor. Besides an essential ratio that shows the energy lost (relative loss factor) to the energy stored (relative dielectric constant) in a material is given as loss tangent tan δ, as shown in Eq. (2):

$$\tan\delta = \varepsilon_r''/\varepsilon_r' \tag{2}$$

The dielectric properties of the concrete including dielectric constant and loss factor are important parameters in microwave-dielectric material interactions. They are strongly dependent on moisture content, temperature, extent of hydration. Reports of prior investigations [17–19] studies did not attempt to correlate experimental results with dielectric properties in order to develop a fundamental link to the field equations listed in Eq. (3), a task that must be accomplished in order to predict real-time changes during microwave curing. The internal distribution of free water in the sample is also an important consideration until the structure has been formed since this will decrease the efficiency of microwave heating.

$$\left.\begin{aligned}
\varepsilon(\omega) &= \varepsilon_\infty + \frac{\varepsilon_s-\varepsilon_\infty}{1+(i\omega\tau)^{1-\alpha}} - j\frac{\sigma(0)}{\omega\varepsilon_0} \quad (Maxwell\text{–}Wagner\ effect)\\
\varepsilon(\omega) &= \varepsilon_\infty + \frac{\varepsilon_s-\varepsilon_\infty}{1+(2i\omega\tau)^{\beta}+i\omega\tau} - j\frac{\sigma(0)}{\omega\varepsilon_0} (Double\ layer\ polarization)\\
\varepsilon(\omega) &= \varepsilon_\infty + \frac{\varepsilon_s-\varepsilon_\infty}{1+(i\omega\tau)} - j\frac{\sigma(0)}{\omega\varepsilon_0} \quad (Debye\ effect)
\end{aligned}\right\} \tag{3}$$

2.2. Measurement techniques and calculation

2.2.1. Measurement techniques

Many techniques have been developed to understand the dielectric property (Table 2), including the transmission/reflection line, perturbation, free-space, and open-ended methods [20,21]. Selection of the appropriate method depends, in part, on the operating frequency of the microwave system (Fig. 2) [21]. For example, at the commonly utilized frequency of 2.45 ± 0.05 GHz, the dielectric property should be measured by transmission line. This method allows the measurement of specimens with a slab-shaped geometry placed across the cavity. However, this method is limited by the air-gap effect. The open-ended probe method could also be used, which involves measuring the phase and amplitude of the reflected signal at the end of an open-ended coaxial line inserted in a specimen. This method, too, has limitations, due to the reflection effect from the specimen.

Choices of the measurement equipment and sample holder design depend on several factors, including the dielectric materials to be

Table 2
A summary of the technique for measuring dielectric properties [20,21].

Technique	*Characteristics*	*Feature*	*Dielectric properties*
Transmission/ reflection line	The Material Under Test (MUT) must be made into slab geometry. *Advantages:* • Common coaxial lines and waveguide • Used to determine both ε_r, μ_r of the MUT *Disadvantages:* • Limit by the air-gap effect • Limit to low accuracy	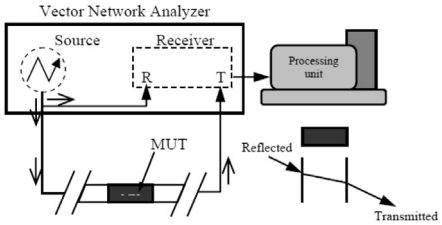	ε_r, μ_r
Perturbation (Cavity) (Resonant)	The measurement is made by placing a sample completely through the center of a waveguide that has been made into a cavity. *Advantages:* • Simple and easy data reduction • Accuracy *and* high temperature capability • Suite to low dielectric loss materials *Disadvantages:* • Need high frequency resolution Vector Network Analysis (VNA) • Limit to narrow band of frequency band only	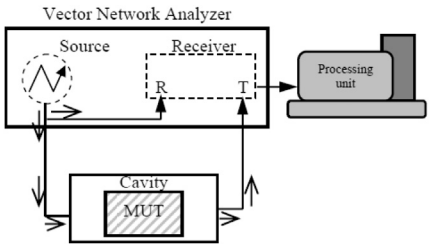	ε_r, μ_r
Free-space	The sample is placed between a transmitting antenna and a receiving antenna, and the attenuation and phase shift of the signal are measured. *Advantages:* • Used for high frequency and allow nondestructive measurement • Measure MUT in hostile environment *Disadvantages:* • Need large and flat MUT and diffraction effects at the edge of sample • Limit to low accuracy	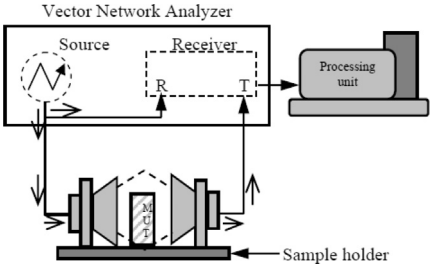	ε_r, μ_r
Open ended probe	The technique calculates the dielectric properties from the phase and amplitude of the reflected signal at the end of an open-ended coaxial line inserted into a sample to be measured. *Advantages:* •After calibration, can be routinely measured in a short time *Disadvantages:* •Available for reflection measurement	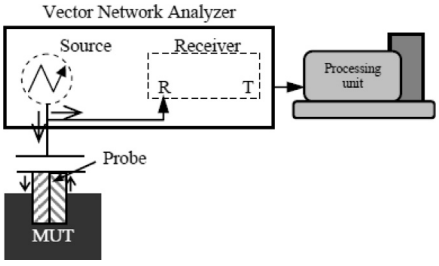	ε_r

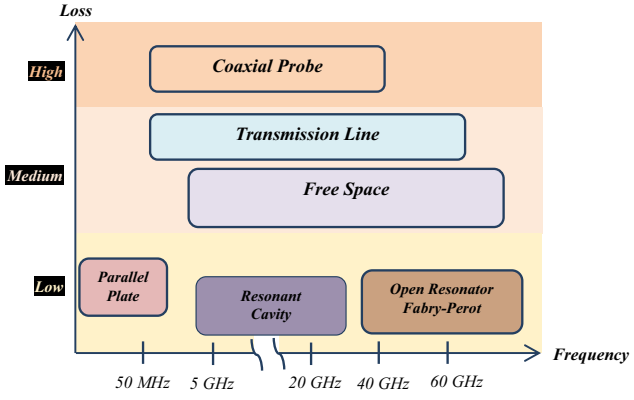

Fig. 2. Summary of dielectric measuring techniques [21].

characterized, extent of the research, as well as the equipment and resources that are available. Two types of dielectric analyzers have recently been used: the scalar network analyzer and the Vector Network Analyzer (VNA). The VNA is quite popular, very versatile, and useful for extensive studies; however, it is also very expensive. Although less expensive, scalar network analyzers and impedance analyzers are generally still too costly for many applications.

The HP 8510 [22] is a VNA that has been used to measure the dielectric properties of cementitious materials, including cement paste, mortar, and concrete. It can measure the magnitude and phase characteristics of linear networks, such as filters, amplifiers, attenuators, and antennae. As with all network analyzers, and as shown in Fig. 3(a), the HP 8510 apparatus measures both reflection and transmission of electromagnetic waves at an interface. An incident signal generated by an RF source is compared with the signal transmission through the analyzer or reflected from the wave input

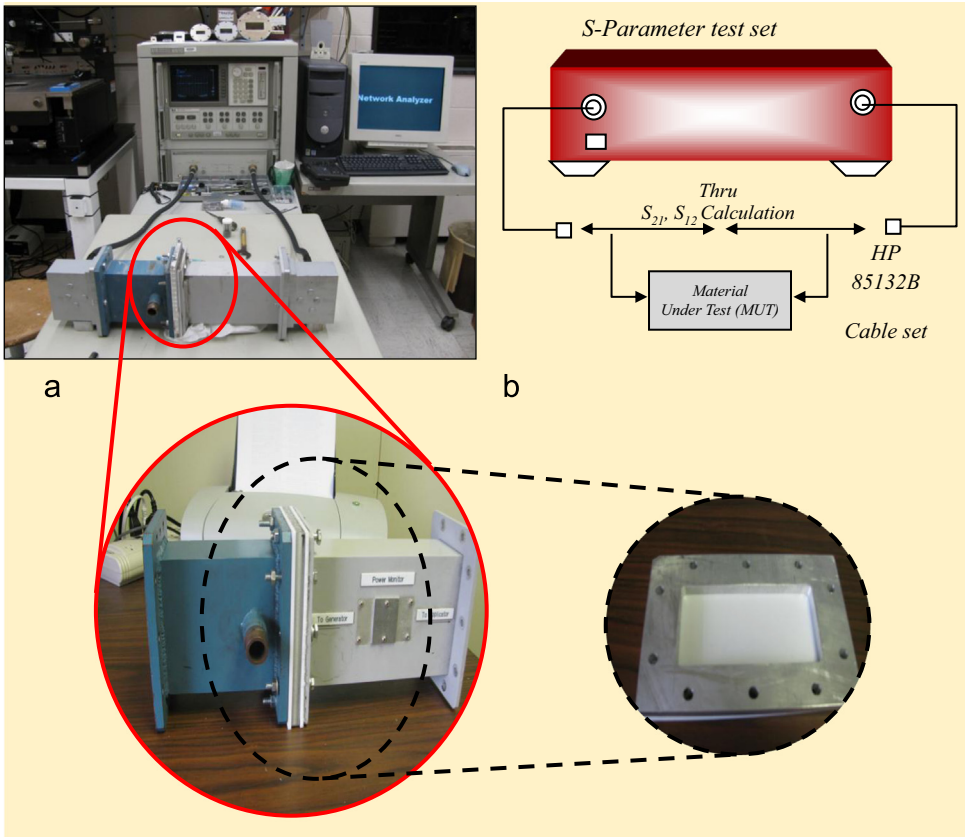

Fig. 3. (a) Network analyzera and (b) schematic of *S*-parameter test [22].

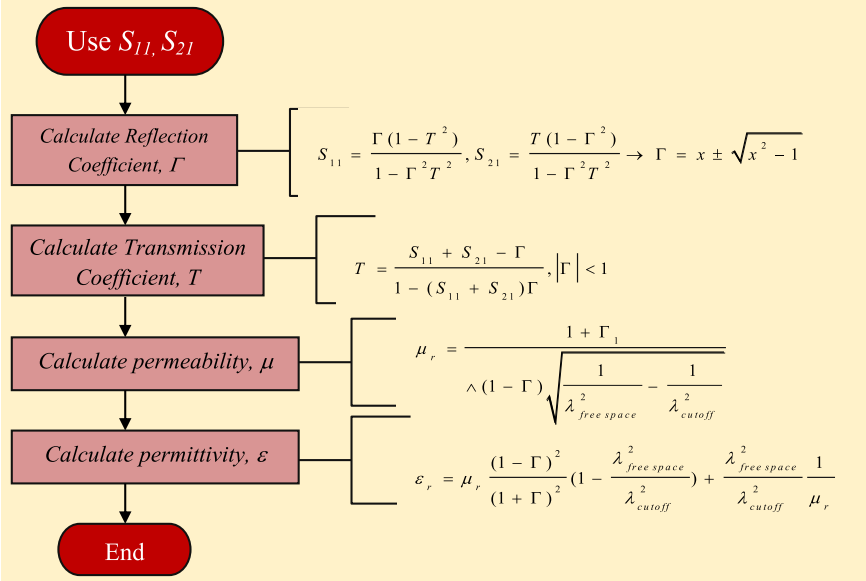

Fig. 4. Nicholson–Ross–Weir conversion process for calculating dielectric permittivity [23].

when passing through the waveguide (Fig. 3(b)). However, this method is strongly affected by the air-gap content, with high air content tending to decrease the dielectric property of the material. It is also influenced by the consistency of the cement and concrete materials. In particular, when materials behave like liquids, the settling of the material under its own weight can result in the non-uniform behavior of the whole specimen. Consequently, the measurement results are not representative of the whole body of the specimen.

A measurement using the transmission/reflection-line technique involves placing a sample in a section of the waveguide or

coaxial line and measuring the two ports' complex scattering parameters with a VNA. Calibration must be carried out before carrying out the measurement, though. The technique involves measuring the reflected (S_{11}) and the transmitted signal (S_{21}). The relevant scattering parameters relate closely to the complex permittivity and permeability of the material by equations. The conversion of *S*-parameters to complex dielectric parameters is computed by solving the equations using a Nicholson–Ross–Weir (NRW) technique as shown in Fig. 4 [23].

2.2.2. Measurement of cement and concrete

There have been several investigations [17–19,24] of the dielectric properties of cement and concrete materials, covering their measurement methods, their behaviors, and the factors influencing their variations. Initially, microwave radiation was used to determine the evaporable moisture (free-water) content in building materials and structural elements by monitoring the absorption level of microwave [17]. Later, Hasted and Shah [18] used the Robert and Von-Hippel method [24], a time-domain reflectometry-based measurement method, to study standing-wave behavior within a waveguide at 10, 3.3, and 1.25 cm. Wittmann and Schlude [19] studied microwave absorption at 9–11 GHz by hardened cement paste, using a free-wave method with a specimen of specified diameter and height. They consistently agreed that the real and imaginary parts of the complex permittivity of cement could be determined as a function of the moisture content, temperature, and hydration duration of the cement, when using the transmission/reflection line method [25] or a cavity-resonant method [26].

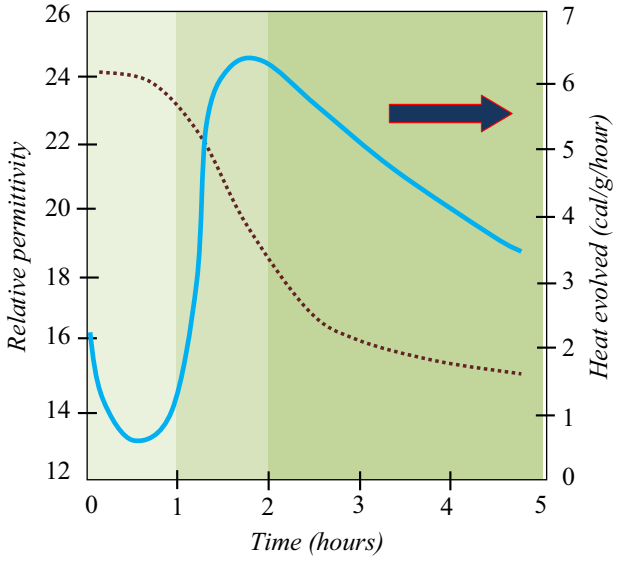

Fig. 5. Correspondent conductivity and heat of hydration for type 1 0.4-*w/c* cement paste [26].

The permittivity of a concrete mixture is influenced by the *w/c* ratio under various free-water volume absorption conditions. Variations in permittivity, due to the effects of the *w/c* ratio, cement type, and superplasticizer use, are closely related to changes during the four stages of cement hydration. The ion concentration is correlated with the mixing of the cement and water particles. When the cement first contacts with water, the ion concentration increases to a relatively high level. It remains constant during the dormant period, decreases rapidly during the hydration reaction, and continues to decrease during the acceleratory period, as shown in Fig. 5 [26]. Some typical dielectric constant (ε') and dielectric loss factor (ε'') values of cementitious materials as a function of temperature are shown in Table 3 [27]. Many microwave-based methods are available for monitoring variations in the dielectric properties during the hydration process. Microwave heating units are commonly operated at 2.45 GHz, which is a suitable frequency for monitoring concrete mixtures using a custom-designed parallel-plate setup with a network analyzer [28,29].

The dielectric properties of cement and concrete materials change drastically and continually in the early stages of concrete formation (*i.e.*, from the time when cement particles first contact with water molecules until the final setting occurs). Parameters that affect the dielectric property during this process should be considered. For example, the measurement method should be able to represent the whole specimen. The method should not be

Table 3
Dielectric constant (ε') and dielectric loss factor (ε'') of cementitious materials as function of temperature [27].

Materials	*Dielectric constant* ε (ε'); $\varepsilon'(t) = at^3 + bt^2 + ct + d$			
	$a \pm$ s.d.	$b \pm$ s.d.	$c \pm$ s.d.	$d \pm$ s.d.
Type 1 Portland cement	$-3.671 \times 10^{-6} \pm 1.276 \times 10^{-7}$	$3.529 \times 10^{-4} \pm 1.869 \times 10^{-5}$	$-2.014 \times 10^{-5} \pm 8.294 \times 10^{-3}$	$3.712 \pm 4.803 \times 10^{-1}$
Type 3 Portland cement	$-1.122 \times 10^{-6} \pm 1.599 \times 10^{-7}$	$4.021 \times 10^{-4} \pm 1.007 \times 10^{-5}$	$-1.476 \times 10^{-3} \pm 5.356 \times 10^{-4}$	$6.023 \pm 3.911 \times 10^{-1}$
Pulverized fuel ash	$3.333 \times 10^{-6} \pm 3.215 \times 10^{-7}$	$-6.667 \times 10^{-4} \pm 5.508 \times 10^{-5}$	$4.200 \times 10^{-2} \pm 2.859 \times 10^{-3}$	$4.138 \pm 3.109 \times 10^{-1}$
Silica fume	$-3.500 \times 10^{-7} \pm 7.071 \times 10^{-8}$	$5.500 \times 10^{-5} \pm 2.121 \times 10^{-5}$	$-3.350 \times 10^{-2} \pm 1.344 \times 10^{-3}$	$2.217 \pm 1.790 \times 10^{-1}$
Superplasticizer (polycarboxylic water-based) (42.5% solid content by weight)	$-2.333 \times 10^{-5} \pm 8.083 \times 10^{-5}$	$4.767 \times 10^{-2} \pm 9.935 \times 10^{-3}$	$-3.260 \times 10^{-1} \pm 2.989 \times 10^{-2}$	$2.865 \pm 1.933 \times 10^{-1}$
Fine aggregate (River sand)	$-1.000 \times 10^{-7} \pm 7.000 \times 10^{-8}$	$-2.333 \times 10^{-5} \pm 1.079 \times 10^{-6}$	$2.333 \times 10^{-4} \pm 6.429 \times 10^{-5}$	$2.600 \pm 1.565 \times 10^{-1}$
Coarse aggregate (Crushed limestone rock)	$-8.500 \times 10^{-7} \pm 1.626 \times 10^{-7}$	$2.600 \times 10^{-5} \pm 4.808 \times 10^{-6}$	$-1.950 \times 10^{-3} \pm 3.606 \times 10^{-4}$	$1.224 \pm 1.409 \times 10^{-1}$
Materials	*Dielectric loss factor* (ε''); $\varepsilon''(t) = et^3 + ft^2 + gt + h$			
	$e \pm$ s.d.	$f \pm$ s.d.	$g \pm$ s.d.	$h \pm$ s.d.
Type 1 Portland cement	$3.333 \times 10^{-7} \pm 4.989 \times 10^{-8}$	$-7.667 \times 10^{-5} \pm 1.115 \times 10^{-6}$	$5.000 \times 10^{-3} \pm 7.874 \times 10^{-4}$	$1.565 \times 10^{-1} \pm 1.844 \times 10^{-2}$
Type 3 Portland cement	$7.987 \times 10^{-7} \pm 3.043 \times 10^{-8}$	$-3.008 \times 10^{-5} \pm 9.453 \times 10^{-6}$	$6.225 \times 10^{-3} \pm 2.114 \times 10^{-4}$	$3.922 \times 10^{-1} \pm 1.042 \times 10^{-2}$
Pulverized fuel ash	$-1.800 \times 10^{-7} \pm 3.111 \times 10^{-8}$	$2.650 \times 10^{-5} \pm 4.738 \times 10^{-6}$	$-1.500 \times 10^{-3} \pm 2.687 \times 10^{-4}$	$2.763 \times 10^{-1} \pm 7.092 \times 10^{-2}$
Silica fume	$-3.667 \times 10^{-7} \pm 2.082 \times 10^{-8}$	$6.333 \times 10^{-5} \pm 3.512 \times 10^{-6}$	$-3.733 \times 10^{-3} \pm 1.850 \times 10^{-4}$	$2.223 \times 10^{-1} \pm 2.045 \times 10^{-2}$
Superplasticizer (polycarboxylic water-based) (42.5% solid content by weight)	$-2.000 \times 10^{-5} \pm 1.414 \times 10^{-6}$	$3.400 \times 10^{-3} \pm 1.273 \times 10^{-3}$	$-1.664 \times 10^{-1} \pm 5.155 \times 10^{-2}$	9.635 ± 1.025
Fine aggregate (river sand)	$7.000 \times 10^{-8} \pm 1.224 \times 10^{-9}$	$-2.000 \times 10^{-5} \pm 2.633 \times 10^{-6}$	$1.000 \times 10^{-3} \pm 1.467 \times 10^{-4}$	$2.645 \times 10^{-1} \pm 6.029 \times 10^{-2}$
Coarse aggregate (crushed limestone rock)	$7.000 \times 10^{-8} \pm 1.453 \times 10^{-9}$	$-2.000 \times 10^{-5} \pm 8.201 \times 10^{-7}$	$1.000 \times 10^{-4} \pm 4.798 \times 10^{-5}$	$5.680 \times 10^{-2} \pm 4.334 \times 10^{-3}$

Remark: s.d.=Standard Deviation.

affected by external moisture or temperature, nor should it be set in the system to be measured, as it is in an adiabatic system. In addition, the strong sensitivity of cement and concrete materials to each microwave range needs to be considered.

2.2.3. Measurement of blended cement and concrete

In addition to conventional cement, researchers have investigated the dielectric properties of cement–pozzolan mixtures, as well as blended cement and concrete. For example, using a perturbation method with microwave systems operated at 8.2–12.4 GHz during the early hydration reaction, researchers found that the dielectric constant increased and the induction period decreased with an increasing percentage of slag in cement paste [30]. A breakthrough in the dielectric measurement of materials containing high-performance cement–pozzolanic materials indicated that the relative dielectric constant at a microwave frequency of 10 kHz ± 1 MHz decreased from 29 to 21 with the addition of increasing silica fume content [31].

Later, Levita et al. [32] studied the electrical properties of liquefied type 1 52.5 R Portland cement (European standard ENV-197/1) containing microsilica fume during the early stage of hydration. These authors made measurements at ambient temperature for up to 40 h, in the frequency interval from 30 Hz to 200 kHz. The electrical properties of the paste mixtures had major variations in the first 40 h of hydration. They reported the values of ε' and ε'' as a function of frequency. At low frequencies, the dielectric constant was very large ($\sim 10^8$) because of an induced dielectric amplification effect, which was previously described by Coverdale et al. [33] and Ding et al. [34]. This effect involved a decrease of the dielectric permittivity with the progression of hydration, due to an increasing amount of calcium–silicate hydrate (C–S-H) or the conversion of free water to combined water in the C–S-H molecule. The permittivity varied depending on the chemical composition of the constituents, the amounts of hydration product phases, and local topological variations. At high frequencies, the dielectric amplification effect was significantly reduced.

Dielectric properties of fresh concrete compositions during the early stage of hydration were also investigated [35]. The dielectric constant varied with time between 30 and 60 min after cement was mixed with water. These results were consistent with the findings of Paul and Stephen, who used frequencies from 100 Hz to 7 MHz [36], Ping and Beudoin, who used frequencies from 1 to 1000 MHz [37], and Youssef et al., who used frequencies from 10 Hz to 1 GHz [38].

The electromagnetic characteristics and absorbing properties of fly ash were studied for cement composite in which fly ash was used as a cement replacement. The ε' was almost constant (~ 3.15) in the whole frequency range from 2 to 8 GHz, whereas ε'' showed obvious changes in the range from 0.03 to 0.1 GHz. Several peaks in ε'' were obtained at fixed positions [39]. The work of Makul et al. [27] comprehensively investigated the behaviors of various blended cement and concrete mixtures during a 24-h first-hydration period at 2.45 ± 0.05 GHz. The dielectric permittivity was relatively high and remained constant during the dormant period. Thereafter, it decreased rapidly when the hydration reaction resumed, and continued to decrease during the acceleratory period, consistent with the works of Moukwa et al. [26] and Zhang et al. [30].

Apart from experimental investigations, Hager and Domszy [40] tried to fit the experimental results of hydrating cement paste to a model over the frequency range of 10 kHz–8 GHz, from initial mixing through several weeks of cure. The model included the following terms: (1) Cole–Davidson relaxation near 1 MHz, (2) Debye relaxation near 100 MHz, (3) free-water relaxation near 10 GHz, and (4) ion conductivity and electrode polarization. The first two terms initially increased, and all four terms decreased with advancing cure. This work was the first to present long-term changes in the dielectric properties of cement, and it is applicable for pozzolanic cements with long-term reactions. The classical effective permittivity theory described by Prasad and Prasad [41] indicates that low-permittivity inclusions can decrease the effective permittivity of composites. In that study, the Cuming equation had the highest degree of acceptability (errors $< \pm 15\%$) in all cases.

Some limitations of the aforementioned investigations should be noted. First, the dielectric constant fluctuates during the early stage of the hydration reaction. Second, other equations may be more optimal than the Cuming equation, such as the Maxwell–Wagner, Webmann, Skipetrov, and modified Cule–Torquato equations, depending on the sensitivity of the moisture (water) content of the cementitious materials.

2.2.4. Modeling work

In addition to the experimental studies described above, theoretical-based analyses of the dielectric properties of cementitious materials have been performed. For example, Finite Difference-Time Domain (FD-TD) modeling has been used to visualize the propagation of electromagnetic fields in concrete (as a dielectric medium) and to predict electromagnetic phenomena associated with concrete targets

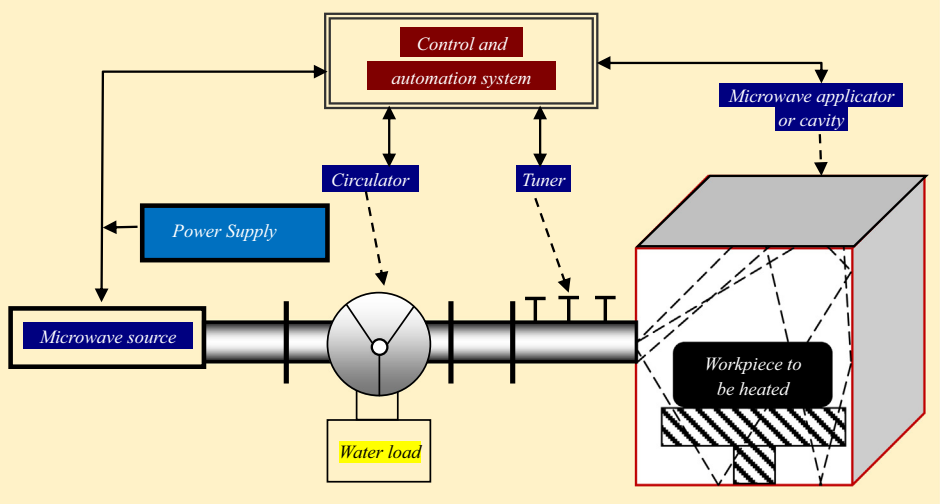

Fig. 6. Microwave system diagram.

for nondestructive testing purposes [16,42]. Klysz et al. [43] proposed a numerical FD-TD model of a ground-penetrating radar-coupled antenna to evaluate the dielectric properties of concrete. Using their method, the permittivity and conductivity of different concretes at different degrees of saturation were in agreement with those provided by Soutsos et al. [44], who used a coaxial transmission line system. These results were later validated in model experiments by an open-ended coaxial probe method over a microwave frequency range from 0.1 to 20 GHz. The results suggested that the outer geometry of the specimens (*i.e.*, shape and size) affected the ability to detect the targets and inclusions [16].

A survey of proposed mathematical models and validations indicated that the model needs to be validated with various concrete mixtures with different internal moisture contents because the latter factor strongly affects the dielectric constant and loss factor of concrete. The dielectric parameters (ε' and ε'') are not linked to the porosity; rather, all of the concrete pores must be filled with moisture in both the saturated and partially saturated states, especially in the early stage of hydration. Therefore, additional *w/c* ratios of concrete will need to be investigated in detail.

3. Microwave systems

This section presents the components and function of existing microwave systems, as well as their practical use for different applications. Conventionally a suitable microwave system is required to generate and introduce microwave energy to material (dielectric) to be heated. A typical microwave system is shown in Fig. 6. Most microwave-heating systems consist of three basic components: microwave power generator (usually magnetron), wave guide, and microwave chamber or cavity where the specimen is to be processed and supplementary components *e.g.* control system, tuner, circulator and so on. In detail, most importantly, microwave power generator connecting to power supply unit: its purpose is to convert the alternating current (a.c.) of 50 or 60 Hz to a desired high frequency microwave radiation. This is achieved by a device called magnetron. Magnetron must also be shielded to prevent the leakage radiation of harmonics, as well as for safety. Waveguide is an important component and it transmits microwave energy through free space and delivers to the specimen. The waveguide is any structure that directs the propagation of energy in the form of an electromagnetic wave along a predetermined path [45]. Waveguides may assume many different physical forms depending up on a large extent on the frequency band. Last is microwave chamber/cavity that obeys with the laws of electromagnetic – transmit, absorb, reflect microwave energy.

Practically, microwave system can be categorized into three subsystems depending on type of applicator associated with supplementary equipment or system as follows:

- Traveling-wave applicators in which a traveling wave is produced by matching the microwave source to a heated load using rectangular and cylindrical waveguide.
- Near-field applicators – this is a resonant open-ended waveguide or cavity attached directly at the end of the waveguide, at which the energy is fed through slots into a cavity.
- Resonant applicators – this is these types can be classified into single and multimode resonators as shown in Fig. 7 (single mode) [46,47] and Fig. 8 (multimode) [48], respectively.
  - For single mode resonant cavity, the standing wave applicator is attached to the end of the waveguide microwave power-feed line. Microwave energy was generated by a magnetron and transmitted directly along the propagation direction ($+z$) of a rectangular wave guide toward a water load situated at the end of the waveguide to ensure that a minimal amount of microwave energy would be reflected back to the sample. A warming water load was circulated through the cooling tower in order to reduce the temperature in the water load system.
  - For multimode applicators, Fig. 8(a), the microwave cavity was rectangular shape with exterior dimensions of 900 mm × 450 mm × 2700 mm. The drier operates at a frequency of 2.45 GHz with maximum working temperature of 180 °C. The microwave power was generated by means of

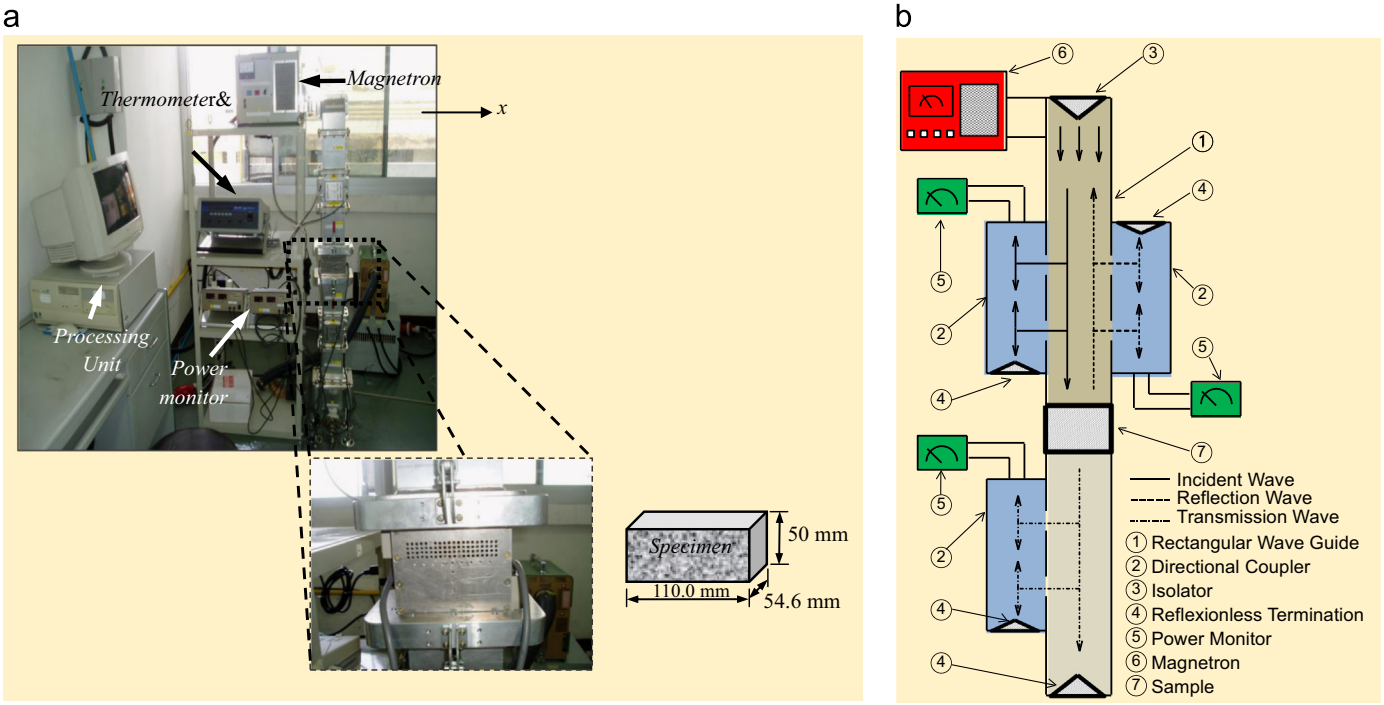

Fig. 7. (a) Experimental set up, (b) schematic showing direction of microwave components (Incident wave, reflected wave, and transmission wave) [46,47].

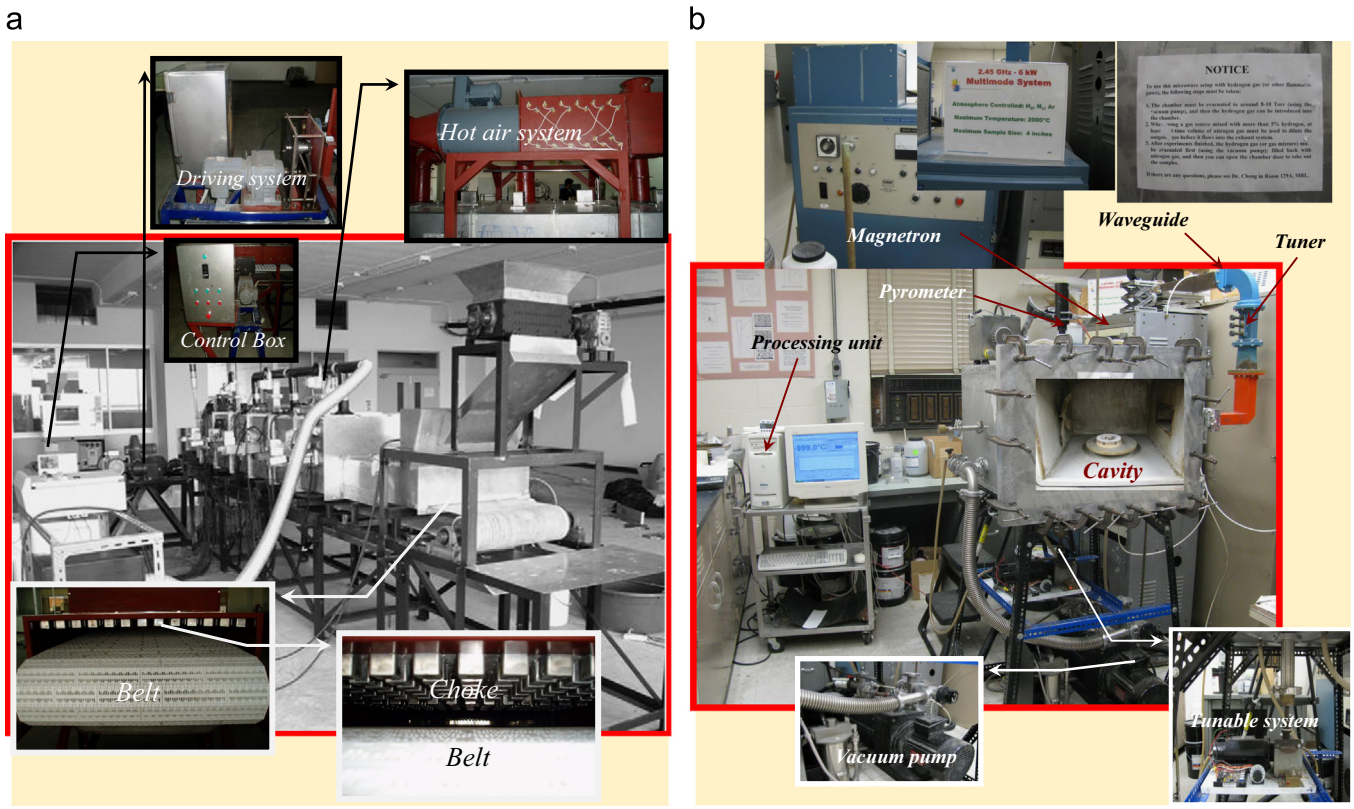

Fig. 8. Microwave system typed multimode resonant cavity: (a) A combined multi-feed microwave-hot air heating with continuous belt system (low temperature multi-mode microwave system) [48] and (b) high temperature multi-mode microwave system [49].

12 compressed air-cooled magnetrons. The maximum microwave capacity was 9.6 kW with a frequency of 2.45 GHz. The power setting could be adjusted individually in 800 W/steps. In the continuous processing equipment, two open ends were essential, through which the material to be heated up on the belt conveyer was put in and taken out. In this equipment, leakage of microwaves was prevented by the countermeasure in double with a combination of mechanical blocking filter (corrugate choke) and microwave absorber zone filter was provided at each of the open ends. The multiple magnetrons (12 units) were installed in an asymmetrical position on the rectangular cavity (Fig. 8(b) [49]). The microwave power was then directly supplied into the drier by using waveguides. An infrared thermometer (located at the opening ends) was used to measure the temperature of the specimens (accurate to ± 0.5 °C). An example is high temperature microwave system. It can generate microwave energy at a frequency of 2.45 GHz and maximum power of 6.0 kW with a multi-mode system. This results in a temperature of 2000 °C being induced in the material.

4. Applications of microwave to cement

Cement is a complicated mixture of calcareous-, silica-, and alumina-based minerals with specific compositions. The manufacturing process consists of grinding and mixing the raw materials, and then roasting at temperatures up to 1450 °C. During this process, a granular clinker is formed, which is composed of tricalcium silicate ($3CaO \cdot SiO_2$ or C_3S), dicalcium silicate ($2CaO \cdot SiO_2$ or C_2S), tricalcium aluminate ($3CaO \cdot Al_2O_3$), and tetracalcium aluminoferrite ($4CaO \cdot Al_2O_3 \cdot Fe_2O_3$). To generate commercial Portland powder, clinkers are ground to a fine powder and 4–5% calcium sulfate is added. The resulting product is ready to be reacted with water.

In the following sections, various applications of microwave energy to cement are presented, covering the use of microwave energy to synthesize cement and to improve cementitious properties.

4.1. Cement synthesis

Microwaves have been utilized at 2.45 GHz to assist in the clinkerization of cement nodules, producing clinkers with similar characteristics to those of conventionally produced industrial cement clinkers. During microwave heating at a maximum temperature of 1450 °C [50,51], the dielectric losses of different cement constituents were adequate to preserve the heating rate and ensure clinkerization, as confirmed by Sutton [52]. In a later work [53], microwave energy at 2.45 GHz was capable of synthesizing regular and colored cement clinkers. Clinkering temperatures required by microwave processing were about 100 °C less than those required for fast-heating by the electric furnace method. Another microwave sintering method involved heating the sample by electric heating to 1500 °C, and then using microwave-assisted heating for 30–60 min to induce C_3S formation [54]. Ion oxides played a very important role in C_3S formation in conventional sintering [55].

Microwave heating has been used to sinter Class F fly ash at temperatures from 800 to 1000 °C for 10 to 20 min. Samples sintered by microwave were denser and had better mechanical properties than samples sintered by conventional processes at the

same sintering temperature and for the same time. The sintered cement nodules were mainly composed of mullite ($Al_6Si_2O_{13}$). At the same heating rate during clinker formation, microwave-assisted sintering improved the formation of C_3S compared to the conventional sintering methods [56–58].

In addition to the use of only microwave heating for cement sintering, a combined electric and microwave clinkering method has been applied for Portland cement. After raw materials had been heated by electric energy to 1000–1200 °C, they were sintered by microwave energy for 1–2 min. The sintering time was reduced by using higher temperature samples in the microwave-sintering step. The same combined method was also applied to make sulphoaluminate belite (SAB) cement clinkers from a raw sulfoaluminate precursor [59]. The combined use of electric heating and microwave processing significantly accelerated the clinkering reaction. For samples that were heated at 1300 °C for 1 h, the free CaO of the obtained clinkers was as high as 1.03–4.78%. When samples of the same composition were heated by microwave alone for 25 min, the $CaCO_3$ in the raw materials did not completely decompose.

4.2. Improving cementitious properties

Microwave can be utilized to improve the cementitious properties of pozzolan materials. For example, rapid sintering of Rice Husk Ash (RHA) at 800–1200 °C by microwave at 2.45 GHz enhanced the cementitious properties of the cementing material. The sintered and ground RHA contained the cristolbalite phase. The strength index of 28-day-old microwave-sintered RHA paste sintered at 800 °C was increased by 30% compared to the index before sintering [60].

5. Applications of microwave to concrete

This section presents various applications of microwave energy to concrete, including microwave-accelerated curing, the decommissioning of decontaminated concrete, nondestructive monitoring, and the drilling/melting of concrete.

5.1. Acceleration of curing

After cement grains are mixed with sufficient water, various reactions occur that result in hydration product formation (*e.g.* calcium silicate hydrate gel, C_x–S_y–H_z) (Eq. (4)). Due to the nature of the cement grains and the reaction kinetics, the strength of the concrete continually increases over time. Immediately after the cement and water are mixed, the $CaO \cdot Al_2O_3$ phase reacts with water to form an aluminate-rich material, and calcium sulfate hemihydrate is converted to its dihydrate form. Both of these reactions contribute to a brief exothermic peak. Subsequently, the gel reacts with sulfate in solution to form ettringite ($3CaO \cdot Al_2O_3$) and, thereafter, enters a dormant period [61].

At the end of the dormant period, $3CaO \cdot SiO_2$ and $2CaO \cdot SiO_2$ in the cement begin to hydrate, forming calcium silicate hydrate (CaO_x–SiO_y–H_2O_z) and calcium hydroxide ($Ca(OH)_2$). This step corresponds to the main period of hydration, when much of the increase in strength occurs. The cement grains react from the surface inwards, and unreacted grains become fewer and eventually are consumed. The period of maximum heat evolution occurs between 6 and 24 h after mixing, followed by a gradual decrease approximately over 1 month period. The sequence of reactions is shown below:

$$\left.\begin{aligned}
&3CaO \cdot SiO_2 + H_2O \rightarrow CaO_x - SiO_{2y} - H_2O_z + Ca(OH)_2 + \Delta Heat\ (500\ J/g)\\
&2CaO \cdot SiO_2 + H_2O \rightarrow CaO_x - SiO_{2y} - H_2O_z + Ca(OH)_2 + \Delta Heat\ (260\ J/g)\\
&2(3CaO \cdot Al_2O_3) + 18H_2O \rightarrow 2CaO \cdot Al_2O_3.8H_2O + 4CaO \cdot Al_2O_3 \cdot 10H_2O + \Delta Heat\ (866\ J/g)\\
&2(3CaO \cdot Al_2O_3) + 32H_2O + 3(Ca^{2+}_{(aq)} + SO^{2-}_{4(aq)}) \rightarrow CaO \cdot Al_2O_3 \cdot 3SO_3 \cdot 32H_2O + \Delta Heat\ (420\ J/g)\\
&6CaO \cdot Al_2O_3 \cdot 3SO_3 \cdot 32H_2O + 23CaO \cdot Al_2O_3 \rightarrow 3(4CaO \cdot Al_2O_3 \cdot SO_3 \cdot 12H_2O)
\end{aligned}\right\} \quad (4)$$

Although cement can react with water under conditions of room temperature and pressure, such cement will require more time to reach an adequate strength for industrial uses [61]. Consequently, various curing methods are used to accelerate strength development in cement-based materials during the early-age phase.

Strength is a crucial factor in structural design. High early strength can benefit concrete production by reducing the construction time, labor, formwork, energy, and environmental impact. Early strength development is strongly influenced by several factors, including the water/cementitious material ratio, cement type and content, age of the paste, and curing method. For example, use of a lower water/cementitious materials ratio (*w/c*) makes a stronger concrete.

Many methods [61] are available for increasing the early strength of concrete. Curing involves maintaining favorable moisture and temperature conditions to ensure that the degree of hydration is sufficient to reduce the porosity to a level at which the desired properties (*e.g.* strength and flexibility) can be attained. Curing affects the rate of strength development. Accelerated gains in strength may be achieved by supplying heat and moisture to the concrete. For example, curing with steam at atmospheric pressure (live steam curing) or at high pressure in an autoclave (high-pressure steam curing) is advantageous when high early strength is necessary or when additional heat is required to accomplish hydration (*e.g.* in cold weather).

Conventional curing methods have many limitations. For instance, when water curing is used, long periods are needed to reach the required strength. With steam curing, non-uniform temperature distributions can occur, resulting in non-homogeneous curing. When admixtures are employed, durability problems may occur. Thermal curing methods are especially susceptible to negative effects on durability in both the early and long-term stages. For example, high-temperature curing at atmospheric pressure was shown to result in reduced long-term strength and durability problems [62,63]. Although the reasons for these problems are not wholly understood, they might include an increase in microcracking and delayed ettringite formation. As mentioned in Verbeck and Helmuth [63], rapidly accelerated hydration during curing can lead to the encapsulation of the anhydrous cement grains by a layer of product with low porosity, which further slows the hydration. Hydration products act as insulating (dielectric) materials that transfer heat at a low, non-uniform rate, resulting in poor properties after curing.

Moving the heat source from the outside surface of a heated cementitious material to the internal structure (*e.g.* through the interaction between the microwave field and the heated material) can result in a violent cement–water interaction and volumetric

heat generation [64,65]. This concept serves as the basis of one method of accelerated curing (microwave curing). The Portland cement–water system inherently reacts to a complex multicomponent system and repletion-coupled temperature- and composition-sensitive hydration products. Therefore, to develop the accelerated curing method further, Portland cement-based materials subjected to high-temperature curing by microwave energy will need to be characterized from a microstructural perspective.

Given the adverse short- and long-term effects that thermal-curing methods have on the properties of concrete, a crucial question is whether microwave heat can be applied in the concrete industry. Theoretically, this application is possible because the materials used to make concrete (*e.g.* hydraulic Portland cement, aggregates, water, and admixtures) are dielectric (*i.e.* they can absorb microwave energy). In particular, the relative dielectric constant (ε_r') and loss tangent ($\tan\delta$) values for water are higher than those of the other components of cement. As a result, when the electric part of the electromagnetic field ($\vec{E}$) interacts with the constituents of concrete, energy is transferred from the electric and magnetic fields and converted (through ion conduction and polar rotation) to the molecular bonds of the water, which is part of the microwave-irradiated material. This mechanism causes the bonds to vibrate. Energy is dissipated as heat and transferred within the concrete, increasing the temperature and accelerating hydration. Free water molecules in the capillary pores of the concrete are quickly removed from the internal concrete structure before setting. Thus, plastic shrinkage occurs, which leads to collapse of the capillary pores and densification of the microstructure [66].

Studies on the use of microwave-assisted curing have numerous aspects. A paper by Watson [67] was the first to extend a microwave dehydration method to concrete. Use of microwave energy accelerated strength development in Portland cement mortar without decreasing the long-term strength of the concrete. The strength of the concrete specimens began to decrease when the final *w/c* ratio was less than 0.40 [68]. In another study, microwave-assisted curing during the first 24 h reduced the induction period of hydration [69]. Key parameters for microwave curing include the microwave power, application time, duration of microwave heating [66], thermal runaway, and overheating within the sample [70]. When optimal microwave power was applied in a discretized fashion through feedback temperature control, very good results were obtained for concrete [71]. The work of Sohn and Johnson [72] obtained the optimal microwave-curing of type 1 Portland cement mortars at 40 and 60 °C, whereas other temperatures were incompatible with curing.

Microwave curing appeared to damage the freeze-thaw durability of high *w/c* concrete, but not low *w/c* concrete [8,73]. In terms of the microstructural characteristics of cement-based materials subjected to microwave energy, microwave-cured paste demonstrates some ettringite. In two studies, the ranges of the Si/*Ca* and Al/*Ca* ratios in the autoclave-cured paste were 0.039–0.052 and 0.207–0.234, respectively, whereas the ratios in the microwave-cured paste ranged from 0.079 to 0.091 [65,74].

Apart from conventional concrete, microwave heating can also be used to cure metakaolin-blended cements. For instance, the pozzolanic activity of metakaolin was improved under microwave curing. Microwave-cured 15% metakaolin was free of $CaOH_2$, whereas 30% or 40% metakaolin was needed for similar outcomes in room-temperature curing [75]. Concrete samples containing 10% silica fume responded well to microwave curing. Microwave heating for 40 min appeared to be the optimal curing time [73].

Microwave energy can also be used in association with a vacuum system, in order to dewater or dehydrate the concrete. The optimal microwave curing time has been shown to be 45 min at a maximum temperature of 60 °C, with a final *w/c* ratio of around 0.38. In this process, microwave curing decreases the amount of free water while increasing the hydration rate of cement, resulting in a compacted/less porous concrete [76]. When microwave energy was applied with a continuous belt drier consisting of 14 compressed air-cooled magnetrons of 800 W each (maximum of 11.2 kW), the microwave energy accelerated the early-age compressive strength of the cement paste, but did not affect the later-age strength. Microwave curing reduced the energy consumption and curing time [77].

Practically, microwave-assisted curing has been shown to be a useful technique for construction applications [6] and for repairing damaged concrete pavements. Leung and Pheeraphan [71] compared the early-age and long-term compressive strengths of concrete specimens developed from microwave-cured type 3 Portland cement to those of commercially available rapid-hardening concrete containing accelerating admixtures. The compressive strength of microwave-cured concrete (*w/c* ratio of 0.55) that was cured for 45 min increased to 19.2 MPa at 4.5 h [71]. Studies based on research by the Commonwealth Scientific and Industrial Research Organization (CSIRO) of Australia [78–83] found that the use of microwave curing cycles of less than 6 h permitted adequate strength for formwork removal and wire-strand prestressing, without impairing the concrete quality.

Microwave heating offers efficient production and high product performance for precast concrete. Heat curing impacts the performance (*i.e.*, thermal response, early-age strength, and durability) of a selected range of concrete materials for bridge construction. Microwave heating produces considerably lower temperature gradients compared to steam heating. For example, when rapid microwave curing cycles of less than 6 h were used, compressive strengths of up to 25 MPa were achieved in high-quality precast concrete. Replicating the bulk heating rate with microwave heating did not cause any deterioration in the near-surface quality, unlike in conventional steam heating.

Several inventions have been developed for the application of microwave-accelerated curing. Mario and Sergio [84] developed a process and device for accelerating the drying of cement mixtures, such as those containing prestressed and non-prestressed concrete components. Ludewig and Steinbach [85] invented a method and device for removing water from buildings, parts of buildings, and/or fixed structures, including those outside buildings, for construction purposes. Birch-Rasmussen et al. [86] invented a process for curing and drying wet reinforced concrete. In their process, the concrete is subjected to short-term electromagnetic heating (for seconds to a few minutes), which increases the temperature of the concrete from 10–25 °C to 50–80 °C. Furthermore, Engelbrecht and Soeren [87] proposed a process for curing and drying concrete by electromagnetic radiation, and a multistep process for accelerating the curing and drying of reinforced concrete products. In their proposals, the cast concrete elements are consecutively subjected to an inductive alternating magnetic field, high-frequency electromagnetic radiation, and electromagnetic microwave radiation.

Although the initial cost of the microwave equipment might be expensive, microwave curing can reduce the amount of cement used in concrete and can accelerate early-age concrete curing in various applications. However, this curing method could have negative impacts on the performance (*i.e.*, thermal response, early-age strength, and durability) of some concrete mixtures. Therefore, a suitable microwave system and appropriate curing procedures need to be determined.

5.2. Decontamination and decommissioning of concrete

Microwave energy has been applied to the decontamination of concrete surfaces [88], including radioactively contaminated surfaces [90,91], and concrete layers, in the case of biological shields [89].

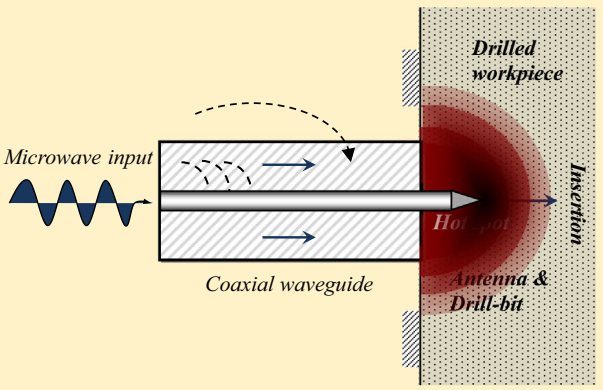

Fig. 9. A typical microwave drill operating system [12].

When a targeted dielectric material is irradiated by microwave energy, the energy is transferred from the electric field to the molecular bonds of the concrete, leading to vibration of molecules within the bond. Due to the nonuniform temperature distribution under the concrete surface, water beneath the surface evaporates, generating a high vapor pressure on the surface. When the accumulated pressure exceeds the tensile strength (maximum tensile stress) of the concrete, the concrete surface will spall off the bulk concrete.

A series of studies investigated the decontamination of concrete by microwave technology [92–94] under operating frequencies of 0.896, 2.45, 10.6, and 18.0 GHz. For microwave frequencies at or above 10.6 GHz, the microwave power dissipation was shifted towards the front surface of the concrete. This finding was verified in theoretical studies by Lagoset al. [95]. When higher microwave frequencies were used, less power was needed to increase the temperature or thermal stress to the same value in the same period of time compared to experiments under lower frequencies. These results are consistent with the findings of Bažant and Zi [11,96], who used microwave to spall off a thin layer of concrete surface that had been contaminated with radionuclide.

More investigations are needed into the use of microwave energy to spall off targeted concrete surfaces for decontamination. The decontamination of steel-reinforced concrete needs to be studied carefully because steel can reflect microwave energy, causing overheating and damage of the bulk concrete. Moreover, the decontamination of the concrete surface to make a break at a specific point or area requires careful analysis. Specifically, the design of an apparatus or machine to control the breaking region should be carefully considered. Finally, the safety of the worker should be taken into consideration.

5.3. Nondestructive monitoring

The early strength and accelerated curing parameters of microwave-cured concrete have been used to predict the 28-day compressive strength of concrete [97]. The 7-day strength of concrete made with rapid-hardening Portland cement and the 28-day strength of concrete made with ordinary Portland cement were predicted from the accelerated strength of concrete by microwave energy. Prediction results were within 15% agreement with actual test results [98].

Near-field microwave-sensing techniques can be used to determine the hydration state of cement paste or concrete [99]. For example, microwave energy has been applied to determine the natural moisture content, percent absorption, and bulk specific gravity values of aggregates [100], to study the hydration kinetics [101], to observe the hydraulic reaction of fresh pastes of C_3S for the first 30 h of hydration [102], and to determine the water content of fresh concrete [103]. The compressive strength of hardened concrete can be estimated from the apparent activation energy using a microwave technique [104,105]. This technique determines the strength in a nondestructive manner, without contacting the sample. In addition, microwave has been used to monitor the residual moisture content in the early hydration stages of cement paste. The residual moisture content decreased in rough proportion to the stage of the hardening process [106–108].

In the case of reinforced or prestressed concrete, microwave can indicate the presence of water, which is important for the diagnosis of concrete. The propagation of electromagnetic waves in concrete is controlled by the electromagnetic properties of the material itself, which are mainly influenced by the presence of water. Concrete-independent linear relationships were observed between the water volume and the propagation velocity of the direct wave and its attenuation [109].

For damaged concrete, microwave can be used to distinguish mortars containing Alkali-Silica Reactive (ASR) aggregate from nonreactive aggregate. Variations in measurements were linked to the production of ASR gel and its tendency to attract free water from its environment. ASR gel in cement-based materials can also be detected by material characterization methods [110,111]. In order to utilize microwave to measure the concrete properties, the status of free and fixed water must be considered. The temperature of free water can increase due to the increase in heat when the concrete interacts with the electromagnetic field. Thus, some of the free water is evaporated, leading to the misinterpretation of the amount of remaining water in the concrete.

5.4. Drilling/melting of concrete

An innovative application of microwave to concrete is the microwave-assisted drilling or melting of concrete [12,13]. High-energy microwave is applied to an area that is much smaller than the wavelength of the microwave (0.001–1.0 m). The microwave behaves like a “focusing injection,” with a monopole antenna conveying the material to be drilled (*e.g.*, concrete, ceramic, *etc.*; Fig. 9). The high-energy microwave energy penetrates the small area of the surface of the material, generating a high temperature locally until the material softens or melts. When a near-field radiator is used to induce microwave energy into a small volume on the surface of the material, a hot spot progresses in a rapid thermal runaway process. This process should be taken into account when determining the microwave drilling spot.

6. Theoretical investigations of microwave processing

This section describes an important theoretical investigation point of view of use of microwave in cement and concrete. It consists of electromagnetic theories involved microwave heating by applying Maxwell's equations, electromagnetic power flow by Poything vector, and the local volumetric heat-generation term based on Lambert's law. In addition, numerical techniques and simulation of microwave heating are presented involving Partial Differential Equations (PDEs) of the Maxwell's equations and the heat transport equations.

6.1. Electromagnetic theories

In essence, the numerical simulation/modeling of microwave heating involves the analysis of multiphase coupling. The mathematic model consists of the electromagnetic field equations (*i.e.* Maxwell's equations) and the heat transport equations, which are interrelated. To capture the interrelationship between the electromagnetic field and heat transport, the heat transport equation

contains at least one inhomogeneous term that reflects the heating source provided by the microwave-dissipated power. Temperature variations during heating can cause changes in the complex permittivity, which can lead to space and time variations of the electromagnetic field. To simulate the microwave heating process, the electromagnetic and heat transport equations with their coupled relationships must be modeled together and solved by suitable numerical methods.

The microwave field includes electric ($\vec{E}$) and magnetic ($\vec{H}$) fields that move simultaneously through space. The relationship between these time-varying fields can be described macroscopically with Maxwell's equations, revealing the following important observations: (a) the displacement current density is the rate at which the electric flux density ($\vec{D}$) varies with time; (b) time variations in the electric field create time variations in the magnetic field, due to the action of ($\partial\vec{D}/\partial t$) as a source of the magnetic field; and (c) the time-varying magnetic and electric fields are interdependent. With the help of boundary characteristics, the propagation conditions of plane waves can be assumed as follows: (a) the components of the field quantities ($\vec{E}$ and $\vec{H}$) lie in a transverse plane that is perpendicular to the direction of wave propagation; and (b) the attenuation of the wave amplitude is reduced by a factor of e^{-1} (0.368) in a dielectric medium (*i.e.* a material that can absorb microwave energy and then can be converted partially into other form of energy), by creating ionic oscillations and continuing dipole relaxation.

The electromagnetic (microwave) waves propagate in free space at the speed of light. Further information on the form of these waves can be obtained by noting that the electric and magnetic fields must also satisfy Maxwell's equations. Although the results derived are general, a specific type of wave is considered: the wave is an unbounded plane, indicating that there exist planes (or wave fronts) that are perpendicular to the direction of propagation, over which all quantities of the wave are constant.

Importantly, Maxwell's equations can be used to predict electromagnetic waves by considering the compacted forms of four equations. The validity of these equations has been proven by their consistency with all existing experiments of electromagnetic phenomena. The physical meanings of these equations are indicated via their specific differential forms below:

(a) *Gauss's law* : $$\nabla\vec{D} = q \tag{5}$$

(b) *Faraday's law* : $$\nabla \times \vec{E} = -\frac{\partial\vec{B}}{\partial t} \tag{6}$$

(c) *Ampére's law* : $$\nabla \times \vec{H} = \vec{J} + \frac{\partial\vec{D}}{\partial t} \tag{7}$$

(d) *Maxwell's equations* : $$\nabla\vec{B} = 0 \tag{8}$$

where $\vec{E}$ is the electric field intensity (V/m), $\vec{H}$ is the magnetic field intensity (A/m), $\vec{D}$ is the electric flux density (C/m), $\vec{B}$ is the magnetic flux density (Wb/m^2), t is time, and q is the electric charge density (C/m^3).

Constitutive relations that relate $\vec{H}$ and $\vec{B}$, $\vec{E}$ and $\vec{D}$, and $\vec{E}$ and $\vec{J}$ are shown in Eqs. (9)–(11), respectively. Substituting Eqs. (9)–(11) into Eqs. (5)–(8) results in Eqs. (12)–(15):

$$\vec{B} = \mu\vec{H} \tag{9}$$

$$\vec{D} = \varepsilon\vec{E} \tag{10}$$

$$\vec{J} = \sigma\vec{E} \tag{11}$$

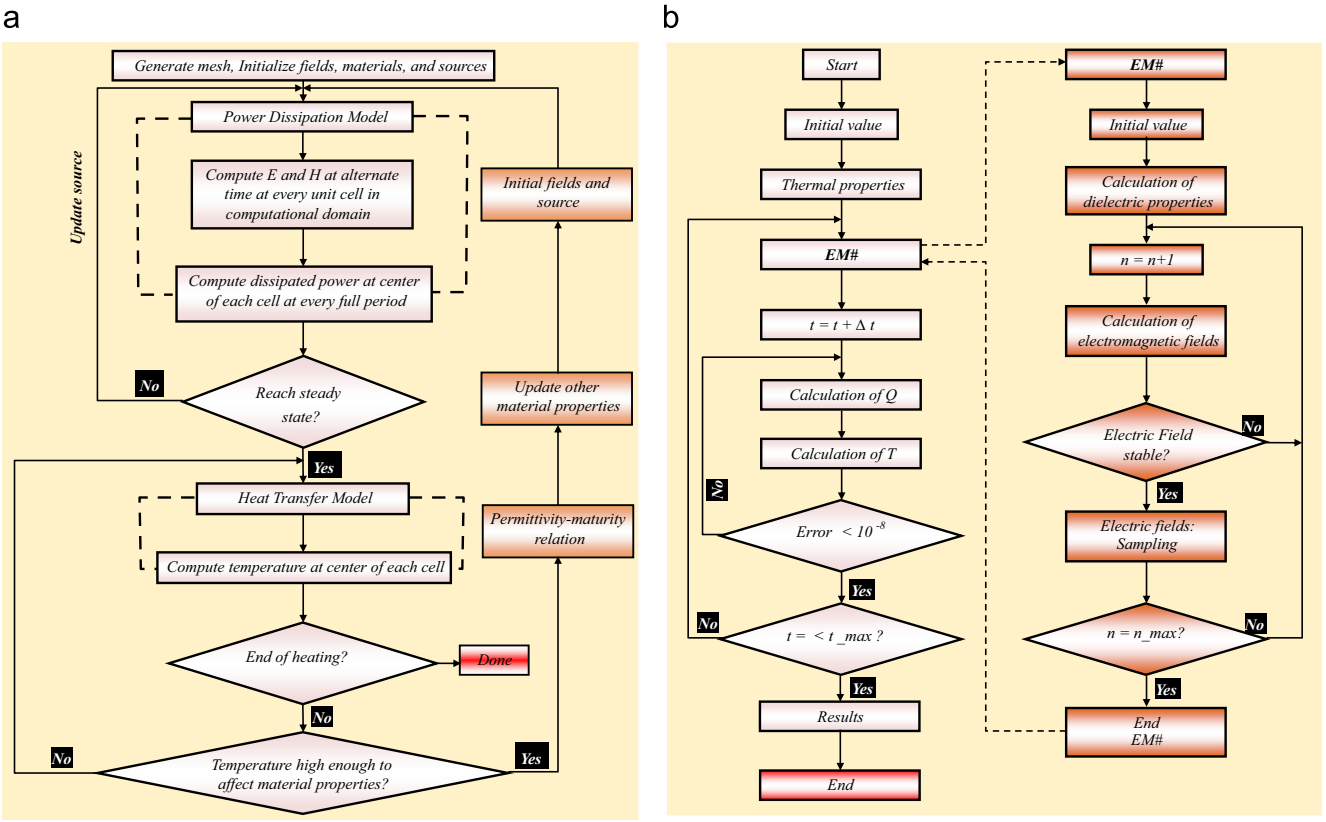

Fig. 10. Microwave heating model. (a) Multi-mode cavity [115] (b) Single mode cavity [46].

where μ is the magnetic permeability (H/m), σ is the electric conductivity (1/Ohm), and ε is the dielectric constant (F/m).

$$\nabla\vec{E} = \frac{q}{\varepsilon} \tag{12}$$

$$\nabla \times \vec{E} = -\mu\frac{\partial\vec{H}}{\partial t} \tag{13}$$

$$\nabla \times \vec{H} = \sigma\vec{E} + \varepsilon\frac{\partial\vec{E}}{\partial t} \tag{14}$$

$$\nabla\vec{H} = 0 \tag{15}$$

During microwave heating, electromagnetic energy is converted into heat, which is liberated into or from the dielectric material. Therefore, the power that flows through a closed medium surface can be calculated from the Poything vector, as shown in integral form in Eq. (16).

$$\vec{P} = \vec{E} \times \vec{H} \tag{16}$$

However, by definition, the average power is given by Metaxas and Meredith [5]

$$P_{av} = -\frac{1}{2}\int_s \mathrm{Real}(\vec{E} \times \vec{H})d\vec{S}' = -\frac{1}{2}\omega\varepsilon_0\varepsilon''\int_V (\vec{E}^{*}\vec{E})dV \tag{17}$$

The temperature change of the processed cement paste during microwave treatment can be obtained by solving the heat-conduction transport equation, in which the microwave power is included as a local electromagnetic heat-generation term:

$$\frac{\partial T}{\partial t} = a\left(\frac{\partial^2 T}{\partial x^2}+\frac{\partial^2 T}{\partial y^2}+\frac{\partial^2 T}{\partial z^2}\right)+\frac{Q}{\rho\cdot C_p} \tag{18}$$

In this equation, T is the temperature (°C), a is the thermal diffusivity (m^2/s), ρ is the density (kg/m^3), and c_p is the heat capacity at constant pressure (J/(kg K)). The local electromagnetic heat-generation term Q depends on the electric field distribution and based on Lambert's law, the microwave energy absorbed or the local volumetric heat-generation term, defined as in Eq. (19).

$$Q = \sigma|\vec{E}|^2 = 2\pi f\varepsilon_0\varepsilon_r'(tan\ \delta)|\vec{E}|^2 \tag{19}$$

where Q is the microwave energy, σ is the effective conductivity, f is the frequency (Hz), ε_0 is the permittivity of free space (8.8514×10^{-12} F/m), ε_r' is the relative dielectric constant, tan δ is the loss tangent coefficient, and $\vec{E}$ is the electric field intensity (V/m).

When microwave energy penetrates a dielectric material, the wave strength fades away exponentially because the microwave energy is absorbed by the dielectric material and is converted to heat. This absorbed ratio varies with frequency and dielectric properties. In general, the penetration depth (D_p) is used to denote the depth at the power density. It decreased to 36.8% or (e^{-1}) of its initial value at the surface [46] and is defined in Eq. (20):

$$D_p = \frac{1}{(2\pi f/\upsilon)\sqrt{\varepsilon_r'(\sqrt{(1+(\varepsilon_r''/\varepsilon_r')^2)}-1)/2}} = \frac{1}{(2\pi f/\upsilon)\sqrt{(\varepsilon_r'(\sqrt{(1+(\tan\ \delta)^2)}-1)/2)}} \tag{20}$$

where D_p is the penetration depth, ε_r'' is the relative dielectric loss factor, and υ is the microwave speed in the dielectric material that can be evaluated by $c/\sqrt{\varepsilon_r'}$.

6.2. Numerical techniques and simulation

The numerical simulation of microwave heating involves an analysis of at least two kinds of interrelated Partial Differential Equations (PDEs): the electromagnetic field equations (*i.e.* Maxwell's equations) and the heat transport equations. Additional differential equations may also be needed; for example, the mass transfer equation may be required for a model of drying porous materials.

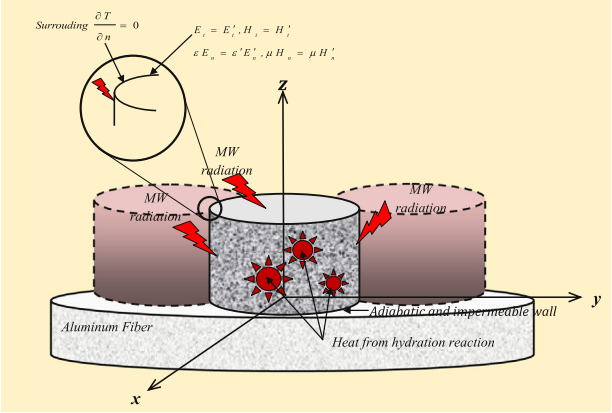

Fig. 11. A physical model and boundary conditions of 0.38-*w/c* cement paste subjected to microwave energy using a multi-mode cavity [116].

To obtain an accurate solution for the above coupled equations, analytical methods cannot be used. Various numerical methods have been applied to simulate microwave heating of cement and concrete. Popular methods include Finite Difference (FD) methods (*e.g.* Finite Differential Time Domain/FDTD method) [112,113], Finite Element Method (FEM), the Moment of Method (MoM), Transmission Line Matrix (TLM) method, Finite-Volume Time-Domain (FVTD) method, and others. Remarkable progress has been achieved in recent years in the numerical simulation of microwave heating. As more refined models, faster numerical methods, and more complete descriptions of the complex permittivity of more materials are developed [114], this progress will continue to accelerate. With the aid of numerical simulation, the complex interaction between microwaves and materials will be better understood, and the critical parameters influencing the process will be identified, allowing for the rapid design of optimized and controllable applicators.

To study the microwave heating process in cement and concrete, this process can be separated into a heat transfer model and a microwave power dissipation model, as shown schematically in Fig. 10(a) [115]. FDTD is a powerful numerical method for solving Maxwell's equations. The FDTD method described by Rattanadecho et al. is a useful approach for solving models in the single-mode cavity, as shown schematically in Fig. 10(b) [46]. Natt et al. [107] used the FEM method to solve Maxwell's equations and heat transfer in the cement paste during microwave curing in the multimode cavity (Fig. 11) [116]. However, Lambert's law cannot be used in numerous situations, such as instances with standing waves.

7. Health and safety of microwave processing

Health and safety of microwave processing cannot be neglected when microwave operates with human and environments. Therefore this issue is explained in this section that entails on the limitations and conditions of microwave exposure regulated by associations relating to the use of microwave energy.

Microwave processing of cement and concrete materials may involve a risk of exposure of microwave to human and biological tissues if certain precautions are not taken. Therefore, the Federal Communication Commission (FCC) and Occupational Health and Safety Administration [117] have provided exposure limits for microwave. These organizations have considered the effects of microwave radiation on human health from the perspectives of

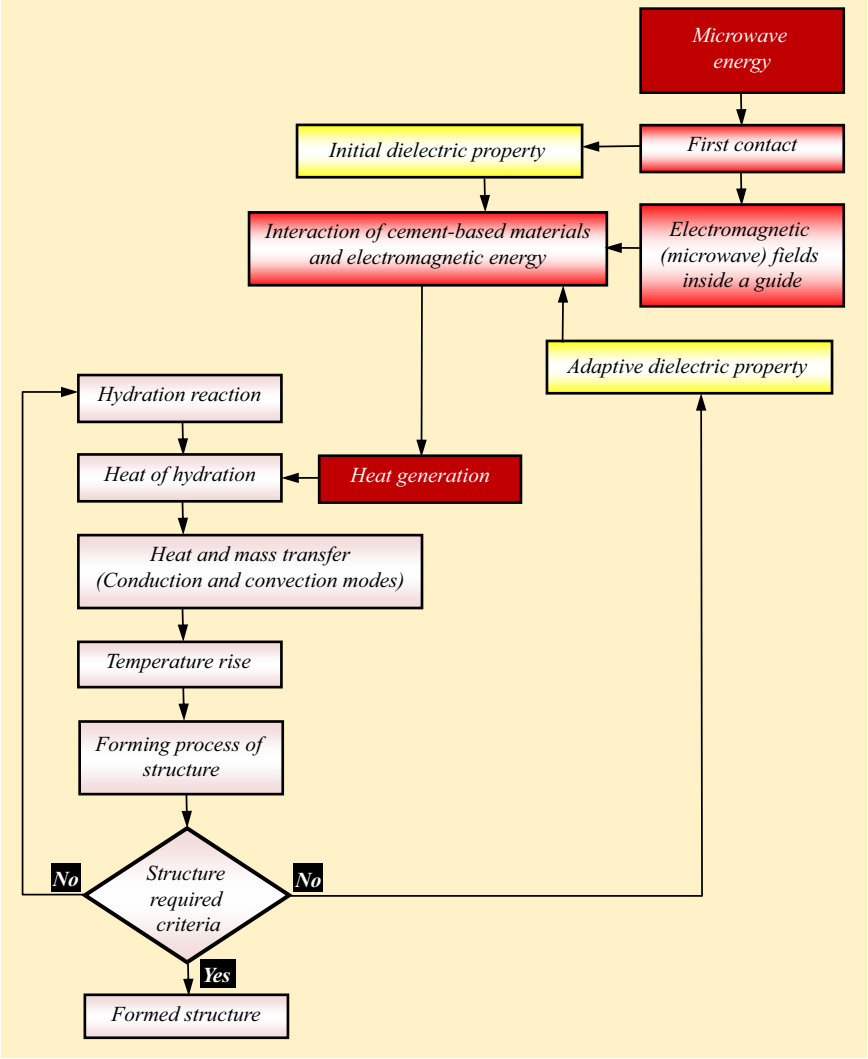

Fig. 12. A proposed schematic model of cement and concrete subjected to microwave energy.

exposure source (*e.g.* medical devices, amateur radio, cellular phone base stations, hand-held cell phones, heating and sealing devices, microwave ovens, radio broadcast antennae, traffic radar devices, *etc.*), hazard location, exposure time and solution.

The absorption and distribution of microwave exposure are strongly dependent on body size and orientation, as well as on the frequency and polarization of the incident radiation. In particular, the Specific Absorption Rate (SAR) refers to the power absorbed by a body when exposed to EM radiation. The current SAR limit is 4 W/kg. To be conservative, organizations generally use 1/10 of this value for setting standards, especially for Radio Frequency (RF) and microwave exposure limits. For occupational exposure, the field strength is averaged over a 6-min time period. For public exposure, the field strength is averaged over a 30-min period, as recommended by the International Radiation Protection Association (IRPA) Guidelines [118], IEEE Standards [119,120], National Radiological Protection Board (NRPB), and the Health Protection Agency [121]. It is strongly recommended that the microwave systems in the laboratory and industry are periodically tested for any leakage, and if any substantial leakage is observed, suitable measures must be taken to stop the leakage before the system is further used.

8. Conclusions

8.1. Major review findings

In this review paper, we have described applications of microwave energy in the cement and concrete field. Microwave heating is a high-performance volumetric heating method suitable for dielectric materials used in various concrete industrial processes. Applications of microwave heating in these systems include cement synthesis, accelerated curing, decommissioning of decontaminated concrete, nondestructive monitoring, and concrete drilling/melting. Numerous studies have experimentally and numerically investigated these processes, to utilize microwave heating to its fullest potential in cement and concrete applications. The following conclusions can be drawn from this review:

- Microwave heating is commonly performed at 2.45 GHz. Concrete mixtures can be monitored during the hydration process with a custom-designed parallel-plate setup using a network analyzer.
- The dielectric permittivity of cement-based materials is affected by the initial *w/c* ratio, cement type, mineral admixture, and

aggregate. Although the volumetric fractions of water and superplasticizer in a given mixture are small, these components strongly affect the dielectric permittivity.

- The dielectric permittivity is relatively high and remains constant during the dormant period of each process. The dielectric permittivity decreases rapidly when the hydration reaction resumes, and it continues to decrease during the acceleratory period. Thus, the dielectric property is related to the temperature rise and setting time behaviors of cement-based materials. This information can be used to accelerate the early strength of the concrete by choosing a suitable curing time (*e.g.*, start time and end time for applying microwave energy).
- The clinkering temperatures required by microwave processing were about 100 °C less than those required for fast-heating by the electric furnace method.
- Microwave-assisted heating for 30–60 min induced C_3S formation. Ion oxides played a very important role in C_3S formation in conventional sintering.
- Microwave-assisted sintering improved the formation of C_3S compared to conventional sintering methods.
- Microwave can be utilized to improve the cementitious properties of RHA-incorporating cement, especially cement that is microwave-sintered at 800 °C.
- Use of microwave energy accelerated strength development in Portland cement mortar without decreasing the long-term strength of the concrete. The strength of the concrete specimens began to decrease when the final *w/c* ratio was less than 0.40.
- Key parameters for microwave curing include the microwave power, application time, duration of microwave heating, thermal runaway, and overheating within the sample.
- Microwave energy at operating frequencies of 0.896, 2.45, 10.6, and 18.0 GHz can be used to decontaminate a concrete surface. At or above 10.6 GHz, the microwave power dissipation was shifted towards the front surface of the concrete.
- Microwave energy can be used for near-field microwave-sensing techniques, such as for determining the natural moisture content, percent absorption, bulk specific gravity of aggregates, hydration kinetics of cement, and water content of fresh concrete.
- High-energy microwave energy (wavelength range: 0.001–1.0 m) is useful for drilling/melting of concrete.
- The numerical simulation of microwave heating involves the analysis of electromagnetic field equations (*i.e.*, Maxwell's equations) and heat transport equations. Simulations should be separated into heat transfer and microwave power dissipation models. FDTD is a powerful numerical method for solving Maxwell's equations.
- The Specific Absorption Rate (SAR) refers to the power absorbed by a body when exposed to electromagnetic radiation. The current SAR limit is 4 W/kg.

8.2. Future trends of research and development

Microwave heating is a high-performance volumetric heating method suitable for the dielectric materials used in various concrete industrial processes. Numerous studies have experimentally and numerically investigated this process, in order to utilize microwave heating to its fullest potential in cement and concrete applications. Some of the investigated topics are outlined as follows:

- The dielectric properties of cementitious materials should clarify the effects of the time-dependent dielectric properties and thermal properties of concrete on microwave heating mechanisms. The dielectric property is a primary factor for determining the interaction of the microwave energy with the material. Theoretically, the complex permittivity comprises the normal dielectric constant ε', which is a measure of how much energy from an external electric field is stored in a material, and the loss factor ε'', which is a measure of how much energy a material loses to an external electric field. In addition, concrete is a heterogeneous material with pores that are partially filled by Si^{3+}, Ca^{2+}, and OH^- ion-rich solution. The ion concentration parameters can vary throughout the hydration and pozzolanic reactions. However, heating concrete by microwave energy leads to a simultaneous change in the dielectric property, which instantaneously affects the interaction between the microwave energy and concrete. Thus, the dielectric property needs to be understood, in order to determine the compatibility of microwave applications with the material's time-dependent concrete properties and thermal properties.
- Studies should investigate the influences of different concrete mixtures and curing conditions on the characteristics of microwave heating, as these conditions strongly affect the strength development of concrete. The primary parameters that characterize a given concrete sample include the *w/c* ratio, the chemical composition of the cement, the "fineness" of the cement (*e.g.* type 1 – normal purpose; type 2 – moderate heat- and sulfate-resistant; type 3 – high early strength; type 4 – low heat; and type 5 – sulfate-resistant), the nature and proportions of aggregates, and the use of chemical and mineral admixtures, among others. Admixtures are increasingly being used in the concrete construction industry. For example, type I cement can be replaced, in part, by silica fume, producing a concrete with high early strength.
- As shown in Fig. 12, Heat and mass transfer mechanisms within the heated concrete during microwave heating should be clarified. Studies have consistently shown that the generation and transport of heat and mass within the heated concrete material are key factors influencing the efficiency of microwave heating. In this process, heat is generated inside the concrete structure, and volumetrically transported towards the outside. These studies assume that no chemical reactions occur within the concrete under consideration. This assumption is not true, however, as hydration and pozzolanic reactions take place. Given the difficulty of this task, one may choose to perform the analysis at specified coupled chemical reactions during microwave curing. Heat generated by the microwave ($Q = \sigma|\vec{E}|^2 = 2\pi f \varepsilon_0 \varepsilon_r' (tan\,\delta)|\vec{E}|^2$) must be applied in synergy with the heat liberated by the hydration (Q_{Hyd}^{Total}) and pozzolanic (Q_{Pozz}^{Total}) reactions ($Q_{\text{Reaction}}^{Total} = Q_{Hyd}^{Total} + Q_{Pozz}^{Total}$). These heat sources should be considered from the perspectives of the setting and hardening processes of concrete, which are influenced by the internal energy from hydration and the external energy from microwave energy. Simply speaking, when external energy is added to the concrete after the final setting time, the energy leads to the generation and expansion of microcracks.

Acknowledgments

The authors gratefully acknowledge the Thailand Research Fund (TRF Contract nos. MRG5580041 and RTA5680007) and National Research Universities Project of the Higher Education Commission for supporting this research. In addition, this paper is dedicated to a great scientist, researcher, philosopher and our guide and colleague, Professor Dr. Rustum Roy (July 3, 1924 – August 26, 2010), Evan Pugh Professor of the Solid State Emeritus. We will always remember Dr. Roy for his wide ranging intellectual

pursuits including his pioneering contributions to advance the field of materials science.

References

[1] ⟨http:/www.cemnet.com/Articles/story/153619/global-cement-2014-outlook.html⟩.
[2] Madlool NA, Saidur R, Hossaina MS, Rahim NA. A critical review on energy use and savings in the cement industries. Renew Sust Energ Rev 2011;15:2042–60.
[3] Energy Efficiency Asia. ⟨http:/www.energyefficiencyasia.org/docs/Industry%20Sectors%20Cement%20draft_May%2005.pdf⟩, 20/08/2010; 2010.
[4] Metaxas AC. Microwave heating. J Microwave Power Electromagn Energy 1991;5:237–47.
[5] Metaxas AC, Meredith RJ. Industrial microwave heating. United Kingdom: Peter Peregrinus; Herts; 1998.
[6] Leung CKY, Pheeraphan T. Microwave curing of Portland cement concrete: experimental results and feasibility for practical applications. Constr Build Mater 1995;9:67–73.
[7] Makul N, Agrawal DK. Microwave-accelerated curing of cement-based materials: compressive strength and maturity modeling. Key Eng Mater 2011;484:210–21.
[8] Pheeraphan T, Leung CKY. Freeze-thaw durability of microwave cured air-entrained concrete. Cem Concr Res 1997;27:427–35.
[9] Mak SL. Microwave accelerated processing for precast concrete production. In: Proceedings of the 4th CANMET/ACI international conference on durability of concrete. Sydney, Australia; 17–22 August, 1997. p. 709–20 (supplementary papers).
[10] Li W, Ebadian MA, White TL, Grubb RG, Foster D. Heat transfer within a radioactive contaminated concrete slab applying a microwave heating technique. ASME Trans J Heat Transf 1993;115:42–50.
[11] Bažant ZP, Zi G. Decontamination of radionuclides from concrete by microwave heating. I: Theory. J Eng Mech 2003;129:777–84.
[12] Jerby E, Dikhtyar V, Aktushev O, Grosglick U. The microwave drill. Science 2002;298:587–9.
[13] Dikhtiar V, Jerby E. Patent No. US 6114676, method and device for drilling, cutting, nailing and joining solid non-conductive materials using microwave radiation, issued in 2000.
[14] Zoughi R, Gray SD, Nowak PS. Microwave nondestructive estimation of cement paste compressive strength. ACI Mater J 1995;92:64–70.
[15] Zoughi R. Microwave non-destructive testing and evaluation. The Netherlands: Kluwer Academic Publishers; 2000 (Chapter 2).
[16] Rhim HC, Büyüköztürk O. Electromagnetic properties of concrete at microwave frequency range. ACI Mater J 1998;95-M25:262–71.
[17] Watson A. Building research station Report A 93. England (DSIR): Garston; 1961.
[18] Hasted JB, Shah MA. Microwave absorption by water in building materials. Br J Appl Phys 1964;15:825, http://dx.doi.org/10.1088/0508–3443/15/7/307.
[19] Wittmann FH, Schlude F. Microwave absorption of hardened cement paste. Cem Concr Res 1975;5:63–71.
[20] Venkatesh MS, Raghevan GSV. An overview of dielectric properties measuring techniques. Can Biosyst Eng 2005;47:15–29.
[21] Tereshchenko OV, Buesink FJK, Leferink FBJ. An overview of the techniques for measuring the dielectric properties of materials. 978-1-4244–6051-9/11/IEEE; 2011.
[22] Hewlett Packard Corporation. Dielectric Probe Kit 85070A. Palo Alto, CA: Research and Development Unit. Test and Measurements Laboratories; 1992.
[23] ⟨www.rohde-schwarz.co.in/file/RAC-0607-0019_1_5E.pdf⟩.
[24] Hippel ARV. Dielectric materials and applications. New York: The Technology Press of M.I.T. and John Wiley & Sons; 1954.
[25] Gorur K, Smit MK, Wittmann FH. Microwave study of hydrating cement paste at Early Age. Cem Concr Res 1982;12:447–54.
[26] Moukwa M, Brodwin M, Christo S, Chang J, Shah SP. The influence of the hydration process upon microwave properties of cements. Cem Concr Res 1991;21:863–72.
[27] Makul N, Keangin P, Rattanadecho P, Chatveera B, Agrawal DK. Microwave-assisted heating of cementitious materials: relative dielectric properties, mechanical property, and experimental and numerical heat transfer characteristics. Int Commun Heat Mass Transf 2010;37:1096–105.
[28] Al-Qadi IL, Hazim O, Su W, Riad S. Dielectric properties of Portland cement concrete at low radio frequencies. J Mater Civ Eng 1995;7:192–8.
[29] Haddad RH, Ai-Qadi IL. Characterization of Portland cement concrete using electromagnetic waves over the microwave frequencies. Cem Concr Res 1998;28:1379–91.
[30] Zhang X, Ding XZ, Lim TH, Ong CK, Tan BTG, Yang J. Microwave study of hydration of slag cement blends in early period. Cem Concr Res 1995;25:1086–94.
[31] Wen S, Chung DDL. Effect of admixtures on the dielectric constant of cement paste. Cem Concr Res 2001;31:673–7.
[32] Levita G, Marchetti A, Gallone G, Principallo A, Guerrini GL. Electrical properties of fluidified Portland cement mixes in the early stage of hydration. Cem Concr Res 2000;30:923–30.
[33] Coverdale RT, Christensen BJ, Mason TO, Jennings HM, Garboczi EJ. Interpretation of impedance spectroscopy of cement paste via computer modeling: Part II. J Mater Sci 1994;29:4984–92.
[34] Ding XZ, Zhang X, Ong CK, Tan BT. Study of dielectric and electrical properties of mortar in the early hydration period at microwave frequencies. J Mater Sci 1996;31:5339–45.
[35] Leon CO. Effect of mixture composition and time on dielectric constant of fresh concrete (Master thesis). North Carolina State University; 2007.
[36] Paul C, Stephen B. Dielectric properties of Portland cement paste as a function of time since mixing. J Appl Phys 1989;66:6007–13.
[37] Ping G, Beudoin JJ. Dielectric behaviour of haredened cement paste systems. J Mater Sci Lett 1996;15:182–4.
[38] Youssef H, Smith A, Bonnet JP, Abelard P, Blanchart P. Electrical characterization of aluminous cement at the early age in the 10 Hz–1 GHz frequency range. Cem Concr Res 2000;30:1057–62.
[39] Baoyi L, Yuping D, Shunhua L. The electromagnetic characteristics of fly ash and absorbing properties of cement-based composites using fly ash as cement replacement. Constr Build Mater 2012;27:184–8.
[40] Hager NE, Domszy RC. Monitoring of cement hydration by broadband time-domain-reflectometry dielectric spectroscopy. J Appl Phys 2004;96:5117–28.
[41] Prasad A, Prasad K. Effective permittivity of random composite media: a comparative study. Physica B 2007;396:132–7.
[42] Büyüköztürk O, Yu T, Ortega J. A methodology for determining complex permittivity of construction materials based on transmission-only coherent, wide-bandwidth free-space measurements. Cem Concr Res 2006;8:349–59.
[43] Klysz G, Balayssac JP, Ferrières X. Evaluation of dielectric properties of concrete by a numerical FDTD model of a GPR coupled antenna-Parametric study. NDT & E Int 2008;41:621–31.
[44] Soustos MN, Bungey JH, Millard SG, Shaw MR, Patterson A. Dielectric properties of concrete and their influence on radar testing. NDT&E Int 2001;34:419–25.
[45] Cronin NJ. Microwave and optical waveguides. London: Taylor & Francis; 1995.
[46] Rattanadecho P, Suwannapum N, Cha-um W. Interactions between electromagnetic and thermal fields in microwave heating of hardened type – cement paste using a rectangular waveguide (influence of frequency and sample size). ASME J Heat Transf 2009;131:1–12.
[47] Suwannapum N, Rattanadecho P. Analysis of heat-mass transport and pressure buildup induced inside unsaturated porous media subjected to microwave energy using a single (TE_{10}) mode cavity. Drying Technol Int J 2011;29:1010–24.
[48] Vongpradubchai S, Rattanadecho P. The microwave processing of wood using a continuous microwave belt drier. Chem Eng Process Process Intensif 2009;48:997–1003.
[49] Agrawal DK. Latest global developments in microwave materials processing. Mat Res Inno 2011;14:3–8.
[50] Quéméneur L, Choisnet J, Raveau B, Thiebaut JM, Roussy G. Microwave clinkering with a grooved resonant applicator. J Am Ceram Soc 1983;66:855–9.
[51] Quéméneur L, Choisnet J, Raveau B. Is it possible to use the microwave for clinkering the cement raw materials? Mater Chem Phys 1983;8:293–303.
[52] Suston WH. Microwave processing of ceramic materials. Am Ceram Soc Soc 1989;68:3–19.
[53] Fang Y, Roy DM, Roy R. Microwave clinkering of ordinary and colored Portland cements. Cem Concr Res 1996;26:41–7.
[54] Jiang H, Hao Q, Zhou J. Microwave synthesis of dicalcium silicate: – comparison with conventional synthesis. Adv Mater Res 2011;306-307:1060–7.
[55] Ke K, Ma B, Wang X. Formation of tricalcium silicate prepared by electric and microwave sintering. Adv Mater Res 2011;148–149:1119–23.
[56] Fang Y, Chen Y, Silsbee MR, Roy DM. Microwave sintering of fly ash. Mater Lett 1996;27:155–9.
[57] Haoxuan L, Agrawal DK, Cheng J, Silsbee MR. Formation and hydration of C_3S prepared by microwave and conventional sintering. Cem Concr Res 1996;29:1611–7.
[58] Abdelghani-Idrissi MA. Experimental investigations of occupied volume effect on the microwave heating and drying kinetics of cement powder in a mono-mode cavity. Appl Therm Eng 2001;21:955–65.
[59] Haoxuan L, Agrawal DK, Cheng J, Silsbee MR. Microwave sintering of sulphoaluminate cement with utility wastes. Cem Concr Res 2001;31:1257–61.
[60] Makul N, Agrawal DK. Microwave (2.45 GHz)-assisted rapid sintering of SiO_2-rich rice husk ash. Mater Lett 2010;64:367–70.
[61] Neville AM. Properties of concrete. Fourth Edition. London England: Pitman Books Limited; 1995.
[62] Ramezanianpour AA, Khazali MH, Vosoughi P. Effect of steam curing cycles on strength and durability of SCC: a case study in precast concrete. Constr Build Mater 2013;49:807–13.
[63] Verbeck GJ, Helmuth RA. Structures and physical properties of cement paste. In: Proceedings of the 5th international congress cement chemistry. Tokyo, Japan; 1969. p. 1–44.
[64] Makul N, Agrawal DK. Influences of microwave-accelerated curing procedures on microstructure and strength characterization of Type I-Portland cement pastes. J Ceram Process Res 2012;13:376–81.
[65] Makul N, Agrawal DK. Comparison of the microstructure and compressive strength of Type 1 Portland cement paste between accelerated curing

methods by microwave energy and autoclaving, and a saturated-lime deionized water curing method. J Ceram Process Res 2012;13:174–7.
[66] Leung CKY, Pheeraphan T. Determination of optimal process for microwave curing of concrete. Cem Concr Res 1997;27:463–72.
[67] Watson A. Curing of concrete. In: Okress EC, editor. Microwave power engineering. New York: Academic Press; 1968.
[68] Xuequan W, Jianbgo D, Mingshu T. Microwave curing technique in concrete manufacture. Cem Concr Res 1987;17:205–10.
[69] Hutchinson RG, Chang JT, Jennings HM, Brodwin ME. Thermal acceleration of Portland cement mortars with microwave energy. Cem Concr Res 1991;21:795–9.
[70] Somaratna J, Ravikumar D, Neithalath N. Response of alkali activated fly ash mortars to microwave curing. Cem Concr Res 2010;40:1688–96.
[71] Leung CKY, Pheeraphan T. Very high early strength of microwave cured concrete. Cem Concr Res 1995;25:136–46.
[72] Sohn D, Johnson DL. Microwave curing effects on the 28-day strength of cementitious materials. Cem Concr Res 1999;29:241–7.
[73] Lee M. Preliminary study for strength and freeze-thaw durability of microwave- and steam-cured concrete. J Mater Civ Eng 2007;19:972–6.
[74] Makul N, Agrawal DK. Influence of microwave-accelerated curing procedures on the microstructure and strength characteristics of type I-Portland cement pastes. J Ceram Process Res 2011;12:376–81.
[75] Oriol M, Pera J. Pozzolanic activity of metakaolin under microwave treatment. Cem Concr Res 1995;25:265–70.
[76] Dongxu L, Xuequan W. A study on the application of vacuum microwave composite dewatering technnique in concrete engineering. Cem Concr Res 1994;24:159–64.
[77] Rattanadecho P, Suwannapum N, Chatveera B, Atong D, Makul N. Development of compressive strength of cement paste under accelerated curing by using a continuous microwave thermal processor. Mater Sci Eng A 2008;472:299–307.
[78] Mak SL, Shapiro TGS. Accelerated heating of concrete with microwave curing. In: Proceedings of the 4th CANMET/ACI/JCI international conference on recent advances in concrete technology. Tokushima, Japan; 7–11 June 1989. p. 531–42.
[79] Mak SL, Taylor AH, Son T, El-Hassan MT. Performance of concrete subjected to microwave accelerated processing. In: Proceedings of the Proceedings of the 4th CANMET/ACI international conference on durability of concrete. Sydney, Australia; 17–22 August 1997. p. 603–15.
[80] Mak SL. Properties of heat cured concrete. Brisbane, Queensland, Australia: Presented to Concrete Institute of Australia Seminar on Heat, Fire, Weather Effects on Concrete; 1999; 156–63.
[81] Mak SL, Banks R, Ritchie R, Shapiro G. Practical industrial microwave technology for rapid curing of precast concrete. Presented to Concrete 2001: 20th Biennial concrete conference. Perth, Western Australia; 11–14 September, 2001.
[82] Mak SL, Ritchie DJ, Shapiro G, Banks RW., Rapid microwave curing of precast concrete slab elements. Presented to 5th CANMET/ACI international conference on recent advances in concrete technology. Singapore; 29 July to 1 August, 2001.
[83] Mak SL, Banks RW, Ritchie DJ, Shapiro G. Advances in microwave curing of concrete. Presented to 4th World congress on microwave & radio frequency applications. Sydney, Australia; 22–26 September, 2002.
[84] Mario P, Sergio L. Patent No. EP0462612A1, Process and Device for Accelerating the Drying of Cement Mixes; Publication date: December 27, 1991.
[85] Ludewig A, Steinbach D. Patent No. WO1997021060A1, Method and Device for Drying out Buildings and or Fixed Components; Publication date: Jun 12, 1997.
[86] Engelbrecht HCL, Birch-Rasmussen S. Patent No. WO2009027813A2, Process for Curing And Drying Reinforced Concrete; Publication date: March 5, 2009.
[87] Engelbrecht HCL, Birch-Rasmussen S. Patent No. EP2197641B1, Process for Curing and Drying Reinforced Concrete; Publication date: February 23, 2011.
[88] Yasunaka H, Shibamoto M, Sukagawa T. Microwave decontaminator for concrete surface decontamination in JPDR. In: Proceedings of the international decommissioning symposium. United States of America; 1987. p. 4-109–16.
[89] Hills DL. The removal of concrete layers from biological shields by microwave EUR 12185. 2nd Ed.. Brussels: Nuclear Science and Technology, Commission of the European Communities, Brussels; 1989.
[90] Ebadian MA, Li W. A theoretical/experimental investigation of the decontamination of a radioactively contaminated concrete surface using microwave technology: final report. DOE Project, DE-AC05-840R2140; 1992.
[91] White TL, Grubb RG, Pugh LP, Foster D Jr, Box WD. Removal of contaminated concrete surfaces by microwave heating – phase I results presented at the 18th American nuclear society symposium on waste management waste management 92. Tucson, Arizona; 1992.
[92] Li W, Ebadian MA, White TL, Grubb RG, Foster D., Heat and mass transfer in a contaminated porous concrete slab subjected to microwave heating. General Papers in Heat Transfer and Heat Transfer in Hazardous Waste Processing, ASME HTD (2nd Ed.), vol. 212; 1992. p. 143–53.
[93] Li W, White TL, Foster D, Ebadian MA. Heat transfer within a steel-reinforced porous concrete slab subjected to microwave heating. J Heat Transf 1995;117 (3):582–9.
[94] Li W, Ebadian MA, White TL, Grubb RG, Foster D. Heat and mass transfer in a contaminated porous concrete slab with variable dielectric properties. Int J Heat Mass Transf 1994;37:1013–27.
[95] Lagos LE, Li W, Ebadian MA, White TL, Grubb RG, Foster D. Heat transfer within a concrete slab with a finite microwave heating source. Int J Heat Mass Transf 1995;38:887–97.
[96] Zi G, Bažant ZP. Decontamination of radionuclides from concrete by microwave heating. II: computations. J Eng Mech 2003;129:785–92.
[97] Neelakantan TR, Ramasundaram S, Shanmugavel R. Prediction of 28-day compressive strength of concrete from early strength and accelerated curing parameters. Int J Eng Tech 2013;5:1197–201.
[98] Pheeraphana T, Cayliani L, Dumangas Jr MI, Nimityongskul P. Prediction of later-age compressive strength of normal concrete based on the accelerated strength of concrete cured with microwave energy. Cem Concr Res 2002;32:521–7.
[99] Reboul JP. The hydraulic reaction of tricalcium silicate observed by microwave dielectric measurements. Rev Phys Appl (Paris) 1978;13:383–6.
[100] Naik TR, Ramme BW. Determination of the water content of concrete by the microwave method. Cem Concr Res 1987;17:927–38.
[101] Henry F, Broncy M, Berteaud AJ. The hydration kinetics studied by means of microwaves. Microwaves 1978;19:608–12.
[102] Watson A. The non-destructive measurement of water content by microwave absorption. CIB No. 3; 1960. p. 15–6.
[103] Nagi M, Whiting D. Determination of water content of fresh concrete using a microwave oven. Cem Concr Aggreg 1994;16:125–31.
[104] Zoughi R, Nowak PS, Bois KJ, Benally AD, Mirshahi R, Campbell H. Near-field microwave inspection of cement based materials – microwave sensor for nondestructive and non-contact estimation of concrete compressive strength, final report. NSF Contract no. CMS-9523264 and EPRI Contact no. WO 8031-09; 1998.
[105] Zhang J, Scherer GW. Comparison of methods for arresting hydration of cement. Cem Concr Res 2011;41:1024–36.
[106] Bois KA, Benally A, Zoughi R. Microwave near-field reflection property analysis of concrete for material content determination. IEEE Trans Instrum Meas 2000;49:49–55.
[107] Bois KA, Benally A, Zoughi R. Near-field microwave non-invasive determination of NaCl in mortar. IEEE Proc Sci Meas Technol Special Issue Non-destr Test Eval 2001;148:178–82.
[108] Hashem M, Al-Mattarneh A, Ghodgaonkar DK, Mahmood W, Majid WA. Determination of compressive strength of concrete using free-space reflection measurements in the frequency range of 8–12.5 GHz. Asia-Pacific Microwave Conference: Taipei, Taiwan; 2001. p. 679–82.
[109] Klysz G, Balayssac JP. Determination of volumetric water content of concrete using ground-penetrating radar. Cem Concr Res 2007;37:1164–71.
[110] Donnell KM, Zoughi R, Kurtis KE. Demonstration of microwave method for detection of alkali-silica reaction (ASR) gel in cement-based materials. Cem Concr Res 2013;44:1–7.
[111] Donnell KM, Hatfield S, Zoughi R, Kurtis KE. Wideband microwave characterization of alkali-silica reaction (ASR) gel in cement-based materials. Mater Lett 2013;90:159–61.
[112] Ayappa KG, Davis HT, Crapiste G, Davis EA, Gordon J. Microwave heating: an evaluation of power formulations. Chem Eng Sci 1991;46:1005–16.
[113] Ayappa KG, Davis HT, Davis EA, Gordon J. Analysis of microwave heating of materials with temperature-dependent properties. AIChE J 1991;37:313–22.
[114] Rattanadecho P, Aoki K, Akahori M. A numerical and experimental investigation of the modeling of microwave drying using a rectangular wave guide. Dry Technol Int J 2001;19:2209–34.
[115] Pheeraphan T. Accelerated curing of concrete with microwave energy (Doctor of Philosophy Dissertation). MIT; 1997.
[116] Makul N, Rattanadecho P, Agrawal DK. Microwave curing at an operating frequency of 2.45 GHz of Portland cement paste at early-stage using a multimode cavity: experimental and numerical analysis on heat transfer characteristics. Int Commun Heat Mass Transf 2010;37:1487–95.
[117] Occupational Health and Safety Administration (OSHA). Radiofrequency and microwave radiation. ⟨www.osha.gov/SLTC/radiofrequencyradiation/⟩ ; 2009 [accessed 04.12.13].
[118] International Radiation Protection Association (IRPA). International commission on non-ionizing radiation protection (ICNIRP) guidelines: for limiting exposure to time-varying electric, magnetic and electromagnetic fields (up to 300 GHz). Health Phys 1988;54:492–522.
[119] Institute of Electrical and Electronics Engineers (IEEE). Technical information statement on: human exposure to microwaves and other radio frequency electromagnetic fields. IEEE Eng Med Biol Mag 1995;14:336–7.
[120] Institute of Electrical and Electronics Engineers (IEEE). Standard for safety levels with respect to human exposure to radio frequency electromagnetic fields 3 kHz to 300 GHz. IEEE/ANSI 2005;C95:1.
[121] National Radiological Protection Board (NRPB) and the Health Protection Agency. Review of the Scientific Evidence for Limiting Exposure to Electromagnetic Fields (0–300 GHz); 2004.

Aqueous Humor Natural Convection of the Human Eye induced by Electromagnetic Fields: In the Supine Position

Teerapot Wessapan
School of Aviation, Eastern Asia University, Pathumthani 12110, Thailand
Email: teerapot@yahoo.com

Phadungsak Rattanadecho
Department of Mechanical Engineering, Faculty of Engineering, Thammasat University, Pathumthani 12120, Thailand
Email: ratphadu@engr.tu.ac.th

***Abstract*—This study presents the simulation of the specific absorption rate (SAR), fluid flow and heat transfer in an anatomical human eye exposed to EM fields in the supine position. In this study, the frequencies of 900 and 1800 MHz were chosen for our simulations. This work focuses on the aqueous humor natural convection of the lying human eye induced by electromagnetic (EM) fields. In this study, the effect of operating frequency on the SAR, fluid flow and heat transfer in the eye was systematically investigated. The SAR value and the temperature distribution in various tissues in the eye during exposure to EM fields were obtained by numerical simulation of EM wave propagation and a heat transfer model was then developed based on the natural convection and porous media theories. The findings demonstrate the potential of aqueous humor natural convection in enhancing heat transfer of the eye in the supine position.**

***Index Terms*—electromagnetic fields, heat transfer, specific absorption rate, human eye, natural convection**

I. Introduction

Since the human eye is one of the most sensitive organs to the EM radiation. The high intensity EM fields can lead to a number of ocular effects. However, the resulting thermo-physiologic response of the eye to EM fields is still not well understood. In order to gain insight into the phenomena of heat and mass transfer in the eye concerned with the temperature distribution induced by EM fields, a detailed knowledge of the absorbed power distribution as well as the temperature distribution is necessary. Therefore, this study investigates the ocular effects occurred during exposure to EM fields. The severity of these effects produced by increasing a small temperature can cause eyesight to worsen. There have been medical case reports of the formation of cataracts in humans following accidental exposure to microwave radiation [1]. Actually, a small temperature increase of 3-5 °C in the eye leads to induce cataracts formation [2]. Additionally, it is reported that the temperature above 41°C is necessary for production of posterior lens opacities [3].

The topic of temperature increase in human tissue when exposed to EM fields, particularly those radiated to the eye, has been of interest for many years. Recently, the modeling of heat transport in human tissue has been investigated by many researchers [4]-[17]. The thermal modeling of human tissue is important as a tool to investigate the effect of external heat sources and to predict the abnormalities in the tissue. In the past, most studies of heat transfer analysis in the eye used heat conduction equation [4]-[10]. Some studies carried out on the natural convection in the eye based on heat conduction model [11], [12]. Ooi and Ng [12], [13] studied the effect of aqueous humor (AH) hydrodynamics on the heat transfer in the eye based on heat conduction model. Meanwhile, the bioheat equation, introduced by Pennes [14], [15] based on the heat diffusion equation for a blood perfused tissue, is used for modeling of the heat transfer in the eye as well [16], [17]. Ooi and Ng also developed a three-dimensional model of the eye [18], extending their two-dimensional model [17]. Recently, porous media models have been utilized to investigate the transport phenomena in biological media instead of a simplified bioheat model [19]-[21]. Shafahi and Vafai [22] proposed the porous media along with a natural convection model to analyze the eye thermal characteristics during exposure to thermal disturbances. The other research groups have been tried to conduct the advanced model using a coupled model of heat and EM dissipation in the eye [6]-[10]. Ooi et al. have been tried to conduct the advanced model using the coupled model of heat and laser irradiation in the eye [23]. Results from a similar model of Ooi *et al.* [23] for various applications were also presented in continuation [24]-[27]. Wessapan *et al.* [28] investigated the SAR and temperature distributions in the eye during exposed to EM waves at 900 MHz using the porous media theory.

Manscript received August 22, 2013; revised October 21, 2013.

©2014 Engineering and Technology Publishing
doi: 10.12720/jomb.3.4.251-258

Most previous studies of the interaction between the EM fields and the eye mainly focused on SAR. They have not been considered heat transfer causing an incomplete analysis of results. Therefore, the modeling of the heat transport is needed to completely explain the actual process of interaction between the EM fields and the eye. Although the porous media and natural convection models of the eye have been used in the previous biomedical studies [11], [12], [30], most studies of the human eye exposed to the EM fields, especially at different frequencies, have not been considering the porous media and natural convection approaches is sparse or non-existent.

This study presents the simulation of the SAR, fluid flow and temperature distributions in an anatomical human eye exposed to EM fields in the supine position. The work described in this paper is substantially extended from our previous work [28] by further enhancing the focus on the transport phenomena in the eye of lying human. In this study, a two-dimensional human eye model was used to simulate the SAR and temperature distributions in the eye model. The EM wave propagation in the eye was investigated by using Maxwell's equations. An analysis of the heat transfer in the eye exposed to TM-mode of EM fields at different frequencies was investigated using a developed heat transfer model (included the conduction and natural convection heat transfer modes) [22]. In the eye model of lying human, the effect of operating frequency on the SAR, fluid flow and temperature distributions in the eye is systematically investigated. The SAR and temperature distributions in various parts of the eye during exposure to EM fields of 900 and 1800 MHz are obtained by numerical simulation of the EM wave propagation and heat transfer equations.

II. Formulation of the Problem

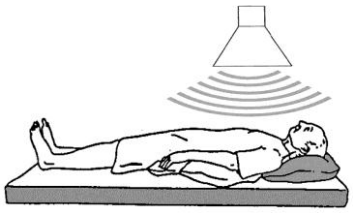

Figure 1. EM fields from an EM radiation device radiated to a supine human body.

Fig. 1 shows the radiation of the EM fields from an EM radiation device to the eye of lying human. These EM fields fall on the eye that causes heating in the deeper tissue, which leads to tissue damage and cataract formation. Due to ethical consideration, exposing the human to EM fields for experimental purposes is limited. It is more convenient to develop a realistic human eye model through the numerical simulation. A highlight of this work is the illustration of the transport phenomena, including the heat and mass transfer in the eye during exposure to EM fields at different frequencies. The analyses of the SAR and the heat transfer in the eye exposed to EM fields will be illustrated in Sec. 3. The system of governing equations as well as the initial and boundary conditions are solved numerically using the finite element method (FEM).

III. Methods and Model

The first step in evaluating the effects of a certain exposure to EM fields in the eye is to determine the induced internal EM fields and its spatial distribution. Thereafter, EM energy absorption which results in temperature increase in the eye and other interactions will be able to be considered.

A. Physical Model

In this study, the two-dimensional model of the eye, which follows the physical model in the previous research [22], is developed. Fig. 2 shows the two-dimensional eye model used in this study. This model comprises 7 types of tissue including cornea, anterior chamber, posterior chamber, iris, sclera, lens and vitreous. These tissues have the different dielectric and thermal properties. In the sclera layer, there are two more layers known as the choroid and retina which are relatively thin compared to the sclera. To simplify the problem, these layers are assumed to be homogeneous. The iris and sclera, which have the same properties, are modeled together as one homogenous region [12]. The dielectric and thermal properties of tissue are given in Tables I and II, respectively. Each tissue is assumed to be homogeneous and electrically as well as thermally isotropic.

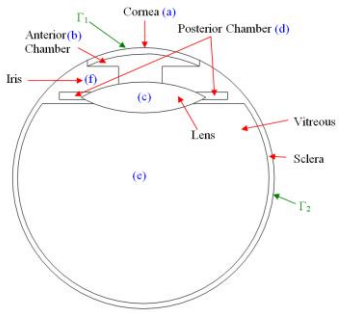

Figure 2. Human eye vertical cross section [22].

TABLE I. Dielectric Properties of Tissues at 900 MHz and 1800 MHz [29]-[31]

	Frequency: 900		Frequency: 1800	
	ε_r	σ (S/m)	ε_r	σ (S/m)
Cornea *(a)*	52.0	1.85	55.0	2.32
Anterior Chamber *(b)*	73.0	1.97	75.0	2.40
Lens *(c)*	51.3	0.89	41.1	1.29
Posterior Chamber *(d)*	73.0	1.97	75.0	2.40
Vitreous *(e)*	74.3	1.97	73.7	2.33
Sclera *(f)*	52.1	1.22	52.7	1.68
Iris *(f)*	52.1	1.22	52.7	1.68

©2014 Engineering and Technology Publishing

TABLE II. THERMAL PROPERTIES OF THE EYE [12]

Tissue	ρ (kg/m^3)	k (W/m°C)	C_p (J/kg°C)	μ (N s/m^2)	β (1/K)
Cornea *(a)*	1050	0.58	4178	-	-
Anterior Chamber *(b)*	996	0.58	3997	0.00074	0.000337
Lens *(c)*	1000	0.4	3000	-	-
Posterior Chamber *(d)*	996	0.58	3997	-	-
Vitreous *(e)*	1100	0.603	4178	-	-
Sclera *(f)*	1050	1.0042	3180	-	-
Iris *(f)*	1050	1.0042	3180	-	-

B. Equations for EM Wave Propagation Analysis

The mathematical models are developed to predict the electric fields and the SAR with respect to the temperature gradient in the eye. To simplify the problem, the following assumptions are made:

1) The EM wave propagation is modeled in two dimensions.
2) The eye in which the EM waves interact with the eye proceeds in the open region.
3) The free space is truncated by scattering boundary condition.
4) The model assumes that dielectric properties of each tissue are constant.
5) In the eye, the EM waves are characterized by transverse magnetic fields (TM-mode).

The EM wave propagation in the eye is calculated using Maxwell's equations which mathematically describe the interdependence of the EM waves. The general form of Maxwell's equations is simplified to demonstrate the EM fields penetrated in the eye as the following equation:

$$\nabla\times\left(\left(\varepsilon_r-\frac{j\sigma}{\omega\varepsilon_0}\right)^{-1}\nabla\times H_z\right)-\mu_r k_0{}^2 H_z=0 \tag{1}$$

where H is the magnetic field (A/m), μ_r is the relative magnetic permeability, ε_r is the relative dielectric constant, $\varepsilon_0 = 8.8542\times10^{-12}$F/m is the permittivity of free space, k_0 is the free space wave number (m^{-1}).

Boundary condition for wave propagation analysis

EM energy is emitted by an EM radiation device and falls on the eye with a particular power density. Therefore, boundary condition for solving EM wave propagation is described as follows:

It is assumed that the uniform wave flux falls on the left side of the eye. Therefore, at the left boundary of the considered domain, an EM simulator employs TM wave propagation port with specified power density,

$$S = \int(E-E_1)\cdot E_1/\int E_1\cdot E_1 \tag{2}$$

Boundary conditions along the interfaces between different mediums, for example, between air and tissue or tissue and tissue, are considered as continuity boundary condition,

$$n\times(E_1-E_2)=0 \tag{3}$$

The outer sides of the calculated domain, i.e., free space, are considered as scattering boundary condition [25],

$$n\times(\nabla\times E_z)-jkE_z=-jk(1-k\cdot n)E_{0z}\exp(-jk\cdot r) \tag{4}$$

where k is the wave number (m^{-1}), σ is the electrical conductivity (S/m), n is the normal vector, $j=\sqrt{-1}$, and E_0 is the incident plane wave (V/m).

C. Interaction of EM Fields and Human Tissues

Interaction of EM fields with biological tissue can be defined in the term of the SAR. When the EM waves propagate through the tissue, the energy of EM waves is absorbed by the tissue. The SAR is defined as power dissipation rate normalized by material density [21]. The SAR is given by,

$$SAR=\frac{\sigma}{\rho}|E|^2 \tag{5}$$

where E is the electric field intensity (V/m), σ is the electric conductivity (S/m), and ρ is the tissue density (kg/m^3).

D. Equations for Heat Transfer and Flow Analysis

To solve the thermal problem, the coupled effects of the EM wave propagation and the unsteady bioheat transfer are investigated. The temperature distribution is corresponded to the SAR. This is because the SAR in the eye distributes owing to energy absorption. Thereafter, the absorbed energy is converted to thermal energy, which increases the tissue temperature.

Heat transfer analysis of the eye is modeled in two dimensions. To simplify the problem, the following assumptions are made:

1) The Human tissue is a bio-material with constant thermal properties.
2) There is no phase change of substance in the tissue.
3) There is a local thermal equilibrium between the blood and the tissue.
4) There is no chemical reaction in the tissue.

This study utilized the pertinent thermal model based on the porous media theory [22] to investigate the heat transfer behavior of the eye when exposed to the EM fields.

©2014 Engineering and Technology Publishing

In this study, the motion of fluid is considered only inside the anterior chamber [12]. There is a blood flow in the iris/sclera part, which plays a role to adjust the eye temperature with the rest of the body [22]. For the rest parts, the metabolic heat generation is neglected based on the fact that these comprise mainly water [12]. The equation governing the flow of heat in cornea, posterior chamber, lens and vitreous are resembled the classical heat conduction equation given in Eq. (6).

$$\rho_i C_i \frac{\partial T_i}{\partial t} = \nabla \cdot (k_i \nabla T_i) + Q_{ext} \quad ; i = a, c, d, e \tag{6}$$

This model accounts for the existence of AH in the anterior chamber. The heat transfer process consists of both the conduction and natural convections, which can be written as follows:

Continuity equation:

$$\nabla \cdot u_i = 0 \quad ; \quad i=b \tag{7}$$

Momentum equation:

$$\rho_i \frac{\partial u_i}{\partial t} + \rho_i u_i \nabla \cdot u_i = -\nabla p_i + \nabla \cdot [\mu(\nabla u_i + \nabla u_i^T)] + \rho_i g \beta_i (T_i - T_{ref}) \quad ;i=b \tag{8}$$

where i denotes each subdomain in the eye model as shown in Fig. 2, ρ is the tissue density (kg/m^3), β is the volume expansion coefficient (1/K), u is the velocity (m/s), p is the pressure (N/m^2), μ is the dynamic viscosity of AH (N.s/m^2), t is the time, T is the tissue temperature (K), and T_{ref} is the reference temperature considered here is 37°C. The effects of buoyancy due to the temperature gradient are modeled using the Boussinesq approximation which states that the density of a given fluid changes slightly with temperature but negligibly with pressure [12].

Energy equation:

$$\rho_i C_i \frac{\partial T_i}{\partial t} - \nabla \cdot (k_i \nabla T_i) = -\rho C_i u_i \cdot \nabla T_i + Q_{ext} \; ; \; i=b \tag{9}$$

The sclera/iris is modeled as a porous medium with the blood perfusion, which assumes that local thermal equilibrium exits between the blood and the tissue. The blood perfusion rate used is 0.0041/s. A modified Pennes' bioheat equation [22], [31] is used to calculate the temperature distribution in the sclera/ iris.

$$(1-\varepsilon)\rho_i C_i \frac{\partial T_i}{\partial t} = \nabla \cdot ((1-\varepsilon) k_i \nabla T_i) + \rho_b C_b \omega_b (T_b - T_i) + Q_{ext} \; ; \quad i=f \tag{10}$$

where C is the heat capacity of tissue (J/kg K), k is the thermal conductivity of tissue (W/m K), T_b is the temperature of blood (K), ρ_b is the density of blood (kg/m^3), C_b is the specific heat capacity of blood (J/ kg K), ω_b is the blood perfusion rate (1/s), and Q_{ext} is the external heat source term (EM heat-source density) (W/m^3).

In the analysis, the porosity (ε) used is assumed to be 0.6. The heat conduction between the tissue and the blood flow is approximated by the blood perfusion term, $\rho_b C_b \omega_b (T_b - T)$.

The external heat source term is equal to the resistive heat generated by the EM fields (EM power absorbed), which defined as

$$Q_{ext} = \frac{1}{2}\sigma_{tissue}\left|\vec{E}\right|^2 = \frac{\rho}{2} \cdot SAR \tag{11}$$

where σ_{tissue} is the electric conductivity of tissue (S/m).

Boundary condition for heat transfer analysis

The heat transfer analysis excluding the surrounding space is considered only in the eye. The cornea surface is considered as the convective, radiative, and evaporative boundary conditions.

$$-n.(-k\nabla T) = h_{am}(T_i - T_{am}) + \varepsilon\sigma(T_i^4 - T_{am}^4) + e$$
$$\text{on } \Gamma_1 \quad i = a \tag{12}$$

where Γ_i is the external surface area corresponding to section i, e is the tear evaporation heat loss (W/m^2), T_{am} is the ambient temperature (K), h_{am} is the convection coefficient (W/m^2.K).

The temperature of blood generally assumed to be the same as the body core temperature causes heat to be transferred into the eye [12]. The surface of the sclera is assumed to be a convective boundary condition

$$-n \cdot (-k_i \nabla T_i) = h_b (T_b - T_i) \qquad \text{on } \Gamma_2 \quad i = f \tag{13}$$

where h_b is the convection coefficient of blood (65 W/m^2.K). Γ_1 and Γ_2 are the corneal surface and sclera surface of the eye, respectively.

E. Calculation Procedure

In this study, the finite element method is used to analyze the transient problems. The computational scheme is to assemble finite element model and compute a local heat generation term by performing an EM calculation using tissue properties. In order to obtain a good approximation, a fine mesh is specified in the sensitive areas. This study provides a variable mesh method for solving the problem as shown in Fig. 3. The system of governing equations as well as the initial and boundary conditions are then solved.

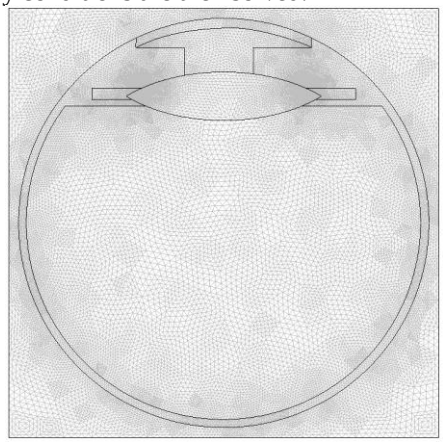

Figure 3. A two-dimensional finite element meshes of the eye model.

©2014 Engineering and Technology Publishing

The 2D model is discretized using triangular elements and the Lagrange quadratic is then used to approximate the temperature and SAR variations across each element. The convergence test is carried out to identify the suitable number of elements required. This convergence test leads to the grid with approximately 10,000 elements. It is reasonable to assume that, at this element number, the accuracy of the simulation results is independent from the number of elements.

IV. Results and Discussion

Since most GSM networks use frequencies in the 900 and 1800 MHz spectrum, therefore, in this analysis, the effects of these operating frequencies on distributions of SAR and temperature in the eye are systematically investigated. In this study, the coupled model of the EM and thermal fields are solved numerically. For the simulation, the dielectric and thermal properties are directly taken from Tables 1 and 2, respectively.

A. Verification of the Model

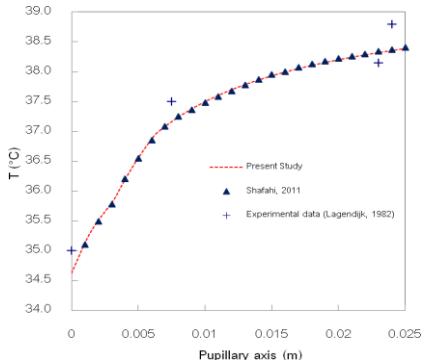

Figure 4. Comparison of the calculated temperature distribution to the temperature distribution obtained by Shafahi and Vafai [22], and the Lagendijk's experimental data [4]; h_{am}=20W/m^2.K and T_{am}=25 °C.

In order to verify the accuracy of the present numerical models, the case without EM fields of the simulated results from this study are validated against the numerical results with the same geometric model obtained by Shafahi and Vafai [22]. Moreover, the numerical results are then compared to the experimental results of the rabbit obtained from Lagendijk [4]. The validation case assumes that the rabbit body temperature is 38.8 °C, the tear evaporation heat loss is 40 W/m^2, the ambient temperature is 25 °C, and the convection coefficient of ambient air is 20 W/m^2.K. The results of the selected test case are depicted in Fig. 4 for temperature distribution in the eye. Fig. 4 clearly shows a good agreement of the temperature distribution in the eye between the present solution and that of Shafahi and Vafai [22] and Lagendijk [4]. In the figure, the simulated results provides a good agreement with the simulated results obtained from Shafahi and Vafai [22]. This favorable comparison lends confidence in the accuracy of the present numerical model.

B. Electric field Distribution

Fig. 5 shows the simulation of an electric field pattern inside the eye exposed to the EM fields in TM mode operating at the frequencies of 900 and 1800 MHz propagating along the vertical cross section human eye model. By comparison, the maximum electric field intensity in outer parts of the eye at the frequency of 900 MHz displays a higher value than that of 1800 MHz. The maximum electric field intensities are 391.8 and 231.2 V/m at the frequencies of 900 and 1800 MHz, respectively. The maximum value for the frequency of 900 MHz is in the cornea while for the frequency of 1800 MHz is in the lens. Mathematically, this result corresponds to Eq. (1) and the dielectric properties (ε_r) in Table I show that the frequency of 900 MHz has lower dielectric properties of cornea, while the frequency of 1800 MHz has lower dielectric properties of lens. It is found that these alterations of electric field distribution between the two chosen frequencies vary in extent with the magnitude of the dielectric property and with the standing-wave pattern.

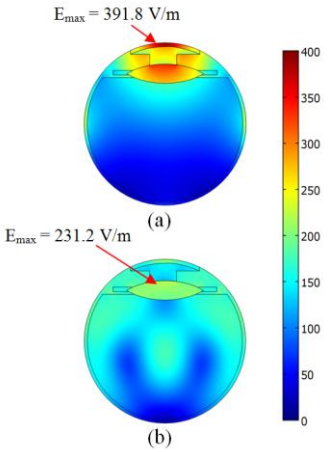

Figure 5. Electric field distribution (V/m) in the eye exposed to the EM power density of 100 mW/cm^2 at the frequencies of *(a)* 900 MHz and *(b)* 1800 MHz.

C. SAR Distribution

Fig. 6 shows the SAR distribution evaluated on the vertical cross section of the eye exposed to the EM frequencies of 900 and 1800 MHz. It is evident from the figure that the results of the SAR values in the eye (Fig. 6) are increased corresponding to the electric field intensities (Fig. 5). Besides the electric field intensity, the magnitude of the dielectric and thermal properties in each tissue will directly affect SAR values in the eye. For both frequencies, the highest SAR values are obtained in the region of the corneal surface. In this region, the frequencies of 900 and 1800 MHz display SAR values of 135.2 and 45.9 W/kg, respectively. This is because the cornea has a much higher value of its electrical conductivity (σ) than those of lens and iris. The second main reason is the position of the cornea located close to the exposed surface, at which the electric field intensity is strongest. It is found that the SAR distribution pattern in the eye, which corresponds to Eq. (5), is strongly depended on the effect of the dielectric properties (σ, shown in Table I) and thermal properties (ρ, shown in Table II). Moreover, the SAR pattern at the frequency of 1800 MHz shows a greater value of the EM power

©2014 Engineering and Technology Publishing

absorption in the deep part of the eye, with less surface heating, compared to those of 900 MHz.

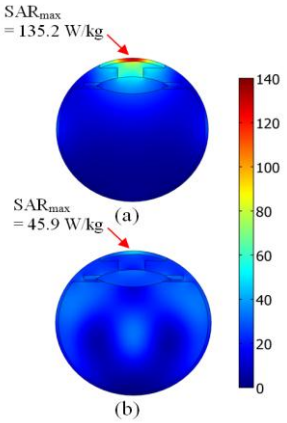

Figure 6. SAR distribution (W/kg) in the eye exposed to the EM power density of 100 mW/cm^2 at the frequencies of *(a)* 900 MHz and *(b)* 1800 MHz.

D. Velocity Fields and Temperature Distributions

In this study, the effect of an ambient temperature variation have been neglected in order to gain insight into the interaction between the EM fields and the tissue as well as the correlation between the SAR and the heat transfer mechanism. For this reason, the ambient temperature has been set to the human body temperature of 37 °C, and the tear evaporation has been neglected. Moreover, the effect of thermoregulation mechanisms has also been neglected due to the small temperature increase occurred during exposure process. The convective coefficient due to the blood flow inside the sclera is set to 65 W/m^2.K [12].

Fig. 7 shows the circulatory patterns in the anterior chamber in the eye exposed to the EM frequencies of 900 and 1800 MHz at various times. These patterns vary corresponding to the temperature gradient in the eye. Therefore, in the case of a lower temperature gradient, the circulatory patterns have a lower speed, where a circulatory pattern with a higher temperature gradient flows faster. For the 900 MHz frequency, at the early stage (t=10s) a counterclockwise circulation thus appears in the anterior chamber, shown in Fig. 7a. This seemed to imply that the heat gradually travels inward passes through the front of the eye to the lens corresponding to the higher SAR value at the cornea surface (Fig. 6a). Later, it is found that the natural convection and formation of two circulatory patterns with opposite direction in the anterior chamber, shown in Fig. 7a, play important roles on the cooling processes in the eye, especially in the inner corneal surface. It is observed that a large temperature gradient is significantly produced by the EM fields after 10 minutes. The circulation pattern implies that the generated heat in the anterior chamber is transferred outward from the lens surface. While for the 1800 MHz frequency, at the early stage the formation of two circulatory patterns with opposite direction in the anterior chamber is occurred in the inward direction. Surprisingly, after 60s, the circulatory patterns in the reverse direction thus appear in the anterior chamber, shown in Fig. 7b. The direction of heat transfer is to reverse outward from the lens surface. In the stage of heating (after 60 s), the effect of convective flow becomes stronger and plays a more important role, especially at the center region of the anterior chamber. However, at the peripheral region of the anterior chamber where the convection flow is small, temperature distributions are primarily governed by the conduction mode. At the steady state, the flow pattern is symmetrical between left and right sides for both frequencies. The flow fields are in the same direction but the magnitudes of velocity are clearly different. The circulation pattern in each case significantly different from each other, this is because each case exhibited a different heating pattern.

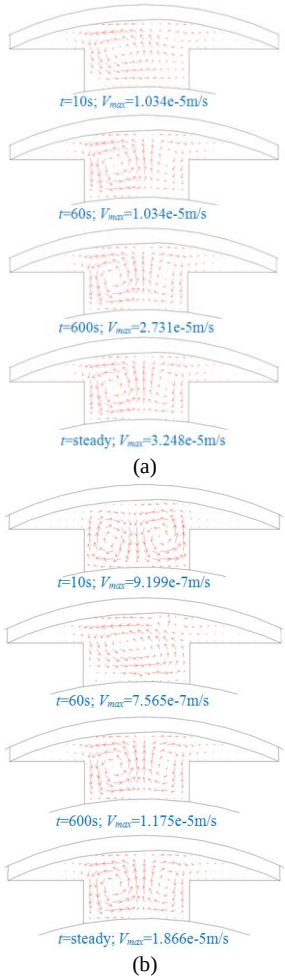

Figure 7. The velocity fields inside the anterior chamber at various time exposed to the EM power density of 100 mW/cm^2 at the frequencies of *(a)* 900 MHz and *(b)* 1800 MHz.

Fig. 8 shows the temperature distribution in the vertical cross section human eye at various time exposed to the EM frequencies of 900 (Fig. 8a) and 1800 MHz (Fig. 8b). For the eye exposed to the EM fields for a period of time, the temperature in the eye (Fig. 8) is increased corresponding to the SAR (Fig. 6). This is because the electric fields in the eye attenuate owing to the energy absorbed and thereafter the absorbed energy is converted to thermal energy, which increases the eye temperature.

For the 900 MHz frequency, even though the maximum values of the electric fields (Fig. 5a) and the

©2014 Engineering and Technology Publishing

SAR (Fig. 6a), are the cornea, the highest temperature is the anterior chamber (Fig. 8a). This is owing to the extensive penetration of the EM power of the internal regions and the higher dielectric properties (ε_r) of the anterior chamber. This higher dielectric property of the anterior chamber represents the stronger absorption ability of EM fields than those of cornea and lens. Moreover, the outer corneal surface has a lower temperature than that of the anterior chamber, even if it has higher SAR value (Fig. 6a). This is because, in this area, the generated heat is dissipated to the ambient via convection and radiation.

While for the 1800 MHz frequency, beside the cornea and lens, the high value of the electric fields is the middle of the vitreous and peripheral vitreous. This is owing to the constructive interference between the forward and reflected waves of the higher frequency of 1800 MHz results in standing wave patterns forming in the EM fields (Fig. 7b) in the vitreous area. This high electric field intensity increases the amount of energy absorption in the vitreous area (Fig. 8b) and consequently causes the temperature to rise (Fig. 9b). In this case, the maximum temperature increase in the peripheral vitreous area has a lower level than that of the middle of the vitreous even if the peripheral vitreous area also has high electric field intensity and the SAR value also. This is due to the presence of blood perfusion in the sclera tissue, which covers an internal surface area of the eye. This blood perfusion provides buffer characteristic to the eye temperature and plays important roles on the cooling processes in the peripheral vitreous area.

A longer exposure time resulted in a higher heat accumulation inside the eye, thereby increasing its temperature. By using the operating frequency of 900 MHz, the maximum temperatures increase are 0.216, 0.849, 2.433, and 3.052 ℃ for the exposure times of 10s, 60s, 600s, and at steady-state conditions of 3600s, respectively. By using the operating frequency of 1800 MHz, the maximum temperatures increase are 0.1, 0.417, 2.068, and 40.323 ℃ for the exposure times of 10s, 60s, 600s, and at steady-state conditions of 3600s, respectively.

In this study, the maximum temperature increase in the eye exposed to the EM fields with the power density of 100 mW/cm^2 at the frequencies of 900 and 1800 MHz are 3.052 and 3.323 ℃, respectively.

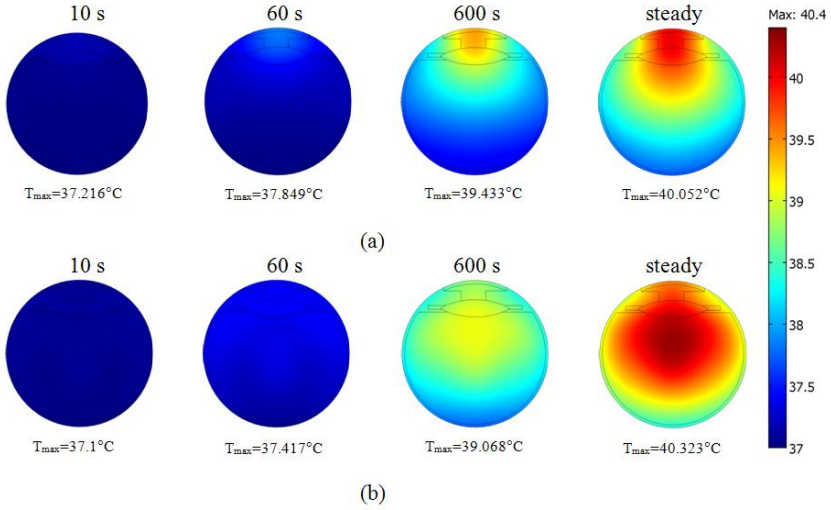

Figure 8. The temperature distribution in the eye at various time exposed to the EM power density of 100 mW/cm^2 at the frequencies of *(a)* 900 MHz and *(b)* 1800 MHz.

V. Conclusions

In this study, the aqueous humor natural convection of the lying human eye induced by electromagnetic (EM) fields is systematically investigated. From the results, the electric field distributions show a strong dependence on the dielectric properties of the tissue. The results of the SAR values are increased corresponding to the electric field intensities. Besides the electric field intensity, the magnitude of the dielectric and thermal properties in each tissue will directly affect the SAR values in the eye. It is found that the convective heat transfer in the anterior chamber plays a significant role in transferring heat. This will allow a better understanding of the realistic situation of the interaction between the EM fields and the eye.

Acknowledgment

This work has been financially supported by the Thailand Research Fund (TRF), the Commission on Higher Education (CHE) and Eastern Asia University.

References

[1] A. F. Emery, P. Kramar, A. W. Guy, and J. C. Lin, "Microwave induced temperature rises in rabbit eyes in cataract research," *ASME J. Heat Transfer*, vol. 97, pp. 123–128, 1975.

[2] C. Buccella, V. D. Santis, and M. Feliaiani, "Prediction of temperature increase in human eyes due to RF sources," *IEEE Trans. Electromagn. Compat.*, vol. 49, no. 4, pp. 825–833, 2007.

[3] J. C. Lin, "Cataracts and cell-phone radiation," *IEEE Antennas and Propagation*, vol. 45, no. 1, pp. 171–174, 2003.

[4] J. J. W. Lagendijk, "A mathematical model to calculate temperature distribution in human and rabbit eye during

©2014 Engineering and Technology Publishing

hyperthermic treatment," *Physics in Medicine and Biology*, vol. 27, pp. 1301–1311, 1982.
[5] J. Scott, "A finite element model of heat transport in the human eye," *Physics in Medicine and Biology*, vol. 33, pp. 227–241, 1988.
[6] J. Scott, "The computation of temperature rises in the human eye induced by infrared radiation," *Physics in Medicine and Biology*, vol. 33, pp. 243–257, 1988.
[7] E. H. Amara, "Numerical investigations on thermal effects of laser–ocular media interaction," *Int. J. Heat Mass Transfer*, vol. 38, pp. 2479–2488, 1995.
[8] A. Hirata, S. Matsuyama, and T. Shiozawa, "Temperature rises in the human eye exposed to EM waves in the frequency range 0.6-6 GHz," *IEEE Trans. Electromagnetic Compat*, vol. 42, no. 4, pp. 386–393, 2000.
[9] K. J. Chua, J. C. Ho, S. K. Chou, and M. R. Islam, "On the study of the temperature distribution within a human eye subjected to a laser source," *Int. Commun. Heat Mass Transfer*, vol. 32, 1057–1065, 2005.
[10] W. Limtrakarn, S. Reepolmaha, and P. Dechaumphai, "Transient temperature distribution on the corneal endothelium during ophthalmic phacoemulsification: A numerical simulation using the nodeless variable element," *Asian Biomedicine*, vol. 4, no. 6, pp. 885–892, 2010.
[11] S. Kumar, S. Acharya, R. Beuerman, and A. Palkama, "Numerical solution of ocular fluid dynamics in a rabbit eye: Parametric effects," *Ann. Biomed. Eng.*, vol. 34, pp. 530–544, 2006.
[12] E. Ooi and E. Y. K. Ng, "Simulation of aqueous humor hydrodynamics in human eye heat transfer," *Comput. Biol. Med.*, vol. 38 pp. 252–262, 2008.
[13] E. H. Ooi and E. Y. K. Ng, "Effects of natural convection inside the anterior chamber," *International Journal for Numerical Methods in Biomedical Engineering*, vol. 27, pp. 408-423, 2011.
[14] H. H. Pennes, "Analysis of tissue and arterial blood temperatures in the resting human forearm," *J. Appl. Physiol*., vol. 1, pp. 93-122, 1948.
[15] H. H. Pennes, "Analysis of tissue and arterial blood temperatures in the resting human forearm," *J. Appl. Physiol*., vol. 85, no. 1, pp. 5-34, 1998.
[16] V. M. M. Flyckt, B. W. Raaymakers, and J. J. W. Lagendijk, "Modeling the impact of blood flow on the temperature distribution in the human eye and the orbit: Fixed heat transfer coefficients versus the pennes bioheat model versus discrete blood vessels," *Physics in Medicine and Biology*, vol. 51, pp. 5007–5021, 2006.
[17] E. Y. K. Ng and E. H. Ooi, "FEM simulation of the eye structure with bioheat analysis," *Comput. Methods Programs Biomed*., vol. 82, pp. 268–276, 2006.
[18] E. H. Ooi and E. Y. K. Ng, "Ocular temperature distribution: A mathematical perspective," *J Mech Med Biol*, vol. 9, pp. 199–227, 2009.
[19] A. Nakayama and F. Kuwahara, "A general bioheat transfer model based on the theory of porous media," *Int. J. Heat Mass Transfer*, vol. 51, pp. 3190–3199, 2008.
[20] S. Mahjoob and K. Vafai, "Analytical characterization of heat transfer through biological media incorporating hyperthermia treatment," *Int. J. Heat Mass Transfer*, vol. 52, pp. 1608–1618, 2009.
[21] K. Khanafer and K. Vafai, "Synthesis of mathematical models representing bioheat transport," *Advances in Numerical Heat Transfer*, vol. 3, pp. 1–28, 2009.
[22] M. Shafahi and K. Vafai, "Human eye response to thermal disturbances," *ASME J. Heat Transfer*, vol. 133, pp. 011009, 2011.
[23] E. H. Ooi, W. T. Ang, and E. Y. K. Ng, "A boundary element model of the human eye undergoing laser thermokeratoplasty," *Computers in Biology and Medicine*, vol. 28, pp. 727–738, 2008.
[24] E. H. Ooi, W. T. Ang, and E. Y. K. Ng, "A boundary element model for investigating the effects of eye tumor on the temperature distribution inside the human eye," *Computers in Biology and Medicine*, vol. 28, pp. 727–738, 2009.
[25] J. H. Tan, E. Y. K. Ng, U. R. Acharya, and C. Chee, "Study of normal ocular thermogram using textural parameters," *Infrared Physics & Technology*, vol. 53, pp. 120-126, 2010.
[26] J. H. Tan, E. Y. K. Ng, and U. R. Acharya, "Evaluation of tear evaporation from ocular surface by functional infrared thermography," *Medical Physics*, vol. 37, pp. 6022-6034, 2010.
[27] J. H. Tan, E. Y. K. Ng, and U. R. Acharya, "Evaluation of topographical variation in ocular surface temperature by functional infrared thermography," *Infrared Physics & Technology*, vol. 54, pp. 469-477, 2011.
[28] T. Wessapan and P. Rattanadecho, "Specific absorption rate and temperature increase in human eye subjected to electromagnetic fields at 900 MHz," *ASME J. Heat Transfer*, vol. 134, pp. 091101, 2012.
[29] P. Bernardi, M. Cavagnaro, S. Pisa, and E. Piuzzi, "Specific absorption rate and temperature increases in the head of a cellular-phone user," *IEEE Trans. Microw. Theor. Tech.*, vol. 48, no. 7, pp. 1118–1126, 2000.
[30] S. Park, J. Jeong, and Y. Lim, "Temperature rise in the human head and brain for portable handsets at 900 and 1800 MHz," in *Proc. Fourth International Conference on Microwave and Millimeter Wave Technology*, vol. 1, 2004, pp. 966-969.
[31] A. Nakayama and F. Kuwahara, "A general bioheat transfer model based on the theory of porous media," *Int. J. Heat Mass Transfer*, vol. 51, pp. 3190–3199, 2008.

Teerapot Wessapan received the Bachelor's degree in Mechanical Engineering from the Srinakharinwirot University, Bangkok, Thailand in March 2002. He received his master's degree in Mechanical Engineering from Kasetsart University, Bangkok, Thailand in 2005. He received Ph.D. degree in Engineering from Thammasat University, Bangkok, Thailand in 2011. His researches involve the numerical analysis of microwave thermal ablation, thermal response of humans exposed to electromagnetic fields, computer simulation of electromagnetic fields. He is now an Assistant Professor of Mechanical Engineering at Eastern Asia University.

Phadungsak Rattanadecho received the Bachelor's degree in Mechanical Engineering from the King Mongkut Institute of Technology Thonburi, Bangkok, Thailand in March 1991. He received the Master's degree in Mechanical Engineering from Chulalongkorn University, Thailand, in March 1994. He received Ph.D. degree in Mechanical Engineering from the Nagaoka University of Technology, Japan, 2002. His researches concern microwave heating/ drying and melting processes in porous medium, numerical analysis of electromagnetic fields (inside multimode cavity), development of numerical schemes based on lattice boltzmann method for flow and dispersion in porous media, heat and mass transport in complexity boundary-layer and so on. He is now a Professor of Mechanical Engineering at Thammasat University.

©2014 Engineering and Technology Publishing

Journal of Electrostatics 72 (2014) 477–486

Contents lists available at ScienceDirect

Journal of Electrostatics

journal homepage: www.elsevier.com/locate/elstat

Numerical and experimental studies of collection efficiency of an ion electrostatic collector for a mini-volume electrical PM detector

Panich Intra [a, *], Artit Yawootti [a], Phadungsak Rattanadecho [b]

[a] Research Unit of Electrostatic Applications in Energy and Environment, College of Integrated Science and Technology, Rajamangala University of Technology Lanna, Chiang Mai 50220, Thailand

[b] Center of Excellence in Electromagnetic Energy Utilization in Engineering, Department of Mechanical Engineering, Faculty of Engineering, Thammasat University,
Pathum Thani 12121, Thailand

ARTICLE INFO

Article history:
Received 9 March 2014
Received in revised form
11 August 2014
Accepted 15 September 2014
Available online 27 September 2014

Keywords:
Ion
Aerosol
Electrostatic
Collector
Collection efficiency

ABSTRACT

The experimental efficiency was numerically and experimentally studied for collecting negative and positive ions in a coaxial cylindrical electrostatic collector for a mini-volume electrical PM detector. The commercial computational fluid dynamics software package COMSOL Multiphysics™ was used to predict the behaviors of the flow and electric fields as well as the particle trajectories in the collecting zone of the ion collector. In the experiment, the ions were generated by a corona-needle ionizer with concentrations greater than 10^{13} ions/m^3, the positively and negatively applied voltages at the inner electrode ranged from 0 to 45 V and the ion flow rates ranged from 1 to 5 L/min. For these ion flow rates, 1–5 L/min, the ion precipitates due to space charge and diffusion effects ranged from 92 to 97 % for positive ions and 91–97 % for negative ions. The total collection efficiency of the collector increased to 100% at collection voltages larger than 5, 20 and 40 V respectively for the ion flow rates of 1, 3 and 5 L/min for both positive and negative ions. Numerical calculation results of the ion trajectory in the collecting zone of the collector; showed good agreement with the experimental results of the total collection efficiency and can be used to support the bettering of designing in order to refine an ion collector after the charger or ionizer in a mini-volume electrical aerosol detector. Finally, this shows that this ion collector was proven to be particularly useful as an electrostatic collector for positive and negative ions after the charger or ionizer in a mini-volume electrical aerosol detector.

© 2014 Elsevier B.V. All rights reserved.

Introduction

Measurement of concentration of the particulate matter (PM), any solid or liquid material suspended in air with aerodynamic diameter in the range of 1 nm–100 μm, have become an important topic in atmospheric pollution monitoring and source characterization. In recent years, considerable interest has been shown to micron-sized aerosol particles, defined as suspended aerosol particles with aerodynamic diameter lower than 2.5 μm, for two main reasons. First, such particles have been associated with adverse health effects in areas of high concentrations, and second, aerosols are believed to have a significant influence on atmospheric quality, climate at a local and global scale and processes in various industries such as food, pharmaceutical and medical, electronic and semiconductor industries [1]. PM detectors have been developed to monitor indoor and outdoor aerosols for pollution and process control industry for this purpose.

A widely used instrument capable of detecting and measuring PM is an electrical PM detector. A typical PM detector consists of an aerosol charger, an ion collector, and an aerosol electrometer. In the PM detector, aerosols are directed into the aerosol charger to charge the aerosol particles by ion-particle collisions via the diffusion charging and field charging mechanisms. The charged aerosol then passes through an ion collector to remove excess ions and moves on to a highly sensitive aerosol electrometer for charge measurement [2,3]. Generally, an ion collector is one of the most important parts of the electrical PM detector because it can prevent contamination of the signal current to be measured by free ions potentially reaching the electrometer [4]. The ion collector typically uses the principle of electrostatic precipitation and has a geometrical configuration similar to the coaxial cylindrical electrostatic precipitator. It consists of an inner electrode placed along the axis of an outer electrode. For generating an electrostatic field inside the

* Corresponding author.
E-mail address: panich_intra@yahoo.com (P. Intra).

http://dx.doi.org/10.1016/j.elstat.2014.09.001
0304-3886/© 2014 Elsevier B.V. All rights reserved.

collector a DC voltage is applied to the inner electrode, while the outer electrode is grounded. When ions are introduced into the collector, the electrostatic force drives them toward the outer electrode where they deposit on the inner surface of the electrode. The design and performance evaluation of the ion collector has received little attention in the literature [5–12]. Higher applied voltages (10–150 V) and flow rates (5–15 L/min) were theoretically and experimentally studied by numerous works [5–7,12]. However, a mini-volume electrical PM detector commonly has been operated at volumetric aerosol flow rates lower than 5 L/min and therefore needed a compactable system for a field test and measurement. Therefore, an ion electrostatic collector needs to be designed and numerically and experimentally evaluated for the efficiency of collecting both negative and positive ions at ion flow rates smaller than 5 L/min and collection voltages lower than 50 V. The geometry, dimension and size of the ion collector would have influenced to the complexity and expense of the ion collector and then to keep it cost effective.

This paper presents the work of designing and evaluating an electrostatic collector that collects highly electrical mobile positive and negative ions after the charger or ionizer of the mini-volume electrical PM detector. Its collection characteristics were experimentally determined at applied voltages at the inner electrode between 0 and 45 V, ion flow rates between 1 and 5 L/min, and an operating pressure of about 1.01×10^5 Pa. The ions precipitates due to space charge and diffusion effects were evaluated. Also, a commercial computational fluid dynamics software package COMSOL Multiphysics™ was used to predict the behavior of the flow and electric fields as well as the ion and particle trajectories in the collecting zone of the ion collector.

Description of an ion electrostatic collector

Fig. 1 shows the schematic diagram of the ion collector used in this study. The geometrical configuration is similar to that in the ion collector used by Intra and Tippayawong [4]. However, the differences between the previous and the present were as follows; (i) short column collector was used to reduce diffusion and space charge losses of the aerosol particles inside the collector; and (ii) it is a low complexity and inexpensive system. This ion collector consisted of a coaxial cylindrical electrode placed along the axis of a metallic cylindrical tube and divided into three sections. The first and third sections (from the upper part to the lower part in the diagram) were made of a stainless steel tube and the second a polytetrafluorethylene (PTFE) tube. The PTFE tube is an electrical insulator and it was placed between the two stainless steel tubes, the hole through which the ion flow, and served to hold the inner electrode coaxial with the outer electrode. The inner electrode could be screwed into the PTFE insulator to connect a DC voltage supply. The outer electrode was 15 mm in an inner diameter and 15 mm in length, and the inner electrode was made of a stainless steel with an outer diameter of 3 mm and a length of 11.5 mm. The inner and outer electrodes were polished to an extremely fine surface finish, and the head of the inner electrode was rounded to a 1.25 mm radius to ensure the uniform flow and electric fields inside the collector. The DC voltage supply applied to the inner electrode, was typically in the range between 0 and 45 V, whereas the outer metallic electrode was grounded.

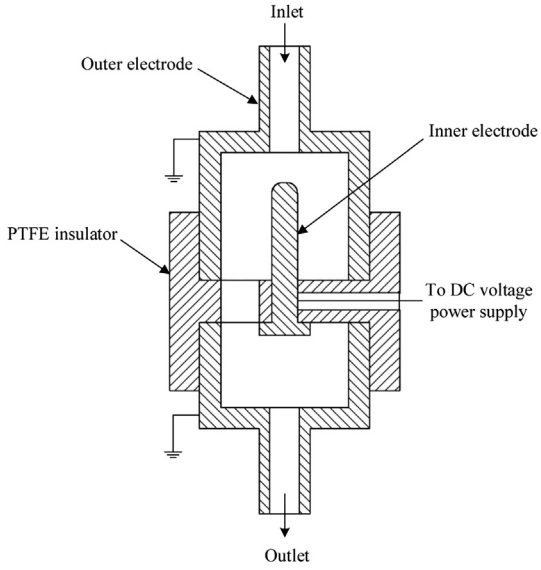

Fig. 1. Schematic diagram of the ion collector.

Mathematical model and numerical simulation

It was well known that the fluid flow, the electric field distribution, and the ion transport behavior within the ion collector has been reported in our previous work by Intra and Tippayawong [12] to have important factors influencing on its collection efficiency depending on the arrangement of major geometrical features inside an ion collector. It is difficult to carry out detailed and reliable measurement of the fluid flow, the electric field distribution, and the ion and particle transport inside an ion collector as the geometry is very complex. Numerical simulation provides an alternative method, which is reliable and less expensive to study the fluid flow, the electric field distribution, and the ion transport behavior inside the ion collector. The mathematical model and numerical simulation used in this study were as follows:

Governing equations

To the accurate model of the ion collector, three partial differential equations (PDE) were selected and coupled in the commercial software package COMSOL Multiphysics™, namely, the Poisson's and Navier–Stokes equations as well as the Khan and Richardson force [13]. The governing equations are given by:

Governing equations for the electrostatics

For electrostatic field modeling, electrostatic fields are generated by a combination of stationary charges and applied potentials. Electrostatics is governed by Gauss's Law, which states that the net electric flux passing through a closed surface is equal to the net charge enclosed by that surface. Therefore, the electric potential V is governed by Poisson's equation and given by.

$$\nabla^2 V = \frac{\rho_v}{\varepsilon_0} \tag{1}$$

where ρ_v is the space charge density and ε_0 is the dielectric permittivity of free space. Since most ion collector application involve aerosol concentration lower than 10^6 particles/cm3, and with low particle charge level, the space-charge effect on the electric field is neglected ($\rho_v = 0$). The electric potential is derived from the electric field intensity E and it is given by

$$E = -\nabla V \tag{2}$$

Governing equations for the air flow

The air flow inside the collector can be assumed to be steady, incompressible and laminar. Based on the principle of momentum conservation, the air flow has been modeled by using COMSOL software incorporating a laminar flow, using the Reynolds averaged Navier–Stokes equations for incompressible gas in this work. The mean velocity, field and pressure and determined using the $\kappa-\varepsilon$ parameters as defined in the software [13].

$$\rho_{\text{gas}}\left(u\cdot\nabla\right)u = -\nabla p + \mu_{\text{gas}}\nabla^2 u + F \tag{3}$$

$$\nabla\cdot u = 0 \tag{4}$$

where u is the air velocity, μ_{gas} is the dynamic viscosity of the air, ρ_{gas} is the air density, p is the pressure and F is the force field. The pressure at the outlet is the atmospheric pressure (P_0) and no viscous stress is used:

$$\eta(\nabla u + (\nabla u)^T n = 0 \text{ and } P = P_0 \tag{5}$$

where T is the transposed matrix. The no slip boundary condition was considered for the wall boundary conditions.

Governing equations for the particle trajectories

There are four forces acting on each particle which is given by gravity force: $\vec{F}_g = \rho_p g 2\pi a^3/3\vec{z}$, archimedes force: $\vec{F}_a = -\rho_{\text{gas}} g 2\pi a^3/3\vec{z}$, electrostatic force: $\vec{F}_e = q_{\max}E(r)\cdot\vec{r}$ and drag force: $\vec{F}_d$; where a is the particle radius, ρ_p is the particle density, $q_{\max}$ is the maximum number of charge per particle, and g is the gravity constant. The drag force is modeled by the Khan and Richardson force which is calculated by the COMSOL software [13].

The following equation describes the total force that a fluid exerts on an immersed spherical particle:

$$\vec{F}_d = \pi a^2 \rho_{\text{gas}}\left(\vec{u} - \vec{u}_p\right)\left[1.84(\text{Re}_p)^{-0.31} + 0.293(\text{Re}_p)^{-0.06}\right]^{3.45} \tag{6}$$

$$\text{Re}_p = \frac{2a\rho_{\text{gas}}(\vec{u} - \vec{u}_p)}{\mu} \tag{7}$$

where Re_p is the particle Reynolds number, $\vec{u}$ is the velocity field of the gas and $\vec{u}_p$ is the particle velocity.

Computational domain and boundary conditions

Computational domain for flow and electric fields of the ion collector is shown in Fig. 2 (a). For the collection zone, the Poisson's Equation (1) and the electric potential Equation (2) were solved using the electrostatic module and the PDE module to obtain a steady state field and charge density distribution. Dirichlet boundary conditions were used in the PDE module, with an initial space charge density on the inner electrode boundary along with zero ion concentration on the outer electrode. In the electrostatic module, a ground (0 V) has been implemented on the outer electrode and the electric potential on the inner electrode (ranging from 0 to 45 V). The zero-charge symmetry boundary condition was applied to the boundaries without walls, and is given by $n\cdot D = 0$ where n is the outward normal from medium and D is the electric flux density. The flow inside the ion collector could be assumed to be steady, incompressible and laminar. Based on the principle of momentum conservation, the incompressible Navier–Stokes

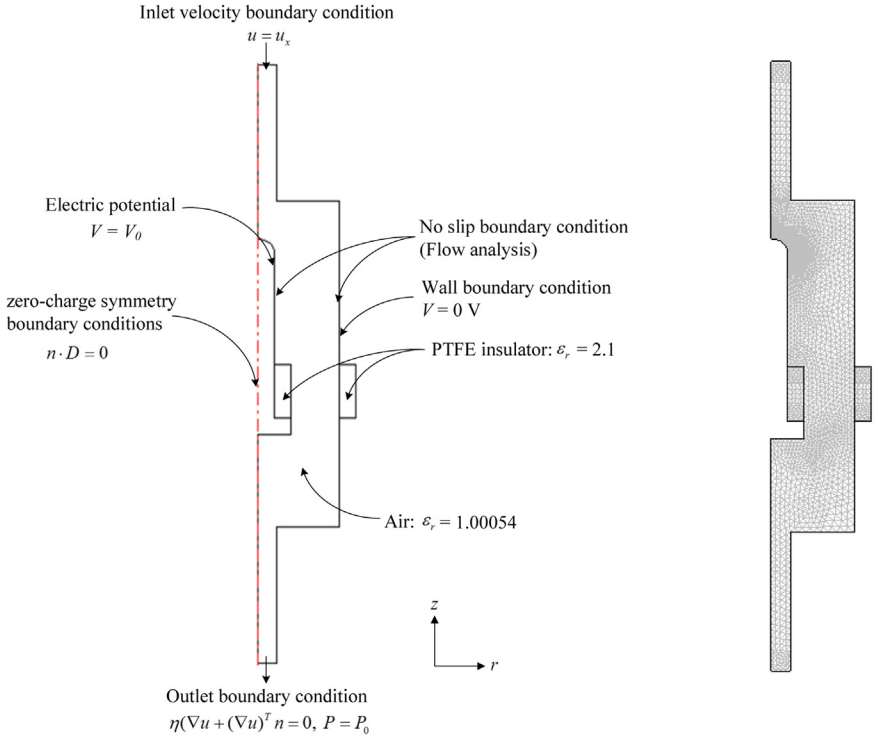

(a) Computational domain (b) Mesh distribution

Fig. 2. Computational domain and mesh distribution for flow and electric fields of the ion collector.

Table 1
Operating condition values of the experiments.

Parameter and operating conditions	Values
Diameter of inner electrode (mm)	3
Diameter of outer electrode (mm)	15
Length of collector (mm)	15
Inner electrode voltage (V)	0 – 45
Ion flow rate (L/min)	1, 3, 5
Operating temperature (K)	294
Operating pressure (atm)	1
Polarity of ions	Positive and negative

equations (N–S equation) can be applied in this case. A wall boundary condition has been implemented on both electrodes, i.e., a pressure of 1.01×10^5 Pa on the outlet and a normal velocity field in the inlet. The operating gas was ambient air (density was 1.19 kg/m^3, viscosity was 1.79×10^{-5} kg/m/s, and the relative permittivity constant was 1.00054). The PTFE insulator permittivity constant was 2.1.

Fig. 2 (b) shows the mesh distribution for the flow and electric fields of the ion collector. The considered problem was discretized with the finite element method (FEM), and utilizing triangular elements for the axis-symmetric two-dimensional model. The mesh was automatically generated by COMSOL and was refined in critical regions such as the inner electrode head and between outer electrode and insulators. This convergence test results in number of triangular elements of approximately 4608. The computations were carried out on a desktop running a 64 bit OS Windows 7. Core i5 processors (each 2.40 GHz) and 4 GB of RAM are allowed for solving the model within the approximation of the 3 min of computation time. The values of various parameters, which have been used in this study, are given in Table 1. After solving the fluid dynamic equations together with the electrostatic parameters, it is possible to trace the particulate trajectories.

Experimental setup

In order to use the numerical simulation to analyze the fluid flow, electric field distribution, and ion and particle transports behavior within the ion collector, it is necessary to evaluate the simulation. Experimental study has been carried out for evaluating the numerical simulation. Fig. 3 shows the experimental setup for investigating the collection efficiency of the ion collector. It consisted of an ionizer, a DC voltage power supply, a Faraday cup, an electrometer, a high efficiency particulate-free air (HEPA) filter, and a flow system. A high concentration of ions was generated by corona discharge with the corona-needle ionizer developed by Intra and Tippayawong [14,15] as shown in Fig. 4. The ion concentration at the ionizer outlet was measured by the Faraday cup electrometer. Fig. 5 shows the number concentration of positive and negative ions as a function of the corona voltage at the ionizer outlet, usually greater than 10^{13} ions/m^3, at operating flow rate between 1 and 5 L/min and the corona voltage between 2.3 and 3.4 kV [15]. As shown in Fig. 5, the ion concentration at the ionizer outlet was found to be relatively high with the same corona voltage at higher air flow rates, because the free ions can be more easily drawn off the ionizer by faster flowing air [14–16].

In this experimental study, the ion collector was connected directly to the ionizer outlet via a very short connecting pipe. The connecting pipe is made of a stainless steel, 3.5 mm in an inner diameter and a length of 10 mm. The airflow was regulated and controlled by a mass flow meter and controller (Dwyer model GFC-1111) with a vacuum pump located at the end of the experimental equipment train. The mass flows were typically in the range between 1 and 5 L/min. A silica gel drying chamber was used to remove any remaining water from an air sample. Dried air samples were filtered through a Pall HEPA capsule filter (model 12144) and were then drawn into the ionizer. An adjustable commercial DC high voltage power supply (Leybold Didactic model 521721) was used to maintain the corona voltage difference in the ionizer,

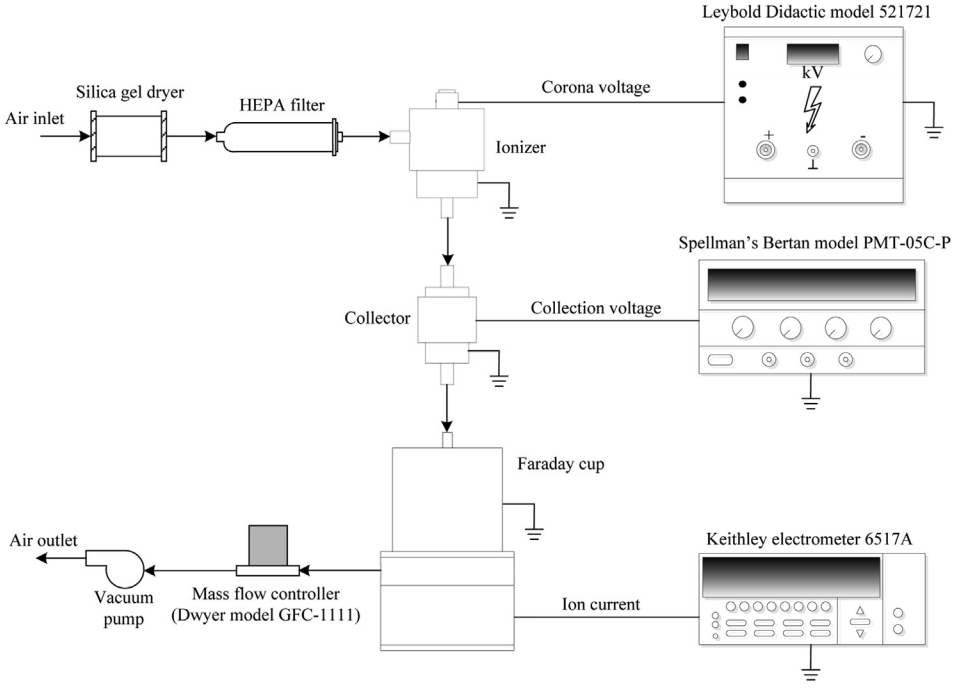

Fig. 3. Experimental setup for investigating the efficiency of the ion collector.

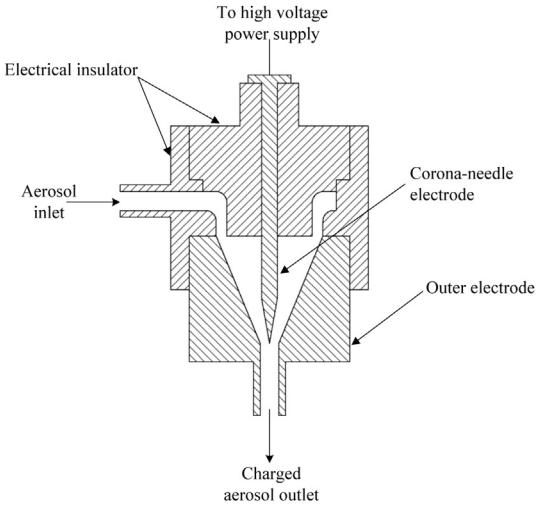

Fig. 4. Schematic diagram of the corona-needle ionizer.

generally 3.0 and 2.7 kV for positive and negative coronas, respectively. The ions produced inside the ionizer then entered the ion collector. A second adjustable commercial DC voltage power supply, Bertan model PMT-05C–P, was used to maintain the positive and negative voltages difference in the collector, generally in the range between 0 and 45 V.

After the ion collector, the air sample with ions entered the Faraday cup as shown in Fig. 6 [16], where the ion current was measured with Keithley 6517A electrometer. In order to eliminate the leakage currents, the collecting electrode (filter holder) of the Faraday cup was connected to the electrometer input that had been carefully shielded against external fields with the low-noise triaxial connection cables, Keithley 237-ALG-2. The Keithley 237-ALG-2 has an insulation resistance of 10^{15} Ω, center conductor to shield, and contact resistance of <0.5 Ω. As shown in Fig. 5, it can be shown that the ion number concentration at the ionizer outlet corresponded to the operating air flow rate. Thus, the number concentration of positive and negative ions at the ionizer outlet, N_p and N_n, could be calculated from the expression by Lehtimaki [5]:

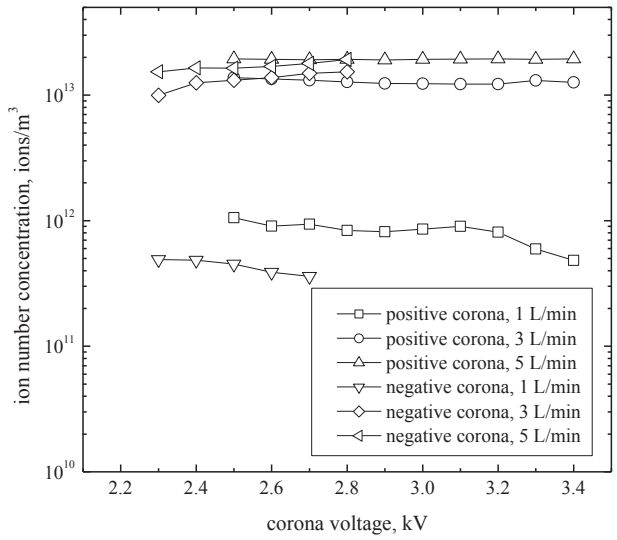

Fig. 5. Variation in ion number concentration with corona voltage at the corona-needle ionizer outlet.

$$N_p = I_p/eQ \tag{8}$$

$$N_n = I_n/eQ \tag{9}$$

where I_p and I_n are the currents of the positive and negative ions from the Faraday cup, e is the value of the elementary charge on an electron (1.60×10^{-19} C) [1], and Q is the volume flow rate of ions. Therefore, the collection efficiency η, was calculated by

$$\eta = 1 - \frac{N_{\text{outlet}}}{N_{\text{inlet}}} \tag{10}$$

where N_{outlet} and N_{inlet} are number concentration of ions at the outlet and inlet. Table 1 shows the values for the operating condition values of the experiment.

Results and discussion

Fig. 7 (a) shows the numerical calculation results of the gas flow field, namely the streamline and velocity field, inside the ion collector. In this calculation, the air flow velocity at the ion collector inlet was about 7.073 m/s or the air flow rate was about 3 L/min. It is noted that the domain is represented at the symmetry plane. It was showed that the flow field has the highest velocity at the inlet and outlet of the ion collector. The flow velocity generally peaks at the axis and decreases towards the wall of the outer electrode. Uniformity of the velocity field was presented in the collecting zone of the collector. Fig. 7 (b) shows the characteristics of the electric field inside the ion collector when 40 V was applied at the inner electrode. It was observed that the electric field was distributed with the highest strength near the head and end of inner electrode whereas electric field decreased in magnitude from the edge of the inner electrode to the outer electrode of the collector. It was also found that the holder insulator of the inner electrode could be used to change the distribution and uniformity of the electric field in the collecting zone as shown in Fig. 7 (b).

It is possible to trace the ions and particles trajectories with COMSOL Multi-physics. Fig. 8 shows the ion trajectories inside the ion collector at different operating collecting voltage of 10–40 V and air flow rate of about 3 L/min or air flow velocity of about 7.073 m/s. In this simulation, the ionic mass and radius was assumed about 3×10^{-18} g and 30×10^{-12} m, respectively [17]. It has been observed that the collection efficiency of ions increases with respect to the applied collecting voltage. It was also found that

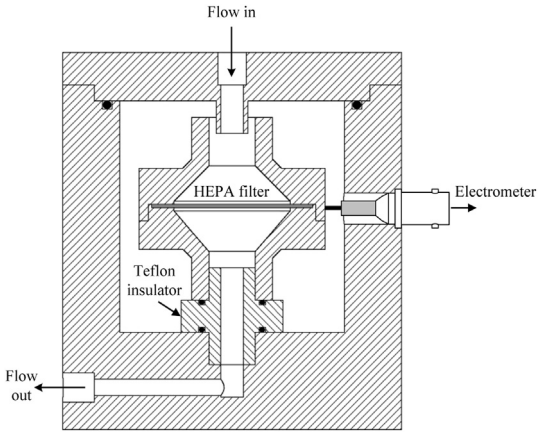

Fig. 6. Schematic diagram of the Faraday cup.

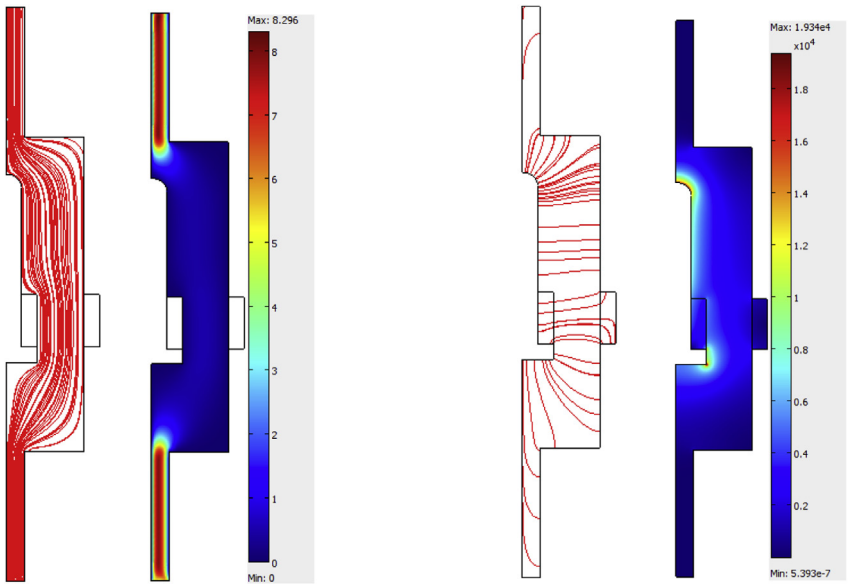

(a) Flow field (b) Electric field

Fig. 7. Flow and electric fields inside the ion collector.

all ions were collected on the outer electrode of the ion collector at a collecting voltage larger than 20 V.

In case of particle trajectories, Fig. 9 shows the particle trajectories inside the ion collector at different particle diameter of 0.1, 1.0, 2.5 and 10 μm and collecting voltage of 40 V with air flow velocity of 8.666 m/s. The particle mass was about 5.22×10^{-19}, 5.15×10^{-16}, 5.0×10^{-15} and 5.17×10^{-13} g corresponding to the particle diameter of 0.1, 1.0, 2.5 and 10 μm, respectively [1]. In this study, the mean of charge per particle was approximated by White's charging equation for the field and diffusion charging [18]. It should be noted that the field charging was dominant for particles larger than 0.5 μm, and for smaller particles smaller than 0.2 μm, thermal diffusion became dominant, and therefore diffusion charging became important [1]. In case of the particle diameter of 1.0, 2.5 and 10 μm, the mean charge per particle were usually based on combined diffusion and field charging where particle charge is the sum of the contributions from field and diffusion charge [19]. Therefore, the mean of charge per particle was about 5.6, 162, 1000 and 16,540 electrons for the particle diameter of 0.1, 1.0, 2.5 and 10 μm, at the $N_i t$ product of 1.28×10^{13} ions/m^3 s, the corona voltage of 3.4 kV, the electric field strength of 2×10^6 V/m, and the dielectric constant of 3.0, respectively. It was well known that the collection efficiency of charged particles mainly depended on the electric field strength inside the collector and the particle

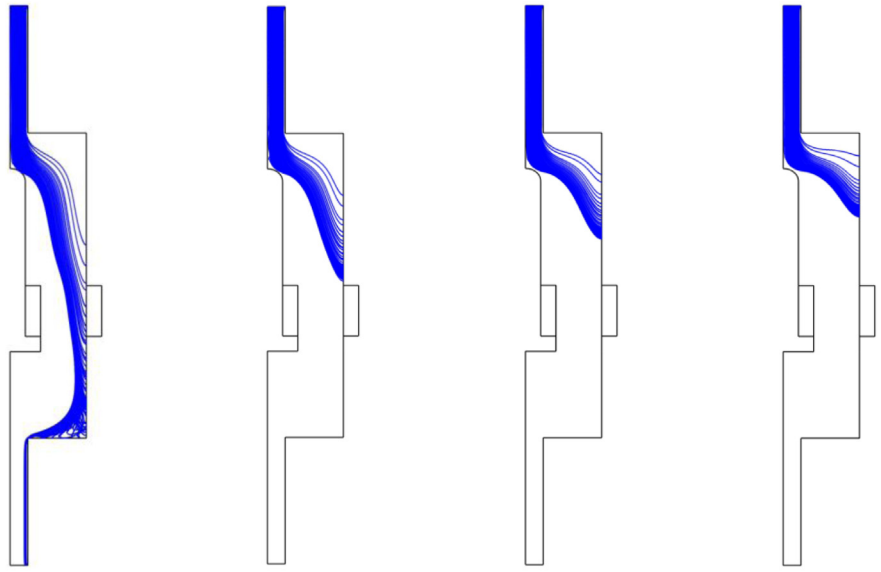

(a) 10 V (b) 20 V (c) 30 V (d) 40 V

Fig. 8. Ion trajectories inside the ion collector at different operating collecting voltage.

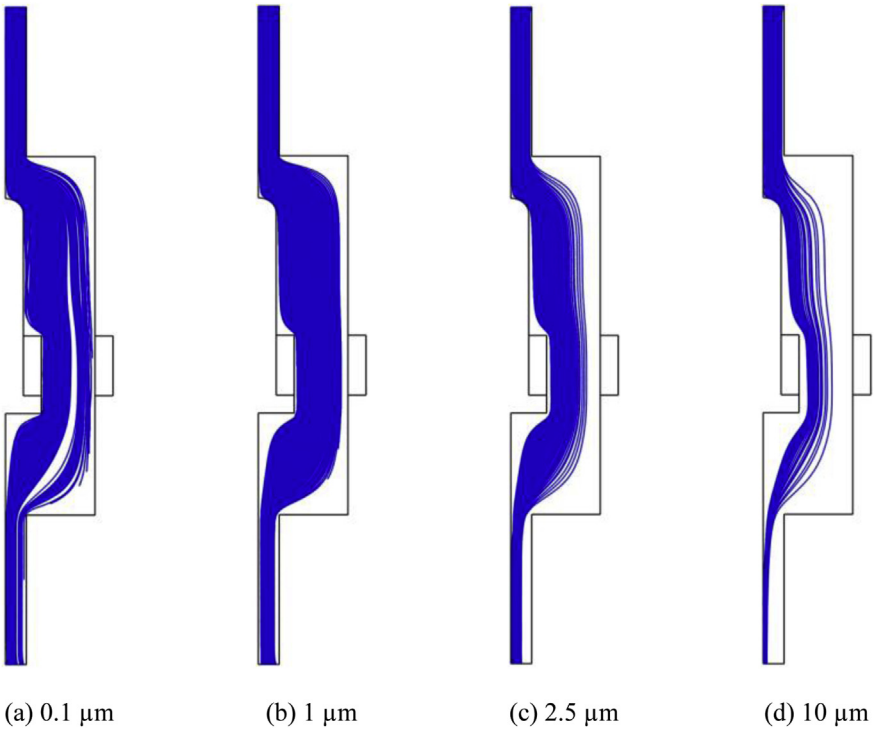

Fig. 9. Particle trajectories inside the ion collector at different particle diameter.

electrical mobility as a function of a particle diameter. Large particle diameter has higher mean charge than small particle diameter, therefore, electrostatic force applied on the particle increased with respect to the mean charge per particle as a function of its diameter. An increase in electrostatic force on the charged particles produced an increase in the collection efficiency of the charged particles of the ion collector. It has been shown in Fig. 9, and it can be observed that all charged particles of 0.1, 1.0, 2.5 and 10 μm can pass through the collector smoothly without precipitate on the outer electrode of the ion collector. It should be noted these calculation results can be used to support the bettering of further modify and refinement of the ion collector and also to understand the mechanisms of the ion transport and collecting inside the ion collector.

Fig. 10 shows the variation of the ion concentration of the ionizer and collector outlets with ion flow rate. At higher ion flow rates, the ion number concentration was high. The magnitude of the ion number concentration at the ionizer outlet was much larger than at the ion collector outlet. It was expected that ions partially would be lost by electrostatic deposition inside the ion collector due to Brownian diffusion, electrostatic dispersion

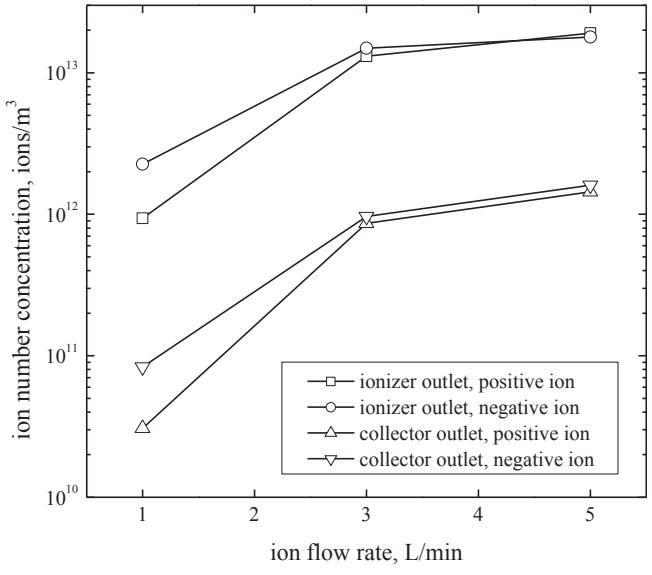

Fig. 10. Variation of ion concentration of ionizer and collector outlets with ion flow rate.

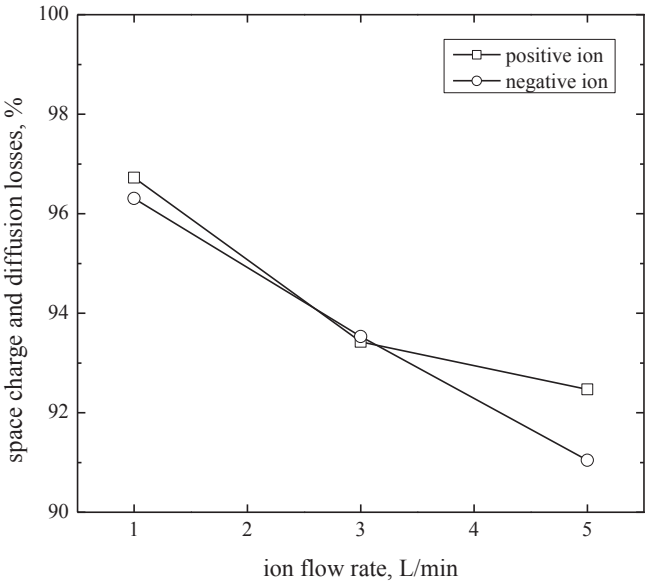

Fig. 11. Space charge and diffusion losses of ions as a function of ion flow rate.

(space charge) and an external electric field. With ion concentrations above 10^{13} ions/m^3, ions may partially deposit onto the inner and outer electrodes of the ion collector by space charge effects in the absence of any applied voltage on the inner electrode. As shown in Fig. 10, the ion number concentration at the ionizer outlet had a range from 9.38×10^{11} to 1.91×10^{13} ions/m^3, and 2.26×10^{12} to 1.79×10^{13} ions/m^3 for positive and negative corona voltages, respectively. The number concentration of both positive and negative ions at the collector outlet was in the range from 3.07×10^{10} to 1.44×10^{12} ions/m^3, and 8.35×10^{10} to 1.60×10^{12} ions/m^3, respectively. At the same ion flow rate, the magnitude of the number concentration for a negative ion was slightly higher than that of the positive ion, again because negative and positive ions differ in mass and electrical mobility. Ionic mobility was inversely proportional to its mass. Generally, values of mobility for positive and negative ions differ by approximately 19.30%. Reischl et al. [20] quote averages for ion motility as 1.15×10^{-4} and 1.425×10^{-4} m^2/V s for positive and negative ions.

Fig. 11 shows the space charge and diffusion precipitates of ions as a function of ion flow rate. Positive and negative ion precipitates due to space charge and diffusion effects ranged from 92 to 97 % and 91–97 % for ion flow rates in the range of 1–5 L/min. Higher ion flow rates resulted in further reducing the space charge and diffusion precipitates of ions. Figs. 12–14 show the time variations of outlet ion concentration with collection voltage at different ion flow rates. For this study the collection voltages varied from 0 to 45 V, the ion flow rates from 1 to 5 L/min and the times of measurement from 0 to 100 s. It was found in Figs. 12–14 that the concentration of positive ions was more stable than that of negative ions. This was because a negative ion had a higher electrical mobility than a positive ion due to a negative corona in the corona discharge ionizer has much higher density of free electrons compared to a positive corona, perhaps a thousandth of the electron density, and a hundredth of the total number of electrons. However, the electrons in a positive corona were concentrated close to the surface of the curved electrode in region of high potential gradient; however, the electrons in a negative corona many

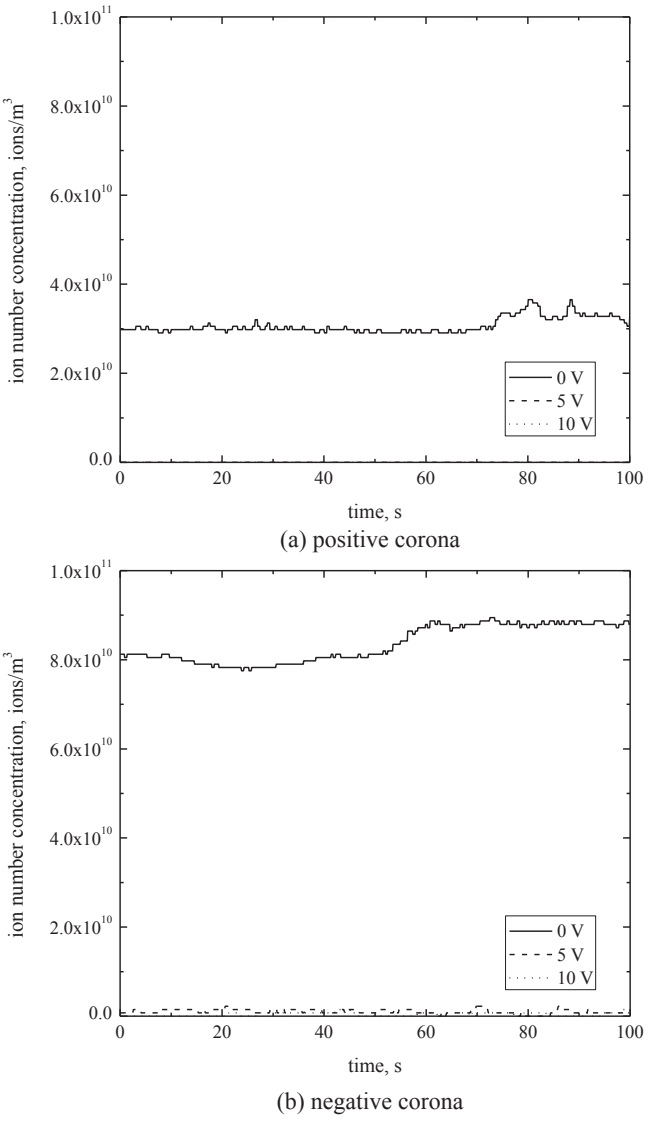

Fig. 12. Time variation of outlet ion concentration with collection voltage at ion flow rate of 1 L/min.

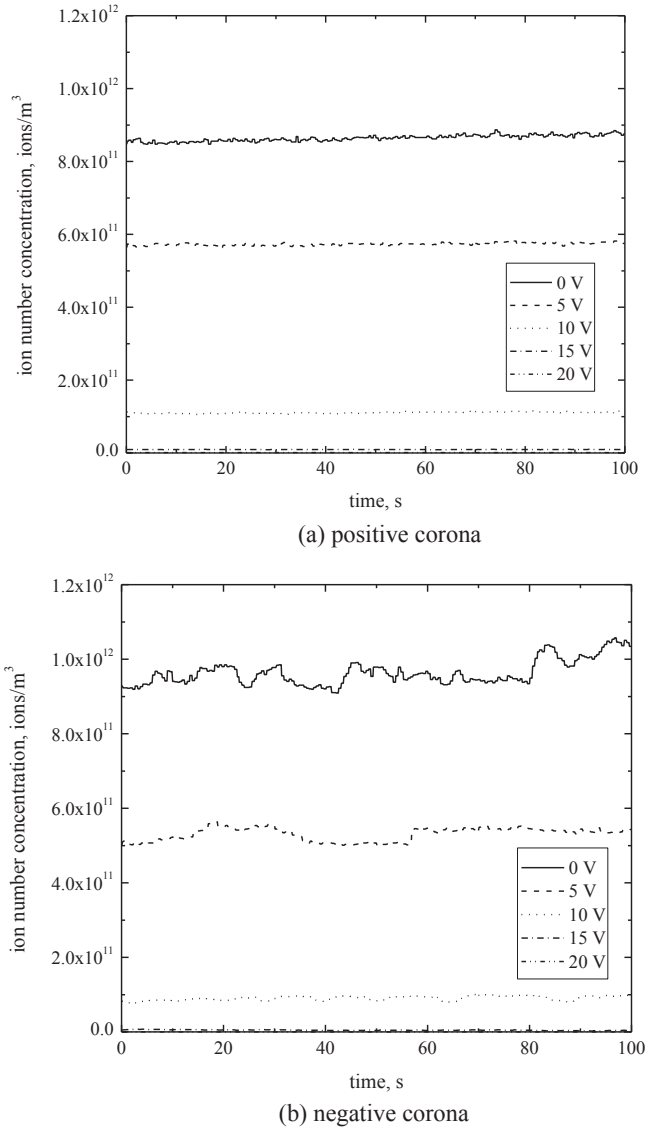

Fig. 13. Time variation of outlet ion concentration with collection voltage at ion flow rate of 3 L/min.

of electrons are in the outer lower-field areas [17]. Increasing the collection voltage resulted in the decrease of the ion number concentration at the collector outlet. Fig. 15 shows the variation of outlet ion concentration with collection voltage at different ion flow rates. Low ion flow rate and high collection voltage resulted in a decrease in the number concentration of ions at the collector outlet. For positive and negative ions, the ion number concentration at the collector outlet decreased to about 0 at collection voltages greater than 5, 20, and 40 V for ion flow rates of 1, 3, and 5 L/min, respectively.

Fig. 16 shows the variation of collection efficiency with collection voltage at different ion flow rates. Generally, an increase in collection voltage produced an increase in the ion collection efficiency of the collector for both negative and positive ions. It was shown that the ion collection efficiency of the collector increased to 100% at a collection voltage larger than 5 and ion flow rate of 1 L/min, for a collection voltage larger than 20 V the ion flow rate needed to be 3 L/min and for 40 V the ion flow rate of 5 L/min also gave 100% collection. This shows that the ion collector proved to be particularly useful in collecting positive and negative ions.

Conclusion

A coaxial cylindrical collector was designed as well as numerically and experimentally studied to determine the collection efficiency of positive and negative ions. The positive and negative ions were generated by a corona-needle ionizer. For positive and negative corona voltages, the number concentration of the ions at the ionizer outlet ranged from 9.38×10^{11} to 1.91×10^{13} ions/m^3 for negative ions and 2.26×10^{12} to 1.79×10^{13} ions/m^3 for positive ions. In this study, the positively and negatively applied voltages at the inner electrode ranged from 0 to 45 V and the ion flow rates ranged from 1 to 5 L/min. For these ion flow rates (1–5 L/min), the positive and negative ion losses due to space charge and diffusion effects ranged from 92 to 97 %, and 91–97 %, respectively. Increasing the collection voltage resulted in a decrease of the ion number concentration at the collector outlet, consequently; an increase in ion collection efficiency of the collector. The total collection efficiency of positive and negative ions of the collector

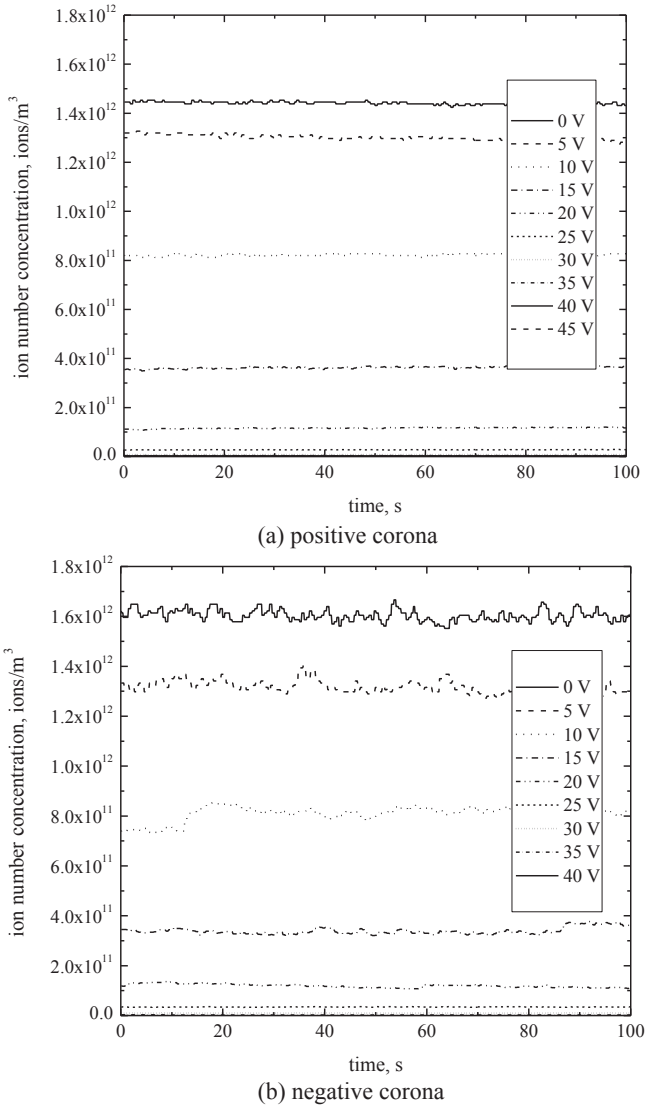

Fig. 14. Time variation of outlet ion concentration with collection voltage at ion flow rate of 5 L/min.

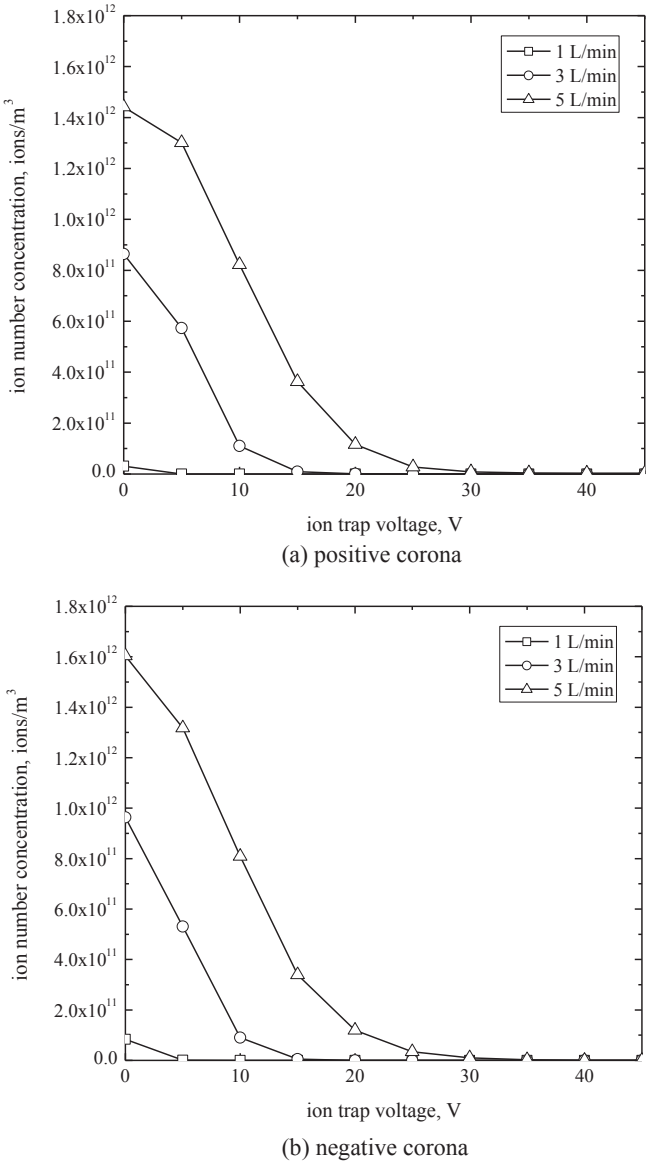

Fig. 15. Variation of outlet ion concentration with collection voltage at different ion flow rates.

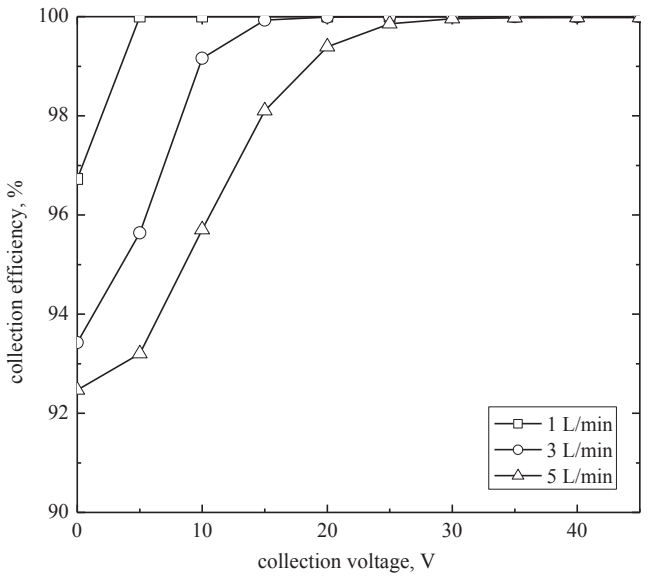

(a) positive corona

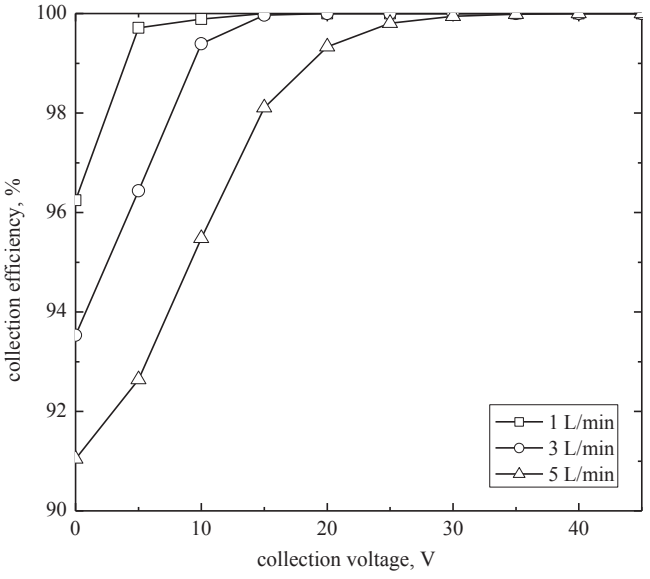

(b) negative corona

Fig. 16. Variation of total collection efficiency with collection voltage at different ion flow rates.

increased to 100% at collection voltages larger than 5, 20, and 40 V for ion flow rates of 1, 3, and 5 L/min, respectively. A commercial computational fluid dynamics software package COMSOL Multiphysics™ was used to predict the behavior of the flow and electric fields as well as the particle trajectories in the collecting zone of the ion collector. Numerical simulation results of the ion trajectory in the collecting zone of the ion collector; showed good agreement with experimental results of the total collection efficiency and can be used to support the bettering of further modify and refinement of the ion collector after the charger or ionizer in a mini-volume electrical aerosol detector. These results can be used as the proper operating conditions for the ion collector. The ion collector proven to be particularly useful for collecting highly electrically mobile and positive and negative ions after the charger or ionizer of a mini-volume electrical PM detector.

Acknowledgments

The authors gratefully acknowledge the Thailand Research Fund under the TRF contract No. RTA5680007.

References

[1] W.C. Hinds, Aerosol Technology, John Wiley & Sons, New York, USA, 1999.
[2] R.C. Flagan, History of electrical aerosol measurements, Aerosol Sci. Technol. 28 (1998) 301–380.
[3] P. Intra, N. Tippayawong, An overview of aerosol particle sensors for size distribution measurement, Maejo Int. J. Sci. Technol. 1 (2) (2007) 120–136.
[4] P. Intra, N. Tippayawong, Performance evaluation of an electrometer system for ion and aerosol charge measurements, Korean J. Chem. Eng. 28 (2) (2011) 527–530.
[5] M. Lehtimaki, Modified Electrical Aerosol Detector, Aerosol in the Mining and Industrial Work Environments, Ann Arbor Science Publishers, Ann Arbor, 1983.
[6] M. Lehtimaki, Studies of Aerosol Measuring Techniques (Ph.D. thesis), Tampere University of Technology, Tampere, Finland, 1986.
[7] J. Keskinen, K. Pietarinen, M. Lehtimaki, Electrical low pressure impactor, J. Aerosol Sci. 23 (1992) 353–360.
[8] A. Medved, F. Dorman, S.L. Kaufman, A. Pocher, A new corona-based charger for aerosol particles, J. Aerosol Sci. 31 (2000) s616–s617.
[9] TSI Incorporated, Operation and Service Manual, Revision B, for Electrical Aerosol Detector™ Spectrometer Model 3070, 2004. Minnesota, USA.
[10] J. Wei, Development of a Method for Measuring Surface Area Concentration of Ultrafine Particles (D.Eng. thesis), University of Duisburg-Essen, Germany, 2007.
[11] D. Park, M. An, J. Hwang, Development and performance test of a unipolar diffusion charger for real-time measurements of submicron aerosol particles having a log-normal size distribution, J. Aerosol Sci. 38 (2007) 420–430.
[12] P. Intra, N. Tippayawong, Use of electrostatic precipitation for excess ion trapping in an electrical aerosol detector, J. Electrost. 69 (2011) 320–327.
[13] COMSOL Inc, COMSOL Multi Physics Modelling Guide, Version 3.5a, 2008.
[14] P. Intra, N. Tippayawong, Effect of needle cone angle and air flow rate on electrostatic discharge characteristics of a corona-needle ionizer, J. Electrost. 68 (2010) 254–260.
[15] P. Intra, N. Tippayawong, Design and evaluation of a high concentration, high penetration unipolar corona ionizer for electrostatic discharge and aerosol charging, J. Electr. Eng. Technol. 8 (5) (2013) 1175–1181.
[16] P. Intra, N. Tippayawong, Measurements of ion current from a corona-needle charger using a faraday cup electrometer, Chiang Mai J. Sci. 36 (1) (2009) 110–119.
[17] E.A. Mason, Ion mobility: its role in plasma chromatography, in: T.W. Carr (Ed.), Plasma Chromatography, Plenum Press, New York, USA, 1984.
[18] H.J. White, Industrial Electrostatic Precipitation, Addison-Wesley Pub Co. U S A, 1963.
[19] B.Y.H. Liu, A. Kapadia, Combined field and diffusion charging of aerosol particles in the continuum regime, J. Aerosol Sci. 9 (1978) 227–242.
[20] G.P. Reischl, J.M. Makela, R. Harch, J. Necid, Bipolar charging of ultrafine particles in the size range below 10 nm, J. Aerosol Sci. 27 (6) (1996) 931–939.

Journal of Electrostatics 74 (2015) 37–46

Contents lists available at ScienceDirect

Journal of Electrostatics

journal homepage: www.elsevier.com/locate/elstat

Influence of the corona-wire diameter and length on corona discharge characteristics of a cylindrical tri-axial charger

Panich Intra [a, *], Artit Yawootti [a], Phadungsak Rattanadecho [b]

[a] Research Unit of Electrostatic Applications in Energy and Environment (RUEE), College of Integrated Science and Technology, Rajamangala University of Technology Lanna, Chiang Mai 50220, Thailand
[b] Center of Excellence in Electromagnetic Energy Utilization in Engineering (CEEE), Department of Mechanical Engineering, Faculty of Engineering, Thammasat University, Pathum Thani 12121, Thailand

ARTICLE INFO

Article history:
Received 27 July 2014
Received in revised form
10 November 2014
Accepted 20 December 2014
Available online 5 January 2015

Keywords:
Aerosol
Charger
Unipolar charging
Corona discharge
Electric field

ABSTRACT

In this paper, the corona discharge characterization in terms of current–voltage relationships of a unipolar cylindrical tri-axial charger on the effects of the corona wire diameter and length have been experimentally studied and discussed. A commercial computational fluid dynamics software package, COMSOL Multiphysics™, was used to predict the electric field distribution in the ion generation and charging zones of the charger and the ion penetration through the perforated screen opening on the inner electrode of the charger. It was found from experimental results that both positive and negative charging currents in the charging zone of the charger increased with increasing corona and ion-driving voltages. At the same corona and ion-driving voltages, both positive and negative coronas were decreased with increasing diameter of the corona-wire. Compared with the corona-wire of 22 mm in length, the magnitude of both positive and negative charging currents were markedly higher for corona-wire of 11 mm in length at the same corona voltage. It was found that the charging currents for negative coronas were about 1.2 times higher than those positive coronas at the same corona and ion-driving voltages. Numerical results of the electric field distribution and the ion and charged particles migrations in the discharge and charging zones of the charger is correlated to have the same direction with the experimental results of the current–voltage relationships. Also, this can be used to guidance in describing the electric field distribution and the behavior of ion and charged particle trajectories that cannot be seen from experiments in order to improve the applicably design and refinement of a unipolar cylindrical tri-axial charger.

© 2014 Elsevier B.V. All rights reserved.

Introduction

Corona discharge is among the most common technique to produce high ion concentrations in a unipolar field and diffusion charging of aerosol particles in a gas [1]. Electrical aerosol charging by the corona discharges is also common in aerosol size determination by electrical mobility analysis [2]. Corona discharge is usually generated by sharp corners, projecting points, edges of metal surfaces, or small diameter wires at highly curved regions on electrodes. When aerosol flow is directed across the corona discharge and is then charged by attachment of ions produced by the corona discharge. Ions are transported by the electric field and/or by thermal diffusion. Particle charging by transported ions in an electric field is called “field charging”. For larger particles (>1 μm), field charging is dominant. For smaller particles (<0.1 μm), thermal diffusion becomes dominant, and “diffusion charging” becomes important [3]. The amount of deposited ion charge on the particle surface depends on resident time, particle radius and shape, electric field, etc.

Electrical aerosol charging by the corona discharge technique has been applied successfully and several designs of aerosol corona charger are employed and described in published literatures for both corona-wire [4–12] and corona-needle chargers [13–19]. In our previous work, Intra [9] was experimentally studied the corona discharge characteristics in a cylindrical tri-axial charger for unipolar diffusion aerosol charging. The ion number concentration in the discharge zone was found larger than that in the charging zone for positive and negative coronas, with values of about 197 and 32 times and 645 and 99 times for the ion-driving voltages of 0 and 310 V, respectively. The average ion penetration for positive and

* Corresponding author.
E-mail address: panich_intra@yahoo.com (P. Intra).

http://dx.doi.org/10.1016/j.elstat.2014.12.002
0304-3886/© 2014 Elsevier B.V. All rights reserved.

negative coronas was 0.64 and 0.19% and 3.62 and 1.93% for the ion-driving voltages of 0 V and 310 V, respectively. By calculation 14% of charged particles with diameter of 10 nm were lost onto the outer cylinder due to electric field effect. However, the effect of the corona wire diameter and length on the corona discharge within a cylindrical tri-axial charger has not been extensively studied in our previous work and literature. Thus, the influence of the corona wire diameter and length on electrostatic discharge characteristics of a cylindrical tri-axial charger is important for corona discharge due to the presence of different electric field distribution, ion migration and space-charge effect in the ion generation and charging zones of the cylindrical tri-axial charger.

The aim of this paper was to characterize the corona discharge of a unipolar cylindrical tri-axial charger. The experimental results of the corona discharge characterizations in terms of current–voltage relationships of the cylindrical tri-axial charger on the effects of the corona wire diameter and length were studied and discussed. A numerical model is also developed to study the electric field distribution and the ion and charged particle migration behaviors inside this charger that cannot be seen from experiments for a better understanding on the charger operation. This is done by providing predictions of the electric field distribution in the ion generation and charging zones of the charger, the behavior of the ion penetration through the perforated screen opening on the inner electrode of the charger, and also the behavior of the charged particle trajectories in the charging zone of the charger.

Description of cylindrical tri-axial charger

A schematic diagram of the prototype cylindrical tri-axial charger is shown in Fig. 1. The charger's geometrical configuration is similar to that in the unipolar triode charger used by Intra [9]. However, there are differences between those from the triode charger by Intra [9] and the present tri-axial charger, as follows; (i) aerosol flow guide inlet and outlet geometries were modified to ensure uniform flow distribution across the annular entrance to the charging zone in order to reduce diffusion and electrostatic effect losses of the particles inside the charger; (ii) the corona wire electrode in the discharge zone was rearranged to ensure a uniform electric field distribution and stabilize discharge current in order to obtain a high ion concentration in the ion generation zone and a high ion penetration over the perforated screen openings on the inner electrode to the charging zone of the charger; and (iii) it is a low complexity and inexpensive system. The prototype triode charger was 126 mm in length and 67 mm in diameter.

As Fig. 1 shows, it consisted of two concentric cylinders with a corona-wire electrode placed along the axis of the cylinders. In this study, the corona-wire diameter was set at 0.3, 0.34 and 0.46 mm and length was set at 11 and 22 mm in order to investigate the corona wire diameter and length effects on corona discharge characteristics of the charger as shown in Fig. 2. The inner and outer cylinders were fabricated using stainless steel, and were polished to an extremely fine surface finish to avoid distortion of the electrical field from small surface scratches and imperfections. Stainless steel was used because it is electrically conductive, inert, corrosion resistant and very hard, and therefore resistant to scratching. The inner and the outer radii of the annular charging zone were 17 mm and 30 mm, respectively. The electrical insulation was provided by a Delrin spacer between the inner and outer cylinder, and the aerosol flows through the space between the cylinders. A DC high voltage was applied to the corona-wire to produce a corona discharge and the generated ions is migrated toward the inner cylinder due to the high electric field in the region. In order to allow ions to flow in the charging zone, a section of the inner cylinder was

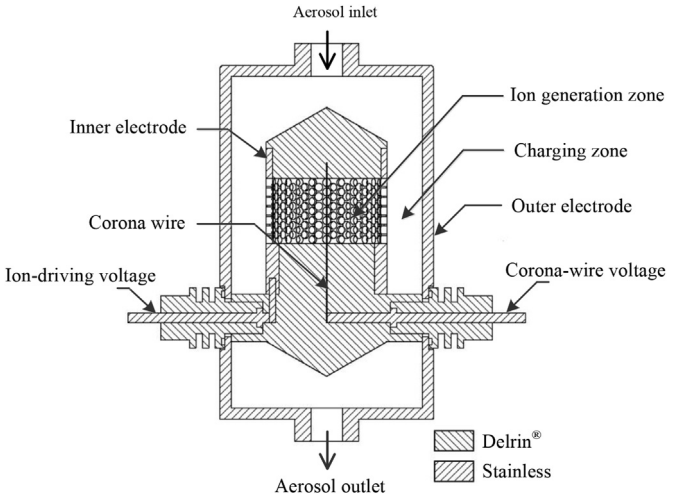

Fig. 1. Schematic diagram of the cylindrical tri-axial charger.

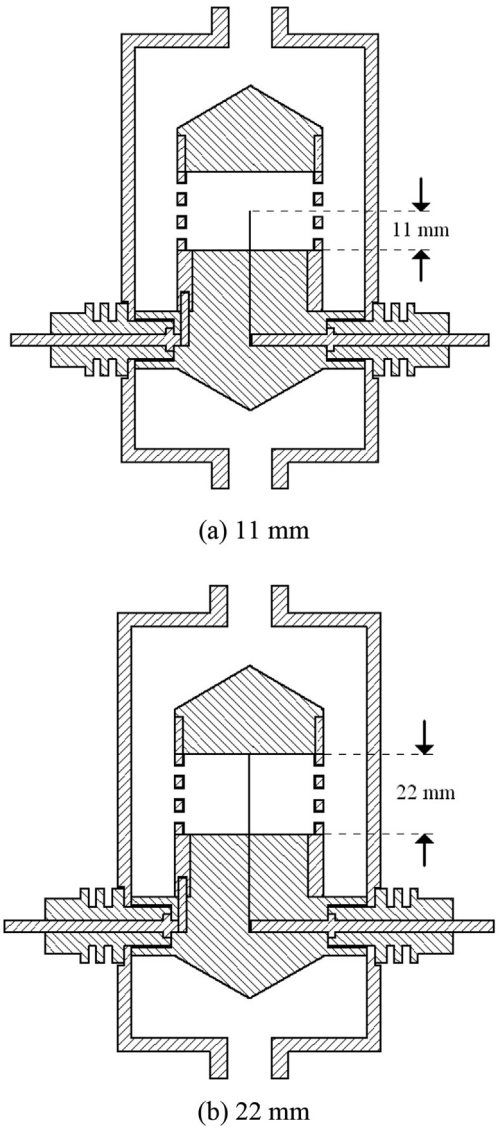

Fig. 2. Arrangements of the corona wire length of the cylindrical tri-axial charger.

made out of a perforated with holes of 2.5 mm in diameter cylindrical tube. The width of the perforated screen opening on the inner cylinder was 20 mm. The ion-driving voltage applied on the inner cylinder forced the ions through the perforated screen openings on the inner cylinder to the charging zone, while the outer cylinder was connected to ground. This ion-driving voltage could regulate the ion current flow through the perforated screen. The fraction of ions drawn into the charging zone is equal to the ratio of the field strengths on either side of the perforated screen opening. In the charging zone, the aerosol particles collided with the ions and were charged electrically.

Ion current density and charging current

The ion current density is the electric current per unit area of cross section (A/m^2), and is given by:

$$j = \rho u_{ion} \tag{1}$$

where $\rho = n_{ion}e$, $u_{ion} = Z_{ion}E$, ρ is the space-charge density (C/m^3), n_{ion} is the ion concentration (ions/m^3), u_{ion} is the ion velocity (m/s), e is the elementary charge (1.60×10^{-19} C), Z_{ion} is the electrical mobility of the ions (m^2/V s), and E is the average electric field inside the charging zones of the charger (V/m). Thus, ion current density (A/m^2) is given by:

$$j = n_{ion}eZ_{ion}E \tag{2}$$

where $j = i_{ion}/A$, with i_{ion} representing the charging currents and A representing the inner surface area of the outer electrode where the charging current is collected. Thus, the ion current or charging current of the cylindrical tri-axial charger in the absence of aerosol particles can be estimated by:

$$i_{ion} = n_{ion}eZ_{ion}EA \tag{3}$$

Mathematical model and numerical simulation

The important factors influencing on the particle charging efficiency of a corona-based unipolar aerosol charger depending on the arrangement of major geometrical features inside the charger has been well known as the electric field distribution of both ion generation and charging zones, the ion penetration behavior from the ion generation zone through the perforated screen openings on the inner cylinder to the charging zone of the charger, and the charged particle transport in the charging zone of the charger. As the geometry is very complex, it is difficult to carry out detailed and reliable measurement of the electric field distribution, the ion migration and charged particle trajectories inside this charger from the experimental study. Numerical simulation provides an alternative approach, which is more reliable and less expensive to guidance in describing the electric field distribution and the ion and charged particle migration behaviors inside this charger that cannot be seen from experiments. The mathematical model and numerical simulation used in this study were as follows:

Governing equations

To the accurate model of the ion collector, three partial differential equations (PDE) were selected and coupled in the commercial software package COMSOL Multiphysics™, namely, the Poisson's and Navier–Stokes equations as well as the Khan and Richardson force [20]. The governing equations are given by:

Governing equations for the electrostatics

For electrostatic field modeling of the cylindrical tri-axial charger, electrostatic fields are generated by a combination of stationary charges and applied potentials. Electrostatics is governed by Gauss's Law, which states that the net electric flux passing through a closed surface is equal to the net charge enclosed by that surface. Therefore, the electric potential V is governed by Poisson's equation and given by

$$\nabla^2 V = \frac{\rho_v}{\varepsilon_0} \tag{4}$$

where ρ_v is the space charge density and ε_0 is the dielectric permittivity of free space. Since most particle charger application involve aerosol concentration lower than 10^6 particles/cm^3, and with low particle charge level, the space-charge effect on the

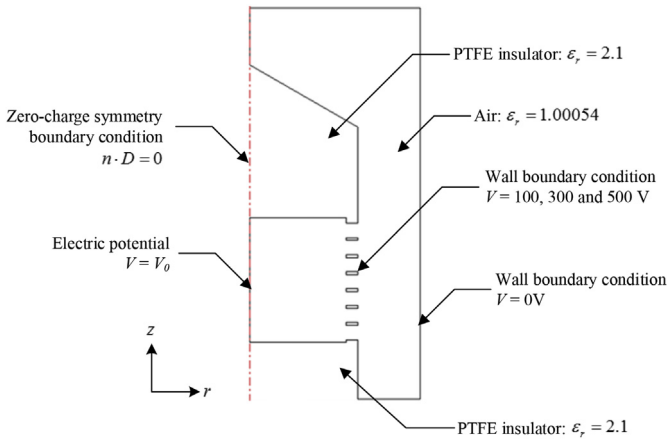

Fig. 3. Computational domain for analysis of electric field inside the cylindrical tri-axial charger.

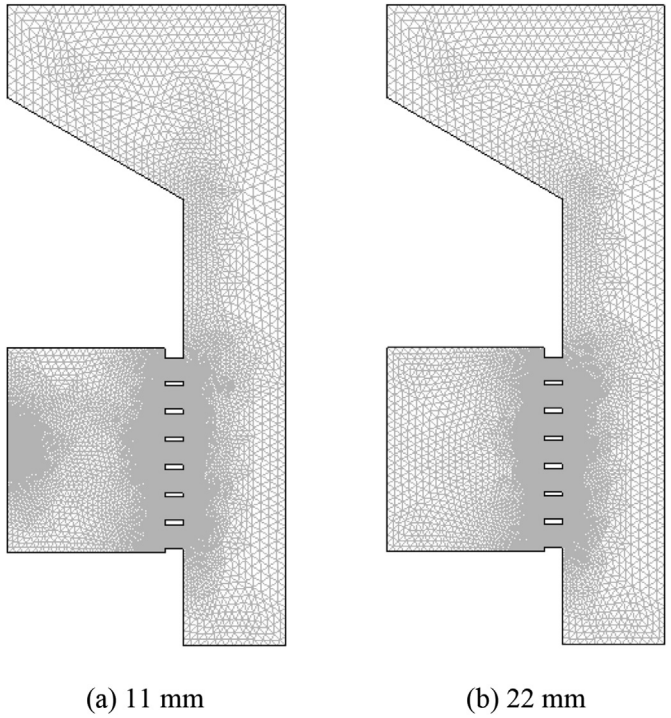

Fig. 4. Mesh distribution for analysis of electric field inside the cylindrical tri-axial charger.

Table 1
Limits of the investigated variables.

Variable	Range
Corona-wire diameter	0.15, 0.17 and 0.23 mm
Corona-wire length	11 and 22 mm
Inner electrode diameter	30 mm
Outer electrode diameter	60 mm
Corona-wire voltage	0–10 kV
Ion-driving voltage	100, 300 and 500 V
Ions generated	Positive ion (+) and negative ion (−)
Ionized gas	Air
Operating pressure	1 atm
Operating temperature	30 °C
Operating humidity	60%

electric field is neglected ($\rho_v = 0$). The electric potential is derived from the electric field intensity E and it is given by

$$E = -\nabla V \tag{5}$$

Governing equations for the air flow

The air flow inside the collector can be assumed to be steady, incompressible and laminar. Based on the principle of momentum conservation, the air flow has been solved by using COMSOL software incorporating a laminar flow, using the Reynolds averaged Navier–Stokes equations for incompressible gas in this work. The mean velocity, field and pressure and determined using the $\kappa - \varepsilon$ parameters as defined in the software [20]:

$$\rho_{gas}(u\cdot\nabla)u = -\nabla p + \mu_{gas}\nabla^2 u + F \tag{6}$$

$$\nabla\cdot u = 0 \tag{7}$$

where u is the air velocity, μ_{gas} is the dynamic viscosity of the air, ρ_{gas} is the air density, p is the pressure and F is the force field. The pressure at the outlet is the atmospheric pressure (P_0) and no viscous stress is used:

$$\eta(\nabla u + (\nabla u)^T n = 0$$

and

$$P = P_0 \tag{8}$$

where T is the transposed matrix. The no slip boundary condition was considered for the wall boundary conditions.

Governing equations for the particle trajectories

There are four forces acting on each charged particle which is given by the gravity force: $\mathbf{F_g} = \rho_p g 2\pi a^3/3\mathbf{z}$, the archimedes force: $\mathbf{F_a} = -\rho_{gas} g 2\pi a^3/3\mathbf{z}$, the electrostatic force: $\mathbf{F_e} = n_p E(r)\cdot\mathbf{r}$ and the drag force: $\mathbf{F_d}$; where a is the particle radius, ρ_p is the particle density, n_p is the maximum number of charge per particle, and g is the gravity constant. The drag force is modeled by the Khan and Richardson force which is calculated by the COMSOL software [20]. The following equation describes the total force that a fluid exerts on an immersed spherical particle:

$$\mathbf{F_d} = \pi a^2 \rho_{gas}(\mathbf{u} - \mathbf{u_p})\left[1.84(\mathrm{Re}_p)^{-0.31} + 0.293(\mathrm{Re}_p)^{-0.06}\right]^{3.45} \tag{9}$$

$$\mathrm{Re}_p = \frac{2a\rho_{gas}(\mathbf{u} - \mathbf{u_p})}{\mu} \tag{10}$$

where Re_p is the particle Reynolds number, $\mathbf{u}$ is the velocity field of the gas and $\mathbf{u_p}$ is the particle velocity.

Computational domain and boundary conditions

Computational domain for analysis of electric field inside the charger is shown in Fig. 3. For the charger, the Poisson's Equation (4) and the electric potential Equation (5) were solved using the electrostatic module and the PDE module to obtain a steady state flow and electric field distributions. Dirichlet boundary conditions were used in the PDE module, with zero space charge density on the corona-wire electrode boundary along with zero ion concentration on the outer electrode. In the electrostatic module, a ground (0 V) has been implemented on the outer electrode. The constant electric potentials were applied to the inner electrode (ranging from 100 to 500 V) as well as the corona-wire electrode (ranging from 0 to 10 kV). The zero-charge symmetry boundary condition was applied to the boundaries without walls, and is given by $n\cdot D = 0$ where n is the outward normal from medium and D is the electric flux density. No heat transfer occurs in the charger could be assumed in this simulation. The flow inside the charger could be assumed to be steady, incompressible and laminar. Based on the principle of momentum conservation, the incompressible Navier–Stokes equations (N–S equation) can be applied in this case. A wall boundary condition has been implemented on both electrodes, i.e., a pressure of 1.01×10^5 Pa on the outlet and a normal velocity field in the inlet. The operating gas was ambient air (density was 1.19 kg/m^3, viscosity was 1.79×10^{-5} kg/m/s, and the relative permittivity constant was 1.00054). The PTFE insulator permittivity constant was 2.1.

In this study, the charged particle with diameter of 2.5 μm and mass of 2.0×10^{-12} g [21] was used to study behavior of the charged particle trajectories in the charging zone of the charger. The mean of charge per particle was approximated by White's charging equation for the field and diffusion charging [3]. It should be noted that the field charging was dominant for particles larger than 0.5 μm, and for smaller particles smaller than 0.2 μm, thermal diffusion became dominant, and therefore diffusion charging became important [21]. In case of the particle diameter of 2.5 μm, the mean charge per particle were usually based on combined diffusion and field charging where particle charge is the sum of the contributions from field and diffusion charge [22]. Therefore, the mean of charge per particle was about a 1000 electrons for the charged particle with diameter of 2.5 μm at the $N_i t$ product of 2.95×10^{13} ions/m^3 s, the corona voltage of 10 kV, the electric field strength of 4.27×10^4 V/m, and the dielectric constant of 3.0, respectively.

Fig. 4 is illustrates the mesh distribution for analysis of the electric field inside the charger. The considered problem was discretized with finite element method (FEM), and utilizing triangular elements for the axis-symmetric two-dimensional model. The mesh was automatically generated by COMSOL [20] and was refined in critical regions such as the inner electrode head and between outer electrode and insulators. This convergence test results in number of triangular elements of approximately 28,960 and 22,368 for corona-wire length of 11 and 22 mm, respectively. The computations were carried out on a desktop running a 64 bit OS Windows 7 Core i5 processors (each 2.40 GHz) and 4 GB of RAM are allowed for solving the model within 5 min of computation time. The values of various parameters, which have been used in this study, are given in Table 1.

Experimental setup

Fig. 5 shows the experimental setup for corona discharge characterization of a cylindrical tri-axial charger. It consisted of a cylindrical tri-axial charger, an adjustable DC high voltage power supply, a Keithley 6517A electrometer, a high efficiency particulate-

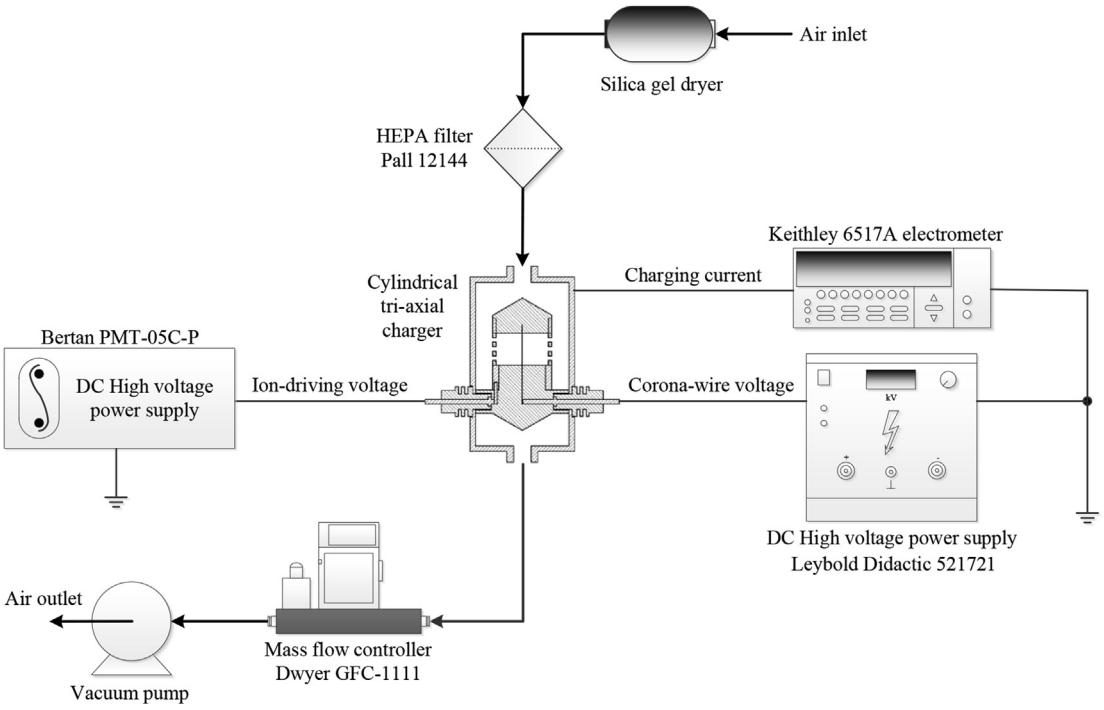

Fig. 5. Experimental setup for electrostatic discharge characterization of a cylindrical tri-axial charger.

free air (HEPA) filter, a Dwyer mass flow controller, and vacuum pump. In order to reduce the space charge and air flow effects in the charging zone, the air flow through the charging zone was regulated and controlled, approximately 5 L/min, by a mass flow meter and controller (Dwyer model GFC-1111) with a vacuum pump located at the end of the experimental equipment train. A diffusion dryer by silica gel drying chamber was used to remove any remaining water from the air sample for stabilize operating humidity, generally is about 60% RH. Dried air samples were filtered through a Pall HEPA capsule filter (model 12144) and were drawn into the charger. The positive and negative high voltage differences on the corona-wire electrode of the charger were applied by a first adjustable commercial DC high voltage power supply (Leybold Didactic model 521721), in the range between 0 and 10 kV. For the ion-driving voltage differences on the inner electrode of the charger, a second adjustable commercial DC high voltage power supply (Bertan model PMT-05C–P) was applied in the range between 100 and 500 V. In order to investigate the ion penetration through the perforated screen opening on the inner electrode into the charging zone of the charger, the charging current from the outer electrode was directly measured by the Keithley 6517A electrometer. It should be noted that the measurements of the charging current was repeated at least three times for each set of operating conditions. Table 1 gives the limits of the evaluated variables.

Results and discussion

The numerical calculation of the vector plot of electric field inside the cylindrical tri-axial charger for the corona-wire length of 11 and 22 mm, the corona-wire voltage of 10 kV and the ion-driving voltage of 100 V, respectively, is shown in Fig. 6. It was shown that non-uniform distribution of electric field appeared at the end of the 11 mm corona-wire in the ion generation zone, on the other hand, a uniform distribution of electric field was observed in the case of 22 mm corona-wire. Fig. 7 shows the numerical results of the electric field distribution inside the cylindrical tri-axial charger for the corona-wire length of 11 and 22 mm, respectively. In this simulation, the corona-wire voltage was about 10 kV and the ion-driving voltage of 100, 300 and 500 V. The high towards low

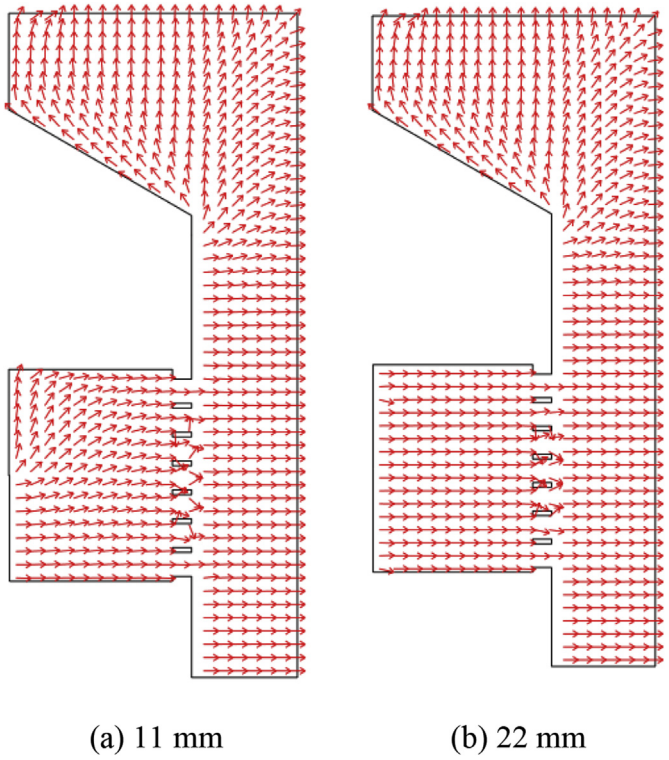

Fig. 6. Numerical calculation of the vector plot of electric field inside the cylindrical tri-axial charger.

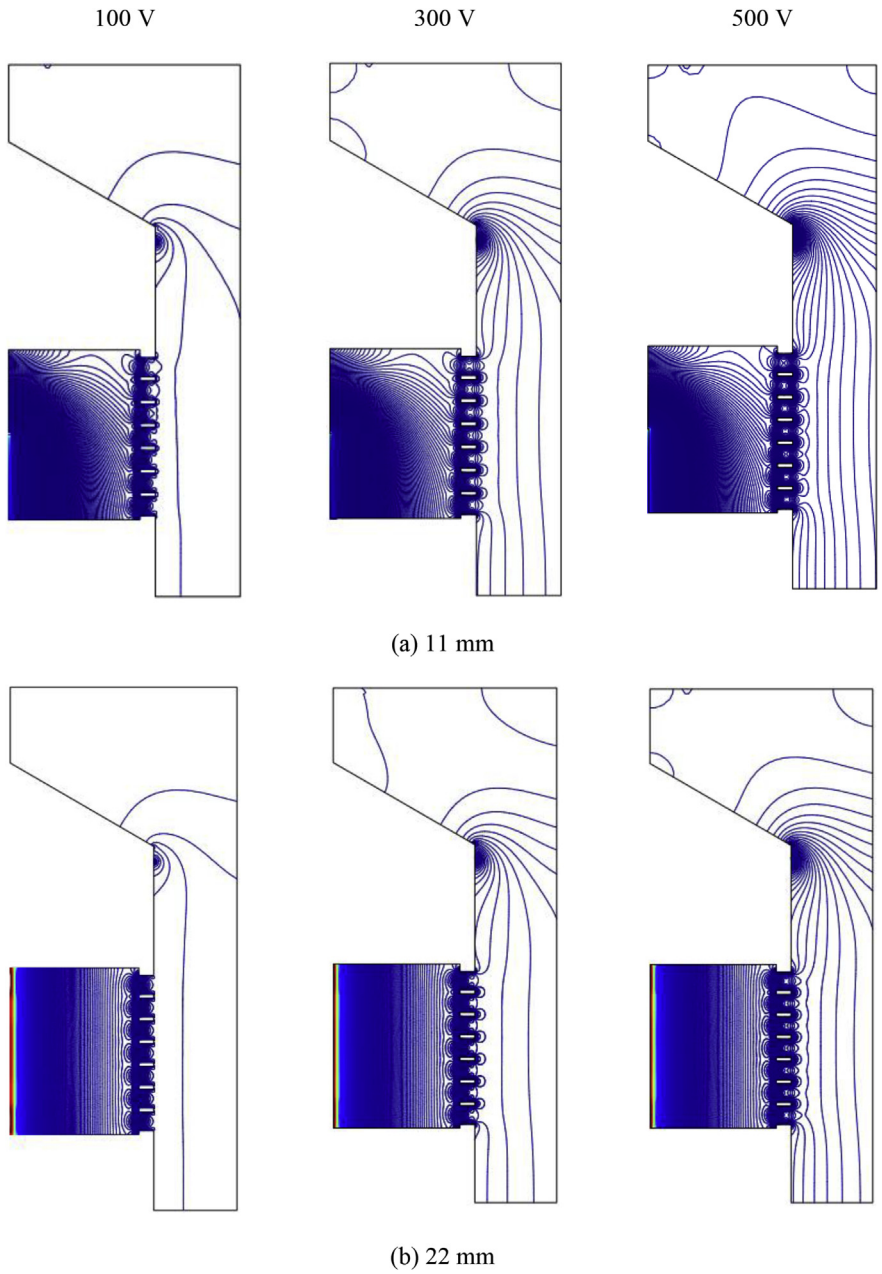

Fig. 7. Numerical calculation of the electric field distribution inside the cylindrical tri-axial charger.

intensity regions are indicated by red (in the web version), yellow, green to blue, respectively It can be seen that electric field gradients are in orderly manner, as expected. Its gradient was more profound at location near to the corona-wire electrodes for both 11 and 22 mm in length. It should be noted that the corona discharge is generally produced by a non-uniform electrostatic field such as that between a wire/needle and plate or a concentric wire and a tube. Air and other gases can undergo electrical breakdown when the electric field strength is high. For the case of the wire and the tube, the only place this breakdown can occur is in the very thin layer at the wire surface. In this corona region, electrons have sufficient energy to knock an electron from gas molecules to create positive ions and free electrons.

Fig. 8 show the numerical calculation of the electric field flow lines in the ion generation and charging zones of the charger at corona wire length of 11 and 22 mm, respectively. In this calculation, the corona-wire voltage was fixed at about 10 kV and the ion-driving voltage was about 100, 300 and 500 V. It was noted that the numerical calculation helped predict the electric field flow lines, on which the ions migrated from the ion generation zone into the charging zone within the charger. Therefore, the number of streamlines passing through the perforated screen opening on inner electrode into the charging zone would then be proportional to the ion penetrating from the ion generation zone into the charging zone. As shown in Fig. 8, it was found that the number of electric field flow lines passing through the perforated inner electrode can be increased by increasing the ion-driving voltage into the inner electrode. In the ion generation zone, the non-uniform distribution of the electric field lines was observed at the end of the corona-wire in case of 11 mm corona-wire while the 22 mm corona-wire

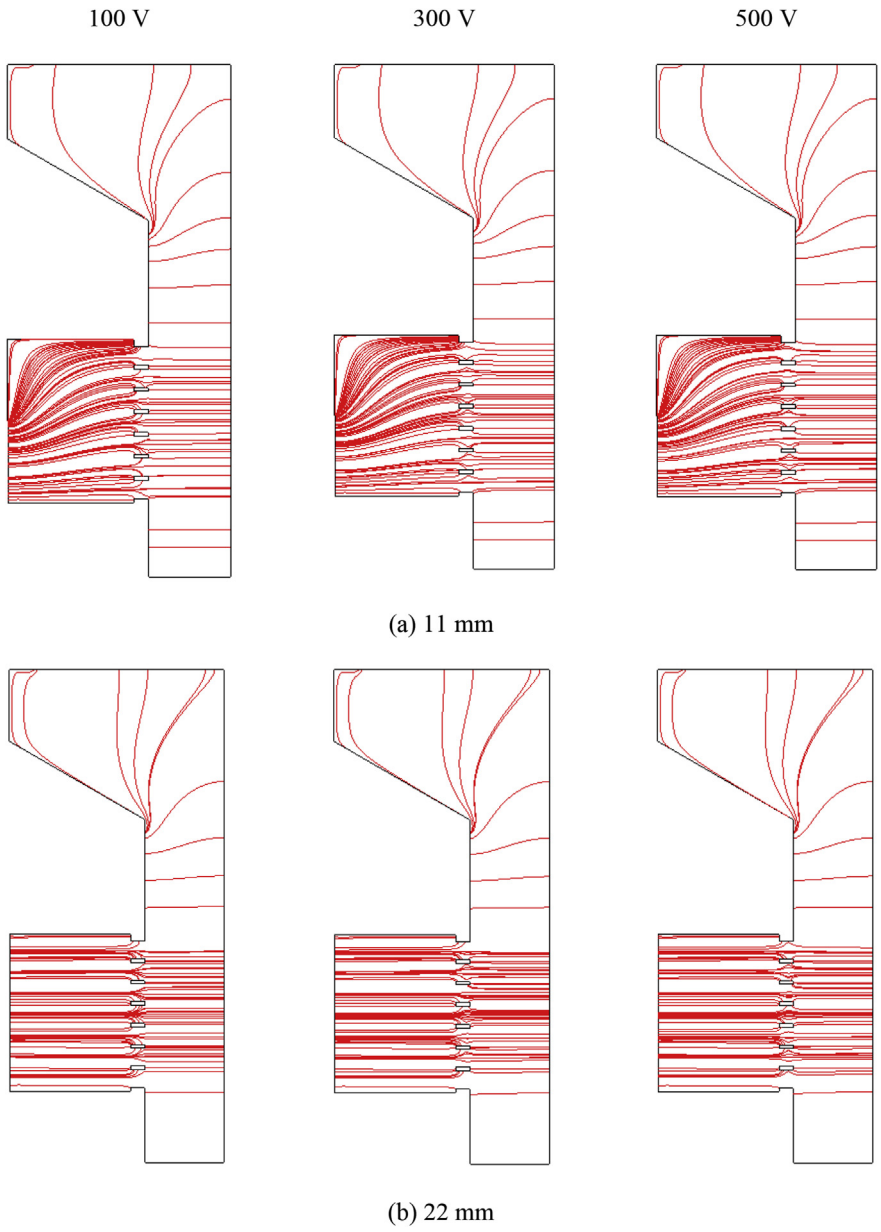

Fig. 8. Numerical calculation of the electric field lines in the ion generation and charging zones of the charger.

appeared to create uniform electric field lines along the radius of the ion generation zone. In the charging zone, it was shown that the number of the electric field lines passing through the perforated screen opening on the inner electrode into the charging zone in the case of 11 mm corona-wire was slightly higher than the case of 22 mm corona-wire. Thus, it can be concluded that the case of 11 mm corona-wire was higher ion penetration corresponding to the ion number concentration in the charging zone of the charger than the case of 22 mm.

In case of particle trajectories, Fig. 9 shows the trajectories of charged particle with diameter of 2.5 μm in the charging zone of the charger at different ion-driving voltage of 100, 300 and 500 V with air flow velocity of 0.05 m/s. As shown in Fig. 9, it can be observed that charged particles with diameter of 2.5 μm can pass through the charger smoothly without precipitate on the outer electrode of the charger. It was well known that the penetration efficiency of charged particles mainly depended on the electric field strength in the charging zone of the charger and the particle electrical mobility as a function of a particle diameter. Large particle diameter has higher mean charge than small particle diameter, therefore, electrostatic force applied on the particle increased with respect to the mean charge per particle as a function of its diameter. An increase in electrostatic force on the charged particles produced a decrease in the penetration efficiency of the charged particles in the charging zone of the charger. These calculation results can be used to support the bettering of further modify and refinement of the charger and also to understand the mechanisms of the charged particle transport inside the charger.

The number concentrations of ions in charging zone of the charger can be determined by measuring the charging current because they are approximately proportional. Figs. 10 and 11 show the variations in the charging current in relation with the corona voltage of the charger at different corona wire diameter and length and ion-driving voltage for both positive and negative ions. In this

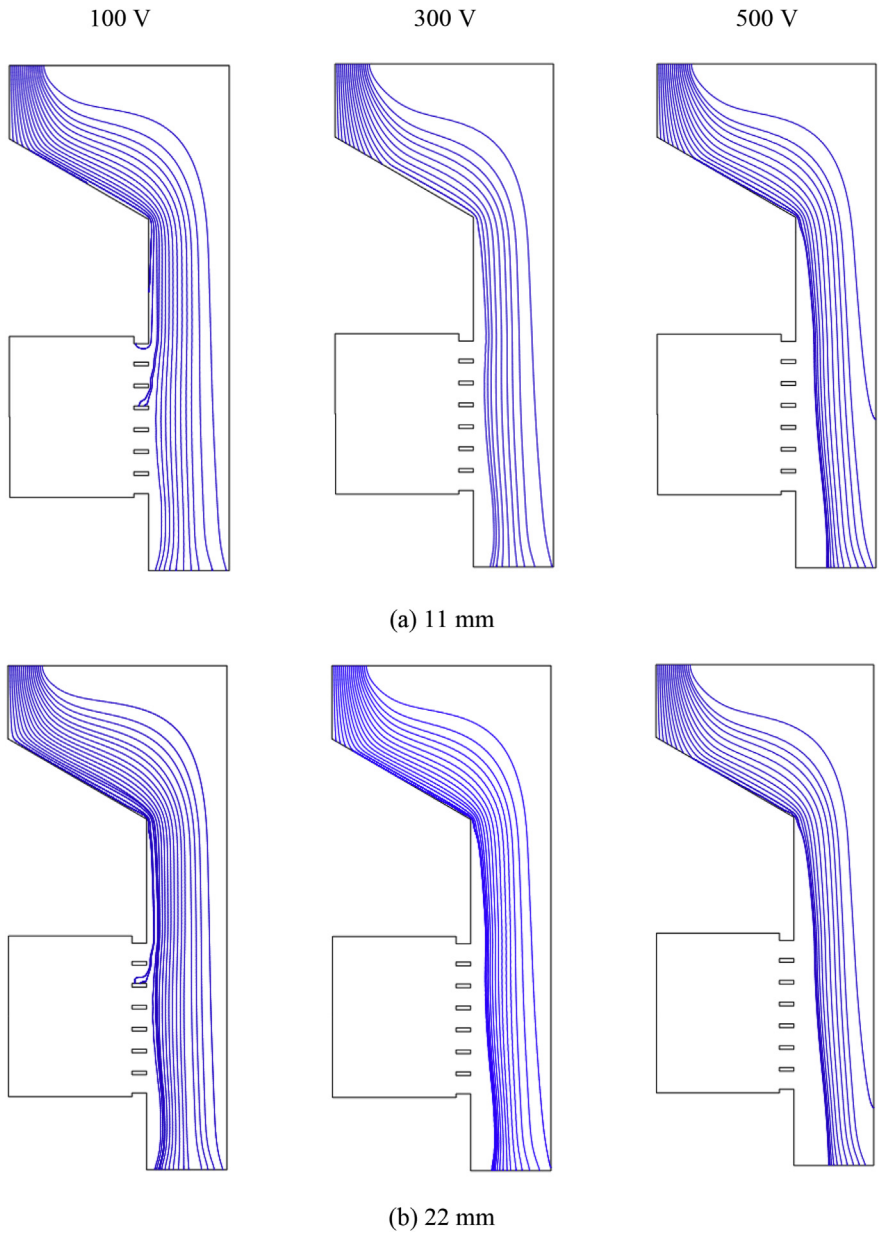

Fig. 9. Numerical calculation of the trajectories of charged particle with diameter of 2.5 μm in the charging zone of the charger at different ion-driving voltage.

experimentation, the corona voltage was maintained in the range between 0 and 10 kV, the ion-driving voltage was about 100, 300 and 500 V, the corona-wire diameter was about 0.15, 0.17 and 0.23 mm, and the corona-wire length was about 11 and 22 mm. Both positive and negative charging currents increased monotonically with increasing corona voltage at the same ion-driving voltage. When the corona voltage is constant, it was found that the both positive and negative charging currents can be increased by increasing the ion-driving voltage. As shown in Fig. 10, the corona onset voltage in the charging zone of positive corona was about 3.5 kV for the ion-driving voltage of 100, 300 and 500 V, respectively. For negative corona in Fig. 11, the corona onset voltage in the charging zone was about 3.0 kV for ion-driving voltage of 100, 300 and 500 V, respectively. At the same corona and ion-driving voltages, both positive and negative coronas were decreased with increasing corona-wire diameter. This was expected as the corona discharge will occur in a very thin layer at the corona wire surface corresponding to high strength (potential gradient) of the electric field around the corona-wire in the ion generation zone.

Compared with corona-wire of 22 mm in length, the magnitude of both positive and negative charging currents was markedly higher for corona-wire of 11 mm in length at the same corona voltage because the corona discharge usually forms at highly curved regions on electrodes, such as sharp corners, projecting points, edges of metal surfaces, or small diameter wires. The high curvature causes a high potential gradient at these locations. For positive corona, the highest charging current was found to be about 4.3×10^{-7}, 5.7×10^{-7} and 7.8×10^{-7} A occurring at the corona voltage of 10 kV for the ion-driving voltage of 100, 300 and 500 V, respectively, and corona-wire diameter of 0.15 and length of 11 mm, respectively. For negative corona, the highest charging current was found to be about 5.2×10^{-7}, 7.2×10^{-7} and 9.4×10^{-7} A occurring at the corona voltage of 10 kV for the ion-

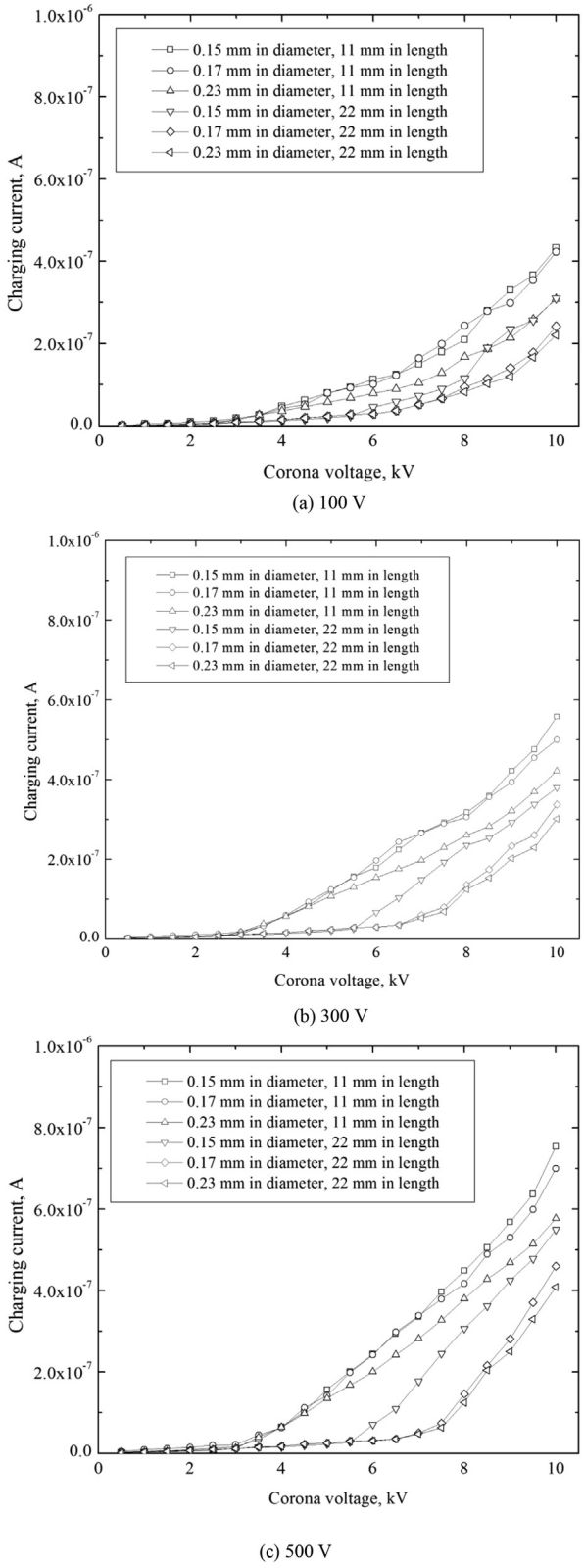

Fig. 10. Variations in charging current with corona voltage of the charger at different corona wire diameter and length and ion-driving voltage for positive ion.

driving voltage of 100, 300 and 500 V, respectively, and corona-wire diameter and length of 0.15 and 11 mm, respectively. At the same corona and ion-driving voltages, the charging currents for negative coronas were about 1.2 times higher than those positive

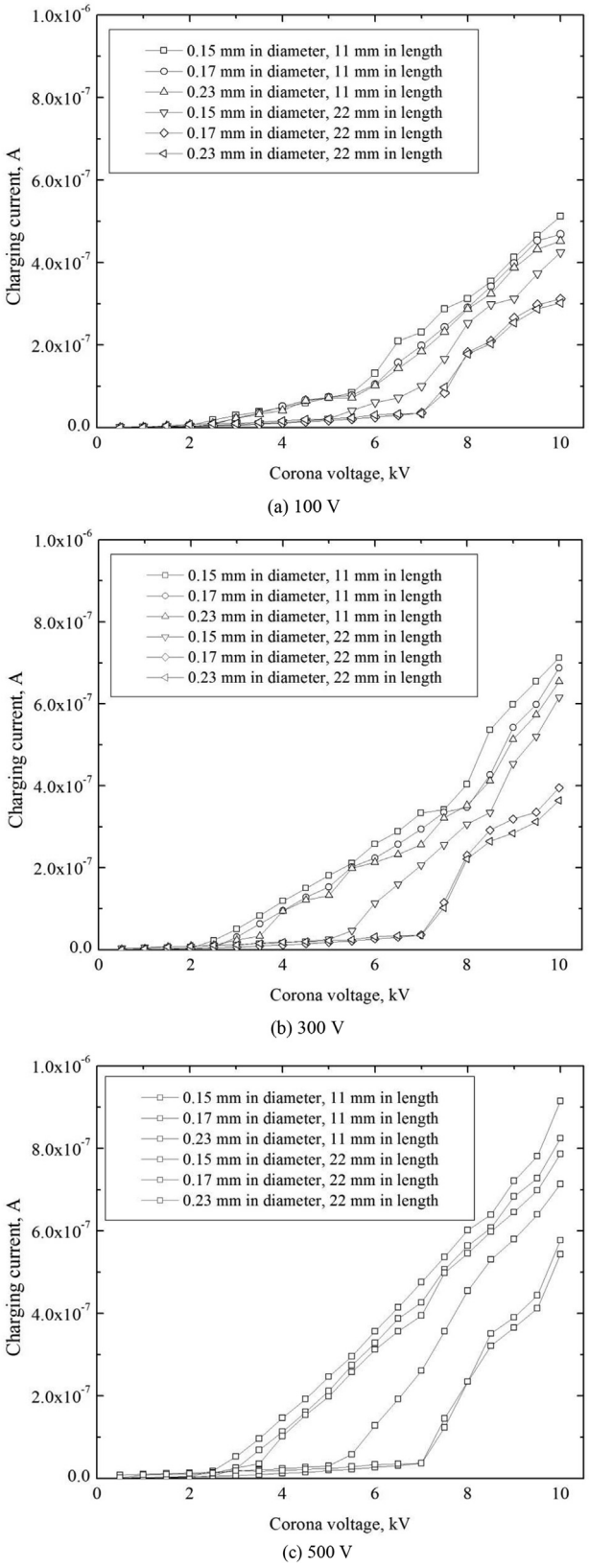

Fig. 11. Variations in charging current with corona voltage of the charger at different corona wire diameter and length and ion-driving voltage for negative ion.

coronas. This was because negative and positive ions differ in mass and electrical mobility. Ionic mobility was inversely proportional to its mass. Generally, values of mobility for positive and negative ions differ by approximately 19.30%. Reischl et al. [23] quote averages for ion motility as $Z_{ion}^{+} = 1.15 \times 10^{-4}$ m^2/V s and $Z_{ion}^{-} = 1.425 \times 10^{-4}$ m^2/V s, respectively.

Conclusion

The effects of the corona wire diameter and length electrostatic discharge characteristics of a unipolar cylindrical tri-axial charger on were numerically and experimentally investigated and presented in this work. A commercial computational fluid dynamics software package, COMSOL Multiphysics™, was used to predict the electrostatic field distribution in the ion generation and charging zones of the charger and the ion penetration through the perforated screen opening on the inner electrode of the charger. In this study, the positively and negatively applied voltages at the corona wire ranged from 0 to 10 kV, the ion-driving voltage between 100 and 500 V, the corona-wire diameter was about 0.15, 0.17 and 0.23 mm, and the corona-wire length was about 11 and 22 mm, respectively. It was found from the experimental results that both positive and negative charging currents in the charging zone of the charger increased with increasing corona and ion-driving voltages. At the same corona and ion-driving voltages, both positive and negative coronas were decreased with increasing corona-wire diameter. Compared with corona-wire of 11 mm in length, the magnitude of both positive and negative charging currents was markedly higher for corona-wire of 22 mm in length at the same corona voltage. It was found that the charging currents for negative coronas were about 1.2 times higher than those positive coronas at the same corona and ion-driving voltages. Numerical calculation results of the electric field distribution and the ion migration in the discharge and charging zones of the charger is correlated to have the same direction with the experimental results of the current–voltage relationships. This can be also used to guidance in describing the electric field distribution and the behavior of ion and charged particle trajectories that cannot be seen from experiments in order to improve the applicably design and refinement of a unipolar cylindrical tri-axial charger.

Acknowledgments

The authors gratefully acknowledge the Thailand Research Fund and the Nation Research University Project of Thailand Office of Higher Education Commission (under the TRF contract No. RTA5680007).

References

[1] P. Intra, N. Tippayawong, Progress in unipolar corona discharger designs for airborne particle charging: a literature review, J. Electrost. 67 (4) (2009) 605–615.
[2] P. Intra, N. Tippayawong, An overview of differential mobility analyzers for size classification of nanometer-sized aerosol particles, Songklanakarin J. Sci. Technol. 30 (2) (2008) 243–256.
[3] H.J. White, Industrial Electrostatic Precipitation, Addison-Wesley, Reading, Massachusetts, 1963.
[4] B.Y.H. Liu, K.T. Whitby, H.H.S. Yu, Diffusion charging of aerosol particles at low pressures, J. Appl. Phys. 38 (4) (1967) 1592–1597.
[5] D.Y.H. Pui, Experimental Study of Diffusion Charging of Aerosols, Ph.D. thesis, University of Minnesota, Minneapolis, MN, USA, 1976.
[6] P. Buscher, A. Schmidt-Ott, A. Wiedensohler, Performance of a unipolar "square wave" diffusion charger with variable nt-product, J. Aerosol Sci. 25 (4) (1980) 651–663.
[7] F.E. Kruis, H. Fissan, Nanoparticle charging in a twin Hewitt charger, J. Nanopart. Res. 3 (2001) 39–50.
[8] G. Biskos, K. Reavell, N. Collings, Electrostatic characterization of corona-wire aerosol charges, J. Electrost. 63 (2005) 69–82.
[9] P. Intra, Corona discharge in a cylindrical triode charger for unipolar diffusion aerosol charging, J. Electrost. 70 (1) (2012) 136–143.
[10] C.J. Tsai, G.Y. Lin, H.L. Chen, C.H. Huang, M. Alonso, Enhancement of extrinsic charging efficiency of a nanoparticle charger with multiple discharging wires, Aerosol Sci. Technol. 44 (10) (2010) 807–816.
[11] C.L. Chien, C.J. Tsai, H.L. Chen, G.Y. Lin, J.S. Wu, Modeling and validation of nanoparticle charging efficiency of a single-wire corona unipolar charger, Aerosol Sci. Technol. 45 (12) (2011) 1468–1479.
[12] C.L. Chien, C.J. Tsai, Improvement of the nanoparticle charging efficiency of a single-wire corona unipolar charger by using radial sheath airflow: numerical study, Aerosol Sci. Technol. 47 (4) (2013) 417–426.
[13] K.T. Whitby, Generator for producing high concentration of small ions, Rev. Sci. Instrum. 32 (12) (1961) 1351–1355.
[14] A. Medved, F. Dorman, S.L. Kaufman, A. Pocher, A new corona-based charger for aerosol particles, J. Aerosol Sci. 31 (2000) s616–s617.
[15] A. Hernandez-Sierra, F.J. Alguacil, M. Alonso, Unipolar charging of nanometer aerosol particle in a corona ionizer, J. Aerosol Sci. 34 (2003) 733–745.
[16] M. Alonso, M.I. Martin, F.J. Alguacil, The measurement of charging efficiencies and losses of aerosol nanoparticles in a corona charger, J. Electrost. 64 (2006) 203–214.
[17] D. Park, M. An, J. Hwang, Development and performance test of a unipolar diffusion charger for real-time measurements of submicron aerosol particles having a log-normal size distribution, J. Aerosol Sci. 38 (4) (2007) 420–430.
[18] P. Intra, N. Tippayawong, Effect of needle cone angle and air flow rate on electrostatic discharge characteristics of a corona-needle ionizer, J. Electrost. 68 (3) (2010) 254–260.
[19] P. Intra, N. Tippayawong, Design and evaluation of a high concentration, high penetration unipolar corona ionizer for electrostatic discharge and aerosol charging, J. Electr. Eng. Technol. 8 (5) (2013) 1175–1181.
[20] COMSOL Inc., COMSOL Multi Physics Modelling Guide, Version 3.5a, 2008.
[21] W.C. Hinds, Aerosol Technology, John Wiley & Sons, New York, USA, 1999.
[22] B.Y.H. Liu, A. Kapadia, Combined field and diffusion charging of aerosol particles in the continuum regime, J. Aerosol Sci. 9 (1978) 227–242.
[23] G.P. Reischl, J.M. Makela, R. Harch, J. Necid, Bipolar charging of ultrafine particles in the size range below 10 nm, J. Aerosol Sci. 27 (6) (1996) 931–939.

This article was downloaded by: [Thammasat University Libraries]
On: 28 April 2015, At: 19:40
Publisher: Taylor & Francis
Informa Ltd Registered in England and Wales Registered Number: 1072954 Registered office: Mortimer House, 37-41 Mortimer Street, London W1T 3JH, UK

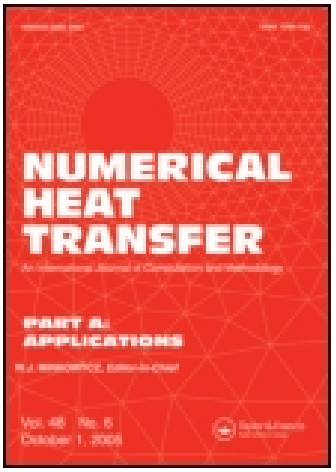

Numerical Heat Transfer, Part A: Applications: An International Journal of Computation and Methodology
Publication details, including instructions for authors and subscription information:
http://www.tandfonline.com/loi/unht20

Heat Transfer Analysis of the Human Eye During Exposure to Sauna Therapy

Teerapot Wessapan[a] & Phadungsak Rattanadecho[b]
[a] School of Aviation, Eastern Asia University, Pathumthani, Thailand
[b] Department of Mechanical Engineering, Faculty of Engineering, Thammasat University (Rangsit Campus), Center of Excellence in Electromagnetic Energy Utilization in Engineering (CEEE), Pathumthani, Thailand
Published online: 23 Apr 2015.

To cite this article: Teerapot Wessapan & Phadungsak Rattanadecho (2015) Heat Transfer Analysis of the Human Eye During Exposure to Sauna Therapy, Numerical Heat Transfer, Part A: Applications: An International Journal of Computation and Methodology, 68:5, 566-582, DOI: 10.1080/10407782.2014.986393

To link to this article: http://dx.doi.org/10.1080/10407782.2014.986393

PLEASE SCROLL DOWN FOR ARTICLE

Taylor & Francis makes every effort to ensure the accuracy of all the information (the "Content") contained in the publications on our platform. However, Taylor & Francis, our agents, and our licensors make no representations or warranties whatsoever as to the accuracy, completeness, or suitability for any purpose of the Content. Any opinions and views expressed in this publication are the opinions and views of the authors, and are not the views of or endorsed by Taylor & Francis. The accuracy of the Content should not be relied upon and should be independently verified with primary sources of information. Taylor and Francis shall not be liable for any losses, actions, claims, proceedings, demands, costs, expenses, damages, and other liabilities whatsoever or howsoever caused arising directly or indirectly in connection with, in relation to or arising out of the use of the Content.

This article may be used for research, teaching, and private study purposes. Any substantial or systematic reproduction, redistribution, reselling, loan, sub-licensing, systematic supply, or distribution in any form to anyone is expressly forbidden. Terms &

Conditions of access and use can be found at http://www.tandfonline.com/page/terms-and-conditions

Downloaded by [Thammasat University Libraries] at 19:40 28 April 2015

Numerical Heat Transfer, Part A, 68: 566–582, 2015
Copyright © Taylor & Francis Group, LLC
ISSN: 1040-7782 print/1521-0634 online
DOI: 10.1080/10407782.2014.986393

Taylor & Francis
Taylor & Francis Group

Downloaded by [Thammasat University Libraries] at 19:40 28 April 2015

HEAT TRANSFER ANALYSIS OF THE HUMAN EYE DURING EXPOSURE TO SAUNA THERAPY

Teerapot Wessapan[1] and Phadungsak Rattanadecho[2]
[1]*School of Aviation, Eastern Asia University, Pathumthani, Thailand*
[2]*Department of Mechanical Engineering, Faculty of Engineering, Thammasat University (Rangsit Campus), Center of Excellence in Electromagnetic Energy Utilization in Engineering (CEEE), Pathumthani, Thailand*

Among the reported health benefits of a sauna session are weight loss, detoxification of the body, and improved blood circulation. Side effects of sauna therapy, both beneficial and detrimental, also exist. It is well known that the human eye is one of the most sensitive parts of the entire human body when exposed to high ambient temperature and humidity levels such as in sauna therapy. This sauna heat interacts with the human eye and may lead to a variety of ocular effects due to radiation emitted by the heater and high ambient temperature. However, the resulting thermophysiologic response of the human eye to various exposure conditions during sauna therapy is not well understood. Therefore, it is of interest to investigate the potential ocular effects that may occur during sauna exposure. This study presents a numerical analysis of heat transfer in a heterogeneous model of a human eye exposed to sauna. The heat transfer model is developed based on porous media theories. In the heterogeneous human eye model, the effects of room air temperature and heater temperature on the intraocular temperature increase are systematically investigated. The study intends to focus attention on the different heat transfer characteristics between conventional sauna (mainly convection) and infrared sauna (mainly radiation). The results show that at the same room air temperature, the circulatory patterns within the anterior chamber of the eye in regard to infrared sauna are more rapid than those for the conventional sauna. Moreover, eye temperature is also higher in the infrared sauna than in the conventional sauna. The maximum temperatures of the eye exposed to conventional and infrared saunas at room air temperature of 80°C are 48.25°C and 52.90°C, respectively. From the values obtained, a guideline can be recommended to indicate the limitations in regard to temperature increase in the human eye due to sauna therapy.

1. INTRODUCTION

A sauna is a small room designed to be heated to very high temperatures with well-controlled humidity. Sauna therapy has been used for hundreds of years as a standard health-promoting practice, and can also be part of an effective weight loss program. Saunas can be divided into two basic types: conventional saunas that warm

Received 2 July 2014; accepted 7 November 2014.

Address correspondence to Phadungsak Rattanadecho, Department of Mechanical Engineering, Faculty of Engineering, Thammasat University (Rangsit Campus), Center of Excellence in Electromagnetic Energy Utilization in Engineering (CEEE), Pathumthani, 12120, Thailand. E-mail: ratphadu@engr.tu.ac.th

Color versions of one or more of the figures in the article can be found online at www.tandfonline.com/unht.

NOMENCLATURE

C	specific heat capacity (J/(kg K))	β	volume expansion coefficient (1/K)
e	tear evaporation heat loss (W/m^2)	ε	porosity
F	view factor	ρ	density (kg/m^3)
G	irradiation (W/m^2)	σ	Stefan–Boltzmann constant
h	convection coefficient (W/m^2 K)	ω_b	blood perfusion rate (1/s)
k	thermal conductivity (W/(m K))	Γ	external surface area
n	normal vector	**Subscripts**	
p	pressure (N/m^2)	am	ambient
Q	heat source (W/m^3)	b	blood
T	temperature (K)	ext	external
t	time	i	subdomain
u	velocity (m/s)	met	metabolic

the air and infrared saunas that warm objects (Figure 1). The conventional sauna relies on indirect means of heat: the air is heated and then the hot air makes contact with the user's skin (convection and conduction). In the infrared sauna, the radiant infrared energy heats the air only slightly while heating the user's body directly (radiation). However, side effects of sauna therapy, both beneficial and detrimental, exist.

Increases in the human eye temperature are important for both laboratory and clinical investigations [1]. Environmental conditions, namely ambient temperature, influence the temperature increase in the eye. It is well known that the eye is one of the organs most sensitive to environmental factors such as extreme temperature conditions. This is due to the fact that the crystalline lens and cornea are nonvascular tissues with a low metabolism, and also that the eye has no thermal sensors or protective reflexes. The severity of the physiological effect produced by small temperature increases can cause deterioration in eyesight. There are medical case reports on the formation of cataracts in humans following accidental exposure to radiation [2]. In fact, a small temperature increase in the eye of 3–5°C can induce the formation

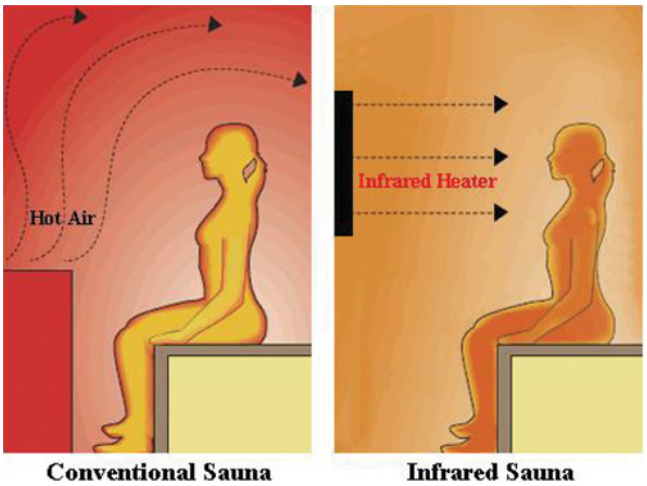

Figure 1. Conventional and infrared saunas.

Downloaded by [Thammasat University Libraries] at 19:40 28 April 2015

of cataracts [3]. Additionally, it is reported that a temperature above 41°C is necessary for the production of posterior lens opacity [4]. However, the resulting thermophysiologic response of the human eye to sauna exposure is not well understood. In order to gain insight into the phenomena occurring within the human eye with temperature distribution induced by sauna use, a detailed knowledge of both absorbed radiation and temperature distribution is necessary. Thus, it is of interest to investigate the potential ocular effects that occur during exposure to sauna.

The thermal modeling of human tissue is important as a tool to investigate the effect of external heat sources and to predict abnormalities in the tissue. Most early studies on heat transfer analysis in human tissue, especially in the eye, used heat conduction equations [5–11]. Some studies were carried out on natural convection in the eye based on heat conduction models [12, 13]. Ooi and Ng [13, 14] studied the effect of aqueous humor (AH) hydrodynamics on heat transfer in the eye based on a heat conduction model. Meanwhile, the bioheat equation introduced by Pennes [15, 16], based on the heat diffusion equation for a blood-perfused tissue, is also used for modeling heat transfer in the eye [17, 18]. Ooi and Ng also developed a three-dimensional (3D) model of the eye [19], extending their 2D model [18]. Porous media models have recently been utilized to investigate the transport phenomena in biological media rather than a simplified bioheat model [20–22]. Shafahi and Vafai [23] proposed porous media along with a natural convection model to analyze ocular thermal characteristics during exposure to thermal disturbances. Other research groups conducted numerical analyses of heat and electromagnetic (EM) dissipation in the eye [24–32]. Ooi et al. conducted advanced numerical modeling of the human eye based on the boundary element method [33–37].

Our research group has numerically investigated the temperature increase in human tissue subjected to EM fields in regard to many problems [37–45]. Wessapan et al. [38, 39] utilized a 2D finite-element method (FEM) to determine the specific absorption rate (SAR) and temperature increase in the human body exposed to leaking EM waves. Wessapan et al. [40, 41] developed a 3D model of the human head in order to investigate the SAR and temperature distributions in the human head during exposure to cellphone radiation. Keangin et al. [42–44] carried out a numerical simulation of liver cancer treatment using a complete mathematical model that considered the coupled model of EM wave propagation, heat transfer, and mechanical deformation in the biological tissue in the couple's way (two or more equations are being solved simultaneously). Wessapan et al. [45–47] investigated the SAR and temperature distribution in the eye during exposure to EM waves using the porous media theory.

Advanced models of the eye based on porous media and natural convection theory have been used in various heat transfer problems [29–36, 45–47]. However, most studies have mainly focused on the effects of convective boundary conditions and have not considered the effects of radiation from high-temperature sources in the simulations. In sauna therapy, these radiation effects result in greater heat transfer toward the eye, which can cause injury to the eye. Therefore, in order to provide adequate information on the levels of exposure and health effects from sauna therapy, it is essential to consider the combined effects of radiation and convection from sauna exposure in the analysis.

This study presents a simulation of the temperature distribution in an anatomical human eye exposed to sauna under various conditions. The temperature

Downloaded by [Thammasat University Libraries] at 19:40 28 April 2015

distribution in various tissues in the eye during exposure is obtained by numerical simulation of a heat transfer model that is then developed based on porous media theories. This study intends to focus attention on the differences in heat transfer characteristics between conventional sauna (mainly convection) and infrared sauna (mainly radiation). A 2D heterogeneous human eye model is used to simulate temperature distribution and fluid flow in the eye model. The analysis of heat transfer in the eye is investigated using a heat transfer model (based on porous media theory) which was first proposed by Shafahi and Vafai [23]. In the heterogeneous eye model, the effects of room air temperature and heater temperature on temperature distribution and fluid flow in the eye during exposure to sauna are systematically investigated. Temperature distribution and fluid flow obtained by numerical simulation of heat transfer equations based on porous media theory are presented. In this work, the model excluded the presence of both eyelid and metabolic heat generation in order to simplify the modeling procedures. The obtained values represent the phenomena accurately in determining temperature increase and fluid flow in the eye, as well as indicating the limitations that must be considered when temperature increases due to sauna exposure under different conditions.

Downloaded by [Thammasat University Libraries] at 19:40 28 April 2015

2. FORMULATION OF THE PROBLEM

In many countries, sauna has always been a part of daily life. However, side effects of sauna therapy, both beneficial and detrimental, exist. Figure 2 shows the eye exposed to sauna under various conditions. The sauna heats the eye primarily by conduction and convection from the heated air and by radiation from the heated surfaces in the sauna room, which leads to tissue damage and cataract formation. Due to ethical considerations, exposure of humans to sauna for experimental purposes is limited; Therefore, it is more convenient to develop a realistic human eye model through numerical simulation. Analysis of the heat transfer in the eye will be illustrated in Section 3. The system of governing equations and the boundary conditions is solved numerically using the FEM.

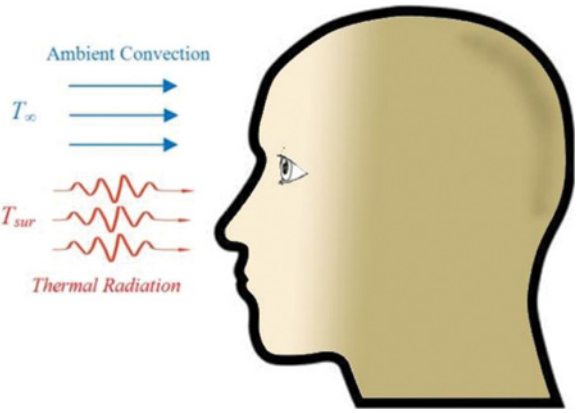

Figure 2. Human eye exposed to sauna therapy.

3. METHODS AND MODEL

The first step in evaluating the effects of exposure to sauna therapy is to determine the energy transferred by convection, radiation, and the evaporation process as well as its spatial distribution. Thereafter, energy absorption which results in a temperature increase in the eye and other processes of transport phenomena can be considered.

3.1. Physical Model

In this study, a 2D model of the eye, which follows the physical model in the previous research [23], is developed. Figure 3 shows the 2D eye model used in this study. This model comprises seven types of tissue: cornea, anterior chamber, posterior chamber, iris, sclera, lens, and vitreous. These tissues have different dielectric and thermal properties. In the scleral layer, there are two further layers known as the choroid and retina, which are relatively thin compared with the sclera. To simplify the problem, these layers are assumed to be homogeneous. The iris and sclera, which have the same properties, are modeled together as one homogenous region [13]. The thermal properties of these tissues are given in Table 1. Each tissue is assumed to be homogeneous and thermally isotropic.

3.2. Equations for Heat Transfer and Flow Analysis

To solve the thermal problem, a model of both unsteady heat transfer and boundary conditions is investigated. Heat transfer analysis of the eye is modeled in two dimensions. To simplify the problem, the following assumptions are made:

1. Human tissue is a biomaterial with constant thermal properties.
2. There is no phase change of substance in the tissue.

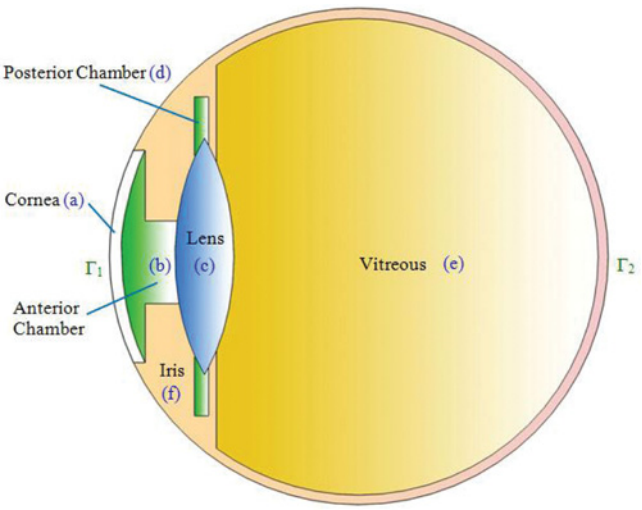

Figure 3. Vertical cross section of the human eye [23].

Downloaded by [Thammasat University Libraries] at 19:40 28 April 2015

Table 1. Thermal properties of the eye [13]

Tissue	ρ (kg/m^3)	k (W/m°C)	C_p(J/kg°C)	μ (N s/m^2)	β (1/K)
Cornea *(a)*	1,050	0.58	4,178	—	—
Anterior chamber *(b)*	996	0.58	3,997	0.00074	0.000337
Lens *(c)*	1,000	0.4	3,000	—	—
Posterior chamber *(d)*	996	0.58	3,997	—	—
Vitreous *(e)*	1,100	0.603	4,178	—	—
Sclera *(f)*	1,050	1.0042	3,180	—	—
Iris *(f)*	1,050	1.0042	3,180	—	—

3. There is a local thermal equilibrium between blood and tissue.
4. There is no chemical reaction in the tissue.

This study utilized a pertinent thermal model based according to porous media theory [23] to investigate the heat transfer behavior of the eye when exposed to sauna.

In this study, the motion of fluid is considered only inside the anterior chamber [13]. There is blood flow in the iris/sclera, which plays the role of adjusting eye temperature to the rest of the body [23]. For the remaining parts of the eye, metabolic heat generation is ignored based on the fact that these comprise mainly water [13]. The equation governing the flow of heat in the cornea, posterior chamber, lens, and vitreous resembles the classical heat conduction equation given by Eq. (1):

$$\rho_i C_i \frac{\partial T_i}{\partial t} = \nabla \cdot (k_i \nabla T_i) \quad ; i = a, c, d, e \tag{1}$$

This model accounts for the existence of AH in the anterior chamber. The heat transfer process consists of both conduction and natural convection, which can be written as follows:

Continuity equation:

$$\nabla \cdot u_i = 0; \quad i = b \tag{2}$$

Momentum equation:

$$\begin{aligned} &\rho_i \frac{\partial u_i}{\partial t} + \rho_i u_i \nabla \cdot u_i = -\nabla p_i + \nabla \cdot [\mu(\nabla u_i + \nabla u_i^T)] \\ &+ \rho_i g \beta_i (T_i - T_{\text{ref}}); \quad i = b \end{aligned} \tag{3}$$

where i denotes each subdomain in the eye model as shown in Figure 3, ρ is the tissue density (kg/m^3), β is the volume expansion coefficient (1/K), u is the velocity (m/s), p is the pressure (N/m^2), μ is the dynamic viscosity of AH (N s/m^2), t is time, T is the tissue temperature (K), and T_{ref} is the reference temperature considered here, which is 37°C. The effects of buoyancy due to temperature gradient are modeled using the Boussinesq approximation, which states that the density of a given fluid changes slightly with temperature but negligibly with pressure [13].

Downloaded by [Thammasat University Libraries] at 19:40 28 April 2015

Downloaded by [Thammasat University Libraries] at 19:40 28 April 2015

Energy equation:

$$\rho_i C_i \frac{\partial T_i}{\partial t} - \nabla \cdot (k_i \nabla T_i) = -\rho C_i u_i \cdot \nabla T_i; \quad i = b \tag{4}$$

The sclera/iris is modeled as a porous medium with blood perfusion, which assumes that local thermal equilibrium exists between blood and tissue. The blood perfusion rate used is 0.004 1/s. A modified Pennes' bioheat equation [20, 23] is used to calculate temperature distribution in the sclera/iris:

$$(1-\varepsilon)\rho_i C_i \frac{\partial T_i}{\partial t} = \nabla \cdot ((1-\varepsilon) k_i \nabla T_i) + \rho_b C_b \omega_b (T_b - T_i)_{ext}; \quad i = f \tag{5}$$

where C is the heat capacity of tissue (J/kg K), k is the thermal conductivity of tissue (W/m K), T_b is the temperature of blood (K), ρ_b is the density of blood (kg/m^3), C_b is the specific heat capacity of blood (J/kg K), and ω_b is the blood perfusion rate (1/s).

In the analysis, the porosity (ε) used is assumed to be 0.6. Heat conduction between tissue and blood flow is approximated by the blood perfusion term, $\rho_b C_b \omega_b (T_b - T)$.

3.3. Boundary Condition for Heat Transfer Analysis

The corneal surface, shown in Figure 4, is considered under convective, radiative, and evaporative boundary conditions. The study focuses on the variation in heat transfer characteristics between a conventional sauna (surface-to-ambient radiation) and an infrared sauna (surface-to-surface radiation).

3.3.1. Conventional sauna (Case I). In this case, the room air temperature is assumed to be equal to the room surface temperature (walls). Therefore, it is reasonable to simplify the radiation at the corneal surface as a surface-to-ambient radiation type:

$$-n.(-k\nabla T) = h_{am}(T_i - T_{am}) + \varepsilon\sigma(T_i^4 - T_{am}^4) + e \ \text{ on } \ \Gamma_1 \, i = a \tag{6}$$

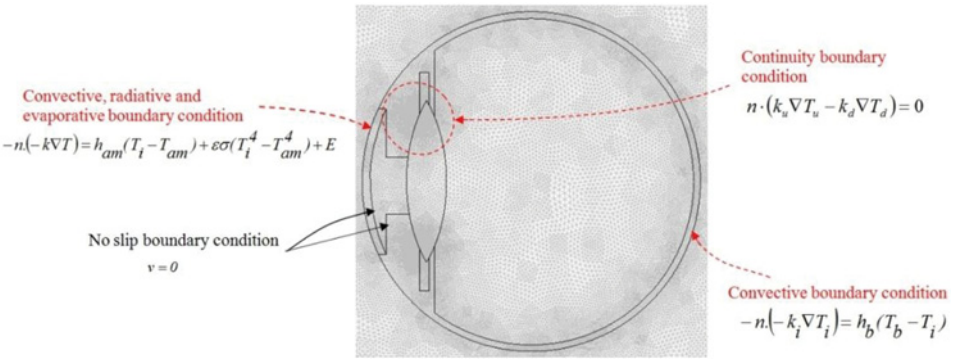

Figure 4. A 2D finite-element mesh of the eye model and boundary conditions for analysis.

3.3.2. Infrared sauna (Case II). In this case, the infrared heater is at a temperature higher than that of the walls, while the room air temperature is assumed to be equal to the wall temperature. Radiation at the corneal surface is a multiple surface radiation exchange, and thus surface-to-surface radiation is modeled using view factor analysis:

$$-n.(-k\nabla T) = h_{\text{am}}(T_i - T_{\text{am}}) + \varepsilon(G - \sigma T_i^4) + e \text{ on } \Gamma_1\, i = a \tag{7}$$

Irradiation, G, can be written as a sum according to

$$G = F_{\text{heater}}\sigma T_{\text{heater}}^4 + F_{\text{am}}\sigma T_{\text{am}}^4 + e \tag{8}$$

where Γ_i is the external surface area corresponding to section *i, e* is the tear evaporation heat loss (W/m^2), T_{am} is the ambient temperature (K), h_{am} is the convection coefficient ($\text{W/m}^2\,\text{K}$), F is the view factor between surfaces, F_{heater} is the heater view factor, and F_{am} is the ambient view factor.

The temperature of blood is generally assumed to be the same as the body core temperature, which causes heat to be transferred to the eye [13]. The surface of the sclera is assumed to be under the convective boundary condition:

$$-n \cdot (-k_i \nabla T_i) = h_{\text{b}}(T_{\text{b}} - T_i) \text{ on } \Gamma_2\, i = f \tag{9}$$

where h_{b} is the convection coefficient of blood ($65\,\text{W/m}^2\,\text{K}$), and Γ_1 and Γ_2 are the corneal and scleral surfaces of the eye, respectively.

3.4. Calculation Procedure

In this study, FEM is used to analyze the transient problems. In order to obtain a good approximation, a fine mesh is specified in the sensitive areas. This study provides a variable mesh method for solving the problem, as shown in Figure 4. The system of governing equations and boundary conditions is then solved. All computational processes are implemented using COMSOL™ Multiphysics to demonstrate the phenomenon that occurs in the eye exposed to sauna.

The 2D model is discretized using triangular elements, and the Lagrange quadratic is then used to approximate the temperature variation across each element. A convergence test is carried out to identify the number of elements required. This convergence test leads to a grid with approximately 10,000 elements. It is reasonable to assume that, at this element number, the accuracy of the simulation results is independent of the number of elements.

4. RESULTS AND DISCUSSION

In this analysis, the effects of room air temperature and heater temperature on temperature distribution and fluid flow in the eye during exposure to sauna are systematically investigated. The following discussion focuses on the transport phenomena that occur within the eye exposed to conventional and infrared sauna.

Downloaded by [Thammasat University Libraries] at 19:40 28 April 2015

In this study, the effect of thermoregulation mechanisms has been ignored. The convective coefficient due to the blood flow inside the sclera is set to 65 W/m^2 K [13]. For the simulation, the thermal properties are taken directly from Table 1.

4.1. Verification of the Model

In order to verify the accuracy of the present numerical model, the simple cases of the simulated results from this study are validated against the numerical results obtained with the same geometric model by Shafahi and Vafai [23]. Moreover, the numerical results are then compared to the experimental results from a rabbit study by Lagendijk [5]. The validation case assumes that the rabbit body temperature was 38.8°C, the tear evaporation heat loss is 40 W/m^2, the ambient temperature is 25°C, and the convection coefficient of ambient air is 20 W/m^2 K. The results of the selected test case are shown in Figure 5 for ocular temperature distribution. Figure 5 clearly shows a good agreement for ocular temperature distribution between the present solution and those of Shafahi and Vafai [23] and Lagendijk [5]. This favorable comparison lends confidence to the accuracy of the present numerical model.

4.2. Conventional Sauna (Case I)

4.2.1. Effect of room air temperature. *In the case of the conventional sauna*, when the room air temperature is higher than the eye temperature, namely 60, 80,

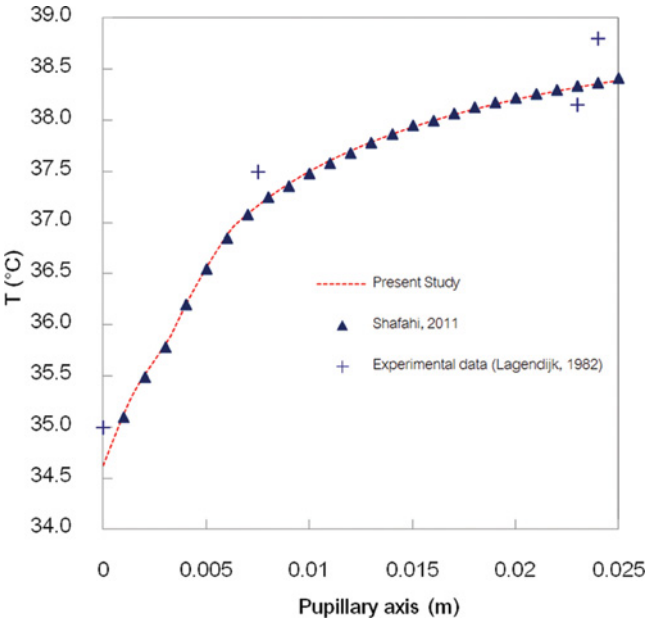

Figure 5. Comparison of the calculated temperature distribution to temperature distribution obtained by Shafahi and Vafai [23] and Lagendijk's experimental data [5]; $h_{am} = 20\ W/m^2$ K and $T_{am} = 25°C$.

Downloaded by [Thammasat University Libraries] at 19:40 28 April 2015

and 100°C (shown in Figure 6), heat convected and radiated from the ambient air flows into the eye and the ocular temperature rises above normal body temperature. At $t = 10$ min, the maximum temperatures inside the eye are 42.91, 48.25, and 53.81°C for room air temperatures of 60, 80, and 100°C, respectively.

4.3. Infrared Sauna (Case II)

This case assumes that the heater view factor (F_{heater}) is 0.1 and the ambient view factor (F_{am}) is 0.9.

In the case of the infrared sauna, infrared heating gives rise to energy transfer to the eye exposed to the sauna. In Figure 7, the effect of heater temperature is also investigated. This figure shows a comparison of temperature distribution within the eye at 10 min with a room air temperature of 80°C corresponding to heater temperatures of 200, 250, and 300°C. It is found that the heater temperature has a

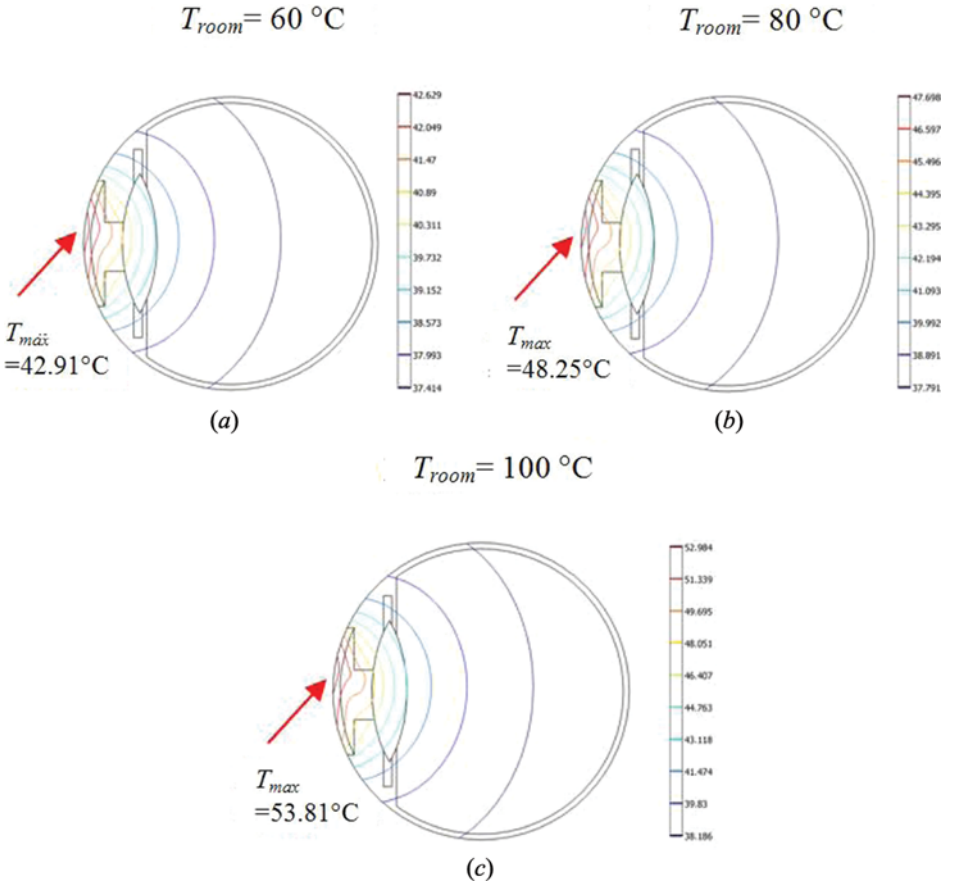

Figure 6. Temperature distribution in the eye exposed to a conventional sauna at room air temperatures of (*a*) 60°C, (*b*) 80°C, and (*c*) 100°C (at $t = 10$ min).

Downloaded by [Thammasat University Libraries] at 19:40 28 April 2015

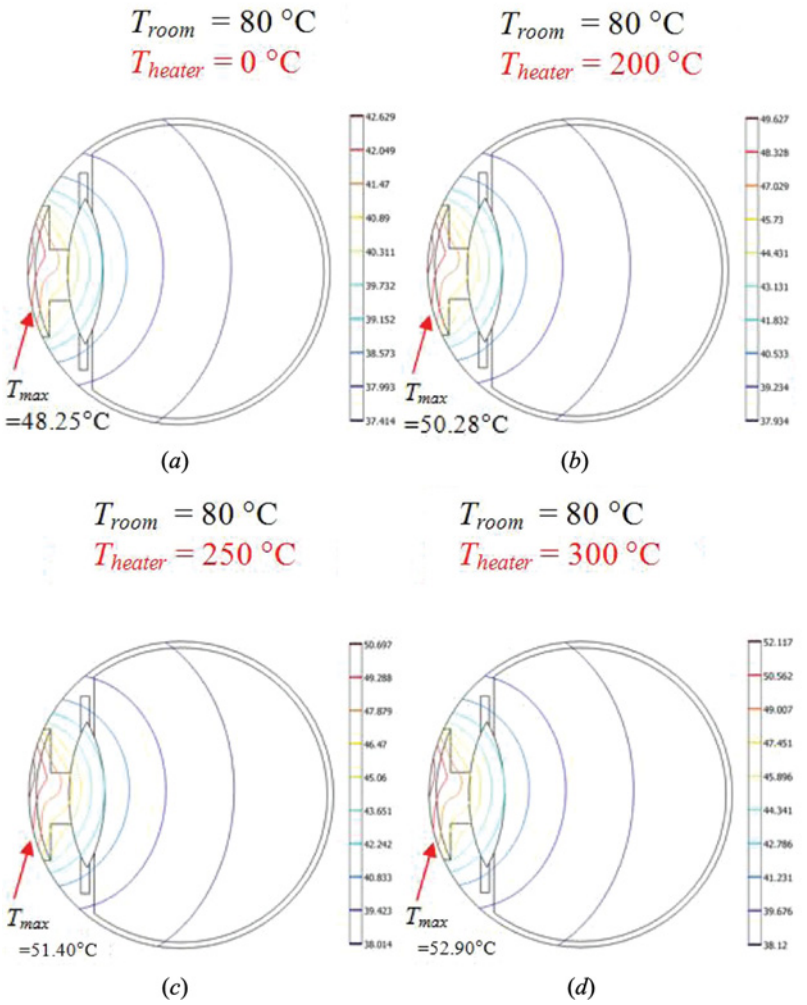

Figure 7. Temperature distribution in the eye exposed to an infrared sauna at a room air temperature of 80°C and heater temperature set to (*a*) no heater, (*b*) 200°C, (*c*) 250°C, and (*d*) 300°C (at $t = 10$ min).

significant influence on temperature increase within the eye. Greater heater temperature provides greater heat radiation to the eye, thereby increasing the ocular temperature. During infrared sauna exposure at $T_{\text{room}} = 80$°C, the maximum temperatures in the eye are 50.28, 51.40, and 52.90°C for heater temperatures of 200, 250, and 300°C, respectively.

4.4. Comparison Between Conventional and Infrared Sauna

Consider the temperature distribution at the extrusion line (Figure 8). Figure 9 shows the temperature distribution versus papillary axis (along the extrusion line) of

Downloaded by [Thammasat University Libraries] at 19:40 28 April 2015

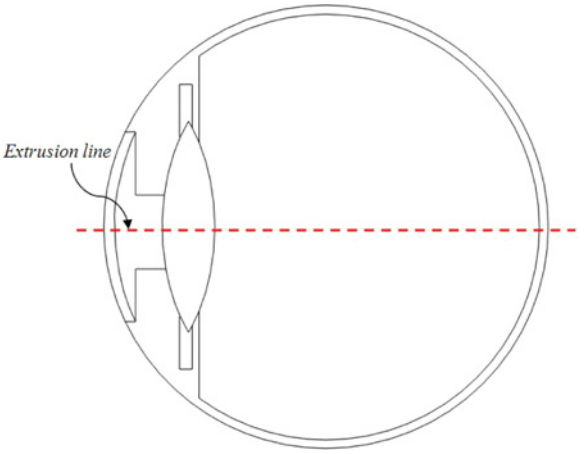

Figure 8. Extrusion line through the eye when temperature distribution is considered.

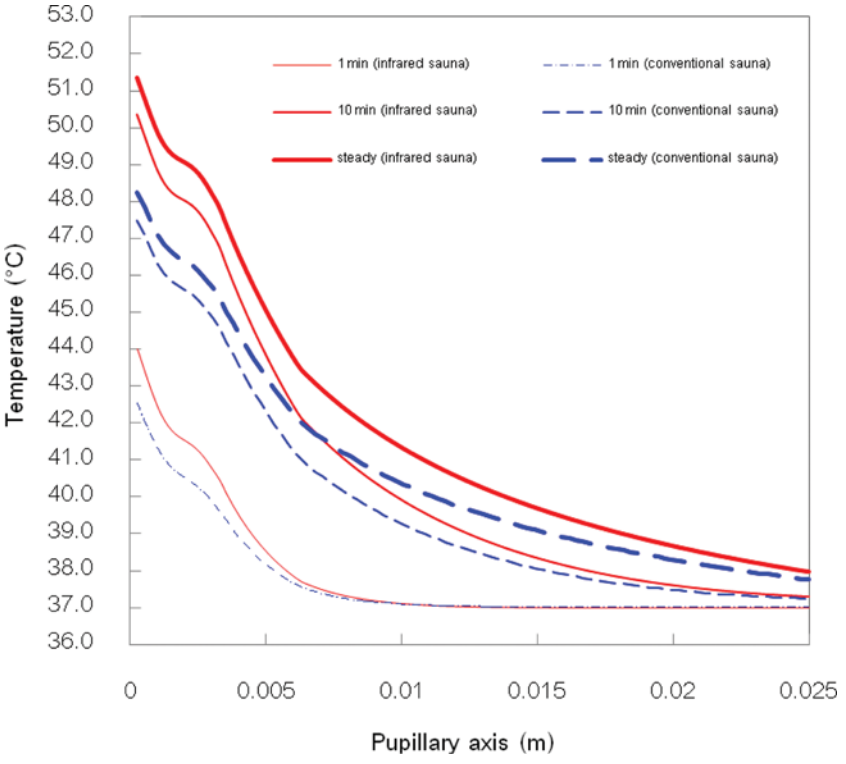

Figure 9. Temperature distribution versus papillary axis of the eye exposed to conventional and infrared sauna at various times.

Downloaded by [Thammasat University Libraries] at 19:40 28 April 2015

the eye exposed to conventional and infrared saunas at various times. This figure shows that the effect of sauna type has a substantial impact on temperature distribution within the eye for all exposure times. In all cases, the maximum temperature occurs at the corneal surface. At all exposure times, the infrared sauna induced a significantly higher temperature increase in the eye than did the conventional sauna.

Figure 10 shows the circulatory patterns within the anterior chamber exposed to conventional and infrared saunas at a room air temperature of 80°C and a heater temperature of 250°C. *In both cases*, a clockwise circulation appeared in the anterior chamber. This seems to imply that the heat gradually travels inward and passes through the front of the eye (cornea) to the lens.

In comparison, *in the conventional case*, the circulatory pattern has a lower speed than that of the *infrared sauna*. At low flow speed, the temperature gradient is less steep in the anterior chamber, where conduction is the dominant heat transfer mode across the fluid layer. On the other hand, *in the case of the infrared sauna* with higher flow speeds, different flow regimes are encountered with progressively increasing heat transfer. In this case, convective heat transfer plays a significant role in transferring heat.

The maximum velocities inside the anterior chamber are 4.06×10^{-4} and 4.63×10^{-4} m/s for the conventional and infrared sauna, respectively. Based on this study, it can be concluded that flow speed varies according to ocular temperature gradient.

In this study, the maximum temperature in the eye exposed to conventional and infrared sauna at $T_{\text{heater}} = 300$°C for a room air temperature of 80°C is 48.25 and 52.90°C, respectively. This may cause potentially serious eye damage, especially in the case of exposure to the infrared sauna. The accumulated heat due to the combination of infrared energy and ambient air raises the eye temperature to 52.90°C;

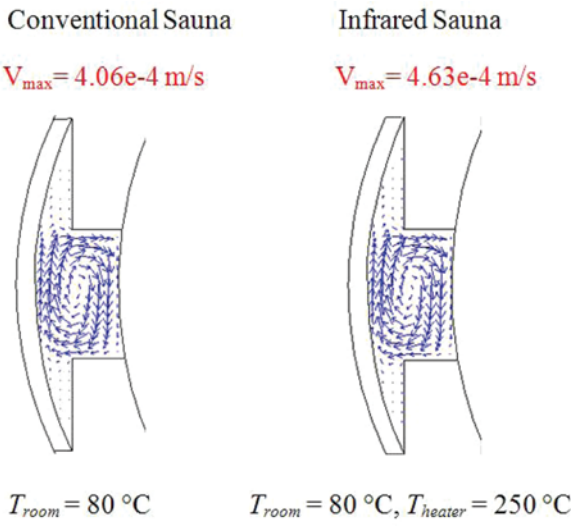

Figure 10. Velocity distribution inside the anterior chamber exposed to conventional and infrared sauna at a room air temperature of 80°C and a heater temperature of 250°C.

Downloaded by [Thammasat University Libraries] at 19:40 28 April 2015

such a high temperature in the regions of the cornea and lens may lead to damaged eyesight and tissue destruction [2, 3].

5. CONCLUSIONS

While all saunas produce sweating, weight loss, detoxification of the body, and improved blood circulation, conventional saunas and infrared saunas do this differently. A conventional sauna warms the air, while an infrared sauna warms the objects in the air (i.e., a human within an enclosed space). This study focuses attention on the different heat transfer characteristics of conventional and infrared saunas. The effects of room air temperature and heater temperature on temperature distribution and fluid flow in the eye during exposure to sauna are systematically investigated. Temperature distribution in various ocular tissues during exposure is obtained by numerical simulation of a heat transfer model, which is then developed based on porous media theories.

It is found that increasing ocular temperature results from an increase in both room air temperature and heater temperature. The results show important information related to a complex interaction among ambient temperature, heater temperature, fluid flow, and temperature distribution in the eye during exposure to sauna. This study also shows that exposure time has a marked influence on temperature increase and fluid flow in the eye. At all exposure times, the infrared sauna induced a significantly higher ocular temperature increase than did the conventional sauna. Based on these results, saunas are potentially harmful to both eye and eyesight, especially the infrared sauna. Excessive or prolonged exposure to infrared sauna carries a higher risk of eye injury than conventional sauna. Staying within recommended time limits and wearing eye protection can help avoid risk.

The results obtained represent the phenomenon sufficiently accurately to determine the ocular temperature increase and enable recommendation of a guideline to indicate the limitations that must be considered at high temperatures due to sauna exposure under different conditions. Thus, the health effect assessment of sauna exposure requires the utilization of the most accurate numerical simulation of the thermal model. A further study will be developed to provide a more realistic 3D model for simulations. This will allow a better understanding of a realistic situation of the heat transfer process during sauna therapy.

Downloaded by [Thammasat University Libraries] at 19:40 28 April 2015

FUNDING

This work was financially supported by the Thailand Research Fund (TRF), the Commission on Higher Education (CHE), and Eastern Asia University.

REFERENCES

1. R. D. Freeman and I. Fatt, Environmental Influences on Ocular Temperature, *Invest. Ophthalmol.*, vol. 12, no. 8, pp. 596–602, 1973.
2. A. F. Emery, P. Kramar, A. W. Guy, and J. C. Lin, Microwave Induced Temperature Rises in Rabbit Eyes in Cataract Research, *J. Heat Transfer ASME*, vol. 97, pp. 123–128, 1975.

3. C. Buccella, V. D. Santis, and M. Feliaiani, Prediction of Temperature Increase in Human Eyes Due to RF Sources, *IEEE Trans. Electromagn. Compat.*, vol. 49, no. 4, pp. 825–833, 2007.
4. J. C. Lin, Cataracts and Cell-Phone Radiation, *IEEE Antennas Propag. Mag.*, vol. 45, no. 1, pp. 171–174, 2003.
5. J. J. W. Lagendijk, A Mathematical Model to Calculate Temperature Distribution in Human and Rabbit Eye During Hyperthermic Treatment, *Phys. Med. Biol.*, vol. 27, pp. 1301–1311, 1982.
6. J. Scott, A Finite Element Model of Heat Transport in the Human Eye, *Phys. Med. Biol.*, vol. 33, pp. 227–241, 1988.
7. T. Wu, P. Li, Q. Shao, J. Hong, L. Yang, and S. Wu, A Simulation-Experiment Method to Characterize the Heat Transfer in Ex-Vivo Porcine Hepatic Tissue with a Realistic Microwave Ablation System, *Numer. Heat Transfer, Part A*, vol. 64, pp. 729–743, 2013.
8. E. H. Amara, Numerical Investigations on Thermal Effects of Laser–Ocular Media Interaction, *Int. J. Heat Mass Transfer*, vol. 38, pp. 2479–2488, 1995.
9. A. Hirata, S. Matsuyama, and T. Shiozawa, Temperature Rises in the Human Eye Exposed to EM Waves in the Frequency Range 0.6–6 GHz, *IEEE Trans. Electromagn. Compat.*, vol. 42, no. 4, pp. 386–393, 2000.
10. K. J. Chua, J. C. Ho, S. K. Chou, and M. R. Islam, On the Study of the Temperature Distribution within a Human Eye Subjected to a Laser Source, *Int. Commun. Heat Mass Transfer*, vol. 32, pp. 1057–1065, 2005.
11. W. Limtrakarn, S. Reepolmaha, and P. Dechaumphai, Transient Temperature Distribution on the Corneal Endothelium during Ophthalmic Phacoemulsification: a Numerical Simulation Using the Nodeless Variable Element, *Asian Biomed.*, vol. 4, no. 6, pp. 885–892, 2010.
12. S. Kumar, S. Acharya, R. Beuerman, and A. Palkama, Numerical Solution of Ocular Fluid Dynamics in a Rabbit Eye: Parametric Effects, *Ann. Biomed. Eng.*, vol. 34, pp. 530–544, 2006.
13. E. Ooi and E. Y. K. Ng, Simulation of Aqueous Humor Hydrodynamics in Human Eye Heat Transfer, *Comput. Biol. Med.*, vol. 38, pp. 252–262, 2008.
14. E. H. Ooi and E. Y. K. Ng, Effects of Natural Convection Inside the Anterior Chamber, *Int. J. Numer. Methods Biomed. Eng.*, vol. 27, pp. 408–423, 2011.
15. H. H. Pennes, Analysis of Tissue and Arterial Blood Temperatures in the Resting Human Forearm, *J. Appl. Physiol.*, vol. 1, pp. 93–122, 1948.
16. H. H. Pennes, Analysis of Tissue and Arterial Blood Temperatures in the Resting Human Forearm, *J. Appl. Physiol.*, vol. 85, no. 1, pp. 5–34, 1998.
17. V. M. M. Flyckt, B. W. Raaymakers, and J. J. W. Lagendijk, Modeling the Impact of Blood Flow on the Temperature Distribution in the Human Eye and the Orbit: Fixed Heat Transfer Coefficients Versus the Pennes Bioheat Model Versus Discrete Blood Vessels, *Phys. Med. Biol.*, vol. 51, pp. 5007–5021, 2006.
18. E. Y. K. Ng and E. H. Ooi, FEM Simulation of the Eye Structure with Bioheat Analysis, *Comput. Methods Program Biomed.*, vol. 82, pp. 268–276, 2006.
19. E. H. Ooi and E. Y. K. Ng, Ocular Temperature Distribution: A Mathematical Perspective, *J. Mech. Med. Biol.*, vol. 9, pp. 199–227, 2009.
20. A. Nakayama and F. Kuwahara, A General Bioheat Transfer Model Based on the Theory of Porous Media, *Int. J. Heat Mass Transfer*, vol. 51, pp. 3190–3199, 2008.
21. P. Rattanadecho, S. Suttisong, and T. Somtawin, The Numerical and Experimental Analysis of Heat Transport and Water Infiltration in a Granular Packed Bed Due to Supplied Hot Water, *Numer. Heat Transfer, Part A*, vol. 65, pp. 1007–1022, 2014.
22. K. Khanafer and K. Vafai, Synthesis of Mathematical Models Representing Bioheat Transport, *Adv. Numer. Heat Transfer*, vol. 3, pp. 1–28, 2009.

Downloaded by [Thammasat University Libraries] at 19:40 28 April 2015

23. M. Shafahi and K. Vafai, Human Eye Response to Thermal Disturbances, *ASME J. Heat Transfer*, vol. 133, p. 011009, 2011.
24. J. Scott, The Computation of Temperature Rises in the Human Eye Induced by Infrared Radiation, *Phys. Med. Biol.*, vol. 33, pp. 243–257, 1988.
25. E. H. Amara, Numerical Investigations on Thermal Effects of Laser–Ocular Media Interaction, *Int. J. Heat Mass Transfer*, vol. 38, pp. 2479–2488, 1995.
26. A. Hirata, S. Matsuyama, and T. Shiozawa, Temperature Rises in the Human Eye Exposed to EM Waves in the Frequency Range 0.6–6 GHz, *IEEE Trans. Electromagn. Compat.*, vol. 42, no. 4, pp. 386–393, 2000.
27. K. J. Chua, J. C. Ho, S. K. Chou, and M. R. Islam, On the Study of the Temperature Distribution within a Human Eye Subjected to a Laser Source, *Int. Commun. Heat Mass Transfer*, vol. 32, pp. 1057–1065, 2005.
28. W. Limtrakarn, S. Reepolmaha, and P. Dechaumphai, Transient Temperature Distribution on the Corneal Endothelium during Ophthalmic Phacoemulsification: a Numerical Simulation Using the Nodeless Variable Element, *Asian Biomed.*, vol. 4, no. 6, pp. 885–892, 2010.
29. E. Y. K. Ng, J. H. Tan, U. R. Acharya, and J. S. Suri, *Human Eye Imaging and Modeling*, CRC Press, Florida, 2012. ISBN: 978-1-4398-6993-2.
30. D. Sumeet, U. R. Acharya, and E. Y. K. Ng, *Computational Analysis of Human Eye with Application*, WSPC Press, Singapore, 2011. ISBN: 978-981-4340-29-8.
31. E. Y. K. Ng, U. R. Acharya, J. S. Suri, and A. Campilho, *Image Analysis and Modeling in Ophthalmology*, CRC Press, Boca Raton, FL, 2014. ISBN: 978-1-4665-5930-1.
32. E. Y. K. Ng, U. R. Acharya, R. M. Rangayyan, and J. S. Suri, *Ophthalmology Imaging and Applications*, CRC Press, Florida, 2014.
33. E. H. Ooi, W. T. Ang, and E. Y. K. Ng, A Boundary Element Model of the Human Eye Undergoing Laser Thermokeratoplasty, *Comput. Biol. Med.*, vol. 28, pp. 727–738, 2008.
34. E. H. Ooi, W. T. Ang, and E. Y. K. Ng, A Boundary Element Model for Investigating the Effects of Eye Tumor on the Temperature Distribution inside the Human Eye, *Comput. Biol. Med.*, vol. 28, pp. 727–738, 2009.
35. J. H. Tan, E. Y. K. Ng, U. R. Acharya, and C. Chee, Study of Normal Ocular Thermogram Using Textural Parameters, *Infrared Phys. Technol.*, vol. 53, pp. 120–126, 2010.
36. J. H. Tan, E. Y. K. Ng, and U. R. Acharya, Evaluation of Tear Evaporation from Ocular Surface by Functional Infrared Thermography, *Med. Physics*, vol. 37, pp. 6022–6034, 2010.
37. J. H. Tan, E. Y. K. Ng, and U. R. Acharya, Evaluation of Topographical Variation in Ocular Surface Temperature by Functional Infrared Thermography, *Infrared Phys. Technol.*, vol. 54, pp. 469–477, 2011.
38. T. Wessapan, S. Srisawatdhisukul, and P. Rattanadecho, Numerical Analysis of Specific Absorption Rate and Heat Transfer in the Human Body Exposed to Leakage Electromagnetic Field at 915 MHz and 2450 MHz, *ASME J. Heat Transfer*, vol. 133, p. 051101, 2011.
39. T. Wessapan, S. Srisawatdhisukul, and P. Rattanadecho, The Effects of Dielectric Shield on Specific Absorption Rate and Heat Transfer in the Human Body Exposed to Leakage Microwave Energy, *Int. Commun. Heat Mass Transfer*, vol. 38, pp. 255–262, 2011.
40. T. Wessapan and P. Rattanadecho, Numerical Analysis of Specific Absorption Rate and Heat Transfer in Human Head Subjected to Mobile Phone Radiation, *ASME J. Heat Transfer*, vol. 134, p. 121101, 2012.
41. T. Wessapan, S. Srisawatdhisukul, and P. Rattanadecho, Specific Absorption Rate and Temperature Distributions in Human Head Subjected to Mobile Phone Radiation at Different Frequencies, *Int. J. Heat Mass Transfer*, vol. 55, pp. 347–359, 2012.

Downloaded by [Thammasat University Libraries] at 19:40 28 April 2015

42. P. Keangin, T. Wessapan, and P. Rattanadecho, Analysis of Heat Transfer in Deformed Liver Cancer Modeling Treated Using a Microwave Coaxial Antenna, *Appl. Therm. Eng.*, vol. 31, no. 16, pp. 3243–3254, 2011.
43. P. Keangin, T. Wessapan, and P. Rattanadecho, An Analysis of Heat Transfer in Liver Tissue during Microwave Ablation Using Single and Double Slot Antenna, *Int. Commun. Heat Mass Transfer*, vol. 38, pp. 757–766, 2011.
44. P. Rattanadecho and P. Keangin, Numerical Study of Heat Transfer and Blood Flow in Two-Layered Porous Liver Tissue During Microwave Ablation Process Using Single and Double Slot Antenna, *Int. J. Heat Mass Transfer*, vol. 58, pp. 457–470, 2013.
45. T. Wessapan and P. Rattanadecho, Specific Absorption Rate and Temperature Increase in Human Eye Subjected to Electromagnetic Fields at 900 MHz, *ASME J. Heat Transfer*, vol. 134, p. 091101, 2012.
46. T. Wessapan and P. Rattanadecho, Specific Absorption Rate and Temperature Increase in the Human Eye due to Electromagnetic Fields Exposure at Different Frequencies, *Int. J. Heat Mass Transfer*, vol. 64, pp. 426–435, 2013.
47. T. Wessapan and P. Rattanadecho, Influence of Ambient Temperature on Heat Transfer in the Human Eye during Exposure to Electromagnetic Fields at 900 MHz, *Int. J. Heat Mass Transfer*, vol. 70, pp. 378–388, 2014.

Downloaded by [Thammasat University Libraries] at 19:40 28 April 2015

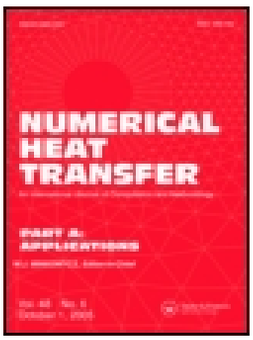

Taylor & Francis
Taylor & Francis Group

Numerical Heat Transfer, Part A: Applications
An International Journal of Computation and Methodology

ISSN: 1040-7782 (Print) 1521-0634 (Online) Journal homepage: http://www.tandfonline.com/loi/unht20

Effect of the body position on natural convection within the anterior chamber of the human eye during exposure to electromagnetic fields

Teerapot Wessapan, Phadungsak Rattanadecho & Patcharaporn Wongchadakul

To cite this article: Teerapot Wessapan, Phadungsak Rattanadecho & Patcharaporn Wongchadakul (2016): Effect of the body position on natural convection within the anterior chamber of the human eye during exposure to electromagnetic fields, Numerical Heat Transfer, Part A: Applications

To link to this article: http://dx.doi.org/10.1080/10407782.2015.1109352

Published online: 22 Mar 2016.

Submit your article to this journal

View related articles

View Crossmark data

Full Terms & Conditions of access and use can be found at
http://www.tandfonline.com/action/journalInformation?journalCode=unht20

Download by: [Teerapot Wessapan] **Date:** 22 March 2016, At: 19:40

NUMERICAL HEAT TRANSFER, PART A
http://dx.doi.org/10.1080/10407782.2015.1109352

Taylor & Francis
Taylor & Francis Group

Effect of the body position on natural convection within the anterior chamber of the human eye during exposure to electromagnetic fields

Teerapot Wessapan[a], Phadungsak Rattanadecho[b], and Patcharaporn Wongchadakul[b]

[a]School of Aviation, Eastern Asia University, Rungsit, Thanyaburi, Pathumthani, Thailand; [b]Center of Excellence in Electromagnetic Energy Utilization in Engineering (CEEE), Department of Mechanical Engineering, Faculty of Engineering, Thammasat University (Rangsit Campus), Khlong Nueng, Khlong Luang, Pathumthani, Thailand

ABSTRACT

Heating is the main biological effect of the electromagnetic (EM) fields to human eye. This study intends to focus attention on the differences in the heat transfer characteristics of the human eye induced by EM fields in different body positions. The effect of three different body positions – sitting, supine, and prone – on natural convection of aqueous humor (AH) in the anterior chamber of the eye is systematically investigated. The specific absorption rate (SAR) value, fluid flow, and the temperature distribution in the eye during exposure to EM fields are obtained by numerical simulation of EM wave propagation. In this study, the frequencies of 900 and 1,800 MHz are chosen for the investigations. The heat transfer model used in this study is developed based on natural convection and porous media theories. The results show that the AH temperature inside the anterior chamber is the highest in the supine position at both frequencies. It is found that during exposure to EM fields, body position plays an important role on AH natural convection and the heat transfer process within the anterior chamber and its periphery in the front part of the eye. However, the body position has no significant effect on temperature distribution for the middle part of the eye. The obtained results provide information on the body position and thermal effects from EM fields exposure.

ARTICLE HISTORY
Received 14 January 2015
Accepted 20 August 2015

Downloaded by [Teerapot Wessapan] at 19:40 22 March 2016

1. Introduction

In the eye, the natural convection is caused by buoyancy effects arising from the gravity force on density differences in a body of the AH in the anterior chamber. The cornea is cooled by the air and tears the evaporation film. This convective flow of the AH is influenced by the difference in temperature between the external cornea and the internal lens. Moreover, the AH natural convection induced by the intense electromagnetic (EM) fields has a significant impact on the temperature increase within the anterior chamber [1–3]. Intense exposure to EM fields causes heating of tissues with potentially harmful effects. It is well known that the eye is one of the organs most sensitive to environmental factors such as EM fields. Recommendations that limit the exposure have been issued by the International Commission on Non-Ionizing Radiation Protection (ICNIRP 1998) [4] and the Institute of Electrical and Electronics Engineers (IEEE 2005) [5]. Normally natural convection is highly dependent on the geometry of the hot surface. Therefore the changes in body position that change the anterior chamber orientation could have a significant effect on the convective flow of the AH. Moreover, body position also affects the natural convection in the eye, especially when subjected to EM fields.

CONTACT Phadungsak Rattanadecho ratphadu@engr.tu.ac.th Center of Excellence in Electromagnetic Energy Utilization in Engineering (CEEE), Department of Mechanical Engineering, Faculty of Engineering, Thammasat University (Rangsit Campus), 99 Moo1, Khlong Nueng, Khlong Luang, Pathumthani 12120, Thailand.
Color versions of one or more of the figures in this article can be found online at www.tandfonline.com/unht.
© 2016 Taylor & Francis

Nomenclature

C	specific heat capacity (J/(kg K))	ε	permittivity (F/m)
E	electric field intensity (V/m)	σ	electric conductivity (S/m)
e	tear evaporation heat loss (W/m^2)	ω	angular frequency (rad/s)
f	frequency of incident wave (Hz)	ρ	density (kg/m^3)
H	magnetic field (A/m)	ω_b	blood perfusion rate (1/s)
h	convection coefficient ($W/m^2 \cdot K$)	Γ	external surface area
j	current density (A/m^2)	**Subscripts**	
k	thermal conductivity (W/(m K))	*am*	ambient
n	normal vector	*b*	blood
p	pressure (N/m^2)	*ext*	external
Q	heat source (W/m^3)	*i*	subdomain
T	temperature (K)	*met*	metabolic
u	velocity (m/s)	*r*	relative
t	time	*ref*	reference
B	volume expansion coefficient (1/K)	0	free space, initial condition
μ	magnetic permeability (H/m)		

Downloaded by [Teerapot Wessapan] at 19:40 22 March 2016

Several numerical models of the eye heat transfer have been investigated to illustrate the temperature distribution in the eye in different environmental conditions. At the beginning, most studies of heat transfer analysis in human tissue, especially in the eye, used heat conduction equations [6–12]. Some studies were carried out on the natural convection in the eye based on heat conduction models [13, 14]. Ooi and Ng [14, 15] studied the effect of aqueous humor (AH) hydrodynamics on heat transfer in the eye based on a heat conduction model. Meanwhile, the bioheat equation, introduced by Pennes [16, 17], based on the heat diffusion equation for a blood perfused tissue, was used for modeling the heat transfer in the eye as well [18, 19]. Ooi and Ng also developed a 3D model of the eye [20], extending their 2D model [18]. Recently, porous media models have been utilized to investigate the transport phenomena in biological media instead of a simplified bioheat model [21–23]. Shafahi and Vafai [24] proposed porous media along with a natural convection model to analyze the eye thermal characteristics during exposure to thermal disturbances. Advanced models of the eye based on natural convection theory have been used in the various applications [25–33]. Ooi et al. and Tan et al. conducted advanced numerical modeling of the human eye based on the boundary element method [29–33]. Furthermore, Heussuer et al. [34] developed a numerical model that includes a vertical blood stream in the choroid.

Our research group has numerically investigated the temperature increase in human tissue subjected to EM fields in several problems [1–3, 35–41]. Wessapan et al. [1–3] investigated the SAR and temperature distributions in the eye during exposure to EM waves using the porous media theory. Wessapan et al. [35, 36] utilized a 2D finite element method (FEM) to obtain the specific absorption rate (SAR) and temperature increase in the human body exposed to leaked EM waves. Wessapan et al. [37, 38] developed a 3D model of the human head in order to investigate the SAR and temperature distributions in the human head during exposure to mobile phone radiation. Keangin et al. [39–41] carried out a numerical simulation of a liver cancer treatment using a complete mathematical model that considered the coupled model of EM wave propagation, heat transfer, and mechanical deformation in the biological tissue in the couple's way.

However, most studies have mainly focused on the modeling and the influence of the external conditions, but they have not considered the effects of eye geometry configuration such as body position and anterior chamber orientation in the simulations, although it directly affects heat transfer from the eye surface. In practical situations, these effects lead to enhanced convection heat transfer within the anterior chamber, which can cause changes in temperature to the eye. Therefore, in order to provide adequate information on the levels of exposure and health effects from EM fields' exposure, it is essential to consider the effect of body position in the analysis.

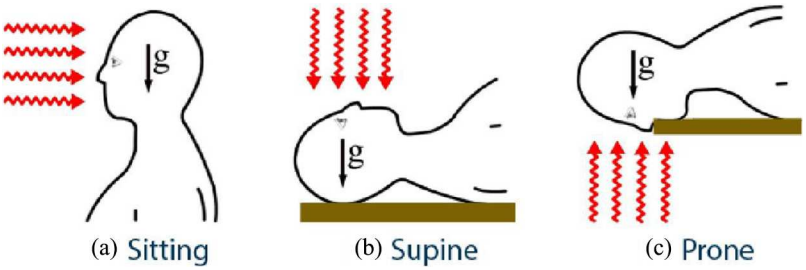

Figure 1. Human eye exposure to EM radiation in different body positions.

This study presents the simulation of the SAR, fluid flow, and temperature distributions in an anatomical human eye exposed to EM fields in different body positions. The work described in this paper is substantially extended from our previous work [1–3] by further enhancing the focus on the effect of change in body position on natural convection within the anterior chamber. A 2D heterogeneous human eye model is used to simulate the SAR, fluid flow, and temperature distributions in the eye model. The EM wave propagation in the eye is expressed mathematically by Maxwell's equations. The analysis of heat transfer is investigated using a recently developed heat transfer model based on natural convection and porous media theory [24]. In the heterogeneous eye model, the effect of three different body positions – sitting, supine, and prone – on natural convection in the anterior chamber of the eye is systematically investigated. The SAR, fluid flow, and temperature distributions in the eye during exposure to EM fields of 900 and 1,800 MHz are obtained by numerical simulation of the EM wave propagation and heat transfer equations. The eye model excluded the presence of the eyelid as well as the metabolic heat generation in order to ease the modeling procedures.

Downloaded by [Teerapot Wessapan] at 19:40 22 March 2016

2. Formulation of the problem

It is well known that the eye consists primarily of water, especially the AH in the anterior chamber. When the eye is exposed to EM fields, the temperature gradient within the anterior chamber plays an important role in AH natural convection. This study investigates the effect of body position on natural convection in the anterior chamber when subjected to EM fields. Figure 1 shows human eye exposure to EM radiation in different body positions. Owing to ethical consideration, exposing the human to EM fields for experimental purposes is limited. It is more convenient to develop a realistic human eye model through the numerical simulation. A highlight of this work is the illustration of the transport phenomena, including the heat and mass transfer in the eye during exposure to EM fields in different body positions. The analyses of the SAR, heat transfer, and fluid flow in the eye exposed to EM fields will be illustrated in Section 3. The system of governing equations as well as the initial and boundary conditions are solved numerically using the FEM.

3. Methods and model

This study focuses on the differences in heat transfer characteristics of the human eye induced by EM fields in different body positions. The first step in evaluating the effects of a certain exposure to EM fields in the eye is to determine the induced internal EM fields and its spatial distribution. Thereafter, EM energy absorption, which results in a temperature increase in the eye and other processes of transport phenomena, can be considered.

3.1. Physical model

A 2D model of the eye, which follows the physical model in the previous research [24], is developed. Figure 2 shows the 2D eye model used in this study. This model comprises seven types of tissue: the

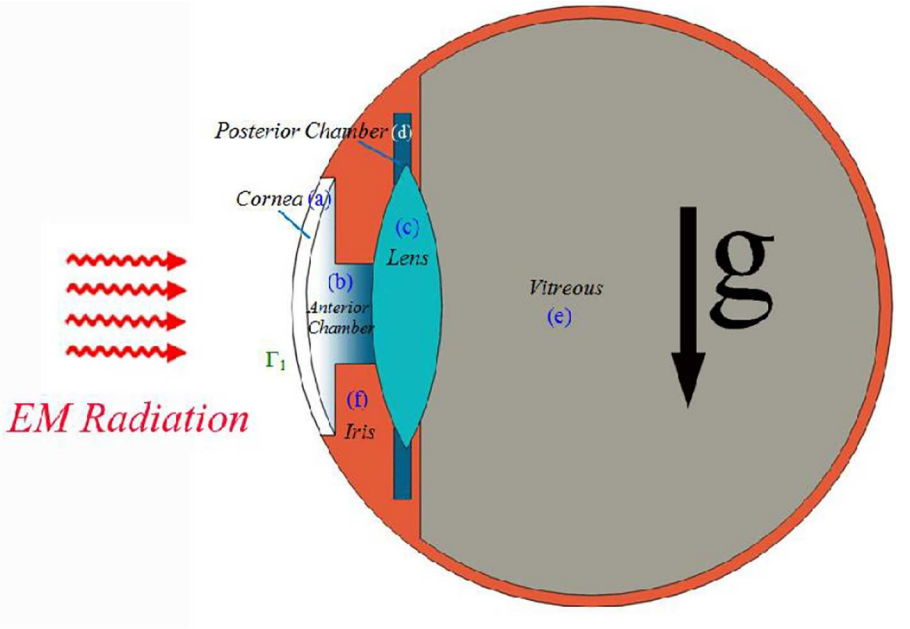

Figure 2. Human eye model vertical cross section [24].

cornea, anterior chamber, posterior chamber, iris, sclera, lens, and vitreous. These tissues have different dielectric and thermal properties. In the sclera layer, there are two more layers known as the choroid and retina, which are relatively thin compared to the sclera. To simplify the problem, these layers are assumed to be homogeneous. The iris and sclera, which have the same properties, are modeled together as one homogenous region. The dielectric and thermal properties of tissues are given in Tables 1 and 2, respectively. Each tissue is assumed to be homogeneous and electrically as well as thermally isotropic.

3.2. Equations for EM wave propagation analysis

The mathematical models are developed to predict the electric fields and the SAR with respect to the temperature gradient in the eye. To simplify the problem, the following assumptions are made:

1. The EM wave propagation is modeled in two dimensions.
2. The eye in which the EM waves interact with the eye proceeds in the open region.
3. The free space is truncated by scattering boundary condition.
4. The model assumes that dielectric properties of each tissue are constant.
5. In the eye, the EM waves are characterized by transverse magnetic fields (TM-mode).

Table 1. Dielectric properties of tissues at 900 MHz and 1,800 MHz [42, 43].

	Frequency: 900 MHz		Frequency: 1,800 MHz	
Tissue	ε_r	σ (S/m)	ε_r	σ (S/m)
Cornea (*a*)	52.0	1.85	55.0	2.32
Anterior Chamber (*b*)	73.0	1.97	75.0	2.40
Lens (*c*)	51.3	0.89	41.1	1.29
Posterior Chamber (*d*)	73.0	1.97	75.0	2.40
Vitreous (*e*)	74.3	1.97	73.7	2.33
Sclera (*f*)	52.1	1.22	52.7	1.68
Iris (*f*)	52.1	1.22	52.7	1.68

Downloaded by [Teerapot Wessapan] at 19:40 22 March 2016

Downloaded by [Teerapot Wessapan] at 19:40 22 March 2016

Table 2. Thermal properties of the eye [14].

Tissue	ρ (kg/m^3)	k (W/m°C)	C_p (J/kg°C)	μ (N s/m^2)	β (1/K)
Cornea (*a*)	1,050	0.58	4,178	–	–
Anterior Chamber (*b*)	996	0.58	3,997	0.00074	0.000337
Lens (*c*)	1,000	0.4	3,000	–	–
Posterior Chamber (*d*)	996	0.58	3,997	–	–
Vitreous (*e*)	1,100	0.603	4,178	–	–
Sclera (*f*)	1,050	1.0042	3,180	–	–
Iris (*f*)	1,050	1.0042	3,180	–	–

The EM wave propagation in the eye in Figure 2 is calculated using Maxwell's equations, which mathematically describe the interdependence of the EM waves. The general form of Maxwell's equations is simplified to demonstrate the EM fields penetrated in the eye as the following equation:

$$\nabla \times \left(\left(\varepsilon_r - \frac{j\sigma}{\omega \varepsilon_0} \right)^{-1} \nabla \times H_z \right) - \mu_r k_0^2 H_z = 0 \tag{1}$$

where H is the magnetic field (A/m), μ_r is the relative magnetic permeability, ε_r is the relative dielectric constant, $\varepsilon_0 = 8.8542 \times 10^{-12}$ F/m is the permittivity of free space, and k_0 is the free space wave number (m^{-1}).

3.2.1. Boundary condition for wave propagation analysis

EM energy is emitted by an EM radiation device and falls on the eye with a particular power density. Therefore, the boundary condition for solving EM wave propagation, as shown in Figure 3, is described as follows:

It is assumed that the uniform wave flux falls on the left side of the eye. Therefore, at the left boundary of the considered domain, an EM simulator employs TM wave propagation port with specified power density:

$$S = \int (E - E_1) \cdot E_1 / \int E_1 \cdot E_1 \, dA_1 \tag{2}$$

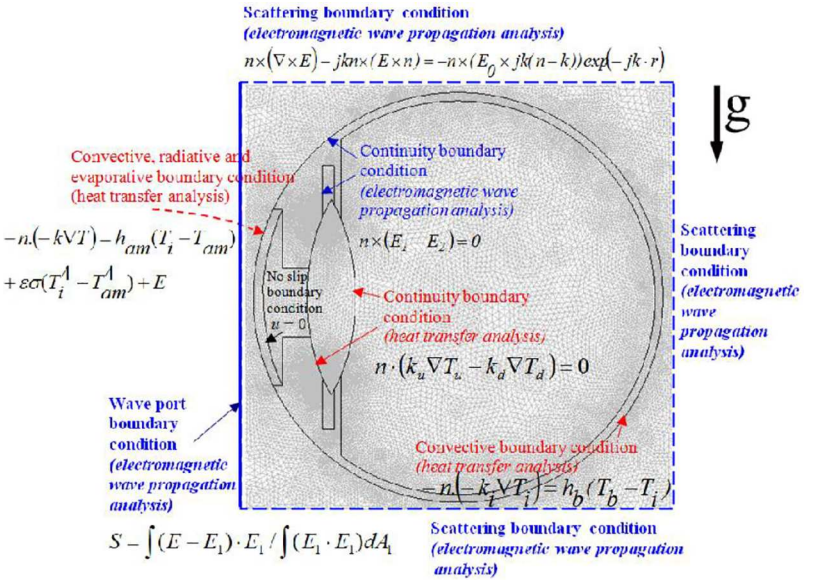

Figure 3. Boundary condition for analysis with a 2D finite element mesh of the eye model.

Boundary conditions along the interfaces between different mediums, for example, between air and tissue or tissue and tissue, are considered as continuity boundary condition

$$n \times (E_1 - E_2) = 0 \tag{3}$$

The outer sides of the calculated domain, i.e., free space, are considered as scattering boundary condition:

$$n \times (\nabla \times E_z) - jkE_z = -jk(1 - k \cdot n)E_{0z} \exp(-jk \cdot r) \tag{4}$$

where k is the wave number (m^{-1}), σ is the electrical conductivity (S/m), n is the normal vector, $j = \sqrt{-1}$, and E_0 is the incident plane wave (V/m).

3.3. Interaction of EM fields and human tissues

Interaction of EM fields with biological tissue can be defined in terms of SAR. When the EM waves propagate through the tissue, the energy of EM waves is absorbed by the tissue. The SAR is defined as the power dissipation rate normalized by material density [23]. The SAR is given by

$$SAR = \frac{\sigma}{\rho}|E|^2 \tag{5}$$

where E is the electric field intensity (V/m), σ is the electric conductivity (S/m), and ρ is the tissue density (kg/m^3).

3.4. Equations for heat transfer and flow analysis

To solve the thermal problem, a coupled effect of the EM wave propagation and the unsteady bioheat transfer are investigated. The temperature distribution corresponds to the SAR. This is because the SAR in the eye distributes owing to energy absorption. Thereafter, the absorbed energy is converted to thermal energy, which increases the tissue temperature.

Heat transfer analysis of the eye is modeled in two dimensions. To simplify the problem, the following assumptions are made:

1. The human tissue is a biomaterial with constant thermal properties.
2. There is no phase change of substance in the tissue.
3. There is a local thermal equilibrium between the blood and the tissue.
4. There is no chemical reaction in the tissue.

This study utilized the pertinent thermal model based on the porous media theory [24] to investigate the heat transfer behavior of the eye when exposed to the EM fields.

In this study, the motion of fluid is considered only inside the anterior chamber (subdomain b in Figure 2) [14]. There is a blood flow in the iris/sclera part, which plays a role to adjust the eye temperature with the rest of the body. For the rest of the parts, the metabolic heat generation is neglected based on the fact that these comprise mainly water. The equations governing the flow of heat in cornea, posterior chamber, lens, and vitreous resemble the classical heat conduction equation given in Eq. (6):

$$\rho_i C_i \frac{\partial T_i}{\partial t} = \nabla \cdot (k_i \nabla T_i) + Q_{ext}; i = a, c, d, e \tag{6}$$

This model accounts for the existence of AH in the anterior chamber. The heat transfer process consists of both conduction and natural convection, which can be written as follows:

Continuity equation:

$$\nabla \cdot u_i = 0; i = b \tag{7}$$

Downloaded by [Teerapot Wessapan] at 19:40 22 March 2016

Momentum equation:

$$\rho_i \frac{\partial u_i}{\partial t} + \rho_i u_i \nabla \cdot u_i = -\nabla p_i + \nabla \cdot [\mu(\nabla u_i + \nabla u_i^T)] + \rho_i g \beta_i (T_i - T_{ref}); i = b \tag{8}$$

where i denotes each subdomain in the eye model as shown in Figure 2, ρ is the tissue density (kg/m^3), β is the volume expansion coefficient (1/K), u is the velocity (m/s), p is the pressure (N/m^2), μ is the dynamic viscosity of AH (N$\cdot$s/m^2), t is the time, T is the tissue temperature (K), and T_{ref} is the reference temperature considered here, which is 37°C. The effects of buoyancy due to the temperature gradient are modeled using the Boussinesq approximation, which states that the density of a given fluid changes slightly with temperature but negligibly with pressure.

Energy equation:

$$\rho_i C_i \frac{\partial T_i}{\partial t} - \nabla \cdot (k_i \nabla T_i) = -\rho C_i u_i \cdot \nabla T_i + Q_{ext}; i = b \tag{9}$$

The sclera/iris is modeled as a porous medium with blood perfusion, which assumes that local thermal equilibrium exists between the blood and the tissue. The blood perfusion rate used is 0.004 1/s. A modified Pennes' bioheat equation [24] is used to calculate the temperature distribution in the sclera/iris.

$$(1-\varepsilon)\rho_i C_i \frac{\partial T_i}{\partial t} = \nabla \cdot ((1-\varepsilon) k_i \nabla T_i) + \rho_b C_b \omega_b (T_b - T_i) + Q_{ext}; i = f \tag{10}$$

where C is the heat capacity of tissue (J/kg K), k is the thermal conductivity of tissue (W/m K), T_b is the temperature of blood (K), ρ_b is the density of blood (kg/m^3), C_b is the specific heat capacity of blood (J/kg K), ω_b is the blood perfusion rate (1/s), and Q_{ext} is the external heat source term (EM heat-source density) (W/m^3).

In this analysis, the porosity (ε) used is assumed to be 0.6. The heat conduction between the tissue and the blood flow is approximated by the blood perfusion term $\rho_b C_b \omega_b (T_b - T)$.

The external heat source term is equal to the resistive heat generated by the EM fields (EM power absorbed), which is defined as

$$Q_{ext} = \frac{1}{2}\sigma_{tissue}|\overline{E}|^2 = \frac{\rho}{2} \cdot SAR \tag{11}$$

where σ_{tissue} is the electric conductivity of the tissue (S/m).

3.4.1. Boundary condition for heat transfer analysis

The heat transfer analysis excluding the surrounding space is considered only in the eye. The corneal surface, shown in Figure 3, is considered under the convective, radiative, and evaporative boundary conditions.

$$-n \cdot (-k \nabla T) = h_{am}(T_i - T_{am}) + \varepsilon\sigma(T_i^4 - T_{am}^4) + e \text{ on } \Gamma_1 \; i = a \tag{12}$$

where Γ_i is the external surface area corresponding to section i, e is the tear evaporation heat loss (W/m^2), T_{am} is the ambient temperature (K), and h_{am} is the convection coefficient (W/m$^2\cdot$K).

The temperature of blood is generally assumed to be the same as the body core temperature, which causes heat to be transferred into the eye [14]. The surface of the sclera is assumed to be under the convective boundary condition

$$-n \cdot (-k_i \nabla T_i) = h_b(T_b - T_i) \text{ on } \Gamma_2 i = f \tag{13}$$

where h_b is the convection coefficient of blood (65 W/m$^2\cdot$K). Γ_1 and Γ_2 are the corneal surface and scleral surface of the eye, respectively.

Downloaded by [Teerapot Wessapan] at 19:40 22 March 2016

3.5. Calculation procedure

In this study, FEM is used to analyze the transient problems. The computational scheme is to assemble finite element model and compute a local heat generation term by performing an EM calculation using tissue properties. In order to obtain a good approximation, a fine mesh is specified in the sensitive areas. This study provides a variable mesh method for solving the problem as shown in Figure 3. The system of governing equations and both the initial and boundary conditions are then solved. All computational processes are implemented using COMSOL™ Multiphysics, to demonstrate the phenomenon that occurs in the eye exposed to the EM fields.

The 2D model is discretized using triangular elements and the Lagrange quadratic is then used to approximate the temperature and SAR variations across each element. A convergence test is carried out to identify the suitable number of elements required. This convergence test leads to a grid with approximately 10,000 elements. It is reasonable to assume that, at this element number, the accuracy of the simulation results is independent of the number of elements.

4. Results and discussion

When the eye is exposed to EM fields, the gravity effect on the AH flow and heat transfer will have a different effect depending on the eye orientation, which is relative to the body position. In this study, the AH is considered to be incompressible, steady-state, Newtonian, and the Boussinesq approximation is applied for natural convection with constant physical properties. The AH natural convection of the human eye at different body positions induced by EM fields is systematically investigated. This work focuses on the effect of three different body positions: sitting, supine, and prone on natural convection in the anterior chamber of the eye. The EM frequencies of 900 and 1,800 MHz are chosen for the investigations since they are used in most parts of the world. The coupled model of the EM propagation and thermal as well as fluid fields is solved numerically. For the simulation, the dielectric and thermal properties are directly taken from Tables 1 and 2, respectively.

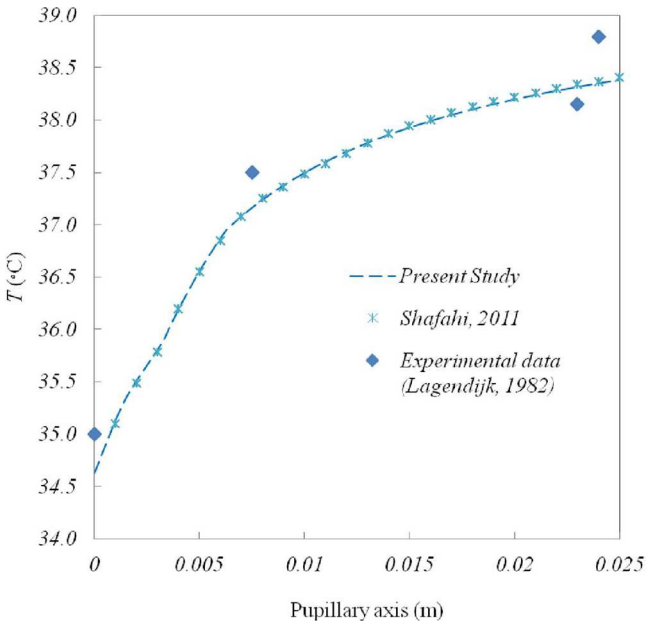

Figure 4. Comparison of the calculated temperature distribution to the temperature distribution obtained by Shafahi and Vafai [24], and Lagendijk's experimental data [8]; $h_{am} = 20\,W/m^2 \cdot K$ and $T_{am} = 25°C$.

Downloaded by [Teerapot Wessapan] at 19:40 22 March 2016

Downloaded by [Teerapot Wessapan] at 19:40 22 March 2016

4.1. Verification of the model

To perform verification of the models presented here, the case without EM fields of the simulated results from this study are validated against the numerical results obtained with the same geometric model by Shafahi and Vafai [24]. Moreover, the comparison between experimental results for a rabbit obtained by Lagendijk [6] and the present numerical results has been performed. The validation case assumes that the rabbit body temperature is 38.8°C, the tear evaporation heat loss is 40 W/m^2, the ambient temperature is 25°C, and the convection coefficient of ambient air is 20 $W/m^2 \cdot K$. The results of the selected test case are depicted in Figure 4 for temperature distribution in the eye. The figure clearly shows a good agreement between experimental and numerical temperature distribution in the eye. This favorable comparison ensures that the numerical model can accurately represent the transport phenomena in the eye.

4.2. SAR Distribution

Figures 5*a* and 6*a* show the SAR distribution evaluated on the vertical cross section of the eye in different body positions during exposure to the EM frequencies of 900 and 1,800 MHz, respectively. The

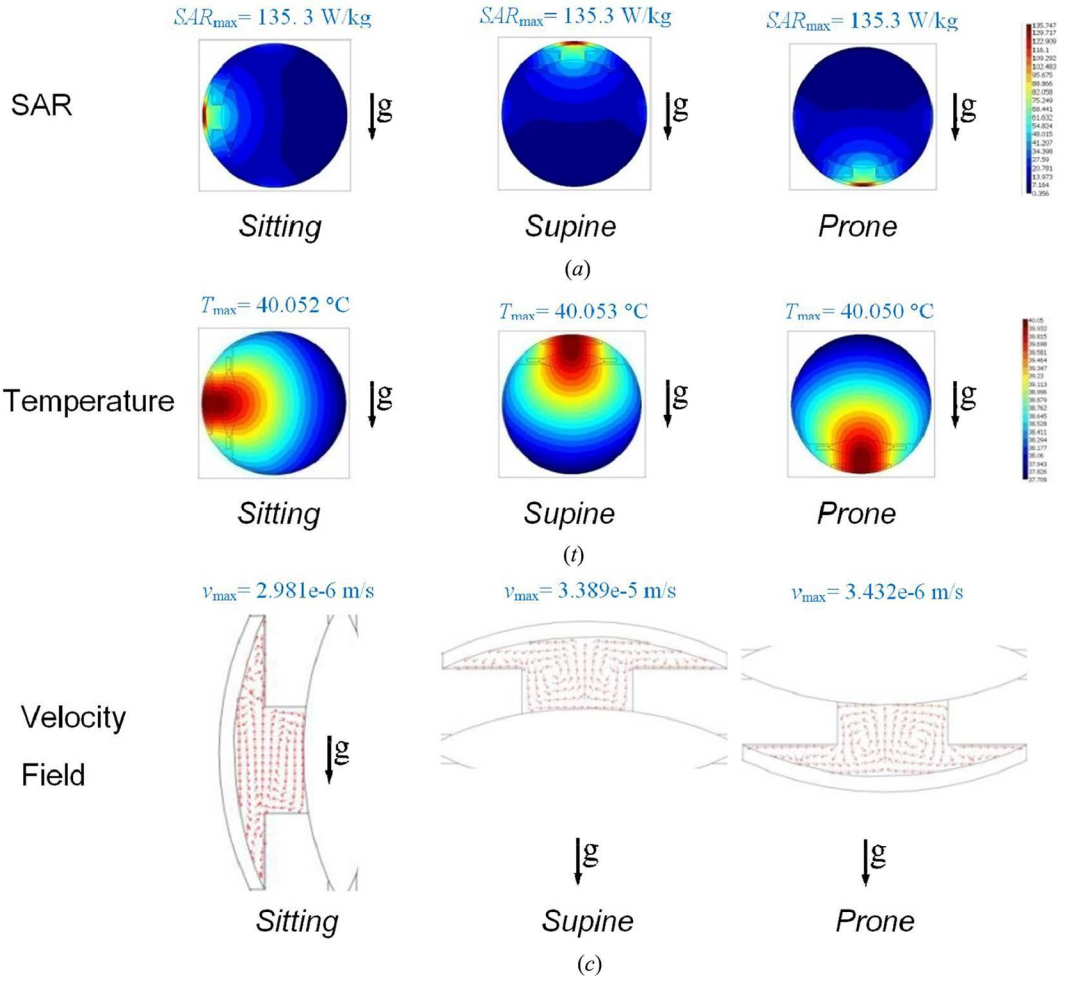

Figure 5. The SAR, temperature distribution, and velocity field in the eye at various body positions exposed to the EM power density of 100 mW/cm^2 at the frequency of 900 MHz.

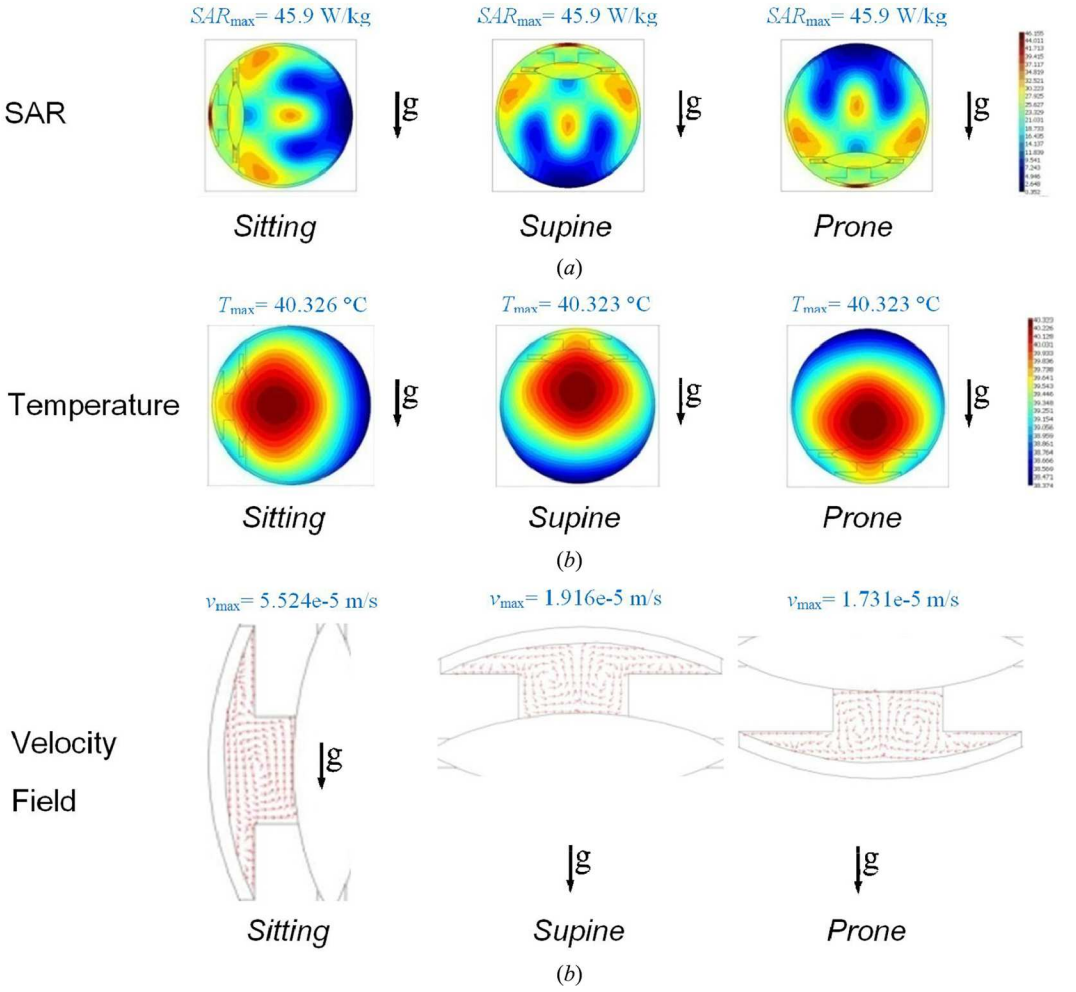

Figure 6. The SAR, temperature distribution, and velocity field in the eye in different body positions exposed to the EM power density of 100 mW/cm^2 at the frequency of 1,800 MHz.

SAR values in the eye are increased corresponding to the electric field intensities. From the previous work [2] at the power density of 100 mW/cm^2, the maximum electric field intensities of the frequencies of 900 and 1,800 MHz are 391.8 and 231.2 V/m, respectively. Besides the electric field intensity, the magnitude of the dielectric and thermal properties (Tables 1 and 2) in each tissue will directly affect SAR distributions in the eye. For all cases, the highest SAR values are obtained in the region of the corneal surface. For all body positions, the frequencies of 900 and 1,800 MHz display maximum SAR values of 135.2 and 45.9 W/kg, respectively. It is found that the body position has no influence on the SAR values in the eye. This is because gravity has a negligible influence on the EM energy absorption behavior of the eye tissue.

4.3. Temperature distributions and velocity fields

Normally natural convection is highly dependent on the geometry of the container surface. Therefore, the changes in body position that change the anterior chamber orientation could have a significant effect on the convective flow of the AH. Moreover, the body position also affects natural convection in the eye, especially when subjected to EM fields. A numerical simulation was carried out to

Downloaded by [Teerapot Wessapan] at 19:40 22 March 2016

investigate the temperature distributions and velocity fields in the human eye exposed to EM fields in different body positions. In order to gain insight into the effects of body position on natural convection within the anterior chamber during exposure to EM fields, effects of an ambient temperature variation and thermoregulation were neglected. The ambient temperature was set to the human body temperature of 37°C. The convective coefficient due to the blood flow inside the sclera was set to $65\,W/m^2 \cdot K$ [14].

Form the simulation of the 900 MHz frequency, the EM energy absorbed (SAR) is the highest over the front part of the eye (Figure 5*a*), corresponding to its large temperature gradient (Figure 5*b*). However, for the 1,800 MHz frequency, it is observed that a large temperature gradient is significantly produced by the EM energy absorbed (Figure 6*a*) at the middle part of the eyeball (Figure 6*b*). For the middle part of the eye, the temperature profile for each body position is almost the same. The temperature profiles especially within the vitreous for three different body positions are closer to each other for both 900 and 1,800 MHz frequencies. It means that body position has little effect on heat transfer in the middle part of the eye when exposed to EM fields. However, the body position still plays an important role on AH natural convection and the heat transfer process within the anterior chamber and its periphery in the front part of the eye.

The effect of body position on velocity field in the eye during exposure to EM fields in different body positions is shown in Figures 5*c* and 6*c*. When the human eye subjected to EM fields, the AH motion in the anterior chamber occurs mainly by natural means such as buoyancy. Since the AH velocity associated with natural convection is relatively low, the heat transfer coefficient encountered in natural convection is also low. This is because the velocity fields vary corresponding to the temperature gradient in the eye. At the peripheral region of the anterior chamber where the convection flow is small, temperature distributions are primarily governed by the conduction mode. Within the anterior chamber, in the case of a lower temperature gradient, the circulatory patterns have a lower speed, where a circulatory pattern with a higher temperature gradient flows faster. Besides the temperature gradient, the changes in body position that change the anterior chamber orientation have a significant effect on the AH natural convection. Figures 5*c* and 6*c* show the circulatory patterns in the anterior chamber in the eye in different body positions during exposure to the EM frequencies of 900 and 1,800 MHz, respectively.

In sitting position velocity field of the 900 MHz (Figure 5*c*) flow is slower than that of 1,800 MHz (Figure 6*c*), but the 900 MHz case has a more complex motion. The natural convection of the 900 MHz forms the two circulatory patterns with opposite direction in the anterior chamber (Figure 5*c*). These patterns imply that the generated heat is transferred in two directions: one is to the corneal surface and the other is to the lens surface. While in the 1,800 MHz, the velocity field becomes faster and the flow circulates in the counterclockwise direction (Figure 6*c*). It is implied that the heat transfer travels outward from the lens surface to the corneal surface. *In the supine position*, double circulation cells are formed. The flow patterns are symmetrical between the left and right sides for both 900 and 1,800 MHz frequencies, but in case of 900 MHz the flow is faster. The primary circulation flows in a counterclockwise direction, whereas the secondary circulation flows in a clockwise direction. This seems to imply that the heat transfers are both traveling outward rising from the lens surface. *In the prone position*, again the two circulatory cells are formed with the opposite direction in the anterior chamber, but in a counter-current direction to the flow of the supine position. Heat flow direction in the anterior chamber changes from outward convection to inward convection with repositioning of the body position from supine to prone.

Figures 7 and 8 illustrate the temperature profile in the front part of the eye during exposure to EM frequencies of 900 and 1,800 MHz, respectively, in different body positions. With the domination of the AH natural convection, the heat transfer rate increases corresponding to the temperature gradient induced by EM fields. In both 900 and 1,800 MHz, the maximum temperatures in the anterior chamber are presented in the supine position. This is due to the fact that the localized heating of the AH near the corneal surface on the top position of the anterior chamber cannot easily be released by the physical mechanism of natural convection. Moreover, there are small differences in the temperature

Downloaded by [Teerapot Wessapan] at 19:40 22 March 2016

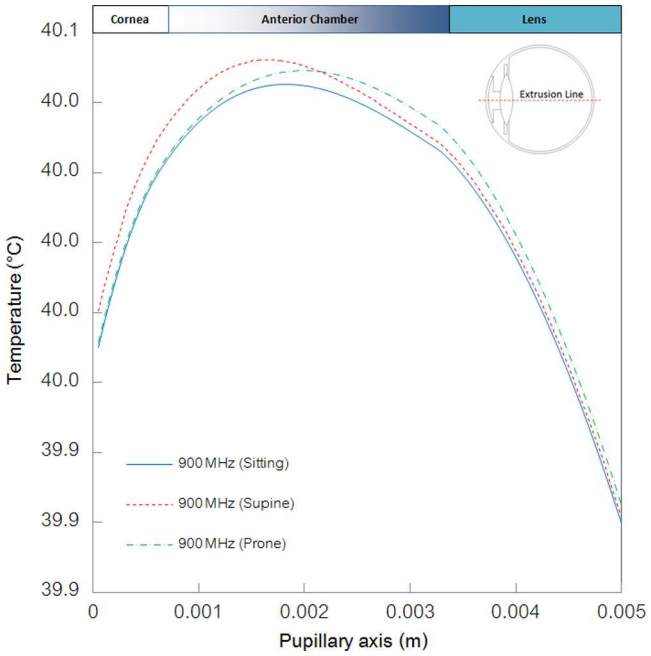

Figure 7. Temperature profile versus papillary axis of the eye exposed to the EM frequency of 900 MHz at 60 minutes.

profiles of sitting, supine, and prone in the lens region due to the domination of conduction heat transfer. However, there are is a huge difference between each body position on the temperature profile in the anterior chamber region, especially at 900 MHz (Figure 7) due to the domination of the difference in the AH natural convection behavior.

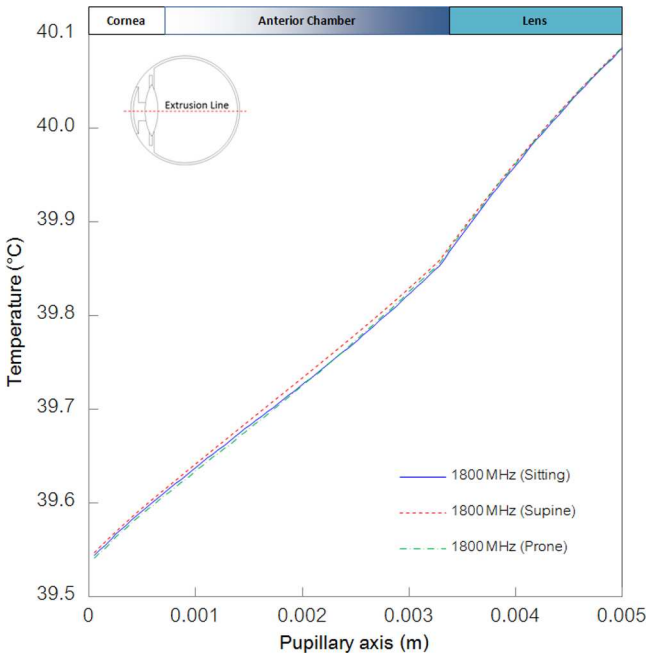

Figure 8. Temperature profile versus papillary axis of the eye exposed to the EM frequency of 1,800 MHz at 60 minutes.

Downloaded by [Teerapot Wessapan] at 19:40 22 March 2016

As a result, it can be concluded that the gravity effects on the AH flow and heat transfer have a different effect depending on the eye orientation, which is relative to the body position. The effect of body position becomes more significant on heat transfer in the front part of the eye where the AH flow exists. This behavior is due to the fact that in the different body positions at the same EM exposure condition, the frontal eye temperature profile is not the same. This indicates that the AH natural convection behavior is different at different body positions for the same EM exposure condition.

5. Conclusions

A numerical analysis of the SAR, AH natural convection, and heat transfer in the eye during exposure to EM fields in different body positions has been performed. The results of the SAR values are increased corresponding to the electric field intensities. Besides the electric field intensity, the magnitude of the dielectric and thermal properties in each tissue will directly affect the SAR values in the eye. In this study, the AH natural convection of the human eye in different body positions induced by EM fields is systematically investigated. It is found that the AH natural convection increases on increasing the anterior chamber temperature gradient. The influence of AH natural convection is particularly strong in the front part of the eye. Body positions affect both AH velocity field and temperature distribution in the anterior chamber and the surrounding area. This is because the gravity effect on the AH flow and heat transfer has a different effect depending on the eye orientation, which is relative to the body position and the AH natural convection in the anterior chamber plays a significant role in transferring heat.

No remarkable change in the temperature increases in the middle part of the eye especially in the vitreous is observed with body repositioning. In this study, the difference in frontal eye temperature profile is caused by the heating pattern (EM frequency) and anterior chamber configuration (body position), which become the dominant mechanisms for the AH natural convection. The obtained results contribute to the understanding of the realistic situation and prediction of the temperature distribution within the eye during exposure to EM fields.

Downloaded by [Teerapot Wessapan] at 19:40 22 March 2016

Funding

The authors gratefully acknowledge the Thailand Research Fund (under TRF contract No. RTA5680007) and the Nation Research University Project of Thailand Office of Higher Education Commission.

References

[1] T. Wessapan and P. Rattanadecho, Specific Absorption Rate and Temperature Increase in Human Eye Subjected to Electromagnetic Fields at 900 MHz, *ASME J. Heat Transfer*, vol. 134, p. 091101, 2012.
[2] T. Wessapan and P. Rattanadecho, Specific Absorption Rate and Temperature Increase in the Human Eye due to Electromagnetic Fields Exposure at Different Frequencies, *Int. J. Heat Mass Transfer*, vol. 64, pp. 426–435, 2013.
[3] T. Wessapan and P. Rattanadecho, Influence of Ambient Temperature on Heat Transfer in the Human Eye during Exposure to Electromagnetic Fields at 900 MHz, *Int. J. Heat Mass Transfer*, vol. 70, pp. 378–388, 2014.
[4] International Commission on Non-Ionizing Radiation Protection (ICNIRP), Guidelines for Limiting Exposure to Time-Varying Electric, Magnetic and Electromagnetic Fields (up to 300 GHz), *Health Phys.*, vol. 74, pp. 494–522, 1998.
[5] IEEE, IEEE Standard for Safety Levels with Respect to Human Exposure to Radio Frequency Electromagnetic Fields, 3 kHz to 300 GHz (1999), IEEE Standard C95 1–1999.
[6] J. J. W. Lagendijk, A Mathematical Model to Calculate Temperature Distribution in Human and Rabbit Eye During Hyperthermic Treatment, *Phys. Med. Biol.*, vol. 27, pp. 1301–1311, 1982.
[7] J. Scott, A Finite Element Model of Heat Transport in the Human Eye, *Phys. Med. Biol.*, vol. 33, pp. 227–241, 1988.
[8] T. Wu, P. Li, Q. Shao, J. Hong, L. Yang, and S. Wu, A Simulation-Experiment Method to Characterize the Heat Transfer in Ex-Vivo Porcine Hepatic Tissue with a Realistic Microwave Ablation System, *Numer. Heat Transfer, Part A*, vol. 64, pp. 729–743, 2013.
[9] E. H. Amara, Numerical Investigations on Thermal Effects of Laser–Ocular Media Interaction, *Int. J. Heat Mass Transfer*, vol. 38, pp. 2479–2488, 1995.

[10] A. Hirata, S. Matsuyama, and T. Shiozawa, Temperature Rises in the Human Eye Exposed to EM Waves in the Frequency Range 0.6–6 GHz, *IEEE Trans. Electromagn. Compat.*, vol. 42, no. 4, pp. 386–393, 2000.
[11] K. J. Chua, J. C. Ho, S. K. Chou, and M. R. Islam, On the Study of the Temperature Distribution within a Human Eye Subjected to a Laser Source, *Int. Commun. Heat Mass Transfer*, vol. 32, pp. 1057–1065, 2005.
[12] W. Limtrakarn, S. Reepolmaha, and P. Dechaumphai, Transient Temperature Distribution on the Corneal Endothelium during Ophthalmic Phacoemulsification: A Numerical Simulation Using the Nodeless Variable Element, *Asian Biomed.*, vol. 4, no. 6, pp. 885–892, 2010.
[13] S. Kumar, S. Acharya, R. Beuerman, and A. Palkama, Numerical Solution of Ocular Fluid Dynamics in a Rabbit Eye: Parametric Effects, *Ann. Biomed. Eng.*, vol. 34, pp. 530–544, 2006.
[14] E. Ooi and E. Y. K. Ng, Simulation of Aqueous Humor Hydrodynamics in Human Eye Heat Transfer, *Comput. Biol. Med.*, vol. 38, pp. 252–262, 2008.
[15] E. H. Ooi and E. Y. K. Ng, Effects of Natural Convection Inside the Anterior Chamber, *Int. J. Numer. Methods Biomed. Eng.*, vol. 27, pp. 408–423, 2011.
[16] H. H. Pennes, Analysis of Tissue and Arterial Blood Temperatures in the Resting Human Forearm, *J. Appl. Physiol.*, vol. 1, pp. 93–122, 1948.
[17] H. H. Pennes, Analysis of Tissue and Arterial Blood Temperatures in the Resting Human Forearm, *J. Appl. Physiol.*, vol. 85, no. 1, pp. 5–34, 1998.
[18] V. M. M. Flyckt, B. W. Raaymakers, and J. J. W. Lagendijk, Modeling the Impact of Blood Flow on the Temperature Distribution in the Human Eye and the Orbit: Fixed Heat Transfer Coefficients Versus the Pennes Bioheat Model Versus Discrete Blood Vessels, *Phys. Med. Biol.*, vol. 51, pp. 5007–5021, 2006.
[19] E. Y. K. Ng and E. H. Ooi, FEM Simulation of the Eye Structure with Bioheat Analysis, *Comput. Methods Programs Biomed.*, vol. 82, pp. 268–276, 2006.
[20] E. H. Ooi and E. Y. K. Ng, Ocular Temperature Distribution: A Mathematical Perspective, *J. Mech. Med. Biol.*, vol. 9, pp. 199–227, 2009.
[21] A. Nakayama and F. Kuwahara, A General Bioheat Transfer Model Based on the Theory of Porous Media, *Int. J. Heat Mass Transfer*, vol. 51, pp. 3190–3199, 2008.
[22] P. Keangin, K. Vafai, and P. Rattanadecho, Electromagnetic Field Effects on Biological Materials, *Int. J. Heat Mass Transfer*, vol. 65, pp. 389–399, 2013.
[23] K. Khanafer and K. Vafai, Synthesis of Mathematical Models Representing Bioheat Transport, *Adv. Numer. Heat Transfer*, vol. 3, pp. 1–28, 2009.
[24] M. Shafahi and K. Vafai, Human Eye Response to Thermal Disturbances, *ASME J. Heat Transfer*, vol. 133, p. 011009, 2011.
[25] E. Y. K. Ng, J. H. Tan, U. R. Acharya, and J. S. Suri, *Human Eye Imaging and Modeling*, CRC Press, Florida, 2012. ISBN: 978-1-4398-6993-2.
[26] D. Sumeet, U. R. Acharya, and E. Y. K. Ng, *Computational Analysis of Human Eye with Application*, WSPC Press, Singapore, 2011. ISBN: 978-981-4340-29-8.
[27] E. Y. K. Ng, U. R. Acharya, J S. Suri, and A. Campilho, *Image Analysis and Modeling in Ophthalmology*, CRC Press, Florida, 2014. ISBN: 978-1-4665–5930-1.
[28] E. Y. K. Ng, U. R. Acharya, R. M. Rangayyan, and J. S. Suri, *Ophthalmology Imaging and Applications*, CRC Press, Florida, 2014. ISBN: 978-1-4665-5913-4.
[29] E. H. Ooi, W. T. Ang, and E. Y. K. Ng, A Boundary Element Model of the Human Eye Undergoing Laser Thermokeratoplasty, *Comput. Biol. Med.*, vol. 28, pp. 727–738, 2008.
[30] E. H. Ooi, W. T. Ang, and E. Y. K. Ng, A Boundary Element Model for Investigating the Effects of Eye Tumor on the Temperature Distribution inside the Human Eye, *Comput. Biol. Med.*, vol. 28, pp. 727–738, 2009.
[31] J. H. Tan, E. Y. K. Ng, U. R. Acharya, and C. Chee, Study of Normal Ocular Thermogram Using Textural Parameters, *Infrared Phys. Technol.*, vol. 53, pp. 120–126, 2010.
[32] J. H. Tan, E. Y. K. Ng, and U. R. Acharya, Evaluation of Tear Evaporation from Ocular Surface by Functional Infrared Thermography, *Med. Phys.*, vol. 37, pp. 6022–6034, 2010.
[33] J. H. Tan, E. Y. K. Ng, and U. R. Acharya, Evaluation of Topographical Variation in Ocular Surface Temperature by Functional Infrared Thermography, *Infrared Phys. Technol.*, vol. 54, pp. 469–477, 2011.
[34] N. Heussner, L. Holl, T. Nowak, T. Beuth, M. S. Spitzer, and W. Stork, Prediction of Temperature and Damage in an Irradiated Human Eye—Utilization of a Detailed Computer Model Which Includes a Vectorial Blood Stream in the Choroid, *Comput. Biol. Med.*, vol. 51, pp. 35–43, 2014.
[35] T. Wessapan, S. Srisawatdhisukul, and P. Rattanadecho, Numerical Analysis of Specific Absorption Rate and Heat Transfer in the Human Body Exposed to Leakage Electromagnetic Field at 915 MHz and 2450 MHz, *ASME J. Heat Transfer*, vol. 133, p. 051101, 2011.
[36] T. Wessapan, S. Srisawatdhisukul, and P. Rattanadecho, The Effects of Dielectric Shield on Specific Absorption Rate and Heat Transfer in the Human Body Exposed to Leakage Microwave Energy, *Int. Commun. Heat Mass Transfer*, vol. 38, pp. 255–262, 2011.
[37] T. Wessapan and P. Rattanadecho, Numerical Analysis of Specific Absorption Rate and Heat Transfer in Human Head Subjected to Mobile Phone Radiation, *ASME J. Heat Transfer*, vol. 134, p. 121101, 2012.

Downloaded by [Teerapot Wessapan] at 19:40 22 March 2016

[38] T. Wessapan, S. Srisawatdhisukul, and P. Rattanadecho, Specific Absorption Rate and Temperature Distributions in Human Head Subjected to Mobile Phone Radiation at Different Frequencies, *Int. J. Heat Mass Transfer*, vol. 55, pp. 347–359, 2012.
[39] P. Keangin, T. Wessapan, and P. Rattanadecho, Analysis of Heat Transfer in Deformed Liver Cancer Modeling Treated Using a Microwave Coaxial Antenna, *Appl. Therm. Eng.*, vol. 31, no. 16, pp. 3243–3254, 2011.
[40] P. Keangin, T. Wessapan, and P. Rattanadecho, An Analysis of Heat Transfer in Liver Tissue during Microwave Ablation Using Single and Double Slot Antenna, *Int. Commun. Heat Mass Transfer*, vol. 38, pp. 757–766, 2011.
[41] P. Rattanadecho and P. Keangin, Numerical Study of Heat Transfer and Blood Flow in Two-Layered Porous Liver Tissue During Microwave Ablation Process Using Single and Double Slot Antenna, *Int. J. Heat Mass Transfer*, vol. 58, pp. 457–470, 2013.
[42] P. Bernardi, M. Cavagnaro, S. Pisa, and E. Piuzzi, Specific Absorption Rate and Temperature Increases in the Head of a Cellular-Phone User, *IEEE Trans. Microw. Theor. Tech.*, vol. 48, no. 7, pp. 1118–1126, 2000.
[43] S. Park, J. Jeong, and Y. Lim, Temperature Rise in the Human Head and Brain for Portable Handsets at 900 and 1800 MHz, *Proceedings of the Fourth International Conference on Microwave and Millimeter Wave Technology*, vol. 1, pp. 966–969, 2004.

Downloaded by [Teerapot Wessapan] at 19:40 22 March 2016

Journal of Electrostatics 77 (2015) 1–7

Contents lists available at ScienceDirect

Journal of Electrostatics

journal homepage: www.elsevier.com/locate/elstat

An experimental study of relative humidity and air flow effects on positive and negative corona discharges in a corona-needle charger

Artit Yawootti [a], Panich Intra [b, *], Nakorn Tippayawong [a], Phadungsak Rattanadecho [c]

[a] Department of Mechanical Engineering, Faculty of Engineering, Chiang Mai University, Chiang Mai 50200, Thailand
[b] Research Unit of Electrostatic Applications in Energy and Environment (RUEE), College of Integrated Science and Technology, Rajamangala University of Technology Lanna, Chiang Mai 50220, Thailand
[c] Center of Excellence in Electromagnetic Energy Utilization in Engineering (CEEE), Department of Mechanical Engineering, Faculty of Engineering, Thammasat University, Pathum Thani 12121, Thailand

ARTICLE INFO

Article history:
Received 26 April 2015
Received in revised form
28 July 2015
Accepted 30 July 2015
Available online xxx

Keywords:
Relative humidity
Corona discharge
Particle charging
Aerosol charger

ABSTRACT

In this paper, the effects of inlet air RH and air flow rate on positive and negative corona discharges in a corona-needle charger have been experimentally studied and discussed. Its corona discharge characterizations in terms of current-to-voltage relationships of the corona-needle charger on the effects of inlet air RH and air flow rate were evaluated at applied corona voltages between 0 and 3.1 kV, an air flow rates between 5 and 15 L/min, a relative humidity between 20 and 90%, and an operating pressure of about 101.3 kPa. Experimental results were shown that discharge current is strongly affected by the RH level of the inlet air. The positive discharge current was found to be decreased with increasing RH value at RH values below 60% and increased with increasing RH value at RH value above 60% in the same corona voltage. The negative discharge current was found to be stable with increasing RH value at RH values below 40% and increased with increasing RH value at RH value above 40% in the same corona voltage. For the air flow rate effects, the positive discharge current was found to slightly decrease when the air flow rate increased at RH value below 90% and to increase with the air flow rate at RH value of 90%. For the negative corona, the discharge current was also found to monotonically decrease when the air flow rate increased.

© 2015 Elsevier B.V. All rights reserved.

1. Introduction

Producing unipolar ions by corona discharging has been applied successfully in unipolar aerosol charging and several designs of aerosol corona charger have been employed and described in the published literature [1]. Unipolar aerosol corona chargers have been widely used in the measurement of aerosol particle charge based on unipolar corona charging and electrostatic detection of charged aerosol particles such as the electrical aerosol detector. This is because of its simplicity and capacity to provide high concentration of ions [2]. A typical electrical aerosol detector consists of two key components, one for unipolar aerosol charging and the other for measuring the electric current on charged aerosol with an electrometer. The output signal of an electrometer depends strongly on the particle charging technique used [3]. However, the detector was very stable at relative humidity (RH) values below 60% but the detector zero reading starts to drift away from the manufacturers expected stable value at RH higher than 60%. This makes the detector unstable, its output unreliable and a strong indication that the detector is not suitable for use under inlet air RH of above 60% such as ambient atmospheric conditions, water content of ambient aerosol particles is usually to be below and above 60% [4]. Placing some silica gel dryer or dehumidifier before enter the detector however reduced the drift, allowing its use under conditions of over 60% RH.

In the aerosol particle charging by corona discharge, the air RH had significant effects on both positive and negative corona discharges and electrostatic characteristics of the charger. Corona discharge is a gas discharge phenomenon and it is influenced by many factors, including air humidity and temperature. At higher RH, the adsorption of water on the surface of a particle will have a significant impact on the corona onset electric field, the electric conductivity enhancement and electrical mobility of ions. The corona onset electric field decreased with the increase of air RH [5–8]. Back in 1920, Peek proposed his well-known empirical

* Corresponding author.
E-mail address: panich_intra@yahoo.com (P. Intra).

http://dx.doi.org/10.1016/j.elstat.2015.07.011
0304-3886/© 2015 Elsevier B.V. All rights reserved.

equation for evaluating the corona onset electric field on conductors [9,10]. This equation included the influence of temperature and pressure, but the effect of air humidity was ignored. Many researchers numerically studied the distribution of electric filed and charge density in electrostatic precipitators (ESPs) [11,12]. Peek equation was used in these studies, which considered the effects of temperature and pressure. But the effect of air RH was not included in these studies. A few modified Peek formulas were suggested to account for the effect of air RH [12,13]. Previous theoretically and experimentally studies, investigating the effect of RH on the electrostatic aerosol charge and on current-to-voltage characteristics have been numerous studied in the past several decades [5–18]. For instance, Young et al. [14] was studied the influence of RH on the electrostatic charge and aerosol performance of dry powder inhaler carrier based systems. The authors reported in this paper that increased storage RH resulted in a reduction in net charge to mass ratio with the greatest reduction at RH >60%. Higher RH would allow a greater degree of electron mobility and thus reduce the charging mechanism. Fouad and Elhazek [7] was studied the effect of humidity on positive corona discharge in a three electrode system. The authors reported in this paper that the corona inception voltage increases as the air relative humidity increases up to a certain limit after which the corona inception voltage begins to decrease with increasing air relative humidity. It is also found that the increase of air relative humidity favors the positive glow formation and affects its stability. Nouria et al. [11] was characterized the behavior of DC corona discharge in wire-to-plane ESPs as influenced by the RH of the inlet air. The authors reported in this paper that discharge current is strongly affected by the RH level of the inlet air. The time-averaged current is lower at higher RH for a given voltage, except when RH of 99%. Time evolution of the discharge current is affected by the RH especially in the case of negative corona. Above various works have been experimentally and theoretically presented the effect of air RH on both positive and negative corona discharges for larger voltage range in various electrode geometries such as the wire-to-cylinder, the wire-to-plane, needle-to-plane and the point-to-plane, but was not have taken in the needle-to-nozzle electrode geometry and was also not introduced explicitly the dependence of the air flow rate in these studies. Since the geometrical configuration of electrodes of the corona-needle charger is similar to the needle-to-nozzle electrode geometry, a coaxial needle electrode placed along the axis of a cylindrical tube with tapered ends, and the corona voltage was applied only within a narrow range, typically 2.5–3.5 kV. Therefore, the effect of inlet air RH and air flow rate on positive and negative corona discharges in a corona-needle charger has not been extensively studied for a narrow voltage range in previous work and literature. The knowledge of the inlet air RH and air flow effects on positive and negative corona discharge behavior in the corona-needle charger is of crucial important for measuring water content of ambient aerosol particle charge by the electrical aerosol detector in ambient atmospheric conditions. Some aspect of this effect require further investigations in order to validate a realistic mathematical model of the physical phenomena, as an essential step towards the accurate numerical simulation of the aerosol particles charging by corona discharge.

The aim of the present paper is to experimentally study the effects of inlet air RH and air flow rate on positive and negative corona discharges in a corona-needle charger. Its corona discharge characterizations in terms of current-to-voltage relationships of the corona-needle charger on the effects of inlet air RH and air flow rate were experimentally studied and discussed at applied corona voltages between 0 and 3.1 kV, an air flow rates between 5 and 15 L/min, a relative humidity between 20 and 90%, and an operating pressure of about 101.3 kPa.

2. Description of corona-needle charger

The schematic diagram of the corona-needle charger used to evaluate the relative humidity and air flow effects in this study is shown in Fig. 1. The corona-needle charger's geometrical configuration is similar to the corona-needle charger used by Intra and Tippayawong [19,20]. The present charger consists essentially of a coaxial needle electrode placed along the axis of a cylindrical tube with tapered end, and divided into three sections. The first and second sections (from top to bottom in the drawing) are made of a polytetrafluoroethylene (PTFE), and the third (outlet section) of stainless steel tube. The PTFE tube is an electrical insulator between needle electrode and outer electrode and served to hold the needle electrode coaxial with the outer electrode. The needle electrode could be screwed into the PTFE insulator to connect to a DC high voltage supply, typically in the range between 2.7 and 3.0 kV. The needle electrode is made of a stainless steel rod, 3 mm in diameter, ending in a sharp tip. The needle electrode was polished to an extremely fine surface finish to avoid undesirable electric field effect on particle motion due to non-uniform electric field which results from small surface scratches and imperfections. The tip radius is about 50 μm, as estimated under a microscope. The needle cone angle is about 10°. The diameter of the outer electrode is 20 mm, its length is 20 mm with conical shape. The orifice diameter is about 3.5 mm. The distance between the needle electrode and the cone apex is 1.75 mm. The needle electrode head is connected to a positive and negative high voltage, while the outer electrode is grounded.

3. Corona current and discharge in humid air

In the absence of aerosol particles, Townsend derived an equation to characterize the DC steady corona current–voltage relationship for point-to-plane geometry is given by Ref. [21].

$$I = AV(V - V_o) \tag{1}$$

where I is the corona discharge current, V is the applied voltage, V_o is the corona onset voltage and A is the dimensional constant depending on the inter-electrode distance, the needle electrode

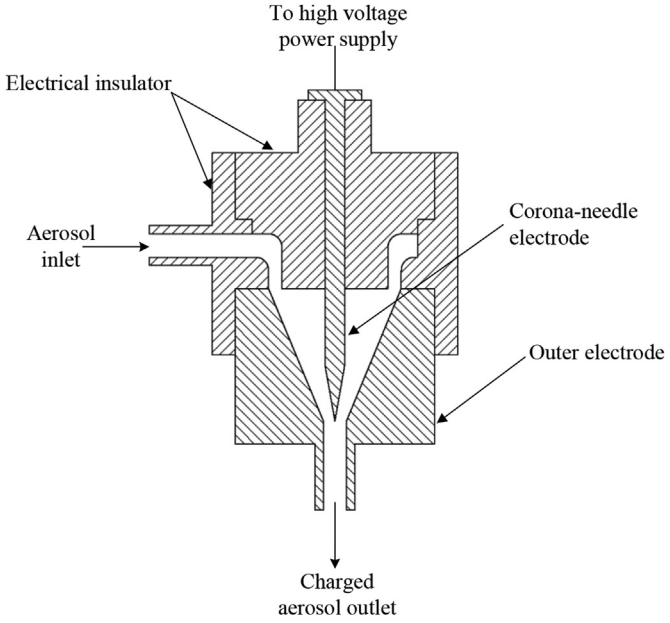

Fig. 1. Schematic diagram of the corona-needle charger.

radius, the charge carrier mobility in the drift region and other geometrical factors. Further, in 1980 Henson [21] theoretically developed a mathematical model for microscopic point-to-plane coronas in the steady-state regime, which was based on his work in liquid helium and expressed as

$$I = (2\pi K\varepsilon/\alpha)[F(\delta/\alpha)]^{-2}(V - V_o)^2 \tag{2}$$

where δ is the minimum corona glow radius, α is the distance between the needle tip and the plane, K is a dimensional constant and $F(\delta/\alpha)$ is a polynomial function of δ/α.

The value of the corona onset electric field strength, E_o, must be known, which has a strong dependence on the electrode tip radius and distance between needle electrode and nozzle [21]. Despite the experimental and theoretical efforts made to predict corona onset electric field accurately, its experimentally observed value varies under different conditions. The critical electric field strength, E_c, for the corona onset is given by the Peeks's equation [9].

$$E_c = m_v E_o \delta\left(1 + \frac{k}{\sqrt{\delta r}}\right) \tag{3}$$

where

$$\delta = \frac{P}{P_r}\cdot\frac{273 + T_r}{273 + T}, \tag{4}$$

m_v is the roughness coefficient of surface of conductor is 1 for smooth cylindrical electrodes, r is the radius of curvature of the needle tip, k is the empirical constant for cylindrical geometry, normally 0.308 $cm^{1/2}$, δ is the relative air density factor, T_r is the absolute temperature of room air, P_r is the normal atmosphere pressure, and T and P are the operating temperature and pressure of the air. For Peek equation, the standard reference atmospheric condition is adopted, i.e. $P_r = 101.3$ kPa and $T_r = 20$ °C. At normal temperature and pressure conditions, this electric field is around 15% larger for nitrogen than for air, i.e. $E_o(N_2) = 3.565 \times 10^6$ V/m. If space-charge effect is neglected, the corona onset voltage V_o can be approximated by

$$V_o = m_v E_o \delta\left(1 + \frac{k}{\sqrt{\delta r}}\right) r \ln\left(\frac{S}{r}\right) \tag{5}$$

where S is the distance between the needle electrode and nozzle.

It was clear from Equation (5) that V_o is independent of air humidity because of Peek's consideration that air humidity does not influence the occurrence of the corona when there is no dewdrop on surface of conductor. In order to take into account the effect of air humidity, the Peek equation was modified with a correction function by Xu et al. [13], and is given by

$$V_o = m_v E_o \delta\left(1 + \frac{k}{\sqrt{\delta r}}\right) r \ln\left(\frac{S}{r}\right) f(H) \tag{6}$$

where $f(H)$ is the correction function of the air humidity and H is the air humidity. The correction function of the air humidity can be calculated by Ref. [13].

$$f(H) = 1 + \left(5.76 - \frac{1.63}{0.69\sqrt{\delta r} + 0.21}\right)\cdot\frac{P_w}{P}\cdot H \tag{7}$$

where P_w is the partial pressure of saturated water vapor can be calculated by using the following equation [22]:

$$P_w = 611 \times 10^{7.5T/(237.3+T)} \tag{8}$$

Substituting Equation (7) into (6), the modified Peek equation which takes into account the air humidity around conductor is given as

$$V_o = m_v E_o \delta\left(1 + \frac{k}{\sqrt{\delta r}}\right) r \ln\left(\frac{S}{r}\right)\left[1 + \left(5.76 - \frac{1.63}{0.69\sqrt{\delta r} + 0.21}\right)\cdot\frac{P_w}{P}\cdot H\right] \tag{9}$$

4. Experimental setup

The experimental setup for relative humidity and air flow effects on positive and negative corona discharges in a corona-needle charger is shown in Fig. 2. It consisted of a corona-needle charger, an adjustable DC high voltage power supply, an electrometer, a high efficiency particulate-free air (HEPA) filter, a Dwyer mass flow controller, a humid air supply, a silica gel dryer, an air compressor pump, and a vacuum pump. The air flow through the charger was regulated and controlled by a mass flow meter and controller (Dwyer model GFC-1111) with a vacuum pump located at the end of the experimental equipment train, typically between 5 and 15 L/min. Air samples were filtered through a Pall HEPA capsule filter (model 12144) before and after the charger in order to remove any particles. The positive and negative high voltage differences on the corona-needle electrode of the charger were applied by an adjustable commercial DC high voltage power supply (Leybold Didactic model 521721), in the range between 0 and 3.1 kV with a maximum load current of 0.5 mA, and the ripple voltage of 3% of maximum value. The discharge current from the outer electrode of the charger was directly measured by the Keithley 6517A electrometer with an input bias current of <3 fA with just 0.75 fA p–p (peak-to-peak) noise, <20 μV burden voltage on the lowest range, and the current measurement range of 1 fA to 20 mA. As shown in Fig. 2, the experiments are carried out inside a closed cylindrical glass vessel with 600 mm in length and 300 mm in diameter filled with clean air. In this study, the effect of the relative humidity of the inlet air, in the range between 20 and 90% RH, is the only parameter taking into account because of the effect of temperature and pressure on the electrical behavior of a corona discharge has been examined extensively in the literature. The operating temperature of 25 °C and the operating pressure of 101.3 kPa inside the test chamber are controlled during each experiment. The relative humidity of the ambient air varies between 20 and 90%. It was reduced by introducing a dry clean air, a diffusion dryer by silica gel drying chamber was used to remove any remaining water for RH less than 10% RH, coming from a vacuum pump and or increased by adding water vapor resulting from the humid air supply after a period of relaxation in a container, during 15 min. The RH of the air inside the test chamber is monitored with the multifunction Fluke 975 AirMeter™, accuracy of about ±2% RH (10% RH–90% RH). It should be noted that the measurements of the discharge current was repeated at least three times for each set of operating conditions. Table 1 gives the ranges and values of variables investigated.

5. Results and discussion

Fig. 3 shows the current–voltage characteristics of the corona-needle charger for positive and negative coronas at different relative humidity. In this experimentation, the corona voltage was maintained to the charger in the range of 0–3.1 kV, the relative humidity was about 20–90%, and the air flow rate was about 5 L/min. As shown in Fig. 3, both positive and negative discharge currents monotonically increase with the applied voltage when it

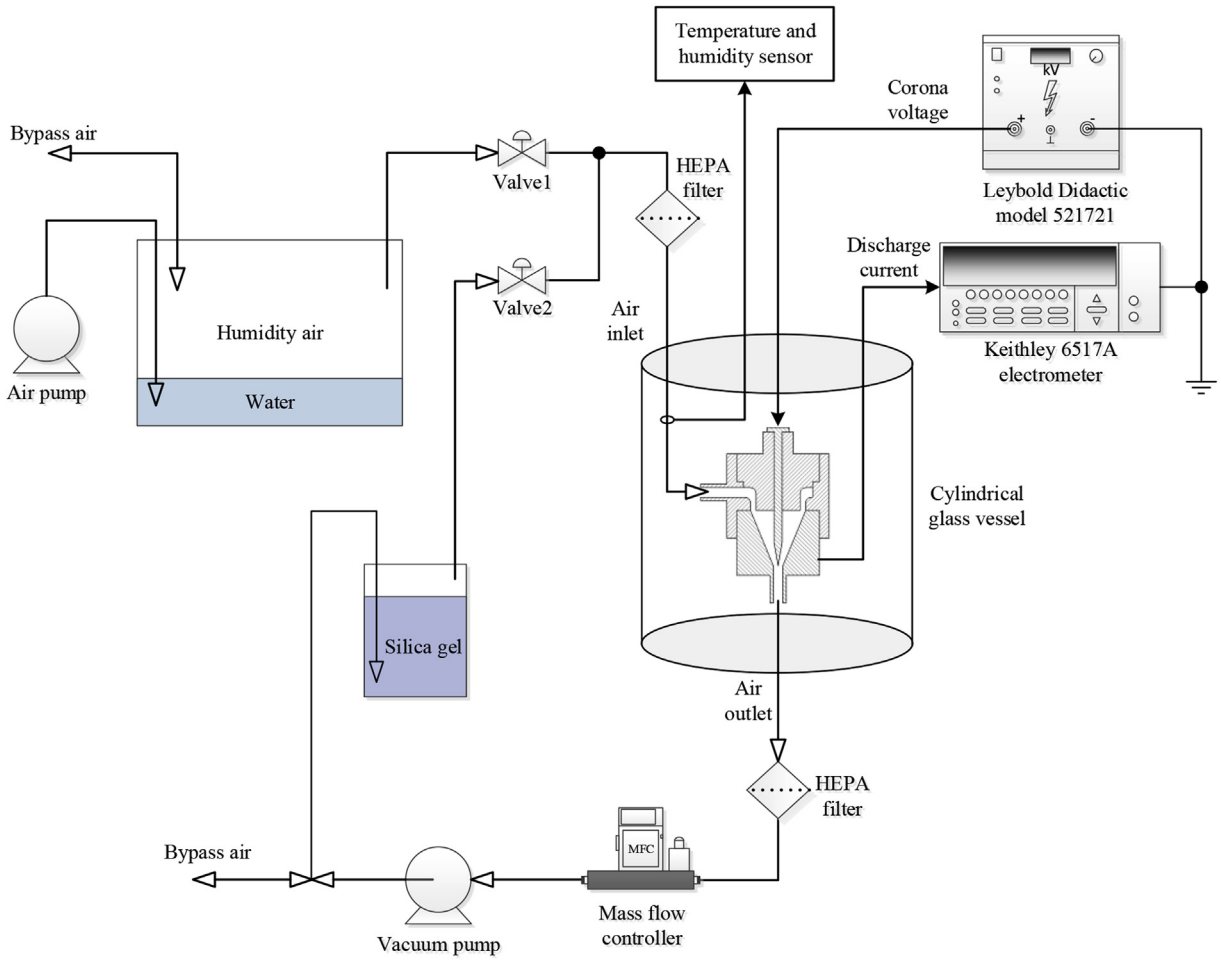

Fig. 2. Experimental setup for relative humidity and air flow effects in a corona-needle charger.

Table 1
Ranges and values of variables investigated.

Variable	Range
Corona voltage	0–3.1 kV
Ion generated	Positive ion (+), Negative ion (−)
Ionized gas	Air
Relative humidity	20–90% RH
Flow rate	5, 10 and 15 L/min
Temperature	25 °C
Pressure	101.3 kPa

exceeds the corona onset voltage until breakdown voltage. At RH value of 60%, the corona onset voltage was found to be about 2.7 and 2.5 kV for positive and negative coronas, respectively, and the breakdown voltage was found to be about 3.2 and 2.8 kV for positive and negative coronas, respectively. At a given voltage, the discharge current is higher with the negative polarity, which is explained by the difference between the apparent mass and electrical mobility of negative charge carriers compared to positive ones. Ionic electrical mobility was inversely proportional to its mass. Generally, values of electrical mobility for positive and negative ions differ by approximately 19.30%. Reischl et al. [23] quote averages for ionic electrical motility as $Z^{+}_{ion} = 1.15 \times 10^{-4}$ m^2/V s and $Z^{-}_{ion} = 1.425 \times 10^{-4}$ m^2/V s, respectively. Additionally, a positive corona has much lower density of free electrons compared to a negative corona; a thousandth of the electron density, and a hundredth of the total number of electrons. However, the electrons in a positive corona are concentrated close to the surface of the curved electrode, in a region of high potential gradient, and therefore the electrons have a high energy, whereas in a negative corona many of the electrons are in the outer, lower-field areas. Therefore, if electrons are to be used in an application which requires a high activation energy, positive coronas may support a greater reaction constants than corresponding negative coronas; though the total number of electrons may be lower, the number of a very high energy electrons may be higher. The RH effect on the positive and negative discharge currents is different depending on the applied voltage.

Fig. 4 shows the theoretical and experimental comparison of corona onset voltage for positive and negative coronas at different relative humidity and air flow rate. It was showed that both positive and negative corona onset voltages decrease with increasing relative humidity for those air flow rate. It should be noted that negative corona discharges appear as discrete points or tufts along the electrode in contrast to the uniform positive corona discharge. At voltages near the corona onset voltage, only a few tufts appear. They are irregularly spaced along the electrode and preferentially appear at imperfections on the surface. As the voltage is increased, the number of tufts increases and the distribution of tufts becomes more uniform [24]. The corona onset voltages with different relative humidity at different air flow rate were approximated by the modified Peek equation, Equation (9), and were in reasonable and systematical agreement with the experiments.

Fig. 5 shows the variation of the discharge current with the

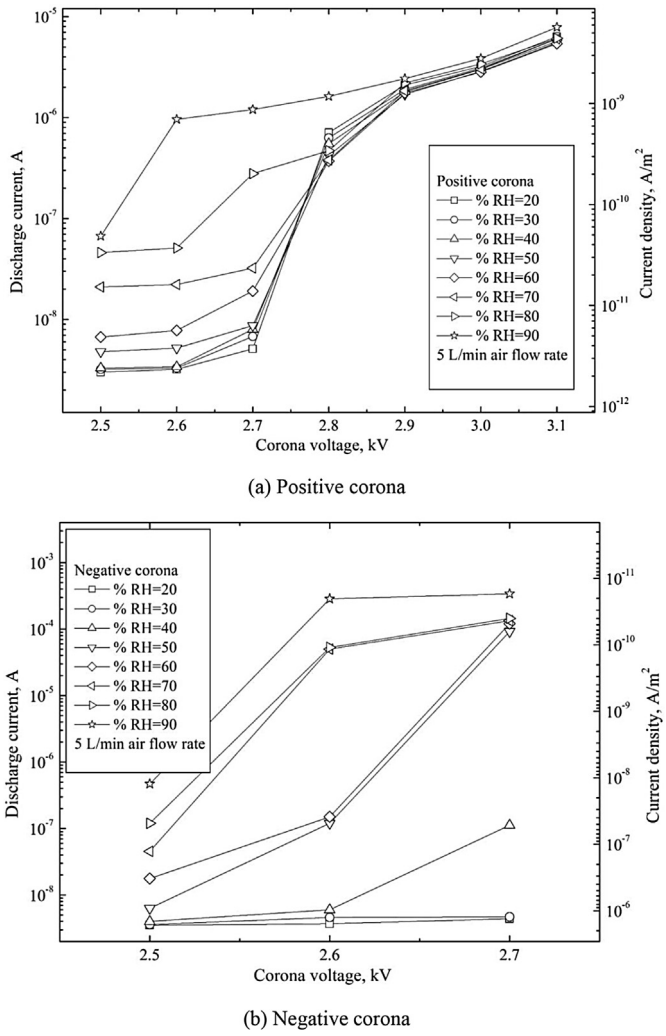

Fig. 3. Current–voltage characteristics of the corona-needle charger for positive and negative coronas at different relative humidity.

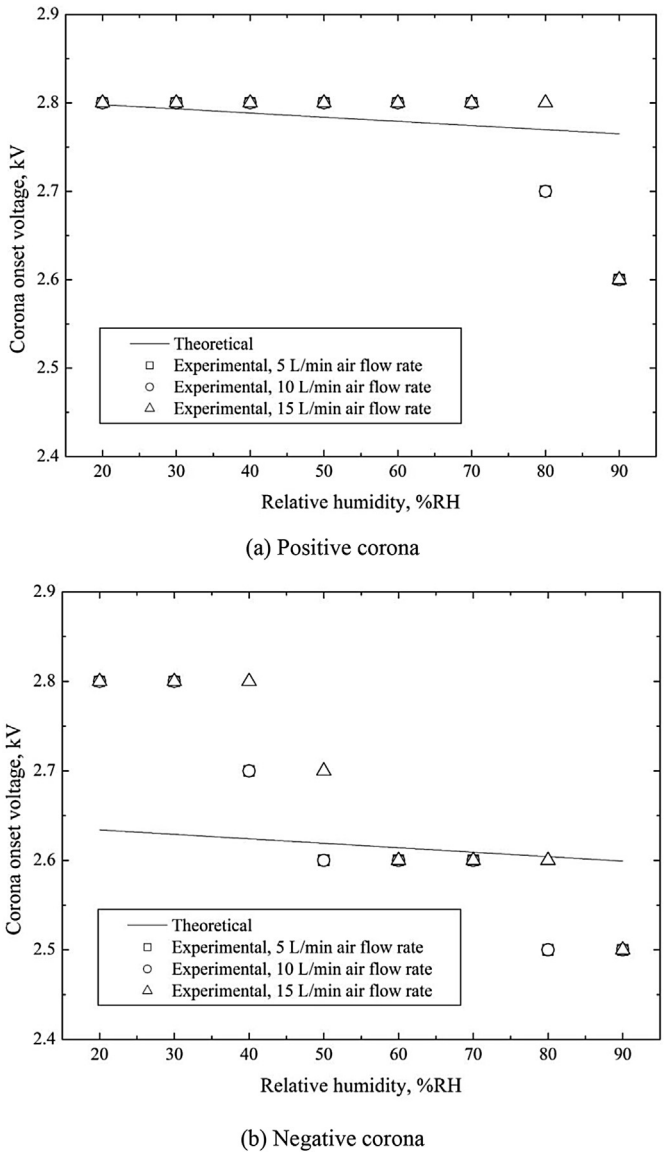

Fig. 4. Theoretical and experimental comparison of corona onset voltage for positive and negative coronas at different relative humidity and air flow rate.

relative humidity at different positive and negative corona voltages. The discharge currents of the charger of both positive and negative coronas were evaluated for the RH of 20–90%, the air flow rate of 5 L/min, and the corona voltage of 2.5–3.1 kV. At the same corona voltage, an increasing RH value in the range of 20–90% resulted in increased the positive discharge current for the corona voltage between 2.5 and 2.7 kV. In case of the corona voltage between 2.8 and 3.1 kV, it was shown that the positive discharge current decreased with increasing RH value at RH values below 60% and increased with increasing RH value at RH value above 60% in the same corona voltage. The negative discharge current was found to be stable with increasing RH value at RH values below 40% and increased with increasing RH value at RH value above 40% in the same corona voltage. In the negative corona, RH effect is unstable and more complex. This effect is due to the water vapor present in the air affects the corona initiation field strength [5,7,8,10,15], the mobility of charge carriers [16,17], and the plasma chemistry [18]. At higher % RH, the discharge current might be increased with RH due to the electric conductivity enhancement. At lower % RH, the discharge current might be decreased with increasing RH due to the decreases of apparent mobility of ions, resulting from their combination with water molecules. Table 2 shows the ratio of the discharge currents between 20 and 90% RH to the 60% RH discharge current in case of the positive corona voltage of about 2.9 kV and the negative corona voltages of about 2.7 kV, respectively. At 20% RH, the positive and negative discharge currents were found about 1.20 and 3.64 $\times$ 10^{-5} times higher than the positive and negative discharge currents at 60% RH, respectively. At 90% RH, the positive and negative discharge currents were also found about 1.39 and 2.81 times higher than the positive and negative discharge currents at 60% RH, respectively.

Fig. 6 shows the variation of the discharge current with the air flow rate at different relative humidity for positive and negative coronas. The resultant discharge currents of the charger of both positive and negative coronas were evaluated for the air flow rate of 5, 10, and 15 L/min, and the corona voltage of 0–3.1 kV. At RH value below 90%, the positive discharge current was found to slightly decrease when the air flow rate increased. This is because the ions can be transported from the charger more easily by faster flowing air. At RH value of 90%, the positive discharge current was found to increase with the air flow rate due to high electrical conductivity enhancement. For the negative corona, the discharge current was found to slightly decrease when the air flow rate increased. It should be noted that the discharge current of negative ions was

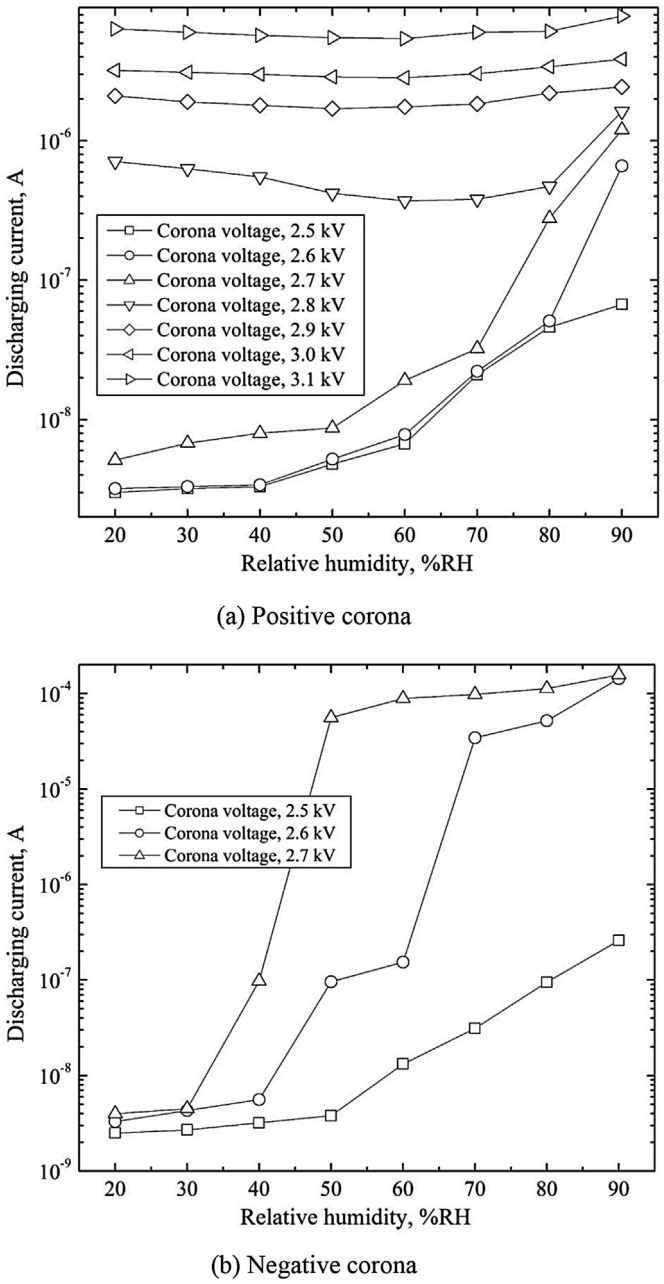

Fig. 5. Variation of the discharge current with the relative humidity at different positive and negative corona voltages.

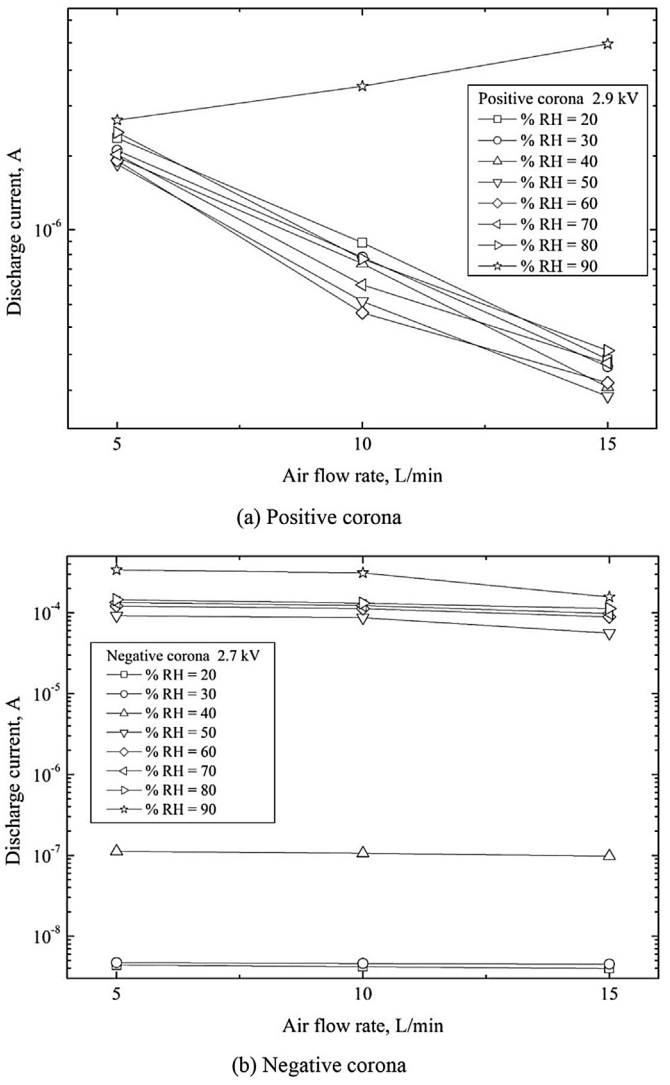

Fig. 6. Variation of the discharge current with the air flow rate at different relative humidity for positive and negative coronas.

Table 2
Ratio of discharge currents between 20 and 90% RH to 60% RH discharge current.

Relative humidity (%)	Ratio of 20–90% RH discharge currents to discharge current at 60% RH	
	Positive corona +2.9 kV	Negative corona −2.7 kV
20	1.20	3.64×10^{-5}
30	1.09	3.88×10^{-5}
40	1.03	9.26×10^{-4}
50	0.97	0.76
60	1.00	1.00
70	1.05	1.11
80	1.26	1.20
90	1.39	2.81

found to be slightly higher than positive ions due to high electrical mobility of negative ion. This negative ion was more likely to impact and deposit on the outer electrode wall of the charger due to the electrostatic force resulted in higher discharge current. Fig. 7 shows the variation of the discharge current with the air flow rate at different positive and negative coronas for 90% relative humidity. It was shown that the discharge current increased with increasing the air flow rate for positive corona but decrease in negative corona. It seems that the electrical mobility of negative ions decreases with the RH and increase with RH for positive ion, which can be explained by the gas/liquid phase transition inducing the formation of ions of water [7].

6. Conclusion

The effects of inlet air RH and air flow rate on positive and negative corona discharges in a corona-needle charger have been experimentally studied and discussed in this paper. The corona discharge characterizations of the charger in terms of current-to-voltage relationships of the corona-needle charger on the effects of inlet air RH and air flow rate were evaluated at applied corona voltages between 0 and 3.1 kV, an air flow rates between 5 and 15 L/

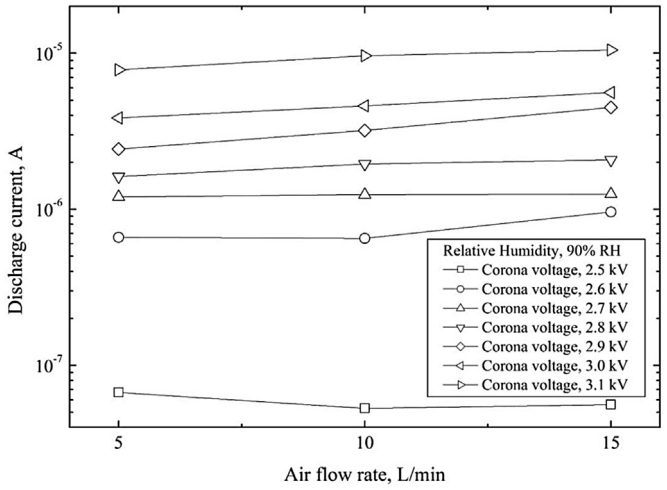

(a) Positive corona

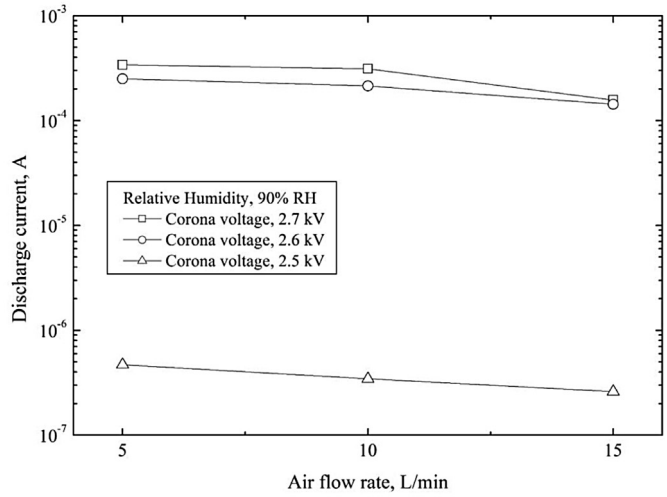

(b) Negative corona

Fig. 7. Variation of the discharge current with the air flow rate at different positive and negative coronas for 90% relative humidity.

min, a relative humidity between 20 and 90%, and an operating pressure of about 101.3 kPa. It was shown that both positive and negative discharge currents monotonically increase with the applied voltage when it exceeds the corona onset voltage until breakdown voltage. As experimental results shown, the discharge current is strongly affected by the RH level of the inlet air. Both positive and negative corona onset voltages were decreased with increasing relative humidity for different air flow rate. The positive discharge current was found to be decreased with increasing RH value at RH values below 60% and increased with increasing RH value at RH value above 60% in the same corona voltage. The negative discharge current was found to be stable with increasing RH value at RH values below 40% and increased with increasing RH value at RH value above 40% in the same corona voltage. This effect is due to the water vapor present in the air affects the corona initiation field strength, the mobility of charge carriers, and the plasma chemistry. For the air flow rate effects, the positive discharge current was found to slightly decrease when the air flow rate increased at RH value below 90% and to increase with the air flow rate at RH value of 90%. For the negative corona, the discharge current was also found to monotonically decrease when the air flow rate increased. Finally, research is in progress on the RH effects on the charging efficiency of the corona-needle charger.

Acknowledgments

The authors gratefully acknowledge the Thailand Research Fund and the Nation Research University Project of Thailand Office of Higher Education Commission (under the TRF contract No. RTA5680007) and the National Science and Technology Development Agency (under the NSTDA contract No. P-14-50757) for the financial support.

References

[1] P. Intra, N. Tippayawong, Progress in unipolar corona discharger designs for airborne particle charging: a literature review, J. Electrost. 67 (4) (2009) 605–615.
[2] P. Intra, N. Tippayawong, An overview of differential mobility analyzers for size classification of nanometer-sized aerosol particles, Songklanakarin J. Sci. Technol. 30 (2) (2008) 243–256.
[3] P. Intra, A. Yawootti, N. Tippayawong, An electrostatic sensor for continuous monitoring of particulate air pollution, Korean J. Chem. Eng. 30 (12) (2013) 2205–2212.
[4] F.O. J-Fatokun, L. Morawska, M. Jamriska, E.R. Jayaratne, Application of aerosol electrometer for ambient particle charge measurements, Atmos. Environ. 42 (38) (2008) 8827–8830.
[5] M. Abdel-Salam, Positive wire-to-plane corona as influenced by atmospheric humidity, IEEE Trans. Ind. Appl. 21 (1985) 35–40.
[6] N.L. Allen, M. Boutlendj, Study of the electric fields required for streamer propagation in humid air, IEE Proc. A Sci. Meas. Technol. 138 (1991) 37–43.
[7] L. Fouad, S. Elhazek, Effect of humidity on positive corona discharge in a three electrode system, J. Electrost. 35 (1995) 21–30.
[8] X.M. Bian, X.B. Meng, L.M. Wang, Negative corona inception voltages in rod-plane gaps at various air pressures and humidities, IEEE Trans. Dielectr. Electr. Insul. 18 (2011) 613–619.
[9] F.W. Peek, Dielectric Phenomena in High Voltage Engineering, McGraw-Hill Press, New York, 1920.
[10] G.T. Hartmann, Theoretical evaluation of Peek's law, IEEE Trans. Ind. Appl. I (1984) 1647.
[11] H. Nouria, N. Zouzou, E. Moreau, L. Dascalescu, Y. Zebboudj, Effect of relative humidity on current–voltage characteristics of an electrostatic precipitator, J. Electrost. 70 (2012) 20–24.
[12] X. Wang, C. You, Effect of humidity on negative corona discharge of electrostatic precipitator, IEEE Trans. Dielectr. Electr. Insul. 20 (2013) 1720–1726.
[13] M.M. Xu, Z.Y. Tan, K.J. Li, Modified peek formula for calculating positive DC corona inception electric field under variable humidity, IEEE Trans. Dielectr. Electr. Insul. 19 (2012) 1377–1382.
[14] P.M. Young, A. Sung, D. Traini, P. Kwok, H. Chiou, H.K. Chan, Influence of humidity on the electrostatic charge and aerosol performance of dry powder inhaler carrier based systems, Pharm. Res. 24 (5) (2007) 963–970.
[15] J.E. Jones, J. Dupuy, G.O.S. Schreiber, R.T. Waters, Boundary conditions for the positive direct-current corona in a coaxial system, J. Phys. D Appl. Phys. 21 (1988) 322–333.
[16] R.G. Stearns, Ion mobility measurements in a positive corona discharge, J. Appl. Phys. 67 (1990) 2789–2799.
[17] H. Ryzko, Drift velocity of electrons and ions in dry and humid air and in water vapor, Proc. Phys. Soc. 85 (1965) 1283–1295.
[18] J.T. Herron, D.S. Green, Chemical kinetics database and predictive schemes for nonthermal humid air plasma chemistry part II. Neutral species reactions, Plasma Chem. Plasma Process. 21 (2001) 459–481.
[19] P. Intra, N. Tippayawong, Effect of needle cone angle and air flow rate on electrostatic discharge characteristics of a corona-needle ionizer, J. Electrost. 68 (3) (2010) 254–260.
[20] P. Intra, N. Tippayawong, Design and evaluation of a high concentration, high penetration unipolar corona ionizer for electrostatic discharge and aerosol charging, J. Electr. Eng. Technol. 8 (5) (2013) 1175–1181.
[21] B.L. Henson, A space-charge region model for microscopic steady coronas from points, J. Appl. Phys. 52 (2) (1981) 709–715.
[22] R.N.C. Anyadike, Assessment of various formulae for the computation of saturation vapor pressures over liquid water, Arch. Met. Geoph. Biocl. Ser. A 33 (1984) 239–243.
[23] G.P. Reischl, J.M. Makela, R. Harch, J. Necid, Bipolar charging of ultrafine particles in the size range below 10 nm, J. Aerosol Sci. 27 (6) (1996) 931–939.
[24] P.A. Lawless, K.J. McLean, L.E. Sparks, G.H. Ramsey, Negative corona in wire-plate electrostatic precipitators. Part I: characteristics of individual tuft-corona discharges, J. Electrost. 18 (1986) 199–217.

Drying Technology
An International Journal

ISSN: 0737-3937 (Print) 1532-2300 (Online) Journal homepage: http://www.tandfonline.com/loi/ldrt20

Microwave-Assisted Drying: A Review of the State-of-the-Art

P. Rattanadecho & N. Makul

To cite this article: P. Rattanadecho & N. Makul (2016) Microwave-Assisted Drying: A Review of the State-of-the-Art, Drying Technology, 34:1, 1-38, DOI: 10.1080/07373937.2014.957764

To link to this article: http://dx.doi.org/10.1080/07373937.2014.957764

Accepted author version posted online: 21 May 2015.

Submit your article to this journal

Article views: 163

View related articles

View Crossmark data

Full Terms & Conditions of access and use can be found at
http://www.tandfonline.com/action/journalInformation?journalCode=ldrt20

Download by: [Thammasat University Libraries] **Date:** 28 December 2015, At: 16:40

DRYING TECHNOLOGY
2016, VOL. 34, NO. 1, 1–38
http://dx.doi.org/10.1080/07373937.2014.957764

Taylor & Francis
Taylor & Francis Group

REVIEW ARTICLE

Microwave-Assisted Drying: A Review of the State-of-the-Art

P. Rattanadecho[a] and N. Makul[b]

[a]Center of Excellence in Electromagnetic Energy Utilization in Engineering (CEEE), Thammasat University (Rangsit Campus), Khlong Luang, Prathum Thani, Thailand; [b]Department of Building Technology, Faculty of Industrial Technology, Phranakhon Rajabhat University, Bangkhen, Bangkok, Thailand

ABSTRACT

Offering advantages of energy-saving rapid drying rates, short processing times, deep penetration of the microwave energy, instantaneous and precise electronic control, and clean heating processes, microwave-assisted drying (MWD) has become a popular method that is currently used for many materials and processes. This article presents a systematic and comprehensive review of experimental and theoretical studies regarding the kinetic mechanisms of MWD. Factors affecting, methods for measuring, and applications of the dielectric property are discussed. From the experimental perspective, laboratory- and commercial-scale MWD systems are elaborated, including the equipment used and the stability, safety, and regulation of MWD systems. Theoretical investigations of thermal and nonthermal equilibrium models and moving-load computational models are discussed. Finally, some future trends in the research and development of MWD systems are suggested.

KEYWORDS

Experimental; microwave-assisted drying (MWD); modeling; thermal applications

Downloaded by [Thammasat University Libraries] at 16:40 28 December 2015

Introduction

Microwaves are electromagnetic waves with radiofrequencies ranging from 300 MHz to 300 GHz (wavelengths from 1.0 mm to 1.0 m). According to the International Telecommunications Union, the electromagnetic frequency band for non-telecommunications (e.g., industrial, scientific, and medical) purposes ranges from 6.765 MHz to 246 GHz, as tabulated in Table 1. Most such systems are operated between 433.92 MHz and 40 GHz.[1,2]

Microwave-assisted drying (MWD) is a complicated phenomenon resulting from microwave heating via liquid vaporization.[3] MWD is a particularly efficient technique for thermal processes. It has been reported to be at least twice as effective as conventional drying methods for dielectric materials, including food,[4–10] biological tissue,[11] wood,[12,13] ceramic,[14–16], oil,[17] and others. In principle, the mechanism and direction of heat transfer differ between conventional and microwave heating methods. In conventional heating, the material is heated by an external heat source (from outside the material to be heated), and the heat is transferred from the outside inward. In contrast, microwave heating is based on the rapid polarization and depolarization of charged groups as the material is subjected to a microwave field, resulting in simultaneous internal heat generation.

Microwave heating offers many advantages compared to conventional methods, including the following[3,18–20]:

- Rapid heating rates and short processing times, which save energy
- Deep penetration of the microwave energy (e.g., in a dielectric material, a microwave system operating at 2.45 GHz can typically penetrate several centimeters), which allows heat to be generated efficiently without directly contacting the materials to be dried
- Instantaneous and precise electronic control
- Unique and fine internal structural development, which may improve many properties of the dried material
- Clean heating processes that do not generate secondary waste

Theoretically, MWD should be useful for materials that exhibit excellent dielectric properties. These materials should be able to absorb microwave energy and convert it into heat very efficiently. Recently, many investigations and practices have reported using microwave heating for numerous applications, such as the drying of paper, textiles, and leather. Other uses have included polymer cross-linking, accelerated vulcanization, and high-temperature casting. Food and related industries are likely the largest consumers of microwave power consumption, as microwave systems are useful for freeze-drying, thawing, cooking, etc. Use of microwave energy can lower the drying temperature for

CONTACT P. Rattanadecho ratphadu@engr.tu.ac.th Center of Excellence in Electromagnetic Energy Utilization in Engineering (CEEE), Thammasat University (Rangsit Campus), 99 Moo 18, Klong 1, Khlong Luang, Pathumthani 12120, Thailand.
Color versions of one or more of the figures in the article can be found online at www.tandfonline.com/ldrt.
© 2016 Taylor & Francis

Downloaded by [Thammasat University Libraries] at 16:40 28 December 2015

Table 1. Electromagnetic frequency ranges for industrial, scientific, and medical non-telecommunications purposes.

Frequency range		Bandwidth		
Value	Unit	Value	Unit	Availability region(s)
6.765–6.795	MHz	30	kHz	Subject to local acceptance
13.553–13.567	MHz	14	kHz	Worldwide
26.957–27.283	MHz	326	kHz	Worldwide
40.660–40.700	MHz	40	kHz	Worldwide
433.050–434.790	MHz	1.74	MHz	Europe, Africa, Iraq, the former Soviet Union,and Mongolia
902.000–928.000	MHz	26	MHz	Americas, Greenland, and some of the eastern Pacific Islands only (with some exceptions)
2.400–2.500	GHz	100	MHz	Worldwide
5.725–5.875	GHz	150	MHz	Worldwide
24.000–24.250	GHz	250	MHz	Worldwide
61.000–61.500	GHz	500	MHz	Subject to local acceptance
122.000–123.000	GHz	1	GHz	Subject to local acceptance
244.000–246.000	GHz	2	GHz	Subject to local acceptance

several dielectric materials, thereby reducing the incidence of drying imperfections, providing better throughput, increasing the energy efficiency, and reducing floor-space needs compared to conventional drying methods.

This article reviews experimental and theoretical studies of the kinetic mechanisms of MWD. Factors affecting methods for measuring and applications of the dielectric property are reviewed. From an experimental perspective, the equipment, stability, safety, and regulation of laboratory- and commercial-scale MWD systems are described in detail. Theoretical investigations of thermal and nonthermal equilibrium models and moving-load computational models are discussed. Finally, some future trends in the research and development of MWD are suggested.

Microwave heating mechanism

Microwave heating is directly associated with dielectric loss of the material. A material will absorb energy when placed in a high-frequency electric field. Consequently, electric dipole polarization and conduction will be generated within a dielectric material composed of polar molecules with positive and negative poles. These orderly dispersed polar molecules vibrate instantaneously and violently in response to the alternative high-frequency electric field of the microwave,[18] as shown in Fig. 1. Resistance to molecular attraction and motion must be overcome. The temperature of the material increases as friction generates heat.

In mathematical terms, heat generation can be calculated from the root mean square of the electric field intensity, $\vec{E}$. According to Lambert's law, the microwave energy absorbed (or local volume of heat generated) can be defined as shown in Eq. (1)[18]:

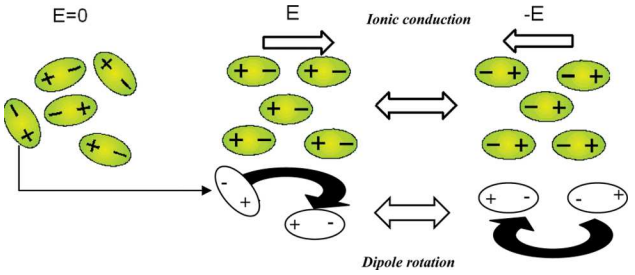

Figure 1. Mechanisms of microwave heating.[18]

$$Q = \sigma|\vec{E}|^2 = 2\pi f \varepsilon_0 \varepsilon_r'(tan\,\delta)|\vec{E}|^2 \quad (1)$$

where Q is the microwave energy, σ is the effective conductivity, f is the frequency (Hz), ε_0 is the permittivity of free space (8.8514×10^{-12} F/m), ε_r' is the relative dielectric constant, $tan\ \delta$ is the loss tangent coefficient, and $\vec{E}$ is the electric-field intensity (V/m).

When microwave energy penetrates a dielectric material, the wave strength fades away exponentially because the microwave energy is absorbed by the dielectric material and converted into heat. This absorbed ratio varies with the frequency and dielectric property. In general, the penetration depth (D_p) is used to denote the depth of the power density. It decreases to 37% (or $1/e$) of its initial value at the surface[18] and is defined in Eq. (2):

$$D_p = \frac{1}{\frac{2\pi f}{\upsilon}\sqrt{\frac{\varepsilon_r'\left(\sqrt{1+\left(\frac{\varepsilon_r''}{\varepsilon_r'}\right)^2}-1\right)}{2}}} = \frac{1}{\frac{2\pi f}{\upsilon}\sqrt{\frac{\varepsilon_r'\left(\sqrt{1+(tan\,\delta)^2}-1\right)}{2}}} \quad (2)$$

where D_p is the penetration depth, ε_r'' is the relative dielectric loss factor, and υ is the microwave speed in the dielectric material, which can be evaluated by $c/\sqrt{\varepsilon_r'}$.

From this equation, the penetration depth of a microwave depends on the dielectric property of the material. If the workpiece has very large dimensions and a high dielectric lossy factor, then its outer layer may overheat intermittently. In contrast, if the thickness of the workpiece is less than the penetration depth, then only a fraction of the microwave energy will be absorbed by the material.

Dielectric property

Theory underlying the dielectric property

As an intrinsic property that describes how a material interacts with the electric and magnetic fields of a

Downloaded by [Thammasat University Libraries] at 16:40 28 December 2015

microwave, the dielectric property can be characterized by two independent properties: the complex electric permittivity, ε^*, and the complex magnetic permeability, μ^*. However, most common concrete materials are non-magnetic and yield a permeability μ^* that is very close to the permeability of free space ($4\pi \times 10^{-7}\,\mathrm{m \cdot kg/s^2 \cdot A^2}$).[18] Thus, the complex electric permittivity, ε^*, which comprises real and imaginary parts, can be defined by the relationship in Eq. (3):

$$\varepsilon_r^* = \varepsilon_r' - \vec{j}\,\varepsilon_r'' \tag{3}$$

where ε_r'' and ε_r'' are the real and imaginary parts, respectively, of the complex permittivity, and $\vec{j} = \sqrt{-1}$ The dielectric constant ε_r'' measures how much energy that is transferred from an external electric field is stored in a material. The relative loss factor ε_r'' measures how lossy a material is to an external electric field. The loss tangent *tan* δ, calculated as shown in Eq. (4), is an essential ratio of the energy lost (relative loss factor) to the energy stored (relative dielectric constant) in a material.

$$tan\ \delta = \varepsilon_r''\varepsilon_r' \tag{4}$$

Factors affecting the dielectric properties of materials to be dried

The dielectric property of a material to be dried affects the microwave heating rate and energy consumption, as described in Eq. (1). The main factors that determine the dielectric behavior of dielectric materials include the frequency and temperature of microwave heating and the moisture content of the material. Llave et al.[21] used the parallel-plate measurement method with an impedance analyzer and a dielectric test fixture to determine the dielectric properties of three ordinary tuna muscles at radiofrequencies of 13.56 and 27.12 MHz from −20 to +10°C. Values of the dielectric constant (ε') were higher from −3 to 1°C than at other temperatures. Tuna samples with higher moisture contents exhibited higher values of the dielectric property than other samples, especially at lower frequencies.

The effects of moisture content on the dielectric constant and dielectric loss are well known. Regardless of the temperature, materials with higher moisture contents consistently exhibit higher values of the dielectric constant and dielectric loss, because the microwave absorption and dissipation increase with increasing free water in the material.[2] However, there is no obvious relationship between temperature and the dielectric property. The ε' values increase lightly with increasing temperature at every moisture level. Nonetheless, a clear decrease in ε' values with increasing water content was found in some investigations.[22–26] As well as the work of Feng et al.,[27] they indicated that the dielectric properties of food products that continually affect microwave drying characteristics are directly influenced by moisture content and temperature. This research also presented the contribution of different dispersion mechanisms in biological materials as affected by frequency and temperature, as shown in Fig. 2. Based on this investigation, it a strong moisture leveling effect was found when drying apples from 50% to 4% at elevated temperatures in 915 MHz or 2.45 GHz microwave drying systems. Further, moisture removal in dehydration operations resulted in a decrease in dielectric properties. Sipahioglu and Barringer[28] found comparable behavior for garlic samples with 57.3% moisture content. Sólyom et al.[29] observed that when the temperature of milled seeds increased, the ε'' value gradually decreased, with a high amount of free water.

The dielectric constant (ε') and loss factor (ε'') of potato purees were observed to decrease considerably after freezing.[32] From −25 to 5°C, the simultaneous addition of sucrose and salt increased the ε' and ε'' values of the samples, with salt having a greater influence than sucrose content on the dielectric properties. The addition of sucrose alone had an insignificant effect on the dielectric properties of thawing samples. In contrast, ε' decreased and ε'' increased with increasing salt content and temperature. In another study, Wang et al.[33] considered the effects of blanching on the dielectric properties of potato purees. The dielectric loss and electrical conductivity values of microwave-blanched samples were two times higher than those of boiling water-blanched samples and five times higher than those of unblanched samples. For stem lettuce

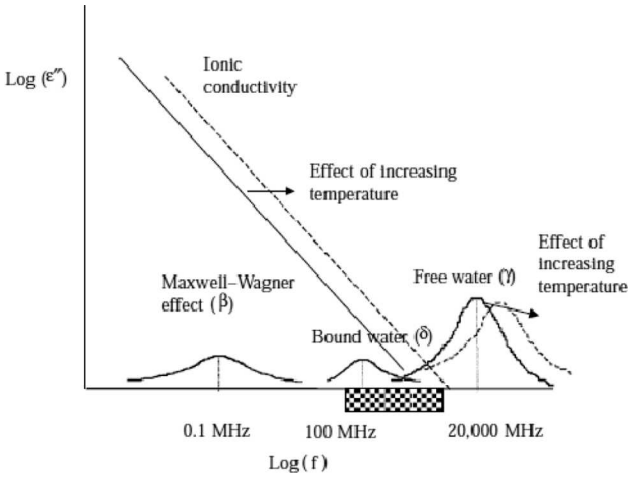

Figure 2. Contribution of different dispersion mechanisms in biological materials as affected by frequency and temperature[30] based on Roebuck and Goldblith.[2,31] The shaded range represents frequency range measured by Feng et al.[27]

Downloaded by [Thammasat University Libraries] at 16:40 28 December 2015

cubes, the values of these dielectric properties decreased considerably after freezing.

One method for creating a porous structure during fruit and vegetable drying is to use an instantaneous controlled pressure drop (DIC), which affects the dielectric properties of the food. Kristiawan et al.[34] used DIC with an open-ended coaxial probe at a frequency of 915 MHz, in the temperature range of 20 to 90°C, with material having a wet bulk moisture content of 5–80%. The dielectric constant and loss factor values increased approximately linearly with increasing moisture content. When the products were treated by the DIC process (with moisture contents <20% wet bulk), the values of the dielectric constant and loss factor were slightly lower than the values of non-treated products.

Techniques for measuring the dielectric property

Many techniques have been developed to understand the dielectric property (Table 2), including the transmission/reflection line, perturbation, free-space, and open-ended methods.[35,36] Selection of the appropriate method depends, in part, on the operating frequency of the microwave system.[36] For example, at the commonly utilized frequency of 2.45 ± 0.05 GHz, the dielectric property should be measured by transmission line. This method allows the measurement of specimens with a slab-shaped geometry to be placed across the cavity. However, this method is limited by the air-gap effect. The open-ended probe method could also be used, which involves measuring the phase and amplitude of the reflected signal at the end of an open-ended coaxial line inserted in a specimen. This method, too, has limitations due to the reflection effect from the specimen.

Choices of the measurement equipment and design of the sample holder depend on several factors, including the dielectric material to be characterized and the extent of the research, as well as the equipment and resources that are available. Two types of dielectric

Table 2. Summary of techniques for measuring the dielectric property.[35,36]

Technique	Characteristics	Feature	Dielectric properties
Perturbation (Cavity) (Resonant)	The measurement is made by placing a sample completely through the center of a waveguide that has been made into a cavity. Advantages: • simple and easy data reduction • accuracy and high temperature capability • suited to low dielectric loss materials Disadvantages: • need high frequency resolution vector network analysis (VNA) • limited to narrow band of frequency band only	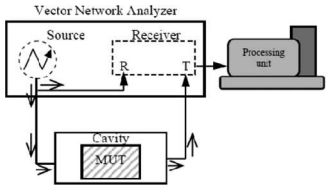	ε_r, μ_r
Transmission/reflection line	The material under test (MUT) must be made into slab geometry. Advantages: • common coaxial lines and waveguide • *used to determine both* ε_r, $\mu_r$of the MUT Disadvantages: • limited by the air-gap effect • limited to low accuracy	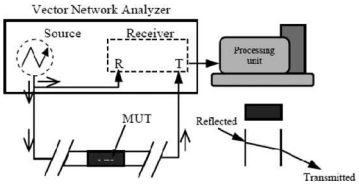	ε_r, μ_r
Open-ended probe	The technique calculates the dielectric properties from the phase and amplitude of the reflected signal at the end of an open-ended coaxial line inserted into a sample to be measured. Advantages: • after calibration, can be routinely measured in a short time Disadvantages: • available for reflection measurement	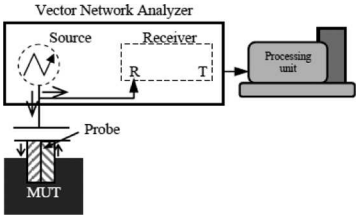	ε_r
Free-space	The sample is placed between a transmitting antenna and a receiving antenna, and the attenuation and phase shift of the signal are measured. Advantages: • used for high frequency and allow non destructive measurement • measure MUT in hostile environment Disadvantages: • need large and flat MUT and diffraction effects at the edge of sample • limited to low accuracy	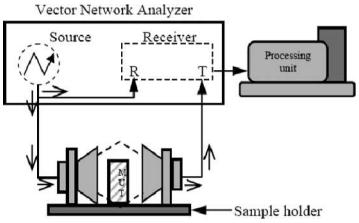	ε_r, μ_r

Downloaded by [Thammasat University Libraries] at 16:40 28 December 2015

Table 3. Test conditions for the C- and F-beds with a constant initial moisture content of 25% (dry basis).

Test condition	Magnetron power (W)	Magnetron position	Air temperature (°C)	Drying time (min)
Case 1	800 × 6	Side (1-10-2-11-3-12)	Ambient, 30	90
Case 2	800 × 6	Top (7-4-8-5-9-6)	Ambient, 30	80
Case 3	800 × 6	Top (7-4-8-5-9-6)	Hot air, 70	80

analyzers have recently been used: the scalar network analyzer and the vector network analyzer. Vector network analyzers are quite popular, very versatile, and useful for extensive studies; however, they are also very expensive. Although less expensive, scalar network analyzers and impedance analyzers are generally still too costly for many applications.

The HP 8510[37] can measure the magnitude and phase characteristics of linear networks, such as filters, amplifiers, attenuators, and antennae. As with all network analyzers, the HP 8510 apparatus measures the reflection and transmission of electromagnetic waves at an interface. An incident signal generated by a radio frequency source is compared with the signal transmission through the analyzer or reflected from the wave input when passing through the waveguide. However, this method is strongly affected by the air-gap content, with high air content tending to decrease the dielectric property of the material. It is also influenced by the consistency of dielectric materials. In particular, when materials behave like liquids, the settling of the material under its own weight can result in the non-uniform behavior of the whole specimen. Consequently, the measurement results are not representative of the whole body of the specimen.

To perform the transmission/reflection-line technique, a sample is placed in a section of the waveguide or coaxial line, and the complex scattering parameters are measured at the two ports with a vector network analyzer. Note that the system must be calibrated before the measurements can be made. Both the reflected signal (S_{11}) and the transmitted signal (S_{21}) are measured. Various equations are used to relate the scattering parameters to the complex permittivity and permeability of the material. The *S*-parameters are converted to the complex dielectric parameters by solving the equations with the Nicholson-Ross-Weir (NRW) technique.[37]

An open-probe technique can be applied to measure the dielectric properties of samples before MWD processing.[14,38] For example, a portable dielectric network analyzer can be used over a frequency band from 1.5–2.6 GHz to measure the dielectric properties of wood, as shown in Fig. 3. A portable

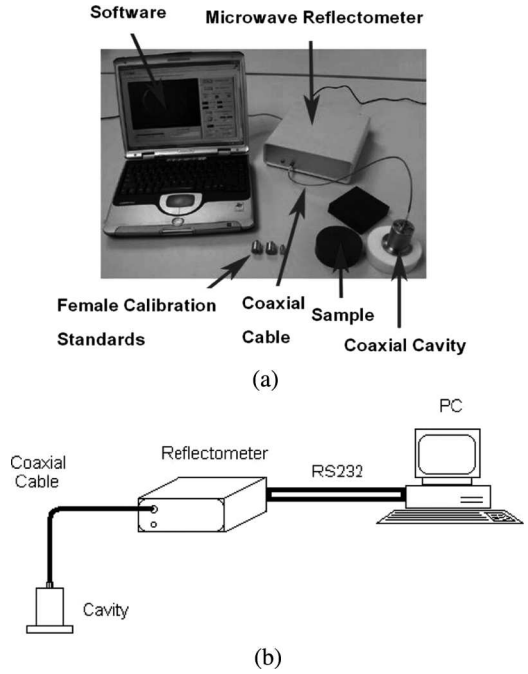

Figure 3. Portable dielectric network analyzer. Reprinted from Vongpradubchai and Rattanadecho[14] with permission from Taylor & Francis.

dielectric measurement kit can be used to measure the complex permittivity values of a wide range of solid, semisolid, granular, and liquid materials. This system performs all of the necessary control functions, microwave signal treatments, calculations, and data-processing steps, and provides a representation of the results. The software controls the microwave reflectometer to measure the complex reflection coefficient of the tested material. It detects the cavity resonant frequency and quality factor, which it converts into the complex permittivity of the tested material. Finally, the measurement results are displayed in a graphical format or saved to disk.

Microwave systems

This section describes existing microwave systems, their components, and their functions, as well as various practical microwave systems based on the type of applicator. Conventionally, a microwave system should generate and introduce microwave energy to the (dielectric) material to be heated. A typical microwave system is shown in Fig. 4. Most microwave-heating systems consist of three basic components: a microwave power generator (usually a magnetron), waveguide, and microwave chamber/cavity where the specimen is processed. The system may also have supplementary components (e.g., control system, tuner, circulator, etc.).

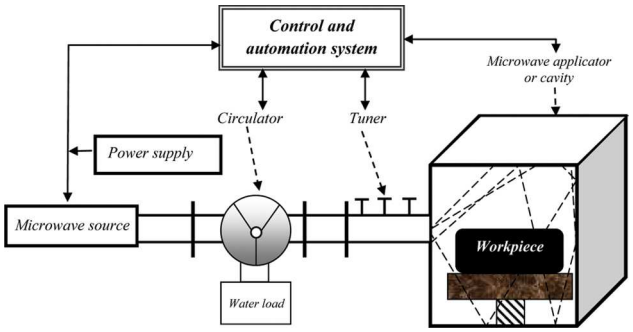

Figure 4. Schematic diagram of a typical microwave system.

As the most important component, the microwave power generator connects to the power supply unit and converts the alternating current of 50–60 Hz to the desired high-frequency microwave radiation. This conversion is typically achieved by a magnetron, which must be shielded for safety and to prevent the leakage of harmonic radiation. The waveguide transmits microwave energy through free space and delivers it to the specimen. The waveguide is any structure that directs the propagation of energy in the form of an electromagnetic wave along a predetermined path.[39] Waveguides may assume different physical forms, largely depending on the frequency band. Finally, the microwave chamber/cavity obeys electromagnetic laws, such that it can transmit, absorb, and reflect microwave energy.

Practically, microwave systems can be categorized according to the type of applicator that is associated

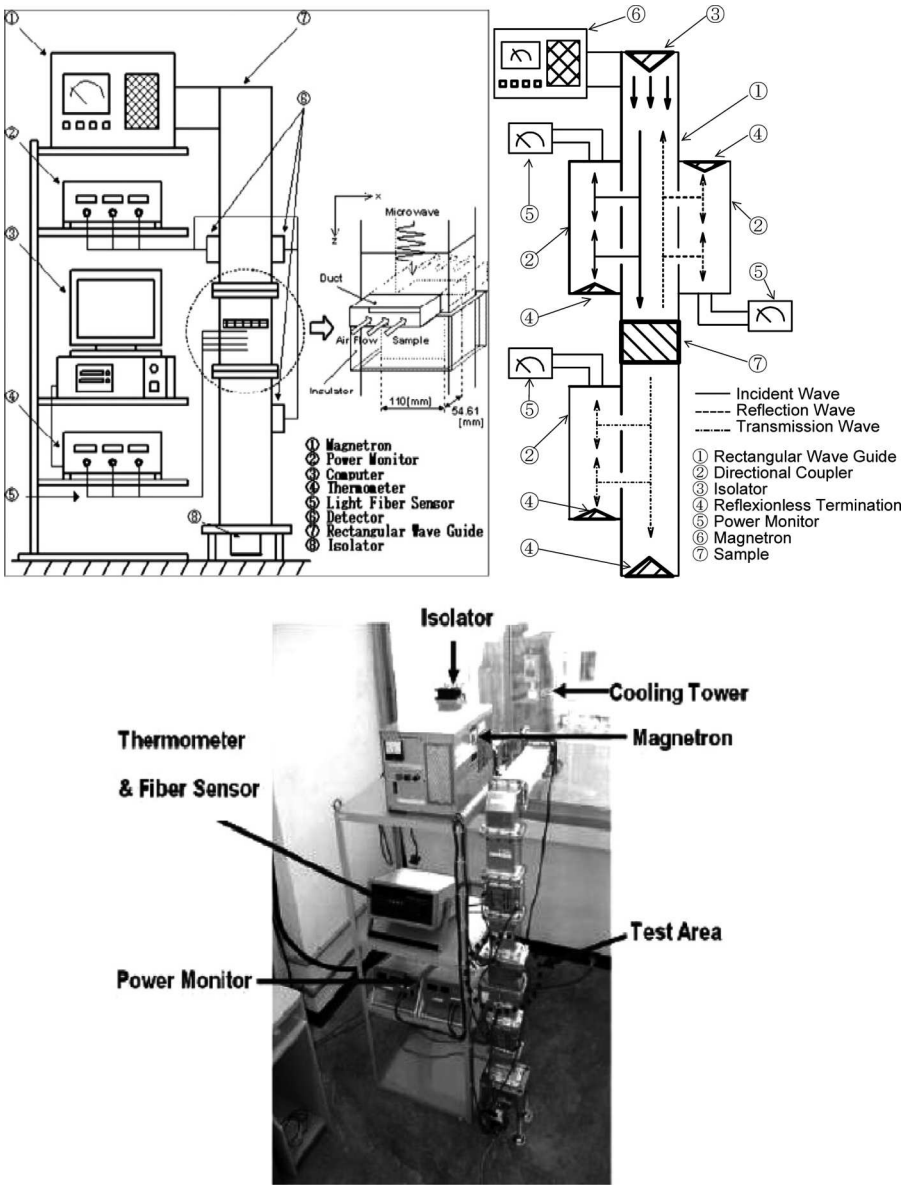

Figure 5. Example of a microwave system using a rectangular waveguide. Reprinted from Vongpradubchai and Rattanadecho[14] with permission from Taylor & Francis.

Downloaded by [Thammasat University Libraries] at 16:40 28 December 2015

Downloaded by [Thammasat University Libraries] at 16:40 28 December 2015

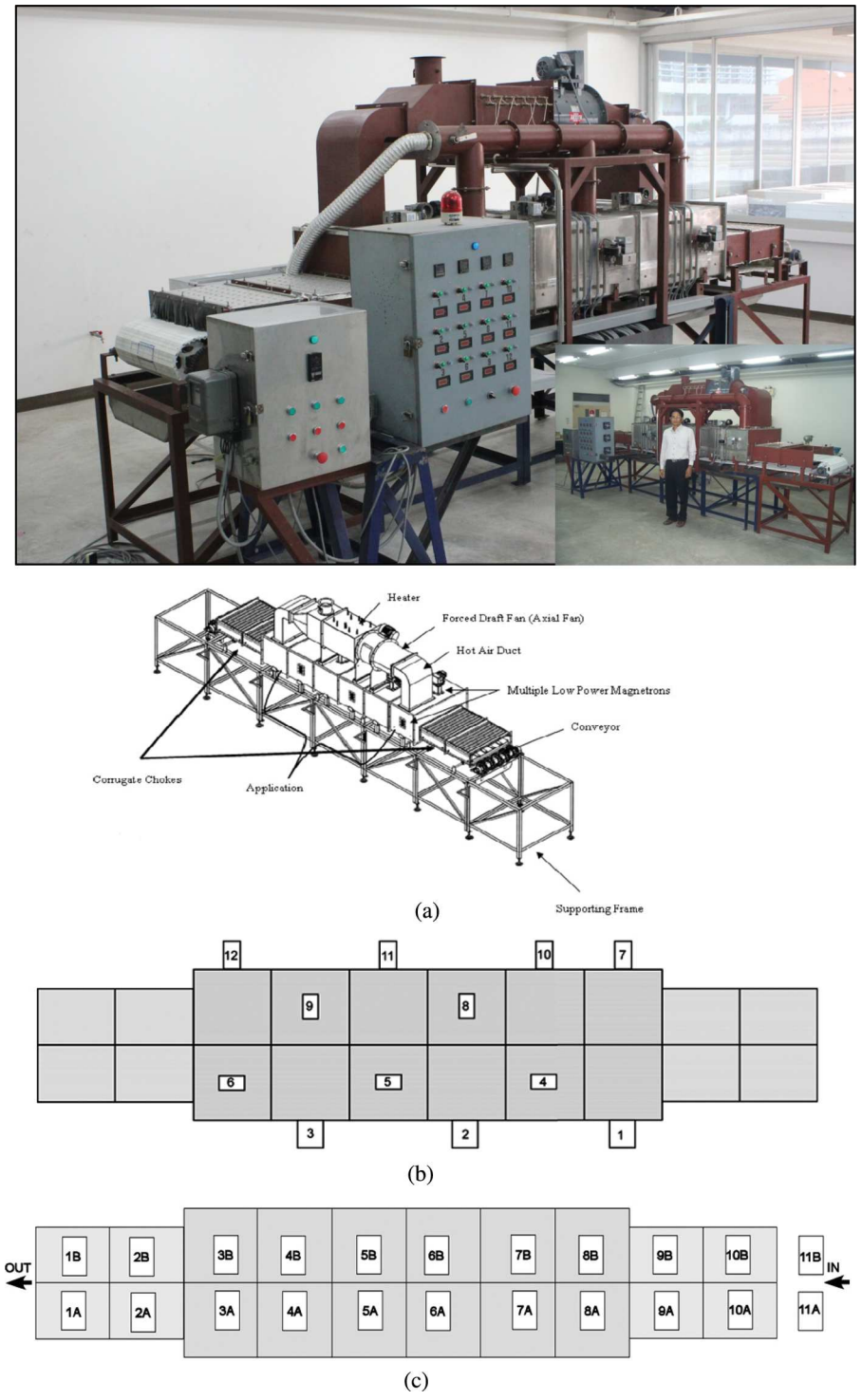

Figure 6. (a) Combined multifeed microwave-convective air and continuous belt (CMCB) system. (b) Schematic diagram of the positioning of the 12 feed magnetrons and (c) 22 packed-bed feed samples. Reprinted from Jindarat et al.[43] with permission from Taylor & Francis.

with the supplementary equipment or system, as follows:

- Traveling-wave applicator—A traveling wave is produced by matching the microwave source to a heated load, by using a rectangular or cylindrical waveguide.
- Near-field applicator–A resonant open-ended waveguide is used, or a cavity is attached directly to the end of a waveguide, and the energy is fed through slots into the cavity.
- Resonant applicators–These applicator types can be classified into single and multimode resonators, as

Downloaded by [Thammasat University Libraries] at 16:40 28 December 2015

shown in Fig. 5 (single mode)[14,40–42] and Fig. 6 (multimode).[43,44]

- Single-mode resonant applicator: A standing wave applicator is attached to the end of a waveguide line that feeds power to the microwave. Magnetron-generated microwave energy is transmitted directly along the propagation direction (+z) of a rectangular waveguide toward a water load, situated at the end of the waveguide. This setup ensures that a minimal amount of microwave energy is reflected back to the sample. The warmed water load is circulated through a cooling tower.
- Multimode resonant applicator (Fig. 6a): Microwave power is generated by 12 compressed air-cooled magnetrons, which are installed in an asymmetric position around a rectangular microwave cavity (exterior dimensions: $900 \times 450 \times 2700$ mm), as shown in Figs. 6b and 6c. Power is supplied directly to the drier by waveguides. The maximum microwave capacity is 9.6 kW at the operating frequency of 2.45 GHz, and the power setting can be adjusted in 800-W steps. The maximum working temperature is 180°C. Two open ends are essential in continuous processing equipment in order to allow the material to be heated to be placed on and removed from the conveyer belt. To maintain the microwave leakage ≤ 5 mW/cm^2 (as required by the U.S. Department of Health and Human Services), a mechanical blocking filter (corrugate choke) and microwave absorber zone filter are used at each of the open ends. To measure the specimen temperature, an infrared thermometer (accurate to ± 0.5°C) is installed at the opening ends after microwave processing. For example, a high-temperature microwave system generating microwave energy at 2.45 GHz and a maximum power of 6.0 kW >with a multimode system can result in a sample temperature of 2000°C.

Experiments

Laboratory-scale

The goal of drying is to remove moisture from a material without causing any adverse effects on its chemical, physical, or related properties.[45] MWD offers a high-performance drying method with multiple advantages, including fast drying rates and enhanced product quality, especially for food or other agricultural products. The microwave energy absorption level is strongly controlled by the initially wet product that can be used for determining heating of interior parts of material to be dried containing moisture and without distressing the exterior parts. MWD is well-characterized and very useful for the period in which the rate of drying is decreasing (also called the *falling rate period*). During this period, the diffusion is rate-limiting, leading to shrinkage of the whole structure and reduced moisture content at the surface.[46] Nevertheless, due to the occurrence of volumetric heating in MWD, gases are generated inside the material, while an internal pressure gradient develops that forces the water outside the material. As a result, MWD avoids the shrinkage of materials during drying. Furthermore, the combined use of MWD with other drying methods can improve the drying efficiency and product quality compared to using MWD or conventional drying alone.

However, especially during the final stages of MWD, excessive temperatures may develop along the corners or edges of the dried products, resulting in burning and byproduct production. It is difficult to control the final product temperature during hot-air MWD, and the product temperature should not exceed the hot-air temperature. For example, the penetration depth of microwave at an operating frequency of 2.45 GHz is inadequate for large-scale drying, whereas heating at 10–300 MHz can provide improved penetration depth. In special cases, fast mass transport might alter the product texture (e.g., cause "puffing" in food), which might be advantageous or disadvantageous depending on the required final product.[46]

Incorporating a conventional drying method with MWD can enhance the drying rate, while maintaining the quality of the final product. In an important work, Feng and Tang[47] evaluated a combined a spouted bed with microwave heating system to improve heating uniformity. A dryer was constructed for the drying tests. The system consisted of microwave source, rectangular cavity, hot-air source, spouted bed, and water load. In part of the spouted bed, it was constructed with microwave-transparent perspex which consisted of a cylindrical section and a 31° conical base as shown in Fig. 7. Based on the experimental investigation, drying

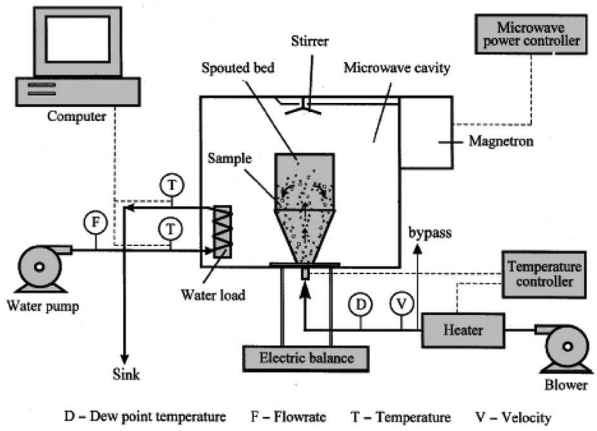

Figure 7. Schematic of microwave and spouted bed (MWSB) drying system. Reprinted from Feng and Tang[47] with permission from Wiley.

Downloaded by [Thammasat University Libraries] at 16:40 28 December 2015

tests were conducted at microwave power levels equivalent to 3.7, 4.9, and 6.1 W/g of evaporated apple dice. Evaporated Golden Delicious and Granny Smith apples were dried with a microwave power intensity of 4.9 W/g (wet basis). The hot air was controlled at 70°C. From this study, it can be found that the microwave and spouted bed (MWSB) method provided much more uniform heating within the microwave cavity. In addition, the drying time can be reduced moisture from evaporated apples to low moisture dehydrated apples (~5%) was significantly shortened as shown in Fig. 8.

Huang et al.[48] compared the effects of conventional freeze drying (CFD), microwave freeze drying (MFD), microwave vacuum drying (MVD), and conventional vacuum drying (CVD) on the texture, color, rehydration, sensory characteristics, and microstructure of chips made by blending apples with potatoes. The equipment consisted of two drying cavities, as shown in Fig. 9. Experimental test results revealed that the quality of MFD chips was better than that of CFD chips, and MFD required about half the time as CFD to dry materials to the same moisture content. The rehydration rate of MFD chips was about the same as that of CFD products, while the water retention of MFD samples was higher.

Jiang et al.[49] prepared banana chips through CFD and MFD methods in a dryer with a vacuum system, cold trap, and heating system. MFD decreased energy consumption by up to 35.7% and drying time by up to 40% compared to CFD. Increasing the heating power in the second drying stage of the MFD process decreased the energy consumption and drying time.

MVD has been widely considered as a high-performance dehydration method to achieve high-quality dried food products.[50] Wang et al.[51] studied the effects of gel type (i.e., cassava starch gel, fish gel, or mixed gel) and thermal treatment on the structure and quality of gel slices submitted to MVD. They used a lab-scale microwave-vacuum dryer in which the materials were rotated in the cavity, as described by Zhang et al.[52] The microwave-vacuum dryer was operated at an absolute pressure of 5 kPa and a turntable rotation speed of 5 rpm. The power intensity for each drying test was 2.1 W/g of the original mass of sample. The gel type and preparation conditions had profound effects on the gel characteristics, influencing the structure and quality attributes of the MVD-derived products.

An essential aspect when using laboratory-scale MWD systems regards the prediction of the final quality of the dried product. Using Young's modulus as a measured parameter for texture, a framework for predicting the effective modulus of a solid food material was developed and extended to four moisture-removal processes: frying, drying, microwave heating, and baking. Moisture and temperature data required for predicting Young's modulus were obtained from multiphase porous media-based models of the processes. In this way, the process and product parameters could be used to make physics-based predictions of texture.[53]

For the important effect on the drying, Namsanguan et al.[54] investigated an innovative two-stage drying concept. The work studied drying of shrimp using

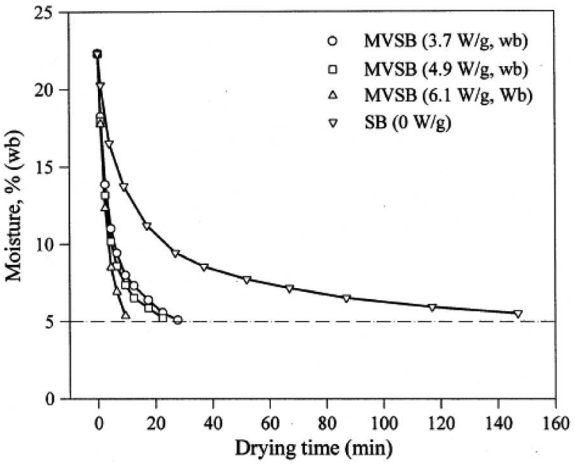

Figure 8. Drying curves of Red Delicious apples dried with MWSB method with different microwave power levels. Reprinted from Feng and Tang[47] with permission from Wiley.

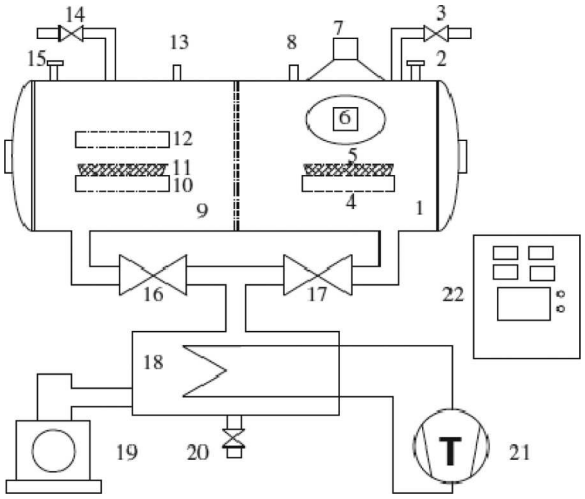

Figure 9. Schematic diagram of the microwave freeze dryer. 1, MFD chamber; 2, optical fiber temperature sensor; 3, MFD vacuum breakage valve; 4, sample supporting plate; 5, MFD sample; 6 and 7, microwave source; 8, pressure sensor for MFD chamber; 9, CFD chamber; 10 and 12, heating plate; 11, CFD sample; 13, pressure sensor for CFD chamber; 14, CFD vacuum breakage valve; 15, temperature sensor; 16, CFD vacuum valve; 17, MFD vacuum valve; 18, cold trap; 19, vacuum pump; 20, draining valve; 21, refrigeration compressor; and 22, control system. Reprinted from *Journal of Food Engineering*, Vol. 103, L. Huang, M. Zhang, A. S. Mujumdar, and R.-X. Lim, "Comparison of four drying methods for re-structured mixed potato with apple chips," pp. 279–284, 2011, with permission from Elsevier.

Downloaded by [Thammasat University Libraries] at 16:40 28 December 2015

a superheated steam dryer. Shrinkage, color, rehydration behavior, toughness and hardness, and microstructure of dried shrimp were measured. The results indicated that a superheated steam dryer followed by a hot air dryer can offer redder shrimp compared to shrimp dried in a single-stage superheated steam dryer and no improvement in terms of shrinkage and rehydration behavior.

Commercial-scale

Hybrid systems associated with supplementary systems

Using a hybrid microwave system associated with supplementary systems can considerably enhance the drying rate and the final product quality. Jindarat et al.[43] constructed a combined multifeed microwaved-convective air and continuous belt (CMCB) system, as shown in Fig. 6. They analyzed the energy consumption during drying of a non-hygroscopic porous packed bed, focusing on conditions of industrialized microwave processing. The overall drying and energy consumption results depended on the porosity of structure, hot-air temperature, and magnetron location. Using continuous microwave application had several advantages over the conventional method, such as shorter processing times, volumetric dissipation of energy throughout the product, and less energy consumption. Their results provide a fundamental understanding of the drying process using an industrial-size CMCB system.

Recently, Charoenvai et al.[55] compared a single microwave dryer with a combination microwave–hot-air dryer in terms of their product properties and energy consumption during the drying of Durian peel particle boards. Their results showed that a CMBM would consume less energy than the single-microwave system (specific energy consumption (SEC) of 0.16509 MJ/kg), while providing the same or better product qualities than the combined system. These findings indicate the potential of the CMCB system to reduce electrical energy consumption. Moreover, using the combined system permitted quicker drying at an increased hot-air temperature. If this CMBM technology were to be implemented in industry, it could decrease production costs by lowering electrical energy consumption microwave–hot-air dryer in terms of their product properties and energy consumption during the drying of Durian peel particle boards. Their results showed that a CMBM would consume less energy than the single-microwave system (SEC of 0.16509 MJ/kg), while providing the same or better product qualities than the combined system. These findings indicate the potential of the CMCB system to reduce electrical energy consumption. Moreover, using the combined system permitted quicker drying at an increased hot-air temperature. If this CMBM technology were to be implemented in industry, it could decrease production costs by lowering electrical energy consumption.

In 2013, Jindarat et al.[56] analyzed the energy consumption during the drying of biomaterials using a combined unsymmetrical double-feed microwave and vacuum system (CUMV). The CUMV drying was more rapid in the continuous than in the pulsed microwave operation mode. Figures 10a and 10b show the rough color shades of tea leaves dried by the pulsed and continuous microwave operation modes, respectively. The best color was achieved by continuous MWD. Furthermore, the specific energy consumption values were relatively low in the continuous compared to the pulsed microwave operation mode.

The industrial-hybrid microwave system has been developed continuously by many microwave manufacturers such as Püschner and his group,[57] such as a microwave freeze drying, which can cut down drying time from days into hours, as well as Micro Denshi,[58] who constructs the microwave continuous equipment. It can be used to drying of equipment of ceramic molding, ferrite products swelling, and equipment for snack foods.

Safety and regulation

The health and safety of microwave processing cannot be neglected when microwave systems are operated by humans or in an environment where humans are present. This section details the limitations and conditions of microwave exposure, as regulated by relevant associations. Microwave processing of dielectric materials may involve a risk of microwave exposure to humans and biological tissues if certain precautions are not taken into account. The U.S. Federal Communication

Figure 10. Tea leaves dried under vacuum pressure at 385 Torr, with the (a) pulsed or (b) continuous microwave operation mode at a microwave power of 800 W. Reprinted from Jindarat et al.[56] with permission from Taylor & Francis.

Downloaded by [Thammasat University Libraries] at 16:40 28 December 2015

Commission and Occupational Health and Safety Administration[59] have provided exposure limits for microwave energy, considering the effects of microwave radiation on human health from the perspectives of exposure source (e.g., medical devices, amateur radio, cellular phone base stations, hand-held cell phones, heating and sealing devices, microwave ovens, radio broadcast antennae, traffic radar devices, etc.), hazard location, exposure time, and solution. Absorption and distribution of microwave energy are strongly dependent on body size and orientation, as well as the frequency and polarization of the incident radiation.

The specific absorption rate refers to the power absorbed by a body when exposed to electromagnetic radiation. The current specific absorption rate limit is 4 W/kg. To be conservative, organizations generally use 1/10th of this value for setting standards, especially for radiofrequency and microwave exposure limits. For occupational exposure, the field strength is averaged over a 6-min time period. For public exposure, the field strength is averaged over a 30-min period, as recommended by guidelines or standards of the International Radiation Protection Association,[60] the Institute of Electrical and Electronics Engineers,[61,62] the National Radiological Protection Board, and the Health Protection Agency.[63] It is strongly recommended that laboratory and industrial microwave systems be tested periodically for any leakage, and that suitable measures be taken to stop any substantial leakage before the system is used further.

In the past, there have been reports on the effects of electromagnetic (EM) fields on the eye.[64,65] Nevertheless, the analysis generally was conducted based on the maximum SAR values permitted by public safety standards.[66,67] The research on transport phenomena in a porous medium subject to EM fields is sparse except for our group. Some researchers investigated the effects of EM fields on the eye temperature.[68] However, most previous studies of human exposed to EM fields hardly considered the heat transfer causing an incomplete analysis to the results. The thermal modeling of human tissue is important as a tool to investigate the effect of external heat sources and to predict the abnormalities in the tissue. At the beginning, most studies of heat transfer analysis in the eye used a heat conduction equation.[69–71] Some studies carried out on the natural convection in the eye based on heat conduction model.[72,73]. Ooi and Ng[73,74] studied the effect of aqueous humor (AH) hydrodynamics on the heat transfer in the eye based on heat conduction model. Meanwhile, the bioheat equation, introduced by Pennes,[75] which is based on the heat diffusion equation for a blood perfused tissue, is used for modeling of the heat transfer in the eye as well.[76,77] Ooi and Ng also developed a three-dimensional model of the eye,[78] extending their 2-D model.[78] Most previous studies of humans exposed to EM fields hardly considered the heat transfer, causing an incomplete analysis to the results. Therefore, modeling of heat transport in human tissue is needed to cooperate with the modeling of electromagnetic (EM) in order to completely explain their interaction characteristics for approaching such phenomena. In 2011, Wessapan et al.[79] proposed a numerical study to simulate the effects of dielectric shield on the specific absorption rate (SAR) and the temperature increase in the human body exposed to leakage microwave energy. Figures 11a and 11b show a vertical cross-section through the middle plane of the human trunk model. The meshes of the human model as well as the SAR and temperature distribution in the case of unshielded human model exposed to the microwave power density of 5 mW/cm^2 at the frequency of 300 MHz. It is found that the temperature distributions are not proportional to the local SAR value, as shown in Fig. 11b.

In 2013, Wessapan and Rattanadech[80] presented a numerical analysis of the SAR and the heat transfer in a heterogeneous human eye model exposed to EM fields of 900 and 1800 MHz. The SAR value and the temperature distribution in various tissues in the eye during exposure to EM fields were obtained by numerical simulation of EM wave propagation, and a heat transfer model was then developed based on the natural convection and porous media theories. EM energy is emitted by an EM radiation device and falls on the eye with a particular power density, as shown in Fig. 12a. Fig. 12b shows the simulation of an electric field pattern inside the eye exposed to the EM fields in TM mode operating at the frequencies of 900 and 1800 MHz propagating along the vertical cross-section human eye model. Due to the different dielectric characteristics of the various tissue layers at different operating frequencies, a different fraction of the supplied EM energy will become absorbed in each layer in the eye. In the next year, Wessapan and Rattanadech[81] also published the influence of ambient temperature on heat transfer in the human eye during exposure to electromagnetic fields at 900 MHz. This work focused on the transport phenomena that occur within the eye exposed to EM fields in hot, moderate, and cold ambient temperatures. In this study, the effect of thermoregulation mechanisms has been neglected due to the small temperature increase occurred during exposure process. The convective coefficient due to the blood flow inside the sclera is set to 65 W/m^2K.[81] In order to study the heat transfer in the eye, the coupled model of EM wave propagation

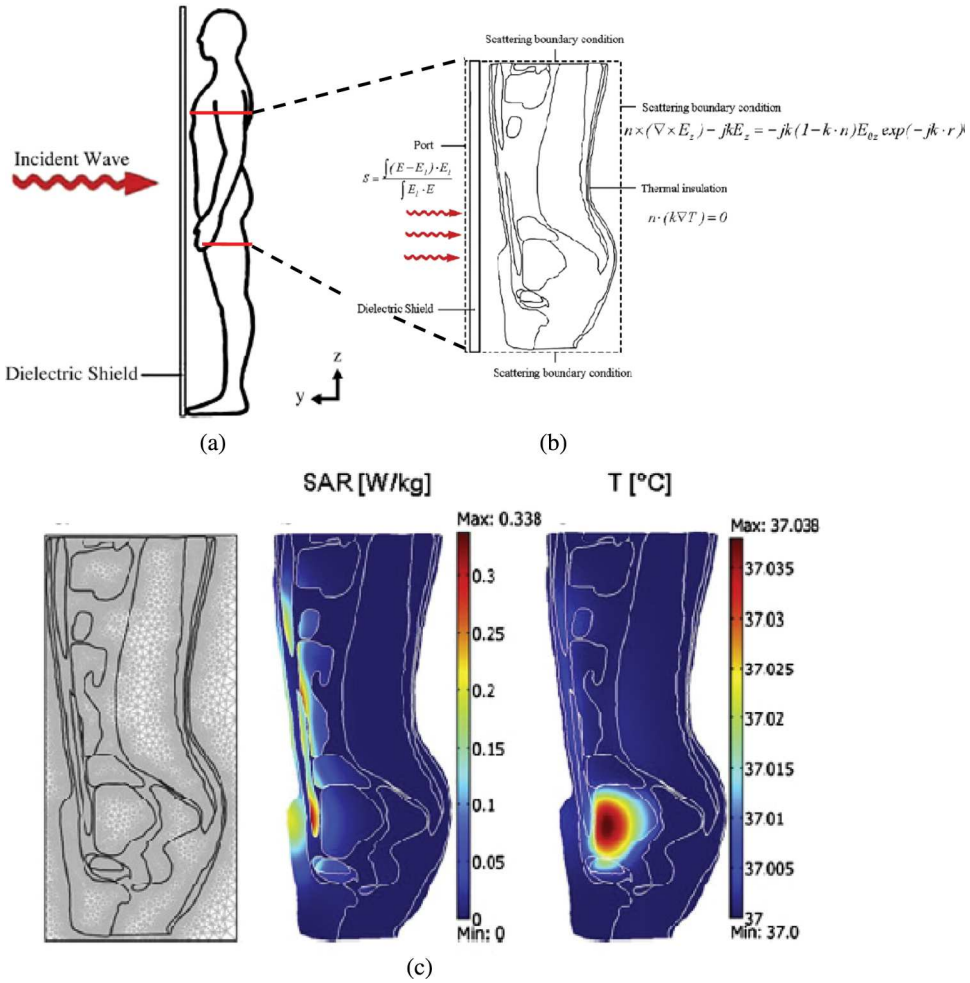

Figure 11. (a) Human model with dielectric shield. (b) Physical model and boundary condition used for analysis. (c) SAR and temperature distribution in the human model exposed to the microwave power density of 5 mW/cm^2 at the frequency of 300 MHz. Reprinted from *International Communications in Heat and Mass Transfer*, Vol. 38, T. Wessapan, S. Srisawatdhisukul, and P. Rattanadecho, "The effects of dielectric shield on specific absorption rate and heat transfer in the human body exposed to leakage microwave energy," pp. 255–262, 2011, with permission from Elsevier.

and unsteady heat transfer as well as the boundary conditions is then investigated. Due to these coupled effects, the electric field distribution in Fig. 13 and the SAR distribution as shown in Fig. 14 are then converted into heat by absorption of the tissue.

Theoretical investigations

In theoretical analysis, the absorbed microwave power is generally assumed to decay exponentially into the absorbed material, as in Lambert's law. Although this law is valid for samples of large dimensions (in which the sample thickness is much larger than the penetration depth), it is not valid for small samples (in which the sample thickness is smaller than the penetration depth).[82] The electromagnetic field within a small sample can be analyzed by solving Maxwell's equations. Two-dimensional (2D) models involving Maxwell's equations have been used in the study of numerous heating processes in microwave applicator configurations.[9,13] Most previous investigations considered simulations of microwave heating of homogeneous materials. Heat and mass transfer processes in porous materials have been studied from a theoretical perspective for several decades. To explain the physical phenomenon of drying in porous materials, most proposed theories use Whitaker's theory[83] as a basis and take one of three approaches:

1. One-variable models employ a single diffusion equation and are used for simple configurations.
2. Two-variable models use two independent variables (temperature and moisture content) and neglect the effects of pressure buildup. These models can be used to describe the most important features of low-temperature drying.
3. Three-variable models use three independent variables (temperature, moisture content, and pressure

Downloaded by [Thammasat University Libraries] at 16:40 28 December 2015

Downloaded by [Thammasat University Libraries] at 16:40 28 December 2015

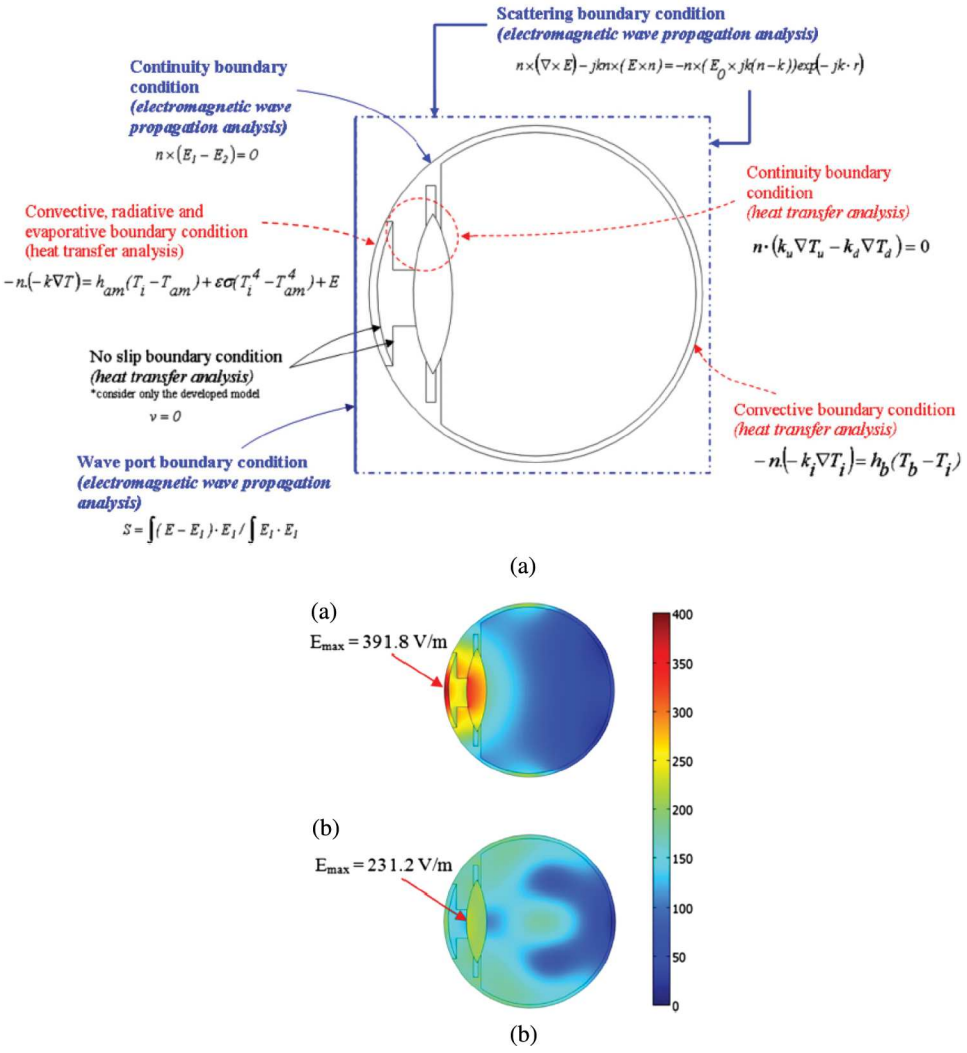

Figure 12. (a) EM wave propagation and heat transfer with boundary conditions and (b) electric field distribution (V/m) in human eye exposed to the EM power density of 100 mW/cm^2 at the frequencies of (a) 900 MHz and (b) 1800 MHz. Reprinted from *International Journal of Heat and Mass Transfer*, Vol. 64, T. Wessapan and P. Rattanadecho, "Specific absorption rate and temperature increase in the human eye due to electromagnetic fields exposure at different frequencies," pp. 426–435, 2013, with permission from Elsevier.

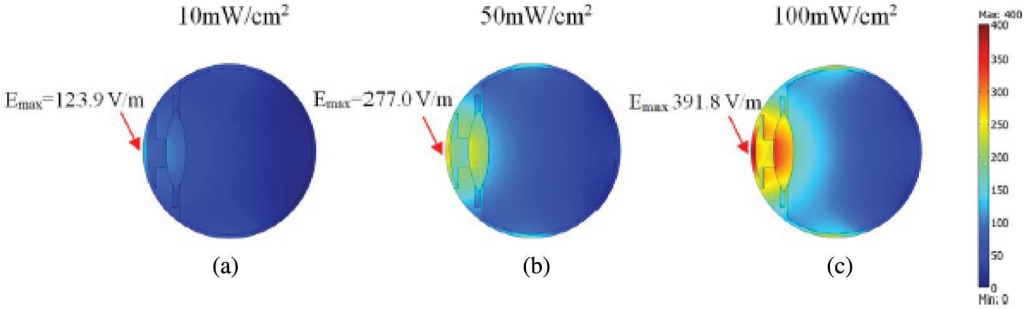

Figure 13. Electric field distribution (V/m) in the eye exposed to the EM power densities of (a) 10 mW/cm^2, (b) 50 mW/cm^2, and (c) 100 mW/cm^2. Reprinted from *International Journal of Heat and Mass Transfer*, Vol. 70, T. Wessapan and P. Rattanadecho, "Influence of ambient temperature on heat transfer in the human eye during exposure to electromagnetic fields at 900 MHz," pp. 378–388, 2014, with permission from Elsevier.

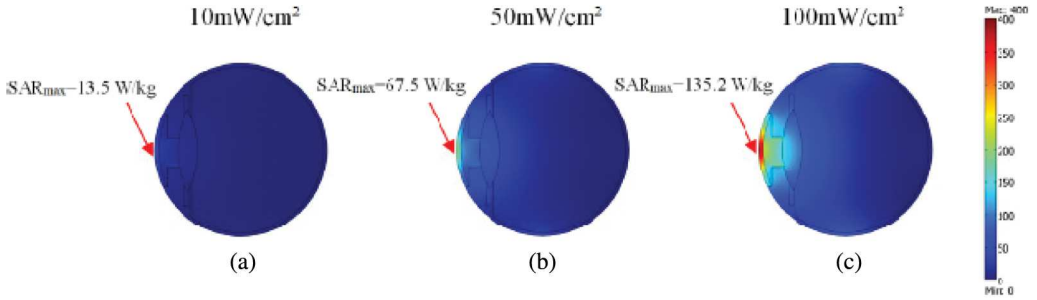

Figure 14. SAR distribution (W/kg) in the eye exposed to the EM power densities of (a) 10 mW/cm^2, (b) 50 mW/cm^2, and (c) 100 mW/cm^2. Reprinted from *International Journal of Heat and Mass Transfer*, Vol. 70, T. Wessapan and P. Rattanadecho, "Influence of ambient temperature on heat transfer in the human eye during exposure to electromagnetic fields at 900 MHz," pp. 378–388, 2014, with permission from Elsevier.

Downloaded by [Thammasat University Libraries] at 16:40 28 December 2015

buildup), thereby providing more detail than two-variable models by describing all of the drying behaviors. Three-variable models can be used in cases of high-temperature convective drying, radio-frequency drying, etc.

Most studies have utilized one- or two-variable models in the case of conventional drying processes,[84,85] because these models are easier to discretize and solve than three-variable models. A few studies have used three-variable models—notably, Perre and Turner,[13] Ni and Datta,[86] Feng et al.,[87] and Rattanadecho et al.[88] Some researchers have studied the interactions between microwave energy and heat and mass transfer phenomena of porous material, such as the microwave heating and drying processes.[13,40,89] Most previous works have not mentioned 2-D pressure buildup or the flow field inside porous materials with varying particle sizes. A recent work performed a systematic investigation of heat and mass transport and pressure buildup phenomena during the MWD of a uniform porous packed bed under microwave energy at a frequency of 2.45 GHz using a rectangular waveguide (TE_{10} mode).[18] The unsaturated porous packed beds were composed by glass beads, water, and air. In this study, the effect of pressure buildup was neglected in the mathematical modeling. It was found that the particle size and thickness of the porous packed bed were primary factors determining heat and mass transport with multiphase flow.

Thermal equilibrium model for drying

Studying microwave-assisted batch fluidized bed drying, Chen et al.[90] examined three microwave heating patterns (uniform, sinusoidal, and rectangular) with a constant average electric field strength of 1000 V/m. An apple was used as are a presentative porous material. Sinusoidal and rectangular heating patterns gave higher drying rates and shorter drying times than the uniform pattern under the same electric field strength. The microwave power absorbed by particles varied with the electrical field strength during drying, and the average value gradually decreased with time. Intermittent microwave heating gave the shortest drying time but consumed the greatest amount of microwave energy.

Another important issue in microwave drying comes from microwave heating process regards hot-spot formation. Bhattacharya and Basak[91] analyzed the temperature dynamics during microwave processing of 2% agar gel, potato, beef, and marinated shrimp. They assessed the role of the absorbed power in forecasting heating scenarios during microwave processing. They assumed uniform plane microwave radiations with incident intensities of I_L and I_R from the left and right sides, respectively, as shown in Fig. 15. The absorbed power distribution showed three distinct behavior regimes (i.e., thin, resonating, and thick sample), depending on the sample length and dielectric property of the material. Nearly uniform power distributions were

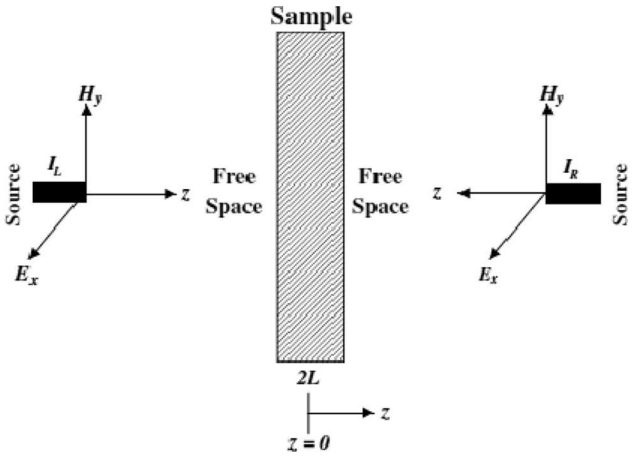

Figure 15. Schematic illustration of a 1-D sample exposed to plane electromagnetic radiations from the left and right sides. Reprinted from *Food Research International*, Vol. 39, M. Bhattacharya and T. Basak, "On the analysis of microwave power and heating characteristics for food processing: Asymptotes and resonances," pp. 1046–1057, 2006, with permission from Elsevier.

Downloaded by [Thammasat University Libraries] at 16:40 28 December 2015

attained within thin samples, compared to exponential distributions within thick samples. In the resonating regime (between the thin and thick sample regimes), power distributions exhibited spatial oscillations.

To develop theoretical and experimental analyses of the MWD of uniform porous materials, Feng et al.[87] developed a mathematical model to predict heat and mass transport in microwave and spouted bed combined (MWSB) drying of porous materials (diced apple). A total gas-pressure equation was taken into account internal vapor generation during microwave drying. The assumptions in the model are as follows: (a) local thermodynamic equilibrium exists. That is the solid, liquid, and gas phases at the same average temperature at any moment in the control volume; (b) solid, liquid, and gas phases are continuous; (c) binary gas mixture of air and vapor obeys the ideal gas; (d) local vapor pressure as a function of moisture content and temperature can be calculated sorption isotherm; and (e) the material used in this model is diced apple. In the model, transport relations as fluid velocity in a multiphase porous medium are given by the generalized Darcy's law. For governing equations considered in this study, mass transfer to occur only in the radial direction and one-dimensional problem in spherical coordinate was formulated. The total moisture transport equation can be written as

$$\frac{\partial X_l}{\partial t} = \frac{1}{r^2}\frac{\partial}{\partial r}\left[D_x r^2 \frac{\partial X_l}{\partial r} + D_T r^2 \frac{\partial T}{\partial r} + D_p r^2 \frac{\partial P_g}{\partial r}\right] \quad (5)$$

where $X_l \approx X_f + X_b$

$$D_X = D_X^f + D_X^b + D_X^v$$
$$D_T = D_T^f + D_T^b + D_T^v$$
$$D_P = D_P^f + D_P^b + D_P^v$$

A MWSB dryer was developed for drying test and validating the model simulation, as shown in Fig. 16. This system consisted of a 2.45 GHz microwave supply system and supply system. In this study, the constructed model can be used as an effective toll to predict moisture, temperature, and pressure for MWSB of the materials to be dried. For example, the case of moisture content for MWSB [microwave power = 4 W/g, air temperature = 70 °C, and SB (air temperature = 70 °C)] drying as shown in Fig. 17. It was found that simulation prediction is in good agreement with experiments for both drying methods.

In another investigation, Suwannapum and Rattanadecho[92] numerically ascertained based on a one dimensional (1-D), three-variable method by studying the effects of sample thickness and size on the overall heat and multiphase flow, and then compared their

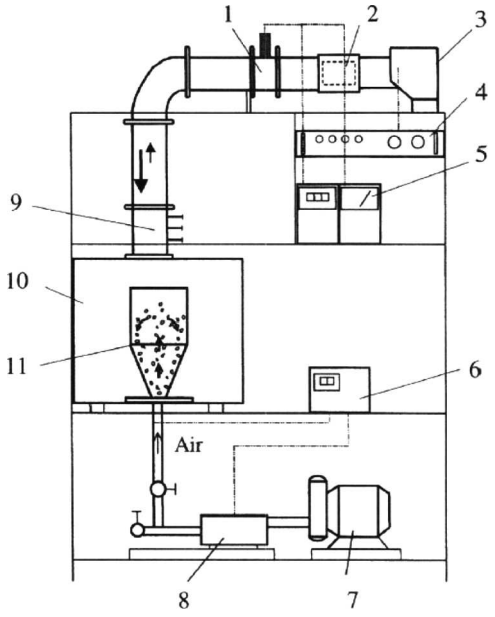

Figure 16. 2.45 GHz MWSB dryer. 1, Direction coupler; 2, circulation; 3, magnetron; 4, power controller; 5, power meter; 6, temperature controller; 7, air pump; 8, heater; 9, three-stub tuner; 10, Microwave cavity; 11, spouted bed. Reprinted from Feng et al.[87] with permission from Wiley.

theoretical findings with experimental results. A schematic of the porous packed bed model used in the heat and mass transport analysis is shown in Fig. 18. Based on the conservation of mass and energy in capillary porous materials, the governing equation of mass and energy of all phases can be derived by the volume-averaging technique.[83] From the results, it can be concluded that the particle size significantly affects the pressure buildup, water saturation, and fluid movement inside the unsaturated porous packed bed. In addition, the saturated distribution can change the electromagnetic field and heat and mass transfer patterns. The sample

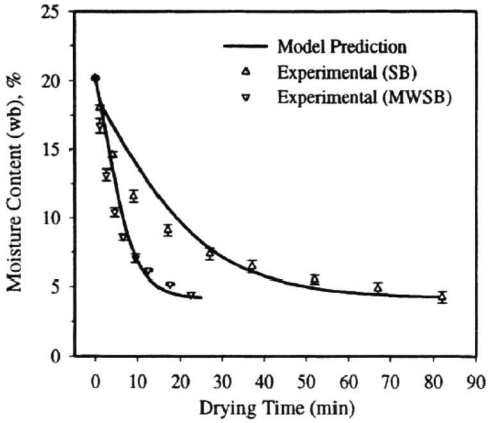

Figure 17. Moisture content: model prediction versus experimental results for MWSB (microwave power = 4 W/g, air temperature = 70 °C, and SB (air temperature = 70 °C) drying. Reprinted from Feng et al.[87] with permission from Wiley.

Downloaded by [Thammasat University Libraries] at 16:40 28 December 2015

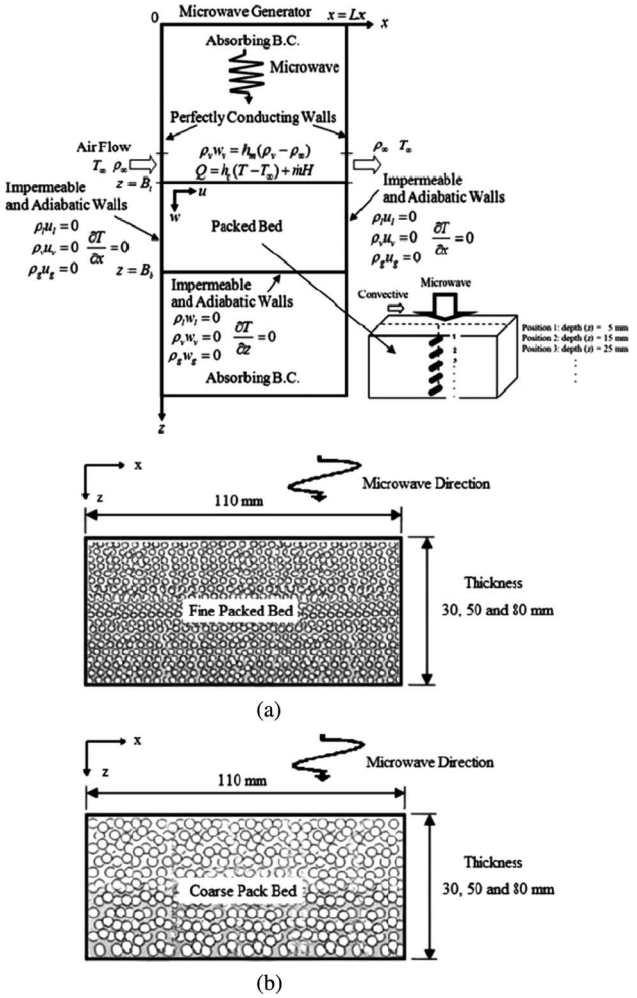

Figure 18. Physical model and measurement points. Reprinted from Suwannapum and Rattanadecho[92] with permission from Taylor & Francis.

thickness strongly influenced heating behavior by changing the electromagnetic field patterns, microwave power absorption, and temperature distribution profile results.

By assuming that moisture transport in a sample can be described by the mass balance equations of water and water vapor, and considering Darcy's and Fick's laws, the moisture transport equation can be expressed in the 2D scalar form, as follows:

$$\phi\frac{\partial}{\partial t}\{\rho_l s+\rho_v(1-s)\}+\frac{\partial}{\partial x}\left[\rho_l\frac{KK_{rl}}{\mu_l}\left(\frac{\partial p_c}{\partial x}-\frac{\partial p_g}{\partial x}\right)+\rho_v\frac{KK_{rg}}{\mu g}\left(-\frac{\partial p_g}{\partial x}\right)-D_m\frac{\partial p_y}{\partial x}\right]+\frac{\partial}{\partial z}\left[\rho_l\frac{KK_{rl}}{\mu_l}\left(\frac{\partial p_c}{\partial z}-\frac{\partial p_g}{\partial x}+\rho_l g_z\right)+\rho\frac{KK_{rg}}{\mu_g}\left(-\frac{\partial p_g}{\partial x}+\rho_l g_z\right)-D_m\frac{\partial p_y}{\partial x}\right]=0 \tag{6}$$

Again, considering Darcy's and Fick's laws and assuming that the gaseous phase is an ideal mixture of perfect gases, the pressure equation can be expressed in the 2D scalar form:

$$\phi\frac{\partial}{\partial t}\{\rho_a(1-s)\}+\frac{\partial}{\partial x}\left[\rho_a\frac{KK_{rg}}{\mu g}\left(-\frac{\partial p_g}{\partial x}\right)-D_m\frac{\partial p_a}{\partial x}\right]+\frac{\partial}{\partial z}\left[\rho_a\frac{KK_{rg}}{\mu g}\left(-\frac{\partial p_g}{\partial z}+\rho_g g_z\right)-D_m\frac{\partial p_a}{\partial z}\right]=0 \tag{7}$$

It is assumed that thermal equilibrium exists among the water, gas, and matrix at any location in the unsaturated packed bed. Considering the enthalpy transport, heat conduction, latent heat transport, and volumetric heat generation, the energy balance equation is represented by:

$$\frac{\partial}{\partial t}\left[\left(\rho C_p\right)_T T\right]+\frac{\partial}{\partial x}\left[\{\rho_l C_{pl}u_l+(\rho_a C_{pa}+\rho_v C_{pv})u_g\}T\right]\frac{\partial}{\partial z}\left[\{\rho_l C_{pl}w_l+(\rho_a C_{pa}+\rho_v C_{pv})w_g\}T\right]+H_v\dot{m}=\frac{\partial}{\partial x}\left[\lambda_{eff}\frac{\partial T}{\partial x}\right]+\frac{\partial}{\partial Z}\left[\lambda_{eff}\frac{\partial T}{\partial z}\right]+Q \tag{8}$$

where $(\rho C_p)_T T$ is the effective heat capacitance of the water-gas matrix mixture:

$$\left(\rho C_p\right)_T T=\rho_l C_{pl}\phi s+\rho_g C_{pg}\phi(1-s)+\rho_p C_{pp}(1-\phi)$$

$$\dot{m}=\frac{\partial}{\partial t}\{\rho_v\phi(1-s)\}+\frac{\partial}{\partial x}\left[D_m\frac{\partial\rho_v}{\partial x}+\frac{\partial}{\partial z}\right]-\frac{\partial}{\partial z}\left[\rho_v\frac{KK_{rg}}{\mu g}\rho_g g_z-D_m\frac{\partial pv}{\partial z}\right]$$

$$\lambda_{eff}=\frac{0.80}{1+3.78exp^{-5.95s}}$$

$$Q=\omega\varepsilon_r' E^2=2\pi f\varepsilon_0\varepsilon\prime_r(tan\,\delta)E_y^2$$

By applying the boundary conditions for solutions of the governing equations, these equations can be applied on a permeable surface, impermeable surface, or layer interface, as detailed below.

Permeable surface

Boundary conditions on a permeable surface (i.e., energy exchange at an open boundary) can be described as follows:

$$-\lambda_{eff}\frac{\partial T}{\partial z}=h_c(T-T_\infty)+\dot{m}H_v \tag{9}$$

Downloaded by [Thammasat University Libraries] at 16:40 28 December 2015

Mass transfer at the permeable surface is modeled by a constant mass transfer coefficient, which is related to the local water vapor flux density:

$$\dot{m} = \rho_v w_v = h_m(\rho_v - \rho_{v\infty}) \tag{10}$$

where ρ_v is the density of water vapor at the permeable surface, and $\rho_{v\infty}$ is the reference vapor density in the gas phase surrounding the permeable surface. Therefore, the total pressure on the permeable surface can be defined as:

$$p_g = p_0 \tag{11}$$

Impermeable surface

The boundary condition at a closed impermeable boundary (i.e., symmetric, without heat or mass exchange) can be described by the following equations:

$$\frac{\partial T}{\partial x} = \frac{\partial T}{\partial z} = 0 \tag{12}$$

$$\frac{\partial u}{\partial x} = \frac{\partial u}{\partial z} = 0 \tag{13}$$

The simulated results for heat, multiphase flow, and pressure buildup in an unsaturated porous packed bed subjected to microwave energy are shown in Figs. 19 and 20. The temperature profiles of thin- and thick-layer packed beds are differen, because the sample thickness affects the electromagnetic wave pattern inside the cavity and the sample (as explained in the previous section). Compared to a thick sample, a thin sample can more easily induce a resonance effect or strong standing wave, corresponding to a greater effect of the absorbed microwave power and the thermal energy transformation inside the sample.

Figure 20 shows the numerical results of the microwave power absorption profile as a function of time for a sample with a thickness of 5 cm. The temperature and microwave power absorption profile results are linked because the absorbed microwave power is mainly electromagnetic energy, which is transformed into thermal energy.

Figure 21 shows the temperature, water saturation, and pressure buildup distributions for an F-bed subjected to microwave heating for 10, 100, and 360 mins, respectively. The profiles displayed a wavy behavior. Regardless of thickness, all of the packed beds had cold- and hot-spot zones inside the samples.

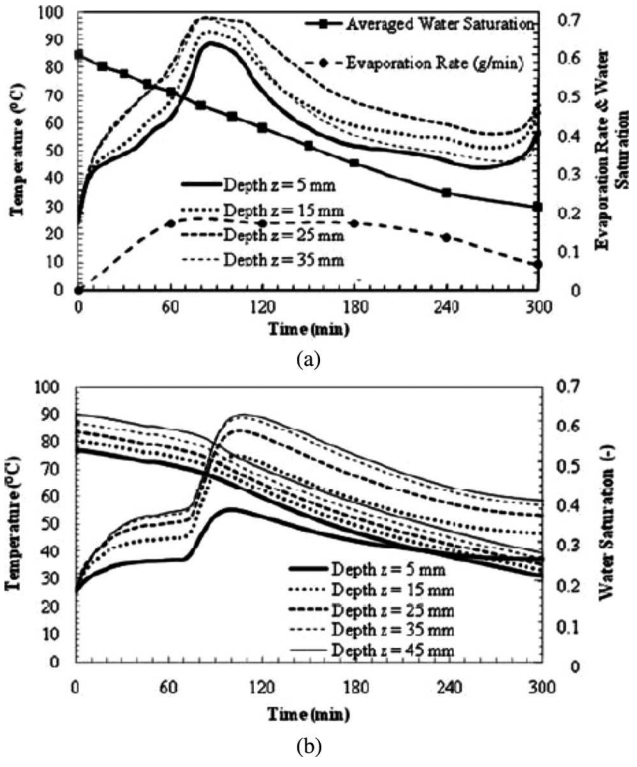

Figure 19. Temperature and water saturation profiles over time at different depths for the F-bed (sample thickness = 50 mm): (a) experimental and (b) simulated results. Reprinted from Suwannapum and Rattanadecho[92] with permission from Taylor & Francis.

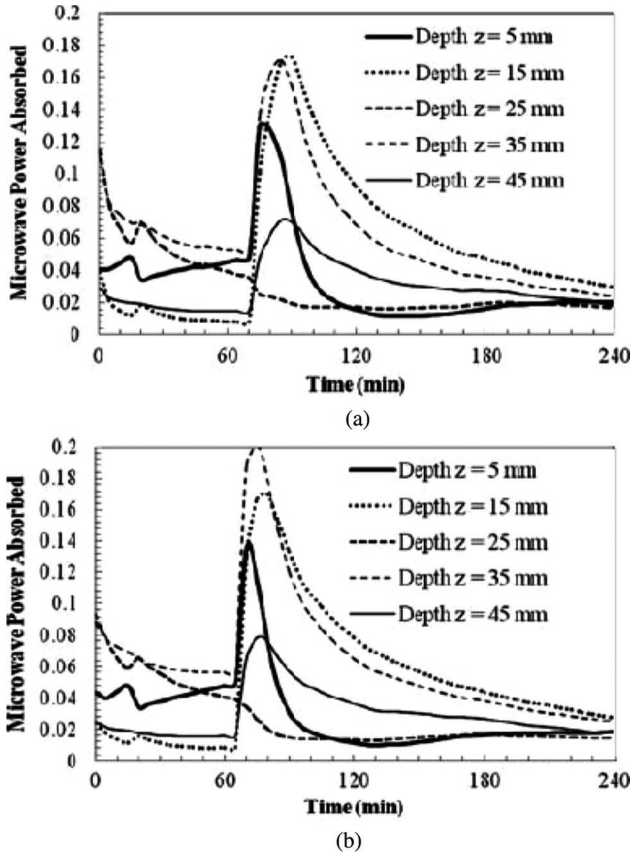

Figure 20. Microwave power absorption profiles overtime at different depths (sample thickness = 50 mm): (a) F- and (b) C-bed. Reprinted from Suwannapum and Rattanadecho[92] with permission from Taylor & Francis.

Downloaded by [Thammasat University Libraries] at 16:40 28 December 2015

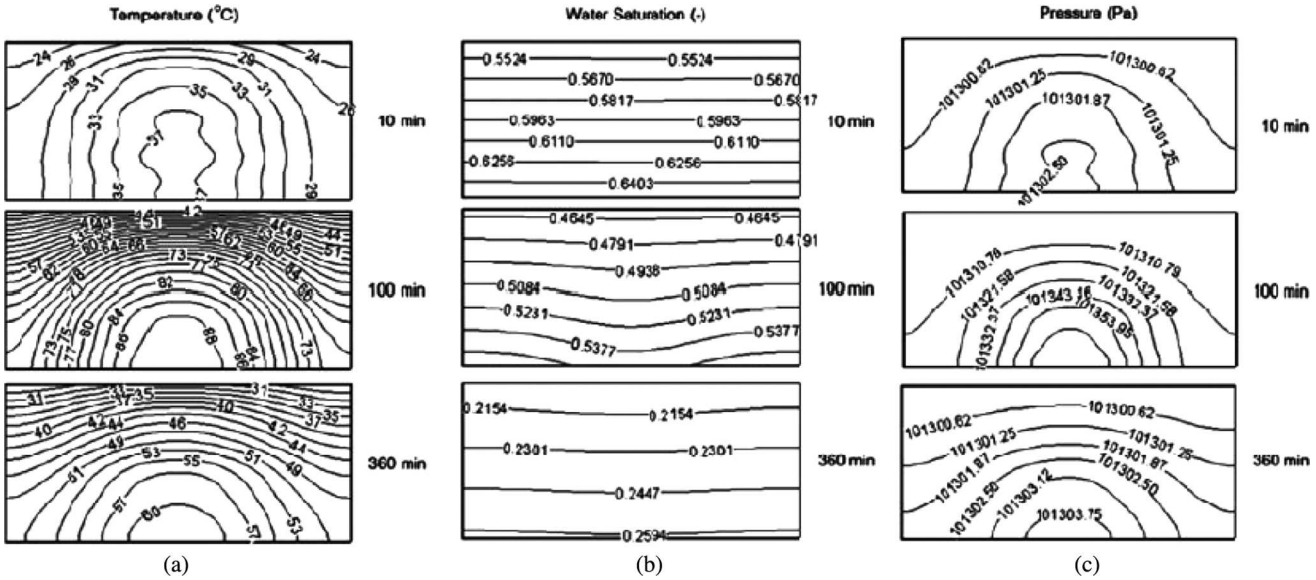

Figure 21. Contour plots for F-bed (50 mm) at drying times of 10, 100, and 360 min. (a) Temperature, (b) water saturation, and (c) pressure contours. Reprinted from Suwannapum and Rattanadecho[92] with permission from Taylor & Francis.

Sungsoontorn et al.[93] proposed a three-variable model by focusing on the microwave frequency, particle size, and electric-field intensity, to predict the heat and mass transfer and pressure build-up profiles in unsaturated porous media subjected to microwave energy. They employed a 1D analytical model for the MWD of the sample, utilizing Eqs. (14)–(16) in association with the boundary and initial conditions in Eqs. (17)–(19). Microwave energy absorption was assumed to decay exponentially into the sample following Lambert's law. This study focused on the absorbed microwave energy, temperature, and moisture distributions within the porous materials, as shown in Figs. 22–25, and discussed the multiphase flow behavior in detail. Variations in frequency, particle size, and electric field intensity were found to play important roles in the overall drying kinetics. This research will serve as a fundamental tool for applications involving the MWD of porous media.

Energy conservation equation

$$\frac{\partial}{\partial t}\left[\left(\rho C_p\right)_T T\right]+\frac{\partial}{\partial z}\left[\left\{\rho_l C_{pl} w_l+\left(\rho_a C_{pa}+\rho_v C_{pv}\right)w_g\right\}T\right] = \frac{\partial}{\partial z}\left(\frac{\partial T}{\partial z}\right)-H_v\left(\frac{\partial}{\partial t}\left(\rho_v\phi(1-s)\right)\right)+\frac{\partial}{\partial z} \times\left(\left(\rho_v\frac{KK_{rg}}{\mu_g}\left(\frac{\partial P_g}{\partial z}+\rho_g g_z\right)-\rho_g D_m\frac{\partial}{\partial z}\left(\frac{\rho_v}{\rho_g}\right)\right)\right)+Q \tag{14}$$

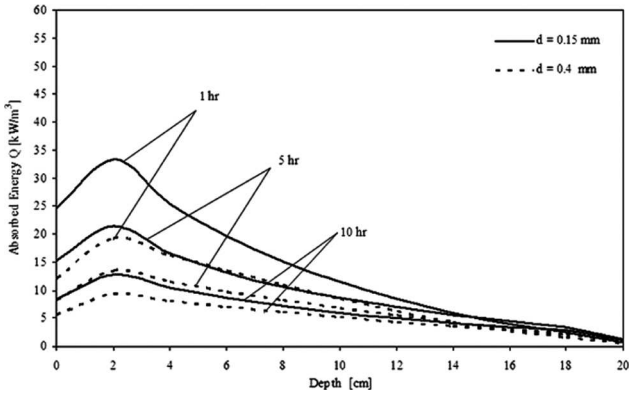

Figure 22. Energy-absorption profiles at various particle sizes ($f = 2.45$ GHz, $E_{in} = 4{,}200$ V/m, $S_{in} = 0.7$). Reprinted from Sungsoontorn et al.[93] with permission from Taylor & Francis.

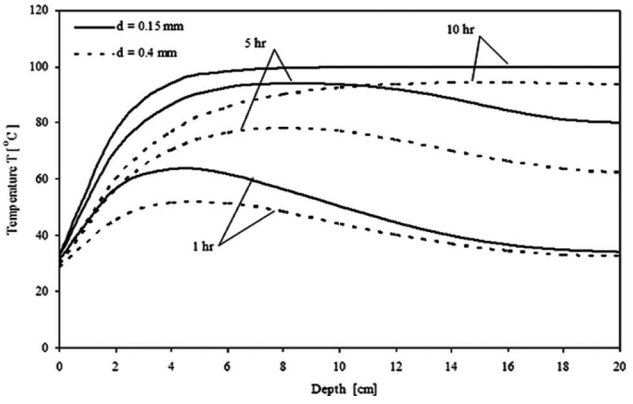

Figure 23. Temperature profiles at various particle sizes ($f = 2.45$ GHz, $E_{in} = 4{,}200$ V/m, $S_{in} = 0.7$). Reprinted from Sungsoontorn et al.[93] with permission from Taylor & Francis.

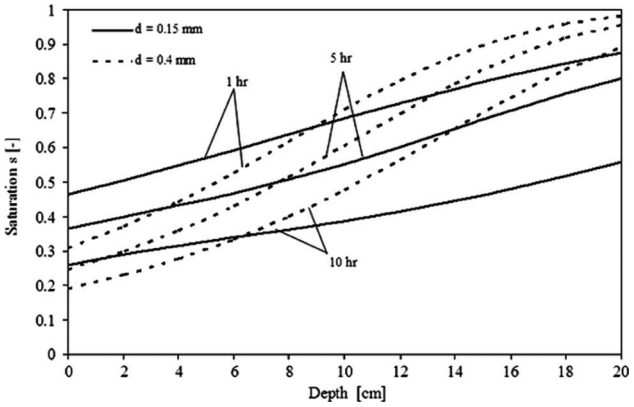

Figure 24. Moisture profiles at various particle sizes ($f = 2.45$ GHz, $E_{in} = 4{,}200$ V/m, $S_{in} = 0.7$). Reprinted from Sungsoontorn et al.[93] with permission from Taylor & Francis.

Mass transport equation

$$\phi\frac{\partial}{\partial t}\{s - Y_v(1-s)\} + \frac{\partial}{\partial z} \times \left[\begin{array}{l} \frac{KK_{rl}}{\mu_l}\left(\frac{\partial P_c}{\partial z} - \frac{\partial P_g}{\partial z} + g_z\right) + \\ Y_v\frac{KK_{rg}}{\mu g}\left(-\frac{\partial P_g}{\partial z} + \rho_g g_z\right) - Y_g D_m \frac{\partial}{\partial z}(W_v) \end{array}\right] = 0 \tag{15}$$

Pressure build-up in porous media

$$\phi\frac{\partial}{\partial t}\{Y_a(1-s)\} + \frac{\partial}{\partial z}\left[Y_a\frac{KK_{rg}}{\mu g} \times \left(-\frac{\partial P_g}{\partial z} + \rho_g g_z\right) - Y_g D_m \frac{\partial}{\partial z}\left(\frac{\rho_a}{\rho_g}\right)\right] = 0 \tag{16}$$

Boundary and initial conditions

$$-\lambda\frac{\partial T}{\partial z} = h_c(T - T_a) \tag{17}$$

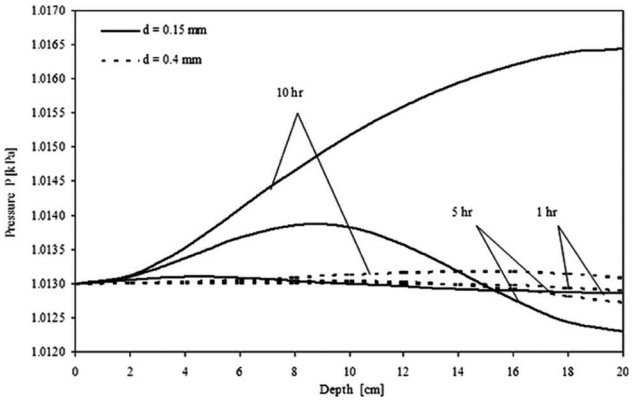

Figure 25. Pressure distribution at various particle sizes ($f = 2.45$ GHz, $E_{in} = 4{,}200$ V/m, $S_{in} = 0.7$). Reprinted from Sungsoontorn et al.[93] with permission from Taylor & Francis.

$$\rho_l w_l + \rho_v w_v = h_m(\rho_v - \rho_{va}) \tag{18}$$

$$\frac{\partial T}{\partial x} = 0, \quad \frac{\partial w}{\partial z} = 0 \tag{19}$$

There have been many investigations of moisture transport during the intensive microwave heating of materials.[94,95] Especially in biomaterials,[96,97] microwaves are assumed to arrive at the open boundary where heat and moisture are convected away from the porous medium. Heat and moisture fluxes at the insulated closed boundary (right side) are zero and also to be a three-variable model, as shown in Fig. 26. Combining microwave with hot-air or infrared heating methods has been suggested to increase the surface temperature and remove accumulated surface moisture.

To maintain product quality, it is crucial to maintain a uniform heat distribution. Factors that influence the distribution of heat include factors related to the load (e.g., dielectric properties, load geometry, and mixture ratio) and the microwave system (e.g., turntable, operating frequency, placement inside the oven, oven size, and geometry). Several parameters must be known to account properly for all phenomena in a dielectric microwave heating process. These parameters include the distributions of the electromagnetic field, microwave power absorption, temperature, and multiphase flow. Understanding these parameters may require the researcher to solve coupled differential equations, including equations for moisture transport, pressure, energy, and the electromagnetic field.

Due to the complexity and number of equations involved, the numerical method is the only approach

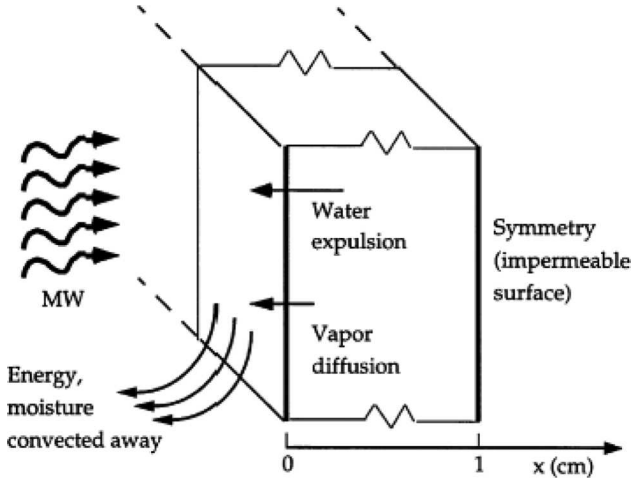

Figure 26. Schematic diagram of the heating process, with boundary conditions.[86,96] Reprinted from *International Journal of Heat and Mass Transfer*, Vol. 42, H. Ni, A. K. Datta, and K. E. Torrance, "Moisture transport in intensive microwave heating of biomaterials: A multiphase porous media model," pp. 1501–1512, 1999, with permission from Elsevier.

Downloaded by [Thammasat University Libraries] at 16:40 28 December 2015

that provides realistic simulations of the process. An attempt to solve these equations was carried out by Rakesh and Datta.[97] They formulated a coupled transport and large deformation model for microwave puffing, which described the individual physics of the process in detail. As shown in Fig. 27, very high temperatures were required to generate the necessary pressures to puff the material. The process may not be successful unless carried out using an intensive heating source, such as a microwave.

Intermittent drying processes utilize time-varying heat input tailored to match the drying kinetics of the material being dried. Chua et al.[98] overviewed the basic process of intermittent drying, selecting results from experiments and mathematical models for various biomaterials dried in a wide assortment of dryers. Intermittent drying can be performed by all types of batch dryers that employ time-varying operating conditions, including periodic or cyclic variations in pressure (from high to atmospheric), vacuum, temperature, or gas flow rate. Intermittent drying is typically performed at low microwave frequencies. It is primarily applicable for materials that are heat sensitive or require long drying periods mainly or exclusively in the falling rate period. A slight-to-moderate increase in drying time should be expected with intermittent drying, but this disadvantage is compensated by a decrease in energy consumption and an enhancement in product quality.

From their finite element model (FEM) results of intermittent MWD, Zhang and Mujumdar[99] recommended employing volumetric heating in a thermal drying process as a potential solution to diminish drying-induced stresses in grain kernels. The tempering period allows time for the internal moisture to distribute. Moisture and temperature gradients are equalized during the resting period when no heat or a reduced level of heat is provided. In the case of intermittent heating, the temperatures of the nodes do not increase constantly. The node temperatures are much lower than those in continuous heating, while the moisture

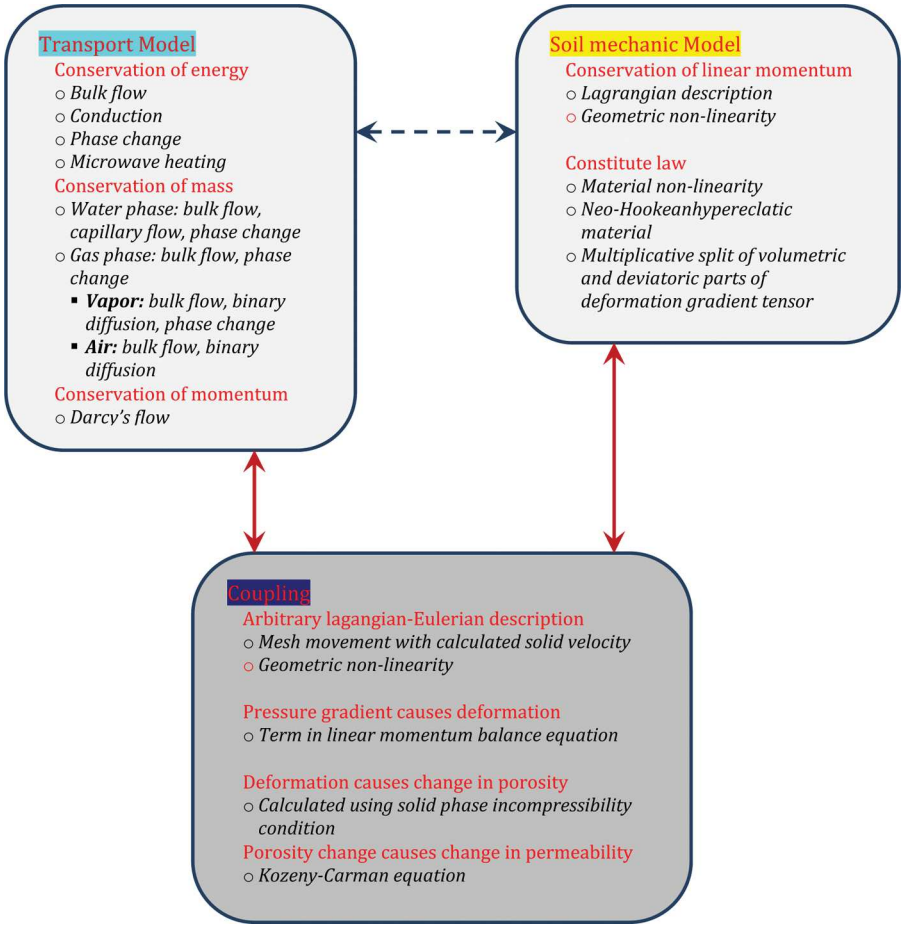

Figure 27. Components of the computational model, the different physical phenomena associated with the puffing process, and the coupling between the different physics. Reprinted from *Journal of Food Engineering*, Vol. 107, V. Rakesh and A.K. Datta, "Microwave puffing: Determination of optimal conditions using a coupled multiphase porous media—large deformation model," pp. 152–163, 2011, with permission from Elsevier.

Downloaded by [Thammasat University Libraries] at 16:40 28 December 2015

Downloaded by [Thammasat University Libraries] at 16:40 28 December 2015

potentials of different points of the body tend to be more uniform. This uniformity implies that the drying-induced stresses must also be decreased. For some heat-sensitive biological materials, intermittent drying should largely mitigate the problems caused by continuous hot-air drying, such as germinability, vigor, protein denaturation, and cracks.

Gong et al.[100] performed a numerical study to understand the effects of intermittent microwave heating on the drying behavior of clay and its internal stress development. When intermittent microwave heating was used, the maximum tensile and compressive stresses within the dried clay were decreased significantly, and the time for the peak stresses to develop was somewhat reduced. Intermittent microwave heating also had a beneficial effect during the MWD of ceramics.[101] Cracks were generated in the ceramic samples with continuous microwave heating. However, with a higher frequency of pulsation, crack formation could be avoided or delayed at lower moisture contents, although the sample did reach a higher temperature.

Gunasekaran[102] verified the advantages of pulsed microwave-vacuum drying of cranberries, in terms of the energy efficiency and quality (color and texture) of the dried product. Energy efficiency and product quality improved with a longer ratio of the power-off to power-on time. Microwaves were operated at 5.33 and 10.67 kPa with power on for 1–6 cycles. These experimental results seemed to suggest that when the power-on time was shorter, more of the microwave energy was used to evaporate moisture, whereas when the power-on time was longer, the product temperature tended to increase, leading to a loss of quality of the heat-sensitive material.

The effect of intermittent MWD on shrinkage behaviors has been investigated.[103,104] Experimental and numerical studies have reported that intermittent MWD improves the quality and temperature distribution of the dried food product. Sanga et al.[105] presented experimental and numerical analyses of intermittent microwave-convection drying of heat-sensitive materials. Using fiber-optic probes, they tested the drying rate and temperature distribution of the product during drying. A diffusion model, which included temperature- and concentration-dependent diffusivity and allowed for shrinkage in an empirical fashion, yielded results that agreed with the measured drying rates. Their FEM may be applied to blends of wet solids with different loss factors for microwave energy absorption. Drying by intermittent microwave input to continuous convection drying provided a product with better quality (color) than continuous microwave input drying alone.

Chen et al.[88] made a theoretical analysis of the effect of intermittent microwave heating patterns on the batch fluid drying of porous particles, considering uniform, sinusoidal, and rectangular patterns of microwave power. Under a constant electric field strength, they computed the temperature and moisture variations of apple particles in batch fluidized bed drying. Their results indicated the magnitude and distribution of the moisture, as well as the temperature and pressure within a particle.

Basak[106] assessed the role of irradiation in the lateral and radial directions on the microwave heating of 2D cylinders for beef and oil samples. Their results revealed various resonance modes with lateral or radial irradiation and with samples having a large radius. The resonance modes corresponded to maxima in power and large processing rates. Hot-spot formation within a sample was a strong function of lateral/radial irradiation for various dielectrics of food. Radial irradiation was not favorable. In particular, a hot spot occurred with radial irradiation at the center of large oil samples, resulting in a larger thermal gradient. This finding was in contrast to earlier works, which established that radial irradiation minimizes the thermal gradient regardless of sample size.

Very recently, Chaiyo and Rattanadecho[107] extended the work of Suwannapum and Rattanadecho,[91] presenting a 2D numerical analysis of an unsaturated porous packed bed, which was placed in a rectangular waveguide and subjected to a combined microwave-vacuum system. The influences of vacuum pressure and microwave frequency on the temperature, absorbed microwave power, saturation distribution, pressure buildup distribution, and fluid movement within the porous media were investigated during drying. The effects on the overall drying kinetics were examined by selecting the dielectric properties as a function of moisture content and temperature. The microwave system was operated as a monochromatic wave of TE_{10} mode (a dominant mode of electromagnetic propagation in a rectangular waveguide due to it has the lowest attenuation of all modes) at an operating frequency of 2.45 GHz. The magnetron-generated microwave energy was transmitted along the z-direction of the rectangular waveguide (inside dimensions: 110×54.61 mm) toward a water load situated at the end of the waveguide (see Fig. 28).

To model the physical single layer, the following assumptions were made:

- Because the microwave field in the TE10 mode does not vary in direction between the broad faces, a 2D model over the x–z plane can be applied to analyze the electromagnetic field inside the rectangular waveguide.

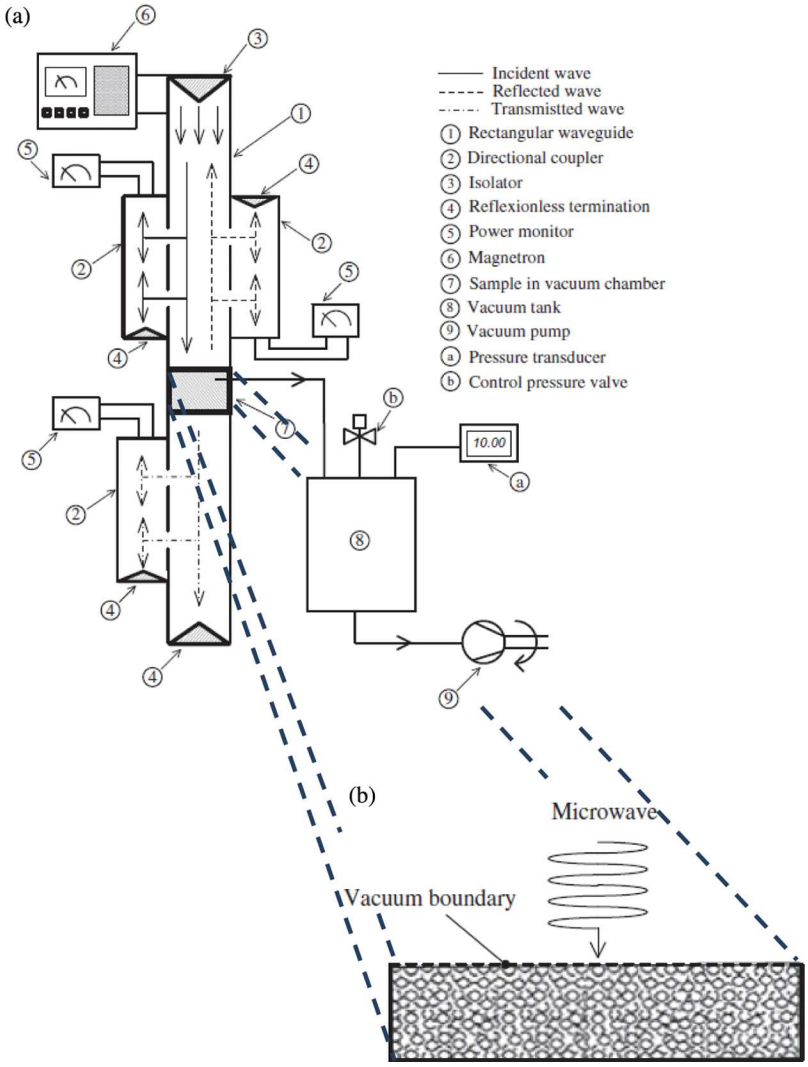

Figure 28. Schematic of (a) the combined microwave-vacuum system, and (b) the single-layer porous packed bed (sample) in a rectangular waveguide. Reprinted from *International Journal of Heat and Mass Transfer*, Vol. 65, K. Chaiyo and P. Rattanadecho, "Numerical analysis of heat-mass transport and pressure buildup of unsaturated porous medium in a rectangular waveguide subjected to a combined microwave and vacuum system," pp. 826–844, 2013, with permission from Elsevier.

- There is negligible absorption of microwave energy by the cavity (including air) in the rectangular waveguide.
- The walls of the rectangular waveguide are perfect conductors.
- The effect of the (quartz) sample container on the electromagnetic field can be neglected because it does not absorb microwave energy.

To obtain a closed set of governing macroscopic equations, the physical model shown in Fig. 29 was applied, and several simplifying assumptions were made:

1. The capillary porous material is rigid, and no chemical reactions occur in the sample.
2. Local thermodynamic equilibrium can be assumed.
3. Simultaneous heat and mass transport processes occur at a constant pressure. The dominant mechanisms are capillary transport, vapor diffusion, and gravity. This situation is generally the case in the drying of capillary porous medium at a specified vacuum or atmospheric pressure when the temperature is lower than the boiling point.
4. The binary gas mixture of air and water vapor behaves like an ideal gas.
5. Darcy's law holds for the liquid and gas phases.
6. Gravity is included for the liquid and gas phases.
7. Permeability of liquid and gas can be expressed in terms of relative permeability.
8. The solid matrix is rigid and non-deformable.
9. In a macroscopic sense, the porous packed bed is homogeneous and isotropic, and water is not bound to the solid matrix. Thus, the volume average model for a homogeneous and isotropic material can be used in the theoretical modeling and analysis.

Downloaded by [Thammasat University Libraries] at 16:40 28 December 2015

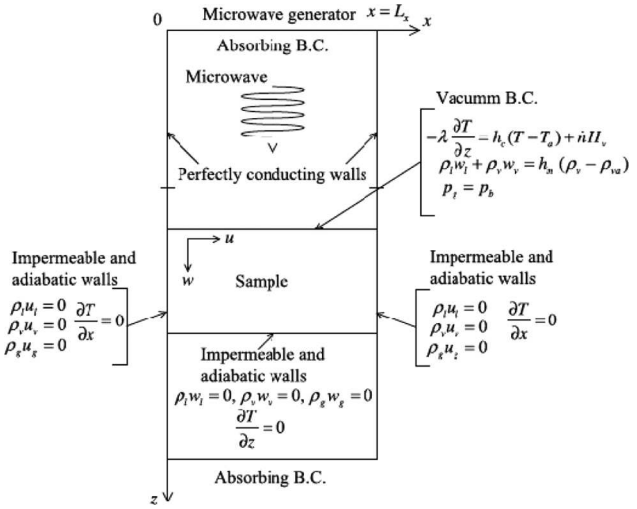

Figure 29. Physical single-layer model. Reprinted from *International Journal of Heat and Mass Transfer*, Vol. 65, K. Chaiyo and P. Rattanadecho, "Numerical analysis of heat-mass transport and pressure buildup of unsaturated porous medium in a rectangular waveguide subjected to a combined microwave and vacuum system," pp. 826–844, 2013, with permission from Elsevier.

10. Similar to the electromagnetic field, the temperature and moisture profiles can be assumed to be 2D in the *x*–*z* plane.

Moisture transport equation

$$\phi\frac{\partial}{\partial t}[\rho_l s + \rho_v(1-s)] + \frac{\partial}{\partial t}[\rho_l u_l + \rho_v u_v] + \frac{\partial}{\partial t}[\rho_l w_l + \rho_v w_v] = 0 \tag{20}$$

Total pressure equation

$$\phi\frac{\partial}{\partial t}[\rho_a(1-s)] + \frac{\partial}{\partial x}\left[\rho_a\frac{KK_{rg}}{\mu g}\left(-\frac{\partial P_g}{\partial x}\right) - D_m\frac{\partial}{\partial z}\rho_a\right] + \frac{\partial}{\partial z}\left[\rho_a\frac{KK_{rg}}{\mu g}\left(-\frac{\partial P_g}{\partial z} + \rho_g g_z\right) - D_m\frac{\partial}{\partial z}\rho_a\right] = 0 \tag{21}$$

Heat transport equation

$$\rho C_p\frac{\partial T}{\partial t} + \frac{\partial}{\partial x}\left[\{\rho_l C_{pl}u_l + (\rho_a C_{pa} + \rho_v)u_g\}T\right] + \frac{\partial}{\partial z}\left[\{\rho_l C_{pl}w_l + (\rho_a C_{pa} + \rho_v C_{pv})w_g\}T\right] + H_v\dot{n} = \frac{\partial}{\partial x}\left[\lambda_{eff}\frac{\partial T}{\partial x}\right] + \frac{\partial}{\partial z}\left[\lambda_{eff}\frac{\partial T}{\partial z}\right] + Q \tag{22}$$

where ρC_p is the effective heat capacitance of the water-gas matrix mixture:

$$\rho C_p = \rho_l C_{pl}\phi s + (\rho_a C_{pa} + \rho_v C_{pv})\phi(1-s) + \rho_p C_{pp}(1-\phi) \tag{23}$$

The phase change term is given by

$$\dot{n}\frac{\partial}{\partial t}\{\rho_v\phi(1-s)\} + \frac{\partial}{\partial x}\left[-D_m\frac{\partial\rho_v}{\partial x}\right] + \frac{\partial}{\partial z}\left[\rho_v\frac{KK_{rg}}{\mu_g}\rho_g g_z - D_m\frac{\partial\rho_v}{\partial z}\right] \tag{24}$$

Figures 30–32 show the temperature profile at various times under atmospheric pressure and a vacuum pressure of 13.3 kPa. The temperature inside the drying sample was higher under MWD than conventional drying, whereas the surface temperature stayed cooler due

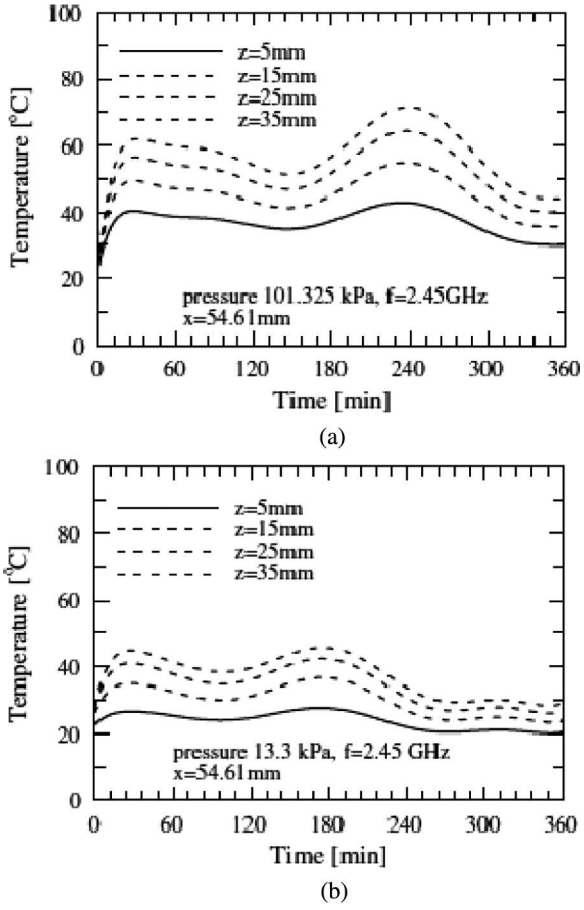

Figure 30. Temperature profile overtime at different *z*-depths (*x*-width = 54.61 mm): (a) atmospheric pressure, (b) vacuum pressure of 13.3 kPa. Reprinted from *International Journal of Heat and Mass Transfer*, Vol. 65, K. Chaiyo and P. Rattanadecho, "Numerical analysis of heat-mass transport and pressure buildup of unsaturated porous medium in a rectangular waveguide subjected to a combined microwave and vacuum system," pp. 826–844, 2013, with permission from Elsevier.

Downloaded by [Thammasat University Libraries] at 16:40 28 December 2015

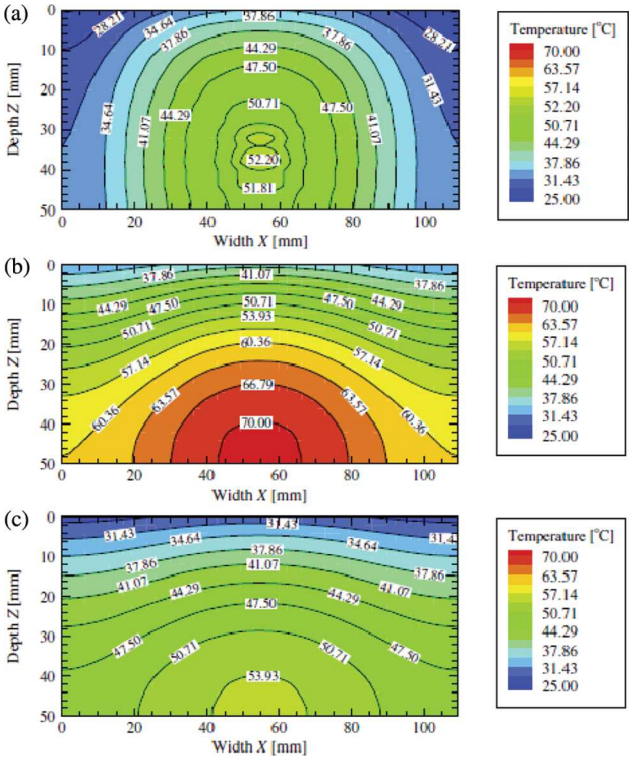

Figure 31. Temperature distribution inside the sample at atmospheric pressure and a microwave frequency of 2.45 GHz. (a) t = 10 min, (b) t = 100 min, and (c) t = 360 min. Reprinted from *International Journal of Heat and Mass Transfer*, Vol. 65, K. Chaiyo and P. Rattanadecho, "Numerical analysis of heat-mass transport and pressure buildup of unsaturated porous medium in a rectangular waveguide subjected to a combined microwave and vacuum system," pp. 826–844, 2013, with permission from Elsevier.

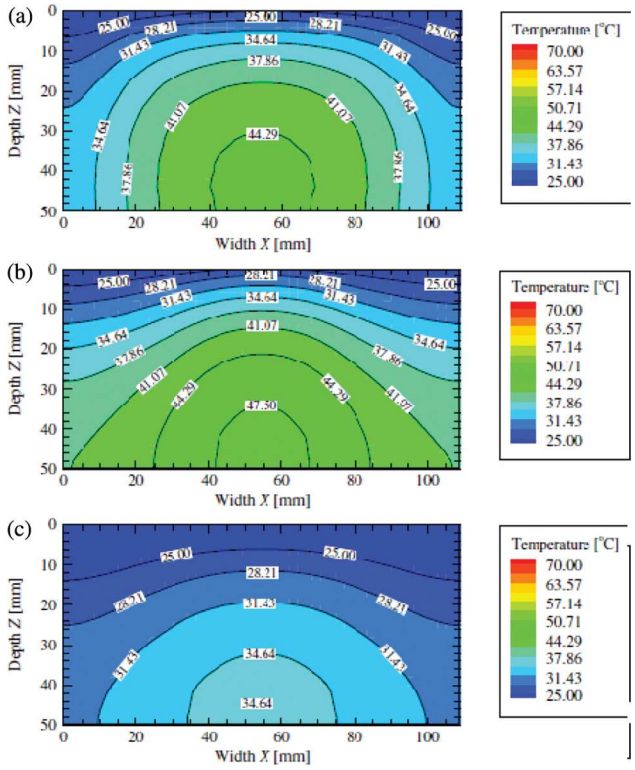

Figure 32. Temperature distribution inside the sample at a vacuum pressure of 13.3 kPa and a microwave frequency of 2.45 GHz: (a) t = 10 min, (b) t = 100 min, and (c) t = 360 min. Reprinted from *International Journal of Heat and Mass Transfer*, Vol. 65, K. Chaiyo and P. Rattanadecho, "Numerical analysis of heat-mass transport and pressure buildup of unsaturated porous medium in a rectangular waveguide subjected to a combined microwave and vacuum system," pp. 826–844, 2013, with permission from Elsevier.

to effect of the surrounding air. Evaporation occurred at a lower temperature at the sample surface, due to evaporative cooling.

Chaiyo and Rattanadecho[107] numerically determined the heat, multiphase flow, and pressure buildup distributions in an unsaturated porous packed bed subjected to microwave energy under atmospheric pressure or a vacuum pressure of 13.3 kPa (100 Torr). Figure 33 shows the electric-field distribution along the center axis (× = 54.61 mm) of the rectangular waveguide when inserted into the sample at different drying times (t = 10, 100, and 360 min). Because the sample was composed of glass beads, water, and air, it can be assumed to be a lossy (moist and porous) material. Under atmospheric pressure, the resonance of the standing wave configuration inside the sample was weak compared to the left-hand side of the sample, as shown in Figs. 33b and 33c. For the electric-field distribution inside the cavity (left-hand side), a stronger standing wave with a large amplitude was formed by interference between the incident and reflected waves from the sample surface, due to the different dielectric properties of the materials (air and sample) at the interface.

For the case of highly deformable products, Perré and May[108] proposed a numerical drying model that accounts for the coupling between transfer and solid mechanics. To describe the drying of porous media that undergo large deformations due to shrinkage, they modified their previous *TransPore* model.[109] In the resultant Model 2, the porous medium is described with two independent variables (temperature and moisture content or equivalent variables). This model can be analyzed as a simplification of Model 3. This model does not account for the internal gaseous pressure. Darcy's law includes only the liquid phase, in which capillary forces are the sole actors. The model assumes that capillary pressure is a function of moisture content alone (rather than moisture and temperature). This approach is worthwhile because it enables the most important feature of drying (i.e., coupling between heat and mass transfer) to be analyzed, as shown in Eqs. (25) and (26). This article presents a typical example of this

Downloaded by [Thammasat University Libraries] at 16:40 28 December 2015

Downloaded by [Thammasat University Libraries] at 16:40 28 December 2015

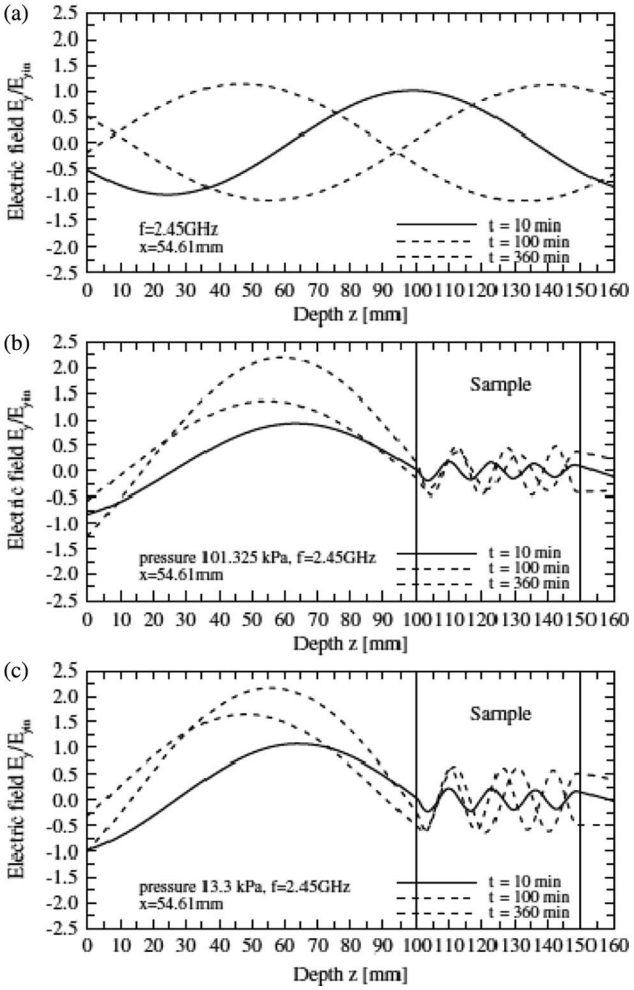

Figure 33. Electric-field distribution a at microwave frequency of 2.45 GHz. (a) Empty rectangular waveguide. (b–c) Sample in the rectangular waveguide at (b) 101.325 kPa or (c) 13.3 kPa. Reprinted from *International Journal of Heat and Mass Transfer*, Vol. 65, K. Chaiyo and P. Rattanadecho, "Numerical analysis of heat-mass transport and pressure buildup of unsaturated porous medium in a rectangular waveguide subjected to a combined microwave and vacuum system," pp. 826–844, 2013, with permission from Elsevier.

model for potato. The computed results reveal dramatic variations of the sample shape as water is removed from the product. Due to exchange surface reduction, the drying rate decreases, even though free water remains available at the surface, as shown in Fig. 34.

Water conservation

$$\frac{\partial}{\partial t}(\rho_s X) + \nabla \cdot (\bar{q}_v) + \nabla \cdot (\bar{q}_l) = 0 \tag{25}$$

with

$$\bar{q}_v = -\rho_v \bar{\bar{K}}_v \nabla X; \quad \bar{q}_l = -\rho_l \bar{\bar{K}}_l \nabla X$$

Energy conservation

$$\frac{\partial}{\partial t}[\rho_s(h_0 + Xh_l)] + \nabla \cdot (\rho_l h_l \bar{q}_l + \rho_v h_v \bar{q}_v) = \nabla \cdot \left(\bar{\bar{\lambda}}_{eff} \nabla T\right) + \Phi \tag{26}$$

Perre and Turner's *TransPore* model,[109] which was based on a discussion by Whitaker,[83] was proposed as a comprehensive heat and mass transfer computational model for simulating the drying of porous media. The necessary governing equations are summarized as follows:

Liquid conservation equation

$$\frac{\partial}{\partial t}\left(\varepsilon_w \rho_w + \varepsilon_g \rho_g + \bar{\rho}_b\right) + \nabla \cdot (\rho_w \bar{v}_w + \rho_v \bar{v}_v + \bar{\rho}_b \bar{v}_b) = \nabla \cdot \left(\rho_g \bar{\bar{D}}_{eff} \nabla \omega_v\right) \tag{27}$$

Energy conservation equation

$$\frac{\partial}{\partial t}\left(\varepsilon_w \rho_w h_w + \varepsilon_g(\rho_v h_v + \rho_a h_a) + \bar{\rho}_b \bar{h}_b\right) + \rho_0 h_s - \varepsilon_g P_g \times \nabla \cdot \left(\rho_w h_w \bar{v}_w + (\rho_v h_v + \rho_a h_a)\bar{v}_g + h_b \bar{\rho}_b h v_b\right) = \nabla \cdot \left(\left(\rho_g \bar{\bar{D}}_{eff}((h_v \nabla \omega_v + h_a \nabla \omega_a)\right) + \bar{\bar{K}}_{eff} \nabla T\right) + \Phi \tag{28}$$

Air conservation equation

$$\frac{\partial}{\partial t}\left(\varepsilon_g \rho_g\right) + \nabla \cdot (\rho_a \bar{v}_a) = \nabla \cdot \left(\rho_g \bar{\bar{D}}_{eff} \nabla \omega_a\right) \tag{29}$$

where the gas and liquid phase velocities are given by the Generalized Darcy's Law:

$$\bar{v}_l = -\frac{\bar{\bar{K}}\,\bar{\bar{k}}}{\mu_l} \nabla \phi_l, \nabla \phi_l = \nabla P_l - \rho_l g \nabla \chi \;\; where \;\; l = w, g \tag{30}$$

The authors demonstrated that their drying model is capable of handling the comprehensive set of macroscopic equations in three spatial dimensions. For example, the evolution of the average moisture content, center temperature, and center pressure over time are depicted in Fig. 35 for concrete and in Fig. 36 for softwood.

Nonthermal equilibrium model for microwave drying

In 2012, Rattanadecho and Klinbun[110] numerically investigated the natural convection of fluid in saturated

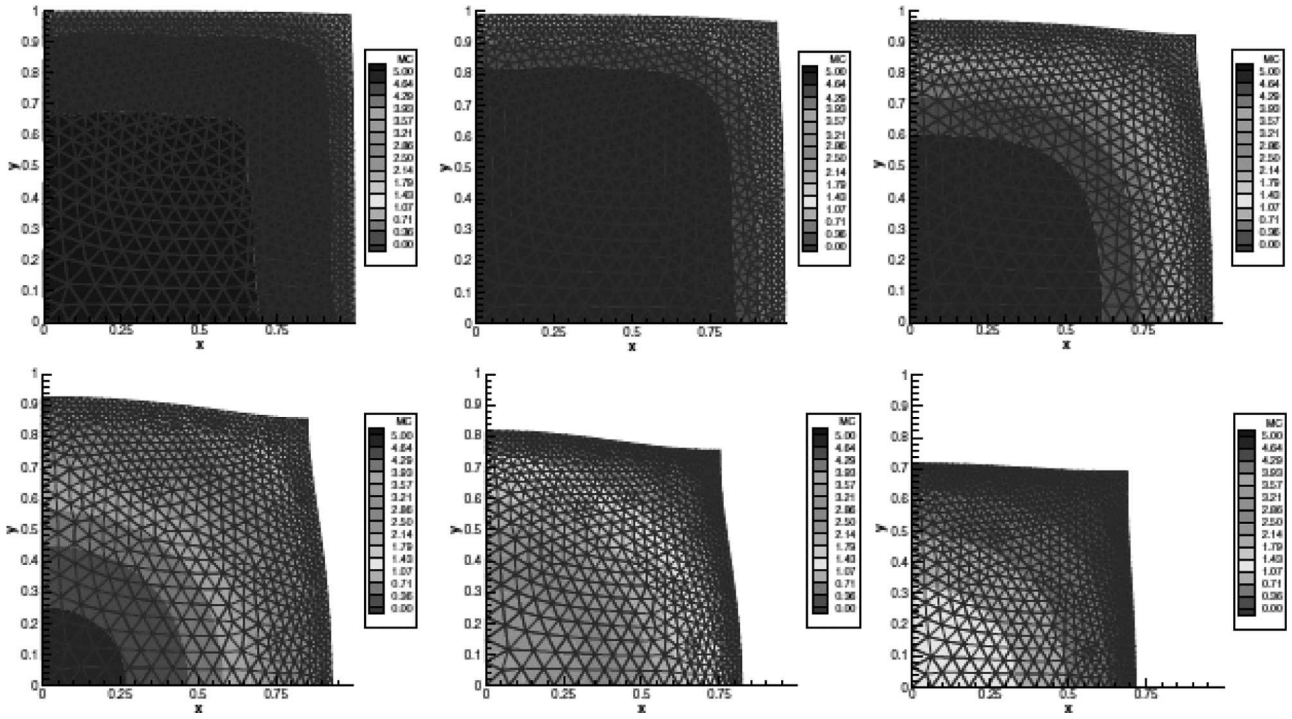

Figure 34. Shape and moisture content iso-values of the shipped section during 1, 2, 5, 10, 20, and 30 h of drying. Mass diffusivity $= 3 \times 10^{-10}$ m^2/s. Reprinted from Perré and May[108] with permission from Taylor & Francis.

porous media under an electromagnetic field. The influences of material properties, microwave power levels, and operating frequencies on the transport processes in porous media were numerically analyzed. By assuming that the porous medium consists of water and spherical solid particles, solving the Brinkman–Forchheimer extended Darcy model for the momentum equation is employed, and two energy equations with local thermal nonequilibrium (LTNE) models. Figure 37 showed a schematic diagram of the problem. The container was filled with a saturated porous medium. The

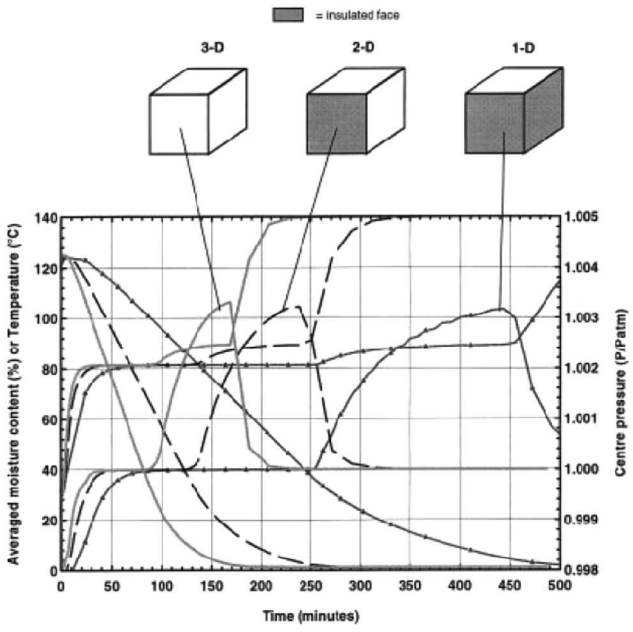

Figure 35. Numerical simulation of concrete drying (140/80°C for dry/wet bulk), showing the effect of the number of spatial dimensions on the overall drying curves. Reprinted from Perré and May[108] with permission from Taylor & Francis.

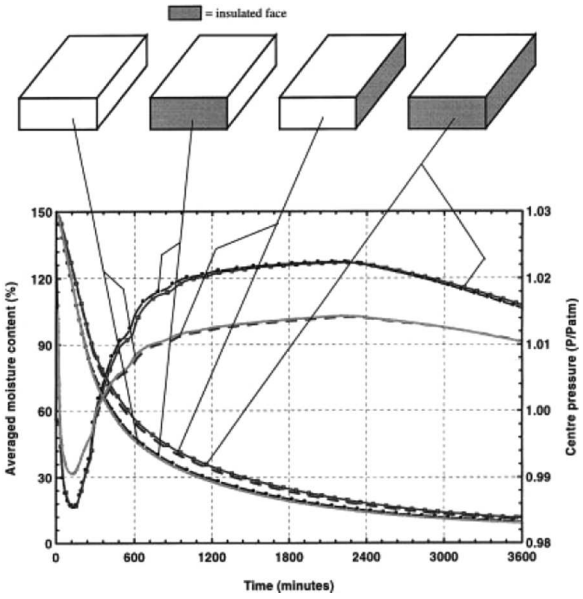

Figure 36. Low-temperature drying of softwood (80/50°C for dry/wet bulk), showing the overall drying and internal pressure curves for different exchange surface configurations. Reprinted from Perré and May[108] with permission from Taylor & Francis.

Downloaded by [Thammasat University Libraries] at 16:40 28 December 2015

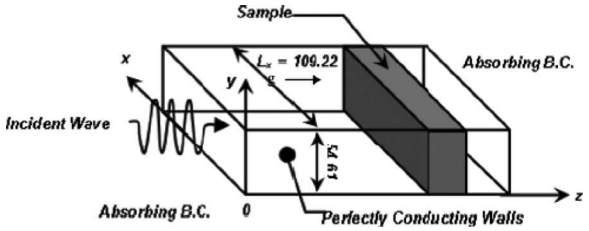

Figure 37. Model geometry of the single-slot MCA. Reprinted from Rattanadecho and Klinbun[110] with permission from Taylor & Francis.

porous medium consisted of water and spherical solid. The results indicated that the phenomena taking place inside the saturated porous media in electromagnetic wave drying processes using LTNE and local thermal equilibrium (LTE) models. Figures 38a and 38b show the temperature distributions of the solid and fluid phases at various power input levels, along with the horizontal axis ($z = 10$ mm) and vertical axis ($x = 54.61$ mm) of a rectangular waveguide, respectively. For water–glass beads, the porous packed bed with P = 1,000 W corresponded to a higher temperature than that for the porous packed bed with P = 300 W for x and z directions. This was due to the high power input, which affected the local electromagnetic heat generation (Q) and thus created the temperature difference.

That same year, Klinbun and Rattanadecho published a second article,[111], in which they numerically studied the heating of a multilayer porous packed bed that was subjected to microwave radiation with a rectangular waveguide.

Keagin and Rattanadecho[112] presented a valuable study on local thermal non-equilibrium (LTNE) in porous material, in the context of microwave ablation (MWA). This research was a preliminary investigation on the effect of phase change due to water evaporation for the future work. In the MWA process, heat from microwave energy is applied to kill cancer cells without damaging the surrounding tissue. These authors investigated the transient distribution of tissue and blood temperatures within porous liver during MWA, using an LTNE model-based single-slot microwave coaxial antenna (MCA). Given the highly complicated tumor structure, the authors simplified the model geometry of the single-slot MCA, as shown in Figs. 39 and 40. These studies[110–112] can be used to extend MWD modeling and have been continuously developing by the authors.

To analyze electromagnetic wave propagation and heat transfer within the porous liver during the MWA process, the authors numerically solved the system of governing equations, initial conditions, and boundary conditions using the FEM via COMSOL Multiphysics. The boundary conditions are described in Fig. 41. To analyze the electromagnetic wave propagation, the following assumptions and relevant equations were used:

1. Electromagnetic wave propagation can be modeled in 2D axially symmetrical cylindrical coordinates (r–z).
2. An electromagnetic wave propagating in an MCA is characterized by transverse electromagnetic fields.
3. An electromagnetic wave in porous liver is characterized by transverse magnetic fields.
4. The wall of an MCA is a perfect electric conductor.
5. The outer surface of the porous liver is truncated by a scattering boundary condition.
6. The dielectric properties of the porous liver are uniform and constant.

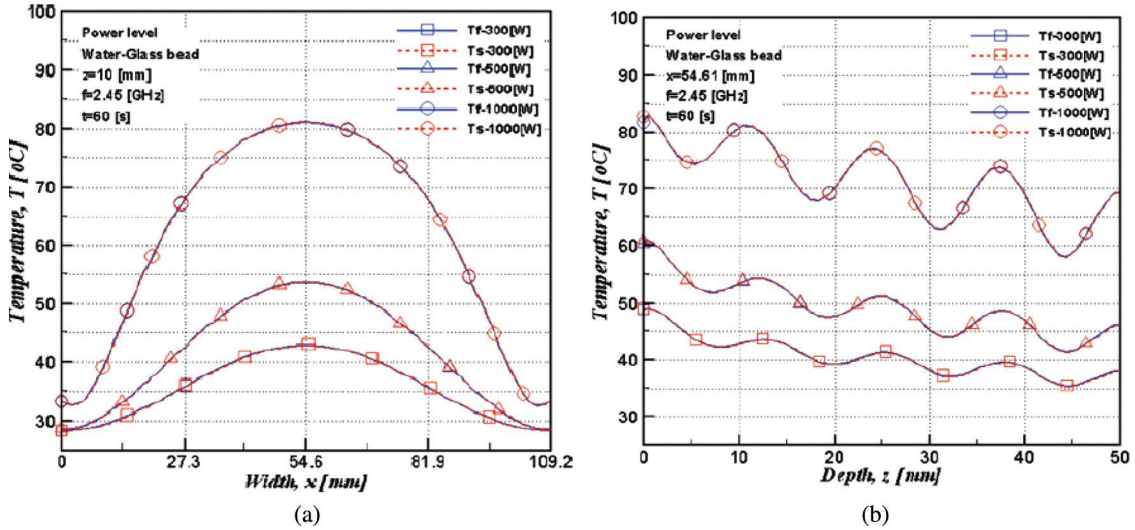

Figure 38. Temperature distributions of the solid and fluid phases at various power input levels: (a) along the x-axis and (b) along the z-axis. Reprinted from Rattanadecho and Klinbun[110] with permission from Taylor & Francis.

Downloaded by [Thammasat University Libraries] at 16:40 28 December 2015

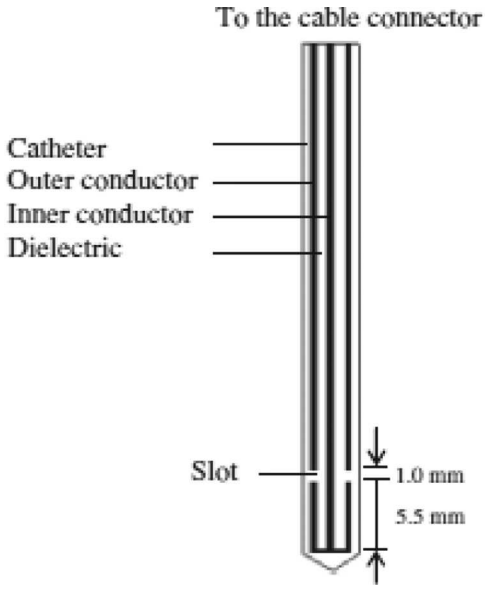

Figure 39. Model geometry of the single-slot MCA. Reprinted from *International Journal of Heat and Mass Transfer*, Vol. 67, P. Keangin and P. Rattanadecho, "Analysis of heat transport on local thermal non-equilibrium in porous liver during microwave ablation," pp. 46–60, 2013, with permission from Elsevier.

Electric field equation

$$\vec{E} = e_r \frac{C}{r} e^{j(\omega t - kz)}, C = \sqrt{\frac{ZP}{\pi . ln(r_{outer}/r_{inner})}} \quad (31)$$

Magnetic field equation

$$\vec{E} = e_\phi \frac{C}{rZ} e^{j(\omega t - kz)}, C = \sqrt{\frac{ZP}{\pi . ln(r_{outer}/r_{inner})}} \quad (32)$$

Wave equation

$$\nabla \times \left(\left(\varepsilon_r - \frac{j\sigma}{\omega \varepsilon_0} \right)^{-1} \nabla \times \vec{H}_\phi \right) - \mu_r k_0^2 \vec{H}_\phi = 0 \quad (33)$$

Boundary conditions

$$\vec{E}_r = 0, \ \frac{\partial \vec{E}_z}{\partial r} = 0 \text{ and } \hat{n} \times \vec{E} = 0 \quad (34)$$

To analyze the heat transfer, tissue and blood temperatures within the porous liver during the MWA process were obtained by solving two energy equations, assuming LTNE and including the microwave power absorbed. To simplify the problem, the following assumptions were made:

1. Corresponding to electromagnetic wave propagation analysis, blood flow and heat transfer can be modeled in 2D axially symmetrical cylindrical coordinates (r–z).
2. Porous liver is homogenous, thermally isotropic, and saturated with a fluid (blood).

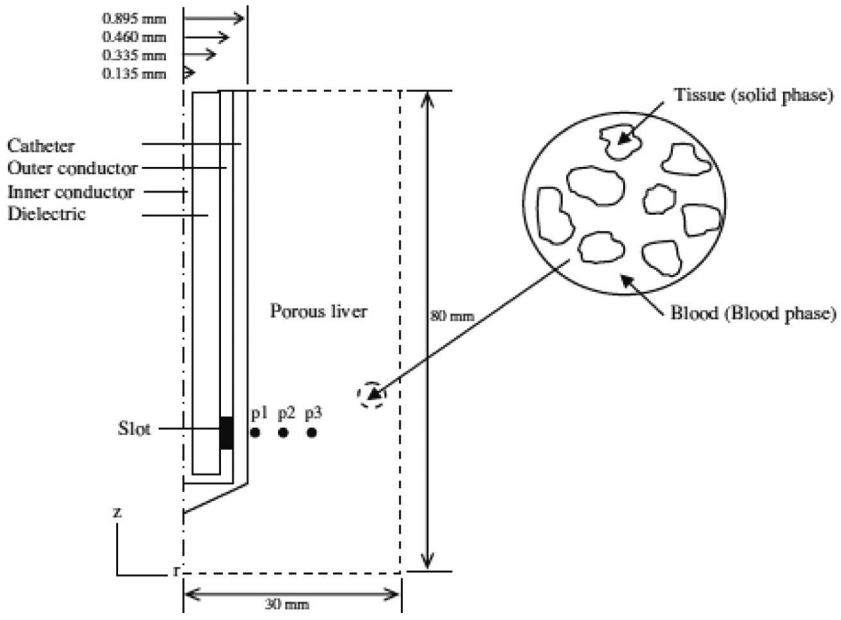

Figure 40. Axially symmetrical model geometry. Three positions of the slot center, p1 (2.5 mm, 16 mm), p2 (4.5 mm, 16 mm), and p3 (8.5 mm, 16 mm), are used to determine the tissue and blood temperatures. Reprinted from *International Journal of Heat and Mass Transfer*, Vol. 67, P. Keangin and P. Rattanadecho, "Analysis of heat transport on local thermal non-equilibrium in porous liver during microwave ablation," pp. 46–60, 2013, with permission from Elsevier.

Downloaded by [Thammasat University Libraries] at 16:40 28 December 2015

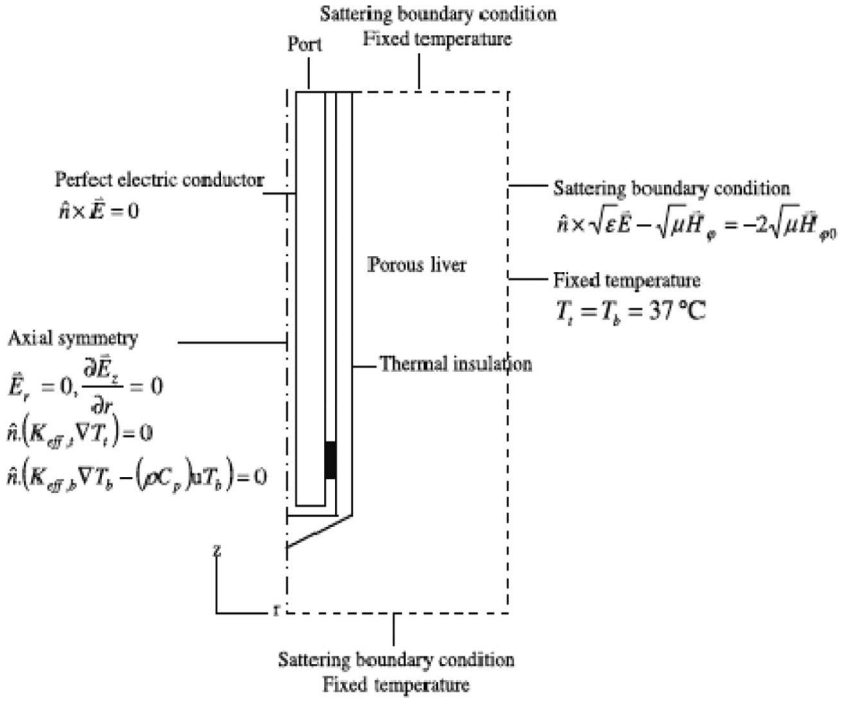

Figure 41. Boundary condition for analysis of electromagnetic wave propagation and heat transfer. Reprinted from *International Journal of Heat and Mass Transfer*, Vol. 67, P. Keangin and P. Rattanadecho, "Analysis of heat transport on local thermal non-equilibrium in porous liver during microwave ablation," pp. 46–60, 2013, with permission from Elsevier.

3. Blood flow is incompressible and Newtonian.
4. No phase change occurs within the porous liver, no energy exchange occurs through the outer surface of the porous liver, and no chemical reactions occur within the porous liver.
5. The porosities and thermal properties of the porous liver are constant.

Governing equations describing the heat-transfer phenomenoa for tissue and blood phases, incorporating the LTNE conditions, can be represented as follows:

Tissue phase equation

$$(1-\phi)(\rho C_p)_t\frac{\partial T_t}{\partial t}=\nabla\cdot\left(K_{t.eff}\nabla T_t\right)-h_{tb}a_{tb}(T_t-T_b)-\omega_b C_b(T_t-T_b)+(1-\phi)Q_{met}+(1-\phi)Q_{ext,t} \quad (35)$$

Blood phase equation

$$\phi(\rho C_p)_b\left(\frac{\partial T_b}{\partial t}+u\cdot\nabla T_b\right)=\nabla\cdot\left(K_{b.eff}\nabla T_b\right)+h_{tb}a_{tb}(T_t-T_b)+\omega_b C_b(T_t-T_b)+\phi Q_{ext,b} \quad (36)$$

where

$$K_{t.eff}=(1-\phi)K_t, K_{b.eff}=\phi K_b$$

The temperature profile formed a nearly ellipsoidal shape around the slot. The temperature was highest near the MCA slot and decreased with distance from the MCA. In the three analyzed cases, the temperature profiles increased with increasing heating time. At locations far from the MCA, the temperatures of tissue and blood from LTNE models and of tissue from local thermal equilibrium models approached the initial temperature of 37°C, as shown in Fig. 42.

Energy and exergy analyses

The main target of designing and optimizing commercial drying processes is to reduce the amount of moisture in a product to a desired value, while utilizing as little energy as possible. Consequently, the energy quantity and quality as well as heat and mass transfer should be evaluated throughout the drying process.[113,114] Exergy is a measurement of the maximum useful work that can be done by a system interacting with an environment at a constant pressure and temperature. Exergy analysis has been increasingly accepted as a useful tool in the design, assessment, optimization, and improvement of energy systems.

For example, Jindarat et al.[56] experimentally investigated the energy consumption during the drying of non-hygroscopic porous packed beds by an industrial CMCB, as shown in Fig. 6, accounting for the effects of drying time, hot-air temperature, porous structure (F- or C-bed), and magnetron location on the overall

Downloaded by [Thammasat University Libraries] at 16:40 28 December 2015

Downloaded by [Thammasat University Libraries] at 16:40 28 December 2015

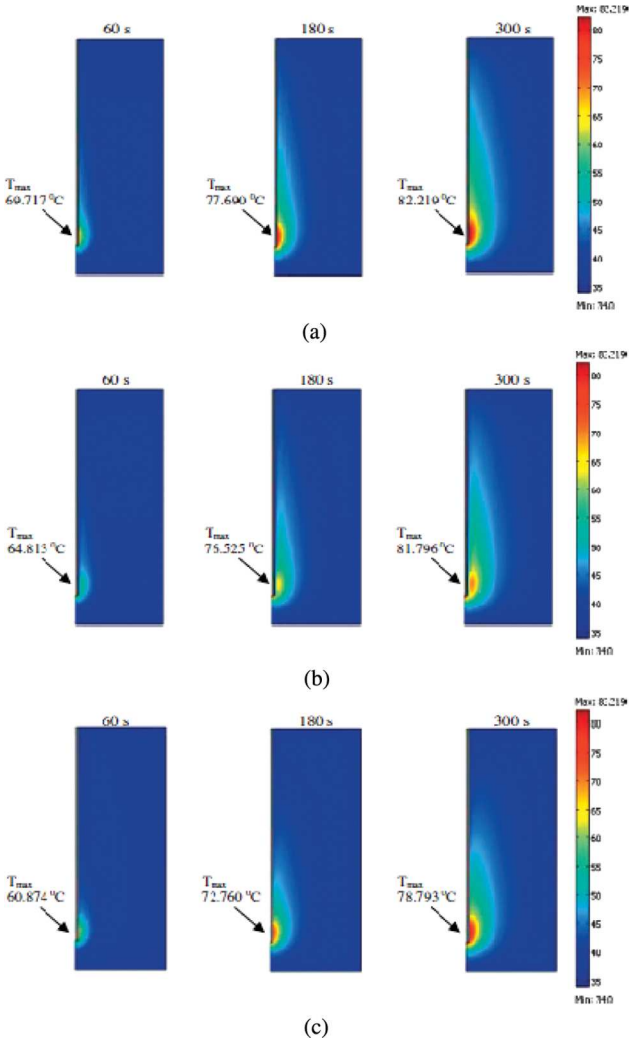

Figure 42. Temperature profiles in the porous liver at various times. (a) Tissue and (b) blood temperature profiles of the LTNE model. (c) Tissue temperature profiles of the local thermal equilibrium model based on the same condition in the figure. Reprinted from *International Journal of Heat and Mass Transfer*, Vol. 67, P. Keangin and P. Rattanadecho, "Analysis of heat transport on local thermal non-equilibrium in porous liver during microwave ablation," pp. 46–60, 2013, with permission from Elsevier.

drying kinetics and energy consumption. A schematic of the conservation of mass for the control volume of the cavity is shown in Fig. 43.

The mass balance equation can be defined as in Eq. (37):

$$\frac{dm_{cv}}{dt} = \dot{m}_{g1} - \dot{m}_{g2} \tag{37}$$

where $\dot{m}_{g1}$ and $\dot{m}_{g2}$ are the mass flow rates at inlet (1) and exit (2), respectively. The energy efficiency (η_e) for the drying process is defined as:

$$\eta_e = \frac{W_d\left[h_{fg}\left(M_{p1} - M_{p2}\right) + c_m(T_{m2} - T_{m1})\right]}{\dot{m}(h_1 - h_0)\Delta t + \Delta t \dot{Q}_{mw}} \tag{38}$$

where W_d is the weight of dried material; h_{fg} is the latent heat of vaporization; M_{p1} and M_{p2} are the particle moisture content on a dry basis at inlet (1) and exit (2), respectively; c_m is the specific heat of the material; T_{m1} and T_{m2} are the temperature at inlet (1) and exit (2), respectively; $\dot{m}$ is the mass flow rate; Δt is the time; and $\dot{Q}_{mw}$ is the microwave energy.

Figures 44–47 show the temperature and moisture variations as a function of time for the C- and F-beds with a constant initial moisture content of 25% (dry basis). In the CMCB at 30°C and 70°C, the moisture profiles of the sample continuously decreased at a faster rate compared to convective drying alone. Thus, the bulk of the sample absorbed the largest amount of microwave energy, which corresponds to the level of absorbed energy in the sample. These findings demonstrate the potential of a technique combining conventional and microwave heating with a continuous belt system to reduce electrical energy consumption. If implemented in industry, this system would decrease production costs by reducing electrical energy consumption.

Prommas et al.[44] investigated the effects of the drying time, hot-air temperature, porous structure

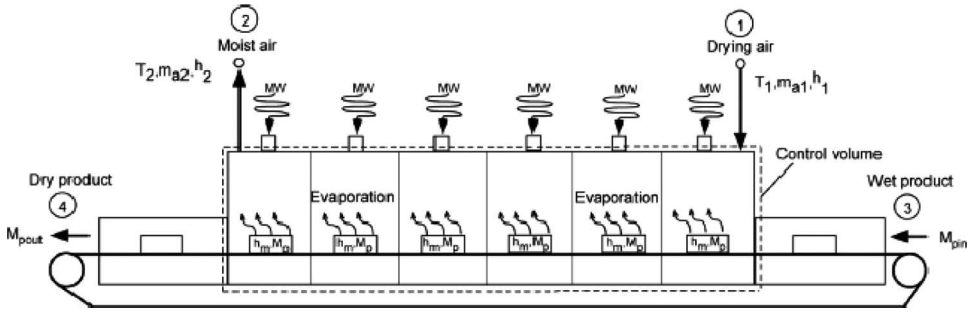

Figure 43. Schematic of the control volume during a drying process in a CMCB. Reprinted from Jindarat et al.[56] with permission from Taylor & Francis.

Downloaded by [Thammasat University Libraries] at 16:40 28 December 2015

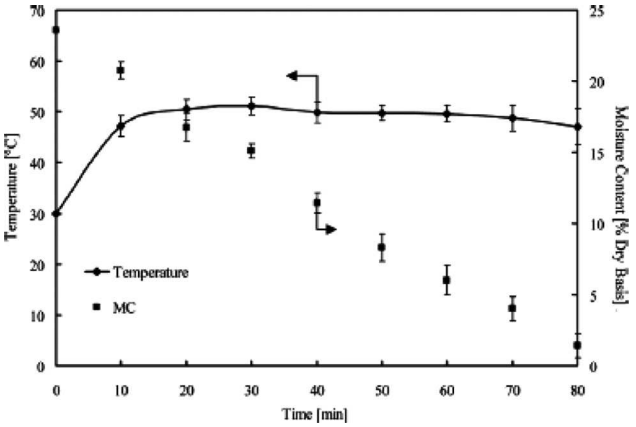

Figure 44. Variations in temperature and moisture over time for drying in the CMCB ($T_1 = 30°C$, case 1, C-bed). Reprinted from Jindarat et al.[56] with permission from Taylor & Francis.

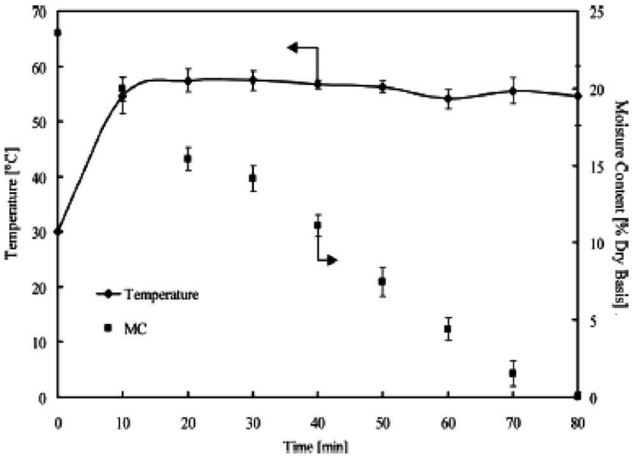

Figure 45. Variations in temperature and moisture over time for drying in the CMCB ($T_1 = 30°C$; case 2, C-bed). Reprinted from Jindarat et al.[56] with permission from Taylor & Francis.

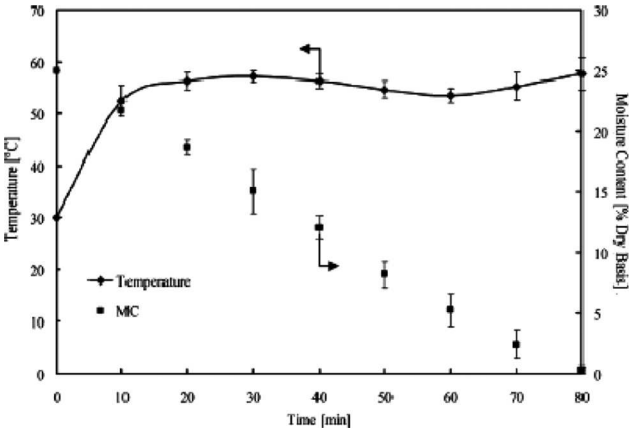

Figure 46. Variations in temperature and moisture over time for drying in the CMCB ($T_1 = 70°C$, case 3, F-bed). Reprinted from Jindarat et al.[56] with permission from Taylor & Francis.

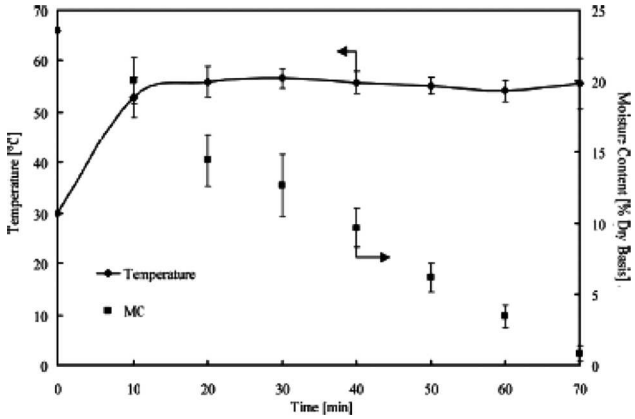

Figure 47. Variations in temperature and moisture over time for drying in the CMCB ($T_1 = 70°C$, case 4, C-bed). Reprinted from Jindarat et al.[56] with permission from Taylor & Francis.

(F- or C-bed), and magnetron location on the overall drying kinetics and energy utilization ratio during the drying of a non-hygroscopic porous packed bed, composed of glass beads and water (saturated porous packed bed, $s_0 = 1$) as shown in Fig. 48. The energy analysis can be calculated as discussed above. For exergy analysis, the authors considered the second law of thermodynamics and estimated the total exergy of inflow, outflow, and

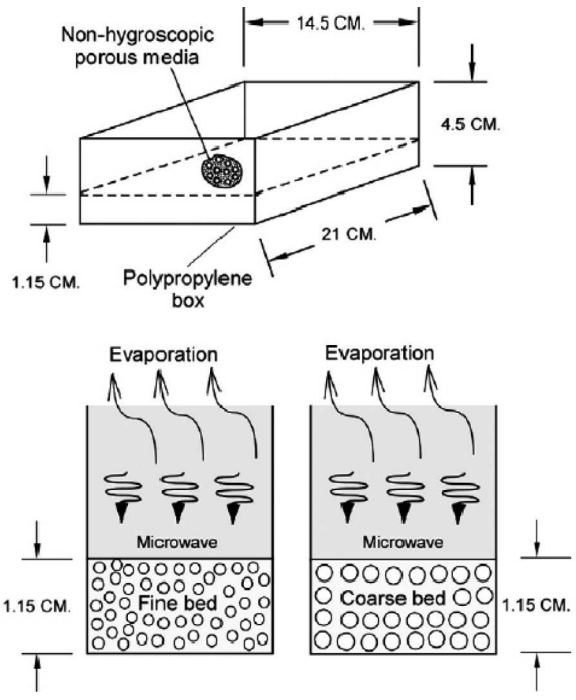

Figure 48. Schematic of drying sample (porous packed bed). Reprinted from *International Communications in Heat and Mass Transfer*, Vol. 39, R. Prommas, P. Rattanadecho, and W. Jindarat, "Energy and exergy analyses in drying process of non-hygroscopic porous packed bed using a combined multi-feed microwave-convective air and continuous belt system (CMCB)," pp. 242–250, 2012, with permission from Elsevier.

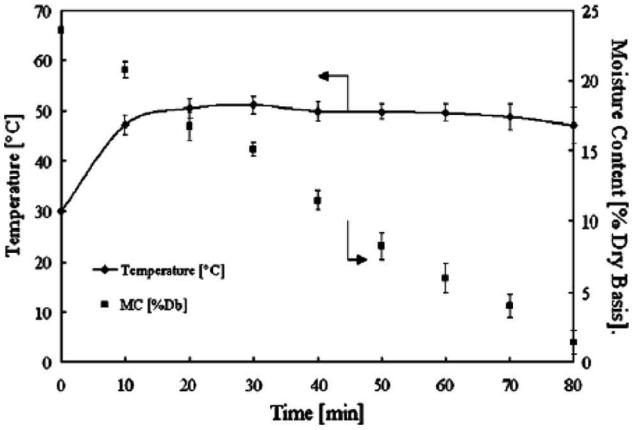

Figure 49. Variations in temperature and moisture over time for drying in the CMCB ($T_1 = 30°C$, case 1, C-bed). Reprinted from *International Communications in Heat and Mass Transfer*, Vol. 39, R. Prommas, P. Rattanadecho, and W. Jindarat, "Energy and exergy analyses in drying process of non-hygroscopic porous packed bed using a combined multi-feed microwave-convective air and continuous belt system (CMCB)," pp. 242–250, 2012, with permission from Elsevier.

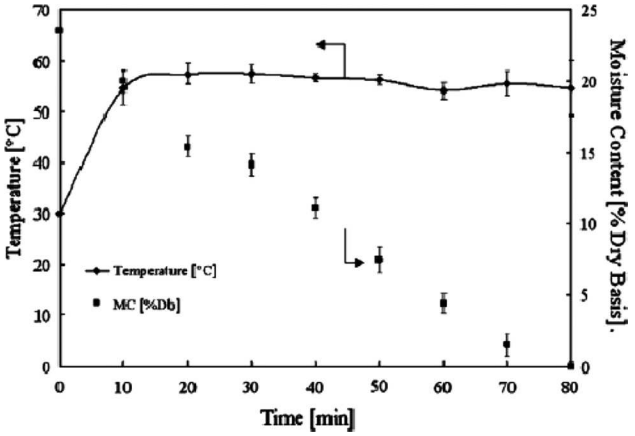

Figure 50. Variations in temperature and moisture over time for drying in the CMCB ($T_1 = 30°C$, case 2, F-bed). Reprinted from *International Communications in Heat and Mass Transfer*, Vol. 39, R. Prommas, P. Rattanadecho, and W. Jindarat, "Energy and exergy analyses in drying process of non-hygroscopic porous packed bed using a combined multi-feed microwave-convective air and continuous belt system (CMCB)," pp. 242–250, 2012, with permission from Elsevier.

losses of the drying chamber. Exergy of the chamber was analyzed by determining the exergy values at steady-state and the reasons for exergy variations from steady-state. Equation (38) provides the mathematical formulation used to evaluate the exergy balance.[114] The temperature and moisture variations were determined as a function of time for the C- and F-beds with a constant initial moisture content of 25% (dry basis). In the case of microwave-convective air drying (30°C and 70°C), the moisture profile of the sample continuously decreased at a faster rate compared to the case of convective drying, as shown in Figs. 49 and 50. The energy utilization ratio and exergy efficiency depended on the particle size, hot-air temperature, and magnetron location.

$$Exergy = \underbrace{(u-u_\infty)}_{\text{Internal energy}} - \underbrace{T_\infty(s-s_\infty)}_{\text{Entropy}} \underbrace{\frac{P_\infty}{J}(v-v_\infty)}_{\text{Work}} + \underbrace{\frac{V^2}{2gJ}}_{\text{Momentum}} + \underbrace{(z-z_\infty)\frac{g}{g_cJ}}_{\text{Gravity}} \underbrace{\sum_c(\mu_c-\mu_\infty)N_c}_{\text{Chemical}} + \underbrace{E_iA_iF_i\left(3T^4-T_\infty^4-4T_\infty T^4\right)}_{\text{Radiation}} + \underbrace{\ldots}_{\text{Emission}} \quad (39)$$

where ∞ is the reference condition.

In 2013, Jindarat et al.[56] analyzed the energy consumption during the drying of biomaterials using a combined unsymmetrical double-feed microwave and vacuum system (CUMV) (Fig. 51). An energy consumption model based on the first law of thermodynamics was developed to evaluate energy efficiency. Influences of microwave power, vacuum pressure, and microwave operation mode on energy consumption were considered in detail. To analyze mass transfer in the drying process, they applied the law of conservation of mass for the control volume, as shown in Fig. 52, in which the mass balance equation can be defined as in Eq. (37). Recently, Jindarat et al.[115] developed an energy model based on the first law of thermodynamics to evaluate

Figure 51. CUMV system. Reprinted from Jindarat et al.[56] with permission from Taylor & Francis.

Downloaded by [Thammasat University Libraries] at 16:40 28 December 2015

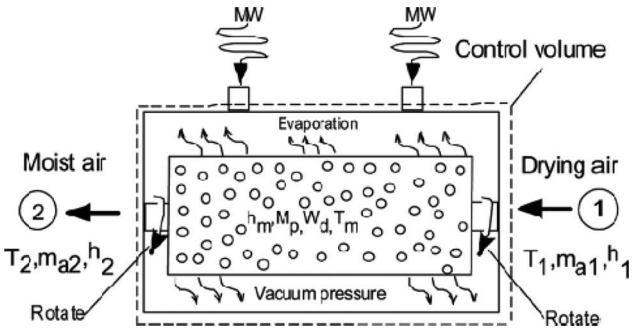

Figure 52. Schematic of the control volume during CUMV drying. Reprinted from Jindarat et al.[56] with permission from Taylor & Francis.

energy efficiency and specific energy consumption in a combined microwave-hot air spouted bed (CMHS) drying of biomaterial (coffee beans). The influences of hot air temperature and initial weight of coffee beans on energy consumption were considered. For analyzing mass transfer in the drying process, the law of conservation of mass for the control volume is applied, as shown in Fig. 53. The results indicated that the CMHS drying method with the drying conditions of hot air temperature of 60°C, air velocity of 12 m/s, and initial coffee bean weight of 280 g gave a good quality dehydrated coffee bean and involved low specific energy consumption in the drying method. Further, the quality

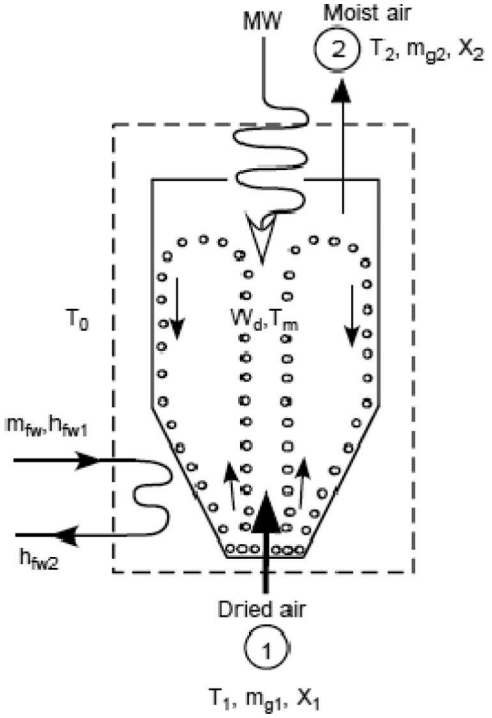

Figure 53. Physical control volume of CMHS drying process using energy analysis. Reprinted from Jindarat et al.[115] with permission from Taylor & Francis.

of coffee beans dehydrated by the CMHS drying method is found to be superior to the HASB drying method.

Conclusions

Published articles on the kinetic mechanisms of MWD have been reviewed systematically. In particular, the dielectric aspects of the materials to be dried have been examined, including factors affecting methods for measuring and applications of the dielectric properties. From the experimental perspective, the equipment, stability, safety, and regulation of laboratory- and commercial-scale MWD systems have been discussed. Theoretical investigations of thermal and non-thermal equilibrium models, and multiple magnetrons have been described. Finally, future trends in the research and development of MWD are suggested, including the limitations of MWD and the three variables that need to be studied in depth to achieve a full understanding of heat and mass transfer in these systems. This review indicates that MWD alone has several limitations for experimental and commercial-scale applications, such as the non-uniformity of the electromagnetic field within the microwave cavity, the high penetration depth within the dielectric materials, and the fast mass transport of the microwave power (which may alter the quality or texture of food). To overcome these problems, materials to be dried should be in constant motion with a uniformity of power absorbed in the cavity to avoid any hot spots. Combining MWD with conventional or other drying techniques can also be employed. Further research of MWD and/or hybrid drying systems must include an examination of macroscopic equations to simulate the drying process in terms of the heat and mass transfer in porous media. Especially, a MWD associated with a hybrid drying system which consists of multiple-microwave sources has been continuously developing by the authors. For example, hot air is applied at initial stage for 30 min and consecutively hot air is applied associated with microwave energy, or infrared is applied at first stage and MWD is consecutively applied, etc. One-, two-, and three-variable models should include chemical reaction terms. Furthermore, using the three variables considered, the moving-load computational models, in-depth investigations enabling the full explanation of heat and mass transfer properties, and pressure build-up should be possible.[61]

Nomenclature

a	thermal diffusivity (m^2/s)
$\vec{B}$	magnetic flux density (Wb/m^2)

Downloaded by [Thammasat University Libraries] at 16:40 28 December 2015

Downloaded by [Thammasat University Libraries] at 16:40 28 December 2015

Cp	specific heat capacity (J/kgK)
c_p	heat capacity at constant pressure (J/(kg · K))
$\vec{D}$	electric flux density (C/m)
D_m	effective molecular mass diffusion (m^2/s)
D_p	penetration depth (m)
e	Euler's number (= 2.7182818 …)
$\vec{E}$	electric field intensity (V/m)
f	frequency (Hz)
g_r	gravitational constant (m/s^2)
h_c	heat transfer constant (W/m^2K)
h_m	mass transfer constant (W/m^2K)
$\vec{H}$	magnetic field intensity (A/m)
H_v	specific heat of vaporization (J/kg)
K	permeability (m^2)
L	material length
$\dot{m}$	phase change term (kg/m^3s)
P	microwave power (W)
$\vec{P}$	energy flux density (W/m^2)
p	pressure (Pa)
q	electric charge density (C/m^3)
Q	microwave power absorbed term (W/m^3)
s	water saturation
S_{11}	reflected scattering coeffient from Port 1
S_{21}	transmitted scattering coeffient from Port 1
S_{22}	reflected scattering coeffient from Port 2
S_{22}	transmitted scattering coeffient from Port 2
T	temperature (°C)
t	time (s)
$tan\,\delta$	loss tangent coefficient
V	volume (m^3)

Greek letters

Γ	reflection coefficient
σ	effective conductivity (S/m)
ε_0	permittivity of free space (=8.8514 × 10^{-12}) (F/m)
ε_∞	permittivity at the high frequency limit
ε_s	static, low-frequency permittivity
ε^*	complex (electric) permittivity, $\varepsilon' - j\varepsilon''$
ε_r	relative permittivity
ε'_r	relative dielectric constant
ε''_r	relative dielectric loss factor
μ^*	complex magnetic permeability, $\mu' - j\mu''$
μ_o	permeability of free space (=4π × 10^{-7}) (m · kg/$s^{2.\ A2}$) or (h/m)
μ_r	relative permeability
υ	microwave speed in the dielectric material (m/s)
ω	angular frequency, field's frequency (s^{-1})
$tan\ \delta$	loss tangent coefficient ($\varepsilon''/\varepsilon'$)
σ	electric conductivity (1/Ω)
τ	characteristic relaxation time (s)
ρ	density (kg/m^3)
λ_g	wavelength in sample
$\lambda_{free\ space}$	wavelength of free space
λ_{cutoff}	wavelength of cutoff frequency

Subscripts

0	free space
a	air
c	capillary
g	gas
l	liquid water
p	particle
r	relative
v	water vapor
x, z	coordinate axis (m)
∞	ambient condition

Funding

The authors gratefully acknowledge the Thailand Research Fund under the TRF contract Nos. RTA5680007 and TRG5780255, and the National Research Universities Project of the Higher Education Commission for supporting this research.

References

[1] Metaxas, A.C. Microwave heating. *Journal of Microwave Power and Electromagnetic Energy* **1991**, *5*, 237–247.
[2] Metaxas, A.C.; Meredith, R.J. *Industrial Microwave Heating*; Peter Peregrinus: Herts, UK, 1998.
[3] Mujumdar, A.S. *Handbook of Industrial Drying*, 4th ed.; CRC Press: Boca Raton, FL, 2014.
[4] Choi, Y.; Okos, M.R. Thermal properties of liquid foods review. In *Physical and Chemical Properties of Food*, Ed.; Okos, M.R. American Society of Agricultural Engineers: St. Joseph, MI, 1986; 5–77.
[5] Chang, K.; Ruan, R.R.; Chen, P.L. Simultaneous heat and moisture transfer in cheddar cheese during cooling. I. Numerical simulation. *Drying Technology* **1998**, *16*(7), 1447–1458.
[6] Kaensup, W.; Wongwises, S.; Chutima, S. Drying of pepper seeds using a combined microwave fluidized bed dryer. *Drying Technology* **1998**, *16*(3–5), 853–862.
[7] Kaensup, W.; Wongwises, S. Combined microwave/fluidized bed drying of fresh pepper corns. *Drying Technology* **2004**, *22*(4), 779–794.
[8] Fakhouri, O.M.; Ramaswamy, S.H. Temperature uniformity of microwave heated foods as influenced by product type and composition. *Food Research International* **1993**, *26*(2), 89–95.
[9] Alibas, I. Microwave, vacuum, and air drying characteristics of collard leaves. *Drying Technology* **2009**, *27*, 1266–1273.
[10] Basak, T.; Meenakshi, A. A theoretical analysis on microwave heating of food slabs attached with ceramic

Downloaded by [Thammasat University Libraries] at 16:40 28 December 2015

plates: Role of distributed microwave incidence. *Food Research International* **2006**, *39*(8), 932–944.

[11] Regier, M.; Schubert, H. Microwave processing. In *The Microwave Processing of Foods*; Schubert, H.; Regier, M. Eds.; Woodhead Publishing, Sawston, Cambridge, UK, 2001.

[12] Afrin, N.; Zhang, Y.; Chen, J.K. Thermal lagging in living biological tissue based on non-equilibrium heat transfer between tissue, arterial and venous bloods. *International Journal of Heat and Mass Transfer* **2011**, *54*, 2419–2426.

[13] Perre, P.; Turner, I.W. Microwave drying of softwood in an oversized waveguide: Theory and experiment. *AIChE Journal* **1997**, *43*(10), 2579–2595.

[14] Vongpradubchai, S.; Rattanadecho, P. Microwave and hot air drying of wood using a rectangular waveguide. *Drying Technology* **2011**, *29*(4), 451–460.

[15] Basak, T.; Meenakshi, A. Influence of ceramic supports on microwave heating for composite dielectric food slabs. *AIChE Journal* **2006**, *52*(6), 1995–2007.

[16] Basak, T.; Rao, B.S. Role of ceramic composites and microwave pulsing on efficient microwave processing of pork meat samples. *Food Research International* **2011**, *44*, 2679–2697.

[17] Basak, T. Role of resonance on microwave heating of oil–water emulsions. *AIChE Journal* **2004**, *50*, 2659–2675.

[18] Ratanadecho, P. Microwave heating using a rectangular wave guide. Ph.D. thesis, Nakaoka University of Technology, Japan, 2002.

[19] Basak, T.; Samanta, S.K.; Jindamwar, A. A novel concept on discrete samples for efficient microwave processing of materials. *Chemical Engineering Science* **2008**, *63*(12), 3292–3308.

[20] Tsotsas, E.; Mujumdar, A.S. *Modern Drying Technology*, Vol. 5; VCH Wiley: Weinheim: Germany, 2014.

[21] Llave, Y.; Terada, Y.; Fukuoka, M.; Sakai, N. Dielectric properties of frozen tuna and analysis of defrosting using a radio-frequency system at low frequencies. *Journal of Food Engineering* **2014**, *139*, 1–9.

[22] Tulasidas, T.N.; Raghavan, G.S.V.; Mujumdar, A.S. Microwave drying of grapes in a single mode cavity at 2450 MHz-I: drying kinetics; and II: quality and energy aspects. *Drying Technology* **1995**, *13*(8–9), 1949–1992.

[23] Dev, S.R.S.; Gariépy, Y.; Raghavan, G.S.V. Measurement of dielectric properties and finite element simulation of microwave pretreatment for convective drying of grapes. *Progress in Electromagnetic Research Online* **2009**, *5*(7), 690–695.

[24] Okiror, G.P.; Jones, C.L. Effect of temperature on the dielectric properties of low acyl gellan gel. *Journal of Food Engineering* **2012**, *113*, 151–155.

[25] Tanaka, F.; Uchino, T.; Hamanaka, D.; Atungulu, G.G.; Hung, Y.-C. Dielectric properties of mirin in the microwave frequency range. *Journal of Food Engineering* **2008**, *89*, 435–440.

[26] Guo, W., Liua, Y.; Zhua, X.; Wanga, S. Dielectric properties of honey adulterated with sucrose syrup. *Journal of Food Engineering* **2011**, *107*, 1–7.

[27] Feng, H.; Tang, J.; Cavalieri, R.P. Dielectric properties of dehydrated apples as affected by moisture and temperature. *Transactions of the American Society of Agricultural Engineers* **2002**, *45*(1), 129–135.

[28] Sipahioglu, O.; Barringer, S.A. Dielectric properties of vegetables and fruits as a function of temperature, ash, and moisture content. *Journal of Food Science* **2003**, *68*(1), 234–239.

[29] Sólyom, K.; Kraus, S.; Mato, R.B.; Gaukel, V.; Schuchmann, H.P.; José Cocero, M. Dielectric properties of grape marc: Effect of temperature, moisture content and sample preparation method. *Journal of Food Engineering* **2013**, *119*, 33–39.

[30] Tang, J.; Feng, H.; Lau, M. Microwave heating in food processing. In Young, X.; Tang, J. eds.; *Advances in Agricultural Engineering*; World Scientific Publishing Co.: Singapore, 2002; 1–43.

[31] Roebuck, B.D.; Goldblith, S.A. Dielectric properties of carbohydrate–water mixtures at microwave frequencies. *Journal of Food Science* **1972**, *37*(1), 199–204.

[32] Wang, R.; Zhang, M.; Mujumdar, A.S.; Jiang, H. Effect of salt and sucrose content on dielectric properties and microwave freeze drying behavior of re-structured potato slices. *Journal of Food Engineering* **2011**, *106*, 290–297.

[33] Wang, Y.; Zhang, M.; Mujumdar, A.S.; Joseph, M.K.; Azam, S.M.R. Effect of blanching on microwave freeze drying of stem lettuce cubes in a circular conduit drying chamber. *Journal of Food Engineering* **2012**, *113*, 177–185.

[34] Kristiawan, M.; Sobolik, V.; Klíma, L.; Allaf, K. Effect of expansion by instantaneous controlled pressure drop on dielectric properties of fruits and vegetables. *Journal of Food Engineering* **2011**, *102*, 361–368.

[35] Venkatesh, M.S.; Raghevan, G.S.V. An overview of dielectric properties measuring techniques. *Canadian Biosystems Engineering* **2005**, *47*, 15–29.

[36] Tereshchenko, O.V.; Buesink, F.J.K.; Leferink, F.B.J. An overview of the techniques for measuring the dielectric properties of materials. In *General Assembly and Scientific Symposium, 2011 XXXth URS*, Istanbul, August 13–20; IEEE: Piscataway, NJ, 2011.I.

[37] Hewlett Packard Corporation. Dielectric Probe Kit 85070A. Palo Alto, CA: Research and Development Unit, Test and Measurements Laboratories, Hewlett Packard Corporation, 1992.

[38] Ratanadecho, P. The simulation of microwave heating of wood using a rectangular wave guide: Influence of frequency and sample size. *Chemical Engineering Science* **2006**, *61*, 4798–4811.

[39] Cronin, NJ. *Microwave and Optical Waveguides*; Taylor & Francis: London, 1995.

[40] Ratanadecho, P.; Aoki, K.; Akahori, M. Experimental and numerical study of microwave drying in unsaturated porous material. *International Journal of Heat and Mass Transfer* **2001**, *28*, 605–616.

[41] Ratanadecho, P.; Aoki, K.; Akahori, M. A numerical and experimental investigation of the modeling of microwave drying using a rectangular wave guide. *Drying Technology* **2001**, *19*(9), 2209–2234.

[42] Ratanadecho, P.; Aoki, K.; Akahori, M. Experimental and numerical study of microwave drying in unsaturated porous material. *International Communications in Heat and Mass Transfer* **2001**, *28*(5), 605–616.

Downloaded by [Thammasat University Libraries] at 16:40 28 December 2015

[43] Jindarat, W.; Rattanadecho, R.; Vongpradubchaia, S.; Pianroj, Y.Y. Analysis of energy consumption in drying process of non-hygroscopic porous packed bed using a combined multi-feed microwave-convective air and continuous belt system (CMCB). *Drying Technology* **2011**, *29*(8), 926–938.

[44] Prommas, R.; Rattanadecho, P.; Jindarat, W. Energy and exergy analyses in drying process of non-hygroscopic porous packed bed using a combined multi-feed microwave-convective air and continuous belt system (CMCB). *International Communications in Heat and Mass Transfer* **2012**, *39*, 242–250.

[45] Cohen, J.S.; Yang, T.C.S. Progress in food dehydration. *Trends in Food Science & Technology* **1995**, *6*(1), 20–25.

[46] Zhang, M.; Tang, J.; Mujumdar, A.S.; Wang, S. Trends in microwave-related drying of fruits and vegetables. *Trends in Food Science & Technology* **2006**, *17*, 524–534.

[47] Feng, H.; Tang, J. Microwave finish drying of diced apples in a spouted bed. *Journal of Food Science* **1998**, *63*(4), 679–683.

[48] Huang, L.; Zhang, M.; Mujumdar, A.S.; Lim R.-X. Comparison of four drying methods for re-structured mixed potato with apple chips. *Journal of Food Engineering* **2011**, *103*, 279–284.

[49] Jiang, H.; Zhang, M.; Liu Y.; Mujumdar, A.S.; Liu, H. The energy consumption and color analysis of freeze/microwave freeze banana chips. *Food and Bioproducts Processing* **2013**, *91*, 464–472.

[50] Markowski, M.; Bondaruk, J.; Błaszczak, W. Rehydration behavior of vacuum-microwave dried potato cubes. *Drying Technology* **2009**, *27*(2), 296–305.

[51] Wang, Y.; Zhang, M.; Mujumdar, A.S. Effect of cassava starch gel, fish gel and mixed gels and thermal treatment on structure development and various quality parameters in microwave vacuum-dried gel slices. *Food Hydrocolloids* **2013**, *33*, 26–37.

[52] Zhang, F.; Zhang, M.; Mujumdar, A.S. Drying characteristics and quality of restructured wild cabbage chips processed using different drying methods. *Drying Technology* **2011**, *29*(6), 682–688.

[53] Thussu, S.; Datta, A. Fundamentals-based quality prediction: Texture development during drying and related processes. *Procedia Food Science* **2011**, *1*, 1209–1215.

[54] Namsanguan, Y.; Tia, W.; Devahastin, S.; Soponronnarit, S. Drying kinetics and quality of shrimp undergoing different two-stage drying processes. *Drying Technology* **2004**, *22*(4), 759–778.

[55] Charoenvai, S.; Yingyuen, W.; Jewyee, A.; Rattanadecho, P.; Vongpradubchai, S. Comparative evaluation on product properties and energy consumption of single microwave dryer and combination of microwave and hot air dryer for durian peel particleboards. *Energy Procedia* **2013**, *34*, 479–492.

[56] Jindarat, W.; Sungsoontorn, S.; Rattanadecho, P. Analysis of energy consumption in drying process of biomaterials using a combined unsymmetrical double-feed microwave and vacuum system (CUMV) —Case study: Tea leaves. *Drying Technology* **2013**, *31* (10), 1138–1147.

[57] Yang, H. C.; Püschner, P. Heat transfer with the speed of light using microwaves in industrial chemical processes. Presented at AchemAsia 2013, Beijing, China, May 13–16, 2013.

[58] Micro Denshi Co., Ltd. http://www.microdenshi.co.jp/en/products/.

[59] Occupational Health and Safety Administration (OSHA). Radiofrequency and microwave radiation. 2009. http://www.osha.gov/SLTC/radiofrequencyradiation/.

[60] International Radiation Protection Association (IRPA). International Commission on Non-Ionizing Radiation Protection (ICNIRP) Guidelines: For limiting exposure to time-varying electric, magnetic and electromagnetic fields (up to 300 GHz). *Health Physics* **1988**, *54*, 492–522.

[61] Institute of Electrical and Electronics Engineers (IEEE). Technical information statement on: Human exposure to microwaves and other radio frequency electromagnetic fields. *IEEE Engineering in Medicine and Biology Magazine* **1995**, *14*, 336–337.

[62] Institute of Electrical and Electronics Engineers (IEEE). Standard for safety levels with respect to human exposure to radio frequency electromagnetic fields 3 kHz to 300 GHz. IEEE/ANSI, C95.1., 2005.

[63] National Radiological Protection Board (NRPB) and the Health Protection Agency. *Review of the Scientific Evidence for Limiting Exposure to Electromagnetic Fields (0–300 GHz)*; 2004.

[64] Fujiwara, O.; Kato, A. Computation of SAR inside eyeball for 1.5-GHz microwave exposure using finite-difference time domain technique. *IEICE Transaction* **1994**, *E77-B*, 732–737.

[65] Karampatzakis, A.; Samaras, T. Numerical modeling of heat transfer and fluid flow transfer in the human eye under millimeter wave exposure. *Bioelectromagnetics* **2013**, *34*, 291–299.

[66] International Commission on Non-Ionizing Radiation Protection (ICNIRP). Guidelines for limiting exposure to time-varying electric, magnetic and electromagnetic fields(up to 300 GHz). *Health Physics* **1998**, *74*, 494–522.

[67] IEEE. IEEE Standard for Safety Levels with Respect to Human Exposure to Radio Frequency Electromagnetic Fields, 3 kHz to 300 GHz. IEEE Standard C95 1999, 1.

[68] Taflove, A.; Brodwin, M.E. Computation of the electromagnetic fields and induced temperature within a model of the microwave-irradiated human eye. *IEEE Transactions on Microwave Theory and Techniques* **1975**, *23*(11), 888–896.

[69] Lagendijk, J.J.W. A mathematical model to calculate temperature distribution in human and rabbit eye during hyperthermic treatment. *Physics in Medicine and Biology* **1982**, *27*, 1301–1311.

[70] Scott, J. A finite element model of heat transport in the human eye. *Physics in Medicine and Biology* **1988**, *33*, 227–241.

[71] Scott, J. The computation of temperature rises in the human eye induced by infrared radiation. *Physics in Medicine and Biology* **1988**, *33*, 243–257.

[72] Kumar, S.; Acharya, S.; Beuerman, R.; Palkama, A. Numerical solution of ocular fluid dynamics in a rabbit eye: Parametric effects. *Annals of Biomedical Engineering* **2006**, *34*, 530–544.

Downloaded by [Thammasat University Libraries] at 16:40 28 December 2015

[73] Ooi, E.; Ng, E.Y.K. Simulation of aqueous humor hydrodynamics in human eye heat transfer. *Computers in Biology and Medicine* **2008**, *38*, 252–262.
[74] Ooi, E.H.; Ng, E.Y.K. Effects of natural convection inside the anterior chamber. *International Journal for Numerical Methods in Biomedical Engineering* **2011**, *27*, 408–423.
[75] Pennes, H.H. Analysis of tissue and arterial blood temperatures in the resting human forearm. *Journal of Applied Physiology* **1948**, *1*, 93–122.
[76] Flyckt, V.M.M.; Raaymakers, B.W.; Lagendijk, J.J.W. Modeling the impact of blood flow on the temperature distribution in the human eye and the orbit: Fixed heat transfer coefficients versus the Pennes bioheat model versus discrete blood vessels. *Physics in Medicine and Biology* **2006**, *51*, 5007–5021.
[77] Ng, E.Y.K.; Ooi, E.H. FEM simulation of the eye structure with bioheat analysis. *Computer Methods and Programs in Biomedicine* **2006**, *82*, 268–276.
[78] Ooi, E.H.; Ng, E.Y.K. Ocular temperature distribution: a mathematical perspective. *Journal of Mechanics in Medicine and Biology* **2009**, *9*, 199–227.
[79] Wessapan, T.; Srisawatdhisukul, S.; Rattanadecho, P. The effects of dielectric shield on specific absorption rate and heat transfer in the human body exposed to leakage microwave energy. *International Communications in Heat and Mass Transfer* **2011**, *38*, 255–262.
[80] Wessapan, T.; Rattanadecho, P. Specific absorption rate and temperature increase in the human eye due to electromagnetic fields exposure at different frequencies. *International Journal of Heat and Mass Transfer* **2013**, *64*, 426–435.
[81] Wessapan, T.; Rattanadecho, P. Influence of ambient temperature on heat transfer in the human eye during exposure to electromagnetic fields at 900 MHz. *International Journal of Heat and Mass Transfer* **2014**, *70*, 378–388.
[82] Ayappa, K.G.; Davis, H.T.; Davis, E.A.; Gordon, J. Analysis of microwave heating of materials with temperature dependent properties. *AIChE Journal* **1991**, *37*(3), 313–322.
[83] Whitaker, S. A theory of drying in porous media. *Advanced Heat Transfer* **1977**, *13*, 119–203.
[84] Bories, S.A. Fundamental of drying of capillary-porous bodies. In *Convective Heat and Mass Transfer in Porous Media*; Kakac, S.; Kilkis, B.; Kulacki, F.; Arinc, F. Eds.; NATO ASI series, Vol. 196; Kluwer Publishers: Dordrecht, the Netherlands, 1991; 39–434.
[85] Boukadida, N.; Ben Nasrallah, S. Two dimensional heat and mass transfer during convective drying of porous media. *Drying Technology* **1995**, *13*(3), 661–694.
[86] Ni, H.; Datta, A.K.; Torrance, K.E. Moisture transport in intensive microwave heating of biomaterials: A multiphase porous media model. *International Journal of Heat and Mass Transfer* **1999**, *42*, 1501–1512.
[87] Feng, H.; Tang, J.; Cavalieri, R.P.; Plumb, O.A. Heat and mass transport in microwave drying of porous materials in a spouted bed. *AIChE Journal* **2001**, *7*, 1499–1512.
[88] Rattanadecho, P.; Pakdee, W.; Stakulcharoen, J. Analysis of multiphase flow and heat transfer: Pressure buildup in an unsaturated porous slab exposed to hot gas. *Drying Technology* **2008**, *26*, 39–53.
[89] Knoerzer, K.; Regier, M.; Hardy, E.H.; Schubert, H.; Schuchmann, H.P. Simultaneous microwave heating and three-dimensional MRI temperature mapping. *Innovative Food Science & Emerging Technologies* **2009**, *10*, 537–544.
[90] Chen, G.; Wang, W.; Mujumdar, A.S. Theoretical study of microwave heating patterns on batch fluidized bed drying of porous material. *Chemical Engineering Science* **2001**, *56*, 6823–6835.
[91] Bhattacharya, M.; Basak, T. On the analysis of microwave power and heating characteristics for food processing: Asymptotes and resonances. *Food Research International* **2006**, *39*, 1046–1057.
[92] Suwannapum, N.; Rattanadecho, P. Analysis of heat–mass transport and pressure buildup induced inside unsaturated porous media subjected to microwave energy using a single (TE10) mode cavity. *Drying Technology* **2011**, *29*, 1010–1024.
[93] Sungsoontorn, S.; Rattanadecho, P.; Pakdee, W. One-dimensional model of heat and mass transports and pressure built up in unsaturated porous materials subjected to microwave energy. *Drying Technology* **2011**, *29*(2), 189–204.
[94] Ayappa, K.G. Modeling transport processes during microwave heating: a review. *Reviews in Chemical Engineering* **1997**, *13*(2), 1–68.
[95] Fu, W.; Metaxas, A.C. A mathematical derivation of power penetration depth for thin lossy materials. *Journal of Microwave Power and Electromagnetic Energy* **1992**, *27*(4), 217–222.
[96] Ni, H.; Datta, A.K. Heat and moisture transfer in baking of potato slabs. *Drying Technology* **1999**, *17*(10), 2069–2092.
[97] Rakesh, V.; Datta, A.K. Microwave puffing: Determination of optimal conditions using a coupled multiphase porous media—large deformation model. *Journal of Food Engineering* **2011**, *107*, 152–163.
[98] Chua, K.J.; Chou, S.K.; Ho, J.C. A comparative study of time-varying thermal and non-thermal drying methods for bioproducts. *Applied Biotechnology Food Science and Policy* **2003**, *1*, 115–123.
[99] Zhang, D.; Mujumdar, A.S. Deformation and stress-analysis of porous capillary bodies during intermittent volumetric thermal drying. *Drying Technology* **1992**, *10*(2), 421–443.
[100] Gong, Z.X.; Mujumdar, A.S.; Itaya, Y.; Mori, S.; Hasatani, M. Microwave drying of clay and non-clay media: Heat and mass transfer and quality aspects. *Drying Technology* **1998**, *16*(6), 1119–1152.
[101] Itaya, Y.; Kobayashi, T.; Hayakawa, K. Three-dimensional heat and mass transfer with viscoelastic strain–stress formation in composite food during drying. *International Journal of Heat and Mass Transfer* **1995**, *38*(7), 1173–1185.
[102] Gunasekaran, S. Pulsed microwave-vacuum drying of food materials. *Drying Technology* **1999**, *17*(3), 395–412.
[103] Raghavan, G.S.V.; Silveira, A.M. Shrinkage characteristics of strawberries osmotically dehydrated in combination with microwave drying. Presented at ADC'99, Bali, Indonesia, 1999.

[104] Raghavan, G.S.V.; Venkatachalapathy, K. Shrinkage of strawberries during microwave drying. *Drying Technology* **1999**, *17*(10), 2309–2321.
[105] Sanga, E.; Mujumdar, A.S.; Raghavan, G.S.V. Principles and applications of microwave drying. In *Drying Technology in Agriculture and Food Sciences*; Mujumdar, A.S. Ed. Oxford IBH: Delhi, India, 2001. Published simultaneously by Science Publishers: Enfield, NH, 2001; 253–289.
[106] Basak, T. Role of lateral and radial irradiations on efficient microwave processing of food cylinders. *Chemical Engineering Science* **2007**, *62*, 3185–3196.
[107] Chaiyo, K.; Rattanadecho, P. Numerical analysis of heat-mass transport and pressure buildup of unsaturated porous medium in a rectangular waveguide subjected to a combined microwave and vacuum system. *International Journal of Heat and Mass Transfer* **2013**, *65*, 826–844.
[108] Perré, P.; May, B.K. A numerical drying model that accounts for the coupling between transfers and solid mechanics: Case of highly deformable products. *Drying Technology* **2001**, *19*(8), 1629–1643.
[109] Perré, P.; Turner, I.W. A 3-D version of TransPore: A comprehensive heat and mass transfer computational model for simulating the drying of porous media. *International Journal of Heat and Mass Transfer* **1999**, *42*(24), 4501–4521.
[110] Rattanadecho, P.; Klinbun, W. Numerical analysis of natural convection in porous media subjected to electromagnetic energy using local thermal non-equilibrium (LTNE) models. *Drying Technology* **2012**, *30*(16), 1896–1905.
[111] Klinbun, W.; Rattanadecho, P. Numerical model of microwave driven convection in multilayer porous packed bed using a rectangular waveguide. *Journal of Heat Transfer* **2012**, *134*, 042605–1–042605–10.
[112] Keangin, P.; Rattanadecho, P. Analysis of heat transport on local thermal non-equilibrium in porous liver during microwave ablation. *International Journal of Heat and Mass Transfer* **2013**, *67*, 46–60.
[113] Akpinar, E.K.; Midilli, A.; Bicer, Y. The first and second law analyses of thermodynamic of pumpkin drying process. *Journal of Food Engineering* **2006**, *72*, 320–331.
[114] Ahern, J.E. *The Exergy Method of Energy Systems Analysis*; John Wiley: New York, 1980.
[115] Jindarat, W.; Sungsoontorn, S.; Rattanadecho, P. Analysis of energy consumption in a combined microwave-hot air spouted bed (CMHS) drying of biomaterial: Coffee beans. *Experimental Heat Transfer* **2015**, *28*(2), 107–124.

Downloaded by [Thammasat University Libraries] at 16:40 28 December 2015

International Communications in Heat and Mass Transfer 70 (2016) 115–126

Contents lists available at ScienceDirect

International Communications in Heat and Mass Transfer

journal homepage: www.elsevier.com/locate/ichmt

Investigation into heat transfer and fluid flow characteristics of liquid two-layer and emulsion in microwave processing☆

Waraporn Klinbun [a], Phadungsak Rattanadecho [b]

[a] Faculty of Engineering and Technology, PANYAPIWAT Institute of Management, Nonthaburi 11120, Thailand
[b] Center of Excellence in Electromagnetic Energy Utilization in Engineering (CEEE), Thammasat University (Rangsit Campus), Khlong Luang, Prathum Thani, 12121 Thailand

ARTICLE INFO

Available online 17 December 2015

Keywords:
Emulsion
Microwave
Rectangular waveguide
Temperature profile

ABSTRACT

Numerical study of fluid flow and heat transfer within two types of liquid (liquid two-layer and oil–water emulsion) when subjected to microwave energy are discussed. In order to obtain the simulation of microwave heating from room temperature, a 2D comprehensive model was integrated with electromagnetic field, incompressible laminar flow and heat transfer. The effects of layered configuration, layered thickness and dispersed fraction of emulsions were investigated. Temporal profiles obtained using fiber optic sensors at four discrete points were compared with the simulated temperature profiles. The simulated outlet temperatures of liquid had a good agreement with experimental data within the maximum prediction error of 5%. The theory presented in this paper can be effectively used to explain fluid transport during microwave heating system using the rectangular waveguide.

© 2015 Elsevier Ltd. All rights reserved.

1. Introduction

The major advantages of microwave heating are rapid and volumetric heating. Microwave can penetrate the surface and produce volumetric heat generation within materials, thus leading to high energy efficiency and short process time. However, non-uniform heating is a disadvantage of microwave heating. The complex interaction of microwaves with sample properties produces non-uniform heating. A particular microwave oven can behave differently for the same sample depending on its physical state such as liquid two-layer and emulsion. This non-uniform heating in a microwave oven not only affects food safety but also influences food quality [1].

Most of the work on microwave heating system design and processes has been done based on only experience and perception of engineers. In addition, experimental study alone is quite difficult to gain the reasons behind non-uniform heating in a microwave oven. A modeling technique is powerful tool can provide a complete platform to study the effects of microwave oven design and food properties on non-uniform heating. Coupled electromagnetic and multi-physics (momentum and heat) equations can describe microwave heating and would help in design microwave ovens and optimize process parameters to minimize non-uniformity issues [2].

Refer to the literature, there were many the theoretical studies on combined microwave and thermal transport [3–20]. The various kinds of dielectric materials are chosen to illustrate microwave heating phenomena.

For liquid sample, Zhang et al. [9] proposed a 3D mathematical model for the heating of water and oil layer with time dependent dielectric properties in microwave cavity. Zhu et al. [16] presented the numerical modeling of continuous flow microwave heating of liquids layer. The results revealed that the heating pattern strongly depends on the dielectric properties of liquids and geometry of the microwave system. Cha-um et al. [19] studied heating process of liquids using microwave with a rectangular waveguide numerically and experimentally. The effects of sample sizes, placement of sample inside the guide, and microwave power were considered in detail. The numerical results agreed well with experimental data. Salvi et al. [21] developed model to simulate temperature profiles in Newtonian and non-Newtonian fluids for continuous flow microwave heating by COMSOL Multiphysics. Recently, Yousefi et al. [22] investigated on microwave heating of flowing water in ANSYS Multiphysics. Various factors were examined; namely, the effects of inlet velocity, applicator height and applicator diameter on the temperature field. A 2D numerical model using COMSOL was developed by Choi et al. [23]. It was to validate uniform heating of particulate foods in a continuous flow microwave and ohmic combination heater. The developed model was included with an electric field, electromagnetic field, incompressible laminar flow, forced-coupling method, heat transfer and arbitrary Langrangian–Eulerian (ALE) moving mesh technique. The simulated outlet temperature of particulate foods was compared with experimental data. The maximum prediction error was 4%.

For layered sample, Rattanadecho [24] investigated the thawing of layered sample using microwave oven. It is shown that, the variation of layered configurations and layer thickness affected to thawing rate

☆ Communicated by W.J. Minkowycz.

E-mail addresses: waraporkli@pim.ac.th (W. Klinbun), ratphadu@engr.tu.ac.th (P. Rattanadecho).

http://dx.doi.org/10.1016/j.icheatmasstransfer.2015.12.005
0735-1933/© 2015 Elsevier Ltd. All rights reserved.

Nomenclature

A	area (m^2)
C_p	specific heat capacity (J/(kg K))
E	electric fields intensity (V/m)
f	frequency of incident wave (Hz)
g	gravitational constant (m/s^2)
h_c	local heat transfer coefficient (W/m^2K)
H	magnetic field intensity (A/m)
k	thermal conductivity (W/mK)
L_x	width of the rectangular waveguide (m)
P	power (W)
p	pressure (Pa)
Q	local electromagnetic heat generation term (W/m^3)
T	temperature (°C)
t	time (s)
tan δ	dielectric loss coefficient (−)
u,w	velocity component (m/s)
Z_H	wave impedance (Ω)
Z_l	intrinsic impedance (Ω)

Greek letters

φ	volume fraction of dispersed phase (−)
α	thermal diffusivity (m^2/s)
β	coefficient of thermal expansion (1/K)
η	dynamic viscosity (Pa/s)
ε	permittivity (F/m)
λ	wavelength (m)
μ	magnetic permeability (H/m)
υ	velocity of propagation (m/s)
ν	kinematics viscosity (m^2/s)
ρ	density (kg/m^3)
σ	electric conductivity (S/m)
ω	angular frequency (rad/s)
ξ	surface tension (N/m)

Subscripts

0	free space
∞	ambient condition
c	continuous phase
d	dispersed phase
eff	effective
r	relative
in	input
x,y,z	axis

due to its dielectric properties of phase change materials during microwave thawing process. Promas et al. [25] concerned with the energy and exergy analyses in the drying process of non-hygroscopic porous packed bed using a combined multi-feed microwave-convective air and continuous belt (CMCB). The results showed that using the CMCB had the several advantages over the conventional method. Klinbun and Rattanadecho [20] studied numerically the heating of multilayer porous packed bed which subjected to microwave power. This study aimed to understand effects of layered configuration, layered thickness and operating frequency. The results were presented in electric field distribution, heat transfer and velocity flow.

The layered liquids and emulsions are the common food systems, such as milk, salad dressing, mayonnaise, sauces, and many more [18]. Therefore, understanding the influences of various parameters during microwave processing of layered liquid and emulsions are required because of the wide usage of microwave systems.

The most emulsions are considered as oil-in-water (o/w) and water-in-oil (w/o). An earlier investigation on microwave heating of multiphase system and emulsions was reported by Barringer et al. [26]. They studied experimentally for various oil–water fractions and layered system with fixed beaker radii in a household microwave oven. They found the dielectric properties and sample size determined in which sample resonant absorption occurred. Chan and Chen [27], Rajaković and Skala [28], and Nour et al. [29] carried out experimental studies on the conditions of demulsification of water-in-oil emulsions by microwave technology. After that, Samanta and Basak [18] carried out the preliminary theoretical analysis on efficient microwave processing of 1D oil–water emulsion (o/w and w/o) placed on ceramic plates (alumina, SiC). The results were shown that an alumina support at the left side may be recommended as the optimal heating strategy for both o/w and w/o emulsion samples whereas SiC support may be favored for o/w emulsion sample due to lesser thermal runaway. In addition, microwave energy was applied to separate or demulsify of emulsions. For example, Palou et al. [30] studied the demulsification of an o/w emulsion prepared with Mexican heavy crude oil. A comparative study was carried out between microwave and oil bath heating with regard to water separation time. From the results, microwave dielectric heating used less time than conventional oil bath heating. Water separation of O/W emulsions increased with microwave power and salt content of the aqueous phase, and in the presence of a chemical demulsifier. Binner et al. [31] was investigated the separation of water-in-oil emulsions using natural gravity settling and microwave heating techniques. The result was found that the thermal effect of microwave heating leads to improvements in settling times.

Due to the large amount of past studies are primarily considered on microwave heating of pure substance or layered system. There are a few works which investigate of microwave processing of multiphase system, especially emulsions. Therefore, the various parameters are still not fully understood and a number of critical issues still remain unsolved. The characteristics of microwave heating of emulsions and layered materials are very complicated, thus the study in more detail should be systemically studied.

This research was to develop a comprehensive fully coupled multiphysics model that includes heat and momentum transfer in model liquid system. In this article, the simulated results were compared with experimental heating profiles of a model. The effects of layered configuration, layered thickness, dispersed phase fraction, and dielectric properties of emulsion are studied. The results presented here provide a basis for fundamental understanding of microwave heating of layered liquid and oil–water emulsions.

2. Experimental study

2.1. Sample preparation

The two-layer and emulsion of oil–water were studied. The oil-in-water emulsion, designated as o/w emulsion and water-in-oil emulsion, designated as w/o emulsions. In case of two-layer is considered in two models: w-o bed (water layer on oil layer), and o-w bed (oil layer on water layer). The sample size is chosen to be 109.22 × 54.61 × 50 mm.

2.2. Apparatus

Fig. 1 shows the experimental apparatus for microwave heating using a rectangular waveguide system. It was a monochromatic wave of TE_{10} mode operating at a frequency of 2.45 GHz. The magnetron (Micro Denshi Co., model UM-1500) generated microwave energy that was transmitted along the z-direction of the rectangular waveguide with inside dimensions of 110 × 55 mm toward a water load that was situated at the end of the guide. The water load ensured that only a minimal amount of microwave was reflected back to the sample. An isolator on the upstream side of sample is used to trap microwave was reflected from the sample in order to prevent the microwave from damaging the magnetron. The sample heated was liquid layer of 50 mm in thickness,

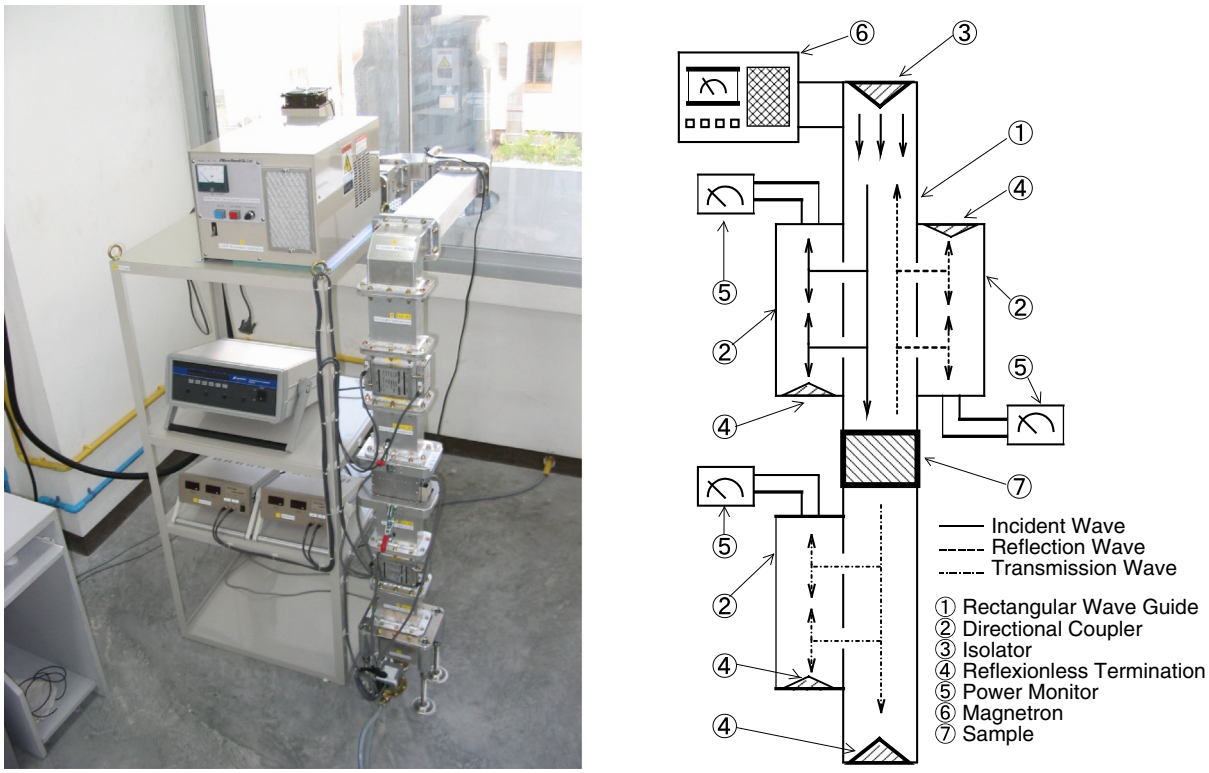

Fig. 1. Experimental apparatus for microwave heating system; (a) equipment setup and (b) microwave measuring system [19].

which is filled in container with a thickness of 0.75 mm and is made from polypropylene. During the experiment, output of magnetron was set at 500 W. The powers of incident, reflected and transmitted waves were measured by a wattmeter using a directional coupler (Micro Denshi Co., model DR-5000). The temperature was measured with a Luxtron fluoroptic thermometer model 790 (accurate to ±0.5 °C) which were placed in the center of the sample at each 10 mm interval.

3. Mathematical modeling

The model was developed to predict heat and fluid flow during heating by microwave energy. The Maxwell's equations of electromagnetic were solved to obtain the electric field inside the cavity and sample and coupled with a multi-physics model to obtain a temperature and velocity distribution in 2D in Fig. 2.

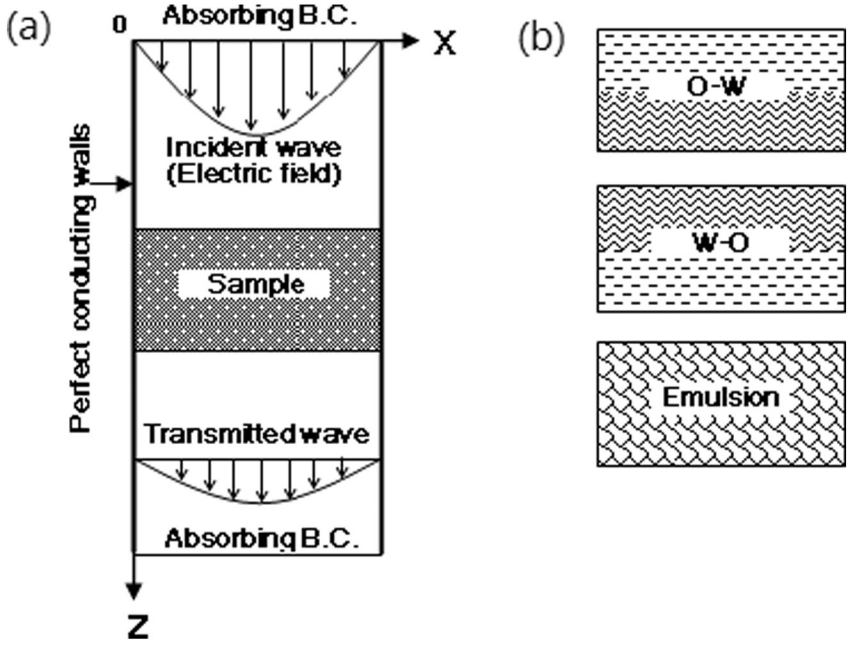

Fig. 2. Physical model; (a) computational domain and (b) sample [20].

3.1. Electromagnetic model

In this work, electromagnetic wave was considered in the TE_{10} mode which does not change in the direction between the broad faces. The Maxwell's equations for electromagnetic wave in TE_{10} mode can be written as [19]:

$$\frac{\partial E_y}{\partial z} = \mu \frac{\partial H_x}{\partial t} \tag{1}$$

$$\frac{\partial E_y}{\partial x} = -\mu \frac{\partial H_z}{\partial t} \tag{2}$$

$$-\left(\frac{\partial H_z}{\partial x} - \frac{\partial H_x}{\partial z}\right) = \sigma E_y + \varepsilon \frac{\partial E_y}{\partial t} \tag{3}$$

where permittivity or dielectric constant ε, magnetic permeability μ and electric conductivity σ are defined by:

$$\varepsilon = \varepsilon_0 \varepsilon_r, \mu = \mu_0 \mu_r, \sigma = 2\pi f \varepsilon \tan\ \delta \tag{4}$$

The dielectric properties are a function of volume fraction and temperature, as follow:

$$\varepsilon_r(\varphi, T) = \varepsilon_r'(\varphi, T) - j\varepsilon_r''(\varphi, T) \tag{5}$$

For water [10]:

$$\varepsilon_r'(T) = 85.56 - 0.3099T - 2.328 \times 10^{-3}T^2 + 4.107 \times 10^{-5}T^3 - 1.728 \times 10^{-7}T^4 \tag{6}$$

$$\tan\ \delta(T) = 0.2314 - 6.405 \times 10^{-3}T + 9.37 \times 10^{-5}T^2 7.415 \times 10^{-7}T^3 + 2.415 \times 10^{-9}T^4 \tag{7}$$

For corn oil [9]:

$$\varepsilon_r'(T) = 2.587 + 0.001313T + 3.998 \times 10^{-6}T^2 \tag{8}$$

$$\varepsilon_r''(T) = 0.1214 + 0.00172T + 1.454 \times 10^{-6}T^2 \tag{9}$$

For o/w emulsions [18]:

$$\varepsilon_r = \frac{\varepsilon_{rc}[\varepsilon_{rd}(1 + a\varphi) + a\varepsilon_{rc}(1 - \varphi)]}{\varepsilon_{rd}(1 - \varphi) + \varepsilon_{rc}(a + \varphi)} \tag{10}$$

For w/o emulsions [18]:

$$\ln \varepsilon_r = \varphi \ln \varepsilon_{rd} + (1 - \varphi) \ln \varepsilon_{rc} \tag{11}$$

Power absorbed per unit volume from the microwaves at any location of the sample was calculated from the electric field distribution inside the sample:

$$Q = 2\pi f \cdot \varepsilon_0 \cdot \varepsilon_r'(\tan\ \delta)(E_y)^2 \tag{12}$$

Boundary conditions: The walls of the rectangular cavity were assumed to be perfect electric conductors and hence the tangential component of the electric field was set to zero.

$$H_n = 0, E_t = 0 \tag{13}$$

At the both ends of cavity was absorbing condition by Mur [32]:

$$\frac{\partial E_y}{\partial t} = \pm v \frac{\partial E_y}{\partial z} \tag{14}$$

The microwave source is simulated by the equations [10]:

$$E_y = E_{yin} \sin\left(\frac{\pi x}{L_x}\right) \sin(2\pi f t) \tag{15}$$

$$H_x = \frac{E_{yin}}{Z_H} \sin\left(\frac{\pi x}{L_x}\right) \sin(2\pi f t) \tag{16}$$

where f is the frequency of microwave, L_x is the width of the incidence plane, Z_H is the wave impedance, and E_{yin} is the input value of the electric field intensity. By applying the Poynting theorem, the input value of the electric field intensity is evaluated by the microwave power input as:

$$E_{yin} = \sqrt{\frac{4Z_H P_{in}}{A}} \tag{17}$$

where P_{in} is the microwave power input and A is the area of the incident plane.

3.2. Heat transfer and fluid flow model

A 2D multi-physics model was formulated to describe the momentum and heat transfer inside the sample. The two samples included in the liquid model were water and corn oil. The energy conservation equation was solved for the mixture and the effect of microwave heating was included as a source term obtained from the electromagnetic model. For momentum balance, the Boussinesq approximation takes into account of the effect of density variation on the buoyancy force.

Continuity equation:

$$\frac{\partial u}{\partial x} + \frac{\partial w}{\partial z} = 0 \tag{18}$$

Momentum equations:

$$\frac{\partial u}{\partial t} + \left(u\frac{\partial u}{\partial x} + w\frac{\partial u}{\partial z}\right) = -\frac{1}{\rho}\left(\frac{\partial p}{\partial x}\right) + \nu\left(\frac{\partial^2 u}{\partial x^2} + \frac{\partial^2 u}{\partial z^2}\right) \tag{19}$$

$$\frac{\partial w}{\partial t} + \left(u\frac{\partial w}{\partial x} + w\frac{\partial w}{\partial z}\right) = -\frac{1}{\rho}\left(\frac{\partial p}{\partial z}\right) + \nu\left(\frac{\partial^2 w}{\partial x^2} + \frac{\partial^2 w}{\partial z^2}\right) + g\beta(T - T_\infty) \tag{20}$$

Energy equation:

$$(\rho C_p)_{eff}\frac{\partial T}{\partial t} + (\rho C_p)_{eff}\left(u\frac{\partial T}{\partial x} + w\frac{\partial T}{\partial z}\right) = k_{eff}\left(\frac{\partial^2 T}{\partial x^2} + \frac{\partial^2 T}{\partial z^2}\right) + Q \tag{21}$$

where

$$(\rho C_p)_{eff} = (1 - \varphi)(\rho C_p)_c + \varphi(\rho C_p)_d \tag{22}$$

$$k_{eff} = (1 - \varphi)k_c + \varphi k_d \tag{23}$$

where the suffixes 'c' and 'd' represent the continuous and dispersed phases, respectively.

Boundary conditions: Only the top surface of the sample was open for energy transfer and the other surfaces were insulted. In addition, the Marangoni flow [10] was incorporated as a boundary condition. Finally, the initial temperature of sample is 28 °C.

$$-k\frac{\partial T}{\partial z} = h_c(T - T_\infty) \tag{24}$$

$$\eta\frac{\partial u}{\partial z} = -\frac{d\xi}{dT}\frac{\partial T}{\partial x} \tag{25}$$

where k, h_c are thermal conductivity and heat transfer coefficient, respectively. η is dynamic viscosity and ξ is surface tension

3.3. Input parameter

Dielectric properties of the samples as function of temperature and volume fraction and thermal properties (heat capacity, thermal conductivity and coefficient of thermal expansion) were obtained from literatures. The detail was showed in Table 1.

3.4. Numerical solution

The electromagnetic and the multi-physics model were fully coupled as the dielectric properties of the sample, which were obtained from literature, were a function of temperature and volume fraction. The coupling procedure was showed in Fig. 3. The Maxwell's equations (Eqs. (1)–(3)) are solved using the finite difference time domain (FDTD) method with boundary conditions given by Eqs. (13)–(16). To ensure stability of the time-stepping algorithm Δt is chosen to satisfy the courant stability condition:

$$\Delta t \le \frac{\sqrt{(\Delta x)^2 + (\Delta z)^2}}{c} \tag{26}$$

And the spatial resolution of each cell defines as:

$$\Delta x, \Delta z \le \frac{\lambda_g}{10\sqrt{\varepsilon_r'}} \tag{27}$$

In this work, a time step of $\Delta t = 2 \times 10^{-12}$ s is used to solve Maxwell's equations. The grid size is $\Delta x = 1.0922$ mm and $\Delta z = 1.0$ mm.

For the sample, energy and momentum equations were solved using a cell centered finite control volume along with the SIMPLE algorithm developed by Patankar [33]. The time step is 0.01 s. The fully implicit time discretization finite difference scheme is used to arrive at the solution in time. The each time step iterations are continued until the relative error is less than 10^{-6}(error $\le 10^{-6}$).

4. Results and discussion

4.1. Characterizing electric field distribution

Because the first objective is to understand the change in electric field density during heating of two-layer and emulsion at various dielectric properties, the coupled models were used to determine the electric field power density within the liquid sample. The electric field distribution inside the cavity and sample was showed in Fig. 4.

Fig. 4 presents the simulation of the typical electric field of TE_{10} mode along the center axis (x = 54.61 mm) of rectangular waveguide. The vertical axis represents the intensity of the electric field E_y, which is normalized to the amplitude of the input electromagnetic wave, E_{yin}.

In Fig. 4(a) and (b), corresponding to that cases of single layer liquid, since the microwave passing through waveguide having low permittivity is directly irradiated to the sample having high permittivity, large part of microwaves are reflected from the surface of the sample and interfered with forward wave propagated from the wave input region

Table 1
Thermal property for computational model.

Properties	Air	Water	Corn oil
ρ (kg m^{-3})	1.205	1000	920
C_p (J kg^{-1} K^{-1})	1007	4186	2100
k (W m^{-1} K^{-1})	0.0257	0.61	0.17
η (kg (ms)$^{-1}$)	1.983×10^{-5}	1.793×10^{-3}	6.072×10^{-3}
β (K^{-1})	3.43×10^{-3}	5.344×10^{-4}	3.8×10^{-4}

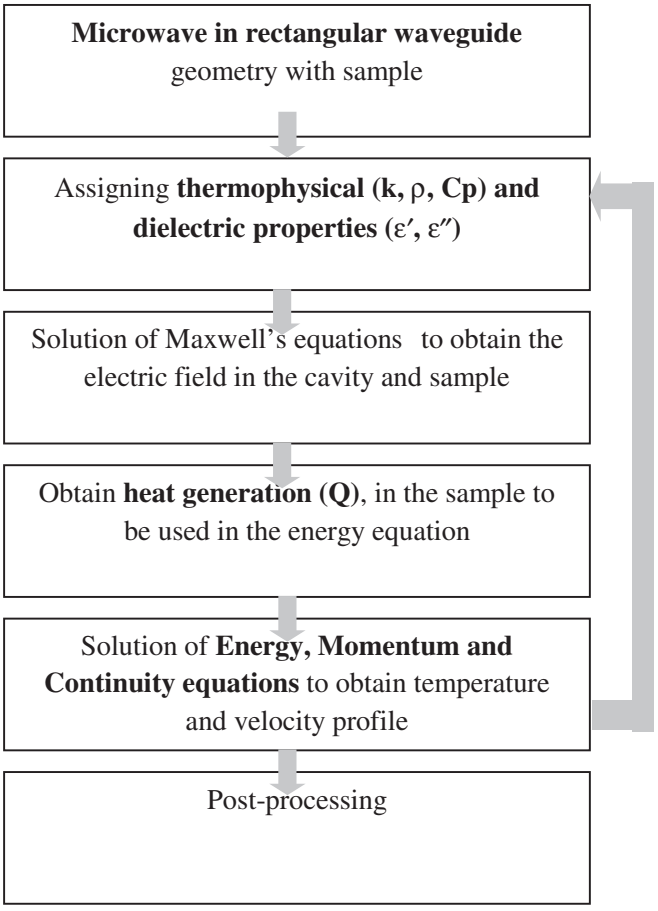

Fig. 3. Algorithm for coupling of electromagnetism and heat transfer and fluid flow.

cause a stronger standing wave with large amplitude is formed within cavity. However, the electric field within the sample is almost extinguished where the electric field attenuated owing to microwave energy absorbed, and thereafter the microwave energy absorbed is converted to the thermal energy. In addition, reflected wave from water layer surface are much higher than that of an oil layer due to permittivity of oil layer is higher than air not so much, the small part of microwave is reflected from the surface of oil layer.

Fig. 4(c) shows the distribution of electric field for the cases of 2o-2w layers. The large part of microwaves can penetrate into the sample; the wave reflected from the lower surface has the same order as propagating wave. The large amplitude and wavelength is formed inside the sample by contribution of propagating and reflected waves, such pattern can lead to higher microwave energy absorbed in the interior in comparison with other cases. Fig. 4(d) shows the distribution of electric field for the cases of 2w-2o layers. It can be observed that the distribution of electric field for this case is nearly the same as that water layer (Fig. 4(b)). Therefore, the presence of water layer at the incident floor slightly affects the distribution of electric field because the major parts of microwaves are reflected from the surface.

By comparing Fig. 4(e) and (f), the small part of microwave is reflected from the surface of 1o-3w. Therefore, the oil layer at thickness of 12.5 mm (1o-3w) strongly affects the distribution of electric field due to large part of microwave can penetrate through the surface.

Fig. 4(g) and (h) were similar; it is observed that electric field within emulsions sample is slightly decreased along the depth of sample. It is also interesting to observe that the electric field intensity for the case of 75% o/w sample is greater than the electric field intensity for the case of 25% o/w emulsions. This is because the higher oil content in the emulsions results in smaller effective dielectric loss and higher

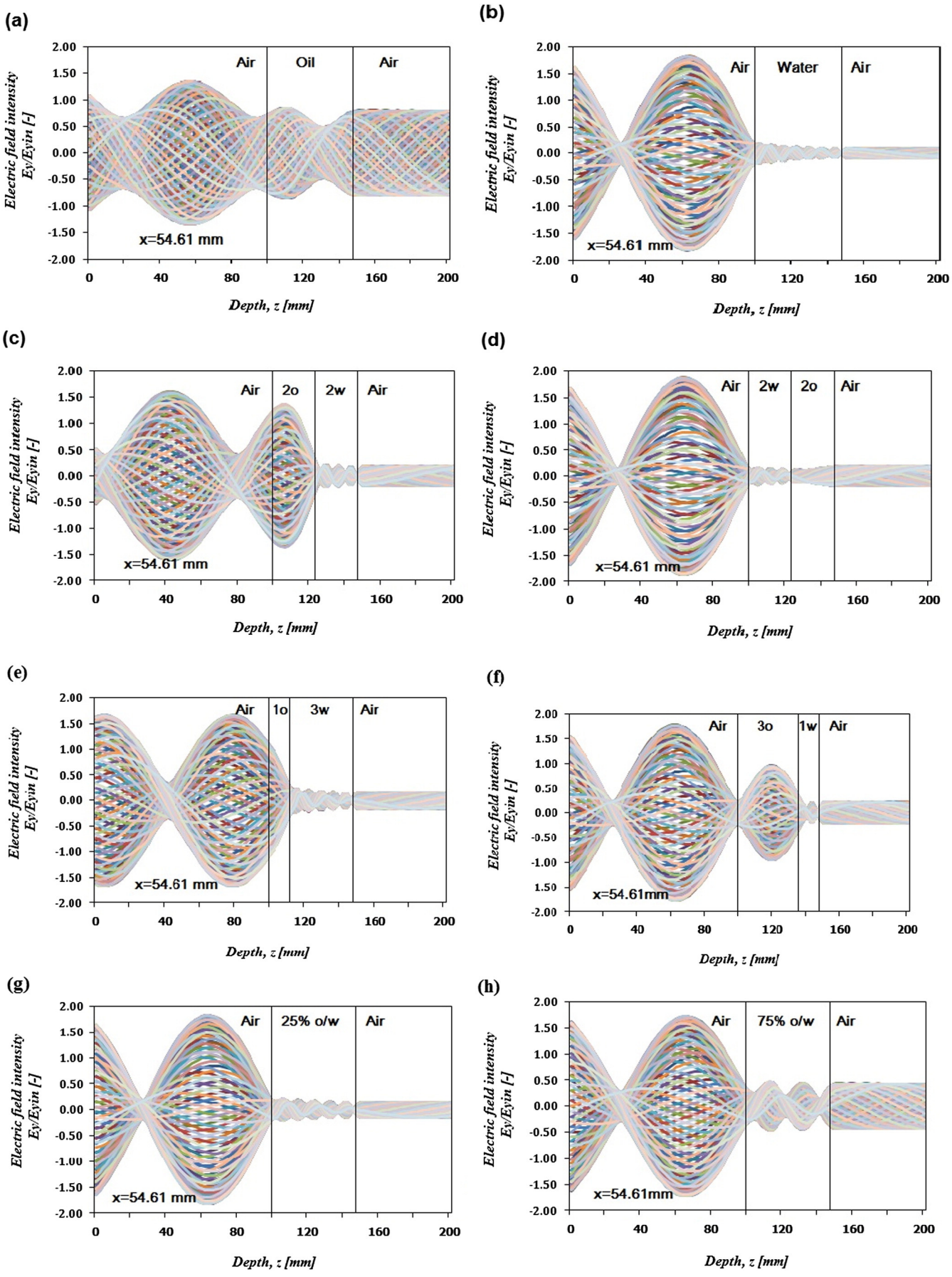

Fig. 4. Electric field distribution inside cavity and sample (P = 500 W, f = 2.45 GHz, t = 60 s).

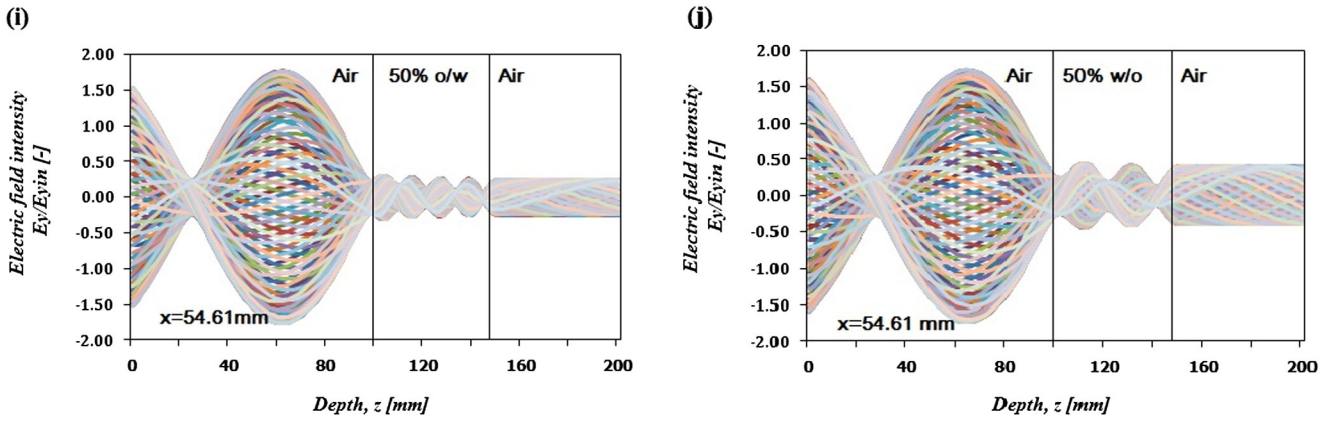

Fig. 4 (*continued*).

penetration depth. Therefore, emulsions with higher oil contents would show the higher electric field intensity.

Fig. 4(i) and (j) was shown that the electric field is depended on the continuous phase of emulsions (o/w or w/o) and an amplitude of electric field for the case of w/o emulsions is found to be higher than that for the case of o/w emulsions.

4.2. Time-temperature profile

Temporal profiles obtained using fiber optic sensors at four discrete points were compared with the simulated temporal profiles. Fig. 5 compared the observed and simulated temperatures during the heating process. Fig. 5(a) showed that temperatures increase with processing time. The comparisons along the horizontal axis (x = 55 mm) was displayed in Fig. 5(b). It was observed that the temperatures decrease along the depth of sample due to its penetration depth effect. From the comparison between the simulated results and experimental data, it was found that it was agree well for all cases of samples and the difference lie below 5 °C. The small discrepancies maybe resulted from keeping constant of some thermal properties during simulation process. In addition, the uncertainty in temperature measurement might come from the error in measured microwave power input where the calculated uncertainty associated with temperature was less than 2%. From this result, it was clear that model can be used as a real tool for investigating in detail this particular microwave heating of dielectric materials at a fundamental level.

4.3. Spatial temperature profile

Fig. 6 depicts simulation of temperature distribution within liquid sample with heating time of 60 s. The results show the greatest temperature in the upper region (this region close to the incoming microwave) of heating sample with the temperature decreasing toward the lower wall. It is found that the temperature contour agree well with distribution of electric field.

By comparing in each layered configurations, it is seen that the temperature field within sample in case of 2o–2w is significantly greater than that of other cases. The high temperatures occur in the center of heating layers with temperature decreasing toward the side walls of the liquid layer corresponding to the characteristic of TE_{10} mode. However, the temperatures increase again near the side walls, which is due to the walls being insulated and low rate of heat loss. The distribution of temperature field near the middle region of liquid layer tends to be uniformed, because the strong effect of Marangoni flow causes the hot spot to move from the middle region to the side walls of the container. The surface of liquid layer, that is close to the incoming microwave, heats up to a higher level at a faster rate than anywhere within the liquid layer. Nevertheless, the temperature decreases slowly along the propagation direction because the penetration depth effect.

In case of effect of layered thickness, it was found that the distribution of temperature in the sample is wavy behavior corresponding to that of electric field. In case of the oil layer with thickness of 25.0 mm,

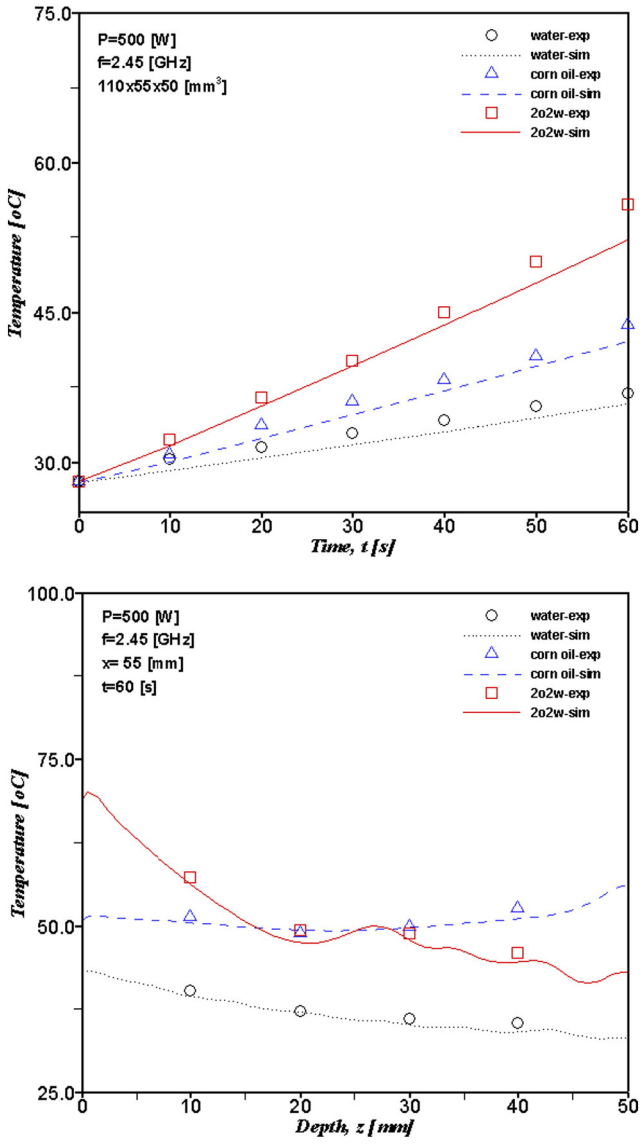

Fig. 5. Simulated and observed time-temperature profile at four locations of sample subjected at 2.45 GHz: (a) during process time and (b) along depth, z [mm].

the distribution of temperature is higher than the cases with oil layer thickness of 12.5 mm and 37.5 mm. It reveals that a stronger standing wave with large amplitude will be formed within the sample with the optimum oil layer thickness. Thus, a higher maximum temperature will be produced. In addition, the temperature contour in the vertical plane (x-z) for the case of 1o-3w and 3o-1w are illustrated the greatest temperature at upper of heating sample where the microwave is incident.

For effect of dispersed phase fraction, the temperature distributions qualitatively follow the electric field intensity within the emulsions. The greater temperature is observed for the case of 75% oil in water emulsions. This is because of the concentration of dispersed phased increased, the number of interfaces, and thus interfacial reflections increased as results in increase power absorption and consequently heating rate [26]. The two maxima in temperatures occur at the center and near the walls of the rectangular waveguide for all cases of oil in water emulsions due to high electric field intensity of TE_{10} mode and the accumulated of heat, respectively. Since the higher microwave power incident at the surface of sample, the maxima in temperature occur at the surface. However, it is found that the maximum temperature occurs at the bottom for the case of 75% o/w sample because the standing waves are formed at the interface between bottom surface and air.

Finally, the comparison of temperature distribution within emulsions between 50% o/w and 50% w/o, it may also be noted that, the greater temperature occurs in the case of o/w emulsions than that the case of w/o emulsions for all directions. The average temperatures within o/w emulsions are 41.62 and 44.89 °C along width, x [mm] and depth, z [mm], respectively whereas average temperatures within w/o emulsions are 38.57 and 41.40 °C along width, x [mm] and depth, z [mm], respectively. The temperature contour for the case of o/w emulsions is higher than that for the case of w/o emulsions.

4.4. Velocity field profile

Fig. 7 illustrated the velocity field within liquid layer and emulsion. The local heating on the surface of liquid layer causes the difference of the surface tension on the surface of liquid layer, which leads to the convective flow of liquid (as Marangoni flow). The liquid flows from the hotter region (higher power absorbed) at the middle of liquid layer to the cold region (lower power absorbed) at the side walls of the container.

By comparing Fig. 7(a) and (b), it is observed that the effect of convective flow in case of water layer becomes stronger than that of oil layer. In Fig. 7(c) and (d), it is seen that the velocity fields are clearly different for each layers.

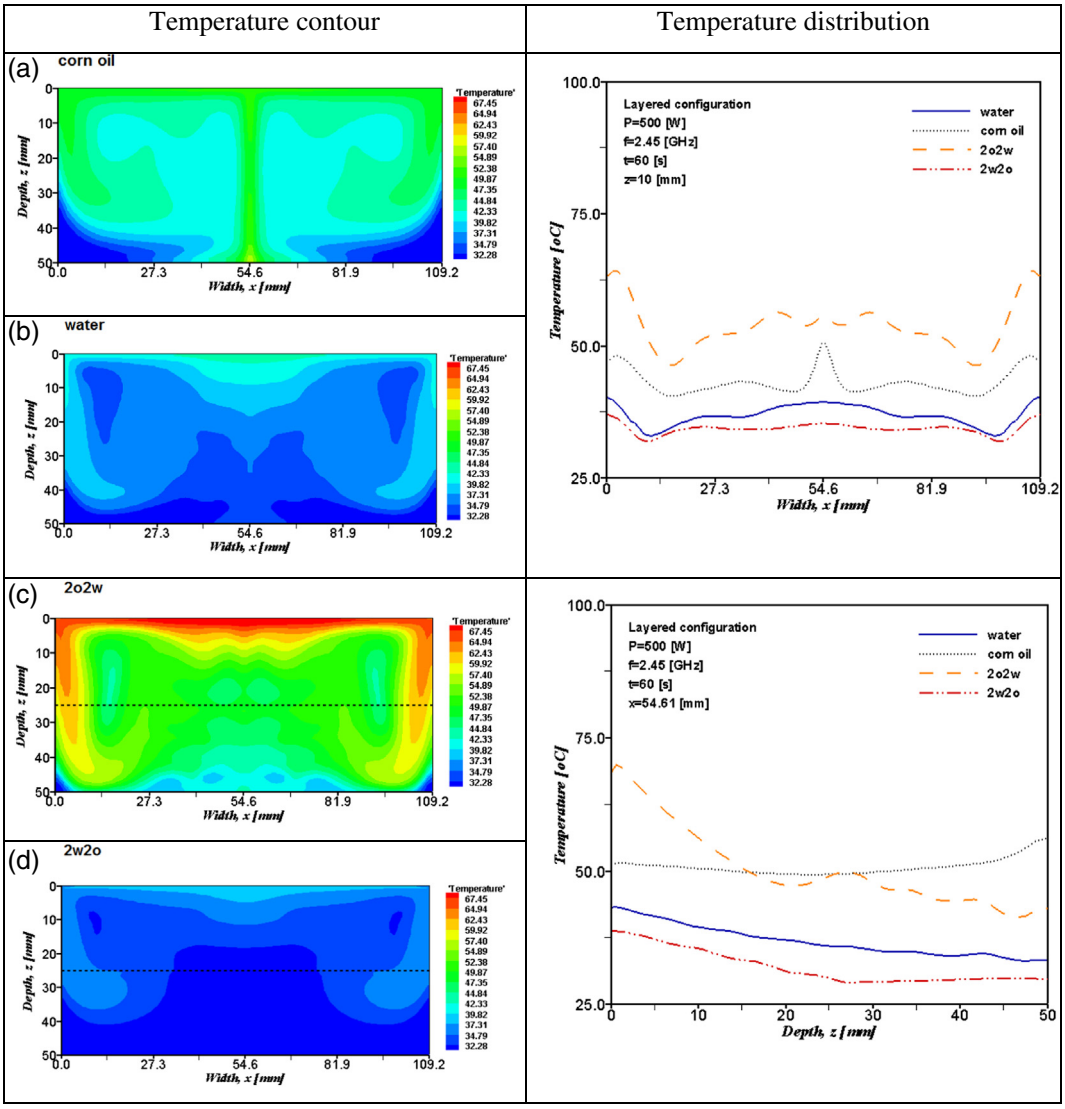

Fig. 6. Spatial temperature profile of the sample due to microwave irradiations (P = 500 W, f = 2.45 GHz, t = 60 s).

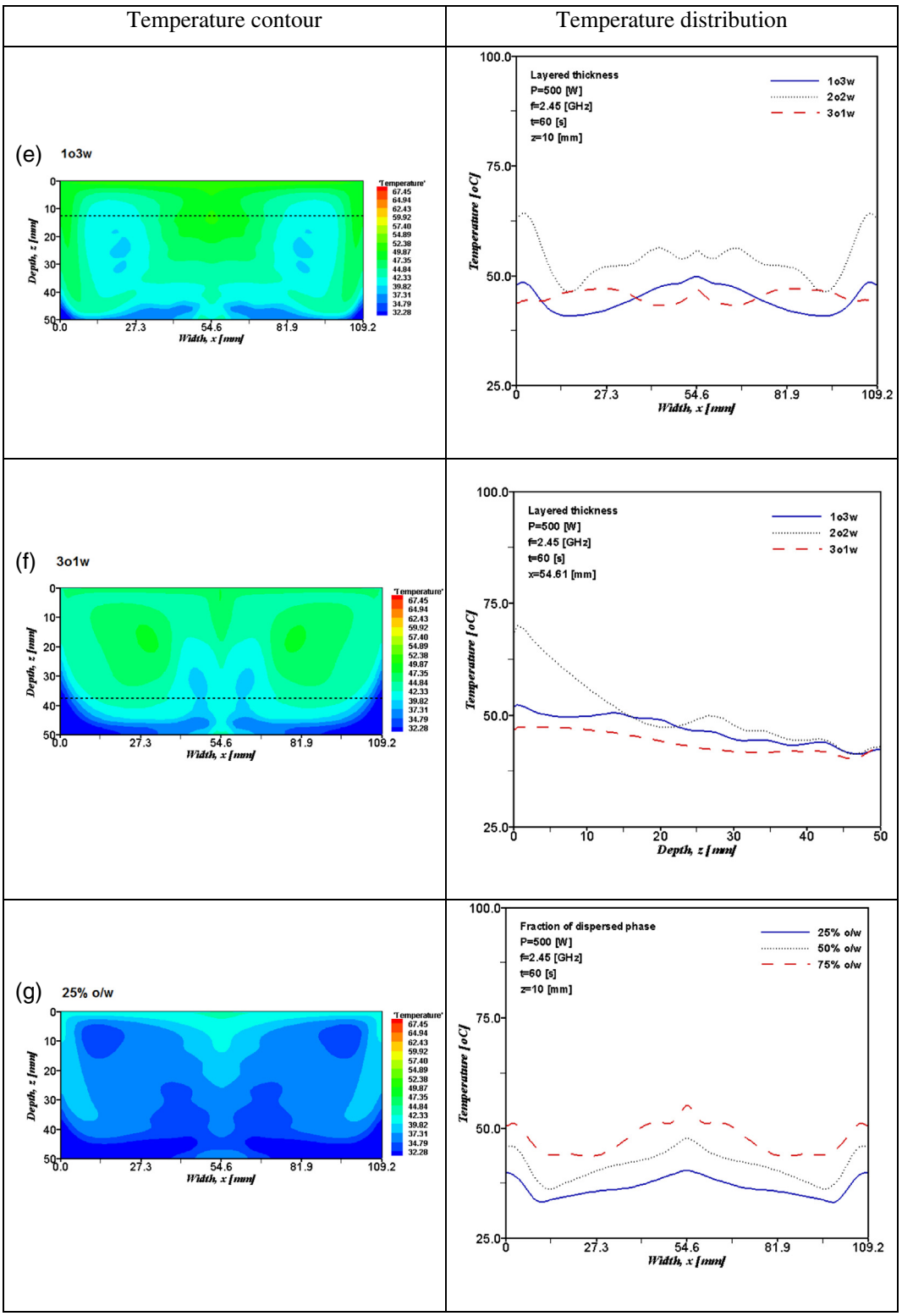

Fig. 6 (*continued*).

From Fig. 7(e) and (f), the velocity fields are related with the temperature contours for microwave heating of two-layered liquid with various layered thicknesses using a rectangular waveguide. It also observed that the flow patterns in case of 1o–3w and 3o–1w are similar to the single layer of water and oil, respectively because the effect of volume of sample in each layer. The sample with higher oil content leads to higher penetration depth and stronger resonance of standing wave.

Fig. 7(g) and (h) displayed the flow patterns in vertical plane (x-z) for the case of 25% o/w and 75% o/w, respectively. The velocity fields qualitatively follow the temperature contour. The velocity field is strongly depended on oil fraction (φ) in o/w emulsions.

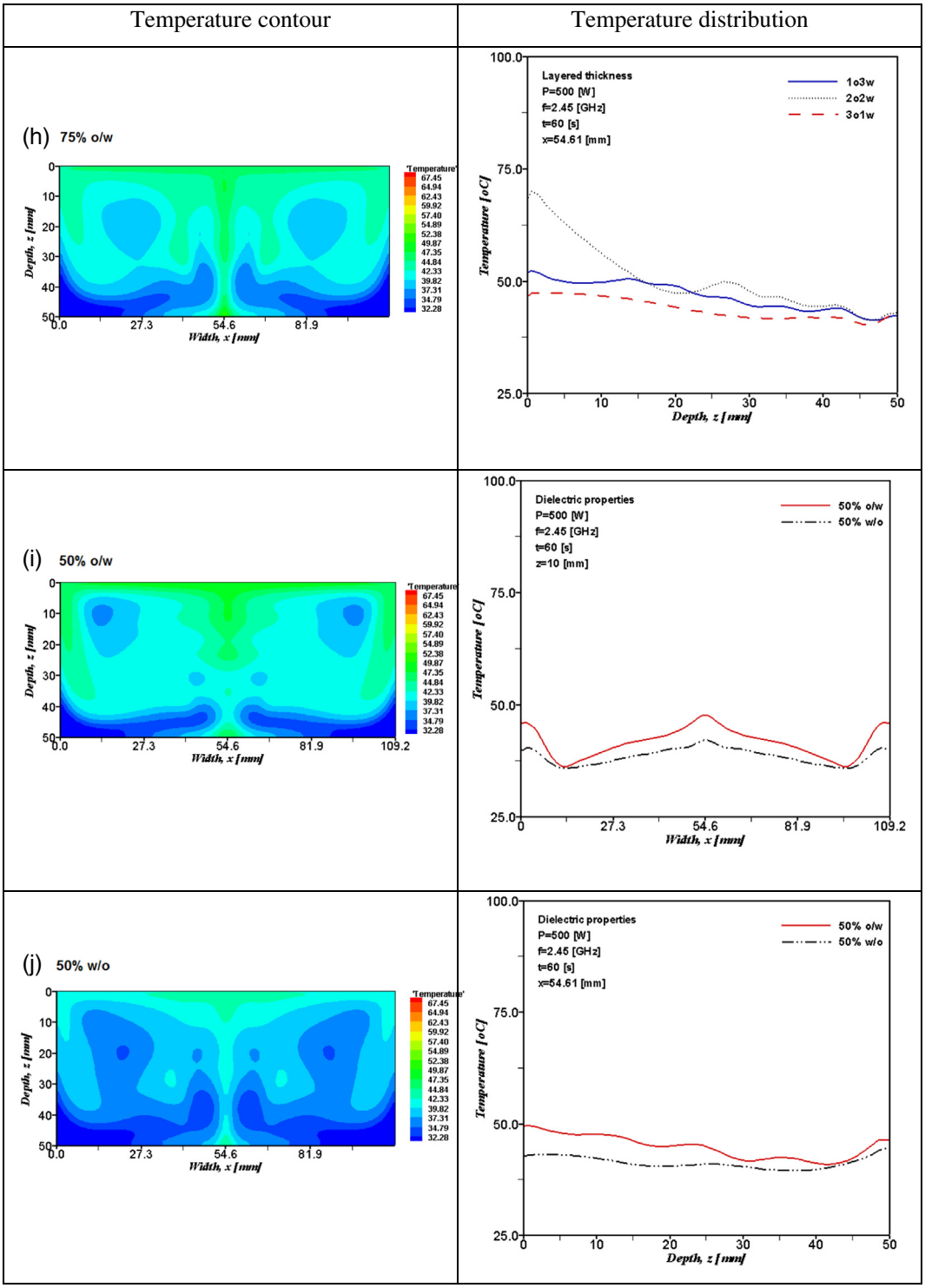

Fig. 6 (*continued*).

Finally, it was also observed that, the flow pattern (Fig. 7(i)) was similar to Fig. 7(j) but the magnitudes of velocity are different. The key parameters affecting to the fluid flow pattern have been already explained in the first subsection.

5. Conclusions

A comprehensive coupled electromagnetic and heat transfer model was developed to simulate microwave heating in rectangular cavity. The simulation results are validated with experimental data at 2.45 GHz. Effects of layered configuration, layered thickness, dispersed fraction, and dielectric properties were studied.

The conclusions of this work can be concluded as followings:

(1) The presenting model of microwave heating of two-layered liquid and emulsions by using a rectangular waveguide (TE_{10} mode) can successfully explain the heating phenomena under various conditions.
(2) The layered configuration of liquid layers has significant affect to heating pattern and velocity field.

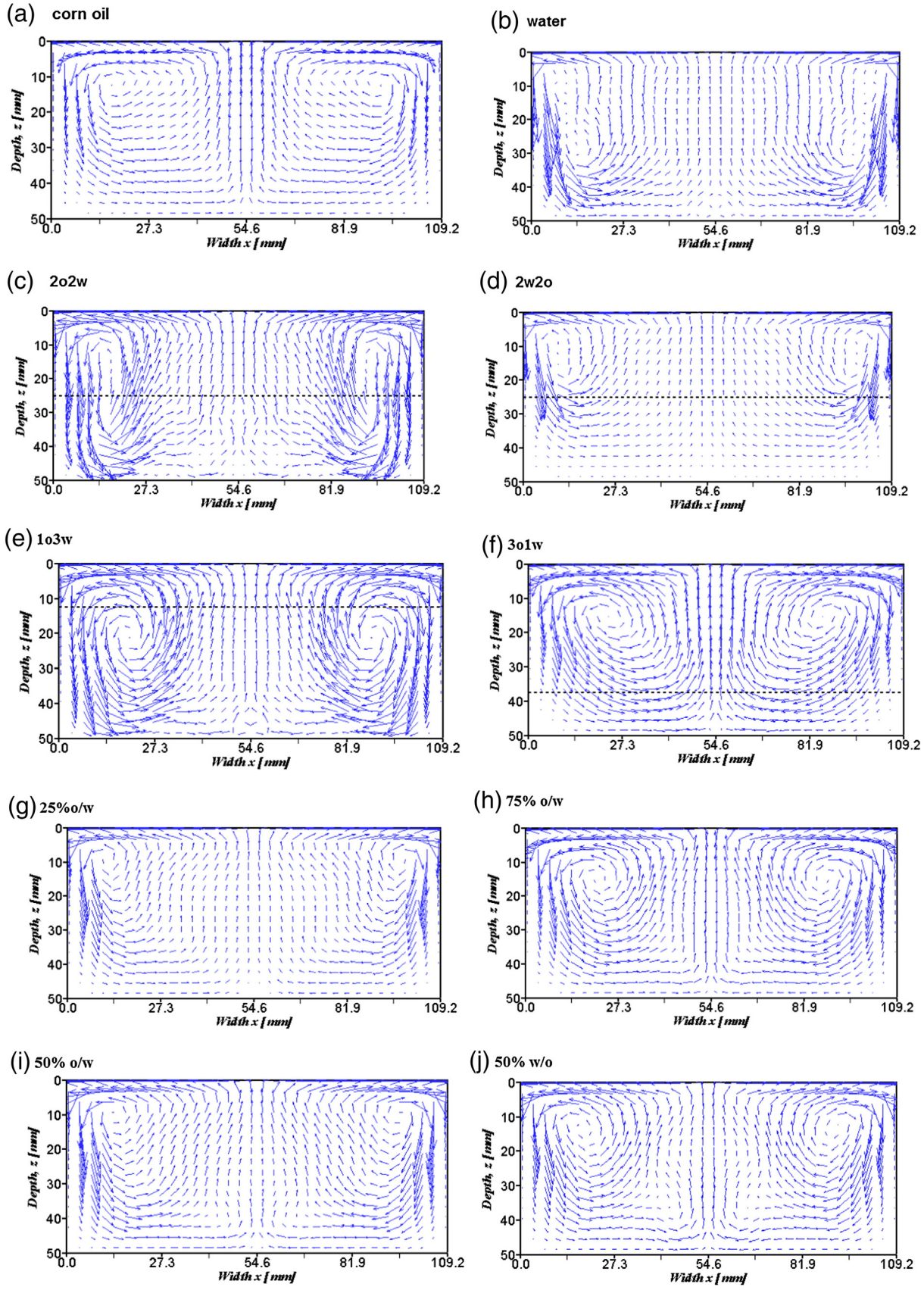

Fig. 7. Spatial velocity profile of the sample due to microwave irradiations (P = 500 W, f = 2.45 GHz, t = 60 s).

(3) The optimum layered thickness of layered system and the higher oil content of o/w emulsion result in the higher temperature, which is related to the increasing microwave power absorbed.
(4) The continuous medium of an emulsion has strongly effect on heating pattern.

The next steps of this work highlight the other materials as Emulsions in Porous Media.

Acknowledgment

The authors gratefully acknowledge the financial support for this work provided by the Thailand Research Fund (under the TRF contract No. RTA5680007) and the Nation Research University Project of Thailand Office of Higher Education Commission.

References

[1] L. Ma, D. Paul, N. Pothecary, C. Railton, J. Bows, L. Barratt, J. Mullin, D. Simons, Experimental validation of a combined electromagnetic and thermal FDTD model of a microwave heating process, IEEE Trans. Microwave Theory Tech. 47 (1995).
[2] H. Chen, J. Tang, F. Lui, Simulation model for moving food packages in microwave heating processes using conformal FDTD method, J. Food Eng. 88 (3) (2008) 294–305.
[3] A. Metaxas, R. Meridith, Industrial Microwave Heating, Peter Peregrinus Ltd, London, 1983.
[4] H. Prosetya, A. Datta, Batch microwave heating of liquids: an experiment study, J. Microwave Power Energy 26 (4) (1991) 215–226.
[5] K. Ayappa, H. Davis, E. Davis, J. Gordon, Two-dimensional finite element analysis of microwave heating, AICHE J. 38 (10) (1992) 1577–1592.
[6] K. Ayappa, H. Davis, G. Crapiste, E. Davis, J. Gordon, Microwave heating: an evaluation of power formulations, Chem. Eng. Sci. 46 (4) (1991) 1005–1016.
[7] K. Ayappa, S. Brandon, J. Derby, H. Davis, E. Davis, Microwave driven convection in a square cavity, AICHE J. 40 (7) (1994) 1268–1272.
[8] H. Ni, A. Datta, K. Torrance, Moisture transport in intensive microwave heating of biomaterials: a multiphase porous media model, Int. J. Heat Mass Transfer 42 (8) (1999) 1501–1512.
[9] Q. Zhang, T. Jackson, A. Ungan, Numerical modeling of microwave induced natural convection, Int. J. Heat Mass Transfer 43 (2000) 2141–2154.
[10] P. Ratanadecho, K. Aoki, M. Akahori, A numerical and experimental investigation of the modeling of microwave heating for liquid layers using a rectangular wave guide (effects of natural convection and dielectric properties), Appl. Math. Model. 26 (3) (2002) 449–472.
[11] D. Dincov, K. Parrott, K. Pericleous, Heat and mass transfer in two phase porous materials under intensive microwave heating, J. Food Eng. 65 (3) (2004) 403–412.
[12] P. Salagnac, P. Glouannec, D. Lecharpentier, Numerical modeling of heat and mass transfer in porous medium during combined hot air, infrared and microwave drying, Int. J. Heat Mass Transfer 47 (2004) 4479–4489.
[13] V. Romano, F. Marra, U. Tammaro, Modelling of microwave heating of foodstuff: study on the influence of sample dimensions with a FEM approach, J. Food Eng. 71 (3) (2005) 233–241.
[14] V. Vegh, I. Turner, A hybrid technique for computing the power distribution generated in a lossy medium during microwave heating, J. Comput. Appl. Math. 197 (1) (2006) 122–140.
[15] S. Chatterjee, T. Basak, S. Das, Microwave driven convection in a rotating cylindrical cavity: numerical study, J. Food Eng. 79 (4) (2007) 1269–1279.
[16] J. Zhu, A. Kuznetsov, K. Sandeep, Mathematical modeling of continuous flow microwave heating of liquids (effects of dielectric properties and design parameters), Int. J. Therm. Sci. 46 (2007) 328–341.
[17] S. Greedipalli, V. Rakesh, A. Datta, Modeling the heating uniforming contributed by a rotating turntable in microwave ovens, J. Food Eng. 82 (2007) 359–368.
[18] S. Samanta, T. Basak, Theoretical analysis of efficient microwave processing oil–water emulsions attached with various ceramic plates, Food Res. Int. 41 (2008) 386–403.
[19] W. Cha-um, P. Rattanadecho, W. Pakdee, Experimental and numerical analysis of microwave heating of water and oil using a rectangular wave guide: influence of sample sizes, position, and microwave power, Food Bioprocess Technol. (2010). http://dx.doi.org/10.1007/s11947-009-0187-x.
[20] W. Klinbun, P. Rattanadecho, Numerical model of microwave driven convection in multi-layer porous pack bed using a rectangular waveguide (effects of layered configuration, layered thickness and frequency), ASME J. Heat Transfer (2012). http://dx.doi.org/10.1115/1.4005254.
[21] D. Salvi, D. Boldor, G. Aita, C. Sabliov, COMSOL multiphysics model for continuous flow microwave heating of liquids, J. Food Eng. 104 (3) (2011) 422–429.
[22] T. Yousefi, S. Mousavi, M. Saghir, B. Farahbakhsh, An investigation on the microwave heating of flowing water: a numerical study, Int. J. Therm. Sci. 71 (2013) 118–127.
[23] W. Choi, S. Lee, C. Kim, S. Jun, A finite element method based flow and heat transfer model of continuous flow microwave and ohmic combination heating for particulate foods, J. Food Eng. 149 (2015) 159–170.
[24] P. Rattanadecho, The theoretical and experimental investigation of microwave thawing of frozen layer using microwave oven (effects of layer configurations and layer thickness), Int. J. Heat Mass Transfer 47 (2004) 937–945.
[25] R. Promas, P. Rattanadecho, W. Jindarat, Energy and exergy analyses in drying process of non-hygroscopic porous packed bed using a combined multi-feed microwave-convection air and continuous belt system (CMCB), Int. Commun. Heat Mass Transfer 39 (2012) 242–250.
[26] S. Barringer, K. Ayappa, E. Davis, H. Davis, J. Gordon, Power absorption during microwave heating of emulsions and layered system, J. Food Sci. 60 (1995) 1132–1136.
[27] C. Chan, Y. Chen, Role of length scales on microwave thawing dynamics in 2D cylinders, Sep. Sci. Technol. 37 (2002) 3407–3420.
[28] V. Rajakovic, D. Skala, Separation of water-in-oil emulsions by freeze/thaw method and microwave radiation, Sep. Purif. Technol. 49 (2006) 192–196.
[29] A. Nour, R. Yunus, Z. Jemaat, Study on demulsification of water-in-oil emulsions via microwave heating technology, J. Appl. Sci. 6 (9) (2006) 2060–2066.
[30] R. Palou, R. Camacho, B. Chavez, A. Vallejo, D. Negrete, J. Castellanos, J. Karamath, J. Reyes, J. Aburto, Demulsification of heavy crude oil-in-water emulsions: a comparative study between microwave and thermal heating, Fuel 113 (2014) 407–414.
[31] E. Binner, J. Robinson, S. Silvester, S. Kingman, E. Lester, Investigation into the mechanisms by which microwave heating enhances separation of water-in-oil emulsions, Fuel 116 (2014) 516–521.
[32] G. Mur, Absorbing boundary conditions for the finite difference approximation of the time domain electromagnetic field equations, IEEE Trans. Electromagn. Compat. 23 (1981) 377–382.
[33] S. Patankar, Numerical Heat Transfer and Fluid Flow, McGraw-Hill, New York, 1980.

International Journal of Heat and Mass Transfer 102 (2016) 645–656

Contents lists available at ScienceDirect

International Journal of Heat and Mass Transfer

journal homepage: www.elsevier.com/locate/ijhmt

Numerical study of vertical solar chimneys with moist air in a hot and humid climate

Sudaporn Sudprasert [a,*], Chatchawin Chinsorranant [a], Phadungsak Rattanadecho [b]

[a] Faculty of Architecture and Planning (Building Technology), Thammasat University, 99 Mu 18 Klongluang, Patumthani, Thailand
[b] Center of Excellence in Electromagnetic Energy Utilization in Engineering (CEEE), Department of Mechanical Engineering, Thammasat University, 99 Mu 18 Klongluang, Patumthani, Thailand

ARTICLE INFO

Article history:
Received 24 November 2015
Received in revised form 16 June 2016
Accepted 18 June 2016

Keywords:
Solar chimney
Moist air
Natural ventilation
CFD
Hot and humid
Species transport

ABSTRACT

The purpose of this study was to investigate numerically the effect of moist air on the performance of a vertical solar chimney. Numerical models were constructed to simulate the heat transfer and fluid flow of dry air and moist air with a relative humidity of 30–80% in a solar chimney. Computational results of air velocity and temperature distribution in the solar chimney with dry air were compared to results with moist air, under a constant chimney wall temperature. Compared to a solar chimney with dry air, the yield of ventilated air flow was 15.4–26.2% less and the overall air temperature was higher for a solar chimney with moist air. To maximize ventilation and reduce backward flow at the opening, an aspect ratio of 14:1 and a limited opening height are recommended for solar chimneys with moist air.

© 2016 Elsevier Ltd. All rights reserved.

1. Introduction

There have been many investigations of the thermal performances of variously designed solar chimneys integrated with buildings. Although invented for use in heating and ventilation applications in a cold climate [1] the solar chimney has been studied and applied under various climatic conditions. The thermal performance, in terms of the volume flow rate, air velocity, and air temperature, depends on the chimney configuration, construction materials, and integrated renewable energy systems [2].

The amount of water vapor in the air is dissimilar in different climates. For example, one study in a hot-dry climate reported a mean ambient temperature in the summer of 30–34 °C and relative humidity (RH) of less than 20% [3]. Another study in a hot–humid climate reported an ambient summertime temperature of 33.4–37.5 °C and RH of 46.0–73.5% [4]. The water content of air was greater in the hot–humid compared to the hot-dry climate by around 10 grams of moisture per kilogram of dry air. In a hot–humid climate, high vapor content in the air will affect the thermal performance of a solar chimney and lead to specific design specifications. Specifically, air flowing inside a solar chimney in a hot–humid climate could behave like moist air, or a mixture of water vapor and dry air.

Studies have covered diverse areas related to the volume flow rate of solar chimneys of various configurations. In India, for example, experiments showed results of 2.4–5.6 air change per hour (ACH) for an absorber area of 0.7–0.9 m^2 [5]. In the hot–dry climate of Iraq, a solar chimney with an incline of 60°, aspect ratio of 13.3, and chimney length of 2 m gave 4–35 ACH for an inflow velocity of 0.3–0.8 m/s [6]. A vertical solar chimney integrated with a water spraying system in Iran [3] gave an average of 4.51–8.28 ACH for an average velocity of 0.2–0.3 m/s. The room temperature approached a comfortable temperature with an indoor RH of 10.7–34.3%. The outdoor RH did not have a significant effect on the air velocity inside the channel.

There have not been many studies of the effects of humidity on solar chimneys in hot–humid climates because the humidity is not considered to have a primary effect on the ventilation. Ventilation performance has been determined by combining the wall and the roof [7], changing the configuration [8] and [9], increasing the inclination angle [3], and increasing the temperature difference between the inlet and outlet [10] and [11] of the solar chimney. Application of direct evaporation has been avoided in hot–humid climates. Only one experiment of an inclined solar chimney with indirect evaporative cooling was found [4], which was performed in Thailand. Solar chimney is used to drive the warm air inside it to rise along the wall, which can be used for building ventilation,

* Corresponding author.
E-mail address: sudaporn@ap.tu.ac.th (S. Sudprasert).

http://dx.doi.org/10.1016/j.ijheatmasstransfer.2016.06.054
0017-9310/© 2016 Elsevier Ltd. All rights reserved.

Nomenclature

c_p	specific heat (J/kg·K)
$D_{i,m}$	mass diffusion coefficient for species i in the mixture (m^2/s)
$D_{i,T}$	thermal diffusion coefficient for species i in the mixture (m^2/s)
g_i	gravitational acceleration in the i direction (m/s^2)
H	height of air gap (m)
h	height of opening (m)
J_i	mass diffusion ($kg/s·m^2$)
k	thermal conductivity (W/m·K)
L	width of air gap (m)
P	static pressure (Pa)
P_{atm}	atmospheric pressure (Pa)
Sc_t	turbulent Schmidt number
t	time (s)
T	time-mean temperature of fluid (°C)
T'	fluctuation temperature (°C)
T_0	reference temperature (=31.0 °C)
T_{w1}	temperature of air contacting the hot surface (°C)
T_{w2}	temperature of air contacting the cold surface (°C)
$T_{\alpha 1}$	ambient temperature (°C)
$T_{\alpha 2}$	air temperature at the inlet (°C)
u_i	mean velocity component corresponding to i direction (m/s)
u'_i	fluctuation velocity component in the i direction (m/s)
x_i	coordinate direction i (m)
Y_i	local mass fraction of each species

Greek symbols

β	coefficient of thermal expansion ($=1/T_0$) (1/K)
ρ	density of fluid (kg/m^3)
μ	laminar dynamic viscosity (kg/m·s)
υ	kinematic viscosity (m^2/s)
γ	diffusion coefficient

power generation, drying, etc. The solar chimney for building ventilation is similar to the solar updraft tower (also called solar chimney) for power generation [12]. In a solar updraft power plant where the buoyancy effect was applied to drive the wind turbine, under high relative humidity, the power generation became smooth, power was increased, and condensation was observed [13].

In the design of solar chimney configurations, the commercial CFD software has been widely used to determine the proper height to width ratio of the air gap [14] and the inlet positions [15] to maximize the mass flow rate. The height of the air gap (H), width of the air gap (L), and height of the opening (h) affected the ventilation rate of the solar chimney. A numerical study showed that the optimal aspect ratio varied with the Raleigh number (Ra_L) under uniform heat flux and uniform wall temperature [16]. On the basis of computational results, Gan (2006) recommended an air–gap height to width ratio (H/L) of 11.11 or 20.0. A wall solar chimney in Thailand showed the highest volume flow rate with H/L = 14 [17].

The purpose of the present study was to compare the air flow and temperature distributions within a vertical solar chimney when using moist air compared to dry air. Here, moist air refers to air with a range of RH typical of Thailand (RH = 40–80%). The air velocity and temperature distribution of moist air in the air gap were obtained simultaneously by using the computational software ANSYS Fluent 14.0. Results obtained from moist air simulated by the species transport model were compared to results from the dry-air model. Effects of moist air on the solar chimney aspect ratio and inlet height were also studied.

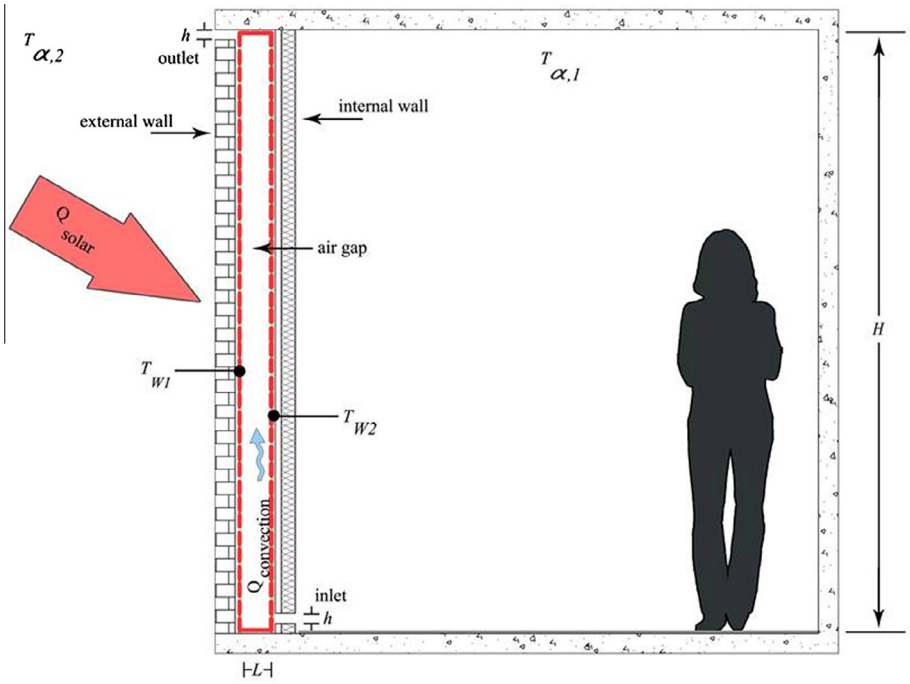

Fig. 1. Air gap of the solar chimney subjected to constant surface temperatures.

Table 1
Temperatures (°C) of solar chimney wall and air gap [17].

Time	Surface W1 (T_{w1})	Surface W2 (T_{w2})	Air in middle (T_a)	Inlet air
16.00	32.28	29.00	31.20	30.80
16.15	32.38	28.79	30.90	27.40
16.30	32.10	28.91	31.20	30.10
16.45	32.38	29.03	31.00	30.70
17.00	32.35	29.09	30.90	27.50

Table 2
Mass fractions of inflow air-vapor mixture.

Relative humidity (%)	Vapor	Dry air
–	0	1.000
40	0.010	0.990
50	0.013	0.987
70	0.019	0.981
80	0.023	0.977

Table 3
Thermal properties of air and vapor at operating temperature [20].

Properties	Unit	Air	Vapor
k	W/mK	0.02588	0.01896
c_p	J/kgK	1007	1874
ρ	kg/m^3	1.164	0.723
υ	m^2/s	1.872×10^{-5}	1.407×10^{-5}

Table 4
Average velocity at the openings of the dry air and air-vapor mixture models.

Relative humidity (RH, %)	Average air velocity (m/s)		Difference from dry air (%)	
	Inlet	Outlet	Inlet	Outlet
Dry air	0.0550	0.0693	–	–
40	0.0408	0.0586	25.8	15.4
50	0.0407	0.0586	26.0	15.4
70	0.0407	0.0585	26.0	15.6
80	0.0406	0.0585	26.2	15.6

2. Problem formulation and numerical modeling

Fig. 1 depicts the physical configuration of a two-dimensional (2-D) air gap of a vertical solar chimney. In this study, the solar induced ventilation is assumed mainly effect across the inlet and outlet openings placed on the right and the left walls, respectively. This assumption is valid when the widths of inlet and outlet openings are identical to the width of the walls and the measurement of air temperature and velocity are conducted at the middle section of the wall. According to the control volume of the solar chimney reported in previous studies [17,18], a 2-D air gap in a solar chimney with an H/L ratio of 14:1 was used (Fig. 1). The height of the inlet and outlet openings was 0.05 m. The surface temperature of the solar chimney was slightly different from that in previous studies [17,18]. Surface temperature along the vertical walls was assumed to be constant and equal to T_{w1} and T_{w2} along the external and internal wall, respectively. The upper roof and bottom walls were assumed to be adiabatic. The bottom inlet was subjected to room air ($T_{\alpha 2}$), and the top outlet was exposed to ambient air ($T_{\alpha 1}$).

Due to the buoyancy effect contributed by heat accumulated on the external wall, warm air in the air gap was discharged to the ambient air via the outlet at the top of the external wall. Then, room air was drawn into the air gap through the inlet opening at the bottom of the internal wall, creating natural ventilation in the adjacent room. The constant surface temperatures were taken from previous research [17], as shown in Table 1. Data were averaged every 15 min for 1 h between 4 and 5 p.m. in a solar chimney installed in the west end of a testing room. The wall temperatures were steady, while the air temperature at the inlet varied from 27.4 to 30.4 °C, during the hour (Table 1).

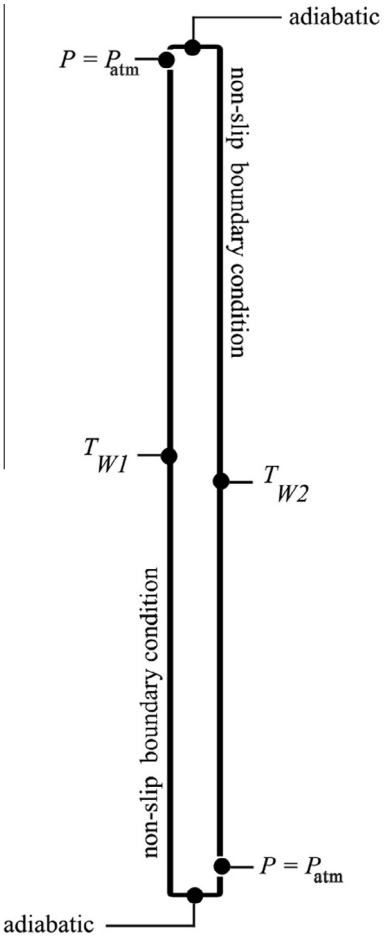

Fig. 2. Boundary conditions for analysis of heat transfer and fluid flow.

As the present work was mainly concerned with the effects of moist air on the volume flow rate and aspect ratio of the solar chimney, dry and moist air were the two working fluids studied in solar chimneys of similar configurations. The dry-air model employed the air property of an ideal gas. Moist air was simulated as an air-vapor mixture using the species transport model [19]. Mass fractions of the air-vapor mixture corresponding to RH = 40–80% are shown in Table 2. Thermal properties of the air and vapor at an operating temperature of 30.5 °C are shown in Table 3. Under the moist-air condition, solar chimney aspect ratios of 30:1, 14:1, and 10:1 were considered. Ratios of the opening height to the solar chimney width (h/L) of 0.25, 0.50, and 0.75 were examined in the solar chimney with an aspect ratio of 14:1.

To analyze the numerical CFD models of dry and moist air, the problem was simplified by assuming constant thermal properties of air and vapor. Air flow in the air gap was assumed to be turbulent, and the k–ε Re-Normalisation Group (RNG) turbulence model was used to simulate the effect of turbulence. The difference in air temperatures between the inlet and outlet of the solar chimney was not high, and the Boussinesq approximation was employed in the dry air model.

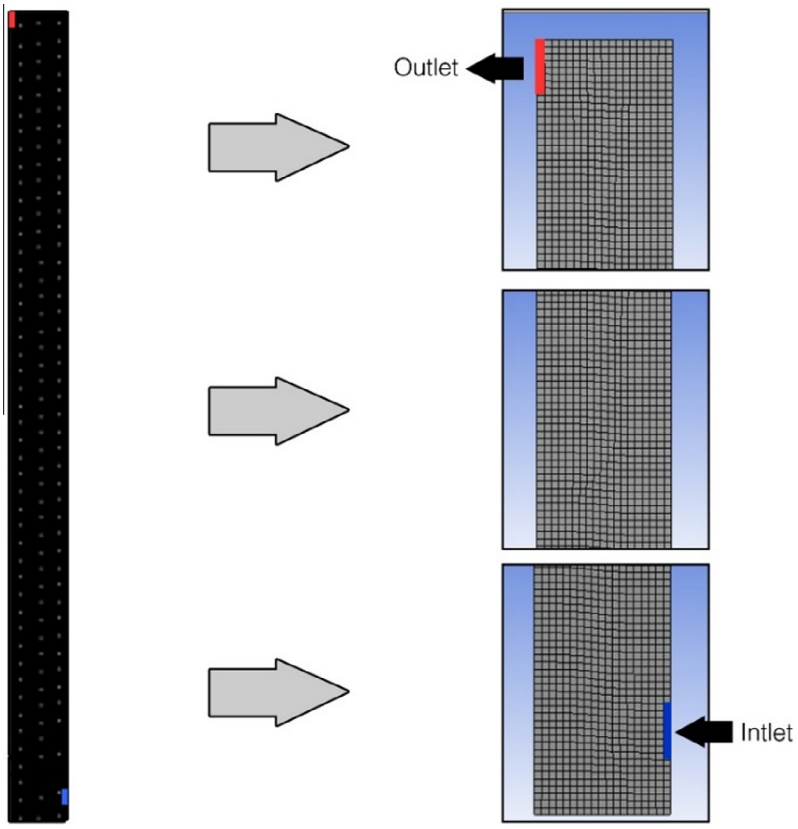

Fig. 3. A two-dimensional finite volume grid of the air gap in solar chimney.

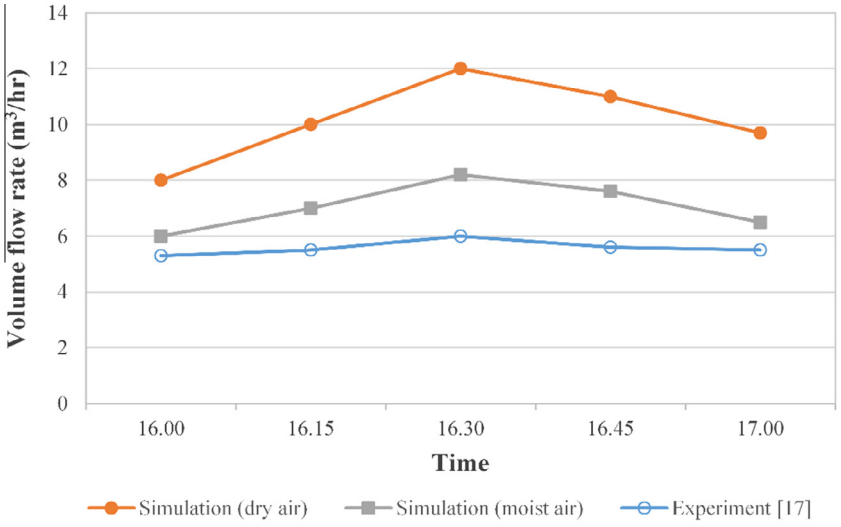

Fig. 4. Comparison of numerical and experimental results of volume flow rates.

In the simulation of moist air, the water vapor had no reaction and no phase change. Moist air was assumed to be a mixture of water vapor (H_2O) and gas (O_2, N_2) molecules. Thus, the species transport model was used to compute air velocity and temperature distribution from the input properties of the air-vapor mixture. Under this assumption, the governing equations can be solved for a 2-D transient turbulent flow, as follows [21]:

Continuity equation:

$$\frac{\partial \rho}{\partial t} + \frac{\partial}{\partial x_i}(\rho u_i) = 0 \tag{1}$$

Momentum equation:

$$\frac{\partial}{\partial t}(\rho u_i) + \rho u_j \frac{\partial u_i}{\partial x_j} = -\frac{\partial P}{\partial x_i} + \frac{\partial}{\partial x_j}\left(\mu \frac{\partial u_i}{\partial x_j} - \rho \overline{u_i u_j}\right) + \rho g_i \beta (T - T_0) \tag{2}$$

Energy equation:

$$\frac{\partial}{\partial t}(\rho T) + \rho u_j \frac{\partial T}{\partial x_j} = \frac{\partial}{\partial x_j}\left(\gamma \frac{\partial T}{\partial x_j} - \rho \overline{u_j' T'}\right) \tag{3}$$

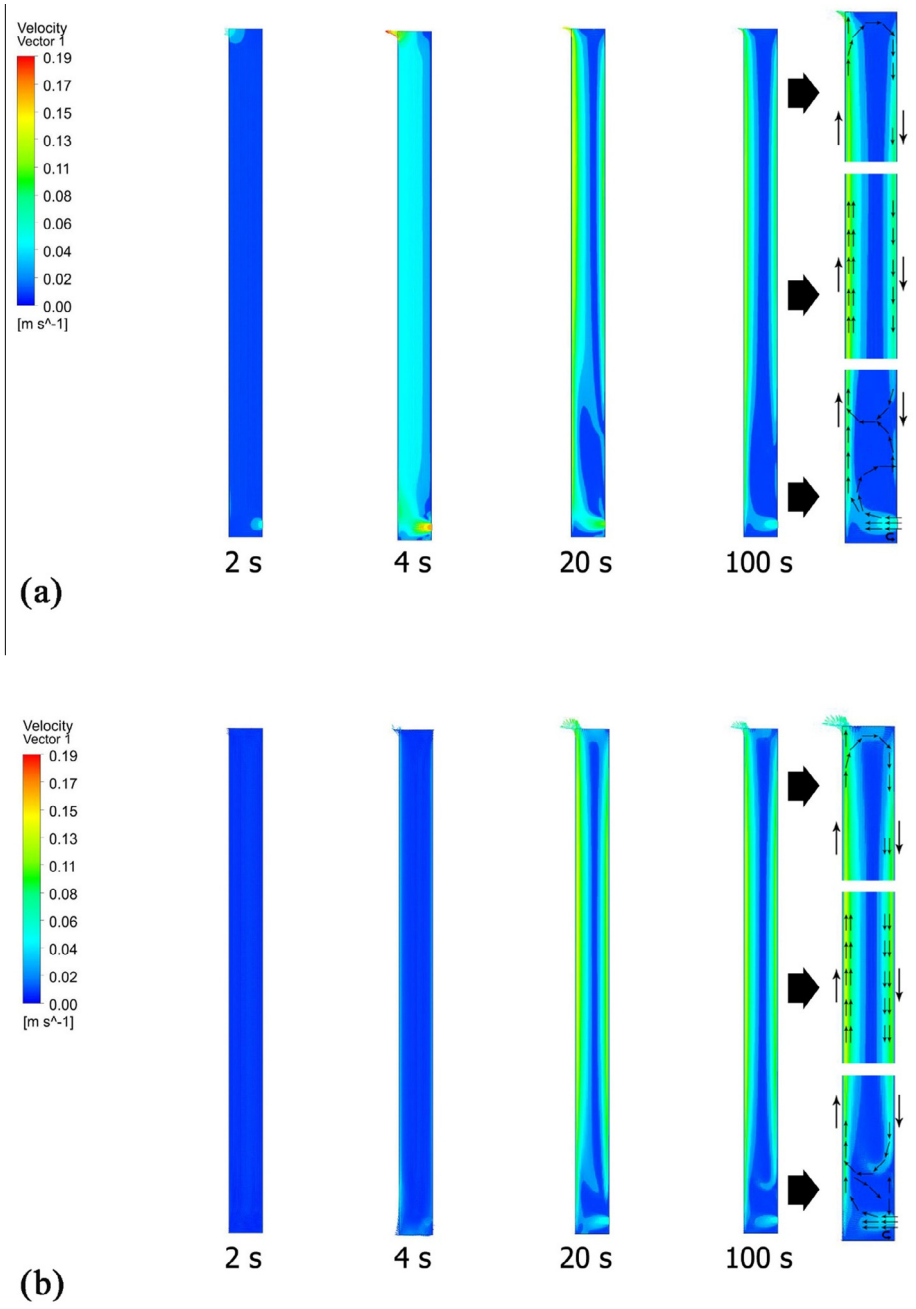

Fig. 5. The transient simulation results of air velocity in the solar chimney with (a) dry air and (b) moist air.

For all flows, the ANSYS Fluent program was used to solve the conservation equations for mass (Eq. (1)) and momentum (Eq. (2)). For flow involving heat transfer, an additional equation for energy conservation (Eq. (3)) was solved. For flows involving a mixture of species, the species conservation equation was solved. To solve conservation equations for species, the ANSYS Fluent software predicts the local mass fraction of each species, Y_i, through solution of a convection–diffusion equation for the ith species. This conservation equation takes the following form:

$$\frac{\partial}{\partial t}(\rho Y_i) + \nabla \cdot (\rho u_i Y_i) = -\nabla \cdot J_i \tag{4}$$

There are two species in the CFD model: water vapor (species 1) and air (species 2). In turbulent flow, ANSYS Fluent computes the mass diffusion in the following form:

$$J_i = -\left(\rho D_{i,m} + \frac{\mu_t}{Sc_t}\right)\nabla Y_i - D_{i,T}\frac{\nabla T}{T} \tag{5}$$

2.1. Boundary conditions

Boundary conditions needed to solve the governing equations are shown in Fig. 2. Air contacting the external or internal wall was considered to have a boundary condition of constant temperature T_{w1} or T_{w2}, respectively. The top wall (#3) and bottom wall (#4) were assumed to be adiabatic. Boundary conditions for solving the momentum equation were no-slip at the boundaries and atmospheric pressure at the openings.

2.2. Calculation procedures

Navier–Stokes and energy equations with boundary condition Eqs. (11)–(15) were solved by using the computational fluid dynamic code ANSYS Fluent. Convective terms in the governing equations for momentum, turbulent kinetic energy, turbulent dissipation rate, and energy were discretized with the second-order

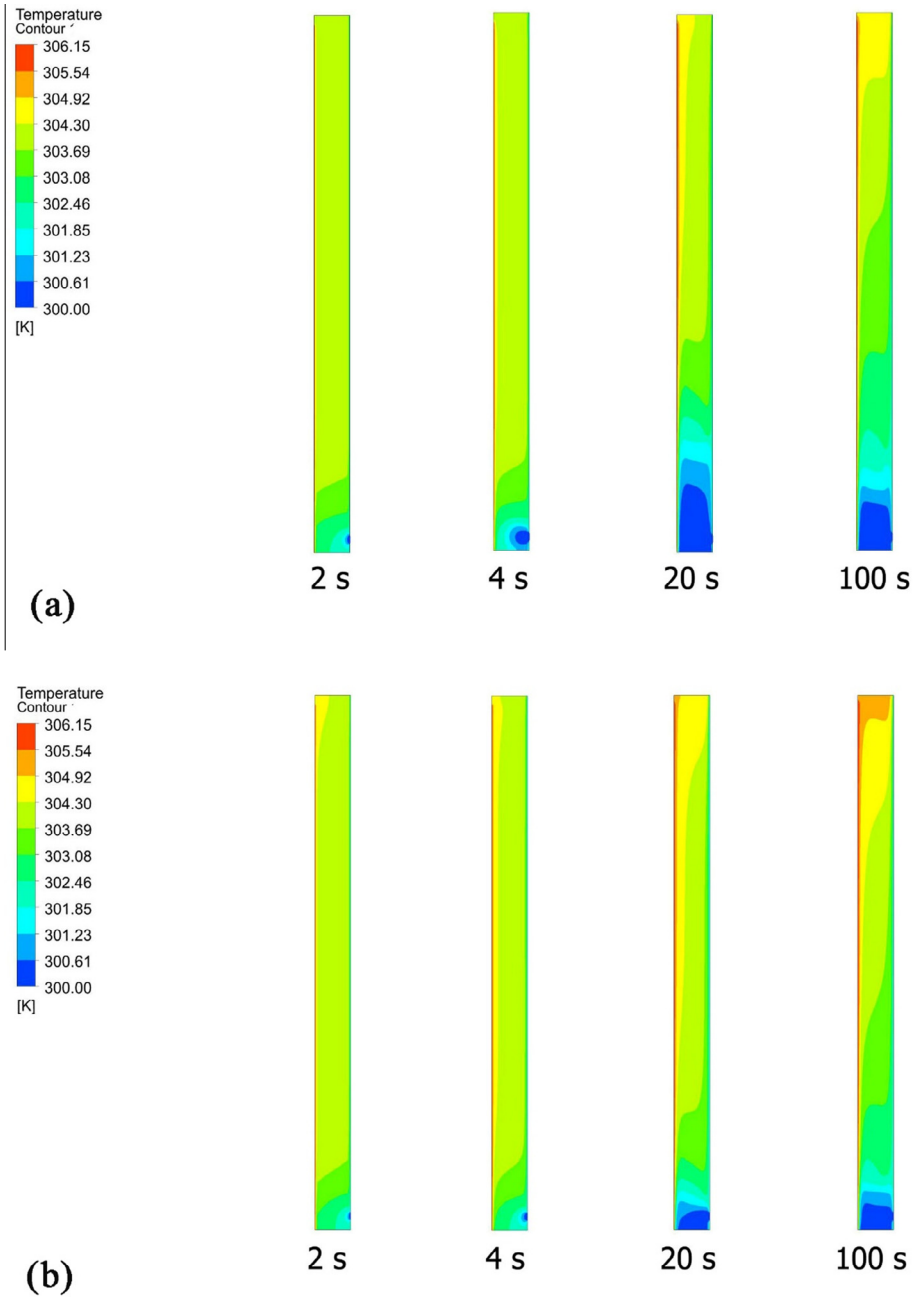

Fig. 6. The transient simulation results of air temperature in the solar chimney with (a) dry air and (b) moist air.

upwind scheme. PRESTO! was used as the pressure interpolation scheme because the solar chimney has natural convective flow with a high Rayleigh number. Coupling between velocity and pressure was performed with the SIMPLE algorithm.

Convergence of the numerical solution was considered to have been achieved when the sum of the normalized residuals for each flow equation was less than 10^{-4}. The convergence test was conducted to identify the appropriate number of grids required. To validate the independence of the solution on the grid, four node numbers (4100, 6400, 11,200 and 24,700) were investigated. Simulation results showed that the temperature distribution and velocity vectors were similar with node numbers of 11,200 and 24,700. Hence, the model with 11,200 nodes was selected for further studies. Fig. 3 shows the results of the uniform grids in the solar chimney.

3. Validation of numerical results

Apart from the investigations of grid independency, the heat transfer and fluid flow characteristics were compared with available experimental results. To validate the reliability of the numerical method being used, the numerical simulation was conducted with the solar chimney with the same geometrical configuration as presented in [17]. Dry and moist air are the working fluids in the simulation models. Temperature values at the wall boundaries and inlet in the simulation models followed the experimental results in Table 1.

Fig. 4 shows the numerical and experimental results of the volume flow rate after 1 h of operation. The volume flow rate from the simulation results of the dry-air model were very different from the experimental results. Simulation results of the moist-air model

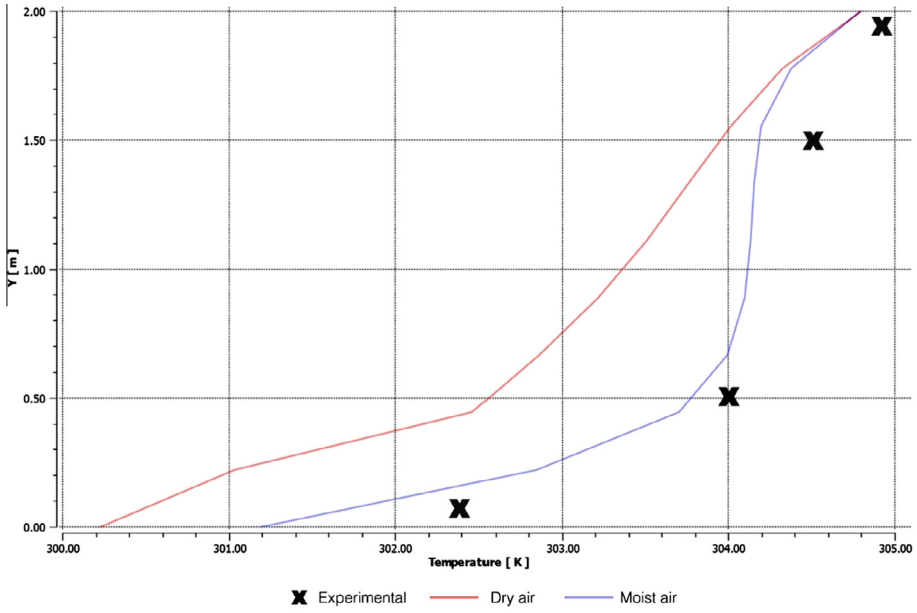

Fig. 7. Temperature profile along the air gap height.

agreed well with experiment results, with a difference of 20–33%. This difference was still high because the results obtained from the 2-D model limit the prediction of the experimental results. The local speed computed at some points may not be real. However, the comparison showed that using the species transport model for the computational modeling of moist air can improve the calculation of volume flow rate through the solar chimney.

4. Results and discussion

The following sections present the numerical results obtained from the 2-D model shown in Fig. 2. The transient simulations approached the steady state at 100 s. Simulations were carried out under a hot wall temperature of T_{w1} = 33 °C and cool wall temperature of T_{w2} = 29 °C. Computational results of air velocity and temperature distribution in the air gap were analyzed through graphical displays produced by the CFD package. Ventilation performances of the solar chimney with different water vapor contents are presented in terms of the volume flow rate.

4.1. Air velocity in the solar chimney with the dry- and moist-air models

Fig. 5 shows the transient simulation results of air velocity in the air gap of the solar chimney with dry or moist air. The dry-air model (Fig. 5a) depicted air close to the hot surface flowing upward from the inlet due to the buoyancy effect, starting from 2 s until 100 s. A portion of the air left the air gap through the outlet, while another portion of air turned back to the cool surface. The backward air flowed down to 0.44 m above the inlet opening and flowed up again close to the hot surface. This recirculation around the borders of the air gap created a region of zero air velocity at the center of the air gap.

In the moist-air model with RH = 70% (Fig. 5b), warm air started moving at 10 s. The flow characteristics were similar to those of the dry-air model. However, the portion of air that turned back was larger in the moist-air model, and the volume of this moist air fell to 0.13 m above the inlet opening. Images on the right-hand side in Fig. 5a and b show the magnification of velocity vectors in the solar chimney at 100 s for the dry- and moist-air models, respectively. There was greater mixing of the room air entering the inlet with the warm recirculation stream in the moist- compared to the dry-air model. Because the disturbance at the inlet was less, dry air flowed into the solar chimney at higher velocity than the moist air.

4.2. Effect of vapor content on air velocity

An increase in RH at a constant mixture temperature involves an increase of the vapor mass fraction in the air-vapor mixture. Increasing the vapor in the mixture by increasing the RH from 40% to 80% reduced the average velocity in the solar chimney (see Table 4). Compared to the results of the dry model, the air-vapor mixture model with RH = 80% delivered 15.6% lower air velocity at the exit. The vapor density was smaller than that of the dry air, resulting in the reduction of buoyancy in the moist-air model. In addition, vapor required higher heat to increase the temperature by 1 °C, due to its higher specific heat compared to dry air of the same mass. Overall, the buoyancy force decreased when vapor was considered in the computational model.

4.3. Temperature distribution in the solar chimney with dry- and moist-air models

Fig. 6 shows the numerical results of air temperature in the solar chimney with the dry- (Fig. 6a) or moist-air model (Fig. 6b). The air temperature was distributed from 300 to 306 K in the dry-air model, with an average air temperature in the air gap of 303.46 K (30.46 °C). Fig. 6b shows the results of the air temperature obtained from the moist-air model with RH = 70%. The temperature distribution was similar for RHs of 40% to 80%. The average air temperature in the moist-air model was 303.96 K (30.96 °C), which is slightly higher than the average temperature in the dry-air model.

The temperature range in the moist-air model was higher than that of the dry-air model, which can be explained by the delayed and reduced discharging of air. Heat quickly dissipated in the air gap, and the temperature increased in the first 2 to 4 s because of the static moist air. At steady state (100 s), the bottom of the air gap with dry air became cool at the inflow air temperature.

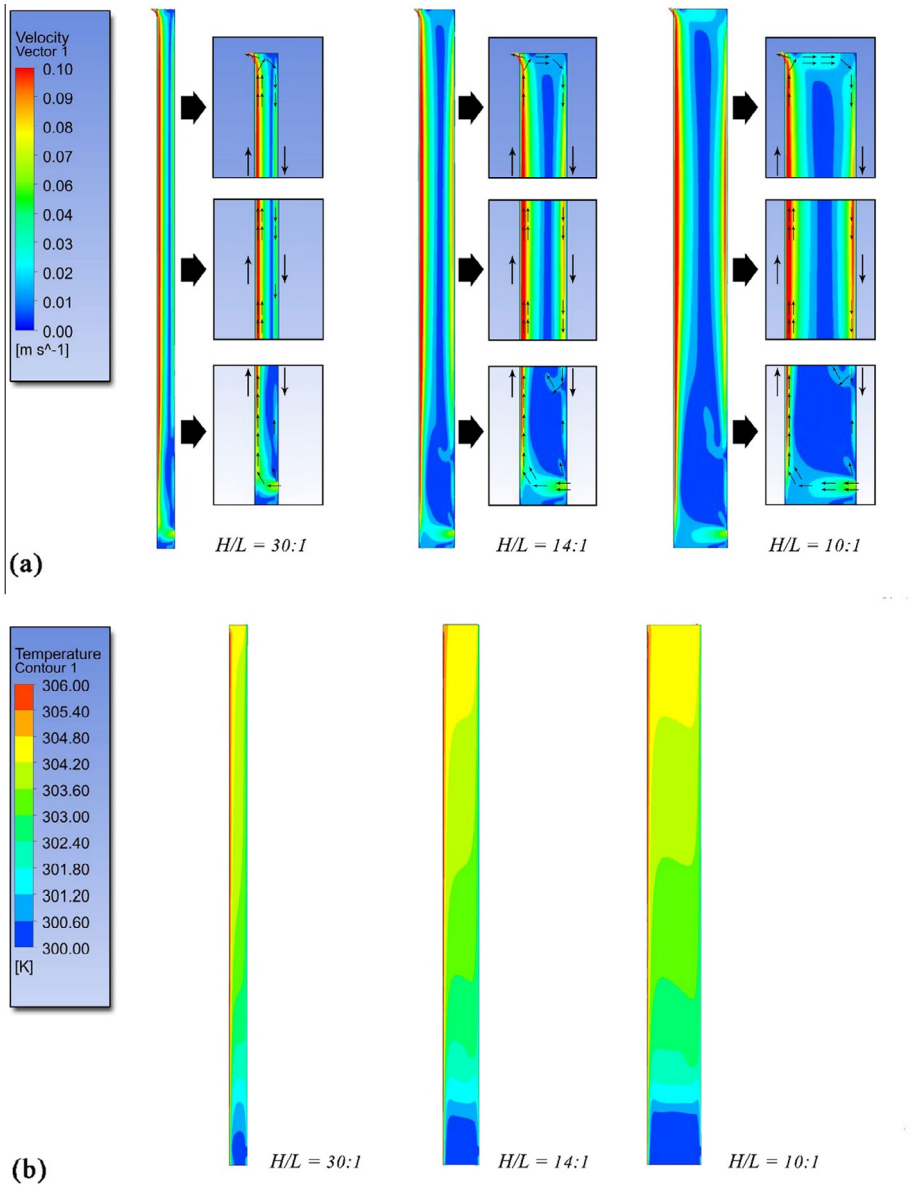

Fig. 8. Simulation results of dry air with aspect ratios of 30:1, 14:1 and 10:1, (a) air velocity and (b) temperature distribution in steady state.

The inlet moist air mixed with the recirculated warm air, and the temperature at the bottom of air gap increased.

Fig. 7 shows the temperature profile along the air–gap height. The dry- and moist-air models had identical temperature profiles; however, the air temperature in the moist-air model was higher than in the dry-air model at equivalent heights in the solar chimney. Compared to experimental research in a hot–humid climate, the moist-air model is more accurate in the prediction of air temperature in the air gap.

4.4. Effect of the aspect ratio

Effects of aspect ratios (H/L) of 30:1, 14:1, and 10:1 (L = 0.1, 0.2, and 0.3 m, respectively, for H = 3.0 m) on the performance of the solar chimney were investigated and compared for the dry- and moist-air models. Fig. 8 shows the simulation results of air velocity (Fig. 8a) and temperature (Fig. 8b) at steady state for the dry-air model. The directions of flow and recirculating air were similar at all three aspect ratios, except for backward flow at the outlet opening with the largest air gap. The largest air gap has a larger portion of backward airflow than the smallest air gap. For L = 0.1, 0.2, and 0.3 m, dry air flowed into the air gap through the inlet and exited through the outlet. Air temperatures at the three aspect ratios were stratified, with a low temperature at the bottom and high temperature at the top of the air gap.

Fig. 9 shows the simulation results for the moist-air model in a solar chimney with different aspect ratios. For a solar chimney with an air–gap width of 0.1 or 0.3 m, two regions of air recirculation separated by static air developed in the steady-state condition (Fig. 9a). Outflow involved only warm air that had collected near the outlet, and excluded the stream of inflow air. Furthermore, reverse flows were found at the inlet. The flow of moist air was clearly inefficient in the air gap with the incorrect aspect ratios. The nonuniformity of air velocity in the air gap led to a variation in temperature distribution (Fig. 9b). The aspect ratio of 14:1,

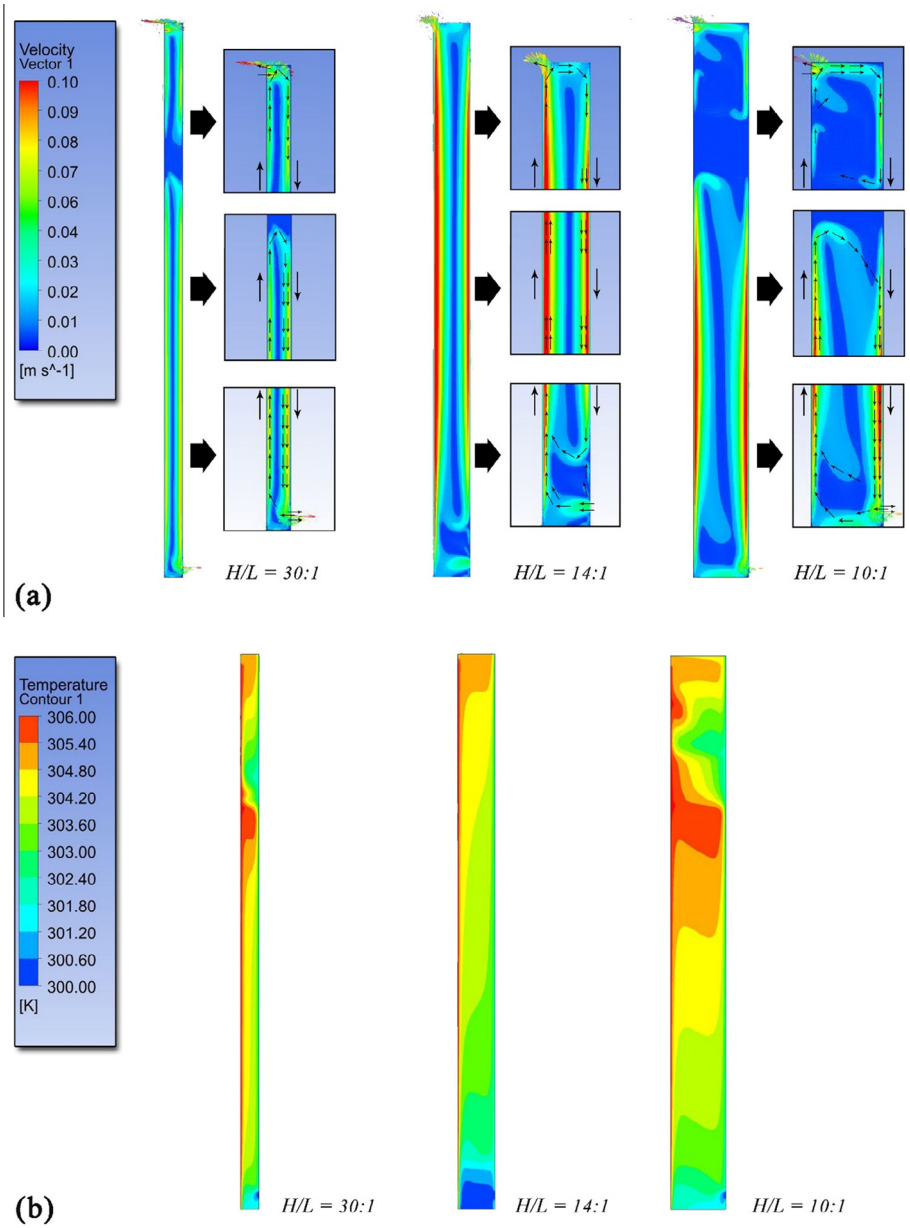

Fig. 9. Simulation results of moist air with aspect ratios of 30:1, 14:1 and 10:1, (a) air velocity and (b) temperature distribution in steady state.

reported in Refs. [17,18] was verified to be appropriate for moist-air application in this study.

4.5. Effect of the height of the opening

Heights of the inlet and outlet openings were varied to study their effect on the ventilation performance of the solar chimney. The recommended opening height was 0.05 m ($h/L = 0.25$) for the inlet and outlet. Simulation results showed the detailed thermal behavior of the dry and moist air. The h/L ratios of 0.25, 0.50, and 0.75 were created for an air gap with a height of 3 m and width of 0.2 m.

Fig. 10 shows the computational results of air velocity (Fig. 10a) at steady state and air temperature (Fig. 10b) for dry air in the air gap. Changing the inlet and outlet opening heights in the dry-air model did not alter the flow pattern or temperature distribution in the air gap. Reverse flow at the inlet and outlet openings was found in the air gap with a large opening ($h/L = 0.50$ and 0.75). The air temperature in the air gap was almost identical for all three h/L ratios, except that reverse flow produced a high temperature at the outlet.

Fig. 11 shows the simulation results obtained from the analysis of moist air in the air gap of the solar chimney with three opening heights. Changing the opening height of the inlet and outlet had different effects on the air gap. Very large openings reduced the upward flow (Fig. 11a), decreasing the magnitude of the upward velocity while increasing the size of static air region, especially for air gaps with $h/L = 0.5$ or 0.75. Reverse flows were found at the inlet and outlet openings. In other words, ambient air entered the air gap through the outlet, and air in the air gap flowed into the room. Nonuniformity of the air flow was also reflected in the temperature distribution (Fig. 11b). High air temperature was found at the middle of the air gap height because of the backward flow. Therefore, the opening

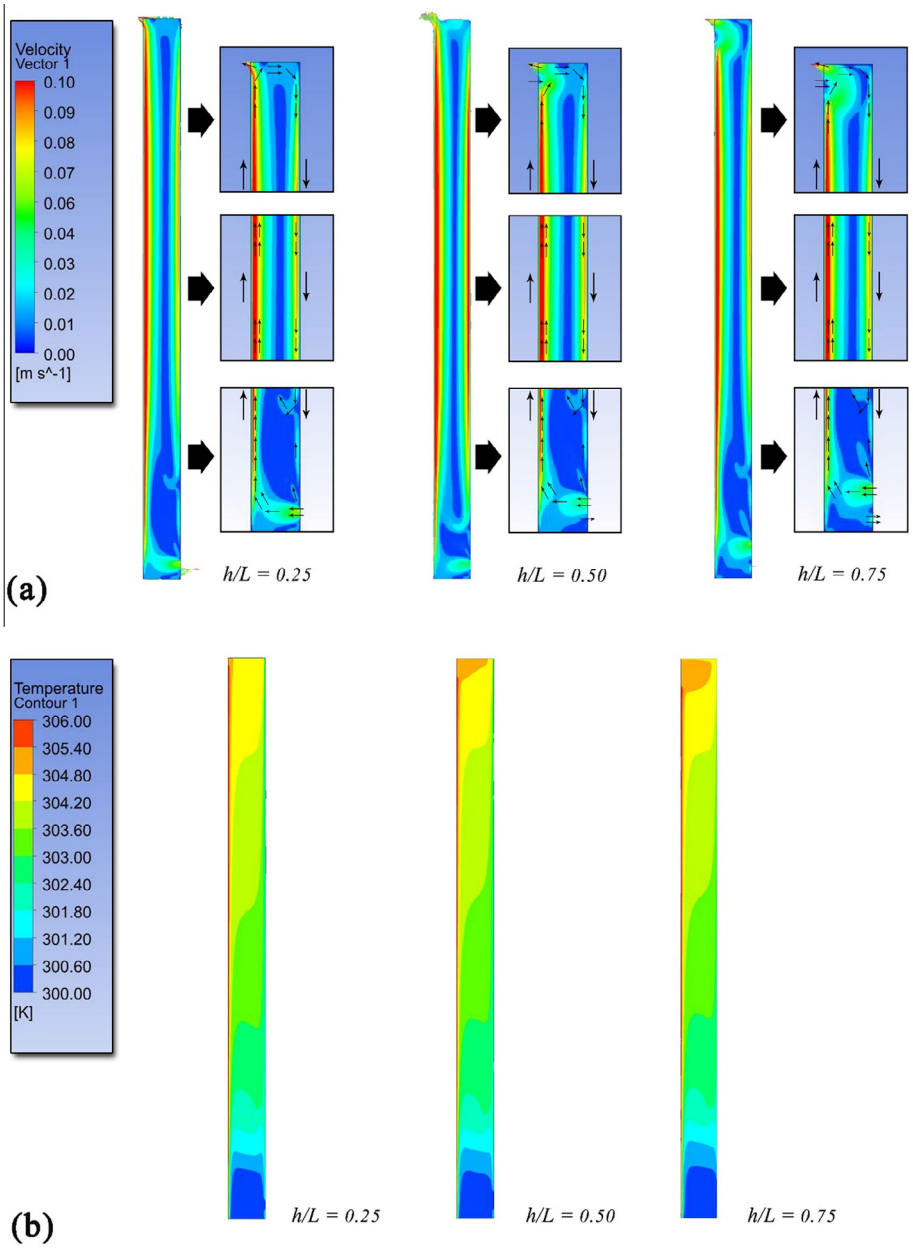

Fig. 10. Computational results of (a) velocity and (b) temperature in steady state of dry air in the air gap with h/L ratios of 0.25, 0.50 and 0.75.

height should be limited to $h/L = 0.25$ for application of a solar chimney with moist or dry air, to avoid reverse flow.

5. Conclusions

This study investigated the effects of the vapor mass fraction in the air-vapor mixture on the temperature distribution and velocity flow patterns in the air gap of a solar chimney. Effects of increasing the RH at a constant temperature on the air temperature distribution and airflow were ascertained by numerically simulating transport models of heat transfer and species conservation. The air temperature distribution was directly influenced by the amount of water vapor in the air. Increasing the vapor mass fraction of the air-vapor mixture reduced the air velocity at the inlet and outlet openings by 26% and 15.6%, respectively, compared to dry air under the same boundary conditions. Furthermore, increasing the vapor mass fraction intensified the recirculation of warm air near the openings and reduced the ventilation through the air gap. The air temperature distribution in the air-vapor mixture model developed similarly to the temperature distribution in the dry-air model, but with a slightly higher air temperature.

From these results, we conclude that the water vapor should be considered in the application of a solar chimney in a hot–humid environment. The suggested aspect ratio (H/L) of 14:1 was verified with the air-vapor mixture simulation model. To increase the upward flow and prevent backward flow into the room, small opening heights, such as $h/L = 0.25$, are recommended for solar chimneys used with moist air.

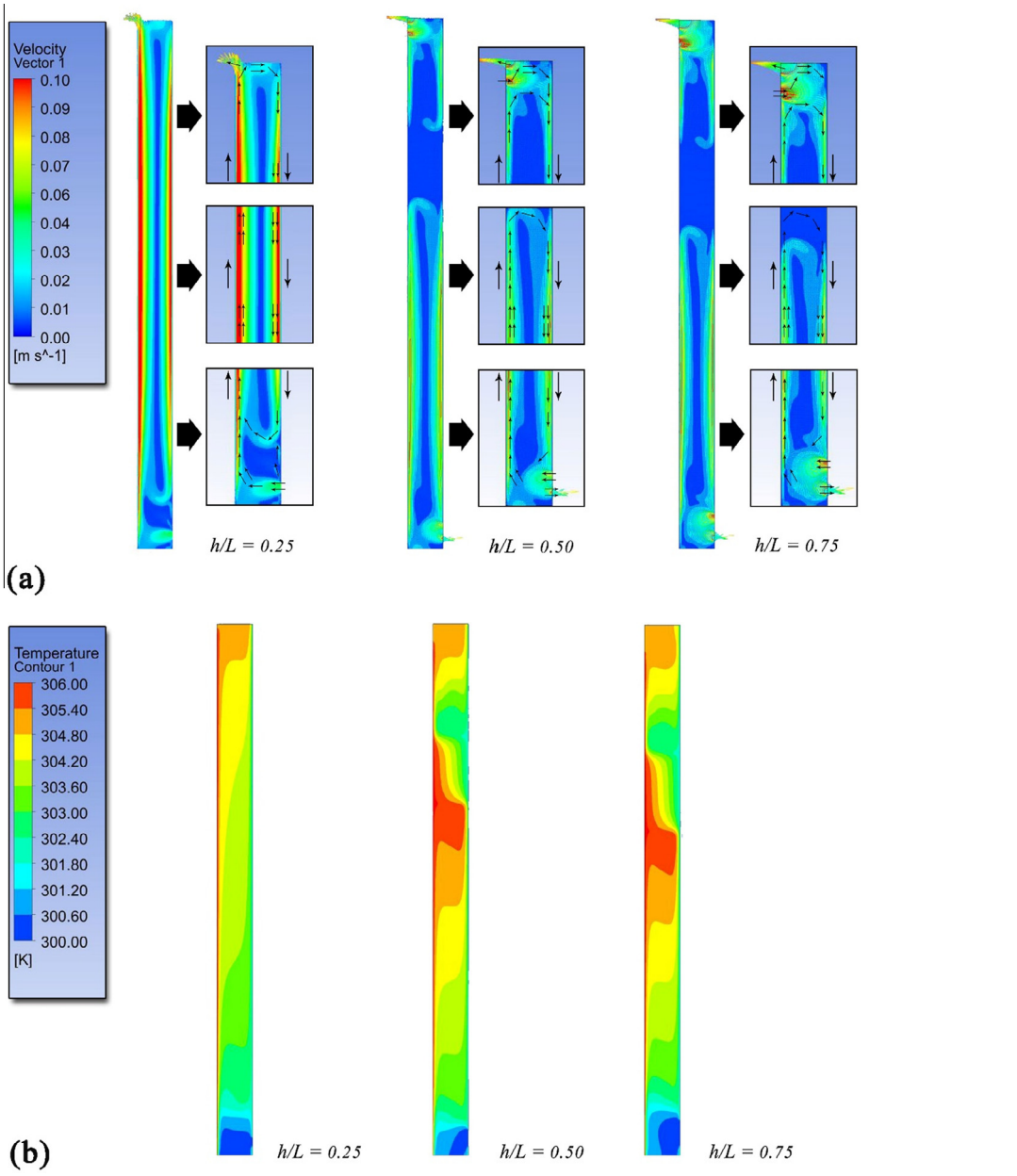

Fig. 11. Computational results of (a) velocity and (b) temperature in steady state of moist air in the air gap with h/L ratios of 0.25, 0.50 and 0.75.

Acknowledgements

The authors gratefully acknowledge the financial support provided by the Thammasat University Research Fund under Research Scholar Contract No. 55/2558, the Thailand Research Fund under TRF Contract Nos. RTA5680007 and TRG5780255, and the National Research Universities Project of Higher Education Commission for supporting this research.

References

[1] O. Saadatian, K. Sopian, C.H. Lim, N. Asim, M.Y. Sulaiman, Trombe wall: a review of opportunities and challenges in research and development, Renewable Sustainable Energy Rev. 16 (2012) 6340–6351.
[2] X.Q. Zhai, Z.P. Song, R.Z. Wang, A review for the applications of solar chimneys in buildings, Renew. Sustain. Energy Rev. 15 (2011) 3757–3767.
[3] M. Rabani, V. Kalantar, A.A. Dehghan, A.K. Faghih, Empirical investigation of the cooling performance of a new designed trobmbe wall in combination with solar chimney and water spraying system, Energy Build. 102 (2015) 45–57.
[4] S. Chungloo, B. Limmeechokchai, Application of passive cooling systems in the hot and humid climate: the case study of solar chimney and wetted roof in Thailand, Build. Environ. 42 (2007) 3341–3351.
[5] J. Mathur, N.K. Bansal, S. Mathur, M. Jain, Anupma, Experimental investigation on solar chimney for room ventilation, Sol. Energy 89 (2006) 927–935.
[6] A.A. Imran, J.M. Jalil, S.T. Ahmed, Induced flow for ventilation and cooling by a solar chimney, Renewable Energy 78 (2015) 236–244.
[7] J. Khedari, B. Boonsiri, J. Hirunlabh, Ventilation impact of a solar chimney on indoor temperature fluctuation and air change in a school building, Energy Build. 32 (2000) 89–93.
[8] J. Hirunlabh, S. Wachirapuwadon, N. Pratinthong, J. Khedari, New configuration of a roof solar collector maximizing natural ventilation, Build. Environ. 36 (2001) 383–391.
[9] R. Khanal, C. Lei, A numerical investigation of buoyancy induced turbulent air flow in and inclined passive wall solar chimney for natural ventilation, Energy Build. 93 (2015) 217–226.
[10] G. Gan, S.B. Riffat, A numerical study of solar chimney for natural ventilation of buildings with heat recovery, Appl. Therm. Eng. 18 (1998) 1171–1187.
[11] J. Waewsak, Hirunlabh, J. Khedari, U.C. Shin, Performance evaluation of the BSRC multi-purpose bio-climatic roof, Build. Environ. 38 (2003) 1297–1302.
[12] X. Zhou, Y. Xu, Solar updraft tower power generation, Solar Energy 128 (2016) 95–125.

[13] Y. Xu, X. Zhou, Q. Cheng, Performance of a large scale solar updraft power plant in a moist climate, Int. J. Heat Mass Transfer 91 (2015) 619–629.
[14] G. Gan, Parametric study of trombe walls for passive cooling of buildings, Energy Build. 27 (1998) 37–43.
[15] G. Gan, Simulation of buoyancy-induced flow in opened cavities for natural ventilation, Energy Build. 18 (2006) 410–420.
[16] B. Zamora, A.S. Kaiser, Optimum wall-to-wall spacing in solar chimney shaped channels in natural convection by numerical investigation, Appl. Therm. Eng. 29 (2009) 762–769.
[17] N. Rachapradit, Field study of performance of solar chimney with air-conditioned building Master Thesis in Thermal Technology, King Mongkut's University of Technology Thonburi, Bangkok, 2000.
[18] J. Khedari, C. Lertsatithanakorn, N. Pratinthong, J. Hirunlabh, The modified trombe wall: a simple ventilation means and an efficient insulating materials, Int. J. Ambient Energy (1998) 104–110.
[19] Z. Li, P.K. Heiselberg, CFD Simulations for Water evaporation and Airflow Movement in Swimming Baths, Institute of Bygningsteknik, Aalborg Universitet, 2005.
[20] Y. Cengel, Heat Transfer, McGraw-Hill, Singapore, 2004.
[21] I.N.C. Ansys, ANSYS Fluent Theory Guide, Pennsylvania, USA, 2013.

Construction and Building Materials 123 (2016) 768–784

Contents lists available at ScienceDirect

Construction and Building Materials

journal homepage: www.elsevier.com/locate/conbuildmat

A novel rapid microwave-thermal process for accelerated curing of concrete: Prototype design, optimal process and experimental investigations

Phadungsak Rattanadecho [a,*], Natt Makul [b], Aumpol Pichaicherd [a], Porncharoen Chanamai [a], Bunyong Rungroungdouyboon [a]

[a] Center of Excellence in Electromagnetic Energy Utilization in Engineering (CEEE), Department of Mechanical Engineering, Faculty of Engineering, Thammasat University Prathum Thani, 12121, Thailand
[b] Building Technology Program, Faculty of Industrial Technology, Phranakhon Rajabhat University, 3 Moo 6 Changwattane Road, Anusaowari Sub District, Bang Khen District, Bangkok 10220, Thailand

HIGHLIGHTS

- Novel rapid microwave-thermal process for accelerated curing of concrete.
- MW at an operating frequency of 2.45 GHz and at powers of 400 W and 800 W.
- A mobile microwave (MW)-assisted curing unit was designed.
- Mathematical models were applied to design a horn-shaped MW cavity.
- MW energizing for 15 min/time and a paused duration of 60 min were included.

ARTICLE INFO

Article history:
Received 14 December 2015
Received in revised form 14 July 2016
Accepted 15 July 2016

Keywords:
Concrete
Heating
Microwave technology
Prototype
Rapid thermal processing

ABSTRACT

In this work, a mobile microwave (MW)-assisted curing unit for the accelerated curing of concrete workpiece is designed based on coupled electromagnetic (MW)–thermal analysis. The design of this unit is described together with experimental investigations into the heating characteristics of concrete workpiece subjected to the MW-accelerated curing process. Mathematical models are applied to design a horn-shaped MW cavity and as a basis for constructing a stationary and a moving MW-accelerated curing unit that uses MW energy at an operating frequency of 2.45 ± 0.05 GHz and at powers of 400 W and 800 W. The experiments included the effects of MW curing on the temperature evolution, moisture content variation, and compressive strength development properties of the concrete. Also, the concrete workpiece was compared to water-cured conventional concretes and air-cured conventional concretes on the basis of these properties. Based on the concept of antenna, a rectangular horn-shaped cavity of 246.7 mm wide × 333.68 mm long is designed showing a uniform thermal distribution for concrete curing. From the experiments, it was found that the application period for curing using the mobile MW-curing unit was considerably shorter than for conventional curing methods. The appropriate preheating interval is 30 min, and MW energizing for 15 min/time and a paused duration of 60 min produces maximum compressive strength. However, the time needed for curing was considerable. When concrete was heated using MW energy for more than 90 min at over 80 °C, the effect was a continuous decrease in compressive strength. Further, at early age, the compressive strength development of the concrete workpiece subjected to MW curing was greater than that achieved by air curing or water wet-curing.

© 2016 Elsevier Ltd. All rights reserved.

1. Introduction

Microwave (MW)-assisted heating has emerged as an innovative and popular heating-process technology for dielectric materials. A particularly efficient technique for thermal processes, MW-assisted heating can considerably reduce the time needed for heating/drying. A number of other analyses of the microwave heating process have appeared in the recent literature [1–4]. MW-assisted heating has been used successful in numerous industrial processes, including the following:

* Corresponding author.
E-mail address: ratphadu@engr.tu.ac.th (P. Rattanadecho).

http://dx.doi.org/10.1016/j.conbuildmat.2016.07.084
0950-0618/© 2016 Elsevier Ltd. All rights reserved.

- Food and biological materials: Regier and Schubert [5] published a book in which they give an account of a wide range of microwave processing applications used worldwide including blanching, thawing, and packaging. Afrin et al. [6] investigated thermal lagging in living biological tissue and found that the phase lag times for temperature gradient and heat flux are indistinguishable in the respective cases of blood and tissue. Irishina et al. [7] studied a level set evolution strategy in microwave imaging for early breast cancer detection. Basak [8] studied thermal MW processing and concluded that it is an efficient way to produce a high temperature in a customized plane-wave oven.
- Wood: Perre and Turner [9] presented the effects of the combined convective and microwave drying of softwood by focusing on predicting the locations of hot spots and thermal runaway within the workpiece from the viewpoint of product quality. Kaensup et al. [10] used a combined microwave fluidized bed dryer to dry pepper seeds. The results indicated that MW energy dried the pepper seeds at a faster rate than a conventional fluidized bed did.
- Accelerated-curing and repairing of concrete: Leung and Pheeraphan [11] showed that MW energy can be used to cure concrete for practical construction applications. Makul et al. [12] used MW energy at an operating frequency of 2.45 GHz and a multi-mode cavity to cure early-stage Portland cement paste. Their research showed that based on steady heat transfer conduction the temperature increased consistently in accord with the mathematical model.

Up to the present time, the focus of research and development pertaining to the technology used to repair concrete has focused on reducing the time taken to complete repairs. However, the time needed to cure concrete is still lengthy and the process relies on conventional curing technology for repairs such as applying a curing compound, water ponding [13], and using a wetting sag to cover the concrete surface so that the concrete retains moisture content. This long period leads to problems; for example, when roads are repaired, traffic jams inevitably ensue as fewer lanes are available. Therefore, any method such as the use of streams or hot air with the potential to reduce the time needed in the initial concrete-curing phase is of great interest. However, these methods have the drawback of producing intermittent thermal distribution in concrete, leading to a reduction in compressive strength and causing the internal structure to break down [14]. Therefore, MW-heating technology applied to concrete curing in the initial phase is advantageous because heat can be produced in a way that is more efficient than with other methods.

It is well known that thermal-curing methods have an adverse effect on the properties of concrete—both at early age and in the long term. Therefore, a crucial question arises: Can the MW-heating method be applied in the concrete industry? Theoretically, it is possible. This is because materials used to make concrete, such as hydraulic Portland cement, aggregates, water, and admixtures are dielectric; i.e., they can absorb MW energy effectively. For example, Xuequan [15] proposed a new kind of MW-curing technique for concrete. Based on removing free water from the internal concrete's structure before any plastic shrinkage and loss of porosity has taken place, the strength and durability of the concrete significantly developed. In addition to Hutchison's [16] research in this area, and Sohn and Johnson [17] used MW energy to accelerate the curing process without incurring any significant loss of compressive strength in the cement mortar.

As a principal material in the production of concrete, water should be considered carefully in regard to the curing process. In particular, compared with the other components of concrete, water has a relative dielectric constant (ε_r') and loss tangent (tan δ) with higher values. As a result, when the electric field $\vec{E}$, which is a main part of the electromagnetic field, interacts with the concrete's constituents, MW electromagnetic energy is quite dramatically transferred and then converted into heat via an interaction with water molecules. This mechanism causes the bonds of polar molecules to vibrate such that energy is dissipated as heat and transferred within the concrete workpiece to be processed, thus giving rise to accelerated hydration reactions. Consequently, free water molecules in the capillary pores of the concrete are quickly removed from the internal concrete structure before setting, which means that plastic shrinkage from drying is taking place. The result is the collapse of the capillary pores collapse and microstructure simultaneously becomes more dense.

However, MW-assisted heating is still limited in terms of the types of concrete materials to which it can be applied. In this regard, Jeppson and Calif [18] reported that MW-assisted heating could only be used for conventional concrete. Until the present time, the non-uniformity of temperature distribution has been a main problem in attempts to use continuous MW heat in concrete applications [19]. The disadvantage of the dielectric materials is that its thermal distribution is inconsistent, which leads to problems associated with hot spots and cold zones [20]. Therefore, MW distribution with multi-mode cavity has been developed using MW technology applications whereby concrete is heated such that its moisture content evaporates while heat is transferred to its top surface.

The present research focuses on the design and construction of a portable prototype for concrete-accelerated curing that relies on applying MW energy. Experiments are performed, and the results are reported. The studied parameters are temperature evolution, moisture content, curing time, and compressive strength. Further, a comparison of MW curing and conventional (air or water) curing is also presented.

2. Design of a horn-shaped cavity using a mathematical model

It is generally accepted that uneven field distribution generates cold and hot spots and that the latter can contribute significantly to the phenomenon of runaway. For dielectric products (such as concrete), cold spots are unwelcome as they induce the internal structure to break or crack, thereby undermining the concrete's performance and rendering the concrete less durable. It is for this reason that a uniform electromagnetic heating is normally required. Researchers have devised multiple ways to improve the electric field as well as to improve heating distribution by varying the degree of achievement by changing either the source, the MW feeding system, the shape of the cavity, or the environment surrounding the load. Some ideas have been developed in regard to empty cavities; however, these do not work in applied situations [21]. For analysis, electromagnetic waves in the cavity were simulated to design the MW–vacuum system. The distributions of electric field strength and mode generation were studied in the simulation. The COMSOL MULTIPHYSICS® program version 3.4 [22] was used to construct domain meshes and the Finite Element Method (FEM) was employed to solve the problems. Generated resonant modes inside the multimode cavity, where the reflections from the cavity walls constructively reinforce each other to produce a standing wave, were calculated by determining the number of half-wavelengths in each of the principal directions. The quality factor (Q-factor) and the maximum electric field strength (E_{max}) were calculated by using the equations found in [19]. The time-average complex power flow through a defined closed surface was calculated from Poynting's theorem [23] when a MW source is connected to the cavity.

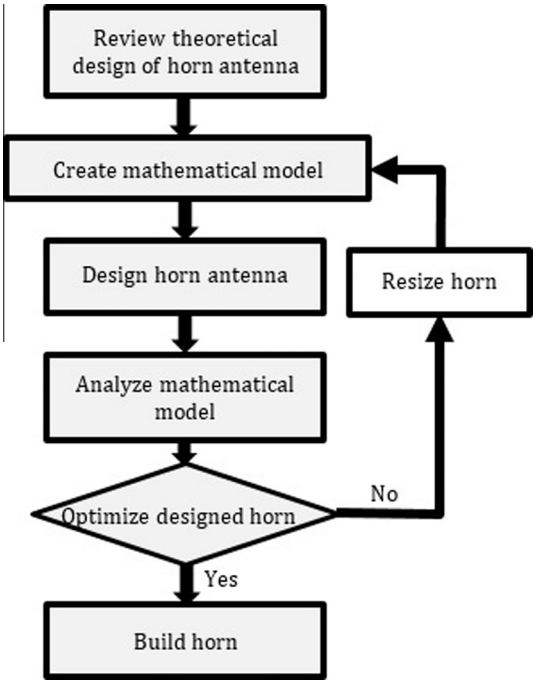

Fig. 1. Horn design process.

As shown in Fig. 1, in the present study, the design processes focus on the study of a horn-shaped cavity and a mathematical model to analyze and determine the horn size and configuration using the coupled electromagnetic and heat transfer analysis of both without load and with load (concrete workpiece) as shown below. A 3D mathematical model is considered, which is analyzed with COMSOL™ MULTIPHYSICS program version 3.4 [22]. After that, the MW-curing prototype is constructed. The horn of this prototype can be adjusted vertically. MW power of 800 W at 2.45 GHz is applied and fixed and movement modes are studied.

2.1. Mathematical formulation

From the calculated horn size, the mathematical model is applied to determine the design size of the horn and to analyze the distribution of the electromagnetic field in the horn (without load case) and the distribution of the concrete's temperature (load case). In this study, COMSOL™ MULTIPHYSICS program version 3.4 [22] is used to create the mathematical model, beginning by calculating the horn size. Then, the mathematical model is used to analyze and determine the optimal horn size before the horn is built.

The mathematical model analysis is divided into two parts: a distribution analysis of the electromagnetic field in the horn and an analysis of the thermal distribution of the concrete. The physical domain is presented in Fig. 2 with the following input MW position:

(a) The walls of the horn are perfect conductors.
(b) The concrete (load) materials are non-magnetic.
(c) The waveguide perfectly conducts the boundaries.

2.2. Analysis of the electromagnetic field in the horn

The distribution of the electromagnetic field in the horn (in terms of the waveguide, the horn, and the load) can be found by using Maxwell's electromagnetic field equation [24,25]. This can be carried out by using the COMSOL™ MULTIPHYSICS program version 3.4 [22], the equation associated with which is as follows:

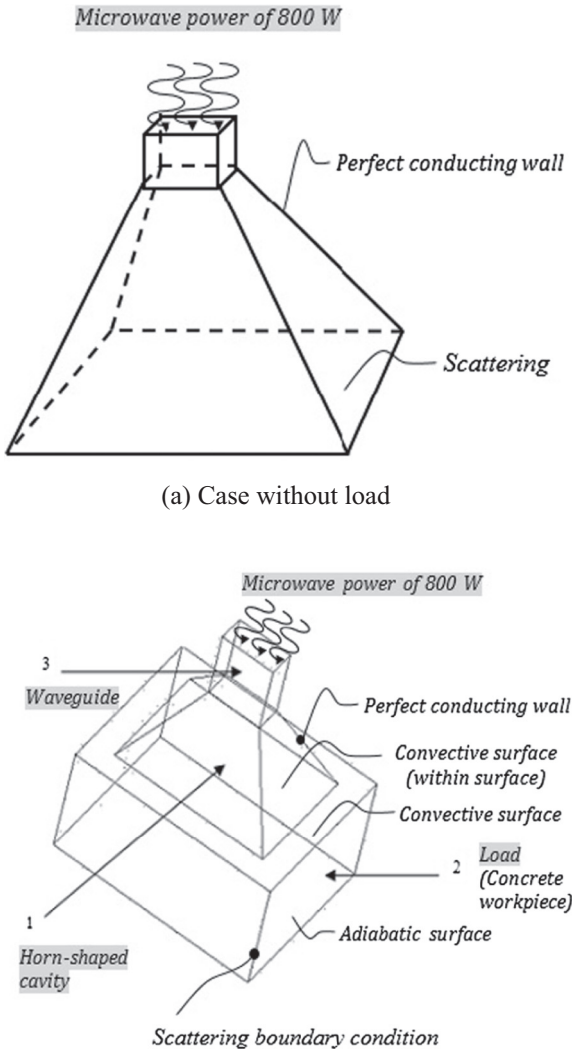

Fig. 2. Physical domain for analysis of the electromagnetic field in the horn and temperature distribution in the concrete. (a) Case without load. (b) Case with load (concrete workpiece).

$$\nabla \times (\mu_r^{-1} \nabla \times E) - k_0^2 \left(\varepsilon_r - \frac{j\sigma}{\omega \varepsilon_0} \right) E = 0 \tag{1}$$

$$\varepsilon_0 = n^2 \tag{2}$$

where E is the electric field intensity (V/m), H is the magnetic field intensity (A/m), J is the current density (A/m^2), σ is the electric conductivity (S/m), μ_r is the relative magnetic permeability, ω is the angular velocity (rad/s), k_0 is the free space wave number, ε_0 is the permittivity of the vacuum (8.85419×10^{-12} F/m), n is the refractive index, and ε_r is the relative dielectric constant that expresses the properties of the material in terms of its absorption capacity to transmit and reflect MW energy.

2.2.1. A case without load

The MW distribution in the waveguide and the horn constitutes the perfect conducting wall. Therefore, the electromagnetic boundary condition of the horn wall can be expressed as in this equation:

$$n \times E = 0 \tag{3}$$

The electromagnetic field condition created by the waveguide, an MW source, presented in Fig. 2, can be expressed as in this equation:

$$port: S = \int (E - E_1) \cdot E_1 \Big/ \int E_1 \cdot E_1 \quad (4)$$

where the port is the MW source at a power of 800 W.

The initial condition of the electromagnetic field is defined as:

$$E_x(t_0), E_y(t_0), E_z(t_0) = 0 \quad (5)$$

2.2.2. A case with load (concrete workpiece)

The coupled Maxwell's equation and heating model in this study is designed to analyze only the thermal distribution covering the concrete load under the electromagnetic field in the horn for the 3D case. On the assumption that the air in the horn cannot absorb the MW energy and transform it into heat, the internal load can transfer heat by conduction and the load can generate internal heat by transforming the MW energy into heat. On this assumption, the heat-exchange equation can be written based on the background from the COMSOL™ MULTIPHYSICS program version 3.4 [22] as in this equation:

$$\rho C_p \frac{\partial T}{\partial t} + \nabla \cdot (-k \nabla T) = Q \quad (6)$$

where T is the temperature (°C), t is time (s), C_p is the heat capacity at constant pressure (J/kg.K), ρ is the density (kg/m^3), k is the thermal conductivity (W/m.K), and Q is the local volumetric heat-generation term generated by the absorption of the MW energy transmitted as heat (W/M^3).

The outer sides of the calculated domain, i.e., the free space, are considered to be the scattering boundary condition as expressed in this equation:

$$n \times (\nabla \times E) - jkn \times (E \times n) = -n(E_0 \times Jk(n-k))(\exp(-Jk \cdot r)) \quad (7)$$

Heat can only be generated by the load or the concrete; therefore, the considered domain in terms of heat focuses directly on load. Thus, the boundary condition of heat occurs only on the top surface of the load (the wall of the load is an insulator, which cannot transmit heat).

The boundary condition of the heat surface at the top of the load (concrete workpiece) is

$$n \cdot (-k \nabla T) = 0 \quad (8)$$

The boundary condition of the heat wall is

$$-n \cdot (-k \nabla T) = 0 \quad (9)$$

The initial condition of the heat analysis is

$$T(t_0) = 303.15\ K \quad (10)$$

3. Materials and methods

Concrete was mixed and poured into molds. Two kinds of cases were explored: conventional curing (air curing and water curing) and MW curing (fixed and movement modes).

3.1. Materials

All the materials used in this study were obtained locally. The cementitious material used in all the mixtures was Type 1 Portland cement (OPC), which complies with ASTM C 150 [26]. The chemical compositions and physical properties of the cement are listed in Table 1. The tap water used conforms to ASTM C 1602 [27]. Further, the fine and coarse aggregates also obtained locally as river sand and crushed limestone rock, respectively, were in accordance with ASTM C 33 [28]. A mix proportion per one cubic meter of concrete used is shown in Table 2.

Table 1
Chemical composition and physical properties of Type 1 Portland cement.

Chemical composition (% by mass)	Type 1 Portland Cement (OPC)
Silicon dioxide (SiO_2)	16.39
Alumina oxide (Al_2O_3)	3.85
Ferric oxide (Fe_2O_3)	3.48
Magnesium oxide (MgO)	0.64
Calcium oxide (CaO)	68.48
Sodium oxide (Na_2O)	0.06
Potassium oxide (K_2O)	0.52
Sodium oxide (SO_3)	4.00
Titanium dioxide (TiO_2)	N/D*
Physical properties	
Loss on Ignition (% by mass)	1.70
Particle size distribution (D [4,3] μm)	23.32
Bulk density (kg/m^3)	1550
Specific gravity	3.20
Specific surface area (m^2/kg)	610

* N/D indicates "Not Detected".

Table 2
Mixture proportion of concrete (per 1 cubic meter of concrete).

Portland Cement (kg)	Water (kg)	River sand (kg)	Crushed limestone rock (kg)	Water–cement ratio (by mass)
350	170	830	1135	0.486

3.2. Equipment

The mobile MW-curing unit for concrete curing is constructed based on coupled MW-thermal analysis in Eqs. (1)–(10) both the without load and with load as presented in Fig. 3. The applied frequency of the MW is 2.45 GHz, which is created by a horn with a magnetron waveguide installed. The power is set at 800 W to produce MW energy. A programmable logic controller (PLC) system is applied to control the movement and on-off mode. The length of the rail is 2.5 m, and a motor to control the driving, AC type, 90 W is installed. A chain is used for driving and use gear (13 pieces that have a gear ratio of 1:5), and the motor drive speed is 5 round/min (rpm.)

3.3. Concrete workpiece preparation

The mixture is weighed, mixed, and poured into an acrylic mold with a thickness of 10 mm, which is designed to protect the mixture from the reflection of the MW. The dimensions of the mold are 150 × 150 × 150 mm, as stated in the British standard BS 1881: Part 3 [29]. The concrete is mixed according to the ASTM C 192 standard [30]. The mixture is left to develop for an initial setting time of 30 min, after which it is cured using MW energy. Next, the frame is removed from the mold, and the curing continues but now in the air by wrapping the mixture in a sealed plastic bag and keeping it at a temperature of 25 ± 2.0 °C for 12 h. Finally, the compressive strength of the mixture is tested.

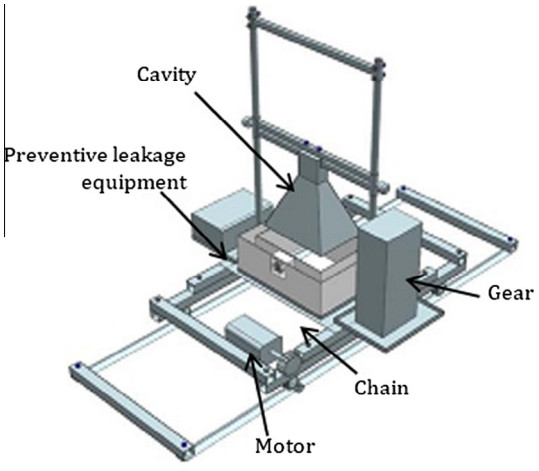

Fig. 3. Prototype for moving mode MW curing.

Table 3
Cases and conditions for concrete curing.

Case	Power (W)	Preheating (minutes)	Pause (minutes)	Heating (minutes)	Total (minutes)
Case A	Air, Water	–	–	–	8 h, and 1, 3, 7, 14, 28 days
Case B	800	Continuity	–	–	30, 60, 90, 120
Case C	400	Continuity	–	–	30, 60, 90, 120
Case D	800	20	120	10	30, 60, 90, 120
Case E	800	30	60	15	30, 60, 90, 120
Case F	800	30	60	10	30, 60, 90, 120

Similarly for curing in water and air, the mixture is poured into a steel mold and cured for 23½ ± ½ h. Then, some concrete workpieces of the mixture are cured in water for respective periods of 8 h, 1 day, 3 days, 7 days, 14 days, and 28 days. Other concrete workpieces are cured in air such that they are wrapped and sealed in a plastic bag and kept in a controlled room where the temperature is maintained in the range of 25 ± 2.0 °C and relative moisture is maintained in the range of 60% ± 5.0%. These workpieces are cured for respective periods of 8 h, 1 day, 3 days, 7 days, 14 days, and 28 days. Finally, the compressive strength of the concrete is tested.

3.4. Cases used to study MW curing

In this study, concrete curing is tested via a conventional method and via MW curing in both the fixed and movement modes. Non-continuous MW curing is carried out in the preheating phase by using MW energy for a fixed period. Then, the heating is paused and the concrete is reheated using MW power. The conditions in which the curing took place are presented in Table 3. The details of each experiment are as follows:

- *Case A: Concrete curing in water and air*

For concrete curing in water and air, the frame is removed from the mold when the mixture is at age 23½ ± ½ h. For water curing, the testing times are 8 h, 1 day, 3 days, 7 days, and 28 days. For air curing, the concrete is wrapped and sealed in a plastic bag and kept in a controlled room where the temperature is held at 25 ± 2.0 °C and where the relative moisture is held at approximately 60% ± 5.0%. The curing is carried out for 8 h, 1 day, 3 days, 7 days, 14 days, and 28 days. Finally, the compressive strength of the concrete is tested.

- *Case B: Concrete curing by using continuous MW power of 800 W*

The concrete is cured by using continuous MW power of 800 W and tested at 30, 60, 90, and 120 min.

- *Case C: Concrete curing by using continuous MW power of 400 W*

The concrete is cured by using continuous MW power of 400 W and tested at 30, 60, 90, and 120 min.

- *Case D: Concrete curing by using non-continuous MW power of 800 W*

The concrete is cured by using non-continuous MW power of 800 W and tested at 30, 60, 90, and 120 min (not including the pause time). The PLC system is used to control the on-off switch for the MW power.

- *Case E: Concrete curing by using non-continuous MW power of 800 W*

The concrete is cured by using non-continuous MW power of 800 W and tested at 30, 60, 90, and 120 min (not including the pause time). The PLC system is used to control the on-off switch for the MW power.

- *Case F: Concrete curing by using continuous MW power of 800 W (movement system)*

The concrete is cured by using MW power of 800 W, and the PLC system is used to control the on-off switch for the MW power and the movement, as shown in Fig. 4. There are six workpieces, each of which is cured by MW energy for 180 min.

3.5. Testing methods

3.5.1. Moisture content measurement

The moisture content is measured is based on the weight of the mixed cubic concrete to find the initial weight of the concrete workpiece. After that, each workpiece is wrapped and sealed in a plastic bag and kept at a temperature in the range of 25 ± 2.0 °C for 12 h. Then, the concrete is weighed to determine the final weight, after which the compressive strength is tested. Further, the wet bulb in the concrete can be calculated by using the following equation:

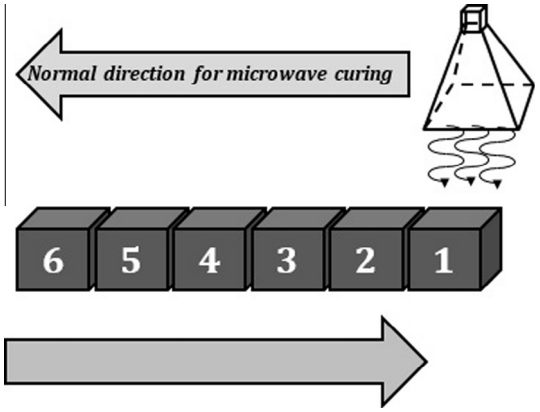

Fig. 4. Flow diagram of process for MW-curing of concrete (movement steps).

$$A = \left(\frac{W_a - W_b}{W_a}\right) \times 100 \quad (11)$$

where A is the wet bulb (%), W_a is the initial weight of the concrete before curing (kg), and W_b is the final weight after curing (kg).

3.5.2. Temperature measurement

The temperature measurement of the concrete can be divided into two aspects: the internal temperature measurement and the external temperature measurement. The process of measuring begins by using a system for measuring temperature connected to a data logger and spike in the middle of the concrete. Three levels of concrete, the top, middle, and bottom, are all measured at 30, 60, 90, and 120 min.

The measurement is carried out at 1 cm from the top surface (top), 7.5 cm from the top surface (middle), and 14 cm from the top surface (bottom), as presented in Fig. 5. The natural heat advection is assumed at the top surface because the wall side is insulated by the 10 mm thick acrylic. In addition, heat transpiration occurs only at the top surface and not at the sides. The internal temperature is measured in order to establish the effect of the MW-curing temperature for Cases B, C, D, and F.

3.5.3. Compressive strength test

Compressive strength—the maximum stress concrete can bear before cracking—is the most important property of concrete. The respective processes for testing the compressive strength of concrete by air curing, water curing, by MW curing are carried out by following the standard set out in BS 1881[31].

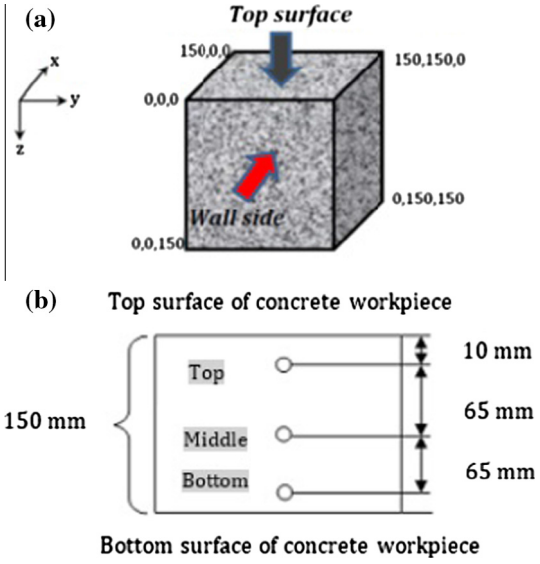

Fig. 5. (a) Dimension of specimen (mm). (b) Installation of a measuring temperature system for measuring the internal temperature of concrete.

4. Model simulation of horn

4.1. Analysis of the horn size

The analysis of the horn size is divided into two parts: an analysis of the distribution of the electromagnetic field within the horn (without load) and an analysis of the thermal distribution of the concrete (with load). Time does not affect the electromagnetic field behavior covering the concrete workpiece in this analysis, but time does affect the distribution of the electromagnetic field covering the concrete workpiece. Thus, this is a steady-state problem. Therefore, the analysis of the distribution of the electromagnetic field covering the concrete workpiece in 3D is carried out using the COMSOL™ MULTIPHYSICS program version 3.4 [22].

In the analysis of the thermal distribution in the concrete, it was found that time had a direct effect on the temperature of the load. This problem is identified as a transient condition. Therefore, the analysis of the distribution of the concrete temperature is performed with the finite element method using the COMSOL™ MULTIPHYSICS program version 3.4 [22].

The input data used to analyze both the electromagnetic field and the heat transfer are presented in Table 4.

4.2. Calculation procedure

In this study, the finite element method is used to analyze the transient problems. The computational scheme is to assemble a finite element model and compute a local heat generation term by performing an electromagnetic calculation using concrete properties.

Table 4
Input data for analysis.

Symbol	Value	Unit	Ref.
ε_0	8.85419×10^{-12}	F/m	–
μ_0	$4\pi \times 10^{-7}$	H/m	–
ε_r	10	–	[Measured by Authors]
t	60	s	–
c_p	650	J/kg.K	[Measured by Authors]
ρ	2300	kg/m^3	[Measured by Authors]
Power	800	W	–
f	2.45	GHz	–
$T(t_0)$	303.15	K	–
k	0.87	w/m.K	–

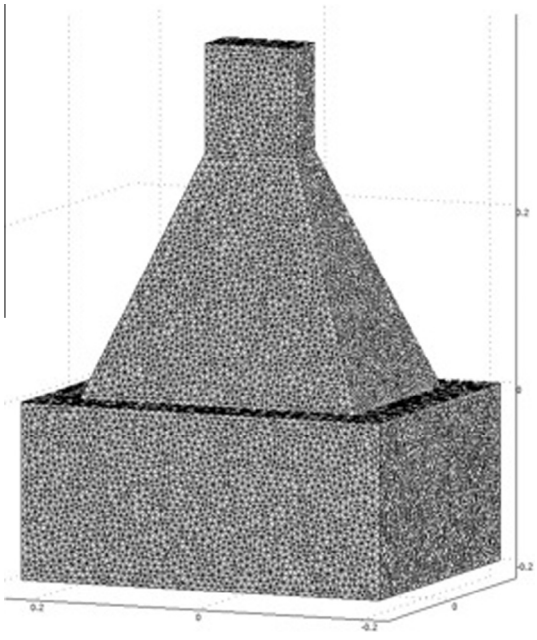

Fig. 6. A three-dimensional finite element mesh of horn and concrete model.

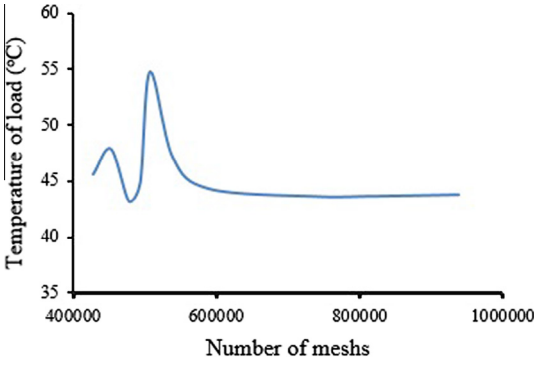

Fig. 7. Grid convergence curve of the 3D model.

In order to obtain a good approximation, a fine mesh is specified in the sensitive areas. This study provides a variable mesh method for solving the problem as shown in Fig. 6. The model of heat equation and Maxwell's equation is then solved. All computational processes are implemented using COMSOL™ MULTIPHYSICS program version 3.4. The electromagnetic power absorption at each point is computed and used to solve the time-dependent temperature distribution. All steps are repeated, until the required exposure time is reached. Convergence tests of the frequency of 2.45 GHz case are carried out to identify a suitable number of elements required. The convergence curve resulting from the convergence test is shown in Fig. 7. This convergence test leads to a grid with approximately 700,000 elements. It is reasonable to assume that, with this element number, the accuracy of the simulation results is independent of the number of elements.

5. Results and discussion

In this section, the modeling results of the electromagnetic field and the results of the tests focused on the thermal behavior of concrete during MW curing.

5.1. Results of the model simulation

The modeling results of the electromagnetic field within the horn in the shape of a horn (without load case) (Fig. 8(a) and the thermal distribution covering the concrete workpiece (with load case) are presented in Fig. 8(b).

In Case 1 (Adjustment on the height of horn), the electric fields are $8.006e^4 \times 10^4$ V/m, $1.062e^5 \times 10^5$ V/m, $1.128e^5 \times 10^5$ V/m, and $8.729e^4 \times 10^4$ V/m, as presented in Fig. 4. The electric fields are similar whereas the increased distribution of the electric field by an increase in the height of the horn from 211.8 to 273 mm provides a progressive electric distribution of $8.729e^4 \times 10^4$ V/m, as presented in Fig. 9(d).

In regard to the thermal distribution in the concrete, it was found that the increased horn height in Fig. 10 produced a temperature of $\lambda/4$, $\lambda/2$, $3\lambda/4$, λ at 64.782, 63.809, 71.743, and 67.481 °C, respectively. When the horn height is increased by λ to achieve a height of 273 mm, as presented in Fig. 10(d), the thermal distribution in the surface of the concrete improves, i.e., becomes more even. In addition, the thermal distribution widens and hot and cold spots are reduced, as presented in Fig. 10.

It is emphasized that the height adjustment of the horn produces an electric field of $8.729e^4 \times 10^4$ V/m, as presented in Fig. 9 (d), and a thermal distribution at 67.481 °C. After this height optimization, the horn width is adjusted by taking the steps described next.

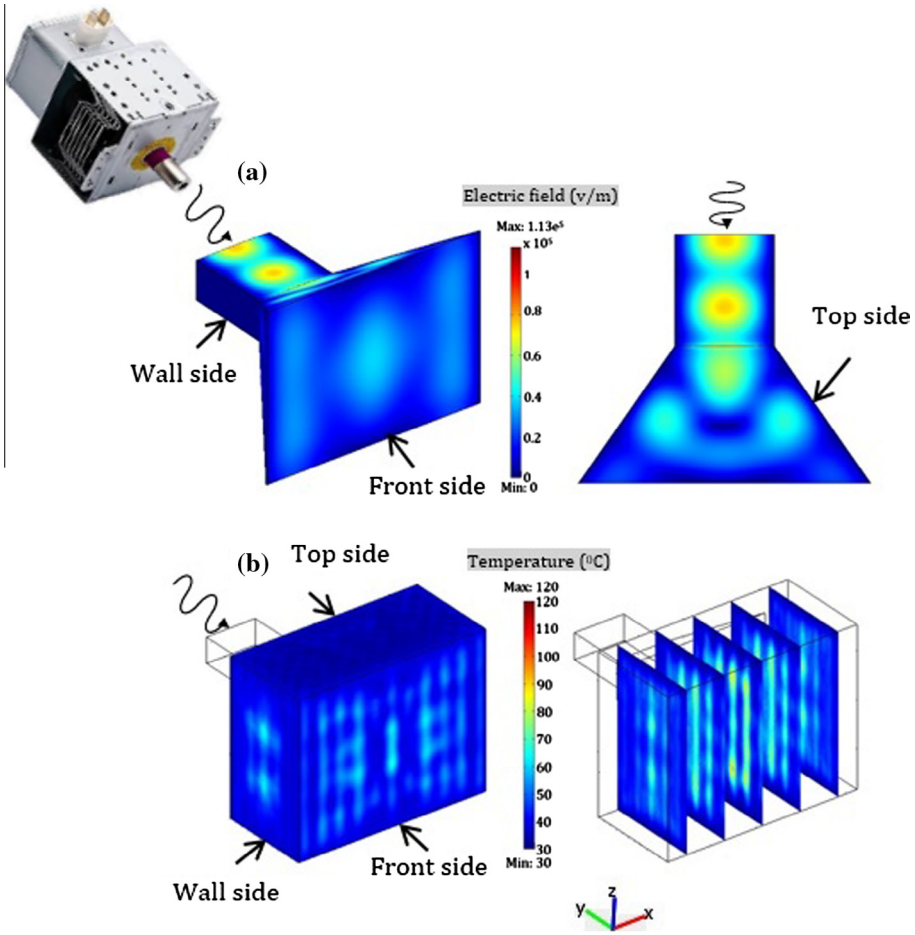

Fig. 8. (a) Distribution of electromagnetic field at a MW power of 800 W within the horn (without load) from the first result of the horn design. (b) Temperature distribution (with load) integrated with the first horn design.

For the simulation in Case 2 (decreasing adjustment on the width of horn), the electric fields are $8.892e^4 \times 10^4$ V/m and $9.05e^4 \times 10^4$ V/m when the horn width is increased, as presented in Figs. 11(a) and 6(b), respectively. In Fig. 11(a), it is shown that the increased horn width produces uniform electric distribution in terms of the electric field. In addition, the distribution of the concrete temperature found at 73.092 °C is presented in Fig. 11 (c) and that found at 69.076 °C, in Fig. 11(d). Therefore, if the horn width is increased, as presented in Fig. 11(a), the electric field in the horn will increase. This increase, in turn, facilitates the process whereby the material or load can receive the electric field, which can produce the concrete thermal distribution and increase the thermal distribution at the surface.

For Case 3 (increasing adjustment on the width of horn), the electric fields of the reduced-width horn, as presented in Fig. 12 (a) and (b), are $8.387e^4 \times 10^4$ V/m and $9.579e^4 \times 10^4$ V/m, respectively. It was found that if the horn width is reduced, the size of the electric field decreases. The thermal distribution covering the concrete load is 73.307 °C and 81.764 °C, as presented in Fig. 12 (c) and (d), respectively.

With the horn design based on the concept of an antenna, the electric distribution within the horn is $7.625e^4 \times 10^4$ V/m, as presented in Fig. 8(a), and the temperature of the load/concrete is 63.731 °C. After increasing the horn height, increasing and reduction of horn found that the electric field is $8.892e^4 \times 10^4$ V/m, as presented in Fig. 11(a), and the concrete temperature is 73.092 °C showing increasing the distribution of electricity, or multimode wave and temperature. The temperature at the center of the concrete for first horn design and adjusted horn of 246.7 mm × 333.68 mm, as presented in Figs. 13 and 14, respectively. It was found temperatures along the x, y and z axis of horn (246.7 mm × 333.68 mm) consistently over.

5.2. Results of the experiments

The results of the thermal behavior of concrete during MW curing, the thermal distribution on the concrete surface, the residual moisture content after MW curing, and the compressive strength of the concrete are discussed.

5.2.1. Thermal behavior of concrete under MW curing (Case B)

Fig. 15 presents the effects of MW curing of concrete with a 0.48 water–cement ratio under a 120 min curing time and 800 W (Case B). It is found that the temperature of the concrete increased continuously. At the beginning of the experiment, the moisture content of the concrete is high, which means that the transfer rate of MW energy to heat takes place rapidly in accord with heat production theory [19]. After 90 min, the temperature is constant because the moisture content at the surface of the concrete is reduced due to the absorption capacity of the MW energy. It can be explained that the dielectric property of concrete is related to the reduced moisture whereas the internal structure of the concrete's voids means that excess water is retained (i.e., the free or residual water remaining after the chemical reaction). After being activated by the MW energy, the concrete is absorbed and transmits heat energy. At the beginning of the curing process, the moisture content in the concrete has a direct effect on the initial temperature because the concrete's dielectric property is high. This causes the concrete's

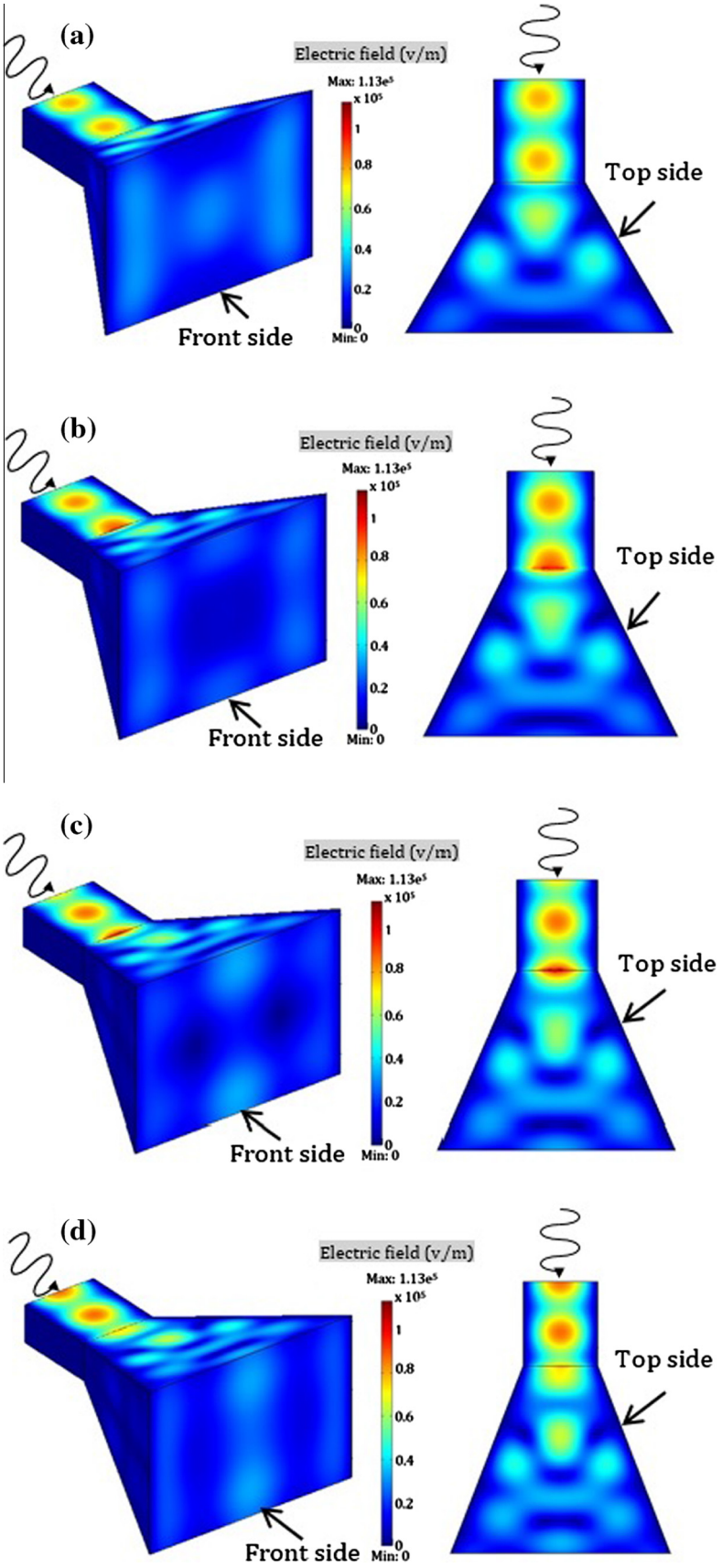

Fig. 9. Distribution of electromagnetic field at a MW power of 800 W within the horn (without load) of (a) Height of original horn of λ/4 is equal to 181.2 mm. (b) Height of original horn of λ/2 is equal to 211.8 mm. (c) Height of original horn of 3 λ/4 is equal to 242.4 mm. (d) Height of original horn of λ is equal to 273 mm.

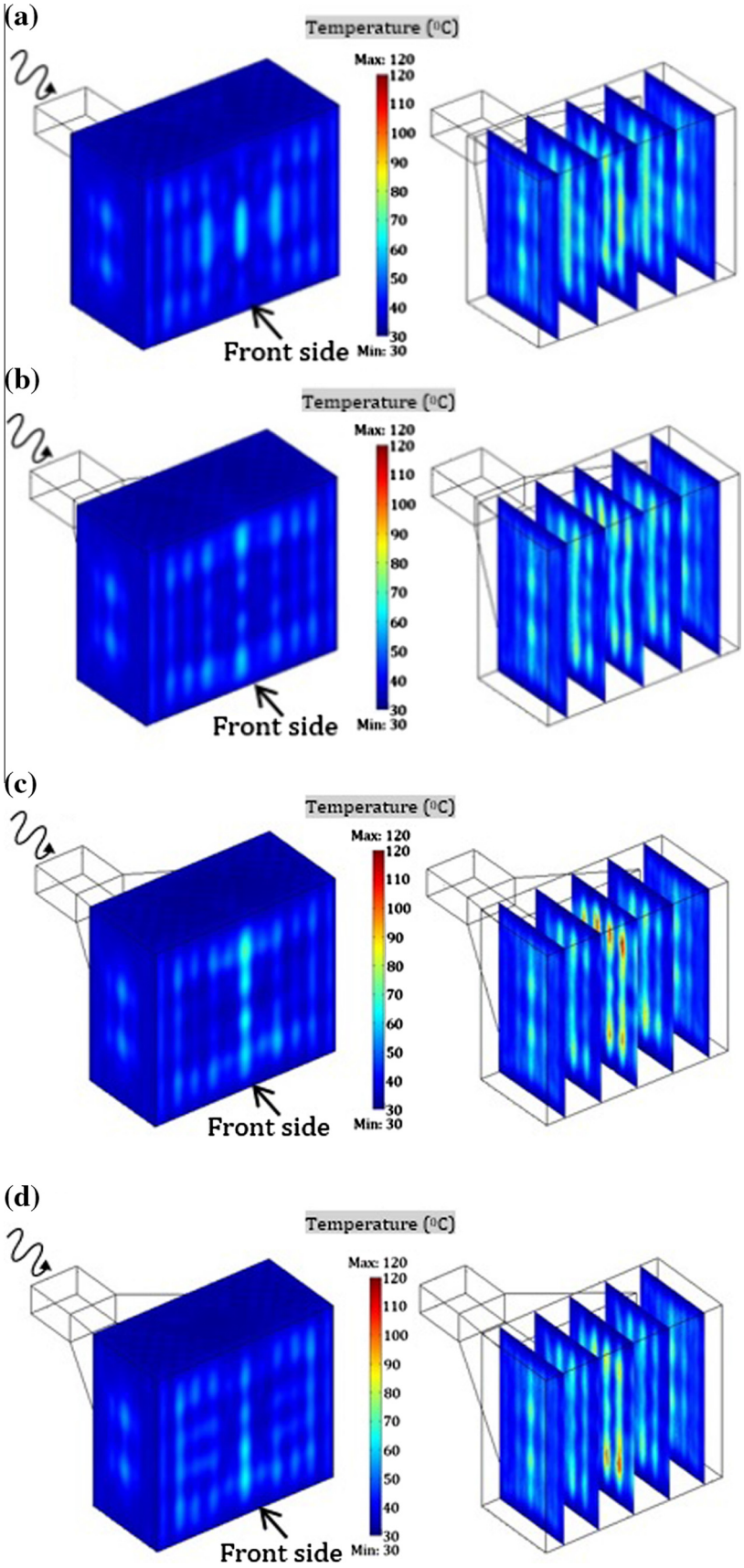

Fig. 10. Temperature distributions at a MW power of 800 W within the horn at (a) height λ/4 is equal to 181.2 mm (b) height λ/2 is equal to 211.8 mm. (c) height 3 λ/4 is equal to 242.4 mm. (d) height λ is equal to 273 mm.

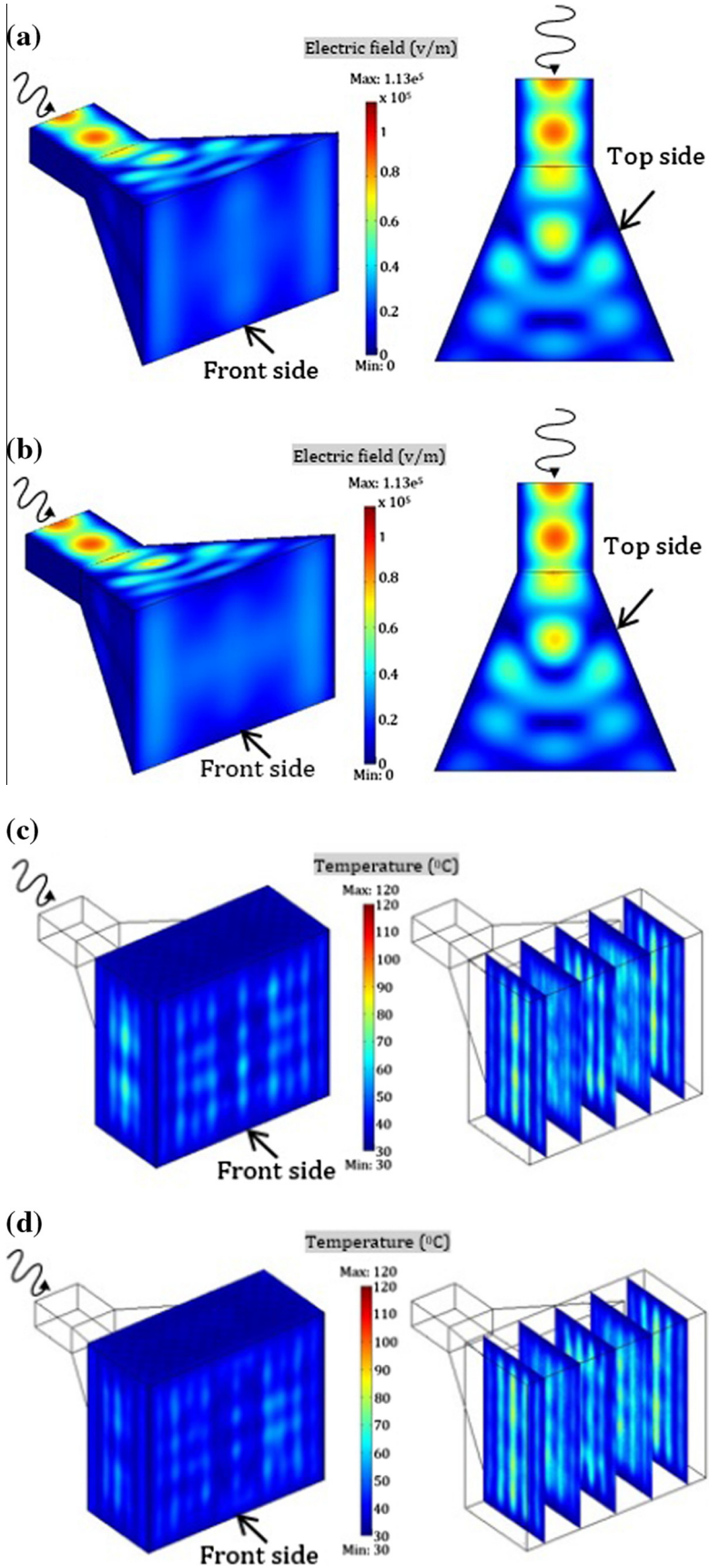

Fig. 11. Distribution of electromagnetic field of (a) adjusted horn of 246.7 mm × 333.68 mm. (b) adjusted horn of 256.7 mm × 347.2 mm, and temperature distributions of (c) adjusted horn of 246.7 mm × 333.68 mm and (d) adjusted horn of 256.7 mm × 347.2 mm.

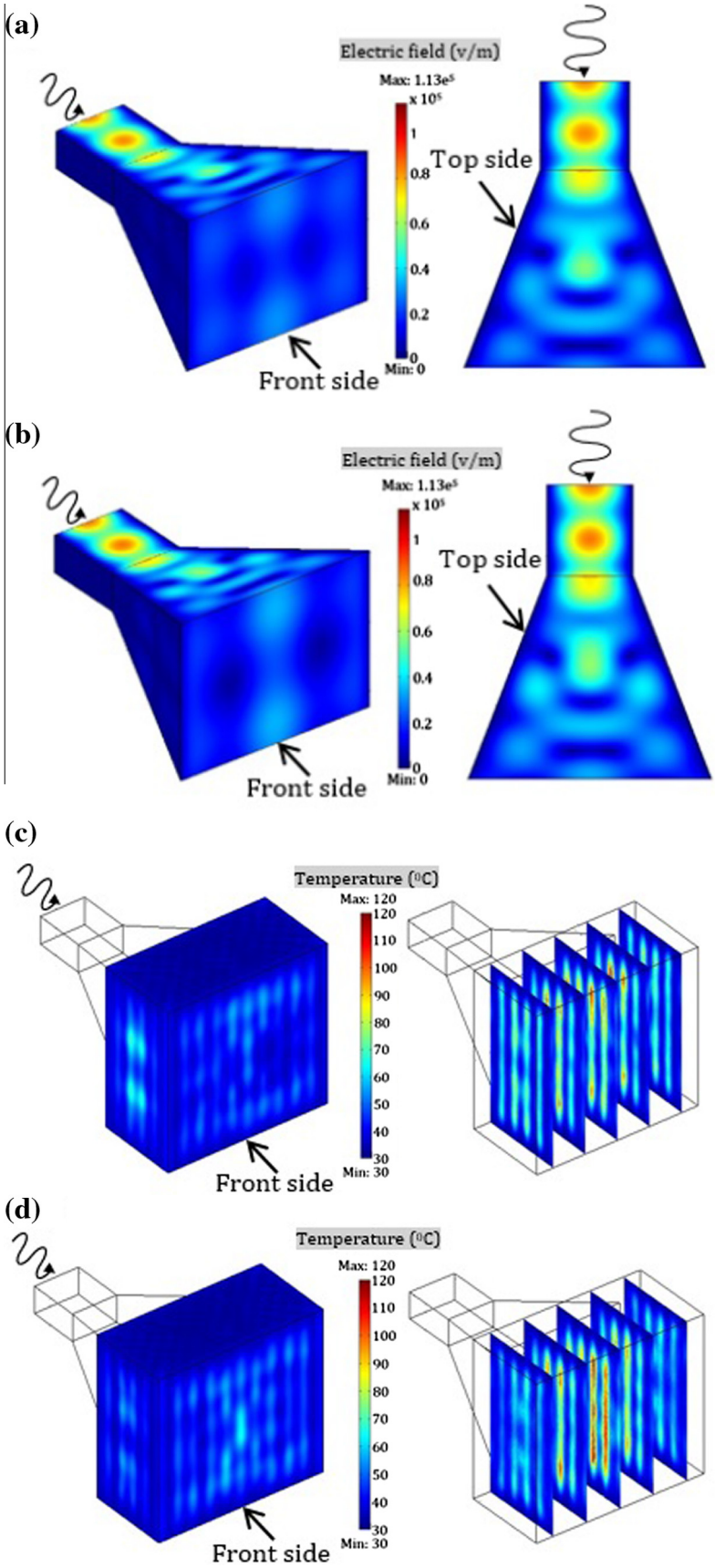

Fig. 12. Distribution of electromagnetic field of (a) Reduction of horn size of 226.7 mm × 306.64 mm. (b) Reduction of horn size of 216.7 mm × 293.12 mm, and temperature distributions of (c) Adjustment of horn size of 226.7 mm × 306.64 mm and (d) Reduction of horn size of 216.7 mm × 293.12 mm.

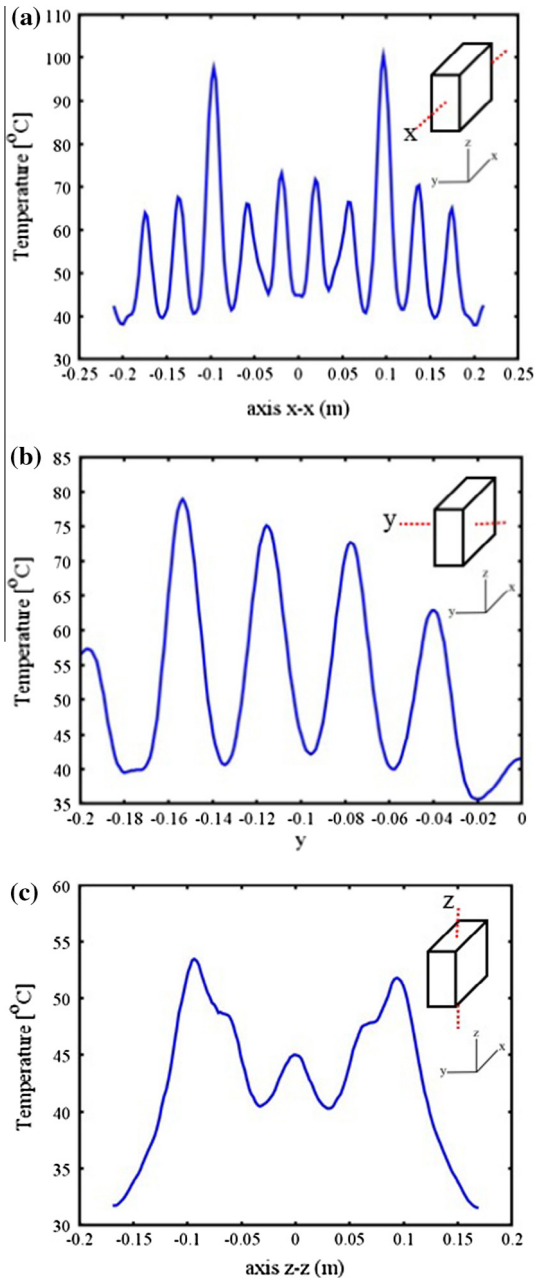

Fig. 13. Temperature at the center of the concrete for first horn design. (a) Temperatures along the x axis. (b) Temperatures along the y axis. (c) Temperatures along the z axis.

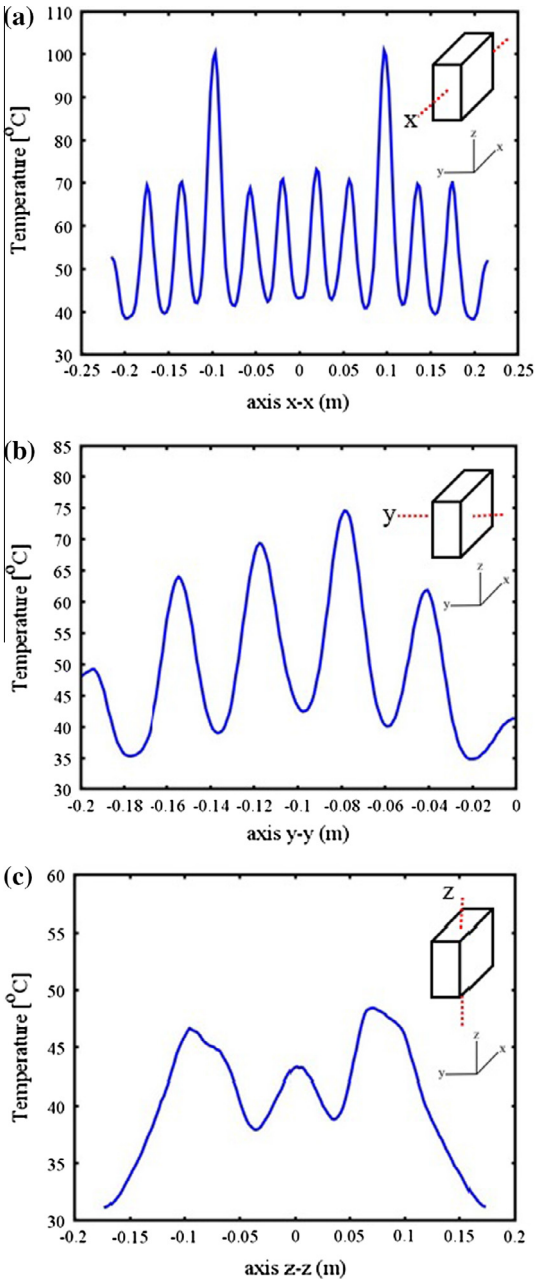

Fig. 14. Temperature at the center of the concrete for adjusted horn of 246.7 mm × 333.68 mm. (a) Temperatures along the x axis. (b) Temperatures along the y axis. (c) Temperatures along the z axis.

temperature to increase rapidly and continuously. However, as the moisture content in the concrete decreases, the dielectric property also decreases, rendering the concrete's temperature constant.

At the beginning of the curing process, the temperature at the top of the concrete increases continuously whereas the temperature in the middle increases intermittently. It can be explained that the top surface contains excess water and that bleeding occurs after curing for 30 min to develop initial setting time. At this stage, the concrete surface absorbs the MW energy to a significant extent after 70 min of curing. However, the temperature in the middle increases rapidly because the temperature of 100 °C at the top surface is high enough to transfer as far down as the middle. In addition, heat accumulates in the middle of the concrete and heat cannot occur because of the insulation wall. At the bottom, the temperature increases slowly due to the heat accumulation and the insulation wall. However, at 95 min, the heat increases dramat-

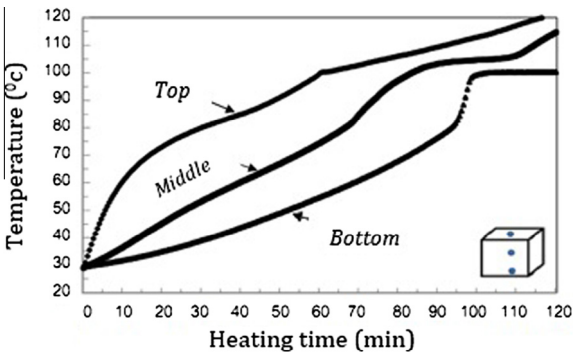

Fig. 15. Temperature profile of concrete during continuous. MW curing with clapsed time and 800 W (Case B).

ically from 70 °C to 100 °C. The temperature at the top surface is 110 °C, and in the middle it is 103 °C. Therefore, the heat transfer is conducted throughout the concrete workpiece. Then, at 100 min, the temperature throughout the concrete increases to 100 °C. In addition, at 120 min, the temperature at the top surface is 125 °C, in the middle it is 110 °C, and at the bottom it is 100 °C.

5.2.2. Influence of MW power on the temperature of concrete under MW curing (Case C)

Fig. 16 presents the results from the MW curing of concrete at 400 W. The results show that the temperature of the concrete increased rapidly due to a change in the amount of electrical power used directly reduces the multi-mode within the horn. Curing the concrete for 30 min at 400 W can increase the concrete's temperature to 70 °C, whereas curing by 800 W for 30 min can increase the concrete's temperature to 80 °C. It was found that the behavior of heat generation within the concrete under both of these conditions is quite similar. At the beginning of the process, the temperature at the top surface is very high due to the high moisture content and the high dielectric property of the concrete, which MW energy can absorb and transform entirely into heat energy. The temperature in the middle of the concrete increases continuously due to penetrated MW can increase the concrete temperature. Heat accumulates at the bottom of the concrete because of the insulation wall and the heat transferred from the surface. After 70 min, the temperature in the middle changes rapidly due to a top surface temperature of 105 °C. Then, the difference in temperature in the middle and at the bottom is constant because 400 W is used to absorb the MW energy of the dielectric material, which is directly related to the electric field. Therefore, heat generation in the concrete decreases. At the bottom, the temperature is constant at 100 °C after 90 min, indicating that electrical or MW power influences the heat generation of concrete due to changes in the electric field.

5.2.3. Thermal behavior of concrete under discontinuous concrete curing (Case D)

In this experiment, the concrete is tested in both the fixed mode and the movement mode at 800 W (Case B). The results show that the concrete's compressive strength decreases continuously after a curing time of 90 min and again after 120 min. When the concrete's temperature is higher than 80 °C [17], compressive strength decreases by 50%. By observation, at a curing time of 120 min, it was found that the temperature at the top, middle, and bottom of the concrete was 125, 115, and 100 °C, respectively. These results may have a negative effect on the internal structure of the concrete, which may crack thereby giving rise to low compressive strength. Therefore, discontinuous MW curing is applied in order to maintain the appropriate temperature, which can increase the compressive strength of concrete. This experiment was carried out by using the PLC system to control the MW supply or on-off mode, as presented in Fig. 17.

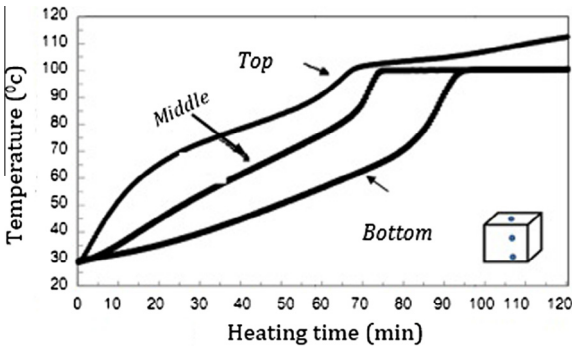

Fig. 16. Internal temperature of concrete during continuous curing by MW energy with clapsed time and 400 W (Case C).

Fig. 17 presents the discontinuous curing by MW energy case (Case D). The experiment is carried out by preheating the workpieces for 20 min, followed by idle time for 2 h, and then energizing by MW power for 10 min and idle time for 2 h until the total time is 2 h. The total time of this experiment is 22 h, and the total MW curing time is 120 min. The results show that in the first 20 min, the temperature at the top, in the middle, and at the bottom of the concrete is approximately 68, 50, and 43 °C, respectively. After that, the PLC serves the function of stopping the MW supply for 2 h and of reheating the workpieces for 10 min. This working loop is operated for 120 min (including only the energizing time and excluding the idle time). During the idle time, the temperature at the top, in the middle, and at the bottom decreases to 20, 10, and 5 °C, respectively. These phenomena can be explained by noting that the top surface is exposed to air because of heat advection, such that the temperature decreases. The temperature in the middle decreases slowly and at the bottom the temperature decreases slightly as there is no heat advection.

5.2.4. Heat evolution from discontinuous curing (Case E)

Fig. 18 presents the discontinuous curing by MW energy case (Case E). In this experiment, the moisture content still retained in and the compressive strength of the concrete increased slightly. Therefore, the energizing time of MW is added and idle time is reduced in order to achieve a high temperature and remove moisture. The experiment is carried out by MW energizing for 30 min, idle time for 1 h, and re-energizing for 15 min followed by a second idle time of 1 h until the total time reaches 120 min. The total time

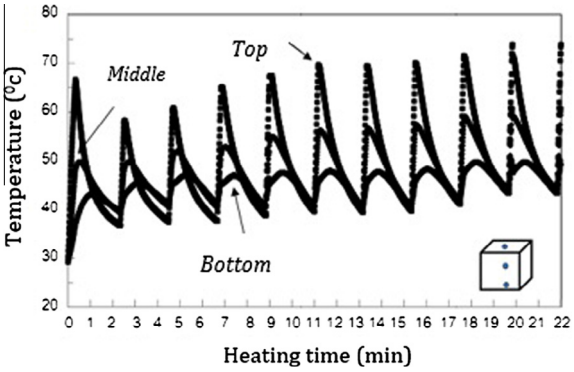

Fig. 17. Temperature of concrete during discontinuous curing by preheating for 20 min, idle time for 2 h, energized by MW power for 10 min and idle time for 2 h until the total time is 2 h (total time of this experiment is 22 h, and the total MW curing time is 120 min).

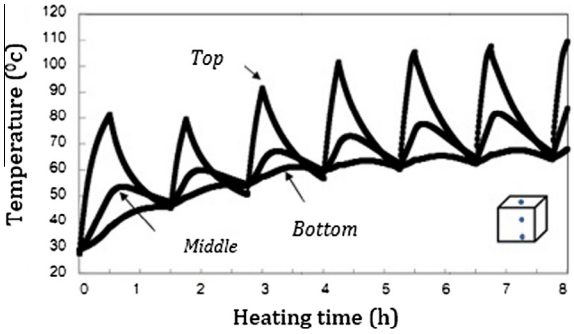

Fig. 18. Internal temperature of concrete after discontinuous MW curing (Case E) by MW energizing for 30 min, idle time for 1 h and re-energizing for 15 min and second idle time for 1 h until the total time reaches 120 min. Total time is 8 h, and curing time is 120 min.

is 8 h, and the curing time is 120 min, which is controlled by the on-off system of the PLC. In the first 30 min, the temperature at the top, in the middle, and at the bottom is 81, 55, and 41 °C, respectively. The operating loop consists of 1 h of idle time and 15 min of energizing MW. The results show that temperature increased continuously because the energizing time was increased and the idle time was reduced. The temperature at the top, in the middle, and at the bottom was 110, 83, and 65 °C, respectively. In addition, the moisture content and the compressive strength of the concrete were both higher than these respective properties under discontinuous curing (Case D).

5.2.5. Thermal distribution at the concrete surface

The internal temperature of the concrete after MW curing is carried out by measuring the temperature in various parts of the workpieces. The absorption phenomenon where by MW energy is transformed into heat energy while the temperature increases continuously is shown in Fig. 19 (Case B). There was two hot spot zone in time 60 min in Fig. 19(b) and one hot spot zone at 90 min in Fig. 19(c).

The external temperature at the top surfaces and sides of the workpieces is recorded by using an infrared camera. The results indicate that heat in the concrete wall is evident at a depth of 3

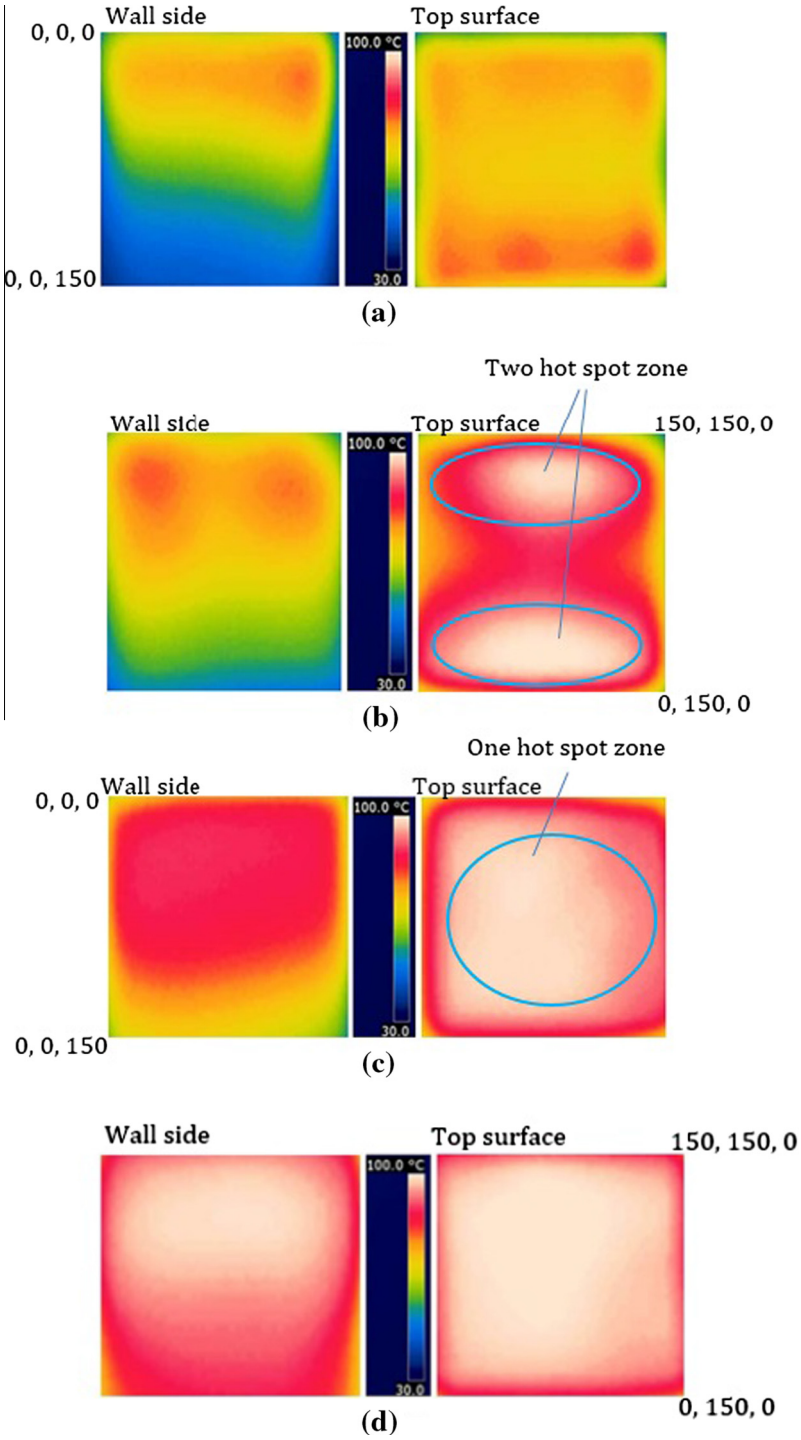

Fig. 19. Temperature distribution at the top surface and wall side after continuous MW curing at 800 W of Case B for (a) 30 min, (b) 60 min, form two hot spot zone. (c) 90 min, form one hot spot zone and (d) 120 min.

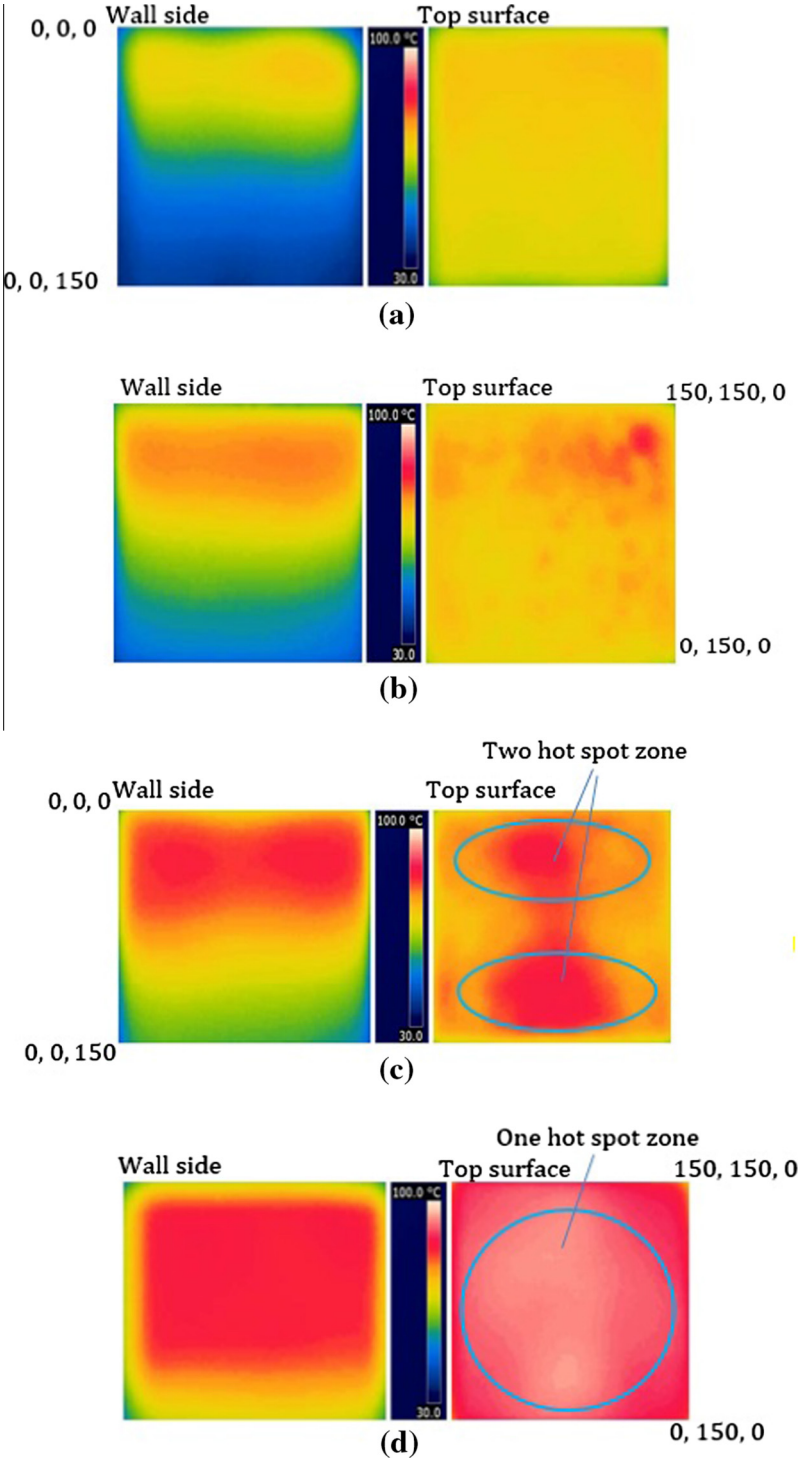

Fig. 20. Temperature distribution after continuous MW curing at 400 W of Case C for (a) 30 min, (b) 60 min, (c) 90 min, form two hot spot zone and (d) 120 min, form one hot spot zone.

to 5 cm from the top surface. As a result, heat is dispersed to the top surface and the wall of the concrete, as shown in Fig. 20 (Case C). There was two hot spot zone in time 90 min in Fig. 20(c) and one hot spot zone at 120 min in Fig. 20(d).

The heat distribution at the concrete surface differs according to whether 800 W or 400 W of MW power are applied. The amount of electrical power used has a direct effect on the intensity of the electric field. In addition, the temperature increases as the curing increases. The maximum temperature in the concrete occurred at 3 to 5 cm from the top surface.

5.2.6. Heating characteristics of a concrete workpiece subjected to MW energy

5.2.6.1. Moisture Loss. In this experiment, the water–cement ratio is 0.486 for all the studied cases. For the purpose of repairing concrete roads, the highway department sets a maximum limit on the water and cement (w/c) of 0.486 by mass. The water or moisture content in concrete means that concrete is a dielectric material capable of absorbing MW energy and transforming it into heat. Therefore, when concrete is energized by MW power, the moisture content of the concrete or the excess water from

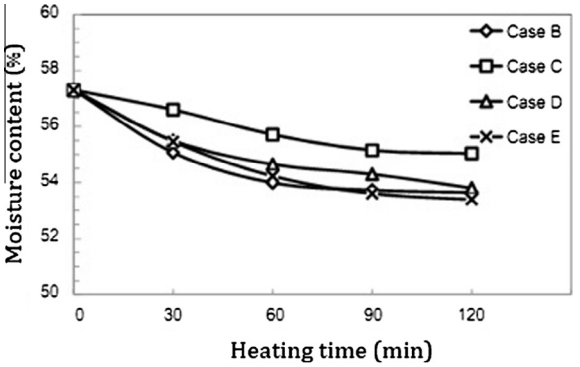

Fig. 21. Moisture content in concrete after MW curing in Cases B, C, D, and E.

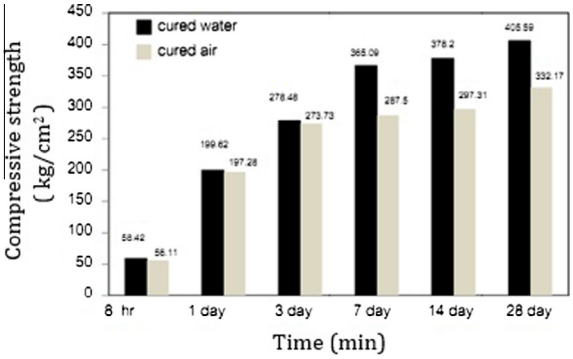

Fig. 22. Compressive strength of concrete after water and air curing (Case A).

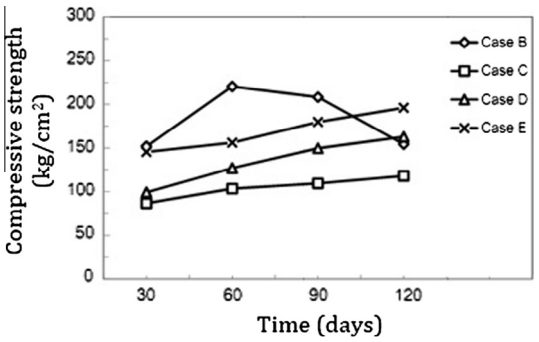

Fig. 23. Compressive strength of concrete after continuous MW curing and discontinuous MW curing for Cases B, C, D, and E.

hydration between the cement and water is reduced. In addition, the concrete is energized by continuous MW power, the moisture content decreases and thereby affects the moisture-transfer mechanism in the concrete (porous material theory).

The results pertaining to the amount of moisture lost from the concrete after MW curing in Cases B, C, D, and E are presented in Fig. 21. Overall, the moisture content of the concrete undergoes rapid changes at the beginning of the curing phase. The moisture distribution and porosity are related to many factors, i.e., the moisture content transfer from within the concrete to its surface, the changing state of fresh concrete from the liquid to gas phase, and the moisture transfer from the thermal distribution. At first, the moisture content at the surface of the concrete absorbs MW energy, which is then transformed into heat energy. The rate of evaporation is equal to the water movement in porous materials that creates the liquid film. The controlled parameter is the level of the heat energy input into the concrete. When the process whereby moisture is removed has been carried out, the internal moisture is reduced, and this reduced moisture content has a direct effect on the concrete's dielectric property. The moisture content is reduced, and the heat generation is reduced likewise (heat transfer and mass in porous material).

5.2.6.2. Compressive strength development. Compressive strength is the most important property of concrete. The main function of concrete is load resistance, which is a direct function of compressive strength. Further, compressive strength is an indicator of other important properties, namely, durability, friction resistance, and porosity resistance.

This research focuses on concrete with compressive strength of at least 325 kg/cm^2 for concrete at age 28 days. MW technology is applied in order to accelerate the curing time because a road repair carried out based on conventional curing can mean that a road is out of use for as many as 14 days. For this special case, compressive strength must be a minimum of 245 kg/cm^2.

The experiment whereby concrete is cured using MW energy is divided into two parts: the conventional water-curing case (Case A), air curing and MW curing (Cases B, C, D, and E, respectively), and moving curing (Case F).

Fig. 22 presents water and air curing (Case A). The results indicate that the concrete's compressive strength increased rapidly in the first 3 days. The initial curing phase can increase this property of concrete. During the first 3 days, water curing and air curing show a similar level of efficiency. After that period, however, under water curing, the concrete's compressive strength increases continuously until the age of 28 days when the compressive strength is equal to 405.59 kg/m^2. On the other hand, under air curing after the first 3 days, the concrete shows only a slight increase in compressive strength until the age of 28 days when the compressive strength is equal to 332.17 kg/cm^2. The results show that water curing yields a higher level of compressive strength than air curing does. This is because under water curing, the moisture content facilitates the chemical reaction between cement and water, which serves to develop this concrete property.

Fig. 23 presents results pertaining to continuous MW curing and discontinuous MW curing for Cases B, C, D, and E. The results show that the compressive strength of the concrete as cured in Case B increased continuously at 30 and 60 min. Then, after 90 and 120 min, the compressive strength decreased continuously. Temperature has an effect on compressive strength development. In Case C, curing at 400 W, electrical power can continuously increase compressive strength. However, the compressive strength of the concrete in Case C increased slightly in comparison with the compressive strength of the concrete in Case B.

For Cases D and E, MW energizing was changed to a discontinuous mode and these two cases show the same level of compressive strength. The preheating together with the reduced idle time and reduced energized time are important factors in developing the concrete strength in Case D.

Fig. 24 presents the compressive strength of MW curing in the movement mode (Case F). The curing time is 18 h, 180 min of MW curing (not including idle time). The results indicate that the compressive strength levels of all six workpieces are similar. The average compressive strength is 193.45 kg/cm^2. The speed of the motor for the movement study is 5 rpm with discontinuous MW energy applied. The PLC is applied in order to control horn movement.

The discontinuous MW curing used in Case E produces a high level of compressive strength when compared with the compressive strength developed in the Case C and Case D workpieces. Therefore, more experiments were performed. The curing time was extended by 60 min. Thus, the total time during which MW energy is applied for Case E is 180 min. The total time of this experiment is 13 h for MW curing.

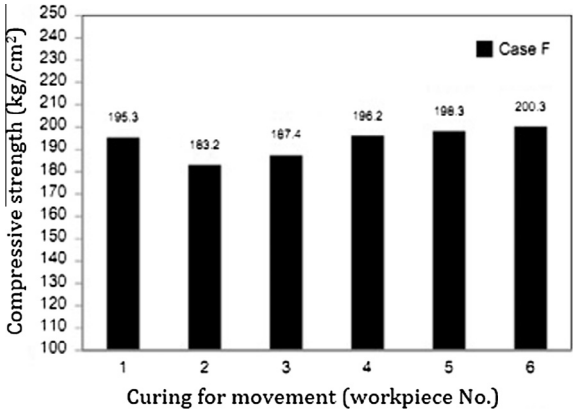

Fig. 24. The compressive strength of MW-cured concrete in the moving mode (Case F) at a curing time of 18 h and 180 min of MW curing (not including idle time).

The results show that compressive strength increases to 239 kg/cm^2 whereas moisture content after curing decreases to 53.3%. It can be concluded that this increased curing time can increase the compressive strength of the concrete and reduce its moisture content. However, the internal temperature is 113 °C, which should be studied in the future in order to determine the appropriate curing time and mixture design given the direct effects of water content in concrete on thermal distribution.

6. Conclusions and recommendation

In this research, MW-heating technology is applied in order to accelerate concrete curing. From the design and construction of a mobile MW-curing unit and an experimental investigation into the compressive strength of concrete dried using the prototype, the following conclusions can be drawn:

- The prototype design has many factors, i.e., the 1-axis movement and horn must be adjusted in a vertical direction [up-down], at 800 W power, and 2.45 GHz frequency.
- At the beginning of microwave curing, temperature of the concrete increased continuously. After 90 min, the temperature is constant because the moisture content at the surface of the concrete is reduced due to the absorption capacity of the MW energy.
- When concrete was heated using MW energy for more than 90 min at over 80 °C, the effect was a continuous decrease in compressive strength. Further, at early age, the compressive strength development of the concrete workpiece subjected to MW curing was greater than that achieved by air curing or water wet-curing.
- To produce maximum compressive strength, the appropriate preheating interval is 30 min combined with MW energizing for 15 min and a paused duration of 60 min.
- The highest strength achieved by MW curing is 239 kg/cm^2, which is equal to 85% of the strength achieved by water curing. Thus, discontinuous MW curing for 120 min represents a significant reduction in curing time as compared with the time needed for water curing.
- In order to manage hot spots taking place during MW curing, moving cavity should be investigated in terms of moving speed, and temperature distribution from one specimen to the others.

Acknowledgments

The authors gratefully acknowledge the Thailand Research Fund under the TRF contract Nos. RTA5680007 and TRG5780255, and the National Research Universities Project of the Higher Education Commission for supporting this research.

References

[1] K.G. Ayappa, H.T. Davis, E.A. Davis, J. Gordon, Two dimensional finite element analysis of microwave heating, AIChE J. 38 (1992) 1577–1592.
[2] C. Saltiel, A. Datta, Heat and mass transfer in microwave processing, Adv. Heat Transfer 30 (1997) 1–94.
[3] P. Heider, Computation of scattering resonances for dielectric resonators, Int. J. Comput. Math. Appl. 60 (2010) 1620–1632.
[4] P. Chen, C.H. Wang, J.R. Ho, A lattice Boltzmann model for electromagnetic waves propagating in a one-dimensional dispersive medium, Int. J. Comput. Math. Appl. 65 (2013) 961–973.
[5] M. Regier, H. Schubert, Microwave processing. In The Microwave Processing of Foods, Woodhead Publishing, Sawston, Cambridge, USA, 2001.
[6] N. Afrin, Y. Zhang, J.K. Chen, Thermal lagging in living biological tissue based on non-equilibrium heat transfer between tissue, arterial and venous bloods, Int. J. Heat Mass Transfer 54 (2011) 2419–2426.
[7] N. Irishina, O. Dorn, M. Moscoso, A level set evolution strategy in microwave imaging for early breast cancer detection, Int. J. Comput. Math. Appl. 56 (2008) 607–618.
[8] T. Basak, Role of resonance on microwave heating of oil–water emulsions, AIChE J. 50 (2004) 2659–2675.
[9] P. Perre, I.W. Turner, Microwave drying of softwood in an oversized waveguide: theory and experiment, AIChE J. 43 (10) (1997) 2579–2595.
[10] W. Kaensup, S. Wongwises, S. Chutima, Drying of pepper seeds using a combined microwave fluidized bed dryer, Dryong Technol. 16 (3–5) (1998) 853–862.
[11] K.Y. Leung, T. Pheeraphan, Microwave curing of Portland cement concrete: experimental results and feasibility for practical applications, Constr. Build. Mater. (1995) 67–73.
[12] N. Makul, P. Rattanadecho, D.K. Agrawal, Microwave curing at operating frequency of 2.45 GHz of Portland cement paste at early-stage using a multi-mode cavity: experimental and numerical analysis on heat transfer characteristics, Int. J. Heat Mass Transfer 37 (2010) 1487–1495.
[13] American Concrete Institute, ACI 318–Building Code Requirements for Structural Concrete and Commentary, 2008. Farmington Hills, MI, USA.
[14] P. Rattanadecho, N. Suwannapum, B. Chatveera, D. Atong, N. Makul, Development of compressive strength of cement paste under accelerated curing by using a continuous microwave thermal processor, Mater. Sci. Eng. A 472 (2008) 299–307.
[15] W. Xuequan, Microwave curing technique in concrete manufacture, Cem. Concr. Res. 17 (2) (1987) 205–210.
[16] R.G. Hutchison, Thermal acceleration of Portland cement mortars with microwave energy, Cem. Concr. Res. 21 (5) (1991) 795–799.
[17] D. Sohn, D.L. Johnson, Microwave curing effect on the 28 day strength of cementitious materials, Cem. Concr. Res. 29 (1999) 241–247.
[18] Microwave Method and Apparatus for Heating Pavement, by M.R. Jeppson, C. Calif, (1981). United States Patent, 425 2 487.
[19] A.C. Metaxas, R.J. Meridith, Industrial Microwave Heating, Peter Peregrinus Ltd, London, 1983.
[20] Concrete Curing Machine, by C.B. Sipherd, J.R. Lease, R.L. Stainbrook, (2002). United States Patent 649 7 531 B1.
[21] T. Chow Ting Chan, H.C. Reader, Understanding Microwave Heating Cavities, Artech House Inc, Norwood, MA 02062 USA, 2000.
[22] COMSOL Inc, COMSOL Multiphysics User's Guide Version 3.4, COMSOL AB, Singapore, 2007.
[23] P. Rattanadecho, K. Aoki, M. Akahori, Experimental and numerical study of microwave drying in unsaturated porous material, Int. J. Heat Mass Transfer 28 (2001) 605–616.
[24] S. Hauck Harold, Design considerations for microwave oven cavities, IEEE Xplore: IEEE Transactions on Industry Applications (1) (1970) 74–80. Vol. IGA-6.
[25] L.A. Campanone, N.E. Zaritzky, Mathematical analysis of microwave heating process, J. Food Eng. 69 (2005) 359–368.
[26] American Society for Testing and Materials, ASTM C150-12 Standard Specification for Portland Cement, Annual Book of ASTM Standards, 4.01, 2012. Philadelphia, PA, USA.
[27] American Society for Testing and Materials, ASTM C1602/C1602M - 12 Standard Specification for Mixing Water Used in the Production of Hydraulic Cement Concrete, Annual Book of ASTM Standards, 4.02, 2012. Philadelphia, PA, USA.
[28] American Society for Testing and Materials, ASTM C33/C33M – 13 Standard Specification for Concrete Aggregates, Annual Book of ASTM Standards, 4.02, 2013. Philadelphia, PA, USA.
[29] British Standards Institution, BS 1881: Part 3, Method of Making and Curing Test Specimens, 2011. London, United Kingdom.
[30] American Society for Testing and Materials, ASTM C192/C192M-14 Standard Practice for Making and Curing Concrete Test Specimens in the Laboratory, Annual Book of ASTM Standards, 4.02, 2014. Philadelphia, PA, USA.
[31] British Standards Institution, BS 1881: Part 4, Method of Testing Concrete for Strength, 2011. London, United Kingdom.

Songklanakarin J. Sci. Technol.
38 (4), , Jul. - Aug. 2016

http://www.sjst.psu.ac.th

Original Article

Design and analysis of a doubly corrugated filter for a combined multi-feed microwave-hot air and continuous belt system

Sopida Sungsoontorn[1], Saysuree Jumrat[2], and Yutthapong Pianroj[2*], and Phadungsak Rattanadecho[3]

[1] *Department of Mechanical Engineering, Faculty of Engineering, Rajamangala University of Technology Rattanakosin, Phutthamonthon, Nakhon Pathom, 73170 Thailand.*

[2] *Faculty of Science and Industrial Technology, Prince of Songkla University, Surat Thani Campus, Mueang, Surat Thani, 84000 Thailand.*

[3] *Center of Excellence in Electromagnetic Energy Utilization in Engineering (CEEE.), Department of Mechanical Engineering, Faculty of Engineering, Thammasat University, Rangsit Campus, Khlong Luang, Pathum Thani, 12120 Thailand.*

Received: 24 April 2015; Accepted: 17 December 2015

Abstract

A doubly corrugated filter was designed for a combined multi-feed microwave-hot air and continuous belt system (CMCB). The proposed filter reduces microwave energy radiation from the open entry of the continuous belt system. Microwave radiation leakage that affects a human should remain below 10 mW/cm^2. The filter was designed for stop-band frequency range 2,300-2,600 MHz, while the operating frequency is 2,450 MHz, and for attenuation greater than 60 dB in this range. We report on optimizing all the design parameters of a doubly corrugated filter and on experimental verification after its installation at the Research Center of Microwave Utilization in Engineering (R.C.M.E) at Thammasat University, Thailand.

Keywords: microwave filter, microwave choke, corrugated choke, waffle-iron filter, radiation energy, drying kinetics

1. Introduction

A continuous microwave heating or drying process necessarily has entry and exit points for the material processed. These points leak microwaves that may interfere with electronic systems, such as communication systems, and might be hazardous to humans or animals. In particular, microwaves at the operating frequency 2.45 GHz of the currently considered equipment are absorbed by organic tissues. They penetrate, and can raise the temperature of blood and tissue, causing serious damage and danger. Therefore, most industrialized countries have established safety standards and limits for intensity of microwave radiation exposure (IEEE, 1992). For example, in the United States microwave energy exposure from microwave equipment at 2.45 GHz is limited to 5 mW/cm^2 at a distance of 5 cm from the equipment surface and the whole body exposure limit is 10 mW/cm^2 at 2.45 GHz. The same intensity limits have been adopted in many countries (Meredith, 1998). Many techniques to reduce or prevent microwave leakage are shown in textbooks (Meredith, 1998; Metaxas *et al.*, 1983), including partially filled choke tunnels (part filled height and part filled width) with a high loss material that absorbs residual microwave leakage. Moreover, a very effective method was proposed in Vankoughnett *et al.* (1973), which is commonly used in many practical system; reactive or reflective choking with a corrugated filter. The design of such filters is traditionally done by an approximate method based on monomode equivalent circuits (Matthaei, 1964; Young *et al.*, 1963). However, a doubly corrugated designed filter or a waffle iron

* Corresponding author.
Email address: yutthapong.p@psu.ac.th

filter has wide-band and stop-band characteristics. Such design of a high power L-band filter, as a singly or a doubly corrugated structure, is shown in Soto *et al.* (2000), and we also applied a multimode analysis method based on the generalized admittance matrix (GAM) (Melcon *et al.*, 1996).

Normally, researchers (De Paolis *et al.*, 2013; Jen-Tsai *et al.*, 2007; Manuilov *et al.*, 2005; Sharp, 1963; Young and Schiffman, 1963) designed and tested the performance of filters by using a waveguide scale, but they did not scaled-up their filters to an industrial scale. Thus, at the Research Center of Microwave Utilization in Engineering (R.C.M.E), we have a combined unsymmetrical multi-feed microwave heater and continuous belt system, which is a prototype of an industrial scale. It has two open entries with the geometry shown in Figures 1 and 2. The first is for workload input and the second for workload pass through the cavity. To address safety issues, we designed doubly corrugated filters. The advantage of doubly corrugated filter is that their periodic structure can be designed for pass-band and stop-band effects, and this paper shows a technique to optimize the design for the residual radiation energy, here with attenuation greater than 60 dB.

The designed filters were implemented at the open entries of the system, and their function validated by measurements. When the CMCB system with doubly corrugated filters was used to run some specimens for drying kinetics studies, also the microwave leakage from the system was checked by a microwave leakage detector. The results of experimental validation are discussed and summarized in the conclusions.

2. Design of Mechanical Blocking Filter (Corrugated Choke)

2.1 Theory

Normally a continuous microwave process has a rectangular open entry, as in Figure 1, and the doubly corrugated filter was designed to fit the open entry. The filter consists of a series of equal length stubs periodically in a grid layout, as shown in Figure 2. The traditional design method is based on a monomode equivalent representation of all the elements in the structure. We modeled the E-plane T-junction of the structure by the monomode equivalent circuit proposed in (Marcuvitz, 1951). The open entry port was considered a rectangular waveguide interconnecting such T-junctions, and was represented by a simple transmission line related to the fundamental mode. The periodicity of the monomode equivalent filter circuit is shown in Figure 3.

The attenuation α in the stop-band is given by the following equations (Matthaei, 1964).

$$A = \cosh^{-1}\left(\left|\cos(\beta l') - \left(\overline{X}_T + m^2{}_T \frac{b}{g}\tan(\beta d')\right)\cdot\frac{\sin(\beta l')}{2}\right|\right) \quad (1)$$

$$\alpha(dB) = 8.686 \cdot n \cdot A \quad (2)$$

Here A represents the attenuation constant in Np/m, n is the number of sections in the E-plane T-junction of filter, β is the propagation constant of fundamental mode ($\beta = \frac{2\pi}{\lambda}$), b and g are physical dimensions of the filter as shown in Figure 3 (a), and l', $\overline{X}_T$, $m^2{}_T$ and d' are electrical parameters derived from the equivalent circuit of a filter section in Figure 3 (b) (Marcuvitz, 1951).

2.2 Design of mechanical blocking filter

The geometry of the open entries is $a \times b$ shown in Figure 1, and x is 695 mm, y is 200 mm, and the web material is polypropylene. The electrical requirements for a filter are a high attenuation level (greater than 60 dB), and a wide stop-band response over ±150 MHz (2.30-2.60 GHz) centered at

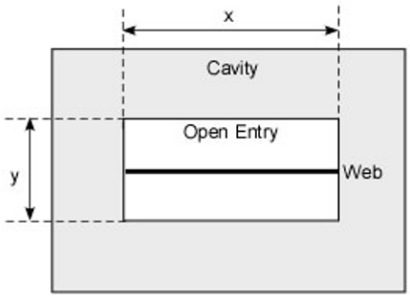

Figure 1. Geometry of open entry.

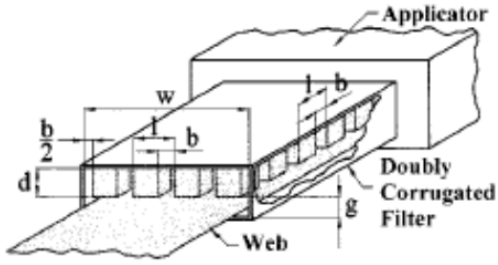

Figure 2. Open entry of the continuous microwave process and the doubly corrugated filter (Soto *et al.*, 2000).

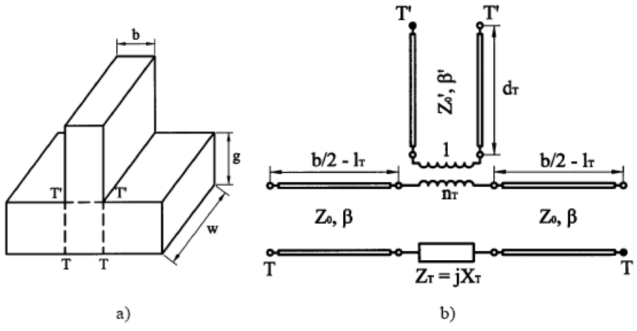

Figure 3. (a) General view and (b) equivalent circuit of E-plane T-junction.

2.45 GHz frequency. As a first step in the design of a doubly corrugated filter, we know from the conditions above that w equals x, and g is 135 mm. The w and g parameters are fixed by the material dimensions. We selected n to be 13, this is the number of sections of E-plane T-Junctions of the filter, and the period of rectangular posts per section was set to *l*, which should be as close as possible to 60 mm. Next we selected the stub height d to be approximately 30 mm, equal to a quarter wavelength (Matthaei, 1964). The last design parameter remaining is b, the stub width of the equivalent T-junction that needs to be carefully selected. When parameter b is one of 19, 21, or 23 mm, the corresponding *l* values are 53.38, 53.54 and 53.69 mm. The attenuation profiles computed for these values are shown in Figures 4, 5, and 6.

The parameters of doubly corrugated filter design given in Soto *et al.* (2000) (w = 172.72 mm, g = 13.97 mm, d = 29.21 mm, *l* = 17.27 mm, b = 6.29 mm, and material inside the waveguide is air with dielectric constant = 1) were used with our computing program to validate it. The design cutoff frequency and infinite attenuation at the operating frequency 2.45 GHz were checked. The given design rejects the energy related to the TE_{10} mode, propagating through the access ports, in the frequency band 2.30-2.60 GHz. The computed results in Figure 7 have the same trends as the graph in Figure 4 of Soto *et al.* (2000), serving as validation of our computations.

The difference between the current work and Soto *et al.* (2000) is in the dimensions of the open entry and the material inside it. Our material inside the open entry is not air, but the polypropylene belt (web) with a dielectric constant of 3.3. We performed some simulations based on Equation 1 with varying parameter values as discussed next.

not only air but also

Figure 4 shows the effects of varying parameters b and *l,* while keeping w, n, d and g fixed. When b equals 19 mm and *l* equals 53.38 mm, the line with symbols '*' shows a pass band of wavelengths from 125 mm to 130 mm (2.40-2.31 GHz). When b is increased, the attenuation also increases. In Equation 1 this increase in attenuation comes from the term tan($\beta d'$) that can become infinite; a higher value of b increases this term providing more attenuation. So the attenuation will increase with b but there is an upper limit for b from the equivalent circuit in Figure 3b. The computed attenuation is not valid if a higher order mode appears, and Equation 1 is no longer appropriate. If the number of sections (n) is changed from 10 to 13, or further to 15, while the other parameters are fixed, the attenuation loss increases. The results are shown in Figure 6, illustrating the effects of the ~~open port height (g)~~ ~~and~~ stub height (d). Changing these values shifts the central frequency of the filter with the penetration of the stubs since d is also modified, and the attenuation and bandwidth of the filter are altered as well.

The design dimensions selected based on these simulations were: w = 675 mm, g = 105 mm, d = 30 mm, n = 13 mm, b = 21 mm and *l* = 53.54 mm, and the doubly corrugated filters were built accordingly as shown in Figure 8. These filters were installed at the open entry of the combined un-

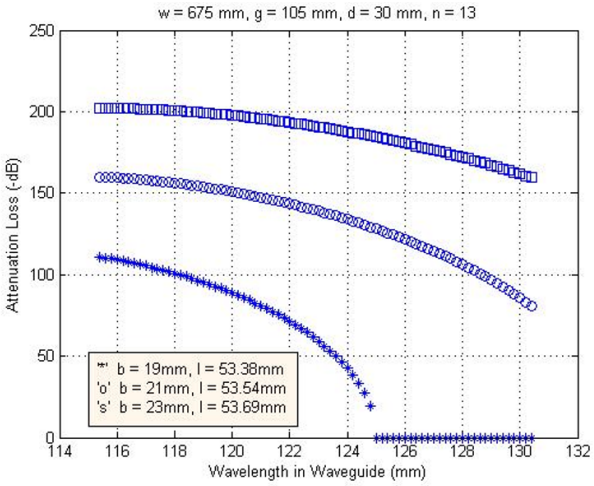

Figure 4. Attenuation loss of the doubly corrugated filter when b and l parameters are varied.

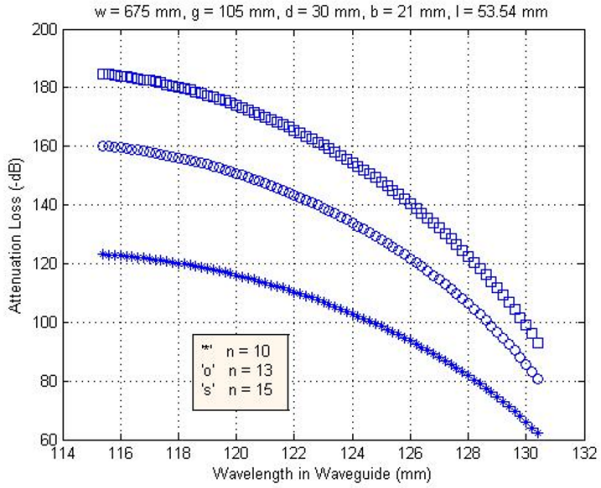

Figure 5. Attenuation loss of the doubly corrugated filter when n parameter is varied.

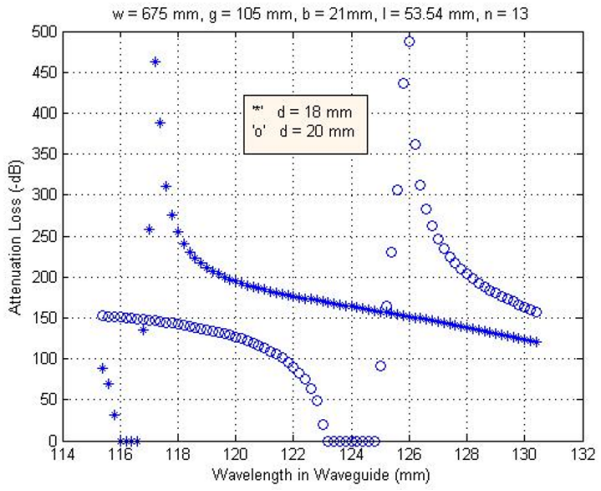

Figure 6. Attenuation loss of the doubly corrugated filter when ~~g and d parameters are~~ varied.

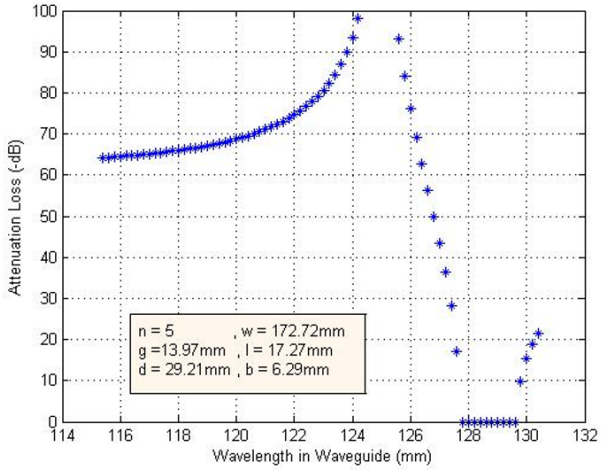

Figure 7. Attenuation loss of the doubly corrugated filter with the parameters from Metaxas *et al.* (1993).

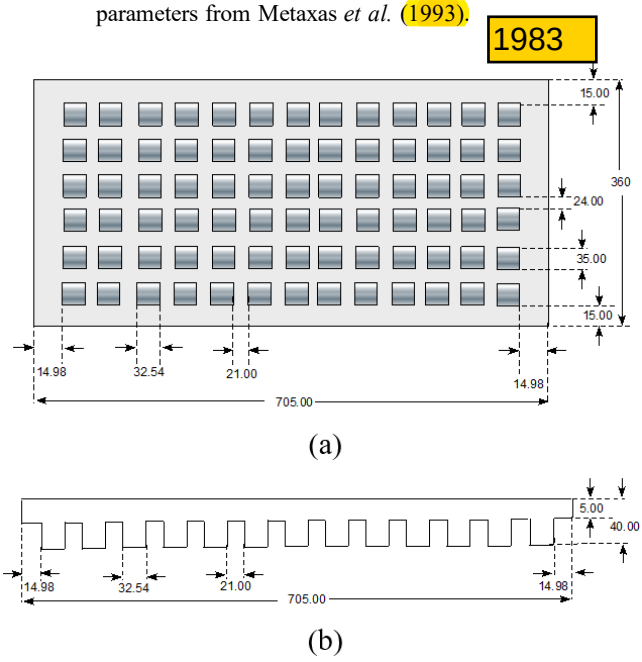

Figure 8. General schematics of the R.C.M.E. doubly corrugated filter, (a) bottom view (b) side view.

symmetrical multi-feed microwave heater and continuous belt system at R.C.M.E., and microwave leakage measurements were done. Moreover, to confirm an attenuation performance of filters which were installed to open-end ports of the system, the commercial simulation software named COMSOL MultiPhysics™, which based on a finite element method (FEM), was applied. The simulation module that used to confirm the result is RF module >> Electromagnetic waves >> Harmonic propagation. The three dimensions of a doubly corrugated filter from Figure 5 of Soto *et al.* (2000) and R.C.M.E. doubly corrugated filter were created, then the transmission coefficient (S_{21}-parameter or attenuation [dB]) were carried out for both filters. The results are depicted in Figure 9. In this figure, it shows a good result trend of the doubly corrugated filter that is similar to the result from Figure 5 of Soto *et al.* (2000). Therefore, these results give more confidence in the R.C.M.E. doubly corrugated filter design, which can achieve the goal of the attenuation level around 60 dB.

3. Experimental Procedure

Microwave-convective air drying was carried out using a combined multi-feed microwave-convective air and continuous belt drier system (CMCB) as shown in Figure 10. The shape of microwave cavity is rectangular with dimensions 90 cm×45 cm×270 cm. The drier was operated at a frequency of 2.45 GHz with a maximum temperature of 180°C.

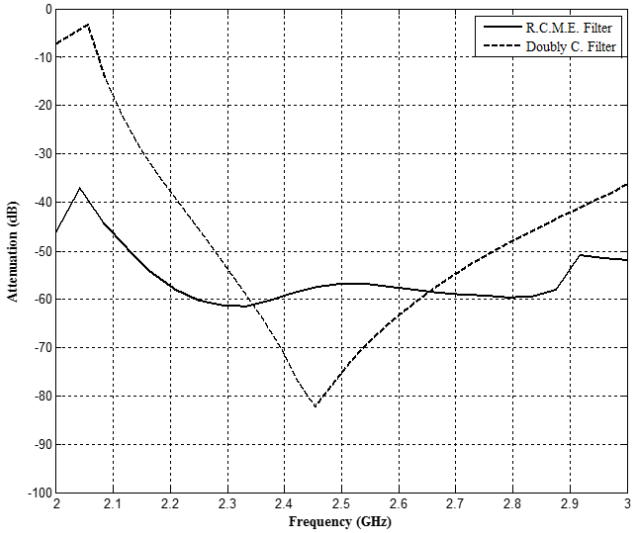

Figure 9. Attenuation results of a doubly corrugated filter with a geometry after Soto et al. (2000) and a R.C.M.E. doubly corrugated filter were carried out with COMSOL MultiPhysics™.

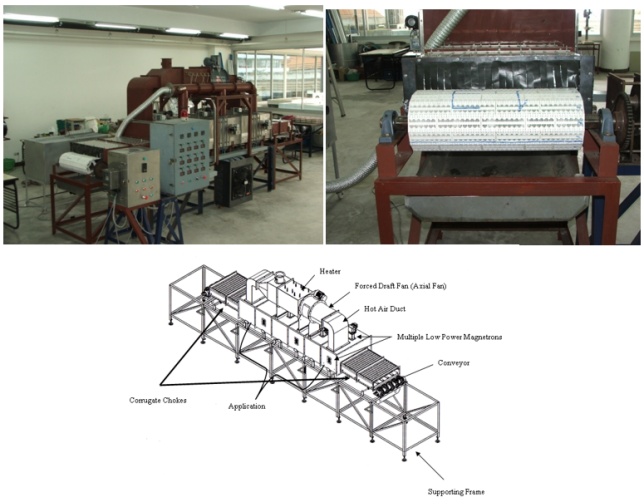

Figure 10. Photos and a schematic diagram of the experimental set-up of a combined multi-feed microwave-convective air and continuous belt system (CMCB).

The microwave power was generated by means of 12 compressed-air-cooled magnetrons. The maximum microwave capacity was 9.6 kW at the operating frequency. The power setting could be adjusted in 800 W steps by turning individual magnetrons on/off. The continuous belt conveyor necessitates two open ends for the material to enter and exit. The leakage of microwaves was prevented by a combination of mechanical blocking filter (corrugated choke) and microwave absorber zone filter, at each open end. The microwave leakage was controlled in compliance with the DHHS (US Department of Health and Human Services) standard to below 5 mW/cm^2. Multiple magnetrons were installed in asymmetrical positions around the rectangular cavity. The microwave power was then directed into the drier by waveguides.

The magnetrons and transformers were cooled down by fans. The belt conveyor system consisted of a drive motor, a tension roller, and the belt. During the drying process, the conveyor speed was held at 0.54 m/min and the motor speed was controlled by the VSD control unit. Hot air was generated using 24 electric heater units with a maximum capacity of 10.8 kW and a maximum working temperature of 240°C. The hot air was blown with a 0.4 kW fan through an air duct into the cavity. The hot air temperature was measured with a thermocouple.

As shown in Figure 11, the drying samples were non-hygroscopic porous packed beds, composed of two sizes of glass beads; fine bed (F-Bed) and coarse bed (C-Bed), with water and air in the pore space. A sample container of dimensions 14.5 cm×21 cm×4.5 cm was made from 2 mm-thick polypropylene. The polypropylene did not absorb microwave energy. In this study, the sample selected for a drying test was non-hygroscopic porous material with dimensions of 14.5 cm × 21 cm × ~~1.5~~ cm, and the 22 packed beds had a total weight of 11 kg.

4. Measurement of Microwave Leakages from Open Ends of Microwave Cavity

The measurement device can report whether or not the amount of radiation from a microwave oven is considered unhealthy, and is useful for testing for defects or problems with door seals. The business end of the MD-2000 and R.C.M.E. microwave leakage detector, Figure 12(a-b), is placed within a couple inches of the oven, along the seam where the door meets the oven's chassis. The device sniffs the oven and gives a reading from 0 to 9.99 mW/cm^2. If it senses levels over 5 mW/cm^2, it flashes a light and emits a warning beep. This usually means there is a problem with the door seal. The device is powered by a 9-Volt battery and comes with a wall-mounting bracket.

The device is zero calibrated before each use, and has sensitivity down to 0.01 mW/cm^2 at 2,450 MHz, giving readings in hundredths of mW/cm^2. The leakage of microwave radiation was measured during the drying trial. The ~~distances~~ from an open end of the microwave cavity ranged from 0 to 200 cm, as shown in Figure 13.

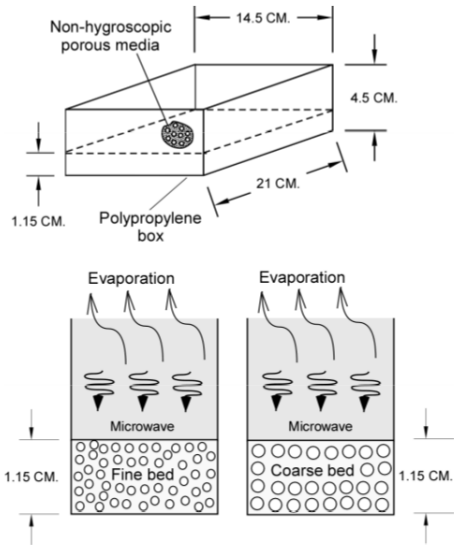

Figure 11. Schematics of a drying sample (packed bed)

(a) (b)

Figure 12. (a) Digital readout microwave leakage detector (MD-2000), and (b) digital readout microwave leakage detector (RCME).

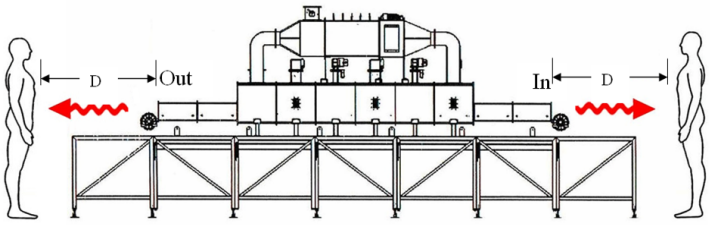

Figure 13. Distance definitions on measuring microwave leakage for CMCB.

The microwave operating power ranged from 0 to 4.8 kW; however, for the leakage experiments, the microwave operating power was fixed at 4.8 kW in all cases. The samples of two types described in the previous section were dried. The first sample type had coarse glass beads as porous substance, and these were labeled as C-Bed samples. They were loaded into the CMCB at the inlet open entry, and the conveyor carried the samples through to the outlet open entry, while the measurements of microwave leakage took place at various distances from the open entries. The experiments were replicated seven times. The other sample type had fine glass beads as the porous substance, and these cases were labeled as F-Bed. The drying and leakage measurements were similar with the C-Bed samples.

5. Results and Discussion

The measured microwave power leakage versus distance is shown in Figure 14. In the top panel, the microwave power leakage at the inlet ranged from 3 to 4 mW/cm^2 is decreasing exponentially with distance so that the leakage level was less than 1 mW/cm^2 for distances greater than 30 cm. There is only a slight difference between the C-Bed and F-Bed sample types, consistently but without statistical significance. In the bottom panel, the microwave leakage at the outlet ranged from 4 to 5 mW/cm^2 at the opening and qualitatively the leakage pattern is similar to the inlet.

Since the radiated power density decreases with distance, it is reasonable to assume that the exposure of a person within 10 to 200 cm from the open entry is much less than the maximum allowed by safety standards. The value 5 mW/cm^2 is considered harmless to humans by the DHHS (US Department of Health and Human Services). Therefore, it can be indicated that the designed doubly corrugated choke has good efficiency and performance.

6. Conclusions

Corrugated chokes are an effective means to reduce radiation leakage from open ports of microwave heating systems. The traditional analysis and design of these filters is based on monomode equivalent representations of the elements integrated in the filter structure. These representations give approximate responses, and particularly with multiple corrugations either multimode or more complete simulations are needed for accurate predictions. The designed corrugated choke was implemented in a combined multi-feed microwave-convective air and continuous belt system (CMCB). The proper function of the choke filter was experimentally established, using a handheld leakage detector. The filter design presented contributes to the safe operation of microwave equipment in industrial processes.

Acknowledgements

Authors dedicate this work to Mr. Wiroj Jindarat, and we gratefully to S. Karrila for his assistance in manuscript preparation. This work was supported by the Higher Education Research Promotion and National Research University Project of Thailand, Office of the Higher Education Commission and Thailand Research Fund under contract no. RTA5680007.

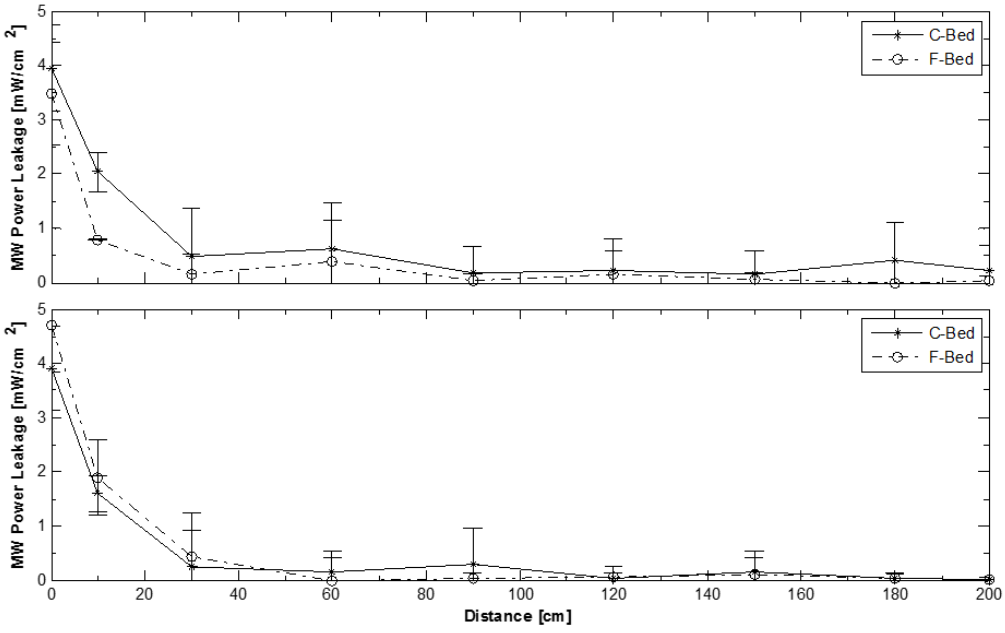

Figure14. Measured microwave power leakage versus distance from an opening to the "oven" cavity. The decaying curves differ slightly between two sample types shown in the labels. The top panel is for leakage at the inlet, while the bottom panel summarizes measurements at the outlet.

References

De Paolis, F., Goulouev, R., Jingliang, Zheng, and Ming, Yu. 2013. CAD Procedure for High-Performance Composite Corrugated Filters. IEEE Transactions on Microwave Theory and Techniques, 61. 3216-3224.

IEEE. 1992. Standard for Safety Issues with Respect to Human Exposure to Radio Frequency Electromagnetic Fields, 3 kHz to 300 GHz, The Institute of Electrical and Electronics Engineers, Inc., New York, U.S.A.

Jen-Tsai, Kuo, Lok, Hou U., and Meng-Huan, Wu. 2007. Novel Corrugated Coupled-Line Stage with Ideal Frequency Response and Its Application to Bandpass Filter Design with Multi-Harmonic Suppression. Proceedings of the IEEE/MTT-S International Microwave Symposium, Hawaii, U.S.A., June 3-8, 2007, 553-556.

Manuilov, M. B. and Kobrin, K. V. 2005. Field theory CAD of waffle-iron filters. Proceedings of the European Microwave Conference, Paris, France, October 4-6, 2005, 4 pp.

Marcuvitz, N. 1951. Waveguide handbook, McGraw-Hill, New York, U.S.A.

Matthaei, G. L. 1964. Microwave filters, impedance-matching networks, and coupling structures, McGraw-Hill, New York, U.S.A.

Melcon, A. A., Connor, G., and Guglielmi, M. 1996. New simple procedure for the computation of the multimode admittance or impedance matrix of planar waveguide junctions. IEEE Transactions on Microwave Theory and Techniques. 44, 413-418.

Meredith, R. J. 1998. Engineers' handbook of industrial microwave heating, Institution of Electrical Engineers, London, U.K.

Metaxas, A. C. and Meredith, R. J. 1983. Industrial microwave heating, P. Peregrinus, Institution of Electrical Engineers, London, U.K.

Sharp, E. D. 1963. A High-Power Wide-Band Waffle-Iron Filter. IEEE Transactions on Microwave Theory and Techniques. 11, 111-116.

Soto, P., Boria, V. E., Catala-Civera, J. M., Chouaib, N., Guglielmi, M., and Gimeno, B. 2000. Analysis, design, and experimental verification of microwave filters for safety issues in open-ended waveguide systems. IEEE Transactions on Microwave Theory and Techniques. 48, 2133-2140.

Vankoughnett, A. L. and Dunn, J. G. 1973. Doubly corrugated chokes for microwave heating systems. Journal of Microwave Power. 8, 101-110.

Young, L. and Schiffman, B. M. 1963. New and improved types of waffle-iron filters. Proceedings of the Institution of Electrical Engineers. 110, 1191-1198.

International Journal of Heat and Mass Transfer 61 (2013) 397–408

Contents lists available at SciVerse ScienceDirect

International Journal of Heat and Mass Transfer

journal homepage: www.elsevier.com/locate/ijhmt

Effects of material properties on heating processes in two-layered porous media subjected to microwave energy

Santiphong Klayborworn [1], Watit Pakdee *, Phadungsak Rattanadecho [2], Somsak Vongpradubchai [3]

Research Center of Microwave Utilization in Engineering (R.C.M.E.), Department of Mechanical Engineering, Thammasat University, Klong Luang, Pathumthani, Thailand

ARTICLE INFO

Article history:
Received 12 October 2012
Received in revised form 7 February 2013
Accepted 7 February 2013
Available online 5 March 2013

Keywords:
Microwave heating
Variable-porosity
Natural convection
Saturated porous media
Material properties
Rectangular waveguide

ABSTRACT

Microwave heating of double-layer porous medium is numerically investigated using a proposed numerical model. A two-dimensional domain composed of two porous layers is considered. The two porous layers have different particle sizes, porosities, thermal and dielectric properties. The generalized non-Darcian model developed takes into account of the presence of a solid drag and the inertial effect. The transient Maxwell's equations are solved by using the finite difference time domain (FDTD) method to describe the electromagnetic field in the waveguide and in the media. The temperature profile and velocity field within the media are determined by solution of the momentum and energy equations given by the SIMPLE (Semi-Implicit Method for Pressure Linked Equations) algorithm. This study focuses on effects of diameter, porosity, position and types of particles that have different thermal and dielectric properties. The computed results agree well with the experimental results. While the particle size and porosity mainly affect fluid flow within porous media, the thermal and dielectric properties strongly influence heat transfer mechanism in each layer of porous media.

© 2013 Elsevier Ltd. All rights reserved.

1. Introduction

Microwave heating of a porous medium is widely implemented in industries, such as heating food, ceramics, biomaterials, concrete manufacture, etc., since microwave energy has many advantages such as short time process, high thermal efficiency, environmentally friendly credentials and high product quality. Microwave radiation penetrates into a material and heats it by a dipolar polarization that occurs millions times per second.

A number of previous works have focused on the drying of unsaturated porous media in which heat and mass transfers were modeled [1–6] however most of these dealt with solid materials and focused on heat conduction within a medium. Some works studied a natural convection induced by microwave heating of fluids, since a complex distribution of electromagnetic waves is shown to be a complicate effect on flow field [7–11]. The effects of natural convection and dielectric properties on liquid layers were studied numerically and experimentally. The heating kinetics strongly depended on the dielectric properties [7]. Natural convection due to buoyancy force strongly affects flow patterns within the water layer during the microwave heating process, and clearly enhances temperature distribution in the layer [8]. Recently, Chaum et al. [8] experimentally investigated the heating process within a packed bed filled with glass beads and water and found that the location of the sample relative to that of heat source had an important effect on the pattern of heating. Other recent works focused on microwave driven convection in pure liquids [9–11]. While the previous studies were based on pure liquids, we pay attention to heating induced by microwave energy in a fluid-saturated porous medium with two layers. One of the apparent applications for microwave heating of fluid-saturated porous medium involves food sterilization or pasteurization [12].

Furthermore, all the previous investigations referred did not account for the effect of variable porosity in the vicinity of the impermeable wall. A region of higher porosity near the wall forms due to the packing of the porous spheres near the column wall is not as efficient as that away from the wall towards the column center [13]. Benenati and Brosilow [14] found a distinct porosity variation with a high porosity region close to the wall in packed beds. Values of porosity those are high close to an impermeable wall decrease to an asymptotic value at about four to five sphere diameters away

* Corresponding author. Address: Department of Mechanical Engineering, Thammasat University (Rangsit Campus), 99 Paholyotin Rd., Klong Luang, Pathumthani 12120, Thailand. Tel.: +66 11 662 5643001–9x3143; fax: +66 11 662 5643023.

E-mail addresses: freshgear@gmail.com (S. Klayborworn), pwatit@engr.tu.ac.th (W. Pakdee), ratphadu@engr.tu.ac.th (P. Rattanadecho), vsomsak@engr.tu.ac.th (S. Vongpradubchai).

[1] Address: 97/3 M.4, T. Tharahat, A. Mueang, Suphanburi 72000, Thailand. Tel.: +66 (0) 81857 9150.

[2] Address: Department of Mechanical Engineering, Thammasat University (Rangsit Campus), 99 Paholyotin Rd., Klong Luang, Pathumthani 12120, Thailand. Tel.: +66 11 662 5643001–5x3153; fax: +66 11 662 5643023.

[3] Address: Department of Mechanical Engineering, Thammasat University (Rangsit Campus), 99 Paholyotin Rd., Klong Luang, Pathumthani 12120, Thailand. Tel.: +66 11 662 5643001–5x3264; fax: +66 11 662 5643023.

0017-9310/$ - see front matter © 2013 Elsevier Ltd. All rights reserved.
http://dx.doi.org/10.1016/j.ijheatmasstransfer.2013.02.020

Nomenclature

C_p	specific heat capacity (J/(kg K))
E	electric fields intensity (V/m)
f	frequency of incident wave (Hz)
g	gravitational constant (m/s^2)
H	magnetic field intensity (A/m)
P	power (W)
p	pressure (Pa)
Q	local electromagnetic heat generation term (W/m^3)
s	Poynting vector (W/m^2)
T	temperature (°C)
t	time (s)
$\tan\delta$	dielectric loss coefficient (–)
u,w	velocity component (m/s)
Z_H	wave impedance (Ω)
Z_l	intrinsic impedance (Ω)

Greek letters

ϕ	porosity (m^3/m^3)
α	thermal diffusivity (m^2/s)
β	coefficient of thermal expansion (1/K)
η	absolute viscosity (Pa s)
ε	permittivity (F/m)
ε'	dielectric constant (F/m)
ε''	dielectric loss factor (F/m)
λ	wavelength (m)
μ	magnetic permeability (H/m)
υ	velocity of propagation (m/s)
ν	kinematics viscosity (m^2/s)
ρ	density (kg/m^3)
σ	electric conductivity (S/m)
ω	angular frequency (rad/s)
ξ	surface tension (N/m)

Subscripts

0	free space
∞	ambient condition
a	air
f	fluid
j	layer number
in	input
p	particle
r	relative

from it [15,16]. Many researchers found that the variation of porosity might significantly affect flow patterns as well as heat transfer features [14,17–19]. The porosity of the bed exhibits sinusoidally damping decay especially at locations near wall [14]. This phenomenon leads to the channeling effect that could significantly modify flow patterns [15,20–22]. Hsiao et al. [18] reported that including the effects of variable porosity and thermal dispersion on natural convection in the region of the heated horizontal cylinder in an enclosed porous medium increased the average Nusselt number and reduced the error between the experimental data and their solutions. Thus, the effects of porosity variation should be taken into account in practice [17,23–25]. For works related to the two-layered porosity medium, Rattanadecho et al. [4] studied influence of time input energy for the microwave on particle size and initial moisture content. It is found that the capillary pressure increases when particle size is smaller and the rate of drying is faster. Prommas et al. [26] showed that the proportion of the benefits of energy and efficiency of exergy depended on the size of the particles, the hydrodynamic properties and the structure of the porous layer. Pakdee and Rattanadecho [27] proposed a mathematical model for the microwave heating of the saturated porous medium with variation-porosity based on distance from the wall of the packed bed. Effects of the size of the particles and the average porosity on the temperature and water flow profile were examined. Numerical results were reliable when compared with values obtained from experiments using a rectangular waveguide for the TE_{10} mode. Recently, effects of electromagnetic field on forced convection in porous media were investigated [28]. The energy separation between solid and fluid phases was modeled using local thermal non equilibrium (LNTE). The results showed that errors stem from assuming local thermal equilibrium the calculation is increased when the Darcy number or power of electromagnetic field or ratio of the thermal diffusivity of solid to fluid increases.

Most previous research studied heating processes in a uniform porosity medium due to microwave heating. Only few studies were interested in microwave heating in a multi-layered medium although microwave heating in a multi-layered saturated materials have been found in broad applications in food applications and hyperthermia system for the treatment of tumor [29,30]. Moreover, no work focusing on effects of material properties have been reported. Therefore, our study aimed to investigate effects of microwave on particle size, porosity and medium properties of particles including thermal and dielectric properties on heating process in two-layered porous materials. The present work particularly includes comparisons between the theoretical analysis, mathematical modeling and experimental results.

2. Experimental setup

Fig. 1 shows the experiment apparatus for microwave heating of a saturated porous medium using a rectangular waveguide. Actual image of the apparatus is shown in Fig. 1(a). The microwave system is a monochromatic wave of TE_{10} mode operating at a frequency of 2.45 GHz. Microwave power used is 300 W. From Fig. 1(b), magnetron (No. 1) generates microwaves and transmits them along the z-direction of the rectangular waveguide (No. 5) with inside cross-sectional dimensions of 109.2×54.61 mm^2 that refers to a testing area (red circle) and a water load (No. 8) that is situated at the end of the wave guide. On the upstream side of the sample, an isolator is used to trap any microwaves reflected from the sample to prevent damage to the magnetron. The powers of incident, reflected and transmitted waves are measured by a wattmeter using a directional coupler (No. 6) (MICRO DENSHI., model DR-5000). Fiberoptic probes (No. 7) (LUXTRON Fluroptic Thermometer (model 790, accurate to ±0.5°C) is employed for temperature measurement. The probes are inserted into the sample, positioned on the XZ plane at $Y = 25$ mm. (see in Fig. 2). Due to the symmetry, temperatures are only measured on one side of the plane. The samples are saturated porous packed beds composed of glass beads and water. The container, with a thickness of 0.75 mm, is made of polypropylene which does not absorb microwave energy.

In our present experiment, the two-layer medium is examined. The glass beads of 0.15 mm and put on top of the glass beads of 0.4 mm in diameter is examined. The averaged (free stream) porosity of the packed bed corresponds to 0.385 and 0.371, respectively.

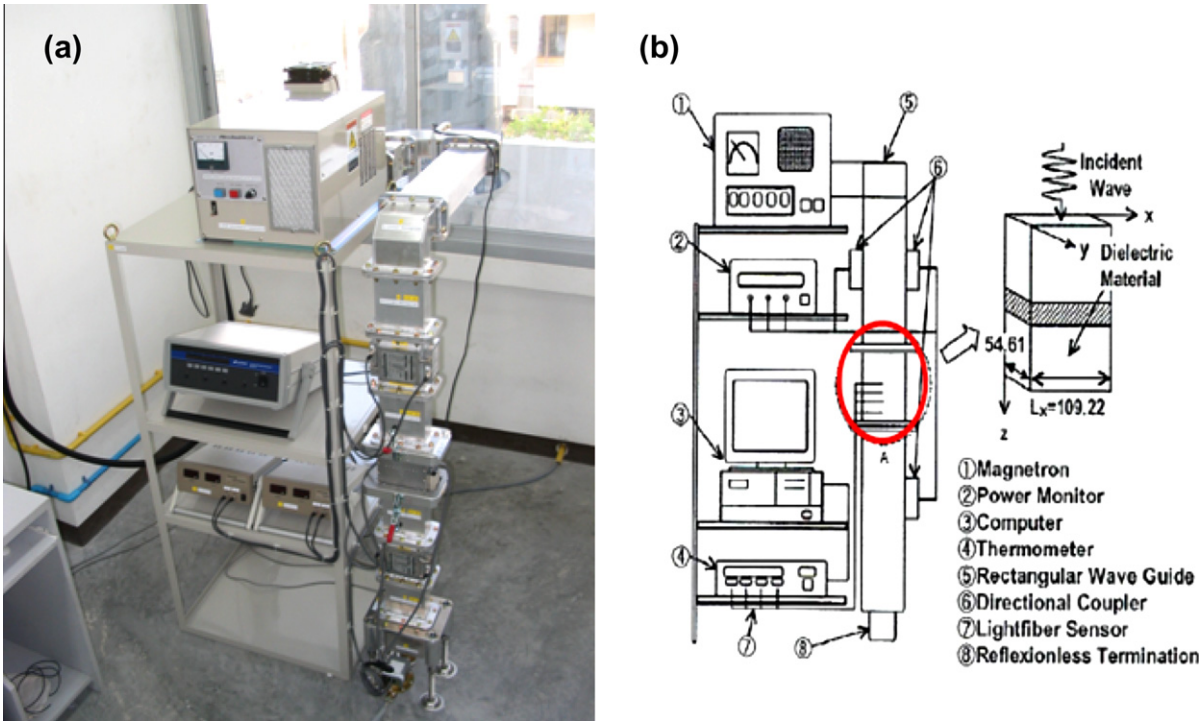

Fig. 1. The microwave heating system with a rectangular waveguide.

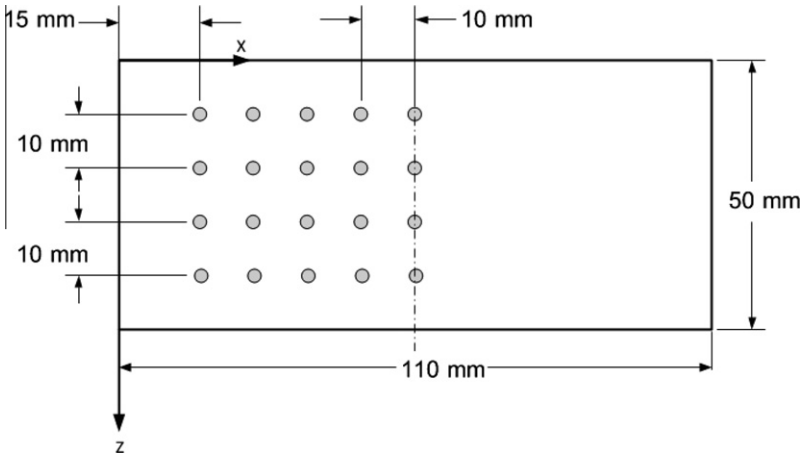

Fig. 2. Locations of temperature measurement in symmetrical *xz* plane.

3. Mathematical formulation

3.1. Analysis of electromagnetic field

Electromagnetic waves are formed with a combination of electric waves and magnetic waves. The magnetic and electric fields of an electromagnetic wave are perpendicular to each other and to the direction of the wave. Microwave is a part of an electromagnetic spectrum that has a particular range of wavelengths. Since the electromagnetic field that is investigated is the microwave field in the TE_{10} mode there is no variation of field in the direction between the broad faces of the rectangular waveguide and it is uniform in the *y*-direction. Consequently, it is assumed that a two dimension heat transfer model in *x* and *z* directions will be sufficient to identify the microwave heating phenomena in a rectangular waveguide [7]. Further assumptions are as follows:

(1) The absorption of microwaves by air in a rectangular wave guide is negligible.
(2) The walls of a rectangular wave guide are perfect conductors.
(3) The effect of the sample container on the electromagnetic and temperature fields can be neglected.

The proposed model is considered in the TE_{10} mode so the Maxwell's equations can be written in term of the electric and magnetic intensities;

$$\varepsilon\frac{\partial E_y}{\partial t}=\frac{\partial H_x}{\partial z}-\frac{\partial H_z}{\partial x}-\sigma E_y \tag{1}$$

$$\mu\frac{\partial H_z}{\partial t}=-\frac{\partial E_y}{\partial x} \tag{2}$$

$$\mu\frac{\partial H_x}{\partial t}=\frac{\partial E_y}{\partial z} \tag{3}$$

where *E* and *H* denote electric field intensity and magnetic field intensity, respectively. Subscripts *x*, *y* and *z* represent the *x*, *y* and

z components of vectors, respectively. Finally, ε is the electrical permittivity, σ is the electrical conductivity and μ is the magnetic permeability. These variables can be defined as follows:

$$\varepsilon = \varepsilon_0 \varepsilon_r \tag{4}$$

$$\mu = \mu_0 \mu_r \tag{5}$$

$$\sigma = 2\pi f \varepsilon \tan\delta, \tag{6}$$

The dielectric properties of porous material depend on temperature in which fractions of fluid and solid are considered based on porosity, ϕ as follows [25]:

$$\varepsilon_r(T) = \varepsilon_r'(T) - j\varepsilon_r''(T) \tag{7}$$

where

$$\varepsilon_r'(T) = \phi\varepsilon_{rf}'(T) + (1-\phi)\varepsilon_{rp}' \tag{8}$$

$$\varepsilon_r''(T) = \phi\varepsilon_{rf}''(T) + (1-\phi)\varepsilon_{rp}'' \tag{9}$$

where ε' and ε'' represent the dielectric constant and the dielectric loss, respectively.

The loss tangent coefficient can be written as:

$$\tan\delta(T) = \frac{\varepsilon_r''(T)}{\varepsilon_r'(T)} \tag{10}$$

When the material is heated unilaterally, it is found that as the dielectric constant and loss tangent coefficient vary, the penetration depth and the electric field within the dielectric material varies. Penetration dept is a measure of how deep the electromagnetic radiation can penetrate into a material. A number of factors can influence penetration depth including properties of the material, intensity and frequency of the electromagnetic wave. The penetration depth is used to denote the depth at which the power density has decreased to 37% of its initial value at the surface [6].

$$D_P = \frac{1}{\frac{2\pi f}{\upsilon}\sqrt{\frac{\varepsilon_r'\left(\sqrt{1+\left(\frac{\varepsilon_r''}{\varepsilon_r'}\right)^2}-1\right)}{2}}} = \frac{1}{\frac{2\pi f}{\upsilon}\sqrt{\frac{\varepsilon_r'\left(\sqrt{1+(\tan\delta)^2}-1\right)}{2}}} \tag{11}$$

where D_p is the penetration depth, ε_r'' is the relative dielectric loss factor and υ is the microwave speed. The penetration depth of the microwave power is calculated according to Eq. (11), which demonstrates how it depends on the dielectric properties of the material. It is noted that products of huge dimensions and with high loss factors may occasionally overheat a considerably thick layer of the outer surface. To prevent such a phenomenon the power density must be chosen so that enough time is provided for the essential heat transfer between boundary and core. If the thickness of the material is less than the penetration depth only a fraction of the supplied energy will become absorbed. For example, the dielectric properties of water show that water moderately dissipate electromagnetic energy into heat. This characteristic depends on the temperature. The water layer at low temperature typically shows slightly greater potential for absorbing microwaves. In the other words, an increase in the temperature typically decreases ε_r'', accompanied by a slight increase in D_p.

The boundary conditions for the TE_{10} mode can be formulated as follows:

(1) Perfectly conducting boundary. Boundary conditions on the inner wall surface of waveguide are given by Faraday's law and Gauss's theorem:

$$E_t = 0, \quad H_n = 0 \tag{12}$$

where subscripts t and n denote the components of tangential and normal directions, respectively.

(2) Continuity boundary condition. Boundary conditions along the interface between sample and air are given by Ampere's law and Gauss's theorem:

$$E_t = E_t', \quad H_t = H_t' \tag{13}$$

(3) The first order absorbing boundary condition applied at both ends of rectangular waveguide:

$$\frac{\partial E_y}{\partial t} = \pm\upsilon\frac{\partial E_y}{\partial z} \tag{14}$$

where ± is represented forward and backward direction and υ is velocity of wave.

(4) The incident wave due to magnetron is given by [7] showing an oscillation of the electric and magnetic intensities by the magnetron:

$$E_y = E_{yin}\sin\left(\frac{\pi x}{L_x}\right)\sin(2\pi f t) \tag{15}$$

$$H_x = \frac{E_{yin}}{Z_H}\sin\left(\frac{\pi x}{L_x}\right)\sin(2\pi f t) \tag{16}$$

where E_{yin} is the input value of electric field intensity, L_x is the length of the rectangular wave guide in the x-direction and Z_H is the wave impedance defined as

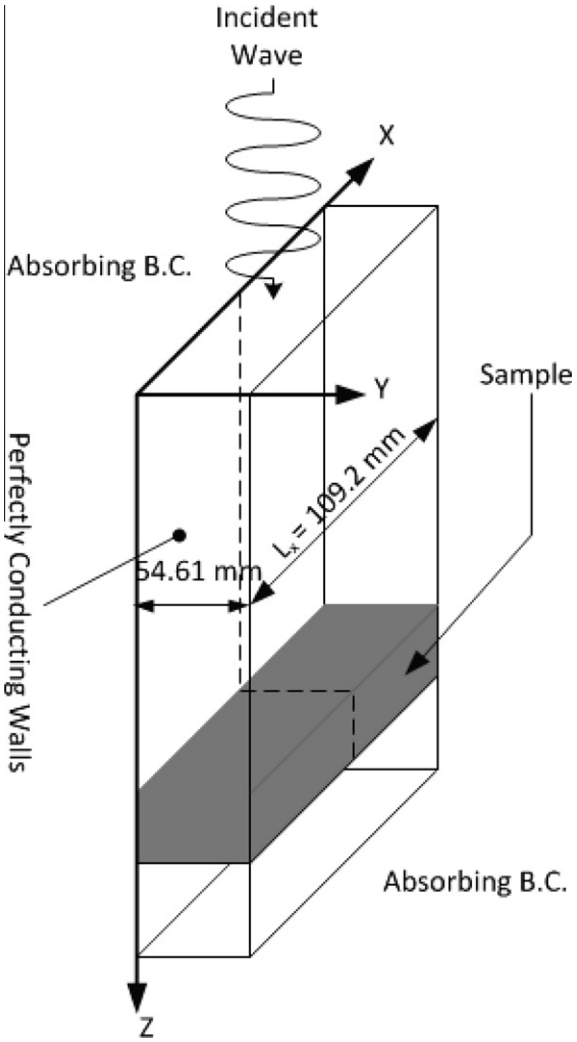

Fig. 3. Schematic of the physical problem.

Table 1
The electromagnetic and thermo physical properties used in the computations [4].

Material property	Air	Water	Glass bead	Alumina	Lead
Heat capacity, C_p ($Jg^{-1}\,K^{-1}$)	1.007	4.186	0.8	1.046	0.448
Thermal conductivity, λ ($W\,m^{-1}\,K^{-1}$)	0.0262	0.610	1.0	26.0	82.0
Density, ρ ($kg\,m^{-3}$)	1.205	1000	2500	3750	7660
Dielectric constant, ε_r'	1.0	$\varepsilon_r'(T)$[a]	5.1	10.8	6.9
Loss tangent, $\tan\delta$	0.0	$\tan\delta(T)$[b]	0.01	0.0145	0.0139

Note: For water, relative permittivity and loss tangent are referenced form Ratanadecho et al. [4] as follow:
[a] $\varepsilon_r'(T) = 85.56 - 0.3099T - 2.328x10^{-3}T^2 + 4.107x10^{-5}T^3 - 1.728x10^{-7}T^4$.
[b] $\tan\delta(T) = 0.2314 - 6.0405x10^{-3}T + 9.37x10^{-5}T^2 + 7.415x10^{-7}T^3 + 2.415x10^{-9}T^4$, T is in °C.

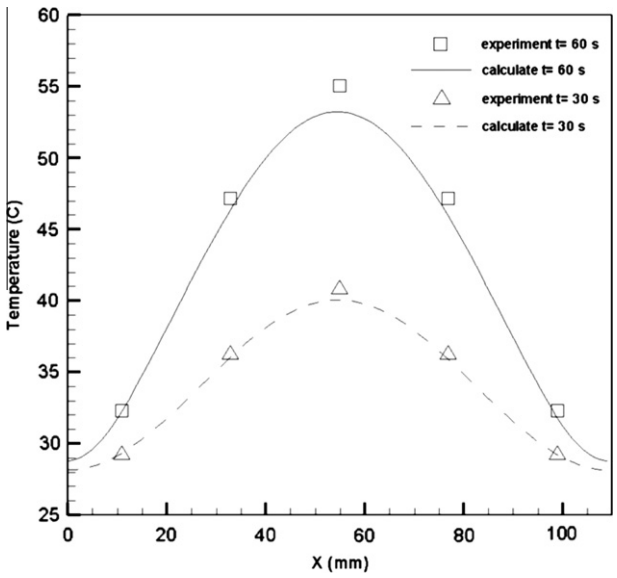

Fig. 4. The distributions of temperature for 30 and 60 s compared to the results from the calculations and experiment.

$$Z_H = \frac{\lambda_g Z_l}{\lambda} = \frac{\lambda_g}{\lambda}\sqrt{\frac{\mu}{\varepsilon}} \tag{17}$$

Here Z_l is the intrinsic impedance dependent on the properties of the material and λ and λ_g are the wave lengths of microwaves in free space and the rectangular wave guide, respectively.

The power flux associated with a propagating electromagnetic wave is expressed by the Poynting vector:

$$s = \frac{1}{2}\mathrm{Re}(E \times H^*) \tag{18}$$

The Poynting theorem allows the evaluation of the microwave power input, which is represented as:

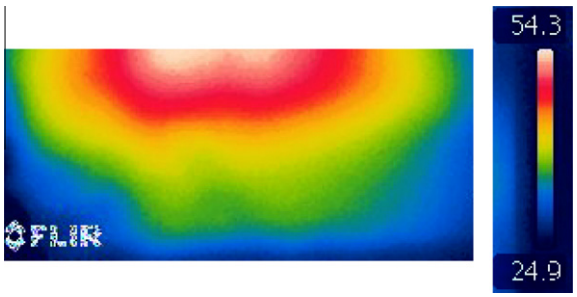

Fig. 5. Photograph taken from infrared camera shows contours of temperature (°C) in the porous packed bed at 60 s in case of porous two layers with glass beads with diameter of 0.15 mm at the top and 0.4 mm at the bottom.

$$P_{in} = \int_A SdA = \frac{A}{4Z_H}E_{yin}^2 \tag{19}$$

3.2. Analysis of temperature profile and flow field

The physical problem and coordinate system are depicted in Fig. 3. The microwave is propagating to the *xy* plane while the transport phenomena on the *xz* plane are currently investigated. To reduce the complexity of the problem, several assumptions have been offered into the flow and energy equations.

(1) Corresponding to the electromagnetic field, the flow and temperature fields can be assumed to be a two-dimensional plane.
(2) The effect of the phase change is neglected.
(3) Boussinesq approximation is used to account for the effect of the density variation on the buoyancy force.
(4) The surroundings of the porous packed bed are insulated except at the upper surface where energy exchanges with the ambient air.

3.2.1. Flow field equation

The porous medium is assumed to be homogeneous and thermally isotropic. The saturated fluid within the medium is in a local thermodynamic equilibrium (LTE) with the solid matrix [29–31]. The validity regime of local thermal equilibrium assumption has been established [32]. The fluid flow is unsteady, laminar and incompressible. The pressure work and viscous dissipation are all assumed to be negligible. The thermophysical properties of the

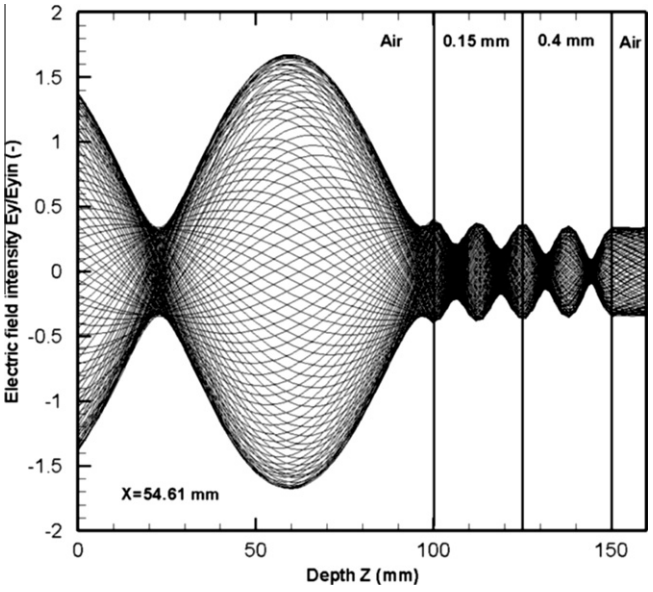

Fig. 6. Distribution of electric field on a porous two layers inside a rectangular waveguide at 60 s.

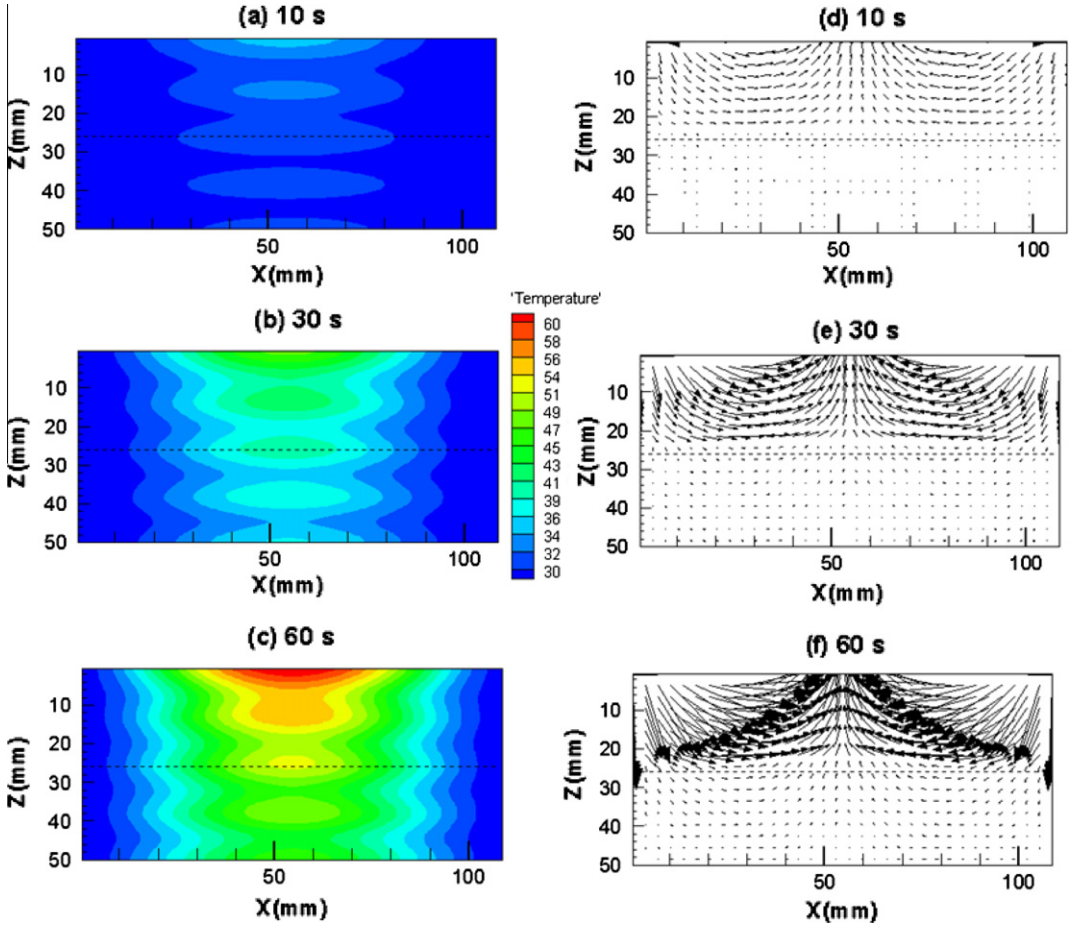

Fig. 7. Contours of temperature (°C) in the porous packed bed (a)–(c) and velocity vectors of water in porous materials, (d)–(f) at 10, 30, 60 s. Glass beads with diameter of 0.4 mm and 0.15 mm on the top and bottom layers, respectively. Both layers have a porosity of 0.385.

porous medium are taken to be constant however, the Boussinesq approximation takes into account of the effect of density variation on the buoyancy force. The Darcy–Forchheimer–Brinkman model was used to represent the fluid transport within the porous medium [32,33]. The Brinkmann's and the Forchheimer's extensions treats the viscous stresses at the bounding walls and the non-linear drag effect due to the solid matrix, respectively [33]. Furthermore, the solid matrix is made up of spherical particles, while the porosity and permeability of the medium are varied depending on the distance from the wall. Using standard symbols, the governing equations describing the heat transfer phenomenon are given by

Continuity equation:

$$\frac{\partial u}{\partial x}+\frac{\partial w}{\partial z}=0 \tag{20}$$

Momentum equations:

$$\frac{1}{\phi}\frac{\partial u}{\partial t}+\frac{u}{\phi^2}\frac{\partial u}{\partial x}+\frac{w}{\phi^2}\frac{\partial u}{\partial z}=-\frac{1}{\rho_f}\frac{\partial p}{\partial x}+\frac{\upsilon}{\phi}\left(\frac{\partial^2 u}{\partial x^2}+\frac{\partial^2 u}{\partial z^2}\right)-\frac{\mu u}{\rho_f \kappa}-F(u^2+w^2)^{1/2} \tag{21}$$

$$\frac{1}{\phi}\frac{\partial w}{\partial t}+\frac{u}{\phi^2}\frac{\partial w}{\partial x}+\frac{w}{\phi^2}\frac{\partial w}{\partial z}=-\frac{1}{\rho_f}\frac{\partial p}{\partial z}+\frac{\upsilon}{\phi}\left(\frac{\partial^2 w}{\partial x^2}+\frac{\partial^2 w}{\partial z^2}\right)-\frac{w\mu}{\rho_f \kappa}-F(u^2+w^2)^{1/2}+g\beta(T-T_0) \tag{22}$$

where ϕ, v and β are porosity, kinematics viscosity and coefficient of thermal expansion of the water layer, respectively. The permeability κ and geometric F function are [17,34]

$$\kappa=\frac{d_p^2\phi^3}{175(1-\phi)^2} \tag{23}$$

$$F=\frac{1.75(1-\phi)}{d_p\phi^3} \tag{24}$$

The porosity is assumed to vary exponentially with the distance from the wall [14,16,22]. Based on these previous studies, we proposed the variation of porosity within three confined walls of the bed; a bottom wall and two lateral walls. The expression that considers the variation of porosity in two directions in the xz plane is given by

$$\phi=\phi_s\left[1+b\left\{exp\left(-\frac{bx}{dp}\right)+exp\left(-\frac{b(W-x)}{dp}\right)+exp\left(-\frac{bz}{dp}\right)\right\}\right] \tag{25}$$

where d_p is the diameter of glass beads, ϕ_s known as the free-stream porosity is the porosity far away from the walls, W is the width of the packed bed and b and c are empirical constants. The dependencies of b and c to the ratio of the bed to bead diameter is small, and b and c were suggested to be 0.98 and 1.0, respectively [15].

3.2.2. Heat transfer equation

The temperature of the liquid layer exposed to the incident wave is obtained by solving the conventional heat transport equation with the microwave power absorbed included as a local electromagnetic heat generation term:

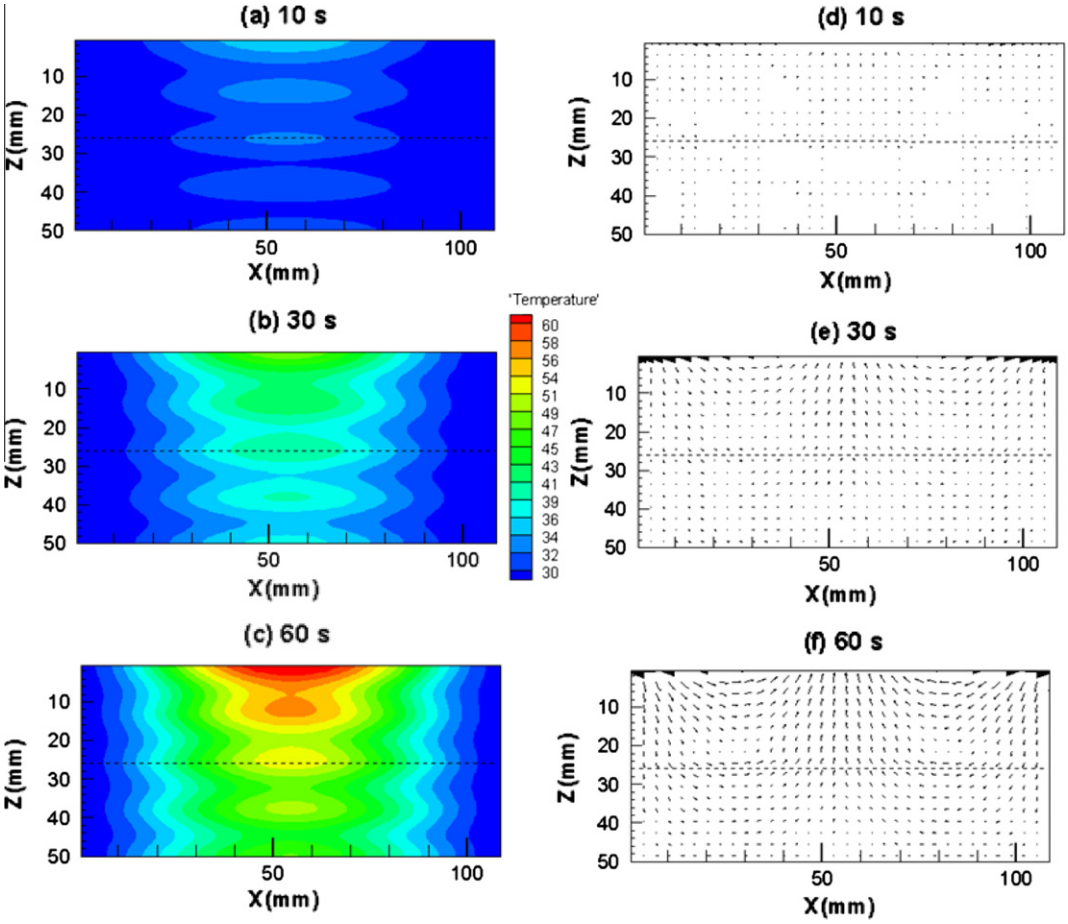

Fig. 8. Contours of temperature (°C) in the porous packed bed (a)–(c) and velocity vectors of water in porous materials, (d)–(f) at 10, 30, 60 s. Glass beads with diameter of 0.15 mm and 0.4 mm on the top and bottom layers, respectively. Both layers have a porosity of 0.385.

$$\sigma\frac{\partial T}{\partial t}+u\frac{\partial T}{\partial x}+w\frac{\partial T}{\partial z}=\alpha\left(\frac{\partial^2 T}{\partial x^2}+\frac{\partial^2 T}{\partial z^2}\right)+Q \tag{26}$$

where specific heat ratio $\sigma=\frac{[\phi(\rho c_p)_f+(1-\varepsilon)(\rho c_p)_s]}{(\rho c_p)_f}$, $\alpha=k_e/(\rho c_p)_f$ is the thermal diffusivity.

The local electromagnetic heat generation term that is a function of the electric field and is defined as

$$Q=2\pi f\varepsilon_0\varepsilon_r'\tan\delta(E_y)^2 \tag{27}$$

Boundary and initial conditions for these equations:

Since the walls of the container are rigid, the velocities are zero. At the interface between the porous layers and the walls of the container, zero slip boundary conditions are used for the momentum equations.

(1) At the upper surface, the velocity in the normal direction (w) and shear stress in the horizontal direction are assumed to be zero, where the influence of Marangoni flow [7] can be applied:

$$\eta\frac{\partial u}{\partial z}=-\frac{d\xi}{dT}\frac{\partial T}{\partial x} \tag{28}$$

(2) The walls, except the top wall, are insulated so no heat or mass exchanges:

$$\frac{\partial T}{\partial x}=\frac{\partial T}{\partial z}=0 \tag{29}$$

(3) Heat is lost from the surface via natural convection and radiation:

$$-k_{eff}\frac{\partial T}{\partial z}=h_c(T-T_0) \tag{30}$$

where

$$k_{eff}=\varepsilon k_f+(1-\varepsilon)k_s \tag{31}$$

(4) The interface boundary condition between layer 1st and layer 2nd are given by:

$$k_{eff}\frac{\partial T_1}{\partial y}=k_{eff}\frac{\partial T_2}{\partial y},\quad T_1=T_2 \tag{32}$$

$$\mu\left.\frac{du}{dy}\right|_1=\mu\left.\frac{du}{dy}\right|_2,\quad u_1=u_2,\quad v_1=v_2 \tag{33}$$

These conditions have been utilized at the interface between two different porous media with reasonably accurate results [35–36].

(5) The initial condition of a medium is defined as:

$$T=T_0\quad \text{at } t=0 \tag{34}$$

When T_0 is initial temperature at 28 °C.

4. Numerical procedure

The description of heat transport and flow pattern of liquid layer eqs. 20, 21, 22, 23, 24 and (26) require specification of temperature (T), velocity components (u,w) and pressure (p). These equations are coupled to the Maxwell's equations (Eqs. (1)–(3)) by Eq. (27), which represents the heating effect of the microwaves in the liquid-container domain.

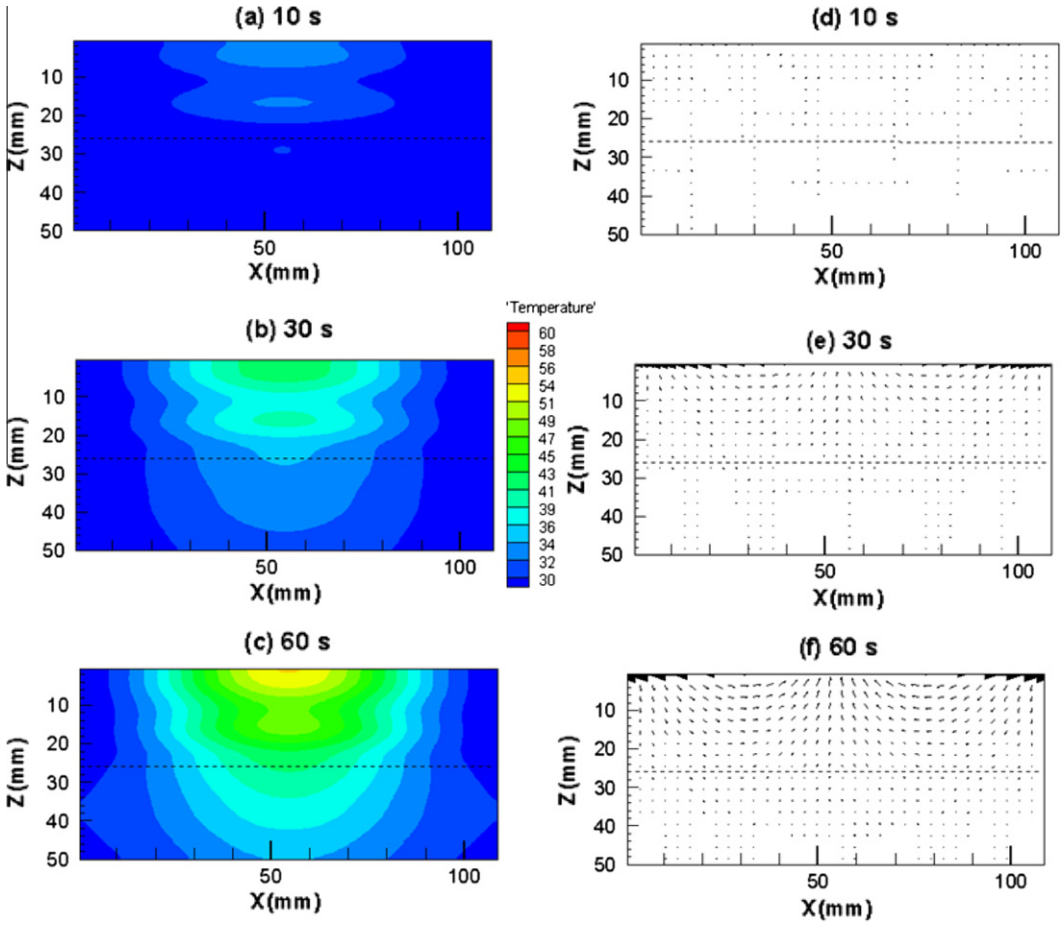

Fig. 9. Contours of temperature (°C) in the porous packed bed (a) (c) and velocity vectors of water in porous materials, (d) (f) at 10, 30, 60 s. Glass beads are on top and alumina balls are in the bottom, both layers have diameter and porosity equal to 0.15 mm and 0.385, respectively.

4.1. Electromagnetic equations and FDTD discretization

The electromagnetic equations are solved by using the finite difference time domain (FDTD) method that provides detailed spatial and temporal information of electromagnetic wave propagation. With this method the electric field components (E) are stored halfway between the basic nodes while magnetic field components (H) are stored at the center. Thus they are calculated at alternating half-time steps. E and H field components are discretized by a central difference method (second-order accurate) in both spatial and time domain. The leapfrog scheme is utilized for time integrations of the Maxwell's equations until the steady-state electromagnetic field behavior is fully evolved.

4.2. Fluid flow and heat transport equations and finite control volume discretization

Eqs. (20)–(24) are solved numerically by using the finite control volume along with the SIMPLE algorithm developed by Patankar [37]. The reason for using this method is the advantage provided from flux conservation that avoids the generation of a parasitic source. The basic strategy of the finite control volume discretization method is to divide the calculated domain into a number of control volumes and then integrate the conservation equations over this control volume and over an interval of time[$\{t, t + \Delta t\}$]. At the boundaries of the calculated domain, the conservation equations are discretized by integrating over half the control volume, taking into account the boundary conditions. At the corners of the calculated domain we used a quarter of the control volume. The fully Euler implicit time discretization finite difference scheme is used to arrive at the solution in time.

4.2.1. The stability and accuracy of calculation

The choice of spatial and temporal resolution is motivated by reasons of stability and accuracy. To ensure stability of the time stepping algorithm, Δt must be chosen to satisfy the courant stability condition and is defined as

$$\Delta t \leqslant \frac{\sqrt{(\Delta x)^2 + (\Delta z)^2}}{\upsilon} \tag{35}$$

and the spatial resolution of each cell is defined as

$$\Delta x, \Delta z \leqslant \frac{\lambda_g}{10\sqrt{\varepsilon_r}} \tag{36}$$

Corresponding to Eqs. (32) and (33) the calculation conditions are as follows:

(1) Grid resolution is 100 (x) × 200 (z).
(2) Grid size: $\Delta x = 1.0922$ mm and $\Delta z = 1.0000$ mm
(3) Time steps: $\Delta t = 2 \times 10^{-12}$ s and $\Delta t = 0.005$ s are used corresponding to the electromagnetic field and temperature field calculations, respectively.
(4) Relative error in the iteration procedures of 10^{-6} was chosen.

The mesh of 100 × 200 was found to be sufficient for the simulations carried out in the present study. Independence of the solutions on the grid size was examined through a number of test

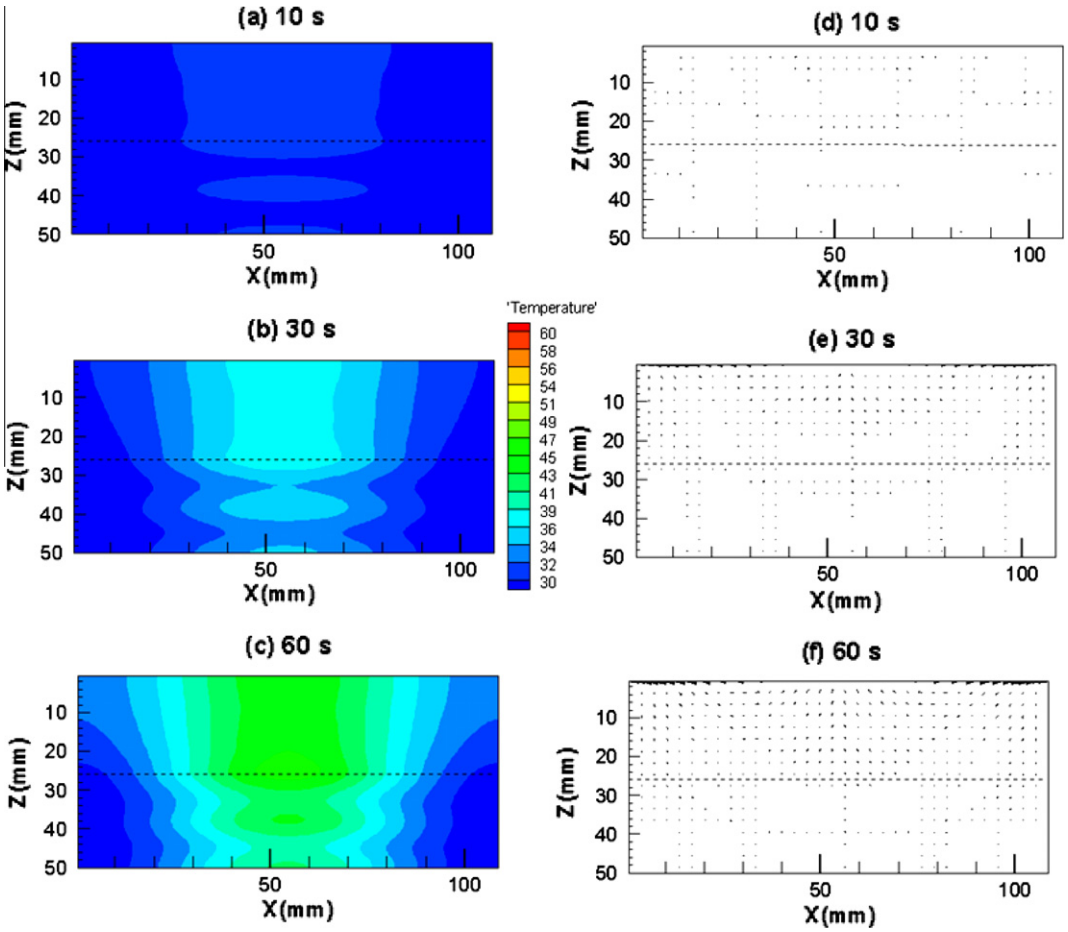

Fig. 10. Contours of temperature (°C) in the porous packed bed (a)–(c) and velocity vectors of water in porous materials, (d)–(f) at 10, 30, 60 s. Alumina balls are on top and Glass beads are in the bottom, both layers have diameter and porosity equal to 0.15 mm and 0.385, respectively.

cases. The results indicate that negligible difference of solutions was achieved above the resolution of 80 × 160 [7].

4.2.2. The iterative computational schemes

Since the dielectric properties of liquid layer samples are temperature dependent, to understand the influence of the electromagnetic fields on the microwave heating of a liquid layer it is necessary to consider the coupling between electric field and temperature and fluid flow fields. For this reason, iterative computational schemes are required to resolve the coupled non-linear Maxwell's equations, momentum and heat transport equations.

The computational scheme is to first computes a local heat generation term by running an electromagnetic calculation with uniform properties determined from initial temperature data. The electromagnetic calculation is performed until a sufficient period is reached in which the representative average rms (root mean square) of the electric field at each point is computed and used to solve the time dependent temperature and velocities field. Using these temperatures new values of the dielectric properties are calculated and used to re-calculate the electromagnetic fields and then the microwave power absorption. All the steps are repeated until the required heating time is reached.

5. Results and discussion

The numerical results are compared against the experimental data. The present analysis involves several types of materials. The dielectric and thermal properties of air, water, glass bead, alumina and lead used for computations are listed in Table 1. The two layered porous medium is composed of smaller glass beads on top of bigger beads with 0.15 mm and 0.4 mm in diameter, respectively. The comparison is shown in Fig. 4 for the temperature distributions in *XZ* plane at the horizontal line $Z = 20$ mm at 30 s and 60 s. The results reveal good agreement between the computations and measurement. It is found that the difference is less than 3.3%. The favorable comparisons lend confidence to accuracy of the present model and further numerical studies herein.

Fig. 5 is a photograph taken by the infrared camera that shows the contour of the temperature (°C) at the *x*–*z* plane surface in the case of a two layers porous medium. This photograph shows glass beads in the packed bed that is 50 mm high, the glass beads 0.15 mm in diameter are placed on top of the bigger glass beads 0.4 mm in diameter. It is observed that temperature is greatest at the top of photograph at about 54 °C. From the photograph we found that the distribution of temperature due to heating by microwave will be similar in many experiments. The temperature contour taken from the camera is consistent with the results given in Fig. 4.

For a better understanding of the electric field inside the rectangular waveguide containing a porous packed bed, an electric field in TE_{10} mode at the center of *x* at 54.61 mm of the rectangular waveguide is extracted and shown in Fig. 6. The sample inside the waveguide is the water saturated packed bed filled with 0.15 mm diameter glass beads on top of 0.4 mm diameter beads. The vertical axis denotes the ratio of the intensity of the electric

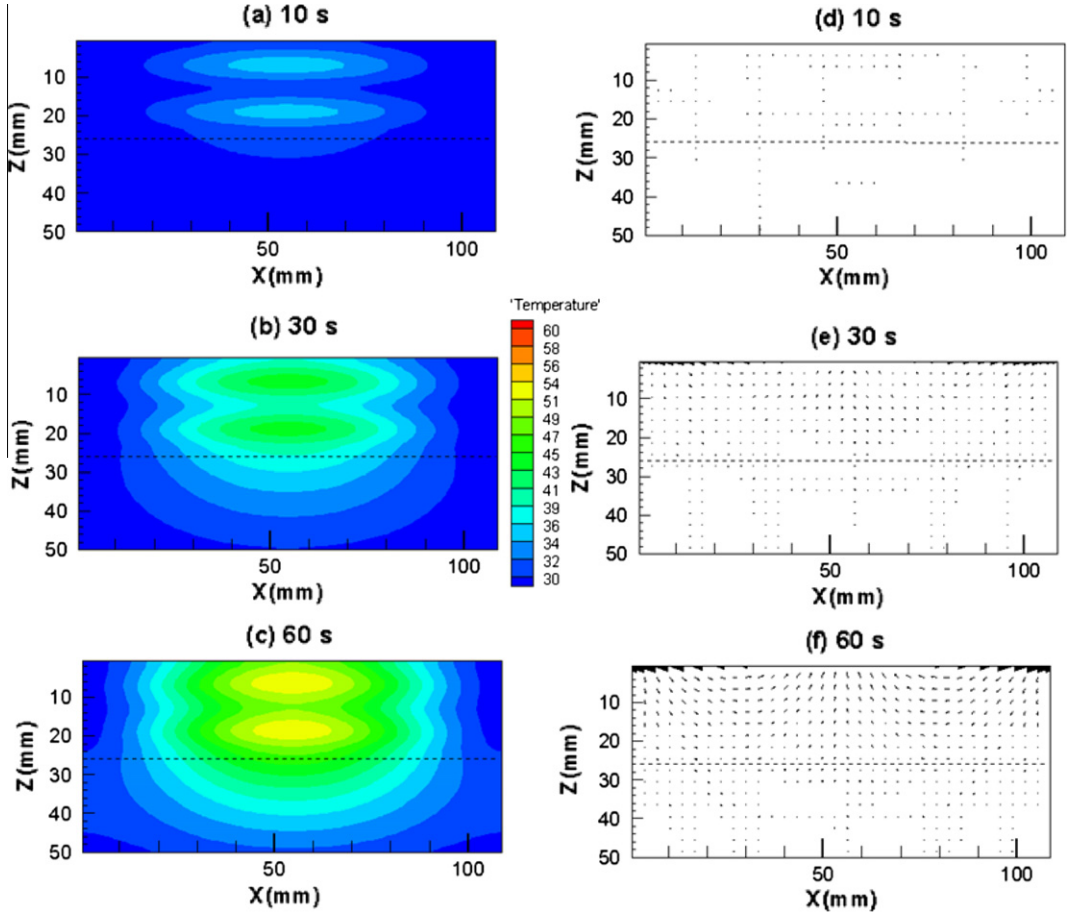

Fig. 11. Contours of temperature (°C) in the porous packed bed (a)–(c) and velocity vectors of water in porous materials, (d)–(f) at 10, 30, 60 s. Glass beads are on top and lead balls are in the bottom, both layers have diameter and porosity equal to 0.15 mm and 0.385, respectively.

field (E_y) and input electric field (E_{yin}). Since the waves transmitted through the cavity with air inside which low relative permittivity travel to the sample has high relative permittivity. Most of the waves are reflected from the surface of the sample occur interference with waves that forward so in front of sample. This phenomenon is called resonance of standing wave that occurs at the empty part waveguide (left side of the example). The amplitude of the wave is increased while the amplitude of the electric field inside the material is reduced due to the microwave energy that is lost into thermal energy. However, distributions of the electric field in this case produce a standing wave in front of porous material are mainly caused by part of water in the porous media. Electrical conductivity and relative permittivity strongly affect formation of standing waves.

Next, effects of particle size and patterns of layers are investigated. Figs. 7 and 8 are numerical results of two-layer porous media compared of glass beads. The two layers have different sizes of glass beads. In Fig. 7, glass beads with diameter of 0.4 mm are filled in the top layers while glass beads with a diameter of 0.15 mm are in the bottom layer. The boundary between layers is at the $Z = 25$ mm. In Fig. 8, the two layers swap over. In both Figs. 7 and 8, porosity is 0.38 for the entire domain and the microwave power of 300 watts is used. It can be seen that, in case of the coarse beads (0.4 mm) on top (Fig. 7) the rate of heat transfer is slower than the case that fine beads (0.15 mm) are on the top (Fig. 8). This result is due to the coarse beads on top that have higher permeability making fluid to flow faster than the bottom layer that contains fine beads. Most of the fluid mass reflects at the interface since it is difficult for fluid to flow through the fine beads that have low permeability. For this reason, the heat transfer within the fine beads is less efficiency.

In order to analyze effects of material properties on heating processes in double layer medium, the two layer porous medium with glass beads and alumina balls is tested. Fig. 9 is the computed results for the case that glass beads are on top of alumina balls. The positions of materials are switched in Fig. 10. Glass beads and alumina balls have different relative dielectric constants 5.1 and 10.8, respectively. Thermal conductivity of the glass beads and alumina balls are 1.0 W/(m K) and 26.0 W/(m K), respectively. The calculated result in Fig. 10 shows that the thermal distribution is wider and its gradients are smaller with lower temperature, compared to Fig. 9. Since alumina in the upper layer has thermal conductivity 26 times greater than glass. High value of thermal conductivity enhances heat transfer rate. In addition, higher relative dielectric constant of alumina indicates less heat absorption in the upper layer. Due to the fact that the penetration depth of the glass beads is greater than the thickness of the layer of glass beads approximately two times, the standing wave or resonance occurs from a combination of forward and reflected waves at the boundary between the glass bead and alumina layers.

Fig. 11 is the calculated domain for which glass beads on top and lead balls in the bottom. Locations of the two layers are switched and shown in Fig. 12. Both of the layers reveal different profiles since their thermal conductivities differ by 82 times. Glass and lead have the thermal conductivity of 1 W/(m K) and 82.0 W/(m K), respectively. It can be noticed that the temperature contour

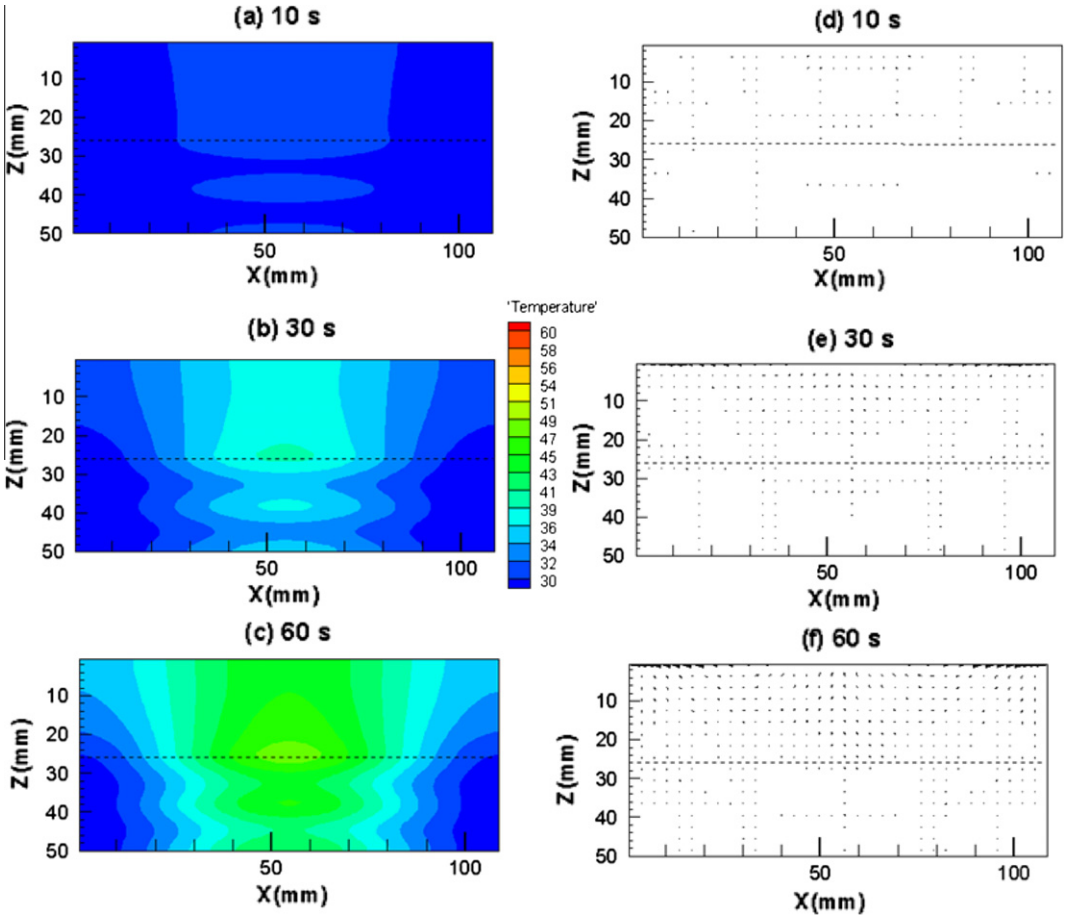

Fig. 12. Contours of temperature (°C) in the porous packed bed (a)–(c) and velocity vectors of water in porous materials, (d)–(f) at 10, 30, 60 s. Lead balls are on top and Glass beads are in the bottom, both layers have diameter and porosity equal to 0.15 mm and 0.385, respectively.

patterns in the Figs. 11 and 12 are similar to Figs. 9 and 10, respectively. However, in the case of lead, the contour spreads more widely since lead has much greater thermal conductivity than alumina. Besides, lead has a dielectric constant less than alumina. Electric wave can be stored into the lead layer more than alumina. When focusing on the top layers which both are filled with glass beads in Figs. 9 and 11, patterns of wave resonance are different within the layers. This result is attributed to the difference of material type in the bottom layer. Lead layer at bottom causes reflected wave as clearly seen in the Figure more than when the bottom material is alumina. Therefore thermal and dielectric properties of material in the bottom layer markedly affect the heating process within the top layer.

6. Conclusions

Heating process in the double-layer porous media subjected to microwave energy is numerically investigated. Effects of particle size thermal and dielectric properties of the media are examined.The porous packed bed as the medium was placed in a waveguide with a rectangular cross section. The two layers have different materials or different particle sizes. The microwave power of 300 W and frequency of 2.45 GHz in TE_{10} mode were used. The calculations based on the mathematical model are consistent with the results of experiment. The major results found are as follows. Regarding fine and course beads, heating rate is higher when fine beads is on top due to the enhanced convective flow in porous materials. Different materials between two layers affect the reflection of waves at the interface. Due to the difference in dielectric properties of materials standing wave are produced in the upper layer, resulting in higher rates of heat transfer within the upper layer. Heat transfer is less efficient when porous material on the top layer has high relative dielectric constant since less electric waves are not absorbed in the material. On the other hand, heat spreads faster in materials with higher thermal conductivity. Finally, heating processes within the top layer are remarkably affected by the thermal and dielectric properties of material in the bottom layer.

References

[1] W.K. Chen, H.T. Davis, E.A. Davis, G. Joan, Heat and mass transfer in water-laden sandstone microwave heating, AIChE J. 31 (5) (1985) 842–848.
[2] H. Ni, A.K. Datta, K.E. Torrance, Moisture transport in intensive microwave heating of biomaterials: porous media model, Int. J. Heat Mass Transfer 42 (1999) 1501–1512.
[3] H. Feng, J. Tang, R.P. Cavalieri, O.A. Plumb, Heat and mass transport in microwave drying of porous materials in a spouted bed, AIChE J. 47 (2001) 1499–1512.
[4] P. Ratanadecho, K. Aoki, M. Akahori, Influence of irradiation time particle sizes and initial moisture content during microwave drying of multi-layered capillary porous materials, ASME J. Heat Transfer 124 (1) (2002) 151–161.
[5] D.D. Dincov, K.A. Parrot, K.A. Pericleous, Heat and mass transfer in two- phase porous materials under intensive microwave heating, J. Food Eng. 65 (2006) 403–412.
[6] P. Ratanadecho, The simulation of microwave heating of wood using a rectangular wave guide: influence of frequency and sample size, Chem. Eng. Sci. (61) (2006) 4798–4811.
[7] P. Ratanadecho, K. Aoki, M. Akahori, A numerical and experimental investigation of modelling of microwave heating for liquid layers using a rectangular wave guide (effects of natural convection and dielectric properties), Appl. Math. Model. 26 (2002) 449–472.

[8] W. Cha-um, P. Rattanadecho, W. Pakdee, Experimental analysis of microwave heating of dielectric materials using a rectangular wave guide (MODE: TE10) (case study: water layer and saturated porous medium), Exp. Therm. Fluid Sci. 33 (3) (2009) 472–481.
[9] K.G. Ayappa, S. Brandon, Microwave driven convection in a square cavity, AIChE J. 40 (7) (1994) 1268–1272.
[10] A.S. Franca, K. Haghighi, Adaptive finite element analysis of microwave driven convection, Int. Commun. Heat Mass Transfer 23 (2) (1996) 177–186.
[11] S. Chatterjee, T. Basak, S.K. Das, Microwave driven convection in a rotating cylindrical cavity: a numerical study, J. Food Eng. 79 (2007) 1269–1279.
[12] A.L. Brody, Advances in microwave pasteurization and sterilization, Food Technol. 65 (2) (2011) 83–85.
[13] S. Lui, J. Masliyah, Single fluid flow in porous media, Chem. Eng. Commun. 148 (1996) 653–732.
[14] R.F. Benenati, C.B. Brosilow, Void fraction distribution in pack beds, AIChE J. 8 (1962) 359–361.
[15] K. Vafai, Convective flow and heat transfer in variable-porosity media, J. Fluid Mech. 147 (1984) 233–259.
[16] A. Amiri, K. Vafai, Analysis of dispersion effects and non-thermal equilibrium, non-Darcian, variable porosity incompressible flow through porous media, Int. J. Heat Mass Transfer 37 (6) (1994) 939–954.
[17] A.K. Abdul-Rahim, A.J. Chamkha, Variable porosity and thermal dispersion effects on coupled heat and mass transfer by natural convection from a surface embedded in a non-metallic porous medium, Int. J. Numer. Methods Heat Fluid Flow 11 (5) (2001) 413–429.
[18] S.W. Hsiao, P. Cheng, C.K. Chen, Non-uniform porosity and thermal dispersion effects on natural convection about a heated horizontal cylinder in an enclosed porous medium, Int. J. Heat Mass Transfer 35 (12) (1992) 3407–3418.
[19] H. Sakamoto, F.A. Kulacki, Effective thermal diffusivity of porous media in the wall vicinity, ASME J. Heat Transfer 130 (2) (2008). art.no. 022601.
[20] K. Vafai, Analysis of the channeling effect in variable porosity media, J. Energy Resour. Technol. 108 (1986) 131–139.
[21] M.L. Hunt, C.L. Tien, Non-Darcian convection in cylindrical packed beds, ASME J. Heat Transfer 110 (1998) 2523–2532.
[22] D. Poulikakos, K. Renken, Forced convection in a channel filled with porous medium, including the effects of flow inertia, variable porosity and Brinkman friction, ASME J. Heat Transfer 109 (1987) 880–888.
[23] H. Shih-Wen, P. Cheng, C. Chao-Kuang, Non-uniform porosity and thermal dispersion effects on natural convection about a heated horizontal cylinder in an enclosed porous medium, Int. J. Heat Mass Transfer 35 (12) (1992) 3407–3418.
[24] Z. Chai, Z. Guo, Study of electro-osmotic flows in microchannels packed with variable porosity media via lattice Boltzmann method, J. Appl. Phys. 101 (2007) 104913.
[25] S. Akbal, F. Baytas, Effects of non-uniform porosity on double diffusive natural convection in a porous cavity with partially permeable wall, Int. J. Therm. Sci. 47 (7) (2008) 875–885.
[26] R. Prommas, P. Kengin, P. Rattanadecho, Energy and exergy analyses in convective drying process of multi-layered porous packed bed, Int. Commun. Heat Mass Transfer 37 (2010) 1106–1114.
[27] W. Pakdee, P. Rattanadecho, Natural convection in a saturated variable-porosity medium due to microwave heating, ASME J. Heat Transfer 133 (6) (2011). art. no. 062502.
[28] W. Klinbun, K. Vafai, P. Rattanadecho, Electromagnetic field effects on transport through porous media, Int. J. Heat Mass Transfer 55 (2012) 325–335.
[29] M.M. El-Refaee, M.M. Elsayed, N.M. Al-Najem, A.A. Noor, Natural convection in partially cooled tilted cavities, Int. J. Numer. Methods Heat Fluid Flow 28 (1998) 477–499.
[30] D.A. Nield, A. Bejan, Convection in Porous Media, Springer, New York, 1999.
[31] A.A. Al-Amiri, Natural convection in porous enclosures: the application of the two-energy equation model, Numer. Heat Transfer Part A 411999 (2002) 817–834.
[32] A. Marafie, K. Vafai, Analysis of non-Darcian effects on temperature differentials in porous media, Int. J. Heat Mass Transfer 44 (2001) 4401–4411.
[33] P. Nithiarasu, K.N. Seetharamu, T. Sundararajan, Natural convective heat transfer in a fluid saturated variable porosity medium, Int. J. Heat Mass Transfer 40 (1996) 3955–3967.
[34] A.J. Chamkha, C. Issa, K. Khanafer, Natural convection from an inclined plate embedded in a variable porosity porous medium due to solar radiation, Int. J. Therm. Sci. 41 (2001) 73–81.
[35] K. Vafai, R. Thiyagaraja, Analysis of flow and heat transfer at the interface region of a porous medium, Int. J. Heat Mass Transfer 30 (1987) 1391–1405.
[36] S.J. Kim, C.Y. Choi, Convection heat transfer in porous and overlaying layers heated from below, Int. J. Heat Mass Transfer 39 (1996) 319–329.
[37] S.V. Patankar, Numerical Heat Transfer and Fluid Flow, Hemisphere, New York, 1980.

OPHTHALMOLOGY IMAGING AND APPLICATIONS

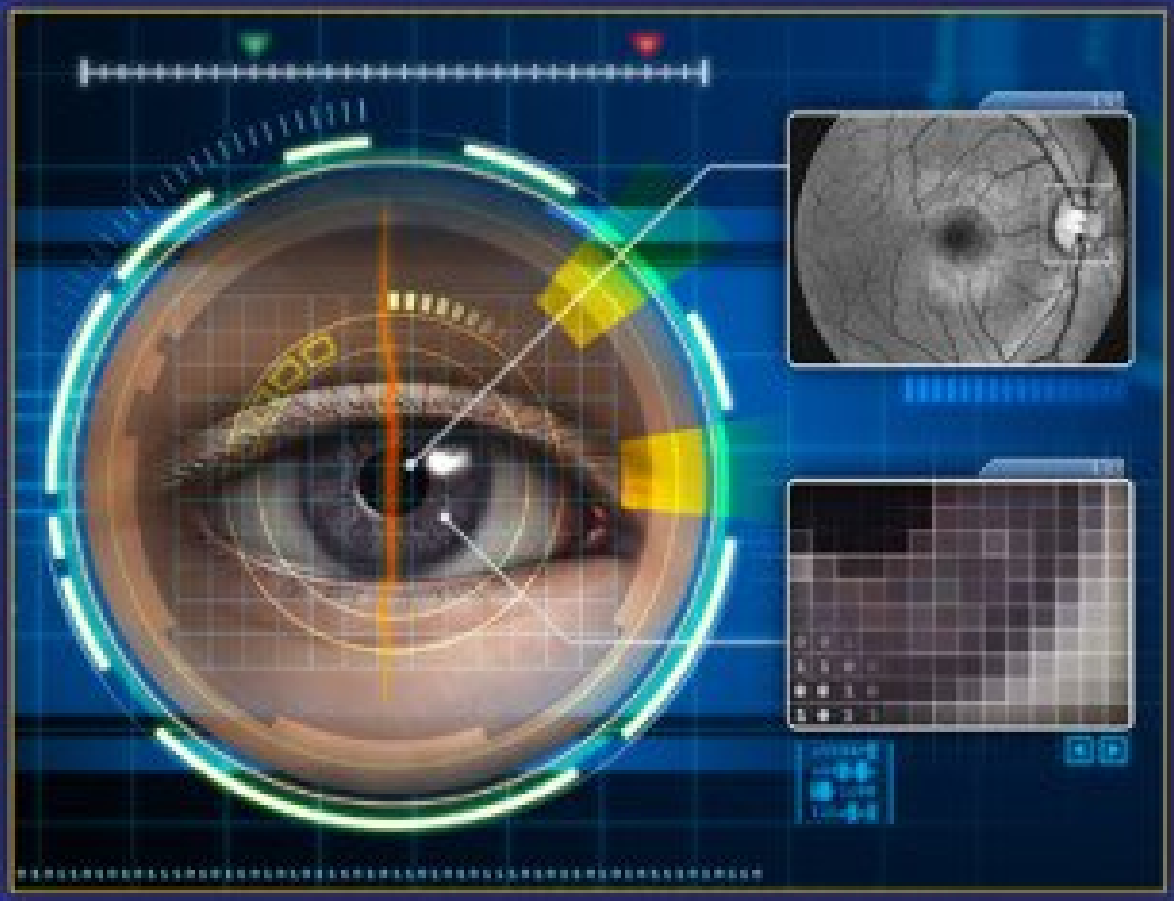

Edited by
E. Y. K. Ng
U. Rajendra Acharya
Rangaraj M. Rangayyan
Jasjit S. Suri

CRC Press
Taylor & Francis Group

22

Effects of Electromagnetic Fields on Specific Absorption Rate and Heat Transfer in the Human Eye

Teerapot Wessapan and Phadungsak Rattanadecho

CONTENTS

22.1 Introduction 426
22.2 Problem Formulation 427
22.3 Mathematical Model Formulation 429
22.3.1 Electromagnetic Wave Propagation Equation 430
22.3.1.1 Boundary Condition for Wave Propagation Analysis 431
22.3.2 Heat Transfer Equation 433
22.3.2.1 Boundary Condition for Heat Transfer Analysis 434
22.3.3 Calculation Procedure 435
22.4 Results and Discussion 435
22.4.1 Verification of the Model 435
22.4.2 Electric Field Distribution 436
22.4.2.1 Effect of Power Density on Electric Field Distribution 436
22.4.3 SAR Distribution 438
22.4.3.1 Effect of Power Density on SAR Distribution 438
22.4.4 Temperature Distribution 439
22.4.4.1 Effect of Heat Transfer Model on Temperature Distribution 439
22.4.4.2 Effect of Power Density on Temperature Distribution 441
22.4.5 Concluding Remarks 443
References 444

Nomenclature

C	Specific heat capacity (J/(kg K))
E	Electric field intensity (V/m)
e	The tear evaporation heat loss (W/m^2)
f	Frequency of incident wave (Hz)
H	Magnetic field (A/m)
h	Convection coefficient ($W/(m^2\ K)$)
j	Current density (A/m^2)
k	Thermal conductivity (W/(m K))
n	Normal vector
p	Pressure (N/m^2)
Q	Heat source (W/m^3)

K15530_C022.indd 425 12/18/2013 2:58:52 PM

T	Temperature (K)
u	Velocity (m/s)
t	Time

Greek Letters

β	Volume expansion coefficient (1/K)
μ	Magnetic permeability (H/m)
ε	Permittivity (F/m)
σ	Electric conductivity (S/m)
ω	Angular frequency (rad/s)
ρ	Density (kg/m^3)
ω_b	Blood perfusion rate (1/s)
Γ	External surface area

Subscripts

am	Ambient
b	Blood
ext	External
i	Subdomain
met	Metabolic
r	Relative
ref	Reference
0	Free space, initial condition

22.1 Introduction

The electromagnetic (EM) waves of the different power levels and frequencies penetrate deep into the human body causing health risks. In recent years, there has been some increasing public concern with the interaction between the human body and the EM fields. Since the eye is one of the most sensitive organs to the EM fields, the high-intensity EM fields may lead to a variety of ocular effects. However, the resulting thermophysiologic response of the eye to EM fields is not well understood. Therefore, it is important to investigate the ocular effects occurred during exposure to EM fields. Although the safety standards written in terms of maximum tissue specific absorption rate (SAR) values are regulated, they are not stated in terms of maximum temperature increase in the eye caused by EM energy absorption. The eye temperature increasing gradually can cause serious long-term effects on eyesight and vision. There have been medical case reports of cataract formation in humans via microwave radiation [1]. It is reported that a temperature increase in the eye of 3°C–5°C leads to induce cataract formation [2] and a temperature above 41°C is necessary for production of posterior lens opacities [3]. Therefore, to gain insight into the phenomenon of eye temperature distribution induced by EM fields, it is necessary to have a detailed knowledge of the absorbed power distribution and the temperature distribution.

Previous studies focused on the effects of EM fields on the human eye [4,5]. Nevertheless, their analysis has been conducted based on the maximum SAR values permitted by public safety standards regulation [6,7]. For example, in studies of an interaction between the EM fields and the human eye, most of them have mainly focused on SAR and have not considered the heat transfer. Consequently, it could not be fully understood. In addition, there

have been few experimental data on the correlation of SAR levels with the temperature increase in the human tissue. Therefore, a modeling of heat transport is needed to completely explain the actual process of interaction between the EM fields and the human eye.

Thermal modeling of human tissue is important as a tool to explore the effects of external heat sources and investigate abnormalities in the tissue. Recently, the modeling of heat transport in human tissue has been considered by many researchers [8–20]. Most studies of heat transfer analysis in the human eye used heat conduction equation [8–14]. Some studies carried out on natural convection in human eye based on heat conduction model [15,16]. Ooi and Ng [16,17] studied the effect of aqueous humor (AH) hydrodynamics on the heat transfer in the eye based on heat conduction model. Meanwhile, the Pennes' bioheat equation [18,19], based on the heat diffusion equation for a blood-perfused tissue, is used for modeling of heat transfer in the human eye as well [20,21]. Ooi and Ng also developed a 3D model of the human eye [22], extending their 2D model [21]. Recently, researchers have used the porous media models to investigate the transport phenomena in biological media instead of a simplified bioheat model [23–25]. Shafahi and Vafai [26] proposed the porous media along with natural convection model to analyze the eye thermal characteristics during exposure to thermal disturbances. Narasimhan and Vishnampet [27] proposed the porous medium model of the sclera and the choroid to study the effect of choroidal blood flow on transscleral drug delivery to the retina. Many researchers have been tried to conduct the advanced model using the coupled model of heat and laser irradiation in the human eye [28–30]. Results from similar models of Ooi et al. [30] for various applications were also presented in continuation [31–34].

Although the porous media and natural convection models of the human eye have been used in the previous biomedical studies [15–16,26,27], most studies of the human eye exposed to EM fields have not been considering the porous media approach, and natural convection approach is sparse or nonexistent. Wessapan and Rattanadecho [35] investigated the SAR and temperature distributions of EM fields in the eye using porous media theory. There are few studies on an interaction between the temperature and the EM fields in realistic physical model of the human organs especially the eye due to its complexity. Therefore, to provide information on exposure levels and health effects from EM fields, it is necessary to simulate both of the EM fields and the heat transfer, based on porous media theory within an anatomical model particularly the eye.

In this study, a 2D eye model was exploited to simulate the SAR and temperature distributions. EM wave propagation in the eye was investigated by using Maxwell's equations. An analysis of heat transfer in the eye exposed to a transverse magnetic (TM) mode of EM fields was investigated using a developed heat transfer model (included the conduction and natural convection heat transfer mode), which was proposed by Shafahi and Vafai [26]. The SAR and the temperature distribution in various parts of the human eye during exposure to EM fields at 900 MHz, which are obtained by numerical solution of EM wave propagation and heat transfer equation, are presented. This book chapter was based on empirical data from the work of Wessapan and Rattanadecho [35], with permission from ASME.

22.2 Problem Formulation

In fact, the human exposures to EM radiation have increased exponentially. The human eye is exposed daily to radiation from sources such as mobile phones, microwave oven,

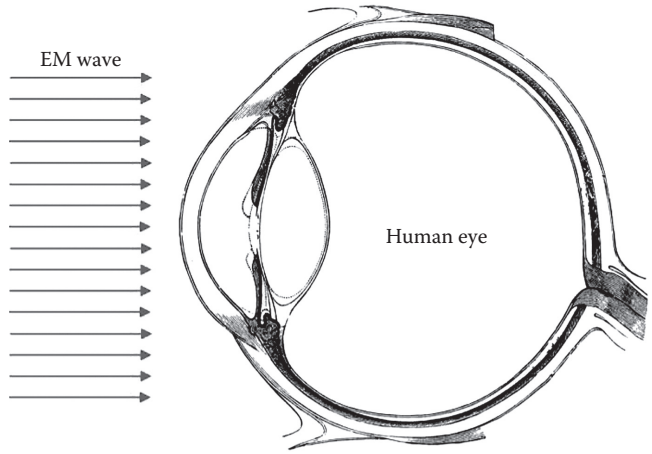

AQ3 **FIGURE 22.1**
EM fields from an EM radiation device.

monitors, and wireless networks and other EM fields commonly found in our daily life. It is known that the human eye is one of the most sensitive organs to EM radiation. This is because the crystalline lens and the cornea are nonvascular tissue with low metabolism and the eye has no thermal sensors and protective reflexes. An investigation of the human eye exposure to EM fields can be done with difficulty due to the eye's complex geometry and its being a heterogeneous tissue. Moreover, this investigation cannot be done by experiments due to the ethical considerations. Exposing a human to EM fields for experimental purposes is still restricted. It is more convenient and ethical to develop a realistic human eye model through numerical simulation. Figure 22.1 shows radiation of EM fields from an EM radiation device to the human body. These EM fields fall on the human eye that causes heating in the deeper tissue, which leads to tissue damage and cataract formation.

Our first step in the evaluation of the effects of a certain exposure to EM fields in the eye is to determine the induced internal EM fields and their spatial distributions. Thereafter, with the EM energy absorption resulting in an increased temperature in the eye, other interactions could be then considered. This study considers the coupling between the EM and heat transfer equations to model the distribution of temperature fields induced by EM radiation in the eye.

In this study, the eye model, which is based on a physical model we developed in the previous research [26], comprises seven types of tissue including posterior chamber, anterior chamber, cornea, iris, sclera, lens, and vitreous. Different types of tissue have different dielectric and thermal properties. In the sclera layer, there are two more layers known as choroid and retina that are relatively thin compared to the size of the sclera itself. To simplify the problem, these layers are assumed to be homogeneous. The iris and the sclera, which have the same properties, are modeled together as one homogenous region [16]. Figure 22.2 shows the 2D eye model used in this study [35]. The dielectric [36,37] and thermal properties [16] of tissue are shown in Tables 22.1 and 22.2, respectively. Each tissue is assumed to be homogeneous and electrically as well as thermally isotropic.

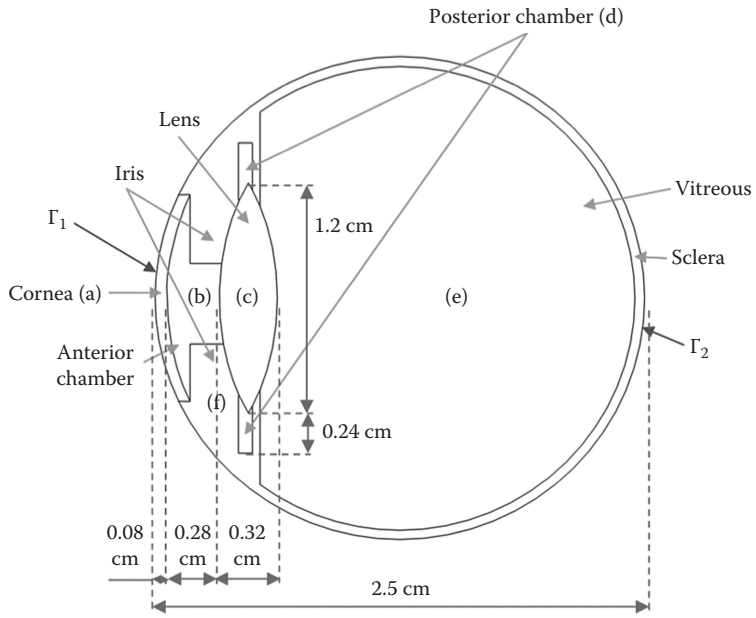

FIGURE 22.2
Human eye vertical cross section. (From Wessapan, T. and Rattanadecho, P., *ASME Trans. J. Heat Transfer*, 134, 091101, 2012. With permission.)

TABLE 22.1

Dielectric Properties of Tissues at 900 and 1800 MHz

	Frequency 900 MHz		**Frequency 1800 MHz**	
Tissue	ε_r	**σ (S/m)**	ε_r	**σ (S/m)**
Cornea (a)	52.0	1.85	55.0	2.32
Anterior chamber (b)	73.0	1.97	75.0	2.40
Lens (c)	51.3	0.89	41.1	1.29
Posterior chamber (d)	73.0	1.97	75.0	2.40
Vitreous (e)	74.3	1.97	73.7	2.33
Sclera (f)	52.1	1.22	52.7	1.68
Iris (f)	52.1	1.22	52.7	1.68

Source: Wessapan, T. and Rattanadecho, P., *ASME Trans. J. Heat Transfer*, 134, 091101, 2012. With permission.

22.3 Mathematical Model Formulation

The intensity of the internal fields in the body depends on various parameters such as an operating frequency, the power intensity, a mode of propagation, the body geometry, the tissue dielectric properties, a distance from EM source, and the presence of other objects in the body vicinity. When the EM waves pass from one medium to another, they can be absorbed, reflected, refracted, or transmitted, depending on the dielectric property of the

TABLE 22.2

Thermal Properties of Human Eyes

Tissue	ρ (kg/m³)	*k* (W/m °C)	C_p (J/kg °C)	μ (N s/m²)	β (1/K)
Cornea (a)	1050	0.58	4178	—	—
Anterior chamber (b)	996	0.58	3997	0.00074	0.000337
Lens (c)	1000	0.4	3000	—	—
Posterior chamber (d)	996	0.58	3997	—	—
Vitreous (e)	1100	0.603	4178	—	—
Sclera (f)	1050	1.0042	3180	—	—
Iris (f)	1050	1.0042	3180	—	—

Source: Wessapan, T. and Rattanadecho, P., *ASME Trans. J. Heat Transfer*, 134, 091101, 2012. With permission.

exposed body and the operating frequency of the EM source. Most of the absorbed EM energies are converted into heat.

22.3.1 Electromagnetic Wave Propagation Equation

EM waves are a phenomenon in the form of self-propagating waves in a free space or in matter. EM waves consist of electric and magnetic fields oscillating in phase perpendicular to each other and to the direction of wave propagation. Maxwell's equations for electric and magnetic fields are used to investigate EM wave propagation in different media and radiation. An EM wave propagating in a linear, isotropic, homogeneous medium can basically be described by Maxwell's equations:

$$\nabla \times \bar{E} = -\frac{\partial \bar{B}}{\partial t} \tag{22.1}$$

$$\nabla \times \bar{B} = \frac{1}{c^2}\frac{\partial \bar{E}}{\partial t} \tag{22.2}$$

$$\nabla \cdot \bar{E} = 0 \tag{22.3}$$

$$\nabla \cdot \bar{B} = 0 \tag{22.4}$$

where

$\bar{E}$ is the electric field intensity (V/m)
$\bar{B}$ is the magnetic flux density (Wb/m² or T)
c is the light velocity in the medium (m/s)
$c_0 = 2.99792458 \times 108$ is the speed of light in free space

$$c = \frac{c_0}{n} \tag{22.5}$$

where n is the refractive index of the medium, $n = \sqrt{\varepsilon_r}$ and ε_r is the relative dielectric constant.

Maxwell's equations for free space are expressed by

$$\nabla \times \bar{E} = j\omega B \tag{22.6}$$

$$\nabla \times \bar{B} = \frac{-1}{c^2} j\omega \vec{E} \tag{22.7}$$

$$\nabla \cdot \bar{E} = 0 \tag{22.8}$$

$$\nabla \cdot \bar{B} = 0 \tag{22.9}$$

where
ω is the angular frequency (rad/s)
$j = \sqrt{-1}$

The general form of Maxwell's equations is simplified to demonstrate the EM fields penetrated in the eye as the following equation:

$$\nabla \times \left(\left(\varepsilon_r - \frac{j\sigma}{\omega \varepsilon_0} \right)^{-1} \nabla \times H_z \right) - \mu_r k_0^2 H_z = 0 \tag{22.10}$$

where
H is the magnetic field (A/m)
μ_r is the relative magnetic permeability
ε_r is the relative dielectric constant
$\varepsilon_0 = 8.8542 \times 10^{-12}$ F/m is the free space permittivity
k_0 is the free space wave number (1/m)

22.3.1.1 Boundary Condition for Wave Propagation Analysis

This study investigated ocular changes during exposure to EM radiation with a particular power density. A schematic description of a boundary condition is shown in Figure 22.3: the uniform wave flux falls on the left side of the eye. Therefore, for the left boundary, an EM simulator uses a TM wave propagation port with a specified power density:

$$S = \frac{\int (E - E_1) \cdot E_1}{\int E_1 \cdot E_1}. \tag{22.11}$$

Boundary conditions along the interfaces between different mediums are considered as continuity boundary conditions:

$$n \times (E_1 - E_2) = 0. \tag{22.12}$$

The outer side of the calculated domain, that is, free space, is considered as a scattering boundary condition:

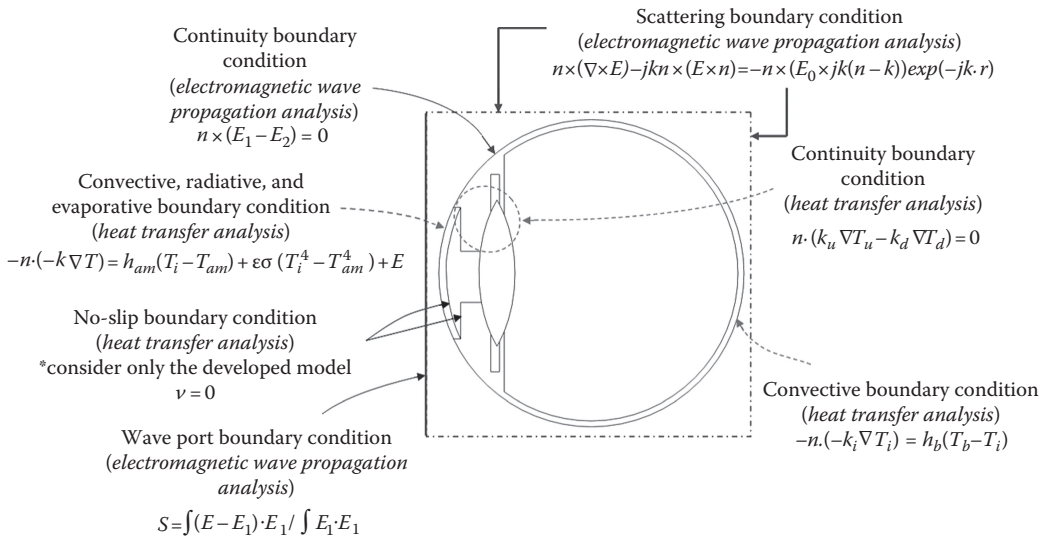

FIGURE 22.3
Boundary condition for the analysis of EM wave propagation and heat transfer. (From Wessapan, T. and Rattanadecho, P., *ASME Trans. J. Heat Transfer*, 134, 091101, 2012. With permission.)

$$n\times\left(\nabla\times E_z\right)-jkE_z=-jk(1-k\cdot n)E_{0z}\exp(-jk\cdot r) \tag{22.13}$$

where

k is the wave number (m^{-1})

AQ4 σ is the electric conductivity (S/m)

n is the normal vector

$j=\sqrt{-1}$

E_0 is the incident plane wave (V/m)

Microwave EM exposure levels are expressed in terms of power density (in W/m^2 or W/ft^2).

However, for microwave band, both the electric field intensity (in V/m) and the magnetic

AQ5 field intensity (in A/m) are used to represent the fields. According to the International Commission of Non-Ionizing Radiation Protection (ICNIRP) guidelines [6], an average SAR (in W/kg) (or whole-body average SAR) is defined as the ratio of the total absorbed power in the exposed body to its mass where the local SAR refers to the absorbed energy value per unit volume or mass, which can be arbitrarily small. The SAR is defined as

$$\text{SAR}=\frac{\sigma}{2\rho}|E|^2 \tag{22.14}$$

where

σ is the electric conductivity (S/m)

ρ is the tissue density (kg/m^3)

AQ6 $\bar{E}_i$ is the electric field intensity (V/m)

The SAR can also be determined from the increase in tissue temperature over a short period of time following the exposure as

$$\frac{\Delta T}{\Delta t} = \frac{\text{SAR}}{C} \tag{22.15}$$

where
ΔT is the temperature increase
Δt is the exposure duration
C is the specific heat

22.3.2 Heat Transfer Equation

From a macroscopic point of view, thermal effects resulting from the EM waves' absorption inside the biological tissue are expressed in terms of the bioheat equation [18,19] based on the heat diffusion equation, which can be written as

$$\rho C \frac{\partial T}{\partial t} = \nabla \cdot (k \nabla T) + \rho_b C_b \omega_b (T_b - T) + Q_{met} + Q_{ext} \tag{22.16}$$

where
ρ is the tissue density (kg/m^3)
C is the tissue heat capacity (J/(kg K))
k is the tissue thermal conductivity (W/(m K))
T is the tissue temperature (°C)
T_b is the blood temperature (°C)
ρ_b is the blood density (kg/m^3)
C_b is the blood heat capacity
ω_b is the blood perfusion rate (1/s)
Q_{met} is the metabolism heat source (W/m^3)
Q_{ext} is the external heat source (EM heat source density) (W/m^3)

$$Q_{ext} = \frac{\sigma}{2} |E|^2 \tag{22.17}$$

This study utilized two pertinent thermal models to investigate the heat transfer behavior of the eye when exposed to the EM fields.

Model I: Conventional heat transfer model [21]

This model assumes the metabolic heat generation and the blood perfusion in the eye to be zero. The governing equation therefore looked just like the classical heat conduction equation:

$$\rho_i C_i \frac{\partial T_i}{\partial t} = \nabla \cdot (k_i \nabla T_i) + Q_{ext}; \quad i = a, b, c, d, e, f \tag{22.18}$$

where
i denotes each subdomain in the eye model as shown in Figure 22.2
ρ is the tissue density (kg/m^3)
C is the tissue heat capacity (J/(kg K))
k is the tissue thermal conductivity (W/(m K))
T is the tissue temperature (K)
t is the time

Model II: Developed heat transfer model [26]

In this model, the fluid motion is considered only inside the anterior chamber [16]. There is a blood flow in the iris/sclera part, by which the blood flow plays a role to adjust the temperature of the eye [26]. For the rest of the parts, the metabolic heat generation is neglected due to the fact that these parts comprise mainly water [16]. The governing equation for the flow of heat in cornea, posterior chamber, lens, and vitreous is the same as Equation 22.18.

This model accounts for the existence of AH in the anterior chamber. The heat transfer process consists of both conduction and natural convection, which can be expressed as follows:

Continuity equation

$$\nabla \cdot u_i = 0; \quad i = b \tag{22.19}$$

Momentum equation

$$\rho_i \frac{\partial u_i}{\partial t} + \rho_i u_i \nabla \cdot u_i = -\nabla p_i + \nabla \cdot [\mu(\nabla u_i + \nabla u_i^T)] + \rho_i g \beta_i (T_i - T_{ref}); \quad i = b \tag{22.20}$$

where

β is the volume expansion coefficient (1/K)
u is the velocity (m/s)
p is the pressure (N/m^2)
μ is the dynamic viscosity of AH (N s/m^2)
T_{ref} is the reference temperature that we consider here as 37°C

The effects of buoyancy due to the temperature gradient are modeled using the Boussinesq approximation, which states that the density changes to the temperature change and the pressure perturbations are negligible [16].

AQ7 The energy equation is expressed as follows:

$$\rho_i C_i \frac{\partial T_i}{\partial t} - \nabla \cdot (k_i \nabla T_i) = -\rho C_i v_i \cdot \nabla T_i + Q_{ext}; \quad i = b. \tag{22.21}$$

The sclera/iris is modeled as a porous medium with blood perfusion, by which the local thermal equilibrium is assumed between the blood and the tissue. A modified Pennes' bioheat equation [26,38] is used to calculate the temperature distribution in the sclera/iris tissue:

$$(1-\varepsilon)\rho_i C_i \frac{\partial T_i}{\partial t} = \nabla \cdot ((1-\varepsilon) k_i \nabla T_i) + \rho_b C_b \omega_b (T_b - T_i) + Q_{ext}; \quad i = f \tag{22.22}$$

where ε is the porosity.

22.3.2.1 Boundary Condition for Heat Transfer Analysis

The heat transfer analysis excluding the surrounding space is considered only in the eye. The cornea surface as shown in Figure 22.3 is considered as the convective, radiative, and evaporative boundary condition for all of the models:

$$-n\cdot(-k\nabla T)=h_{am}(T_i-T_{am})+\varepsilon\sigma(T_i^4-T_{am}^4)+e \quad \text{on } \Gamma_1 \;\; i=a \tag{22.23}$$

where
Γ_i is the external surface area corresponding to section i
e is the tear evaporation heat loss (W/m^2)
T_{am} is the ambient temperature (K)
h_{am} is the convection coefficient (W/(m^2 K))

The blood temperature generally assumed to be the same as the body's core temperature causes heat to be transferred into the eye [16]. The surface of the sclera is assumed to be a convective boundary condition for all of the models:

$$-n\cdot(-k_i\nabla T_i)=h_b(T_b-T_i) \quad \text{on } \Gamma_2 \;\; i=f \tag{22.24}$$

where
h_b is the convection coefficient of blood
Γ_1 and Γ_2 are the corneal surface and the sclera surface of the eye, respectively.

22.3.3 Calculation Procedure

The computational scheme used in this study is applied to assemble a finite element model and compute a local heat generation. The EM calculation is carried out by using tissue properties. To obtain a good approximation, a fine mesh is specified in the sensitive areas, by which a variable mesh method for solving the problem is proposed as in Figure 22.4. The governing equations with initial and boundary conditions are then solved. The 2D model with triangular elements is used to discretize the domain, and the Lagrange quadratic is then used to approximate temperature and SAR variation across each element. To reduce the global mesh size, a mesh convergence test was performed. The mesh with approximately 10,000 elements is obtained.

22.4 Results and Discussion

In this analysis, the effect of power density (5, 10, 50, and 100 mW/cm^2) on distributions of SAR and temperature profiles in the eye is systematically investigated using two models: the conventional heat transfer model and the developed heat transfer model. The models of the EM and thermal fields are solved numerically. The dielectric and thermal properties as in Tables 22.1 and 22.2, respectively, are used for the simulation. In this study, we follow the guidelines of the ICNIRP, the radiated power used at the maximum SAR value of 2 W/kg (general public exposure) and 10 W/kg (occupational exposure) [6].

22.4.1 Verification of the Model

In order to verify the accuracy of the present numerical models, the simulated results from this study are validated against the numerical results obtained by Shafahi and Vafai [26] who studied the same geometric model as this. Moreover, the numerical results are then

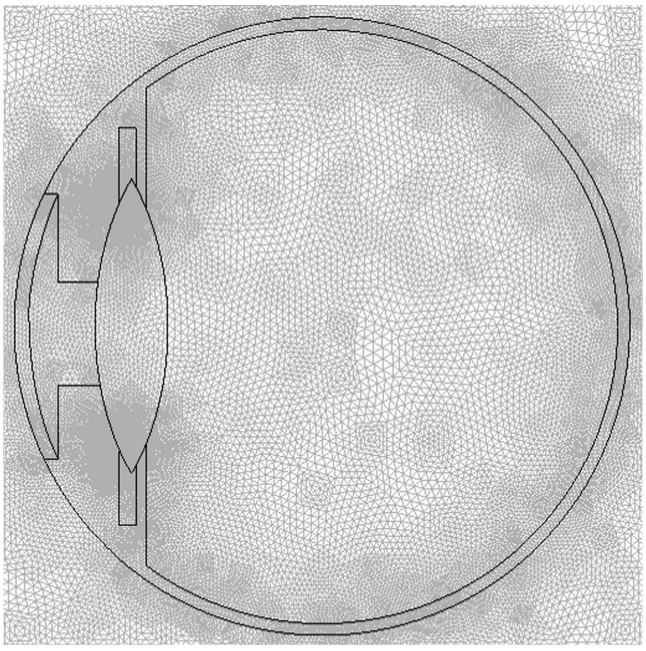

FIGURE 22.4
A 2D finite element mesh of human eye model.

compared to the experimental results of the rabbit obtained from Lagendijk [8]. The validation case assumes that the rabbit body temperature is 38.8°C, the tear evaporation heat loss is 40 W/m^2, the ambient temperature is 25°C, and the convection coefficient of ambient air is 20 W/(m^2 K). The results of the selected test case are presented in Figure 22.5 for the temperature distribution in the eye. Figure 22.5 clearly shows a good agreement of the temperature distribution in the eye between the present solution and that of Shafahi and Vafai [26] and Lagendijk [8]. In the figure, the simulated results of the conventional heat transfer model and the developed heat transfer model provides a good agreement with the simulated results obtained from Shafahi and Vafai [26]. This favorable comparison provides confidence in the results of the present numerical model.

22.4.2 Electric Field Distribution

To illustrate the penetrated electric field distribution inside the eye, the predicted results obtained from our proposed models are required.

22.4.2.1 Effect of Power Density on Electric Field Distribution

Due to the different dielectric characteristics of the various tissue layers, a different fraction of the supplied EM energy will become absorbed in each layer in the eye. Consequently, the reflection and transmission components at each layer contribute to the resonance of standing wave in the eye. Figure 22.6 shows the simulation of an electric field pattern inside the eye exposed to EM field in TM mode operating at the frequency of 900 MHz propagating along the vertical cross section of the eye model, by which the varying power densities are done. As is obvious from Figure 22.6, the higher values of the electric fields in

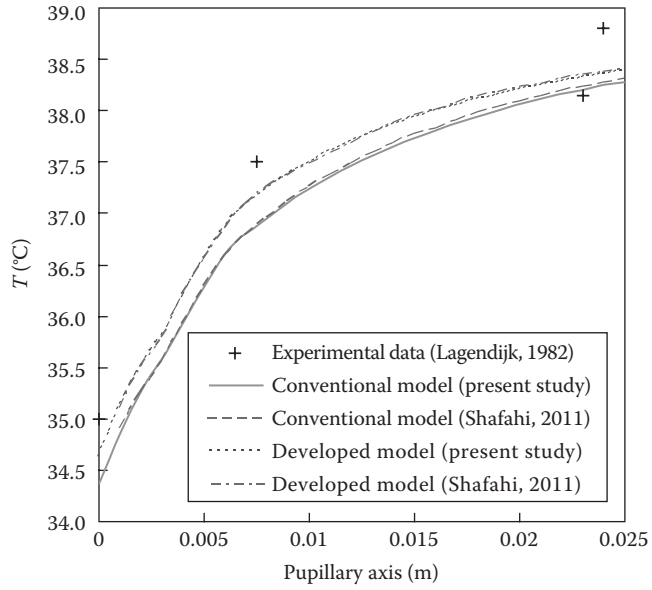

FIGURE 22.5
Comparison of the calculated temperature distribution to the temperature distribution obtained by Shafahi and Vafai and the Lagendijk's experimental data; h_{am} = 20 W/(m² K) and T_{am} = 25°C. (From Wessapan, T. and Rattanadecho, P., *ASME Trans. J. Heat Transfer*, 134, 091101, 2012. With permission.)

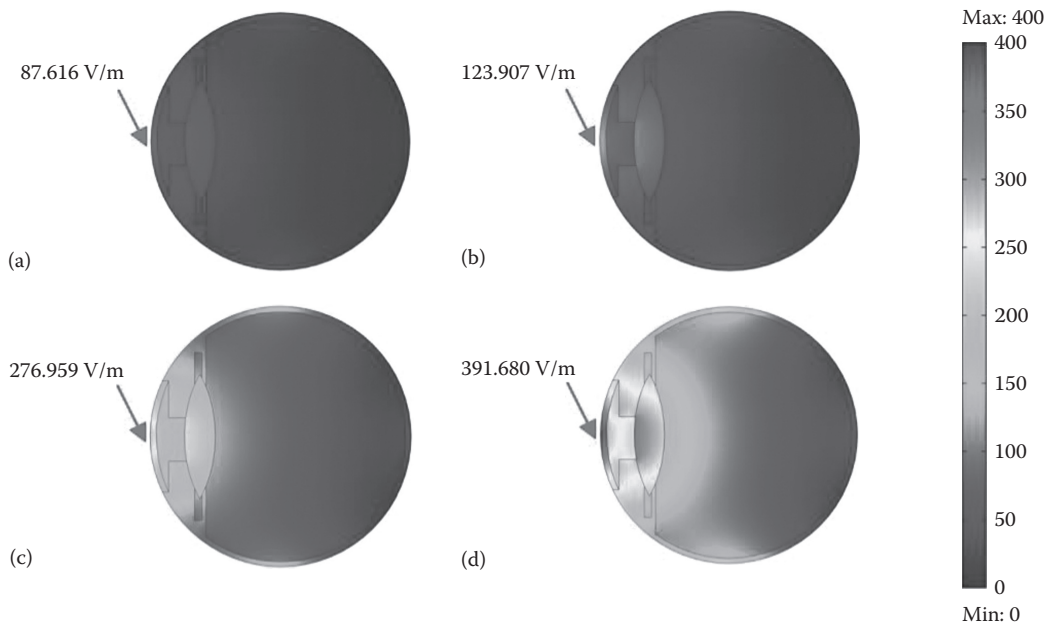

FIGURE 22.6
Electric field distribution (V/m) in human eye exposed to the EM frequency of 900 MHz at the power densities of (a) 5 mW/cm², (b) 10 mW/cm², (c) 50 mW/cm², and (d) 100 mW/cm². (From Wessapan, T. and Rattanadecho, P., *ASME Trans. J. Heat Transfer*, 134, 091101, 2012. With permission.)

all cases occur in the outer part area of the eye, especially in the cornea and lens. The three highest electric field intensity values in the eye at all power densities occur in the cornea, AQ8 lens, and iris, respectively. This is because the lower value of their dielectric properties (ε_r) shown in Table 22.1 corresponds to Equation 22.10, as well as these tissues are located close to the exposed surface, by which it causes the EM fields to penetrate easily into these tissues. The electric fields deep inside the eye are extinguished where the electric field attenuates due to the absorbed EM energy and the electric fields are then converted to heat. Moreover, the electric field distribution also showed a strong dependence on the dielectric properties of the tissue. Certainly, the maximum electric field intensity at the higher power density is greater than that of the lower power density. The maximum electric field intensities are 391.680, 276.959, 123.907, and 87.616 V/m at the power densities of 100, 50, 10, and 5 mW/cm^2, respectively.

22.4.3 SAR Distribution

22.4.3.1 Effect of Power Density on SAR Distribution

For the SAR distribution in the eye, we found that the amplitude corresponds to the electric fields. Figure 22.7 shows the SAR distribution evaluated on the vertical cross section of AQ9 the eye exposed to the EM frequency of 900 MHz at various power densities. The results of the SAR values in the eye are evident from Figure 22.7. The SAR values are increased corresponding to the electric field intensities (Figure 22.6). The maximum SAR values are 135.15, 67.575, 13.525, and 6.763 W/kg at the power densities of 100, 50, 10, and 5 mW/cm^2, respectively. Comparing to the maximum SAR value of 2 W/kg (general public exposure)

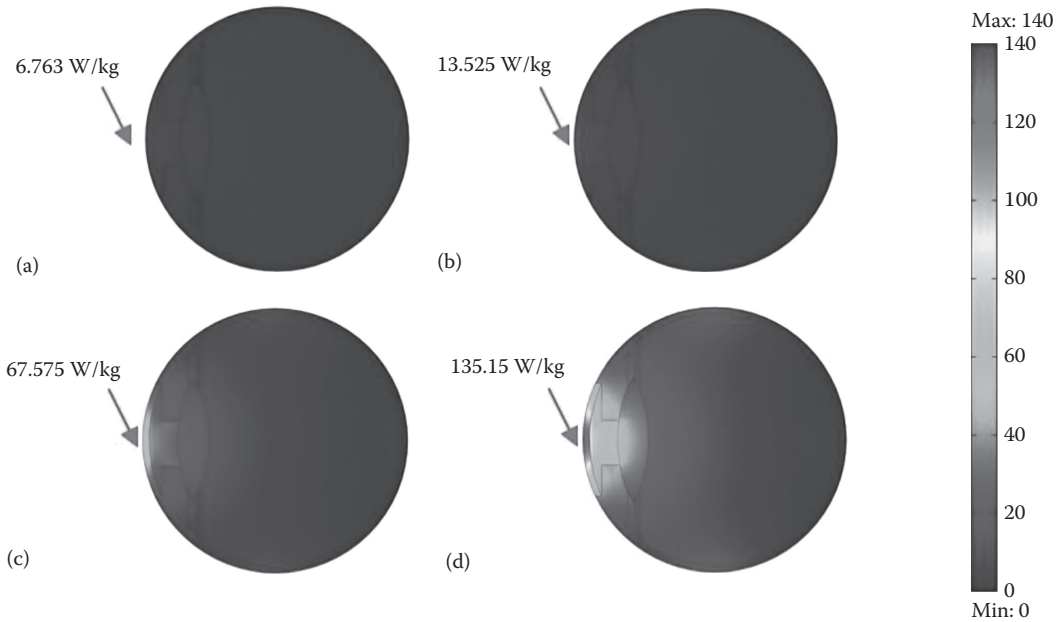

FIGURE 22.7
SAR distribution (W/kg) in human eye exposed to the EM frequency of 900 MHz at the power densities of (a) 5 mW/cm^2, (b) 10 mW/cm^2, (c) 50 mW/cm^2, and (d) 100 mW/cm^2. (From Wessapan, T. and Rattanadecho, P., *ASME Trans. J. Heat Transfer*, 134, 091101, 2012. With permission.)

and 10 W/kg (occupational exposure) [6], the resulting SAR values from this study are higher than the ICNIRP exposure guidelines for occupational exposure in most cases except for the power density of 5 mW/cm^2. Besides the electric field intensity, the magnitude of dielectric and thermal properties in each tissue will directly affect the amount of SAR in the eye. For all power densities, the highest SAR values are obtained only in the region of the cornea, but not in lens and iris as electric field distributions. This is because the cornea has a much higher value of its dielectric properties (σ) than those of the lens and iris, as well as the cornea located close to the exposed surface, at which the electric field intensity is strongest. It is found that the SAR distribution pattern in the eye, which corresponds to Equation 22.14, strongly depends on the effect of the dielectric properties (σ, shown in Table 22.1) and thermal properties (ρ, shown in Table 22.2). With penetration into the eye, the SAR values decrease rapidly along the distance from the EM source.

22.4.4 Temperature Distribution

In order to study the heat transfer in the eye, the coupled effects of the EM wave propagation, the unsteady heat transfer, and the initial and boundary conditions are then investigated. Due to these effects, the electric field distribution (see Figure 22.6) and the SAR distribution (see Figure 22.7) are then converted into heat by absorption of the tissue.

22.4.4.1 Effect of Heat Transfer Model on Temperature Distribution

Since this study has focused on the volumetric heating effect into the multilayer tissues of the eye induced by EM fields, the effect of ambient temperature variation has been neglected in order to gain insight into the interaction between the EM fields and the human tissue as well as the correlation between the SAR and the heat transfer mechanism. For this reason, the ambient temperature has been set to the human body temperature of 37°C, and the tear evaporation has been neglected. Moreover, the effect of thermoregulation mechanisms has also been neglected due to the small temperature increase occurred during exposure process. The convective coefficient due to blood flow inside the sclera is set to 65 W/m^2 K [16].

For the eye exposed to the EM fields for a period of time, the temperature in the eye (Figure 22.8) is increased corresponding to the SAR (Figure 22.7). This is because the electric fields in the eye attenuate owing to the energy absorbed and thereafter the absorbed energy is converted to the thermal energy, which increases the eye temperature. Figure 22.8 shows the temperature distribution in the vertical cross section of the eye at various times exposed to the EM frequency of 900 MHz at the power density of 100 mW/cm^2 calculated using the conventional heat transfer model (Model I) (Figure 22.8a) and developed heat transfer model (Model II) (Figure 22.8b).

It is found that by using the different heat transfer models, the distribution patterns of temperature at a particular time are quite different. The hot spot zone is strongly displayed at 10 min for both heat transfer models at the anterior chamber area, owing to the extensive penetration of EM power of internal regions and higher dielectric properties (ε_r) of the anterior chamber tissue. This higher dielectric property of the anterior chamber represents the stronger absorption ability of EM fields than those of the cornea and lens. The outer corneal surface has a lower temperature than that of the anterior chamber, even if it has higher SAR value (Figure 22.7). This is because heat is dissipated to the ambient via convection and radiation since the main heat transfer mechanism of the conventional heat transfer model is the thermal conduction of the eye, whereas the developed heat transfer AQ10

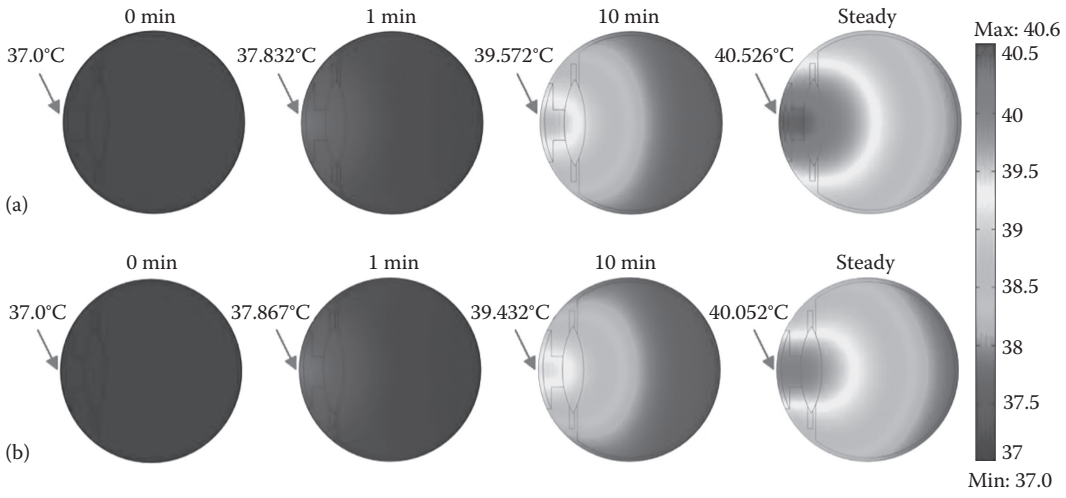

FIGURE 22.8
The temperature distribution in the human eye at various times exposed to the EM frequency of 900 MHz at the power density of 100 mW/cm^2 calculated using (a) the conventional heat transfer model and (b) the developed heat transfer model. (From Wessapan, T. and Rattanadecho, P., *ASME Trans. J. Heat Transfer*, 134, 091101, 2012. With permission.)

model accounts for the natural convection in the anterior chamber as well. Therefore, the developed heat transfer model with higher dissipation rates of heat generated by EM fields can obtain higher cooling effect than that of the conventional heat transfer model.

Consider the temperature increase distribution at the extrusion line (Figure 22.9). Figure 22.10 shows the temperature increase versus papillary axis (along the extrusion line) of the eye exposed to the EM frequency of 900 MHz at various times. In the early stage of

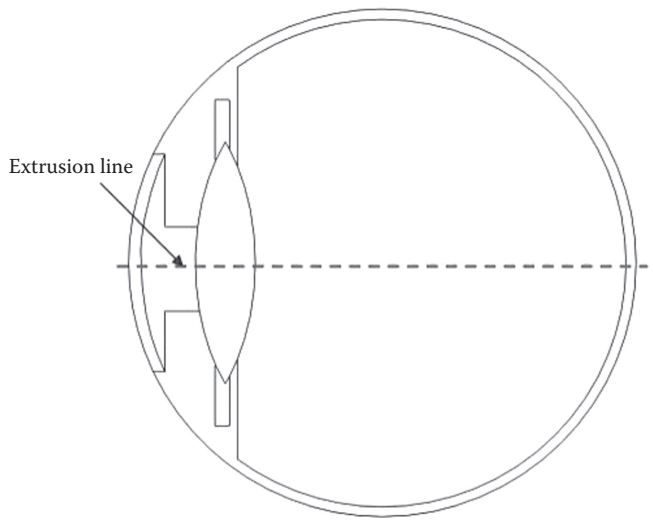

FIGURE 22.9
The extrusion line in the human eye where the temperature distribution is considered. (From Wessapan, T. and Rattanadecho, P., *ASME Trans. J. Heat Transfer*, 134, 091101, 2012. With permission.)

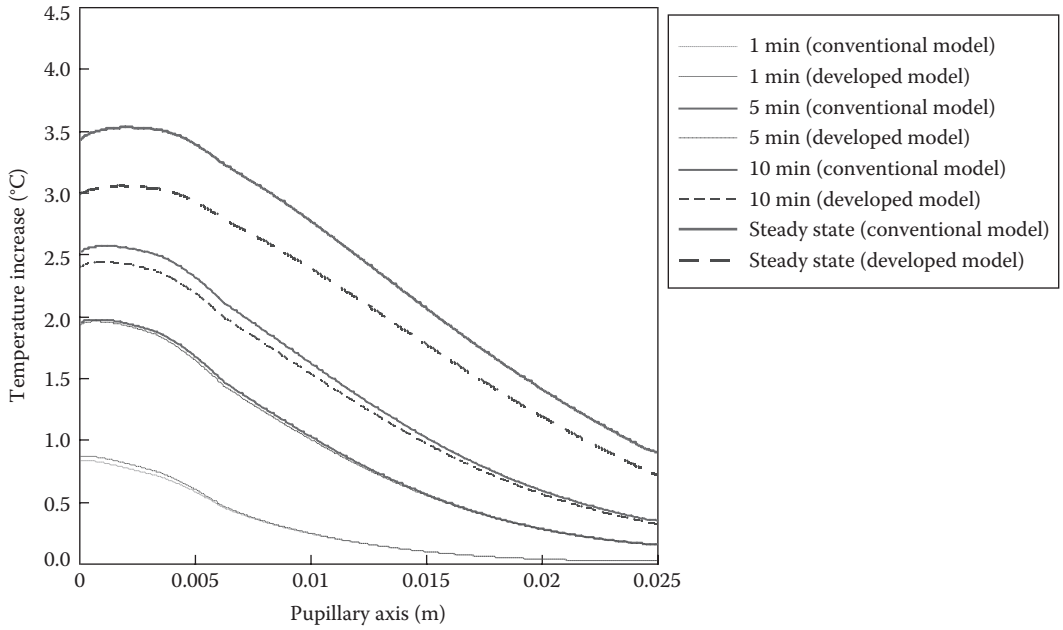

FIGURE 22.10
Temperature increase versus papillary axis of the human eye exposed to the EM frequency of 900 MHz at various times. (From Wessapan, T. and Rattanadecho, P., *ASME Trans. J. Heat Transfer*, 134, 091101, 2012. With permission.)

exposure (1 min), the calculated temperature in the anterior chamber, obtained from the conventional heat transfer model, is little lower than that of developed heat transfer model. This is because natural convection in the developed heat transfer model causes a substantial accumulation of warmer fluid in the upper half of the anterior chamber. Surprisingly, just after 10 min of exposure, the temperature increase of the conventional heat transfer model is higher than that of developed heat transfer model. This is due to the presence of blood perfusion in the iris/sclera tissue, which covers an internal surface area of the eye. This blood perfusion provides buffer characteristic to the eye temperature, which is expected to occur in the realistic physiological conditions. Moreover, the natural convection and formation of two circulatory patterns with opposite direction in the anterior chamber, shown in Figure 22.11, play the important roles on the cooling processes in the eye, especially inner corneal surface, when a large temperature gradient is produced by EM fields after 10 min. The circulation pattern implies that the generated heat in the anterior chamber is convected in two directions: one is to the corneal surface and the other is to the lens surface.

22.4.4.2 Effect of Power Density on Temperature Distribution

In addition, each power density level is applied to investigate the effects of power density (the power irradiated on the eye surface). Figure 22.12 shows the comparison of the temperature distribution in the eye at time approaching to steady-state condition with the frequency of 900 MHz corresponding to the power densities of 5, 10, 50, and 100 mW/cm^2. It is found that the power densities significantly influence the temperature increase in the eye.

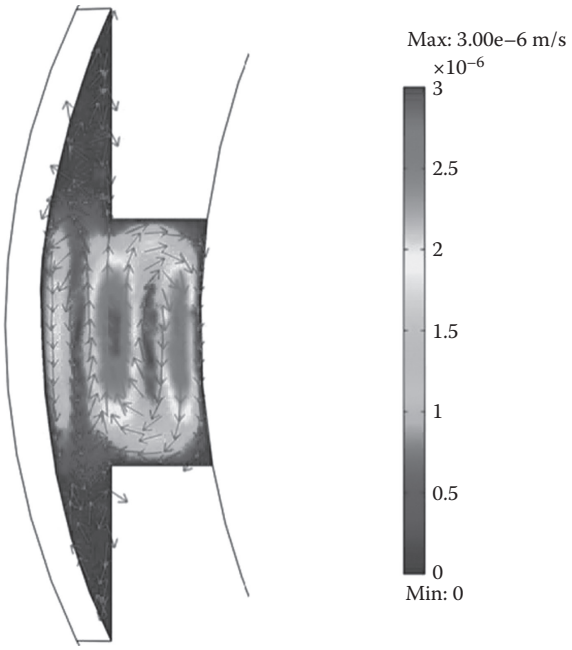

FIGURE 22.11
The velocity distribution inside the anterior chamber in the human eye when exposed to the EM frequency of 900 MHz. (From Wessapan, T. and Rattanadecho, P., *ASME Trans. J. Heat Transfer*, 134, 091101, 2012. With permission.)

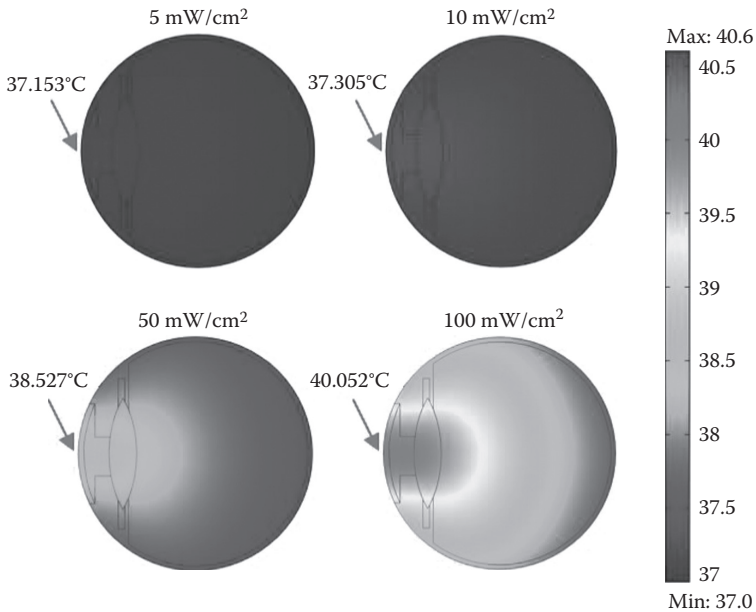

FIGURE 22.12
The temperature distribution in the eye exposed to the EM frequency of 900 MHz at various power densities calculated using (a) the conventional heat transfer model and (b) the developed heat transfer model. (From Wessapan, T. and Rattanadecho, P., *ASME Trans. J. Heat Transfer*, 134, 091101, 2012. With permission.)

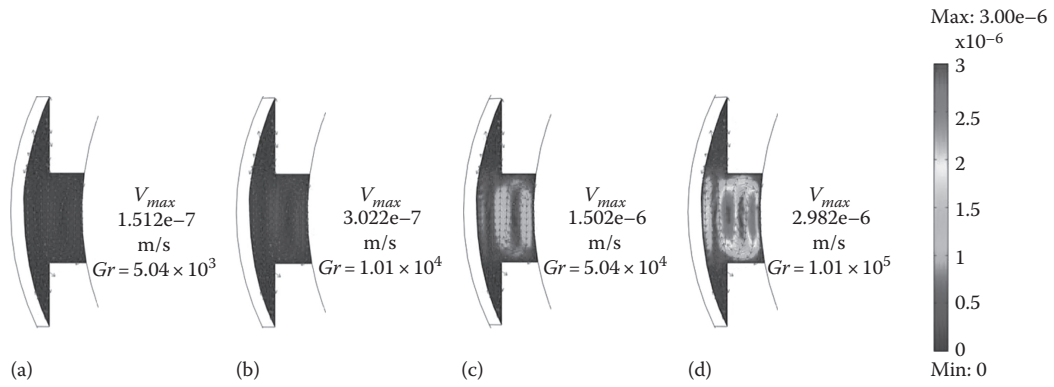

FIGURE 22.13
The velocity distribution inside the anterior chamber in the eye exposed to the EM frequency of 900 MHz at the power densities of (a) 5 mW/cm^2, (b) 10 mW/cm^2, (c) 50 mW/cm^2, and (d) 100 mW/cm^2. (From Wessapan, T. and Rattanadecho, P., *ASME Trans. J. Heat Transfer*, 134, 091101, 2012. With permission.)

Greater power density provides greater heat generation inside the eye, thereby increasing the rate of temperature rise. By using the developed heat transfer model, the maximum temperature increases are 0.153°C, 0.305°C, 1.527°C, and 3.052°C at the power densities of 5, 10, 50, and 100 mW/cm^2, respectively.

Figure 22.13 shows the circulatory patterns in the anterior chamber in the eye exposed to the EM frequency of 900 MHz at various power densities. These circulatory patterns in the anterior chamber vary corresponding to the power densities that produced the temperature gradient in the eye. Therefore, in the case of a lower power density, the circulatory patterns have a lower speed, where a circulatory pattern with a higher power density flows faster. At the lower power density with low flow speed, the heat transfer in the anterior chamber occurs mainly by conduction across the fluid layer. In the case of the higher power density with higher flow speed, different flow regimes are encountered, with a progressively increasing heat transfer. The fluid motion within the anterior chamber is driven by the power density that is associated with the Grashof number Gr. The Grashof number is defined as $Gr = g\beta qD^5/(kv^2)$, in which D is the eye diameter (m), q is the internal power density (W/m^2), and v is the kinematic viscosity (m^2/s). The range of Grashof numbers investigated is 5.04×10^3 to 1.01×10^5 as shown in Figure 22.13.

22.4.5 Concluding Remarks

This study presents the numerical simulation of the SAR and temperature distributions in the eye exposed to TM mode of EM fields. The results of the SAR values in this study are increased corresponding to the electric field intensities. Besides the electric field intensity, the magnitude of dielectric and thermal properties in each tissue will directly affect the amount of SAR in the eye.

In this study, it is found that the highest level of SAR value is the cornea, while the highest temperature is the anterior chamber. In different heat transfer models, the temperature results obtained from a developed heat transfer model, considered natural convection and porous media theory, are compared to the results obtained from a conventional heat transfer model in order to highlight the advantages and the weakness of each model. It is found that by using the different heat transfer models, the distribution patterns of temperature

at a particular time are quite different. In all cases, the temperatures obtained from the developed heat transfer model have a lower temperature than that of the conventional heat transfer model. This is due to the presence of blood perfusion that provides buffer characteristic to the eye temperature, as well as the natural convection in the anterior chamber. It is found that greater power density results in a greater heat generation inside the eye, thereby increasing the rate of temperature increase. Moreover, it is found that the temperature distributions in the eye induced by EM fields are not directly related to the SAR distribution due to the effect of dielectric properties, thermal properties, blood perfusion, and penetration depth of the EM power.

The numerical simulations in this study show several important features of the energy absorption in the eye. This information can be used as a guideline for limiting human eye exposure from EM wave radiation.

References

1. Emery, A. F., Kramar, P., Guy, A. W., and Lin, J. C. 1975. Microwave induced temperature rises in rabbit eyes in cataract research. *J. Heat Transfer—T ASME* 97:123–128.
2. Buccella, C., Santis, V. D., and Feliaiani, M. 2007. Prediction of temperature increase in human eyes due to RF sources. *IEEE Trans. Electromagn. Compat.* 49:825–833.
3. Lin, J. C., 2003. Cataracts and cell-phone radiation. *IEEE Ant. Prop. Magazine* 45:171–174.
4. Fujiwara, O. and Kato, A. 1994. Computation of SAR inside eyeball for 1.5-GHz microwave exposure using finite-difference time domain technique. *IEICE Trans.* E77-B:732–737.
5. Gandhi, O. P., Lazzi, G., and Furse, C. M. 1996. Electromagnetic absorption in the human head and neck for mobile telephones at 835 and 1900 MHz. *IEEE Trans. Microw. Theory Tech.* 44:1884–1897.
6. International Commission on Non-Ionizing Radiation Protection (ICNIRP). 1998. Guidelines for limiting exposure to time-varying electric, magnetic and electromagnetic fields (up to 300 GHz). *Health Phys.* 74:494–522.
7. IEEE. 1999. IEEE standard for safety levels with respect to human exposure to radio frequency electromagnetic fields, 3 kHz to 300 GHz. IEEE Standard C95.1-1999.
8. Lagendijk, J. J. W. 1982. A mathematical model to calculate temperature distribution in human and rabbit eye during hyperthermic treatment. *Phys. Med. Biol.* 27:1301–1311.
9. Scott, J. 1988. A finite element model of heat transport in the human eye. *Phys. Med. Biol.* 33:227–241.
10. Scott, J. 1988. The computation of temperature rises in the human eye induced by infrared radiation. *Phys. Med. Biol.* 33:243–257.
11. Amara, E. H. 1995. Numerical investigations on thermal effects of Laser–Ocular media interaction. *Int. J. Heat Mass Transfer* 38:2479–2488.
12. Hirata, A., Matsuyama, S., and Shiozawa, T. 2000. Temperature rises in the human eye exposed to EM waves in the frequency range 0.6–6 GHz. *IEEE Trans. Electromagn. Compat.* 42:386–393.
13. Chua, K. J., Ho, J. C., Chou, S. K., and Islam, M. R. 2005. On the study of the temperature distribution within a human eye subjected to a laser source. *Int. Commun. Heat Mass Transfer* 32:1057–1065.
14. Limtrakarn, W., Reepolmaha, S., and Dechaumphai, P. 2010. Transient temperature distribution on the corneal endothelium during ophthalmic phacoemulsification: A numerical simulation using the nodeless variable element. *Asian Biomed.* 4:885–892.
15. Kumar, S., Acharya, S., Beuerman, R., and Palkama, A. 2006. Numerical solution of ocular fluid dynamics in a rabbit eye: Parametric effects. *Ann. Biomed. Eng.* 34:530–544.

16. Ooi, E. and Ng, E. Y. K. 2008. Simulation of aqueous humor hydrodynamics in human eye heat transfer. *Comput. Biol. Med.* 38:252–262.
17. Ooi, E. H. and Ng, E. Y. K. 2011. Effects of natural convection inside the anterior chamber. *Int. J. Numer. Methods Biomed. Eng.* 27: 408–423.
18. Pennes, H. H. 1948. Analysis of tissue and arterial blood temperatures in the resting human forearm. *J. Appl. Physiol.* 1:93–122.
19. Pennes, H. H. 1998. Analysis of tissue and arterial blood temperatures in the resting human forearm. *J. Appl. Physiol.* 85:5–34.
20. Flyckt, V. M. M., Raaymakers, B. W., and Lagendijk, J. J. W. 2006. Modeling the impact of blood flow on the temperature distribution in the human eye and the orbit: Fixed heat transfer coefficients versus the pennes bioheat model versus discrete blood vessels. *Phys. Med. Biol.* 51:5007–5021.
21. Ng, E. Y. K. and Ooi, E. H. 2006. FEM simulation of the eye structure with bioheat analysis. *Comput. Methods Programs Biomed.* 82:268–276.
22. Ooi, E. H. and Ng, E. Y. K. 2006. Ocular temperature distribution: A mathematical perspective. *J. Mech. Med. Biol.* 9:199–227.
23. Nakayama, A. and Kuwahara, F. 2008. A general bioheat transfer model based on the theory of porous media. *Int. J. Heat Mass Transfer* 51:3190–3199.
24. Mahjoob, S. and Vafai, K. 2009. Analytical characterization of heat transfer through biological media incorporating hyperthermia treatment. *Int. J. Heat Mass Transfer* 52:1608–1618.
25. Khanafer, K. and Vafai, K. 2009. Synthesis of mathematical models representing bioheat transport. In *Advances in Numerical Heat Transfer*, eds. W. J. Minkowycz, E. M. Sparrow, and J. P. Abraham, pp. 1–28. London, U.K.: Taylor & Francis.
26. Shafahi, M. and Vafai, K. 2011. Human eye response to thermal disturbances. *J. Heat Transfer—T ASME* 133:011009.
27. Narasimhan, A. and Vishnampet, R. 2012. Effect of choroidal blood flow on transscleral retinal drug delivery using a porous medium model. *Int. J. Heat Mass Transfer* 55:5665–5672.
28. KumarJha, K. and Narasimhan, A. 2011. Three-dimensional bio-heat transfer simulation of sequential and simultaneous retinal laser irradiation. *Int. J. Thermal Sci.* 50:1191–1198.
29. Narasimhan, A. and Sadasivam, S. 2013. Non-Fourier bio heat transfer modelling of thermal damage during retinal laser irradiation. *Int. J. Heat Mass Transfer* 60:591–597.
30. Ooi, E. H., Ang, W. T., and Ng, E. Y. K. 2008. A boundary element model of the human eye undergoing laser thermokeratoplasty. *Comput. Biol. Med.* 28:727–738.
31. Ooi, E. H., Ang, W. T., and Ng, E. Y. K. 2008. A boundary element model for investigating the effects of eye tumor on the temperature distribution inside the human eye. *Comput. Biol. Med.* 39:667–677.
32. Tan, J. H., Ng, E. Y. K., and Acharya, U. R. 2011. Evaluation of topographical variation in ocular surface temperature by functional infrared thermography. *Infrared Phys. Technol.* 54:469–477.
33. Tan, J. H., Ng, E. Y. K., and Acharya, U. R. 2010. Evaluation of tear evaporation from ocular surface by functional infrared thermography. *Med. Phys.* 37:6022–6034.
34. Tan, J. H., Ng, E. Y. K., Acharya, U. R., and Chee, C. Study of normal ocular thermogram using textural parameters. *Infrared Phys. Technol.* 53:120–126.
35. Wessapan, T. and Rattanadecho, P. Specific absorption rate and temperature increase in human eye subjected to electromagnetic fields at 900 MHz. *ASME Trans. J. Heat Transfer* 134:091101.
36. Bernardi, P., Cavagnaro, M., Pisa, S., and Piuzzi, E. 2000. Specific absorption rate and temperature increases in the head of a cellular-phone user. *IEEE Trans. Microw. Theory Tech.* 48:1118–1126.
37. Park, S., Jeong, J., and Lim, Y. 2004. Temperature rise in the human head and brain for portable handsets at 900 and 1800 MHz. *4th International Conference on Microwave and Millimeter Wave Technology*, *ICMMT 2004*, Beijing, China. AQ11
38. Nakayama, A. and Kuwahara, F. 2008. A general bioheat transfer model based on the theory of porous media. *Int. J. Heat Mass Transfer* 51:3190–3199.

AUTHOR QUERIES

[AQ1] Please check if edit to the sentence starting "Since the eye..." is okay.
[AQ2] Please check if edit to the sentence starting "For example, in…" is okay.
[AQ3] Please check the caption of Figures 22.1 through 22.13 for correctness.
[AQ4] "σ" is not provided in Equation 22.13. Please check.
[AQ5] Please check if edit to the sentence starting "According to the..." is okay.
[AQ6] "$\bar{E}_i$" is not mentioned in Equation 22.14. Please check.
[AQ7] Please check if edit to the sentence starting "The energy equation..." is okay.
[AQ8] Please check if edit to the sentence starting "This is because…" is okay.
[AQ9] Please check if edit to the sentence starting "The results of…" is okay.
[AQ10] Please check if edit to the sentence starting "This is because..." is okay.
[AQ11] Please check the conference title and location for Ref. [37].

FIRI DIPLOMA

PRESENTED TO

Thammasat University

P. Wongchadakul, P. Rattanadecho, T. Wessapan

FIRI AWARD FOR THE BEST INVENTION

Computer Simulation Based on FEM of Laser-induced Thermotherapy in Human Layered Skin-Tissue

44th International Exhibition of Inventions of Geneva

April 13 - 17 , 2016. Geneva, Switzerland

Hossein Vaezi Ashtiani

Head of International Relations

First Institute Researchers and Inventors in Iran (FIRI)

DIPLÔME

Inventions Geneva

SALON INTERNATIONAL DES INVENTIONS

GENÈVE

Après examen, le Jury International a décidé

de remettre à: P. Rattanadecho, P. Keangin and P. Wongchadakul

pour l'invention: Traitement du cancer du foie, utilisant une antenne coaxiale à micro-ondes

MÉDAILLE D'ARGENT
SILVER MEDAL
SILBERMEDAILLE

Genève, le 15 avril 2016

Le Président du Jury: David Taji

Le Président du Salon: Jean-Luc Vincent

(10)

DIPLÔME

Inventions Geneva

SALON INTERNATIONAL DES INVENTIONS

GENÈVE

Après examen, le Jury International a décidé

de remettre à: P. Wongchadakul, P. Rattanadecho and T. Wessapan

pour l'invention: Simulation informatique d'un modèle de transfert de la bio-chaleur transitoire

MÉDAILLE DE BRONZE
BRONZE MEDAL
BRONZEMEDAILLE

Genève, le 15 avril 2016

Le Président du Jury: David Taji

Le Président du Salon: Jean-Luc Vincent